CO_2 Capture by Aqueous Absorption

Summary of Third Quarterly Progress Reports 2014

by Gary T. Rochelle

Supported by the Texas Carbon Management Program

and the

Industrial Associates Program for CO_2 Capture by Aqueous Absorption

McKetta Department of Chemical Engineering

The University of Texas at Austin

October 31, 2014

Introduction

This research program is focused on the technical obstacles to the deployment of CO_2 capture from flue gas by alkanolamine absorption/stripping. The objective is to develop and demonstrate evolutionary improvements to monoethanolamine (MEA) absorption/stripping for CO_2 capture from gas-fired and coal-fired flue gas. The Texas Carbon Management Program and the Industrial Associates Program for CO_2 Capture by Aqueous Absorption support 17 graduate students. Most of these students have prepared detailed quarterly progress reports for the period July 1 to September, 2014.

Conclusions

Thermodynamics and Rates

The secondary amine solvent 7 m DEA has competitive CO_2 absorption rates compared to 7 m MEA. The measured CO_2 liquid film mass transfer coefficient (k_g') at coal flue gas conditions is about 10% higher than 7 m MEA. DEA has double the intrinsic capacity of MEA. The CO_2-carrying capacity of 7 m DEA is 60% higher than 7 m MEA and other primary unhindered amine solvents. The heat of absorption of CO_2 for 7 m DEA is estimated to be lower than or about the same as 7 m MEA.

Modeling

- As the CO_2 rich loading varies from 0.37 to 0.43 in 5 m PZ, the optimum lean loading occurs at a loading difference of 0.14 mol/equivalent PZ CO_2. The minimum total equivalent work decreases from 36.2 kJ/mol CO_2 to 30.7 kJ/mol,
- The Second Law efficiency of the advanced flash stripper varies from 45 to 70% as the delta loading varies from 0.06 to 0.22. At the optimum delta loading of 0.14 the efficiency is 65%.
- The energy cost of using MDEA/PZ is lower than using 5 m PZ. For Case 19, equivalent work using 5 m MDEA/5 m PZ (32.41 kJ/mol CO_2) is less than using 5 m PZ (33.24 kJ/mol CO_2).

- Adding reflux and purge can separate ammonia from the amine scrubbing system efficiently. As reflux ratio increases from 0.8 to 1, the mole fraction of NH_3 in the purge increases from 0.160 to 0.347. The normalized amount of NH_3 in purge has a peak value (0.0118 mole NH_3/mole CO_2 removed) at 30.5 kg purge/ton CO_2 removed.
- The k_g' of CO_2 absorption into glycerol/water/NaOH was measured by the WWC with μ_L from 0.9–60 cP. The k_g' was found to initially increase about 25% when glycerol increases to 10 wt % because of the catalytic effect of glycerol, and then decrease about 75% when glycerol increases to 89 wt % because of the impeding effect of elevated μ_L on mass transfer.
- The amine scrubbing process has a fast time scale associated with large recycle flow rates and a slow time scale associated with small feed and product flow rates. The linear system model is ill-conditioned. An effective control strategy should take into consideration the different time scales that occur in the process.
- The pressure drop in dry structured packing increases steadily with gas flow rate (F-factor) to the power of 1.6–1.9. The pressure drop increases by 30% from dry condition to a liquid load of 5 gpm/ft^2 (12 m^3/m^2*h), and increases slightly with increasing liquid flow rate.
- The effective mass transfer area increases with liquid velocity to the 0.15 power and is essentially independent of gas velocity. The fractional effective area decreases as packing surface area increases because of the inefficient wetting in the higher specific surface area packings. Rivulets, ripples, and droplets also provide additional mass transfer area in lower specific surface area packings. The effective mass transfer area is not a function of packing corrugation angle.
- The liquid film mass transfer coefficient (k_L) is a function of liquid velocity and independent of gas velocity. The gas film mass transfer coefficient (k_G) is a function of gas velocity and independent of liquid velocity. The k_L increases with liquid velocity (u_L) to the power of 0.5–0.77 for all packings in this work. The k_G increases with liquid velocity (u_G) to the power of 0.43–0.76 for all packings in this work. Summaries of k_L and k_G are given in Figures 4.27 and 4.28.
- With high inlet CO_2, compared to 5 m PZ, 5 m MDEA/5 m PZ results in twice the delta loading and half of the lean solvent flow rate due to the high CO_2 capacity, but results in more than twice the amount of absorber packing due to low absorption rate. Compared to 5 m PZ, absorber costs increase by 50% and advanced flash stripper costs decrease by 47%. The total equipment costs go down by 13%.

Solvent Management

- PZ-activated tertiary morpholines were found to be the most stable solvent class, with T_{MAX} values greater than 150 °C.
- PZ-activated acyclic tertiary amines without methyl groups were of an intermediate stability, with T_{MAX} values between 130 and 140 °C.
- PZ-activated acyclic tertiary amines with at least one methyl group were stable below 130 °C.
- Acyclic PZ-activated hindered amines had T_{max} from 128 °C to 147 °C, with the least stable acyclic hindered amines having the greatest number of hydroxyl groups.
- Cyclic PZ-activated hindered amines had T_{max} below 130 °C.

- Increasing amine chain length between the amino function and the end amino or hydroxyl function of linear amines decreased the initial rate of thermal degradation and increased the activation energy of thermal degradation.
- Ethylenediamine was found to be the most corrosive amine tested, and propylenediamine was the least corrosive.
- Propylenediamine and monopropanolamine were found to be oxidatively stable and did not show any appreciable oxidative degradation.
- Ammonia production, and by proxy amine oxidation, increased along with the accumulation of stainless steel metals in solution with 4 m PZ in the HTOR.
- Ethylenediamine was the most significant oxidation product observed to accumulate in the PZ solvent during the HTOR experiment. It appeared to be reaching a steady state of 35 mmol/kg by the end of the run. 0.24 moles of total formate were produced per mole of ammonia emitted during the HTOR experiment. N-methyl-piperazine was also observed at a similar concentration to total formate.
- Removal of dissolved oxygen with N_2 sparging in a bubble column before the high temperature section of the HTOR reduced the ammonia rate by 20%.
- In samples received from a pilot plant campaign conducted at NCCC in June using 7 m MEA, HEGly was the most significant degradation product quantified, at a concentration in excess of 1 wt % by the end of the campaign. Organic heat stable salts, chiefly formate, acetate, and oxalate, were observed in similarly high concentrations. No significant accumulation of thermal degradation products or nitrosamines was observed.
- Reclaimer waste from a pilot-scale vacuum reclaimer contained 2 to 3 moles of MEA per mole of heat stable salt. MEA recovery decreased as the concentration of contaminants in the solvent feed was increased. No significant contaminants were observed in the reclaimed MEA product stream.

NO_2 absorption in sulfite

- An uninhibited sulfite system is not effective for NO_2 absorption. The ratio of SO_3^{2-} oxidized/NO_2 absorbed is on the order of 1000.
- Thiosulfate drastically reduces sulfite oxidation; addition of 0.1M $S_2O_3^{2-}$ reduced $k_{1\ obs}$ by a factor of 33.
- Increasing sulfite does not affect $k_{1\ obs}$, but produces a first-order correlation between SO_3^{2-} oxidized/NO_2 absorbed and sulfite.
- Sulfite oxidation is half order in NO_2 and is removed more efficiently at higher partial pressures (SO_3^{2-} oxidized/NO_2 absorbed is inverse half order with NO_2).
- Iron and other metals can catalyze oxidation, but NO_2 catalysis is dominant.
- EDTA or a similar chelating agent should be added to chelate the metal ions; 0.01 mM Fe^{2+} has $k_{1\ obs}$ and SO_3^{2-} oxidized/NO_2 absorbed 2.8 times greater than 0.02 mM EDTA.
- Sulfite oxidation rates follow the Arrhenius law with an apparent activation energy of 24.1 kJ/mol.
- Oxygen concentrations do not have an effect on the oxidation rate until below roughly 5 kPa O_2.

NO_x Absorption Kinetics

- NO_x absorption at ppm levels of NO_x is dominated by the free radical absorption of NO_2.

- Free radical absorption of NO_2 is first order in NO_2 partial pressure and half order in free amine concentration.
- Absorption can be modeled as mass transfer with fast reaction in the pseudo-first-order regime.
- NO_2 absorption kinetics are fastest with tertiary amines and slowest with primary amines similar to ClO_2 free radical absorption into amines.
- 70–99% of NO_2 will absorb in amine scrubbers designed to capture 90% of CO_2; only 4% of NO_2 absorption can be attributed to hydrolysis.
- A prescrubber with an A/G of $1*10^6$ $s \cdot Pa \cdot m^2/mol$ can scrub 90% of flue gas NO_2 with 0.17 m free MDEA.
- MDEA oxidation is not catalyzed by NO_2 absorption in the presence of air and stainless steel metals.

NO_x Absorption Products

- 10 ppm of NO_2 absorbs into 0.1 m MDEA with a 95% nitrite yield and a 5% nitrate yield.
- Nitrite yield is independent of NO and oxygen, proving that the absorption species is NO_2 directly instead of N_2O_3.
- NO_2 hydrolysis through N_2O_4 becomes the dominating absorption mechanism when NO_2 partial pressure is above 10 Pa (100 ppm at atmospheric pressure).
- Nitrosamine is less than 3% of total absorption product in 0.1 m MDEA.
- NO can be directly absorbed into amine solution by reacting with the free radical formed by NO_2 absorption.
- In PZ solution, NO absorption forms MNPZ with yields of 20–35% of total absorbed NO_x at 20 °C.
- PZ free radicals can also react with themselves or free radical scavengers to lower the yield to MNPZ.
- MNPZ yield is independent of amine concentration and loading, but yield increases as the ratio of NO_2:NO_x decreases.
- PZ free radicals can also react with themselves or with free radical scavengers to lower the MNPZ yield.
- Increasing absorption temperature from 20 °C to 60 °C decreases MNPZ yield by 60% due to the decreased solubility of NO.
- MNPZ yield at 40 °C in 5 m PZ with an NO_2:NO_x ratio of 1:10 is 17% with nitrite closing the mole balance.
- High temperature nitrosation from nitrite is the dominating mechanism for nitrosamine formation in amine scrubbing.

From neat 4 m PZ, Amberlite 748i showed high removal of Ni and Mn at 81% and 71% respectively. The resin showed moderate removal of Fe and Cr, at 47% and 36%. Breakthrough of metals was not reached at 16 bed volumes of solvent. The initial concentrations of metals were Cr: 0.10 mM, Fe: 0.09 mM, Mn: 0.12 mM, and Ni: 0.14 mM.

From neat 4 m MEA, Amberlite 748i showed high removal of Ni and Mn at 88% and 94% respectively. In addition, the resin showed moderate removal of Fe, at 40%. Breakthrough of metals was not reached by about 14 bed volumes of amine. The initial concentrations of metals were Cr: 0.20 mM, Fe: 0.22 mM, Mn: 0.21 mM, and Ni: 0.21 mM.

From PP2 PZ, Amberlite 748i showed complete Ca, Mg, and Mn removal (100%). In addition, the resin showed moderate removal of Ni and Fe, at 52% and 43%. The resin showed low removal of Cr, Mo, Ni and Se. Breakthrough of Fe, Ni, and Mn was not reached by 15 bed volumes. The initial metal concentrations for stainless steel metals were Cr: 2.0 mM, Fe: 0.45 mM, Mn: 0.14 mM, and Ni: 1.6 mM.

Laboratory Safety

All experimental work is performed under the Laboratory Safety Guidelines (http://www.utexas.edu/safety/ehs/lab/manual/) of the University of Texas. The laboratory personnel have all completed four safety training courses certified by the University: general lab safety, hazardous materials, fire extinguisher, and site specific safety. Routine personal safety protection includes safety glasses, lab coats, gloves, long pants, and closed-toe shoes. Goggles are used for specific hazardous operations. Food and drink are prohibited in the laboratories. Safety inspections of all labs are conducted by a different student every month. The University Office of Environmental Health and Safety conducts random safety evaluations of each lab, usually about twice a year. An industrial visitor conducts a safety evaluation of each lab once per year. A Standard Operating Procedure is followed for three of our major experiments.

Most of the experimental work with amines is conducted in exhaust hoods. Ventilated gas cabinets are used with cylinders of nitrogen mixed with ammonia, NO, NO_2, and SO_2. All work on undiluted nitrosamine samples is contained in one laboratory that has no desks assigned to students for continuous occupancy. We have developed a standard operating procedure to be used in an experiment with closed cylinders of amine solution heated to 175 ^{o}C in convection ovens. These experiments are also contained in the nitrosamines lab.

Dr. Rochelle is the Chairman of the Safety Committee of the Department of Chemical Engineering. The committee meets once a month to review safety issues and safety experiences, and to address initiatives for improving safety.

1. Aqueous Piperazine Blends for CO_2 Capture *p. 14*

by Yang Du

A Ph.D. research proposal has been prepared on aqueous piperazine blends for CO_2 capture. A number of contributions are expected from this work:

1. Review existing relationships between amine structure and its properties, such as thermal stability and volatility.
2. Experimentally screen PZ-based amine blends for thermal and oxidative stability, volatility, CO_2 cyclic capacity, and CO_2 absorption rate.
3. Investigate the relationship between pKa of the blended tertiary amine and CO_2 cyclic capacity of the PZ/tertiary amine blend using wetted wall column.
4. Characterize and evaluate selected PZ-based amine blends for low partial pressure CO_2 capture.
5. Develop rigorous thermodynamic and kinetic models for selected PZ-based amine blends in Aspen Plus®.

2. CO_2 solubility and mass transfer rates by the wetted wall column *p. 41*

by Lynn Li

The secondary amine diethanolamine (DEA) was tested as a solvent for CO_2 capture using the wetted wall column (WWC). The concentration of the amine in the solvent was 7 m, so the results are directly comparable to the base case solvent, 7 m monoethanolamine (MEA). The CO_2 absorption rate and solubility in 7 m DEA was measured at 20, 40, 60, and 80 °C. The absorption performance of the solvent in an absorber for coal flue gas is estimated from the mass

transfer data. The CO_2 carrying capacity and heat of absorption are calculated from the CO_2 solubility data. The performance of 7 m DEA is then compared to 7 m MEA and other primary unhindered amine solvents. The absorption rate of 7 m DEA at coal flue gas conditions is about 10% higher than that of 7 m MEA. The intrinsic capacity of DEA is double that of MEA. The CO_2 capacity of 7 m DEA is about 60% higher than that of 7 m MEA. The heat of absorption of CO_2 for 7 m DEA is lower or about the same as for 7 m MEA.

3. Absorber Intercooling Evaluation *p. 53*

by Darshan Sachde

The evaluation of intercooling benefits (solvent capacity and packing) was completed and summarized in the GHGT manuscript attached to this report. Three flue gas sources were included for the evaluation with 8 m PZ: natural gas combined cycle (NGCC, 4.1% CO_2), coal-fired boiler (13.5% CO_2), and steel blast furnace (27.4% CO_2). As an extension to the intercooling evaluation work, a shortcut method using an energy balance around the absorber was developed to predict the lean loading for each flue gas application where a temperature-related mass transfer pinch becomes limiting and intercooling is necessary to achieve maximum solvent capacity. The new method consistently over-predicts the pinch formation point, but provides a reasonable approximation of lean loading where maximum intercooling benefit could be achieved (within ~10% for all flue gas applications). The method only requires the use of a thermodynamic model for flash calculations and eliminates the need for the rigorous rate-based modeling to identify conditions for maximum intercooling benefit.

4. Modeling and Optimization of Advanced Stripper Configurations *p. 62*

by Yu-Jeng Lin

The work done in this quarter was prepared as a paper manuscript and is in the Attachments to this report. The objective of this work is to identity inefficiencies and improve the process accordingly. The regeneration process and the compressor train were simulated in Aspen Plus®. The lost work of each unit operation was quantified by the exergy balance. The results showed that the two major sources of lost work for the simple stripper are the lean/rich solvent cross exchanger and overhead condenser. The advanced flash stripper was proposed to reduce the lost work of the condenser by recovering the stripping steam heat from the stripper. The advanced flash stripper reduces the heat duty and total equivalent work by 16% and 11%, respectively, compared to the simple stripper. Lean vapor compression was also evaluated, which reduces heat duty and total equivalent work by 8% and 3%, respectively. After reducing the stripping steam heat, the major source of lost work is from the cross exchanger, which should be optimized by including both energy and capital cost.

5. Absorber performance with 5 m MDEA/5 m PZ *p. 63*

by Yue Zhang

In a hybrid-parallel process combining amine scrubbing with membrane technology, the CO_2 concentration in the flue gas is enriched to 23.4% and removal level is increased to 95% (Case 19). This work simulates absorber performance of Case 19 with the Independence model for 5 molal (m) MDEA/5 molal (m) PZ in Aspen Plus®. Different packing types, intercooling configurations, and absorber operating conditions have been tested to get better absorber performance and minimize stripper energy use.

5 m MDEA/5 m PZ offers higher CO_2 capacity but a lower absorption rate than 5 m PZ. Compared to 5 m PZ, absorber costs increase by 50% and advanced flash stripper costs decrease by 47%. The total equipment costs go down by 13%.

6. Stripper Performance and Equipment Costs using 5 m PZ and MDEA/PZ and Design of Ammonia Purging System *p. 72*

by Junyuan Ding

Also supported by a Phillips 66 Fellowship.

Previous work optimized stripping with 5 m piperazine (PZ) with rich loading from 0.37 to 0.43 mol CO_2/mol N. Advanced flash with warm rich bypass and cold rich exchanger bypass is used for stripping. The Independence model for PZ in Aspen Plus® was used to simulate the stripping performance.

In this quarter, stripping data for 24 cases, including heat duty, equivalent work, CO_2 output pressure, and optimal cold and warm rich bypass, were used to build a correlation with CO_2 rich and lean loading. The Second Law efficiency based on the ratio of stripping minimum work and total ideal work was introduced to explain the stripping work. The Second Law efficiency has a maximum value at a specific CO_2 loading.

In previous work, four cases whose inlet CO_2 concentration and CO_2 removal rate were given by MTR (Cases 13, 14, 18, and 19) were simulated based on absorber performance. Since 5 m MDEA/5 m PZ has a higher CO_2 capacity than 5 m PZ, Case 19-MDEA/PZ (rich loading of 0.398 mol CO_2/mol N and lean loading of 0.209 mol CO_2/mol N) using 5 m MDEA/5 m PZ was studied to reduce the heat duty, compared with Case 19 (rich loading of 0.411 mol CO_2/mol N and lean loading of 0.303 mol CO_2/mol N) using 5 m PZ. The base-case stripping configuration was the advanced flash with warm rich bypass and cold rich exchanger bypass. The Independence model for MDEA/PZ in Aspen Plus® was used to simulate the stripping performance. Equipment costs for Case 19 using 5 m PZ and 5 m MDEA/5 m PZ were both analyzed according to the economic part of Peter Frailie's dissertation.

Ammonia purging design is required for amine scrubbing. Amine scrubbing may create an air quality problem by releasing ammonia. Some amine is converted to ammonia through oxidative or thermal degradation in the absorber and reboiler. Ammonia emits into air with the treated flue gas from the absorber, serving as a significant precursor of $PM_{2.5}$.

In this work, a top stripper and a reflux flow of the condensate over the stripper is used to concentrate ammonia and the rest is purged. Different reflux ratios are chosen to see the ammonia concentration and flowrate of the purge. 1 kg/1000 kg mass ratio of NH_3/H_2O is set for the ammonia amount. The base-case stripping configuration was the advanced flash with warm rich bypass and cold rich exchanger bypass. The Independence model for PZ in Aspen Plus® was used to simulate the stripping performance.

7. Packing characterization: hydraulic and mass transfer results overview *p. 91*

by Chao Wang

In this quarter, review of hydraulic and mass transfer results containing all 14 packings measured in this work was presented. The experimental results serve as Chapter 4 of the Ph.D. dissertation. The effects of liquid superficial velocity (u_L), gas superficial velocity (u_G), packing

surface area (a_P), and packing corrugation angle (θ) on hydraulic properties and mass transfer performance were explored. In general, pressure drop increases steadily with gas flow rate (F-factor) to the power of 1.6–1.9. The pressure drop increases by 30% from dry condition to a liquid load of 5 gpm/ft^2 (12 m^3/m^2*h), and increases slightly with increasing liquid flow rate. The liquid hold-up increases slightly with gas flow rate in the pre-loading region, and increases sharply with gas flow rate in the loading region until flood. Liquid hold-up increases with liquid flow rate at the constant gas flow rate. Both pressure drop and liquid hold-up increase with packing surface area and decrease with packing corrugation angle.

The effective mass transfer area increases with liquid velocity to the 0.15 power and is essentially independent of gas velocity. The fractional effective area decreases as packing surface area increases because of the inefficient wetting in the higher specific surface area packings. Rivulets, ripples, and droplets provide additional mass transfer area in lower specific surface area packings. The effective mass transfer area is not a function of packing corrugation angle.

The liquid film mass transfer coefficient (k_L) is a function of liquid velocity and independent of gas velocity. Conversely, the gas film mass transfer coefficient (k_G) is a function of gas velocity and independent of liquid velocity. The k_L increases with liquid velocity (u_L) to the power of 0.5–0.77 for all packings in this work. The k_G increases with liquid velocity (u_G) to the power of 0.43–0.76 for all packings in this work. Summaries of k_L and k_G are shown in Figures 4.27 and 4.28 of the attached Chapter 4.

8. Effect of liquid viscosity on the liquid film mass transfer coefficient in packed columns *p. 114*

by Di Song

In this quarter, a model of surface tension (σ) for NaOH/H_2O/glycerol was built based on literature data. A modified correlation for liquid flow rate (L) of the rotameter in the wetted wall column (WWC) was built, introducing corrected terms for liquid viscosity (μ_L). Based on the updated data for L, surface depletion of each WWC case was calculated, and surface-depletion correction was made to part of the k_g' data. Models of the overall reaction rate constant (k_{Alk}) were built based on empirical data for k_g'. A paper for GHGT-12 was completed summarizing the previous work.

9. Kinetic Modelling of 4 m 2MPZ/4 m PZ and 4 m AMP/2 m PZ *p. 119*

by Brent Sherman

Also supported by CCSI

The kinetics of two different piperazine (PZ) blends were regressed: 4 m 2-methylpiperazine (2MPZ)/4 m PZ and 4 m 2-amino-1-propanol (AMP)/2 m PZ. For each, wetted wall column (WWC) flux data covering a wide loading and temperature range were regressed using activity-based kinetics. The pseudo-first-order rate constants show that the fastest reaction for 2MPZ/PZ is the formation of $PZ(COO^-)_2$ catalyzed by free 2MPZ, and for AMP/PZ it is the formation of $AMPCOO^-$ catalyzed by free AMP. While this is reasonable for the AMP/PZ system, it is suspicious for the 2MPZ/PZ system as the formation of $PZCOO^-$ catalyzed by free PZ should be the fastest. Further, the rate-based absorber model with kinetics could not be converged for 2MPZ/PZ due to an unreasonable 2MPZ zwitterion activity coefficient. While a working

process model was achieved by removing zwitterion reactions, this model lacks some physical significance.

10. Time Scale Analysis of Amine Scrubbing *p. 142*

by Matt Walters
Co-supervised by Thomas Edgar

The process dynamics of amine scrubbing exhibit time scale multiplicity as a result of significant material and energy recycle. A low-fidelity model of the process has been developed using lumped parameters, approximate thermodynamics, and adjustable heat and mass transfer coefficients. The material states of the low-fidelity model were demonstrated to be in non-standard singularly perturbed form. In this model form, only the stripper vapor mole fractions evolve exclusively on the slow time scale; all other variables have both fast and slow components. A coordinate transform using the total liquid material hold-ups can be used to explicitly separate the slow and fast dynamics. This work has been presented at the GHGT-12 conference. The system model was demonstrated to be ill-conditioned based on the eigenvalues of the linear system.

11. Amine Degradation *p. 146*

by Omkar Namjoshi

Three papers were prepared and presented at the GHGT-12 conference. These are included in the appendix to the quarterly report.

The first paper, "Thermal Degradation of PZ-Activated Tertiary Amines and Hindered Amines" (Namjoshi), presented thermal degradation rate measurements for a range of PZ-activated tertiary amines at an initial loading of 0.23 mol CO_2/mol alkalinity and an initial concentration of 5 m PZ/5 m tertiary amine, as well as PZ-activated hindered amines at an initial loading of 0.23 mol CO_2/mol alkalinity and an initial concentration of 1.33 m PZ/2.67 m hindered amine. These rate measurements were interpreted in the context of maximum stripping temperatures (T_{MAX}). PZ-activated tertiary morpholines were found to be the most stable solvent class, with T_{MAX} values greater than 150 °C. PZ-activated acyclic tertiary amines without methyl groups were of an intermediate stability, with T_{MAX} values between 130 and 140 °C. PZ-activated acyclic tertiary amines with at least one methyl group were stable below 130 °C. Acyclic PZ-activated hindered amines had stability temperatures ranging from 128 °C to 147 °C, with the least stable acyclic hindered amines having the greatest number of hydroxyl groups. Cyclic PZ-activated hindered amines had stability temperatures below 130 °C.

The second paper, "Thermal Degradation of Linear Amines" (Hatchell), presented thermal degradation rate measurements for a range of linear diamines and alkanolamines with an initial concentration of 10 m alkalinity (5 m alkalinity for hexamethylenediamine) and an initial loading of 0.4 mol CO_2/mol alkalinity. Increasing amine chain length between the amino function and the end amino or hydroxyl function decreased the initial rate of thermal degradation and increased the activation energy of thermal degradation. Ethylenediamine was found to be the most corrosive amine tested, whereas propylenediamine was the least corrosive.

The third paper "Oxidative Degradation of Diamines and Structural Derivatives," (Liu), presented oxidative degradation rate measurements for a range of linear diamines and alkanolamines with an initial concentration of 10 m alkalinity (5 m alkalinity for hexyamethylenediamine) and an initial loading of 0.4 mol CO_2/mol alkalinity and in the presence

of 0.4 mM Fe, 0.2 mM Mn, 0.1 mM Ni, and 0.05 mM Cr. Propylenediamine and monopropanolamine were found to be oxidatively stable and did not show any appreciable oxidative degradation, whereas all amines tested lost about 80% of their mass after 2 weeks.

12. Aerosol Mitigation in CO_2 Capture *p. 148*

by Steven Fulk

Work completed this quarter is divided between this report and a manuscript prepared for the GHGT-12 conference (appended to this report).

In the GHGT-12 work, inlet aerosols of variable (0.5 m PZ and 0.05 vol % H_2SO_4) composition were generated by vaporizing a metered liquid stream kept at 1 mL/min sucked through an eductor by a preheated (310 ºC) motive N_2 stream at 1.035 SCFM. The solvent flowrate (6–36 GPH), inlet CO_2 concentration (0–8 vol %), and the inlet solvent temperature (40 and 50 ºC) were changed independently and the outlet PZ concentration was measured using FTIR.

The baseline outlet gas CO_2 and PZ concentrations relative to the solvent (0.9 m PZ) flowing at 12 GPH were 110.4 and 2.8 ppmv, respectively. Injection of PZ and H_2SO_4 aerosols increased the outlet PZ value to 65 and 6.5 ppmv, respectively.

Increasing the inlet concentration of CO_2 to 4 vol % doubled the measured PZ in the exhaust gas under PZ aerosol load; however, further increase of CO_2 produced very minor relative changes. PZ seems to be inversely related to inlet CO_2 concentration in the case of H_2SO_4 aerosols.

Changes to the solvent flowrate had far greater impact on the exhaust rate of amine. PZ decreased from 75 to 20 ppmv when the solvent rate was reduced from 36 to 6 gpm for the PZ aerosol case in the presence of no inlet CO_2. Solvent rate was found to have the opposite behavior for the H_2SO_4 aerosol case; PZ emissions increased from 6 to 20 ppmv as the solvent rate was increased from 6–36 GPH. Similar behavior was found during multivariable (CO_2 and flowrate) studies, though the absolute changes in measured PZ were much smaller.

Finally, PZ emissions were found to have a reciprocal relationship to inlet solvent temperature for the PZ aerosol case. No clear trend was observed during H_2SO_4 aerosol testing.

In this document, LVI flow measurements and a new multi-point FTIR sampling system were tested. The LVI flow rate and vacuum level were verified against vendor data and matched closely to the Air-Vac HAVR093SS eductor. The multi-point FTIR sampling system flow rate was measured for variable inlet throttling. The flow rate for both sample lines (10’ and 30’) was 8.9 and 6.3 SLPM at 70% throttle between 25–60 Hz. The flow rate for both sample lines (10’ and 30’) was 6.6 and 5.3 SLPM at 90% throttle between 25–60 Hz.

13. Aerosol Observation and Separation in Amine-Based CO_2 Capture p.159

by Matt Beaudry

Amine emissions in aerosol form have been observed as a significant problem for amine-based CO_2 capture plants. Unarrested soot and hydrolyzed SO_3 condense in the absorber while collecting amine. Conventional water wash columns are ineffective at removing the amine once it is captured in the aerosols. While Brownian diffusion units have proven to be fairly effective at reducing amine emissions, cyclonic separators offer the potential for improved capture performance with a simpler system at a lower cost. A swirl tube cyclonic separator has been designed and will be implemented in both the Aerosol Growth Column and the PRC Pilot Plant.

The flexibility of the design will allow for capture of aerosols at controllable sizes. Another aerosol sampling system has been designed to utilize centrifugal forces to control the size of particles sampled by FTIR analysis. It is hoped that this will provide similar data to the PDI with more robust and less expensive equipment.

14. Amine Degradation in Pilot Plants *p. 168*

by Paul Nielsen

In a oxidation experiment using 4 m PZ in the HTOR degradation rig cycled from 40 °C to 150 °C, the rate of ammonia production, a major oxidation product, was approximately half that previously observed with 8 m PZ at similar conditions. The ammonia rate increased over the course of the experiment, and appeared to be tracking along with the accumulation of dissolved metal ions in solution. The metal ions may be participating in a free radical shuttling mechanism to oxidize the amine. A nitrogen bubble column designed to remove dissolved oxygen was partially effective, reducing ammonia generation by 20%. 0.24 moles of total formate were produced per mole of ammonia generated.

Degraded MEA solvent samples were analyzed from a 2-week campaign conducted at the NCCC pilot plant in June 2014. 55 mmol/kg of N-(hydroxyethyl)-glycine and 19 mmol/kg of formate accumulated during the campaign. No significant accumulation of nitrosamine was observed.

Samples were analyzed from a new vacuum reclaimer being tested at the Searles Valley Minerals Facility pilot plant operated by HTC in Trona, California, using 20 wt % MEA. The reclaimer waste typically contained 2 to 3 moles of MEA per mole of heat stable salt. The purified MEA product stream had no significant contamination.

15. NO_2 Absorption into Aqueous Amines and Sulfite *p. 178*

by Nathan Fine and Virbin Nath Sapkota

Nitric oxide (NO) and nitrogen dioxide (NO_2) were absorbed into aqueous amine to determine the absorbing species, the absorption kinetics, and the aqueous products at the ppm-level NO_x concentrations typical of flue gas from fossil fuel power plants. At flue gas conditions of 0.5–5 ppm of NO_2, absorption is dominated by free radical absorption of NO_2 as nitrite. NO_2 absorption kinetics are first order in NO_2 partial pressure, half order in free amine concentration, and fastest in methyldiethanolamine (MDEA). The reaction-enhanced liquid mass transfer coefficient for NO_2 absorption in 8 m piperazine (PZ) at absorber conditions is $9.7*10^{-7}$ mol/s·m^2·Pa, yielding 92% NO_2 absorption at a typical A/G of $3.3*10^6$ s·Pa·m^2/mol. Similarly, 9 m monoethanolamine (MEA) will absorb roughly 70% of the inlet NO_2 while 7 m MDEA/2 m PZ will absorb over 99% of the NO_2. Nitrite and nitrate are the main NO_x absorption products in MDEA with nitrite dominating at low NO_2 partial pressures. In PZ, the amine free radical formed during NO_2 absorption will react directly with NO to form n-nitrosopiperazine (MNPZ), or react with itself to form 2-piperazinol (2-PZOH). Typical nitrosamine yields in 5 m PZ are around 15% of total absorbed NO_x and can be halved with the addition of 200 mM Inhibitor A (Inh A), a free radical scavenger. Nitrate and nitramine are minor products of NO_x absorption, accounting for less than 5% of total absorbed NO_x.

This quarter, rates of sulfite (SO_3^{2-}) oxidation during nitrogen dioxide (NO_2) absorption into sulfite solutions were measured using the high gas flow apparatus. The SO_3^{2-} absorbs NO_2 via a free radical mechanism that produces sulfite radical ($SO_3^{-}\cdot$) and nitrite. The radical then catalyzes SO_3^{2-} oxidation to form sulfate. Free radical scavengers such as thiosulfate can be

added to suppress radical concentrations and inhibit sulfite oxidation. The effects of thiosulfate, sulfite, NO_2 absorption, temperature, and O_2 partial pressure were investigated. Under normal industrial conditions, oxidation is inverse half-order in thiosulfate, first order in sulfite, and half order in NO_2 absorbed. Sulfite oxidation shows little dependence on O_2 partial pressures above 5 kPa but has a strong dependence on O_2 at lower partial pressures. Oxidation from 20 °C to 65 °C was fit using the Arrhenius equation with an activation energy of 24.1 kJ/mol. The addition of 0.01 mM Fe increased oxidation rates by a factor of 3 compared to solutions with 0.01 mM EDTA added to chelate metals.

16. Ion Exchange for Metals Removal from Amine Solutions p. 194

by Kent Fischer

Several experiments were conducted to test metals removal from amine solutions using an ion exchange resin. Amines tested include MEA, PZ, and a degraded PZ solution from a pilot plant. The resin tested was Amberlite IRC748i, a resin which shows promising selectivity for cations from high pH solutions. High metal selectivity is due to the very favorable complex formed between the resin functional group and strongly cationic metals.

Attachments

Papers and posters presented at *GHGT-12*

Aqueous piperazine blends for CO_2 Capture

Quarterly Report for July 1 – September 30, 2014

by Yang Du

Supported by the Texas Carbon Management Program

McKetta Department of Chemical Engineering

The University of Texas at Austin

October 31, 2014

Abstract

A Ph.D. research proposal has been prepared on aqueous piperazine blends for CO_2 capture. A number of contributions are expected from this work:

1. Review existing relationships between the amine structure and its properties, such as thermal stability and volatility;
2. Experimentally screen PZ-based amine blends for thermal and oxidative stability, volatility, CO_2 cyclic capacity, and CO_2 absorption rate;
3. Investigate a) the relationship between pKa of the blended tertiary amine and CO_2 cyclic capacity of the PZ/tertiary amine blend using the wetted wall column, and b) the relationships between the amine structure and its properties (thermal stability and volatility) for ether amines, piperidines, morpholines, and imidazoles;
4. Characterize and evaluate selected PZ-based amine blends for low partial pressure CO_2 capture;
5. Develop a rigorous thermodynamic and kinetic model for selected PZ-based amine blend in Aspen Plus®.

The University of Texas at Austin

McKetta Department of Chemical Engineering

Aqueous Piperazine Blends for CO_2 Capture

Ph.D. Research Proposal

Yang Du

Supervisor: Prof. Gary T. Rochelle

November, 2014

Summary

Amine scrubbing has shown the most promise for effective capture of CO_2 from coal-fired flue gas. However, the high capital expenditure (CAPEX) and operational expenditure (OPEX), as a result of low CO_2 partial pressure in flue gas and potential Environmental Health and Safety (EHS) issues, impede its commercial application. Novel solvent development and process optimization are two important approaches to solving these issues. This study will focus on the first approach. Concentrated piperazine (PZ) has the most outstanding properties for low partial pressure CO_2 capture (high cyclic CO_2 capacity, high CO_2 absorption rate, high solvent stability, and low volatility), but its industrial application is limited by its low solubility in water. The objective of this work is to find a suitable amine to blend with less concentrated PZ, so that this blend maintains the desired properties of concentrated PZ for low partial pressure CO_2 capture but alleviates the solvent solubility issue.

Five research goals are proposed:

- Review existing relationships between amine structure and its properties, such as thermal stability and volatility;
- Experimentally screen PZ-based amine blends for thermal and oxidative stability, volatility, CO_2 cyclic capacity, and CO_2 absorption rate;
- Investigate a) the relationship between pKa of the blended tertiary amine and CO_2 cyclic capacity of the PZ/tertiary amine blend using the wetted wall column, and b) the relationships between the amine structure and its properties (thermal stability and volatility) for ether amines, piperidines, morpholines, and imidazoles;
- Characterize and evaluate selected PZ-based amine blends for low partial pressure CO_2 capture;
- Develop a rigorous thermodynamic and kinetic model for selected PZ-based amine blend in Aspen Plus®.

These five goals are expected to be finished by 2016 May, and a dissertation and three journal papers will be published. A detailed research timeline is shown below.

	2014	2015	2015	2016
	Sep-Dec	Jan-Jun	Jul-Dec	Jan-May
Review amine structure-property relationships	V			
Screen PZ-based amine blends	V			
Investigate amine structure – property relationships		V		
Characterize selected solvent		V		
Develop Aspen Plus® model			V	
Write dissertation				V

BACKGROUND AND MOTIVATION

Anthropogenic greenhouse gas emissions are changing climates worldwide (IPCC, 2014). Mitigation of greenhouse gas emissions can substantially reduce risks of climate change in the second half of the 21st century (IPCC, 2014). CO_2 emissions from fossil fuel combustion and industrial processes contributed about 78 % of the total GHG emission increase from 1970 to 2010, and accounted for 65% of the total anthropogenic GHG emissions in 2010 (IPCC, 2014).

The coal fired power plant is the largest single source of carbon emissions, accounting for 29% of U.S. CO_2 emissions (IEA, 2014) and 31% of world emissions (IEA, 2013). In 2013, the U.S. Environmental Protection Agency (EPA) announced the new carbon emission standard for the new and existing coal-fired power plant, aiming to reduce 30% carbon emissions by 2030, from 2005 levels (EPA, 2014). Under this regulation, the power sector has to add the carbon control technology to the coal-fired power plant or shift to other carbon-free power generation.

Amine scrubbing has shown the most promise for effective capture of CO_2 from coal-fired flue gas (Rochelle, 2009). A typical amine scrubbing process for CO_2 capture is shown in Figure 1. Desulfurized flue gas from coal combustion with 12% CO_2 is contacted with the aqueous amine in the absorber where 90% of the CO_2 is removed. The rich solvent from the bottom of the absorber is sent to the stripper and heated for CO_2 regeneration. The hot lean solvent is cooled by the cold rich solvent in the cross exchanger before being recycled back to the absorber. The stripped CO_2 is then compressed to 150 bar for further storage and sequestration. Aqueous monoethanolamine (MEA) with a concentration of 15–30 wt % has been previously used in similar applications such as CO_2 removal from natural gas and hydrogen, and is currently considered the benchmark solvent for flue gas CO_2 capture (Rochelle, 2009).

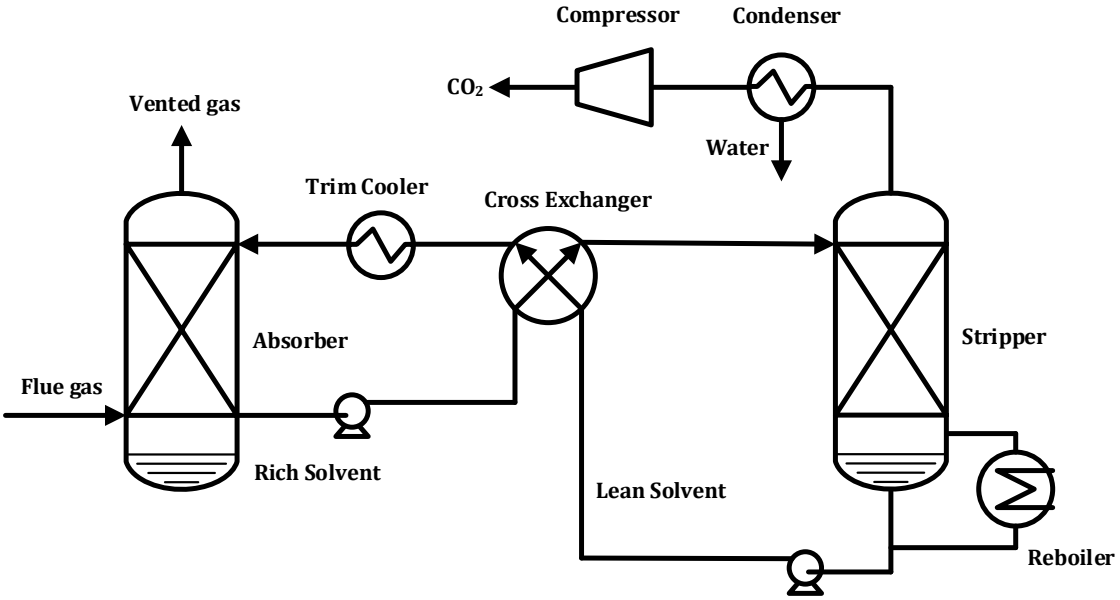

Figure 1 Basic amine scrubbing process for CO_2 capture.

Although amine scrubbing is a mature technology and has been used in the gas treating industry for around 100 years (Bottoms, 1930), the low CO_2 partial pressure in flue gas will lead to high capital and operating costs of the amine scrubbing unit. Current estimates suggest a 40–70% increase in electricity prices to remove 90% CO_2 from a coal-fired power plant (NETL, 2008). To minimize capital and operating costs, current research efforts focus on 1) finding new

solvents with desirable chemical and physical properties at low costs; and 2) optimizing process design to improve efficiency (Rochelle, 2009). This work focuses on the first category by screening piperazine (PZ)-based amine blends in terms of their CO_2 capture performance, and potential Environmental Health and Safety (EHS) issues. Generally, a desired solvent should have the following properties.

1. High cyclic CO_2 capacity

The cyclic CO_2 capacity of a solvent can be calculated using the difference between the lean and rich loading ($\Delta\alpha_{CO2}$) and the total alkalinity in solution (Equation 1):

$$Capacity = \frac{(\propto_{rich} - \propto_{lean}) \cdot mol\ alkalinity}{kg\ (amine + H_2O)} = \frac{mol\ CO_2}{kg} \quad (1)$$

CO_2 loading (α_{CO2}) of lean and rich solvent is calculated using Equation 2.

$$\propto = \frac{n_{co2}}{n_{alkalinity}} \quad (2)$$

For coal-fired flue gas, the normal operation lean and rich loading correspond to equilibrium CO_2 partial pressures of 0.5 kPa and 5 kPa at 40 ^{o}C, respectively, in order to maintain enough driving force for CO_2 absorption throughout the absorber. Cyclic CO_2 capacity represents the amount of CO_2 removed per unit mass of solvent. With higher capacity, less solvent is required to remove the same amount of CO_2. The capacity value directly relates to the sensible heat requirement for stripping, pump work, and the size and cost of the cross-exchanger (Li et al., 2011).

2. Fast Rate

The absorption rate of CO_2 by amine can be described by Equation 3.

$$G_{gas} \cdot \mathrm{x}_{CO2} \cdot \text{Removal Percentage} = \text{Area}_{\text{packing}} \cdot k_g^{'} \left(P_{CO_2} - P_{CO_2}^{*} \right) \quad (3)$$

Where,

G_{gas} is the flue gas flow rate.

x_{CO2} is the percentage of CO_2 in flue gas.

P_{CO2} is the partial pressure of CO_2 in flue gas.

P_{CO2}* is the equilibrium CO_2 partial pressure of loaded amine solvent.

k_g' is the liquid film mass transfer coefficient defined in gas film units.

The removal of CO_2 is a function of packing area, mass transfer coefficient (k_g') and driving force. With same driving force, large k_g' reduces the amount of packing required for the same amount of CO_2 removal, which leads to smaller absorber size and thus lower capital cost. A simple absorber design estimated that for unit volume of flue gas, the required packing area for fast amines such as 5 m N-methyl-diethanolamine (MDEA)/5 m PZ is only 1/2 to 1/3 of that for slow solvents like Diglycolamine® (DGA®), methyl-amino-propane amine (MAPA), and 2-amino-2-methyl-1-propanol (AMP) (Chen, 2011). On the other hand, for an absorber with fixed amount of packing and CO_2 removal, larger k_g' also allows smaller driving force to be used and thus less solvent circulate rate.

3. Resistance to thermal degradation

At high temperature, amines can degrade by different mechanisms, resulting in solvent makeup cost and potential EHS issues. While the rate of amine degradation increases with increase in temperature, the energy performance of the process improves with higher stripper operating temperature (Oyenekan and Rochelle, 2007). Stripper operating temperature is limited by the rate of thermal degradation, and the optimum corresponds to the maximum tolerable rate of amine loss. Previous work by Davis (2009) suggests the acceptable rate of degradation (k_1) for 7 m MEA is 2.9×10^{-8} s^{-1} with stripper temperature at 121 °C. This optimum is calculated by the trade-off between the cost of MEA loss and the energy benefits of higher stripper temperature and pressure (Oyenekan and Rochelle, 2007).

4. Resistance to oxidation

Oxidation is the degradation of amine in response to the oxygen in the flue gas (Sexton, 2009). Oxidation causes the major amine loss in CO_2 capture process for coal-fired flue gas. In addition, some oxidative degradation products are corrosive or toxic (Karl et al., 2011).

5. Low volatility

Amine volatility is one of the key criteria used in screening an amine solvent for CO_2 capture due to a number of reasons including: (1) amine losses up the stack can react in the atmosphere to form ozone and other toxic compounds; (2) high volatility losses can result in greater solvent make-up costs; (3) additionally high losses will require the use of larger water wash units, and more water, to capture fugitive amines prior to venting - these translate to higher capital and operating costs (Nguyen, 2011).

6. Low solvent cost

Due to the low CO_2 partial pressure and high flow rate of flue gas in coal-fired power plant, a large amount of solvent is required for CO_2 capture. For a 300 MW coal-fired power plant, around 3000 gal solvent is needed. Solvent cost accounts for 5% of total capital cost.

7. Others

High solvent solubility and low viscosity are also preferred, as they allow high amine concentration used in the solvent, and give better CO_2 absorption performance in general.

Concentrated piperazine (PZ) has been proposed as a possible alternative to 30 wt % MEA (Rochelle et al., 2011). PZ has about twice the CO_2 absorption rate and CO_2 capacity, and greater resistance to oxidative and thermal degradation than 30 wt % MEA, which can lower the heat duty for the stripper in amine scrubbing systems by approximately 10 % (Rochelle et al., 2011). In spite of desirable characteristics, the application of concentrated PZ in industry may be limited by solid precipitation at both lean and rich CO_2 loading (Rochelle et al., 2011). At room temperature (20 ˚C), 8 m PZ requires a loading of 0.26 mol CO_2/mol alkalinity to stay in solution, and it also forms solids at high CO_2 loading. Blending solvents already in use is one approach to combine desirable characteristics. Several PZ-based amine blends were identified as alternative to 8 m PZ, such as 5 m PZ/5 m methyldiethanolamine (MDEA), 2 m PZ/4 m 2-amino-2-methyl-1 propanol (AMP), 5 m PZ/2 m N-(2-aminoethyl) piperazine (AEP), and 4 m PZ/4 m 2-Methylpiperazine (2-MPZ). Although these PZ-based blends alleviate the solubility issue of straight PZ to some extent, they suffer from other problems. PZ/MDEA and PZ/AMP are not

thermally stable. AMP has a much higher volatility than PZ. 5 m PZ/2 m AEP has a 20% lower capacity than 8 m PZ. 4 m PZ/4 m 2MPZ has a 20% lower absorption rate than 8 m PZ.

OBJECTIVES OF THIS WORK

The objective of this work is to find a suitable amine to blend with less concentrated PZ, so that this blend maintains the desired properties of concentrated PZ for low partial pressure CO_2 capture but alleviates the solvent solubility issue.

Five research goals are proposed:

1. Review amine structure-property relationships

It is not feasible to screen every amine for CO_2 capture. However, with the understanding of desired amine properties and amine structure-property relationships, we can largely narrow down the list of amine to be screened. As amine scrubbing is believed to be the most feasible method to capture CO_2 from coal-fired flue gas, which accounts for one third of the total CO_2 emission (IEA, 2013), some research efforts were made to understand the amine structure-property relationships (Nguyen, 2013; Freeman 2011; Chen, 2011). It is necessary to review and summarize these empirical or theoretical rules as a guideline for our screening work.

2. Screen PZ-based amine blends

As mentioned earlier, although concentrated PZ has better CO_2 absorption performance than 30 wt % MEA (Rochelle et al., 2011), its industrial application is limited by its narrow solubility window in water at low temperature. Blending solvents already in use is one approach to combine desirable characteristics. The objective of this work is to find a suitable amine to blend with less concentrated PZ, so that this blend maintains the desired properties of concentrated PZ for low partial pressure CO_2 capture but alleviates the solvent solubility issue.

3. Investigate the amine structure – property relationships

The CO_2 solubility of an amine depends on both pKa and carbamate stability of the amine. Due to the lack of carbamate stability information, no general correlation has been established to relate amine structure to its CO_2 solubility. However, as tertiary amine cannot

form carbamate, its CO_2 solubility primarily depends on its pKa. In the case of PZ/tertiary amine blends, the CO_2 cyclic capacity also primarily depends on the pKa of tertiary amines, and thus a semi-empirical correlation can be established with sufficient CO_2 solubility data in PZ/tertiary amines with a wide range of pka.

Although recent years some research efforts were made to understand the amine structure-property relationships (Nguyen, 2013; Freeman 2011; Chen, 2011), most of them focused on acyclic alkanolamines, acyclic diamines, and PZ derivatives. There is a lack of understanding on the CO_2 absorption of ether amines, piperidines, morpholines, and imidazoles. Therefore, this study will investigate 1) the relationship between pKa of the blended tertiary amine and CO_2 cyclic capacity of the PZ/tertiary amine blend using the wetted wall column, 2) the relationships between the amine structure and its properties (thermal stability and volatility) for ether amines, piperidines, morpholines, piperazines, and imidazoles.

4. Characterize selected solvent

The selected PZ-based amine blend will be rigorously characterized and evaluated. CO_2 solubility and absorption rate will be measured using the wetted wall column. Thermal stability will be measured using Swagelok® 3/8-inch OD 316 stainless steel thermal cylinders. Oxidation will be measured in a low gas flow agitated reactor with 100 mL/min of a saturated 98%/2% O_2/CO_2 gas mixture fed into the reactor headspace. Volatility will be measured in a stirred reactor coupled with a hot gas FTIR analyzer (Fourier Transform Infrared Spectroscopy, Temet Gasmet Dx-4000).

5. Develop Aspen Plus® model

To predict the overall performance of the selected PZ-based amine blend, it is necessary to develop a rigorous model which can accurately predict the thermodynamic properties and kinetic properties of the solvent. Electrolyte-Nonrandom Two-Liquid (eNRTL) model will be used as the thermodynamic framework in Aspen Plus®. Experimental data (CO_2 solubility, CO_2

absorption rate, solvent volatility, NMR speciation, and viscosity) will be regressed to obtain model parameters.

References

Bottoms, R. R. (Girdler Corp.), "Separating acid gases," U.S. Patent 1783901, 1930.

Chen, X.; Rochelle, G. T. (2011). Aqueous piperazine derivatives for CO_2 capture: Accurate screening by a wetted wall column. *Chem Eng Res Des*. 89(9): 1693-1710.

Davis J. Thermal Degradation of Aqueous Amines used for Carbon Dioxide. The University of Texas at Austin. Ph.D. Dissertation. 2009.

EPA (2014). Clean Power Plan Proposal.

Freeman, S. A. (2011). Thermal Degradation and Oxidation of Aqueous Piperazine for Carbon Dioxide Capture, The University of Texas at Austin.

IEA (2013). CO_2 Emissions from Fuel Combustion Highlights.

IEA (2014). Monthly Energy Review. Environment. Table 12.6 Carbon Dioxide Emissions From Energy Consumption: Electric Power Sector.

IPCC (2014). Climate Change 2014: Impacts, Adaptation, and Vulnerability.

Karl, M.; Berglen, T.F.; Denby, B. (2011). Worst case scenario study to assess the environmental impact of amine emissions from a CO_2 capture plant. *Int J Greenh Gas Con*. 5(3): 439-447.

Li, L., Voice, A. K., et al. (2013). Amine blends using concentrated piperazine. *Energy Procedia*. 37(0): 353-369.

NETL (2008). The Cost of Carbon Dioxide Capture and Storage in Geologic Formations.

Nguyen, T., Hilliard, M., et al. (2011). Volatility of aqueous amines in CO_2 capture. *Energy Procedia*. 4(0): 1624-1630.

Oyenekan, B.; Rochelle, G. (2007). Alternative Stripper Configurations for CO_2 Capture by Aqueous Amines. *AIChE J*. 53.

Rochelle, G. T. (2009) Amine Scrubbing for CO_2 Capture. *Science*. 325:1652–1654.

Rochelle, G.; Chen, E.; Freeman, S.; Van Wagener, D.; Xu, Q.; Voice, A. (2011) Aqueous Piperazine as the New Standard for CO_2 Capture Technology. *Chem Eng J*. 171: 725–733.

Rochelle, G. T. (2012) Thermal Degradation of Amines for CO_2 Capture. *Curr Opin Chem Eng.* 1: 183−190

Sexton, A. J. and Rochelle, G. T. (2009). Catalysts and inhibitors for oxidative degradation of monoethanolamine. *Int J Greenh Gas Con*. 3(6): 704–711.

Appendix A: Literature Review for Amine Structure-Property Relationships

1. Volatility

Nguyen (2011) investigated the volatilities of amine solvents used in post-combustion CO_2 capture from coal-fired power plants. Nguyen's work is one of the largest sources of experimental data available for amine-water volatility measurements, and for the first time it provided a large amount of amine volatilities in CO_2 loaded systems. A group contribution model was proposed by Nguyen to correlate amine volatilities to molecular structures. Nguyen's model gives accurate predictions of aqueous volatilities for saturated aliphatic amines. In general, amines having one or more polar groups, such as amino, hydroxyl, and ether groups, tend to be less volatile due to favorable interactions with water. The presence of one or more methyl groups in a structure contributes to non-polarity or greater volatility as is the case of AMP. As a second order effect, the presence of an N-CH_3 contribution in a straight chained amine, or a C-CH_3 contribution in a cyclic amine, correlates to lower volatility, respectively. Finally, to a small extent, the cyclic amines appear to be less volatile than straight chain amines (Nguyen, 2011).

2. Thermal degradation

Thermal degradation for an extensive list of amines was investigated in Rochelle's group (Freeman, 2011; Davis, 2009). Five mechanisms were proposed by Rochelle (2012) for thermal degradation of amines.

a) Cyclic urea formation (Ethylenediamine)

Diamine structures where two secondary or primary N's are separated by two or three carbons readily degrade at lower temperature in the presence of CO_2 to produce cyclic ureas (imidazolidinone), such as the production of imidazolidinone from ethylenediamine (EDA):

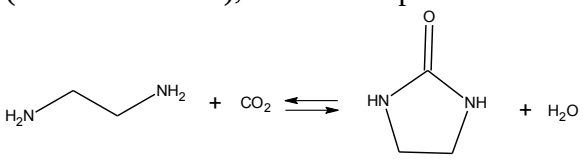

This reaction is reversible, especially at greater temperature. However, the equilibrium concentration of the cyclic urea is substantial and represents an unacceptable loss of active amine.

b) Carbamate Polymerization

Primary and secondary alkanolamines with two or three carbons between the N and O degrade by reversibly forming a cyclic oxazolidinone from the carbamate, which then reacts with another amine to form a dimer of the starting amine or form urea:

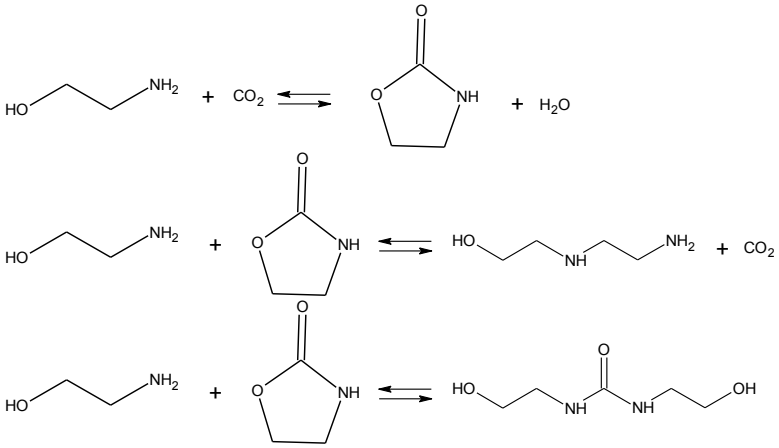

c) Transalkylation and elimination

Tertiary amines appear to degrade by two mechanisms. All of the tertiary amines participate in transalkylation, especially in the presence of secondary N's in the parent molecule or from other degradation mechanisms. These SN_2 reactions are catalyzed by CO_2 or acid loading to protonate the tertiary amine. Tertiary amines react even more readily with a quaternary amine. Elimination from the quatenary amine will result in the net production of the secondary amine. Elimination may be faster with ethyl alcohol or ethyl amine attached to the tertiary N.

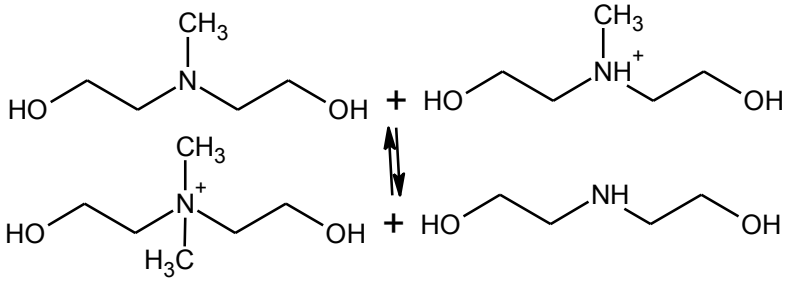

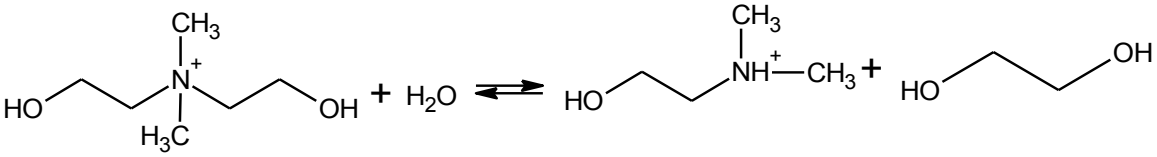

d) Ring closing or opening

Amines with a ring structure, such as piperazine (PZ) degrade by ring opening. The initial product of PZ degradation, aminoethylaminoethylpiperazine (AEAEPZ) is subject to further degradation by cyclic urea formation. The cyclic urea reacts with PZ to produce oligomers and fragments such as ethylenediamine (EDA) and ammonia.

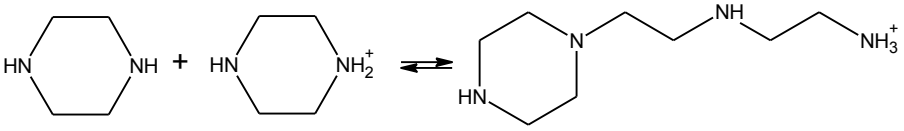

Long chain diamines, such as DGA®, degrade by ring closing.

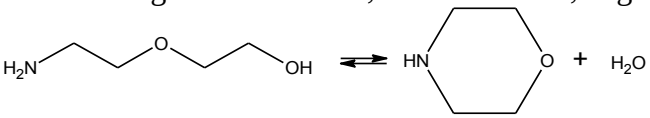

e) Blend Synergism

A blend of amines may degrade faster than either amine, as in the case of PZ/MEA and PZ/MDEA, or slower than either amine, as in the case of PZ/AEP. The blend of MEA with PZ degrades fast because the reactive PZ readily reacts with the MEA oxazolidinone to produce the cross dimer.

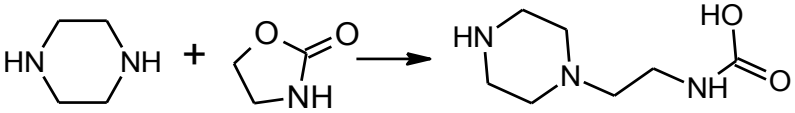

The blend of AEP with PZ degrades slowly because they are the major degradation products for each other, and thus reach equilibrium faster when blended.

Generally, cyclic amines without a side chain, diamines where two secondary or primary N's are separated by more than three carbons, and alkanolamines with more than three carbons between the N and O show the highest thermal stability. Hindered amines show medium thermal stability.

Appendix B: Experimental Methods

1. Viscosity Measurements

Viscosity of amines was measured using a Physica MCR 300 cone and plate rheometer (Anton Paar GmbH, Graz, Austria). The method was described by Freeman (2011). The average value and standard deviation calculated from 10 individual measurements for each sample was reported.

2. Thermal Degradation

Thermal degradation was measured in 3/8-inch OD 316 stainless steel thermal cylinders. Cylinders were filled with 4 mL of amine solution with around 1 mL of headspace, sealed with two Swagelok® end caps, and placed in forced convection ovens maintained at the target temperature. Individual cylinders were removed from the ovens at each sampling point and then analyzed for degradation products, degradation rate, and CO_2 loading, using a Dionex ICS-2500 cation ion chromatograph, a Dionex ICS-3000 modular Dual Reagent-Free anion ion chromatograph (Dionex Corporation) and an infrared CO_2 analyzer (Horiba Instruments Inc., Spring, TX). The details of the experimental apparatus, procedure, and analytical methods were described by Freeman (2011).

3. Oxidative Degradation

Oxidative degradation experiments for amines spiked with 0.05 mM Cr^{3+}, 0.1 mM Ni^{2+}, 0.4 mM Fe^{2+} and 0.1 mM Mn^{2+} were conducted in a low gas flow agitated reactor with 100 mL/min of a saturated 98%/2% O_2/CO_2 gas mixture fed into the reactor headspace. The duration of the experiment was 1–2 weeks and 3 ml samples were taken every two to three days and water was added periodically to maintain the water balance of the reactor contents. The liquid samples were analyzed for amines, and their degradation products using ion chromatography. The details of the experimental apparatus, procedure, and analytical methods were described by Sexton (2009).

4. Volatility

Amine volatility was measured in a stirred reactor coupled with a hot gas FTIR analyzer (Fourier Transform Infrared Spectroscopy, Temet Gasmet Dx-4000). This was the same method and apparatus used by Nguyen to measure amine volatility and CO_2 partial pressure in loaded solutions (Nguyen, 2011).

5. WWC

CO_2 absorption rate and equilibrium partial pressure in amines were measured from 20 to 100 °C using a wetted wall column (WWC), which countercurrently contacted an aqueous amine solution with a saturated N_2/CO_2 stream on the surface of a stainless steel rod with a known surface area to simulate the situation of CO_2 absorption in an absorber. The detailed description of wetted wall column measurement was given by Li (2013).

Appendix C: Amine Table for Solvent Screening

Table C1: Amine table for solvent screening

No.	Amine	Structure	MW
	Piperidines		
1	4-amino-piperidine	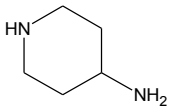	100.16
2	4-aminomethyl-piperidine	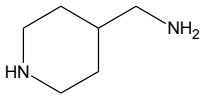	114.19
3	3-aminomethyl-piperidine	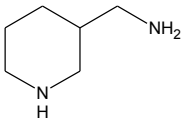	114.19
4	2-aminomethyl-piperidine	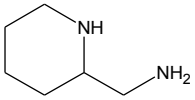	114.19
5	nortropine	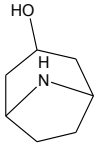	127.18
6	3-quinuclidinol	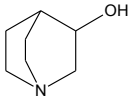	127.18
7	4-hydroxypiperidine	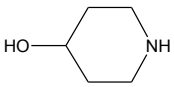	101.15
8	3-hydroxypiperidine	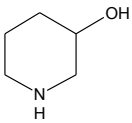	101.15
9	2-piperidinoethanol	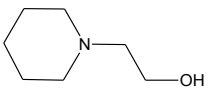	129.2

	Morpholines		
0	3-morpholino-1,2-propanediol	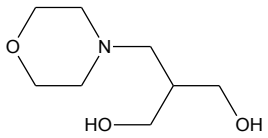	161.20
11	1-(2-hydroxyethyl)morpholine	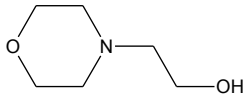	131.17
12	4-(2-aminoethyl)morpholine	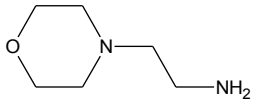	130.19
13	3-(4-morpholinyl)propylamine	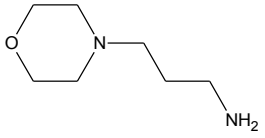	144.22
	Piperazines		
14	1,4-diazabicyclo [2.2.2] octane	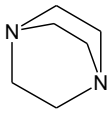	112.18
15	1-ethylpiperazine	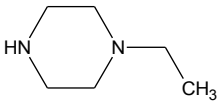	114.19
16	1-(2-hydroxyethyl)piperazine	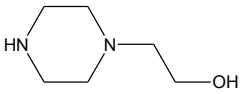	130.19
17	1,4-bis(3-aminopropyl)piperazine	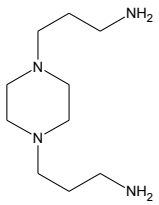	200.32
	Imidazoles		
18	imidazole	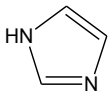	68.08

19	1-methylimidazole	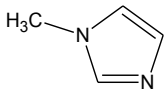	82.1
20	2-methylimidazole	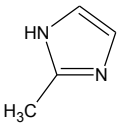	82.1
21	4(5)-methylimidazole	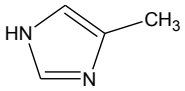	82.1
22	1,2-dimethylimidazole	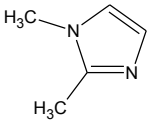	96.13
23	2-ethylimidazole	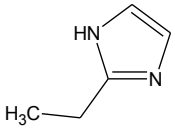	96.13
24	2-ethyl-4-methylimidazole	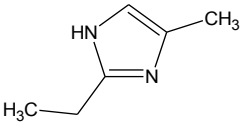	110.16
25	1-(3-aminopropyl)imidazole	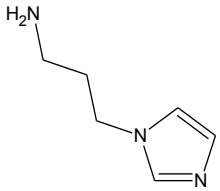	125.17
	Acyclic tertiary and hindered amines		
26	2-amino-2-methyl-1,3-propanediol	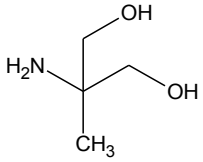	105.14
27	2-amino-2-ethyl-1,3-propanediol	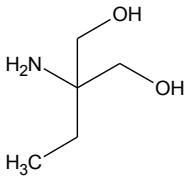	119.16

28	2-amino-1-butanol	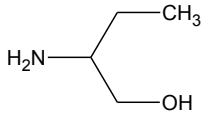	89.14
29	diisopropanolamine	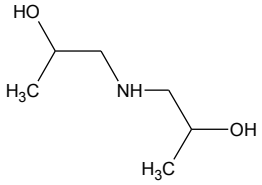	133.19
30	2-(Isopropylamino)ethanol	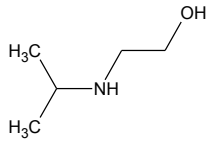	103.16
31	3-(dimethylamino)-1,2-propanediol	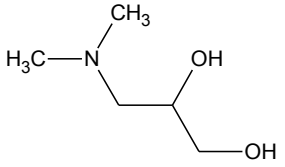	119.16
32	3-diethylamino-1,2-propanediol	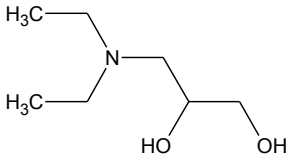	147.22
	Acyclic primary and secondary amines		
33	1,2-bis(2-aminoethoxy)ethane	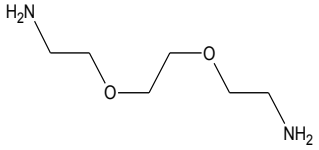	148.20
34	bis(2-methoxyethyl)amine	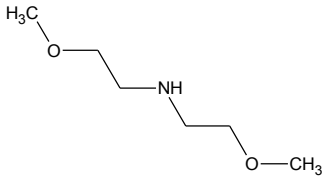	133.19
35	1,1-dimethoxy-2-methylaminoethane	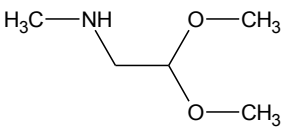	119.16

Appendix D: Preliminary Results

1. Thermal degradation

A thermal degradation screening test was conducted for the PZ-based amine blends (Table C1). The thermal degradation of 6 m PZ/2 m amine with 0.2 mol CO_2/mol alkalinity was measured at 150 °C for 2 weeks. The thermally stable amines (amine loss is less than 10%) are summarized in Table D1.

Table D1: Thermally stable amines

No.	Amine	Structure	MW
	Piperidines		
1	4-amino-piperidine	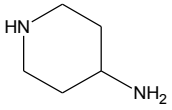	100.16
2	4-aminomethyl-piperidine	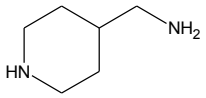	114.19
3	3-aminomethyl-piperidine	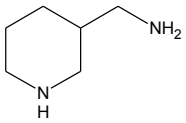	114.19
4	4-hydroxypiperidine	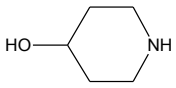	101.15
5	3-hydroxypiperidine	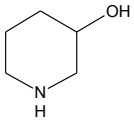	101.15
	Morpholines		
6	1-(2-hydroxyethyl)morpholine	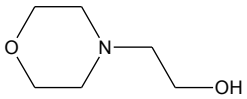	131.17
7	3-(4-morpholinyl)propylamine	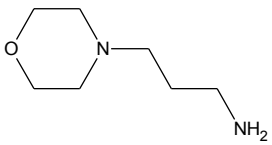	144.22

	Piperazines		
8	1-ethylpiperazine	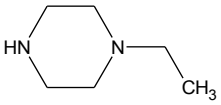	114.19
9	1-(2-hydroxyethyl)piperazine	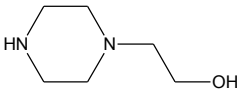	130.19
	Imidazoles		
10	imidazole	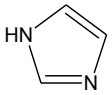	68.08
11	1-methylimidazole	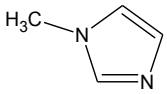	82.1
12	2-methylimidazole	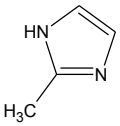	82.1
13	4(5)-methylimidazole	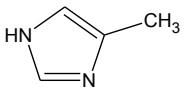	82.1
14	1,2-dimethylimidazole	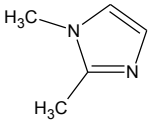	96.13
15	2-ethylimidazole	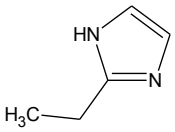	96.13
16	2-ethyl-4-methylimidazole	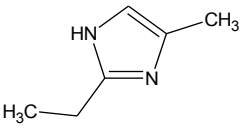	110.16
	Acyclic primary and secondary amines		

17	bis(2-methoxyethyl)amine	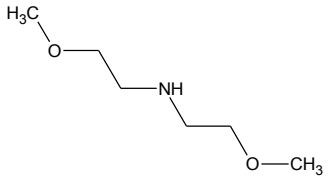	133.19

2. Oxidation

Oxidation of 5 m PZ/5 m 2-ethylimidazole (2E-IMI) at 70 °C in the presence of 0.1 mM Mn^{2+} and the typical SSM mixture (0.4 mM Fe^{2+}, 0.05 mM Cr^{3+}, and 0.1 mM Ni^{2+}), was investigated in the low flow gas apparatus for 2 weeks. The amine loss is shown in Figure D1. It can be seen from Figure D1 that both PZ and 2E-IMI in the blend are resistant to oxidation.

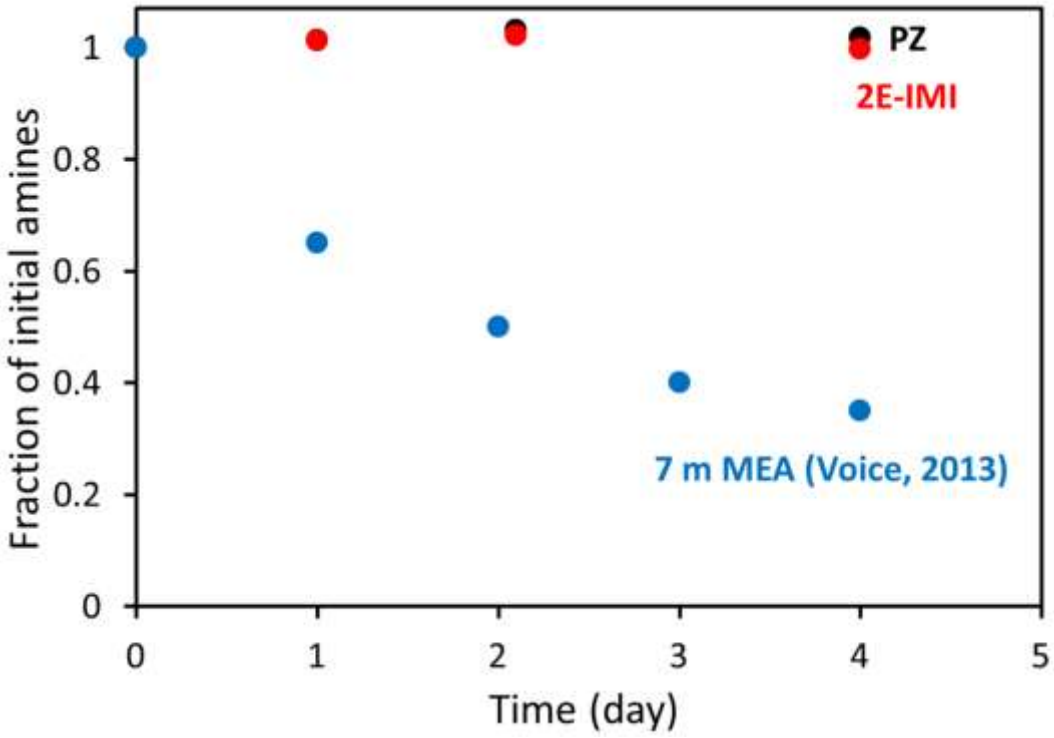

Figure D1: Amine loss for 5 m PZ/5 m 2E-IMI at 70 °C in the presence of O_2, as well as 0.1 mM Mn^{2+}, 0.4 mM Fe^{2+}, 0.05 mM Cr^{3+}, and 0.1 mM Ni^{2+}

3. WWC

The CO_2 solubility in loaded 5 m PZ/5 m 2E-IMI was measured at 40 °C (Figure D2). The CO_2 partial pressure of 8 m PZ is given for comparison. Figure D2 shows that CO_2 partial pressure of 5 m PZ/5 m 2E-IMI at 40 °C is consistently higher than that of 8 m PZ at the same temperature, indicating a

lower CO_2 solubility in 5 m PZ/5 m 2E-IMI. Although CO_2 absorption rate into 5 m PZ/5 m 2E-IMI is higher than 8 m PZ during normal loading range (Figure D3), the working capacity of 5 m PZ/5 m 2E-IMI (0.64 mole per kg amines + water) is 25% lower than that of 8 m PZ (0.86 mole per kg amines + water) (Li et al., 2013). However, as 5 m PZ/5 m 2E-IMI has a much lower viscosity than 8 m PZ, its normalized CO_2 capacity is similar to that of 8 m PZ. The normalized CO_2 capacity and average absorption rate of 5 m PZ/5 m 2E-IMI is shown in Figure D4, with 8 m PZ, 7 m MEA, and 5 m PZ/5 m MDEA as comparison.

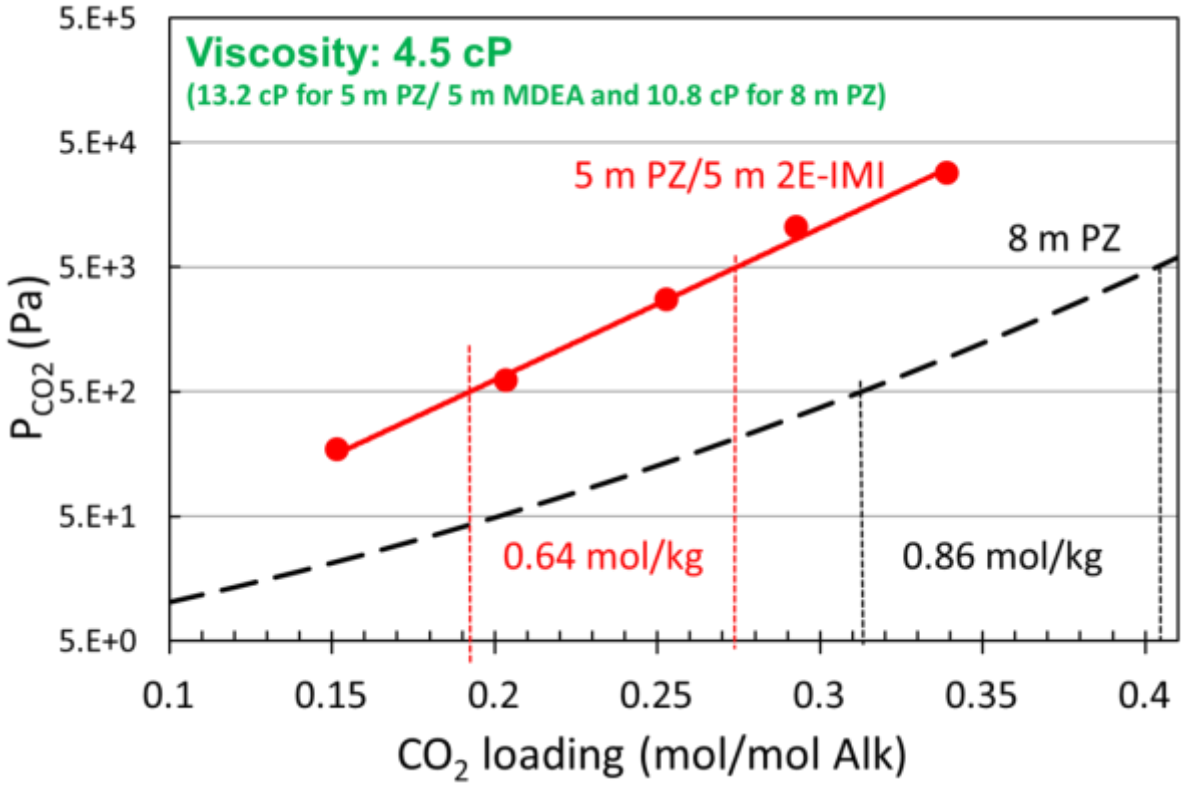

Figure D2: CO_2 solubility for 5 m PZ/5 m 2E-IMI (Dashed lines: 8 m PZ equation model at 40 °C from Xu (2011)).

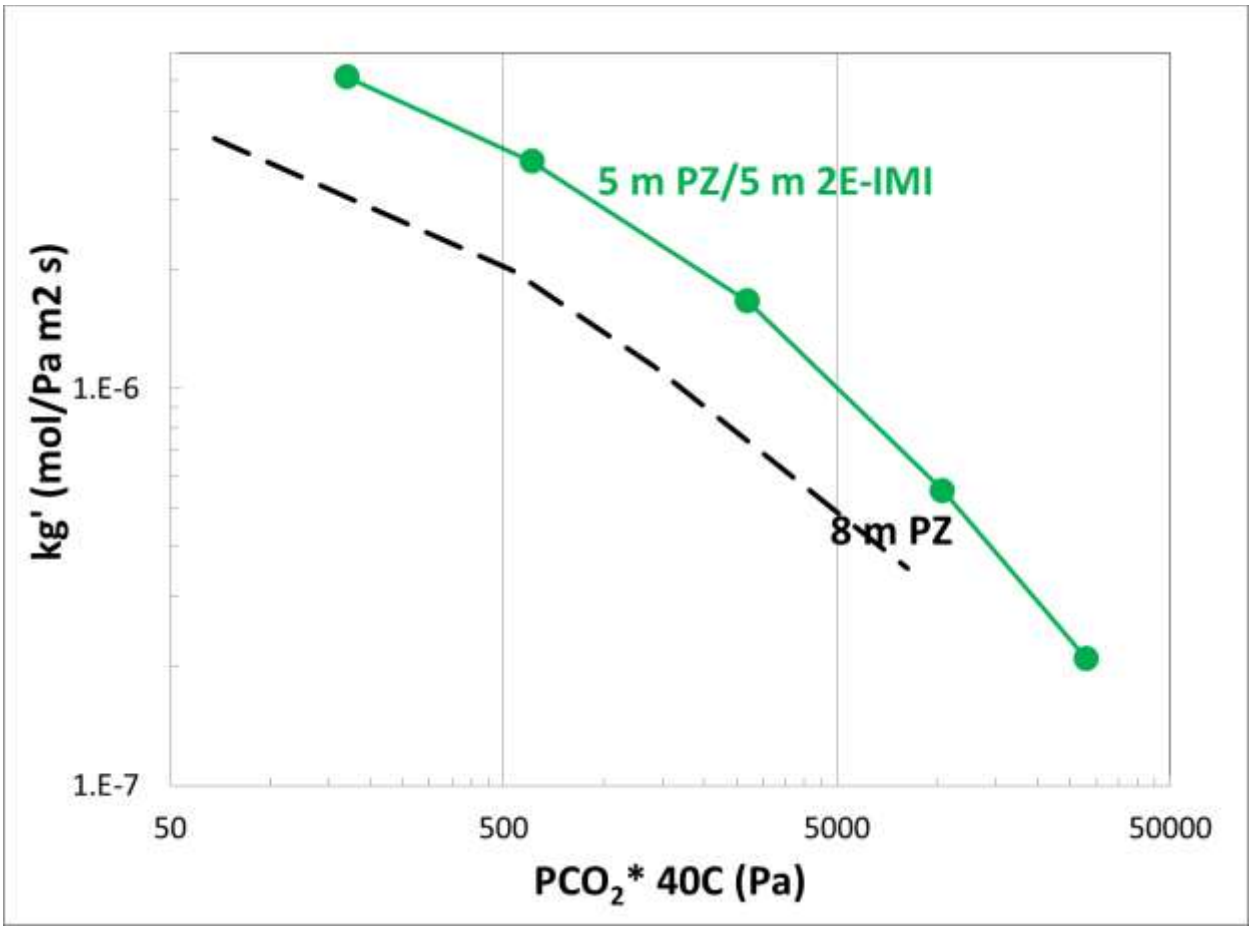

Figure D3: Mass transfer coefficients (kg') in 5 m PZ/5 m 2E-IMI (solid lines) at 40 °C, compared to that in 8 m PZ (dashed line) at 40 °C.

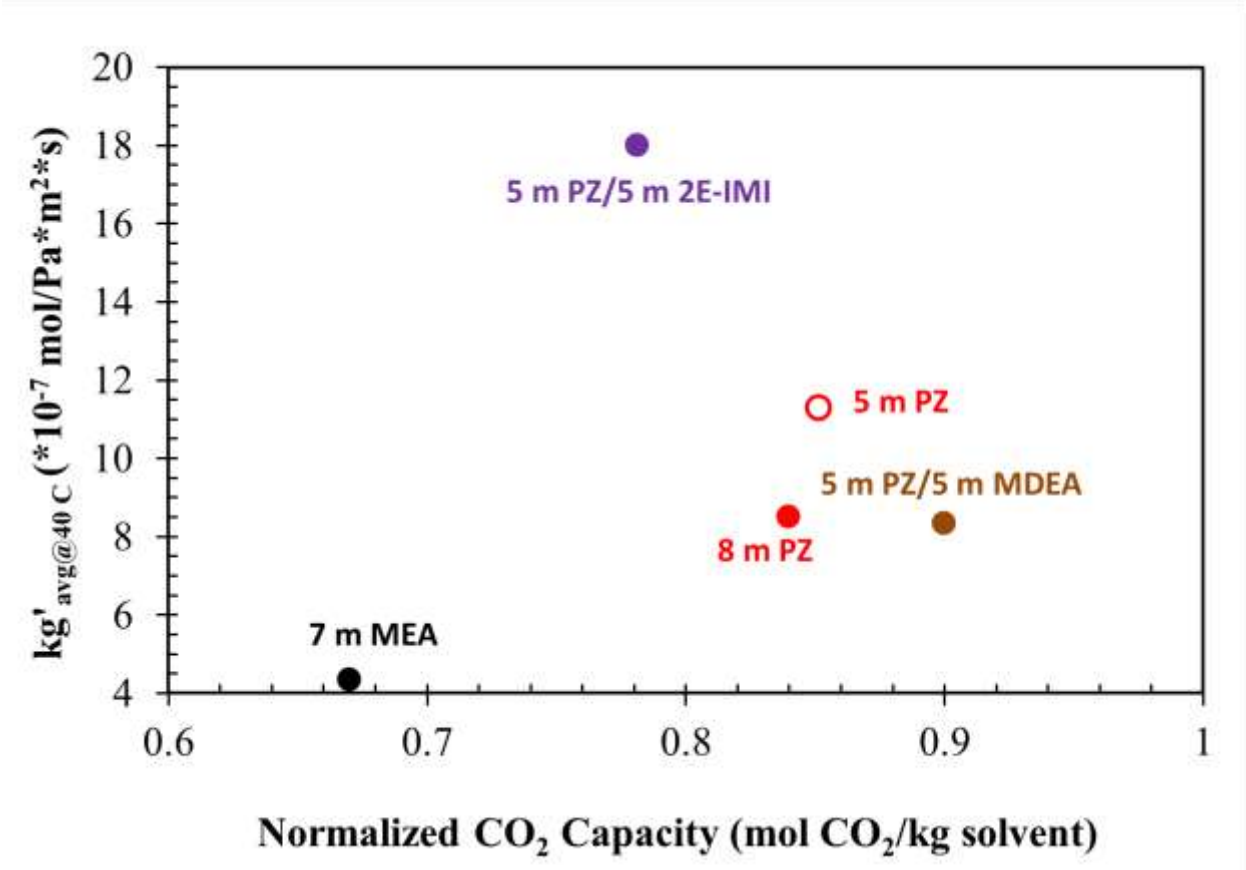

Figure D4: Normalized CO_2 capacity and average mass transfer coefficients (kg') for 5 m PZ/5 m 2E-IMI, compared to other common amines.

CO_2 solubility and mass transfer rates by the wetted wall column

Quarterly Report for July 1 – September 30, 2014

by Le Li

Supported by the Texas Carbon Management Program

McKetta Department of Chemical Engineering

The University of Texas at Austin

October 31, 2014

Abstract

The secondary amine diethanolamine (DEA) was tested as a solvent for CO_2 capture using the wetted wall column (WWC). The concentration of the amine in the solvent was 7 m, so the results are directly comparable to the base case solvent, 7 m monoethanolamine (MEA). The CO_2 absorption rate and solubility in 7 m DEA was measured at 20, 40, 60, and 80 °C. The absorption performance of the solvent in an absorber for coal flue gas is estimated from the mass transfer data. The CO_2 carrying capacity and heat of absorption are calculated from the CO_2 solubility data. The performance of 7 m DEA is then compared to 7 m MEA and other primary unhindered amine solvents. The absorption rate of 7 m DEA at coal flue gas conditions is about 10% higher than that of 7 m MEA. The intrinsic capacity of DEA is double that of MEA. The CO_2 capacity of 7 m DEA is about 60% higher than that of 7 m MEA. The heat of absorption of CO_2 for 7 m DEA is lower or about the same as for 7 m MEA.

Introduction

An aqueous amine solvent using 7 m diethanolamine (DEA) was tested in the wetted wall column during this quarter. The molecular structure of DEA is shown in Figure 1. DEA is a secondary amine with a low pKa of 8.89 at 25 °C. The aim of this work is to understand the effect of primary vs. secondary molecular structure, as well as pKa, on the absorption rate and capacity of CO_2 in the solvent. The CO_2 liquid film mass transfer coefficient and solubility in 7 m DEA was measured at 20, 40, 60, and 80 °C. The average absorption rate of CO_2 in an absorber and the CO_2 capacity of 7 m DEA are estimated from the mass transfer and solubility data. The results of 7 m DEA are compared with 7 m MEA (Dugas, 2009), 7 m monoisopropanolamine (MIPA), and 7 m methylpropanolamine (MPA), to demonstrate the effect of pKa and molecular structure on the performance of the amine as a capture solvent.

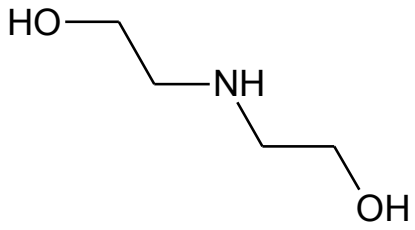

Figure 1: Molecular structure of diethanolamine (DEA)

Experimental Methods

The wetted wall column apparatus and experimental methods are the same as those used by Chen (2011). The current standard operating procedure for the WWC experiment is included in the second quarterly report of 2012 (Rochelle et al, 2012).

Materials

The amine solvents were prepared gravimetrically. To achieve each CO_2 loading, gaseous CO_2 (99.99%, Matheson Tri-Gas) was bubbled into the solvent. The chemicals used in solvent preparation are listed in Table 1.

Table 1: Materials Used for Solvent Preparation

Chemical	Purity	Source
Diethanolamine	99%	Fisher Scientific

Analytical Methods

Liquid samples from each WWC experiment were analyzed for CO_2 content and total alkalinity. The total inorganic carbon (TIC) method was used to measure the total moles of CO_2 per unit mass of liquid sample. For each sample, TIC was performed in triplicate and the average value was reported. The acid titration method was used to determine total alkalinity in each sample, and the reported values are an average of triplicates. The apparatus and method for both TIC and acid titration are identical to those used by Freeman (2011).

Safety considerations

The wetted wall column apparatus is set up in a fully vented hood. At high temperature and pressure operating conditions, the sample collection process could result in projection of hot liquid solvent and must be performed with care. When the apparatus cools from high temperatures, the system must maintain pressure around 5 psi or more to avoid flashing of the liquid solvent. During the experiment, it is important to ensure the gas line remains open at all times to avoid a drastic increase in system pressure.

Results and discussion

Absorption rates

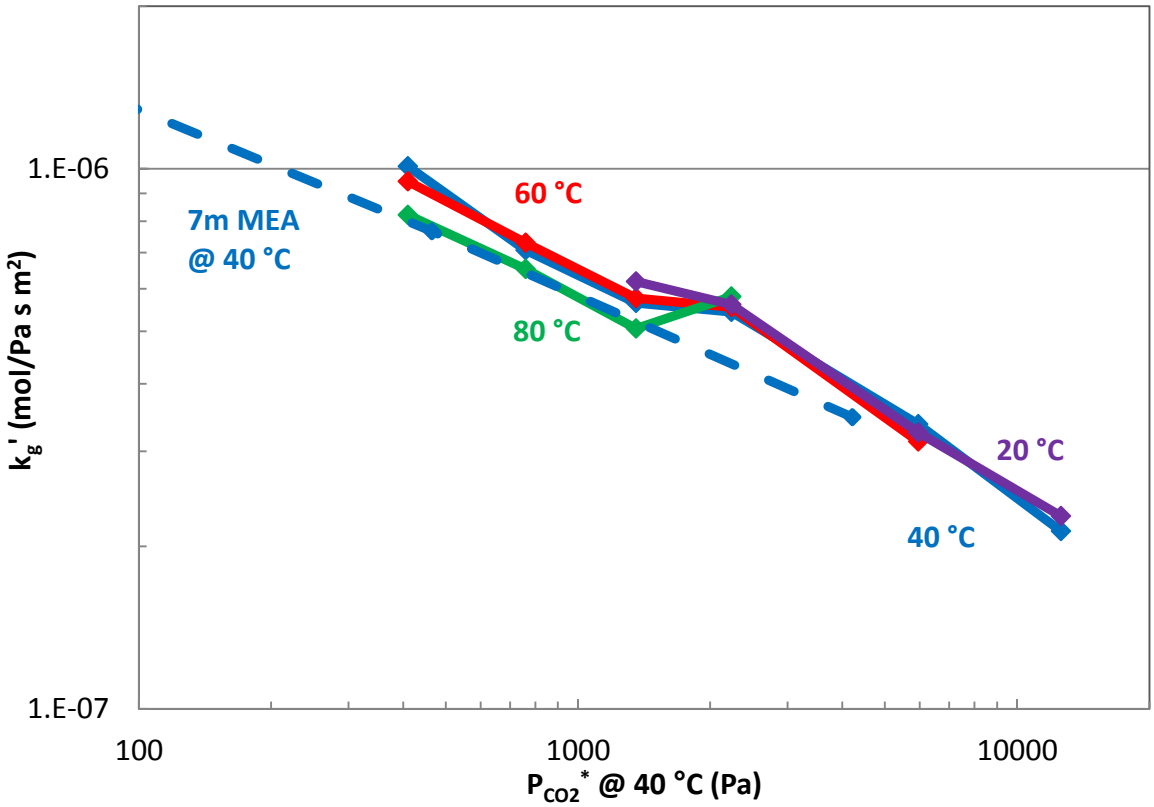

Figure 2: Absorption rate result of 7 m DEA, compared with 7 m MEA at 40 °C (Dugas, 2009).

The liquid film mass transfer coefficient (k_g') of CO_2 into 7 m DEA was measured at 20, 40, 60, and 80 °C, and six different CO_2 loadings in the estimated operating range of a capture plant. The measured result is plotted in Figure 2, and compared with the k_g' of 7 m MEA at 40 °C. The k_g' of 7 m DEA shows little temperature dependence over the entire temperature and CO_2 loading range of the experiment. At 40 °C, 7 m DEA has slightly higher k_g' than 7 m MEA over the range of CO_2 loading tested.

The k_g' at 40 °C for 7 m DEA is compared with other amines in Figure 3. The solvents include 7 m MEA (Dugas, 2009), 10 m Diglycolamine® (DGA®) (Chen, 2011), 7 m methylpropanolamine (MPA), and 7 m monoisopropanolamine (MIPA) (Li, 2013). Also included is a primary hindered amine 4.8 m 2 amino 2 methyl 1 propanol (AMP) (Chen, 2011). The k_g' for 7 m DEA is slightly higher than all primary unhindered amines, and much higher than the hindered amine solvent 4.8 m AMP.

The k_g' at 40 °C measured by the WWC can be used to estimate the performance of the solvent in an absorber. The $k_g'_{avg}$ is calculated using Equation 1, which represents the average absorption rate of CO_2 in an isothermal absorber between the operating lean and rich loadings for coal flue gas (P_{CO2}* at 0.5 and 5 kPa).

$$k'_{g\,avg} = \frac{Flux_{CO_2,LM}}{(P_{CO_2} - P^*_{CO_2})_{LM}} = \frac{(Flux_{CO_2,top} - Flux_{CO_2,bottom})/Ln(Flux_{CO_2,top}/Flux_{CO_2,bottom})}{\left(P_{CO_2,top} - P^*_{CO_2,lean}\right) - \left(P_{CO_2,bottom} - P^*_{CO_2,rich}\right) \Big/ Ln\left(\frac{P_{CO_2,top} - P^*_{CO_2,lean}}{P_{CO_2,bottom} - P^*_{CO_2,rich}}\right)} \quad (1)$$

The calculated $k_{g'avg}$ for 7 m DEA is reported in Table 3, and compared with other solvents.

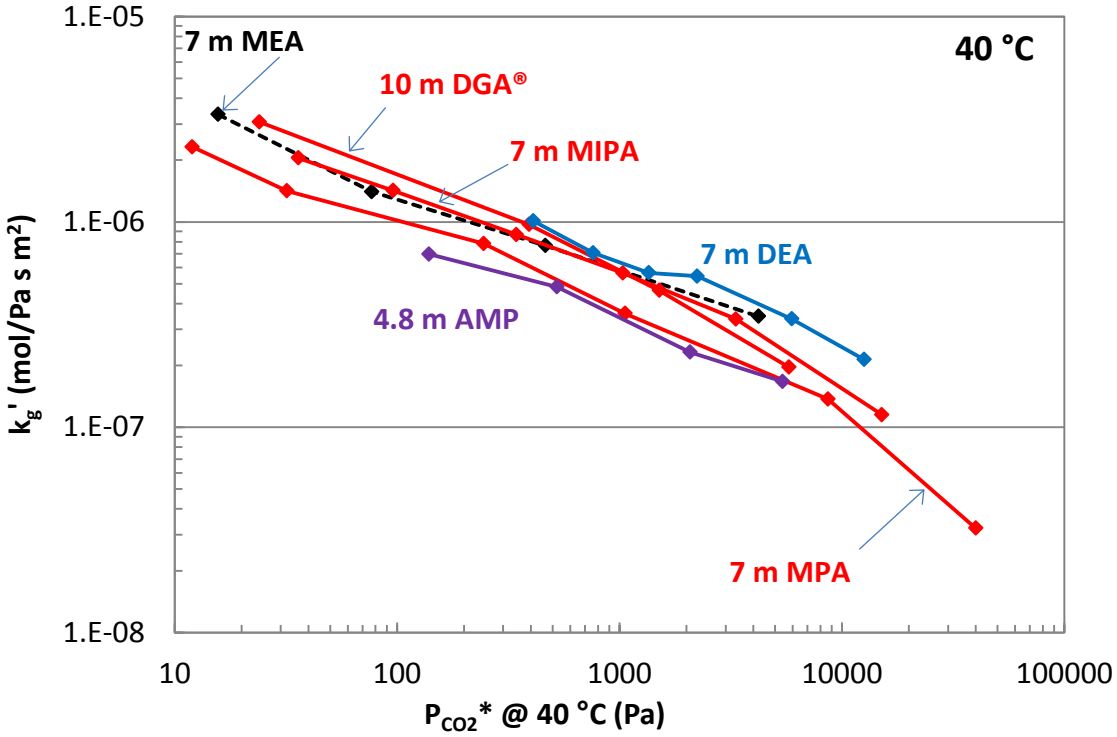

Figure 3: Absorption rate of CO_2 at 40 °C for 7 m DEA and other primary amines

CO_2 solubility

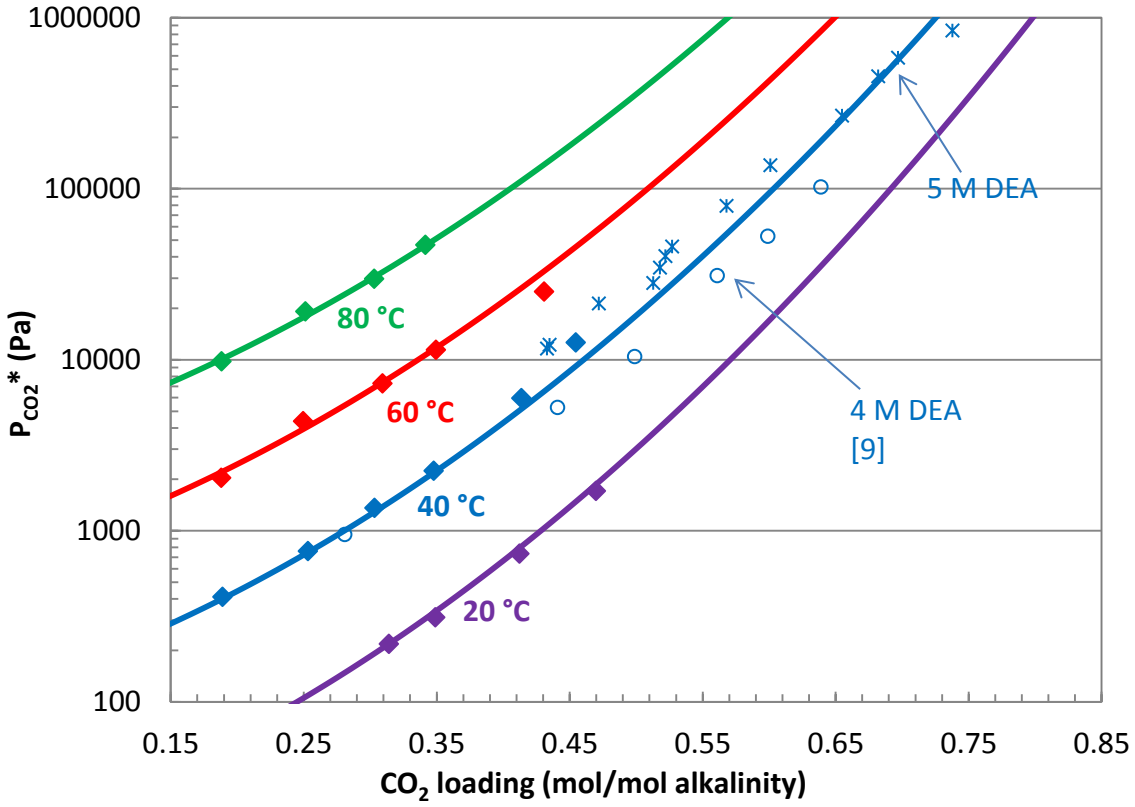

Figure 4: CO_2 solubility of 7 m DEA at 20, 40, 60, and 80 °C. Compared with semi-empirical model (Equation 2, Table 2), data for 4 M DEA (empty circles) and 5 M DEA (asterisks) at 40 °C.

The CO_2 solubility in 7 m DEA was measured in the WWC at 20, 40, 60, and 80 °C. The measured results are plotted in Figure 4. The experimental data was regressed to fit a semi-empirical VLE model, which has the form shown in Equation 2.

$$\ln\left(P^*_{CO_2}\right) = a + \frac{b}{T} + c \cdot \alpha_{CO_2} + d \cdot {\alpha_{CO_2}}^2 + e \cdot \frac{\alpha_{CO_2}}{T} + f \cdot \frac{{\alpha_{CO_2}}^2}{T} \qquad (2)$$

The parameters of Equation 2 are regressed by fitting the experimental data by the WWC. The values of the parameters and the R^2 of the regression are summarized in Table 2. The model shows a good fit to the experimental data, with an R^2 value of 0.995. The data collected using the WWC and the model results are compared with literature values of DEA solvents at similar concentrations. The data for 4 M DEA (Haji-Sulaiman, 1998) and 5 M DEA (Lee, 1972) are plotted in Figure 4. The WWC data and the empirical model result show good agreement with both sets of literature values.

Table 2: Parameter values for the semi-empirical VLE model for 7 m DEA (Equation 2)

Parameter	Value
a	33.5
b	-9046.0
c	5.13
d	0
e	0
f	3236.5
R^2	0.995

Table 3: Summary of performance parameters for 7 m DEA compared with other amines

Amine	Con (m)	$k_g'_{avg}$ @ 40 ˚C x 10^7 mol/Pa s m^2	Capacity mol/kg solv	Δldg mol/mol alkalinity	$-H_{abs}$ @ P_{CO2}^* =1.5 kPa kJ/mol
DEA	7	4.86	0.8	0.2	73
MIPA	7	3.71	0.35	0.08	80
MPA	7	2.52	0.27	0.055	73
MEA	7	4.35	0.5	0.096	73

The CO_2 carrying capacity of the solvent was calculated using experimental VLE data and the semi-empirical model. In Equation 3, it is shown that capacity is calculated as the product of the intrinsic capacity of the amine (Δldg) and the concentration of total alkalinity in solution.

$$\Delta C_{solv} = \frac{\Delta ldg \cdot mol\ alkalinity}{kg\ (amine + H_2O)} \quad (3)$$

The heat of absorption of 7 m DEA can be estimated from the CO_2 VLE data using the semi-empirical model. The thermodynamic definition for heat of absorption can be approximated as the temperature dependence of the gas-liquid equilibrium (Equation 4). The thermodynamic relationship is applied to the semi-empirical VLE model to generate an expression for the heat of absorption of CO_2. In this approximation, the heat of absorption of CO_2 is a function of the CO_2 loading.

$$-\Delta H_{abs} = -R\frac{\partial \ln(P_{CO_2})}{\partial(1/T)} = -R(b + e \cdot \alpha_{CO_2} + f \cdot \alpha_{CO_2}{}^2) \quad (4)$$

The calculated CO_2 capacity and heat of absorption for 7 m DEA are summarized in Table 3, and the results are compared with other solvents. The capacity of 7 m DEA is much higher than the primary unhindered amine solvents at the same total amine concentration. The CO_2 heat of absorption in 7 m DEA is estimated to be lower or similar to the primary amine solvents.

The measured k_g' and CO_2 solubility data are summarized in Table 4. The detailed WWC results are included in the Appendix.

Table 4: P_{CO2}^{*} and k_g' measurement for 7 m DEA

CO_2 loading mol/mol alk	T ˚C	k_g' X 10^{7} mol/Pa s m^2	P_{CO2}* kPa
0.314	20	6.18	0.22
0.349	20	5.61	0.31
0.412	20	3.25	0.73
0.470	20	2.28	1.71
0.189	40	10.10	0.41
0.253	40	7.07	0.76
0.303	40	5.65	1.36
0.348	40	5.44	2.23
0.414	40	3.37	5.95
0.455	40	2.14	12.59
0.188	60	9.48	2.04
0.250	60	7.29	4.35
0.309	60	5.76	7.26
0.349	60	5.54	11.39
0.431	60	3.13	24.97
0.188	80	8.21	9.76
0.251	80	6.53	19.08
0.303	80	5.06	29.64
0.342	80	5.80	46.84

Conclusions

The secondary amine solvent 7 m DEA has competitive CO_2 absorption rates compared with 7 m MEA. The measured CO_2 liquid film mass transfer coefficient (k_g') at coal flue gas condition is about 10% higher than 7 m MEA. The secondary amine DEA has double the intrinsic capacity of MEA. The CO_2 carrying capacity of 7 m DEA is 60% higher than 7 m MEA and other primary unhindered amine solvents. The heat of absorption of CO_2 for 7 m DEA is estimated to be lower than or about the same as 7 m MEA.

Future Work

Two secondary amine solvents are to be tested in the WWC during the next quarter. The CO_2 solubility results measured by the WWC will be used in the simplified speciation model developed in MATLAB to estimate the carbamate stability constant of the amines.

References

Chen X. *Carbon dioxide thermodynamics, kinetics, and mass transfer in aqueous piperazine derivatives and other amines*. The University of Texas at Austin. Ph.D. Dissertation. 2011.

Dugas RE. *Carbon dioxide absorption, desorption, and diffusion in aqueous piperazine and monoethanolamine*. The University of Texas at Austin. Ph.D. Dissertation. 2009.

Freeman SA. *Thermal degradation and oxidation of aqueous piperazine for carbon dioxide capture*. The University of Texas at Austin. Ph.D. Dissertation. 2011.

Haji-Sulaiman MZ, Aroua MK, Benamor A. Aqueous solutions of diethanolamine, methyldiethanolamine and their mixtures using the modified Kent Eisenberg model. *Chem Eng Res Des.* 1998;76 (8):961–968.

Lee JI, Otto FD, Mather AE. Solubility of carbon dioxide in aqueous diethanolamine solutions at high pressures. *J Chem Eng Data.* 1972;7(4):465–468.

Li L, Rochelle GT. CO_2 mass transfer and solubility in aqueous primary and secondary amine. Presented at *GHGT-12*, Austin, Texas, USA, October 5–9, 2014.

Rochelle GT et al. "CO_2 Capture by Aqueous Absorption, Second Quarterly Progress Report 2012." Luminant Carbon Management Program. The University of Texas at Austin. 2012.

Xu Q. *Thermodynamics of CO_2 loaded aqueous amines*. The University of Texas at Austin. Ph.D. Dissertation. 2011.

Appendix

Table A.1. Detailed WWC results for 7 m DEA

DEA	CO_2 ldg	P^*_{CO2}	T	P	Gas_{Dry}	Gas	$P_{CO2in,\ dry}$	$P_{CO2in,\ wet}$	$P_{CO2out,\ dry}$	$P_{CO2out,\ wet}$	CO_2 flux	K_G	k_g	K_G/k_g	k_g'
m	mol/mol	Pa	°C	psig	Std L/min	Std L/min	Pa	Pa	Pa	Pa	mol/s cm^2	mol/s Pa cm^2	mol/s Pa cm^2		mol/s Pa cm^2
7	0.348	2234	40	40	5	5.1	0	0	381	373	-9.8E-08	4.57E-11	2.87E-10	0.159	5.44E-11
							573	562	837	821	-6.8E-08				
							1139	1116	1312	1286	-4.4E-08				
							3341	3275	3175	3113	4.25E-08				
							4434	4347	4095	4014	8.69E-08				
							5550	5441	5022	4924	1.35E-07				
							0	0	381	374	-9.8E-08				
							1136	1114	1296	1271	-4.1E-08				
							3330	3265	3164	3102	4.25E-08				
7	0.349	11386	60	40	5	5.28	0	0	1987	1882	-5.1E-07	4.67E-11	2.98E-10	0.157	5.54E-11
							2251	2132	3778	3578	-3.9E-07				
							3363	3185	4675	4428	-3.4E-07				
							18810	17816	17717	16780	2.8E-07				
							21638	20494	20130	19066	3.86E-07				
							24881	23566	22845	21637	5.21E-07				
7	0.342	46835	80	60	5	5.51	0	0	10437	9477	-2E-06	4.62E-11	2.28E-10	0.203	5.80E-11
							12497	11347	20477	18593	-1.5E-06				
							22537	20464	28046	25466	-1E-06				
							80308	72920	75056	68151	9.85E-07				
							89062	80868	80823	73387	1.54E-06				
							97454	88488	88547	80400	1.67E-06				
7	0.253	760	40	40	5	5.1	0	0	159	156	-4.1E-08	5.67E-11	2.87E-10	0.197	7.07E-11
							253	248	363	356	-2.8E-08				
							419	411	472	463	-1.4E-08				
							1175	1152	1092	1071	2.12E-08				
							1726	1692	1544	1513	4.67E-08				
							2272	2228	1982	1943	7.43E-08				
7	0.250	4354	60	60	5	5.2	0	0	1056	1015	-2E-07	5.45E-11	2.16E-10	0.253	7.29E-11
							1159	1114	1951	1876	-1.5E-07				
							2240	2153	2832	2722	-1.1E-07				
							9639	9266	8485	8157	2.16E-07				
							11997	11533	10195	9800	3.38E-07				
							17352	16680	14160	13612	5.99E-07				

Table A.2. Detailed WWC results for 7 m DEA

DEA	CO_2 ldg	P^*_{CO2}	T	P	Gas_{Dry}	Gas	$P_{CO2in,\ dry}$	$P_{CO2in,\ wet}$	$P_{CO2out,\ dry}$	$P_{CO2out,\ wet}$	CO_2 flux	K_G	k_g	K_G/k_g	k_g'
m	mol/mol	Pa	°C	psig	Std L/min	Std L/min	Pa	Pa	Pa	Pa	mol/s cm^2	mol/s Pa cm^2	mol/s Pa cm^2		mol/s Pa cm^2
7	0.251	19082	80	60	5	5.51	0	0	4279	3885	-8E-07	5.07E-11	2.28E-10	0.223	6.53E-11
							11992	10889	13846	12572	-3.5E-07				
							32948	29917	30889	28047	3.86E-07				
							51896	47122	45563	41371	1.19E-06				
							71565	64981	60032	54509	2.16E-06				
7	0.314	217	20	20	5	5.05	0	0	27	27	-1.1E-08	5.43E-11	4.46E-10	0.122	6.18E-11
							41	41	64	63	-9.2E-09				
							75	75	93	92	-7.2E-09				
							402	398	379	375	9.27E-09				
							514	509	478	473	1.48E-08				
7	0.303	1356	40	40	5	5.1	0	0	234	229	-5.99E-08	4.72E-11	2.87E-10	0.164	5.65E-11
							310	303	486	476	-4.52E-08				
							592	581	718	703	-3.21E-08				
							2272	2228	2117	2076	3.96E-08				
							2544	2494	2370	2324	4.44E-08				
							2856	2801	2604	2553	6.47E-08				
7	0.309	7257	60	60	5	5.2	0	0	1509	1450	-2.8E-07	4.55E-11	2.16E-10	0.211	5.76E-11
							1740	1673	2971	2856	-2.3E-07				
							3419	3287	4289	4123	-1.6E-07				
							11899	11439	11075	10647	1.54E-07				
							14474	13913	13084	12577	2.61E-07				
							17203	16537	15092	14507	3.96E-07				
7	0.303	29640	80	60	5	5.51	0	0	5782	5250	-1.1E-06	4.14E-11	2.28E-10	0.182	5.06E-11
							6524	5924	11637	10566	-9.6E-07				
							12203	11080	15704	14259	-6.6E-07				
							76411	69380	68481	62181	1.49E-06				
							85421	77562	75741	68773	1.81E-06				
							93042	84481	82126	74570	2.05E-06				
7	0.412	732	20	40	5	5.03	0	0	79	79	-2E-08	2.91E-11	2.82E-10	0.103	3.25E-11
							131	130	193	192	-1.6E-08				
							247	245	297	296	-1.3E-08				
							903	897	892	886	2.8E-09				
							1156	1148	1116	1109	1.02E-08				
							1388	1380	1311	1302	1.99E-08				

Table A.3. Detailed WWC data for 7 m DEA

DEA	CO_2 ldg	P^*_{CO2}	T	P	Gas_{Dry}	Gas	$P_{CO2in,\ dry}$	$P_{CO2in,\ wet}$	$P_{CO2out,\ dry}$	$P_{CO2out,\ wet}$	CO_2 flux	K_G	k_g	K_G/k_g	k_g'
m	mol/mol	Pa	°C	psig	Std L/min	Std L/min	Pa	Pa	Pa	Pa	mol/s cm^2	mol/s Pa cm^2	mol/s Pa cm^2		mol/s Pa cm^2
7	0.414	5952	40	40	5	5.1	0	0	709	695	-1.8E-07	3.02E-11	2.87E-10	0.105	3.37E-11
							2828	2772	3118	3057	-7.4E-08				
							5222	5120	5309	5205	-2.2E-08				
							12597	12350	11918	11685	1.74E-07				
							14859	14568	13917	13644	2.41E-07				
							16895	16564	15689	15381	3.09E-07				
7	0.431	24971	60	60	5	5.2	0	0	3429	3296	-6.4E-07	2.73E-11	2.16E-10	0.127	3.13E-11
							6616	6360	9134	8781	-4.7E-07				
							12563	12077	14263	13711	-3.2E-07				
							23067	22174	23428	22521	-6.8E-08				
							42994	41330	40728	39152	4.25E-07				
							62508	60089	57977	55733	8.5E-07				
							81560	78402	74145	71275	1.39E-06				
7	0.470	1705	20	40	5	5.03	0	0	145	144	-3.7E-08	2.11E-11	2.82E-10	0.075	2.28E-11
							306	304	416	414	-2.8E-08				
							581	578	665	661	-2.1E-08				
							2275	2261	2211	2197	1.64E-08				
							2837	2819	2758	2741	2.03E-08				
							3342	3321	3221	3201	3.09E-08				
7	0.455	12591	40	40	5	5.1	0	0	1052	1031	-2.7E-07	1.99E-11	2.87E-10	0.069	2.14E-11
							3695	3623	4366	4281	-1.7E-07				
							6372	6247	6757	6624	-9.8E-08				
							42232	41405	39932	39151	5.89E-07				
							51658	50647	48906	47948	7.05E-07				
							61122	59925	57615	56487	8.98E-07				
7	0.189	410	40	40	5	5.1	0	0	100	98	-2.6E-08	7.50E-11	2.87E-10	0.261	1.01E-10
							127	125	200	196	-1.9E-08				
							238	233	293	288	-1.4E-08				
							689	676	617	605	1.85E-08				
							912	895	782	766	3.35E-08				
							1354	1327	1125	1103	5.84E-08				
7	0.188	2037	60	60	5	5.2	0	0	608	584	-1.1E-07	6.59E-11	2.16E-10	0.306	9.48E-11
							587	564	994	955	-7.6E-08				
							1159	1114	1457	1401	-5.6E-08				
							3960	3806	3460	3326	9.36E-08				
							4516	4341	3841	3692	1.26E-07				
							5530	5316	4521	4346	1.89E-07				

Table A.4. Detailed WWC data for 7 m DEA

DEA	CO_2 ldg	P^*_{CO2}	T	P	Gas_{Dry}	Gas	$P_{CO2in,\ dry}$	$P_{CO2in,\ wet}$	$P_{CO2out,\ dry}$	$P_{CO2out,\ wet}$	CO_2 flux	K_G	k_g	K_G/k_g	k_g'
m	mol/mol	Pa	°C	psig	Std L/min	Std L/min	Pa	Pa	Pa	Pa	mol/s cm^2	mol/s Pa cm^2	mol/s Pa cm^2		mol/s Pa cm^2
7	0.188	9760	80	60	5	5.2	0	0	2430	2207	-4.6E-07	6.04E-11	2.28E-10	0.265	8.21E-11
							4444	4035	6184	5615	-3.3E-07				
							7729	7018	8619	7826	-1.7E-07				
							22547	20473	19715	17901	5.31E-07				
							27490	24961	23423	21268	7.63E-07				
							33103	30057	27130	24634	1.12E-06				

Absorber Intercooling Evaluation

Quarterly Report for July 1 – September 30, 2014

by Darshan Sachde

Supported by the Texas Carbon Management Program

McKetta Department of Chemical Engineering

The University of Texas at Austin

October 31, 2014

Abstract

The evaluation of intercooling benefits (solvent capacity and packing) was completed and summarized in the GHGT manuscript attached to this report. Three flue gas sources were included for the evaluation with 8 m PZ: natural gas combined cycle (NGCC, 4.1% CO_2), coal-fired boiler (13.5% CO_2), and steel blast furnace (27.4% CO_2). As an extension to the intercooling evaluation work, a shortcut method using an energy balance around the absorber was developed to predict the lean loading for each flue gas application where a temperature-related mass transfer pinch becomes limiting and intercooling is necessary to achieve maximum solvent capacity. The new method consistently over-predicts the pinch formation point, but provides a reasonable approximation of lean loading where maximum intercooling benefit could be achieved (within ~10% for all flue gas applications). The method only requires the use of a thermodynamic model for flash calculations and eliminates the need for the rigorous rate-based modeling to identify conditions for maximum intercooling benefit.

Introduction

Previous work used the minimum solvent rate (or maximum rich loading) to evaluate potential benefits of intercooling for a wide range of lean loading for three CO_2 flue gas feed concentrations representative of potential capture applications (NGCC, coal-fired boiler, steel blast furnace). The analysis isolated conditions where intercooling could provide capacity (energy performance) benefits. The current work expands on the previous analysis by developing a shortcut method to estimate the operating condition (lean loading) where a capacity-limiting, temperature-related mass transfer pinch forms. The development of a simplified method should allow a quick assessment of when intercooling is required for a given flue gas application and preferred lean loading operating condition. This method should eliminate the requirement of a rigorous rate-based model and the extensive number of cases required in the previous L_{MIN} analysis.

Shortcut Method for Evaluating Solvent Capacity Benefits of Intercooling

In previous work, the minimum solvent flow rate (L_{MIN}) was used to assess potential benefits of intercooling configurations (Rochelle et al., 2014a). L_{MIN} for any absorption process can be defined as the solvent rate required to achieve a specific solute removal (or specific gas inlet and outlet compositions) for a given inlet solvent composition (loading) with infinite mass transfer area available. L_{MIN} also corresponds to the maximum rich loading (maximum solvent capacity)

achievable and serves as a proxy for the best energy performance that can be achieved with the design and operating conditions of a given absorber

For each operating condition, an isothermal absorber represents the best possible performance (lowest L_{MIN}) and an adiabatic (no intercooling) absorber represents the worst case performance (highest L_{MIN}). Intercooled absorbers will fall between these limiting cases. The ratio of the adiabatic L_{MIN} to the isothermal L_{MIN} at each condition can serve as a screening tool for the conditions where intercooling will be beneficial for energy performance. High values of the preceding ratio indicate large potential benefits of intercooling. A ratio equal to (or approaching) unity indicates that the benefits of intercooling are negligible or non-existent. Figure 1 summarizes the L_{MIN} results for the coal-fired boiler case.

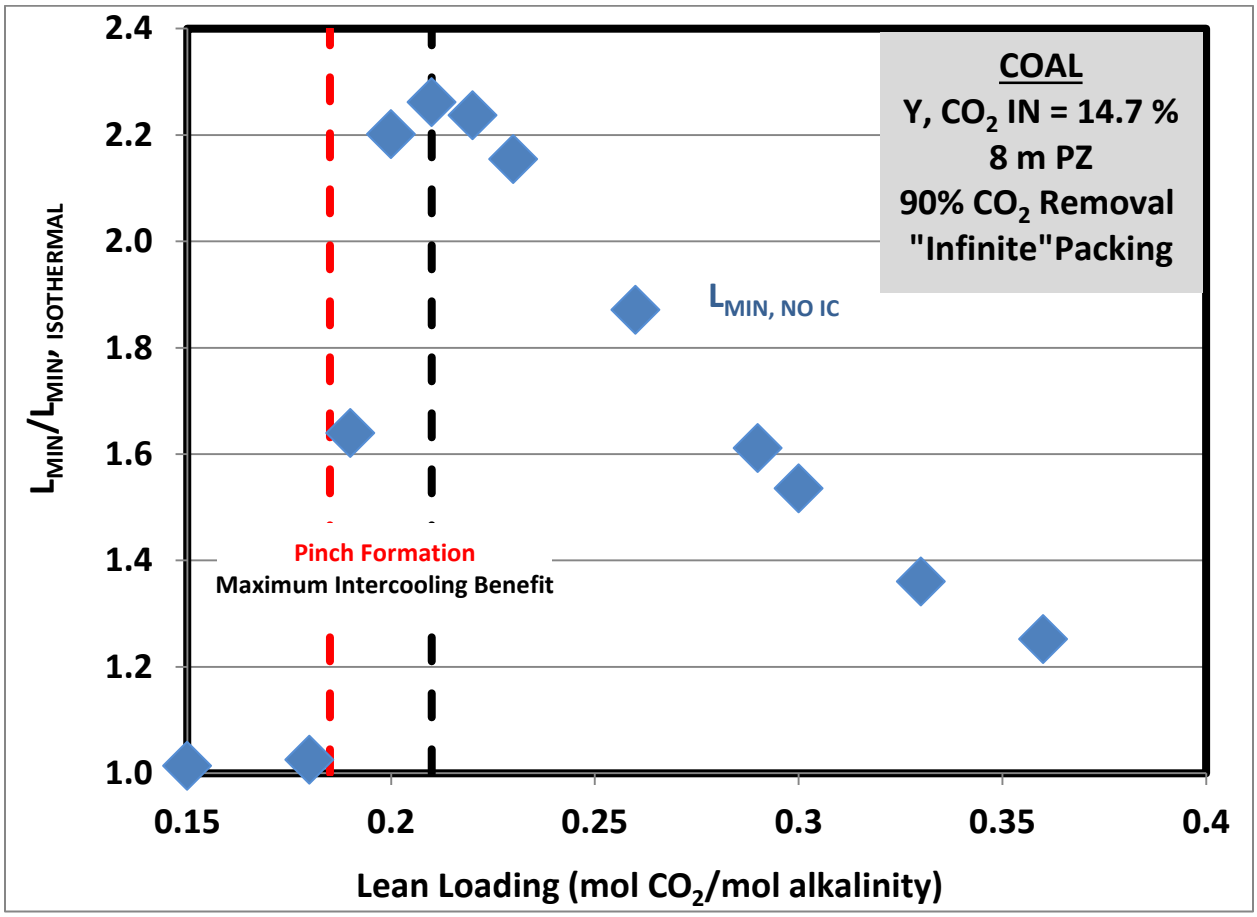

Figure 1: Ratio of the minimum solvent rate ("infinite" packing) for an adiabatic absorber (no intercooling) to an isothermal absorber (40 °C) for 90% CO_2 capture from a coal-fired boiler (13.5% CO_2) using 8 m PZ. Lean loadings for the transition to a temperature-related pinch (- - -) and the maximum deviation from isothermal performance (- - -) are identified.

The figure also identifies the lean loading where a temperature-related pinch forms (~ 0.18 mol CO_2/mol alkalinity) and the lean loading where the maximum deviation from isothermal performance occurs (~0.21 mol CO_2/mol alkalinity). The formation of the pinch and the

transition to significant deviation from isothermal behavior were described in detail in previous work (Rochelle et al., 2014b). These loadings represent important points for absorber design for a given flue gas application. The formation of a temperature-related pinch marks the onset of solvent capacity penalties if intercooling is not implemented in an absorber design and the maximum identifies where this penalty will be most severe. Therefore, if a loading in this range can be approximated for each flue gas application, a decision regarding intercooling implementation can be made quickly without performing the full analysis used to generate Figure 1.

The goal of the shortcut method is to estimate a lean loading to represent the transition region represented in Figure 1. The method requires a relationship between the lean loading and the conditions at the mass transfer pinch (temperature, loading, and gas composition at the pinch). Several observations during the L_{MIN} analysis allow assumptions to develop the relationship between the lean loading and pinch conditions.

First, the temperature-related mass transfer pinch, which signifies the transition in Figure 1, occurs at the maximum temperature in the column. Therefore, the first step in developing a shortcut method requires estimation of the maximum temperature. Figure 2 provides information regarding inlet, outlet, and maximum temperatures in the column as a function of lean loading alongside the trend in the L_{MIN} ratio.

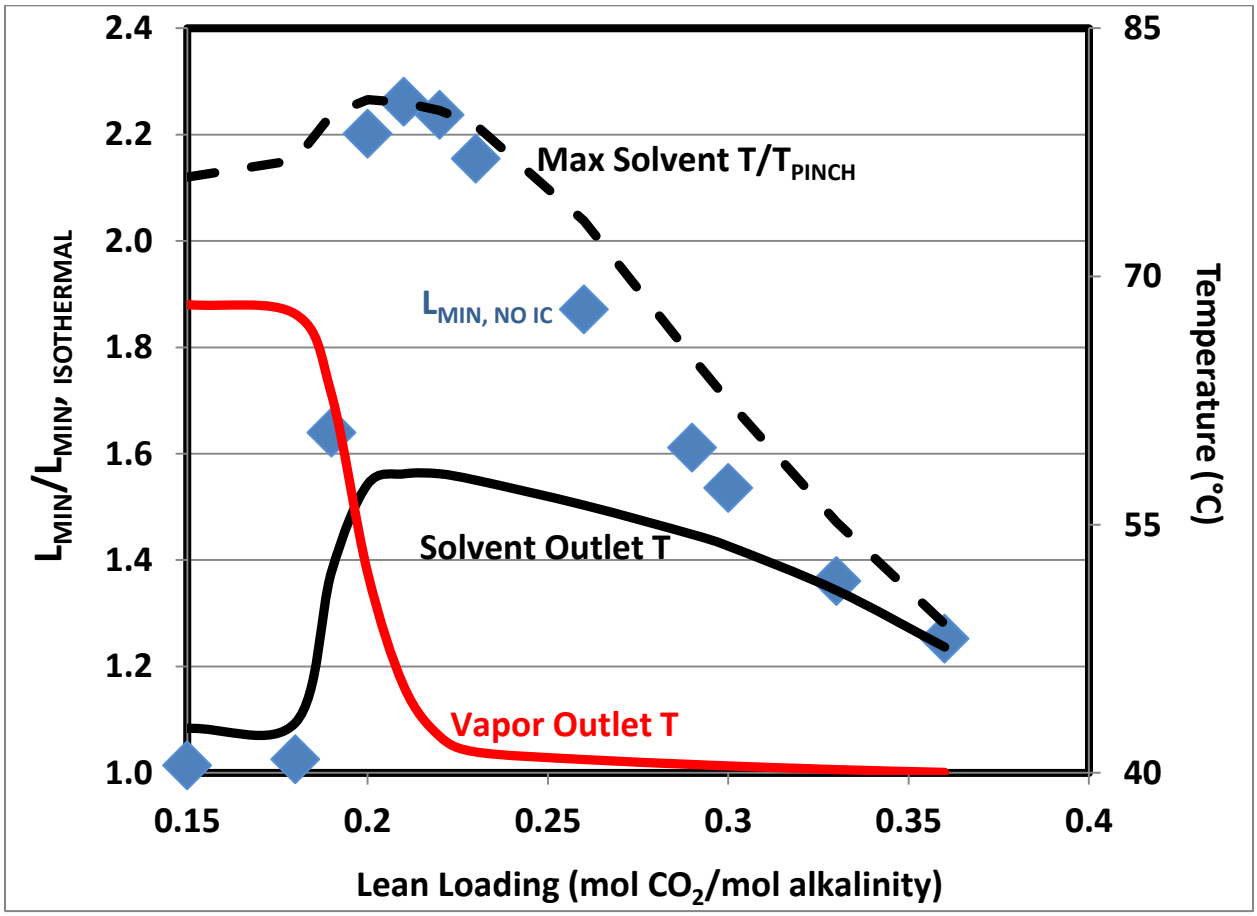

Figure 2: Ratio of the minimum solvent rate ("infinite" packing) for an adiabatic absorber (no intercooling) to an isothermal absorber (40 °C) for 90% CO_2 capture from a coal-fired boiler (13.5% CO_2) using 8 m PZ. Vapor outlet (solid red), solvent outlet (solid black), and maximum column temperature (dashed black) are shown to explain trends in the L_{MIN} ratio.

The temperature plot reveals that prior to the formation of a lean end temperature-related pinch (< 0.19 mol CO_2/mol alkalinity), the vapor temperature leaving the column is significantly higher than the solvent temperature leaving the column. In other words, the gas is carrying a majority of the heat generated by CO_2 absorption out of the top of the column. This is supported by the observation that the total gas heat capacity (including capacity to carry water) is much higher than the solvent heat capacity in this lean region. As the lean end pinch forms, the solvent rate is increased significantly to overcome the pinch and achieve 90% CO_2 removal. This is reflected in the crossover of the solvent outlet and vapor outlet temperatures. The solvent carries an increasingly large portion of the heat and eventually begins to wash the heat out of the column and moderate the temperature effect.

The important approximation for the shortcut method is that the gas carries all of the heat generated by CO_2 when operating near the lean loading where the temperature-related pinch forms. This allows estimation of the maximum temperature achieved near the lean end pinch conditions using only one phase. An energy balance (Equation 1) around an adiabatic absorber was used as the starting point to estimate the pinch (or maximum) temperature.

$$\begin{aligned} &N_{Gas,OUT}\widetilde{C}_{P,GAS,OUT}\left(T_{GAS,OUT}-T_{REF}\right)-N_{Gas,IN}\widetilde{C}_{P,GAS,IN}\left(T_{GAS,IN}-T_{REF}\right)\\ &\quad+\Delta N_{H2O,GAS}\Delta H_{VAP,T_{REF}}+\Delta N_{CO2,GAS}\Delta H_{ABS,T_{REF}}\\ &\quad=N_{Solvent,IN}\widetilde{C}_{P,Solvent,IN}\left(T_{Solvent,IN}-T_{REF}\right)\\ &\quad-N_{Solvent,OUT}\widetilde{C}_{P,Solvent,OUT}\left(T_{Solvent,OUT}-T_{REF}\right) \end{aligned} \tag{1}$$

where:

N = Molar flow rate of given phase (gas or solvent) (kmol/s);
C_P = Molar heat capacity of given phase (kJ/kmol-K);
T = Temperature of given phase (gas or solvent) (K);
T_{REF} = Reference temperature to allow integration sensible heat (K);
ΔH_{VAP} = Heat of vaporization of water at T_{REF} (kJ/kmol);
ΔH_{ABS} = Average heat of absorption of CO_2 at T_{REF} (kJ/kmol).

The steady-state enthalpy balance in Equation 1 requires detailed information regarding both phases at the lean loading conditions discussed previously. However, several steps can be taken to simplify the energy balance:

1) Assign a reference temperature that is equal to the inlet temperatures of the gas and solvent ($T_{REFERENCE}$ = $T_{SOLVENT,\ IN}$ = $T_{GAS,\ IN}$ = 40 °C). This eliminates the inlet enthalpy contributions from the energy balance in Equation1.
2) Assume the gas carries all the heat generated by CO_2 absorption. Therefore, the outlet solvent temperature is equal to the inlet solvent temperature ($T_{REFERENCE}$ = $T_{SOLVENT,\ IN}$ = $T_{SOLVENT,\ OUT}$ = 40 °C). The outlet enthalpy contribution from the energy balance is eliminated, and the liquid phase has been completely eliminated from the energy balance.

Equation 2 provides the simplified energy balance that results from applying the preceding assumptions.

$$N_{Gas,OUT}\widetilde{C}_{P,GAS,OUT}\left(T_{GAS,OUT}-T_{REF}\right)+\Delta N_{H2O,GAS}\Delta H_{VAP,T_{REF}}+\Delta N_{CO2,GAS}\Delta H_{ABS,T_{REF}}=0 \quad (2)$$

The remaining unknowns in Equation 2 are the CO_2 and water transfer contributions to the energy balance. Additional assumptions are required to estimate these quantities.

First, for all three flue gas applications, the formation of the temperature-related pinch occurred near the lean end of the column. In other words, a majority of the CO_2 removal occurred below the pinch. Table 1 includes the lean loading where the temperature-related pinch forms for each application, the loading at the mass transfer pinch, and the removal above the pinch.

Table 1: Lean End Pinch Evaluation

Flue Gas Source	**Lean Loading: Pinch Formation** mols CO_2/mols alk.	**Loading at Mass Transfer Pinch**	**Portion of CO_2 Removal Above Pinch**
Natural Gas Combined Cycle (NGCC)	0.22	0.221	0.69%
Coal-Fired Boiler	0.19	0.194	3%
Steel Blast Furnace	0.18	0.187	5.3%

From the data in Table 1, it is apparent that the temperature-related end pinch occurs essentially at the inlet loading of the column (minimal removal above pinch). The energy balance is simplified by assuming the column is pinched at the solvent inlet condition (lean loading = loading at the pinch) and that all CO_2 removal (90% removal) has occurred below the pinch.

Finally, the CO_2 mass transfer pinch coincides with a mass transfer pinch for H_2O. By assuming the solvent is in equilibrium with water at the lean inlet conditions, the water balance component of the energy balance in Equation 2 can be approximated. An iterative approach can now be implemented to estimate the temperature at the pinch and the loading at the pinch:

1) Guess a maximum temperature (pinch temperature), assume 90% CO_2 removal ($T_{INITIAL}$).
2) Solve the energy balance in Equation 2 for the water transferred and estimate the composition of water in the exiting gas. Perform a flash calculation to estimate the lean loading required to achieve equilibrium to the water content in the exiting gas at the maximum temperature from step 1.
3) Perform a flash calculation to estimate a new maximum temperature (T_{FINAL}) required to achieve equilibrium to CO_2 in the exiting gas at the lean loading from step 3.
4) Use the new temperature estimate to iterate over steps 1 through 3 until the $T_{INITIAL}$ = T_{FINAL}.

This process yields the temperature and lean loading that represents the transition lean loading range in Figure 1. Figures 3–5 superimpose the loading estimates from the shortcut method over the full L_{MIN} analysis for each of the three flue gas applications.

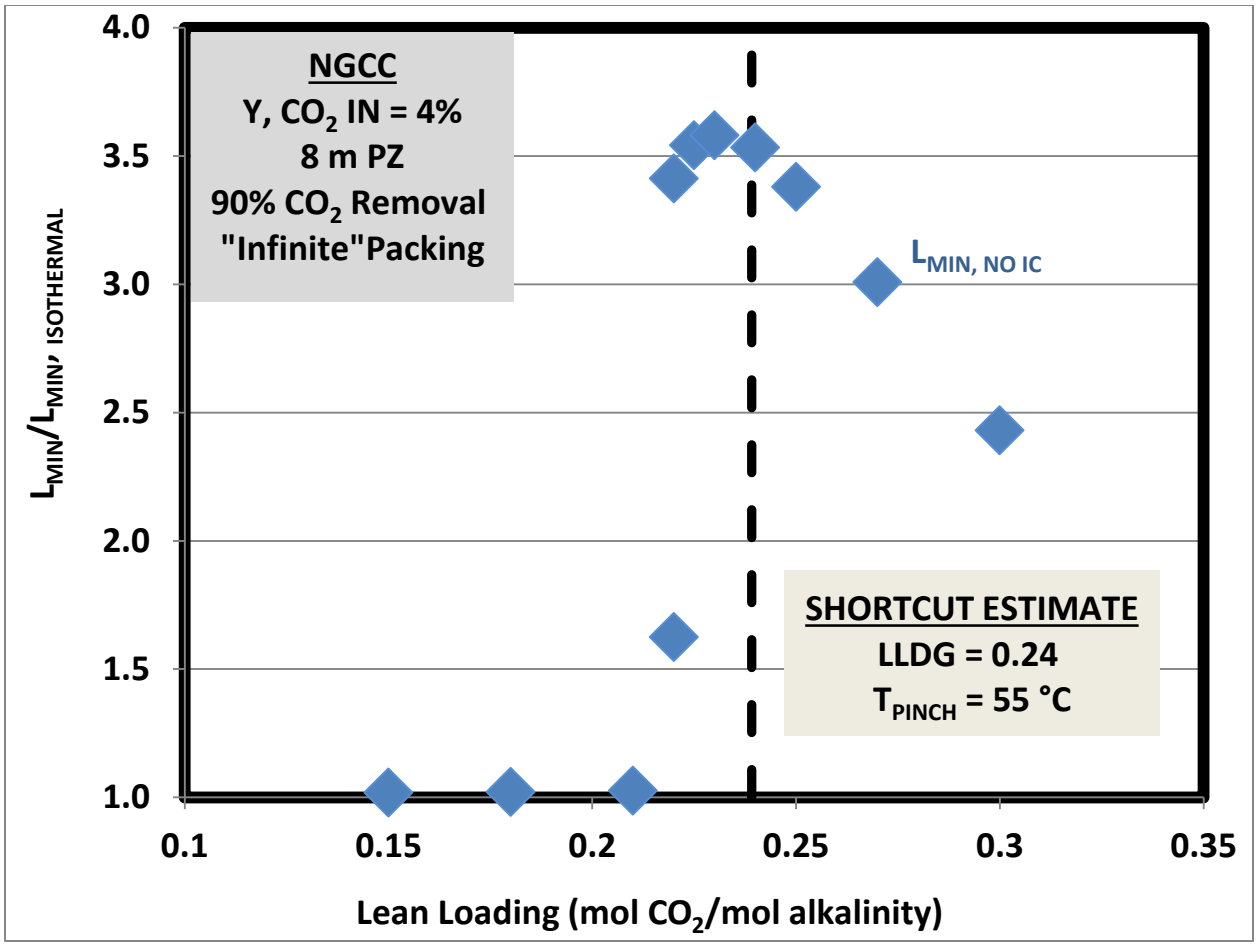

Figure 3: Ratio of the minimum solvent rate ("infinite" packing) for an adiabatic absorber (no intercooling) to an isothermal absorber (40 °C) for 90% CO_2 capture from a natural gas combined cycle turbine (4.1% CO_2) using 8 m PZ. The lean loading approximation for the transition to a temperature-related pinch and the maximum deviation from isothermal performance is identified by the dashed line.

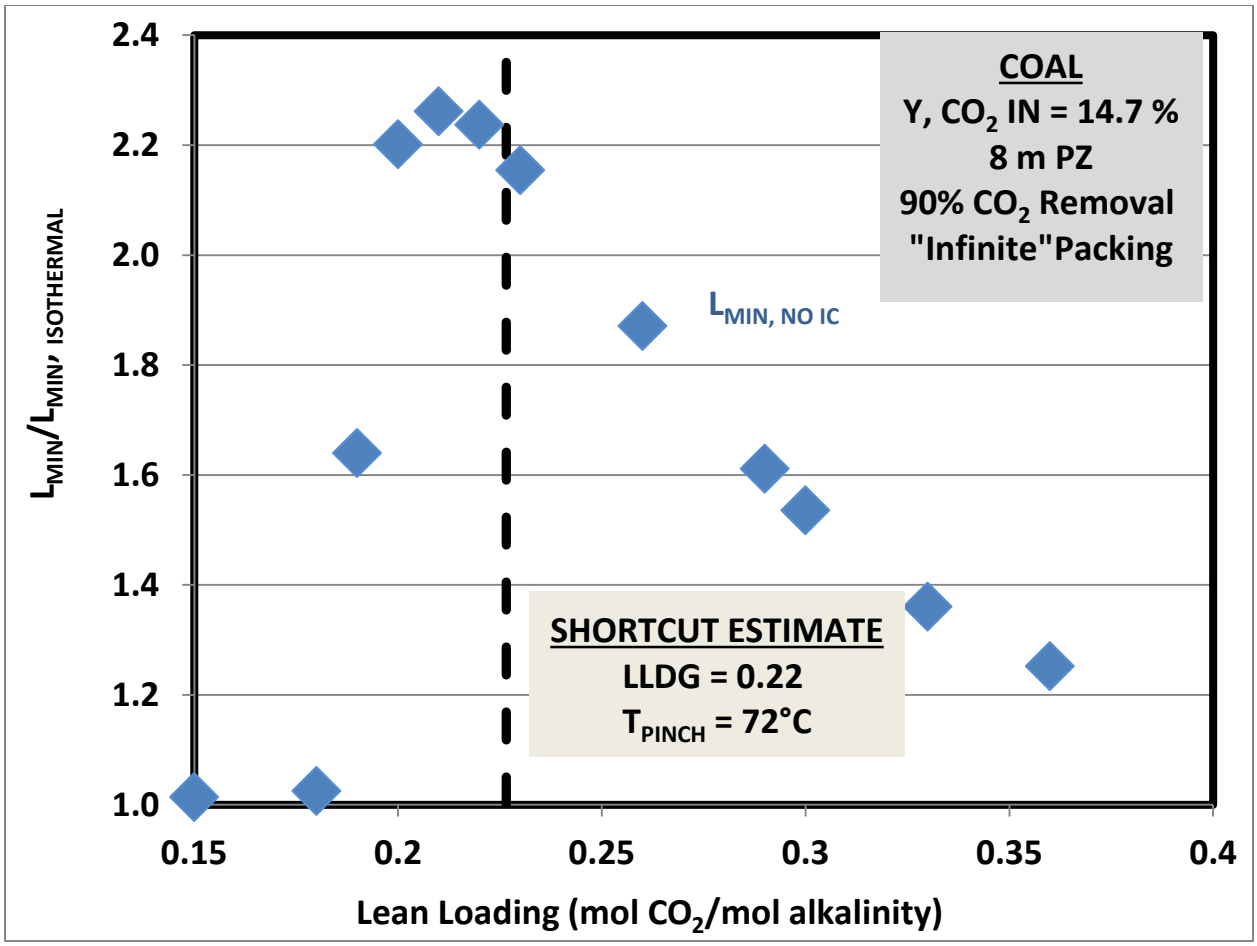

Figure 4: Ratio of the minimum solvent rate ("infinite" packing) for an adiabatic absorber (no intercooling) to an isothermal absorber (40 °C) for 90% CO_2 capture from a coal-fired boiler (13.5% CO_2) using 8 m PZ. The lean loading approximation for the transition to a temperature-related pinch and the maximum deviation from isothermal performance is identified by the dashed line.

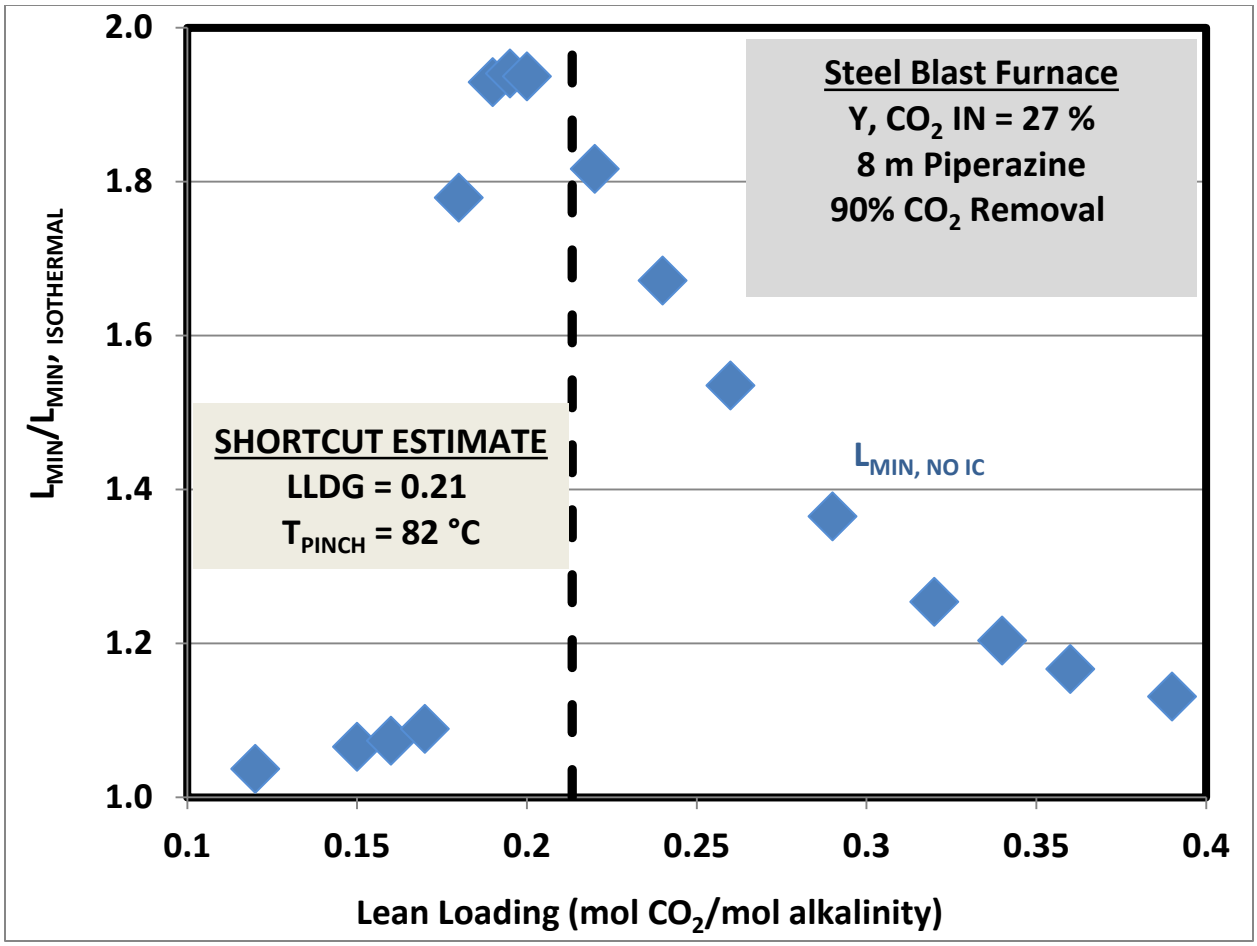

Figure 5: Ratio of the minimum solvent rate ("infinite" packing) for an adiabatic absorber (no intercooling) to an isothermal absorber (40 °C) for 90% CO_2 capture from a steel blast furnace (27% CO_2) using 8 m PZ. The lean loading approximation for the transition to a temperature-related pinch and the maximum deviation from isothermal performance is identified by the dashed line.

Each of the figures indicates that the shortcut method consistently overestimates the transition lean loading where a lean end pinch forms. The method is not a perfect approximation of this condition primarily due to the assumption that the maximum temperature can be estimated by letting the gas carry all of the heat out of the column. Figure 2 clearly shows that while gas does carry a majority of the heat, it is not a close approximation to the maximum temperature in the column. This is due to the fact that the solvent is carrying or "trapping" some of the heat in the column, and creates a temperature maxima in the interior of the column. To rigorously approximate the maximum temperature, the solvent side of the energy balance is required. This complication is not suitable for a simple or approximate shortcut approach.

However, the shortcut loading does provide a reasonable estimate of the maximum potential benefit of intercooling (within ~10% for all cases) and is a good indicator of the loading range where intercooling is required to avoid significant energy penalties of poor solvent capacity. This estimate is developed by using only a simple energy balance and flash calculations (thermodynamic model). Rate-based calculations were not required (as in the full L_{MIN} analysis),

thus significantly simplifying calculation and providing a quick method to determine if intercooling is required for a selected lean loading.

Conclusions

The use of an energy balance around an adiabatic (no intercooling) absorber and several simple assumptions regarding the formation of a temperature-related lean end pinch allows the estimation of the lean loading for each flue gas application where intercooling is critical to achieve maximum solvent capacity. For each flue gas application, the shortcut method over-estimated the lean loading where a capacity limiting pinch formed, but provided a reasonable estimate of the loading where maximum capacity benefits could be obtained from intercooling (within ~10% of actual loading). The predicted loadings from the shortcut method can be compared to the actual lean loading for maximum benefit for each flue gas application:

- NGCC: Actual = 0.23 vs. Predicted = 0.239
- Coal: Actual = 0.21 vs. Predicted = 0.227
- Coal: Actual = 0.195 vs. Predicted = 0.213.

The approach only requires a simplified energy balance and a thermodynamic model for flash calculations.

Future Work

The shortcut method developed in this work will be investigated further to provide better estimation of the transition loading for each flue gas application. In addition, sensitivity analyses to determine controlling mass transfer resistance for each flue gas application will be developed. The analysis will include evaluation of the controlling resistance as a function of position in the absorber column (i.e., function of loading). Finally, the results of the intercooling benefits analysis and mass transfer sensitivity analysis will be used to propose absorber configurations for detailed economic analysis.

Safety

One of the primary safety issues associated with the absorber unit operation in an amine scrubbing facility is exposure to the amine. One method for reducing the overall risk of amine exposure is to reduce overall solvent inventory in the system. This analysis continued the evaluation of potential solvent capacity benefits of intercooling in the absorber. At conditions where intercooling may significantly improve solvent capacity (reduce the solvent circulation rate), a secondary benefit is a potentially significant reduction of the overall solvent inventory in the system.

References

Rochelle GT et al. "CO_2 Capture by Aqueous Absorption, First Quarterly Progress Report 2014." Texas Carbon Management Program. The University of Texas at Austin. 2014a.

Rochelle GT et al. "CO_2 Capture by Aqueous Absorption, Fourth Quarterly Progress Report 2013." Texas Carbon Management Program. The University of Texas at Austin. 2014b.

Modeling and Optimization of Advanced Stripper Configurations

Quarterly Report for July 1 – September 30, 2014

by Yu-Jeng Lin

Supported by the Texas Carbon Management Program

McKetta Department of Chemical Engineering

The University of Texas at Austin

October 31, 2014

Abstract

The work done in this quarter was prepared as a paper manuscript and is in the Attachments to this report. The objective of this work is to identity inefficiencies and improve the process accordingly. The regeneration process and the compressor train were simulated in Aspen Plus®. The lost work of each unit operation was quantified by the exergy balance. The results showed that the two major sources of lost work for the simple stripper are the lean/rich solvent cross exchanger and overhead condenser. The advanced flash stripper was proposed to reduce the lost work of the condenser by recovering the stripping steam heat from the stripper. The advanced flash stripper reduces the heat duty and total equivalent work by 16% and 11%, respectively, compared to the simple stripper. Lean vapor compression was also evaluated, which reduces heat duty and total equivalent work by 8% and 3%, respectively. After reducing the stripping steam heat, the major source of lost work is from the cross exchanger, which should be optimized by including both energy and capital cost.

Future Work

1. Economics of the advanced flash stripper using 5 m PZ will be analyzed and compared to 8 m PZ.

2. Energy performance of natural gas and steel/iron plant applications will be evaluated.

Absorber performance with 5 m MDEA/5 m PZ

Quarterly Report for July 1 – September 30, 2014

by Yue Zhang

Supported by the

Howard A. Halff Endowed Graduate Fellowship in Chemical Engineering

and the Texas Carbon Management Program

McKetta Department of Chemical Engineering

The University of Texas at Austin

October 31, 2014

Acknowledgement: This material is based on work supported in part by the Department of Energy under Award Number DE-FE0013188.

Abstract

In a hybrid-parallel process combining amine scrubbing with membrane technology, the CO_2 concentration in the flue gas is enriched to 23.4% and removal level is increased to 95% (Case 19). This work simulates absorber performance of Case 19 with the Independence model for 5 molal (m) MDEA/5 molal (m) PZ in Aspen Plus®. Different packing types, intercooling configurations, and absorber operating conditions have been tested to get better absorber performance and minimize stripper energy use.

5 m MDEA/5 m PZ offers higher CO_2 capacity but a lower absorption rate than 5 m PZ. Compared to 5 m PZ, absorber costs increase by 50% and advanced flash stripper costs decrease by 47%. The total equipment costs go down by 13%.

Introduction

Compared to 5 m PZ, 5 m MDEA/5 m PZ offers higher CO_2 capacity but a lower absorption rate. It is expected to result in greater delta loading and lower stripper energy cost, but it may also result in a higher absorber packing height. Absorber diameter is fixed by 70% flooding of the middle section during the simulation. This work simulates absorber performance of Case 19 using 5 m MDEA/5 m PZ under different absorber packing types, intercooling configurations, and operating conditions.

Absorber Performance with simple pump-around intercooling

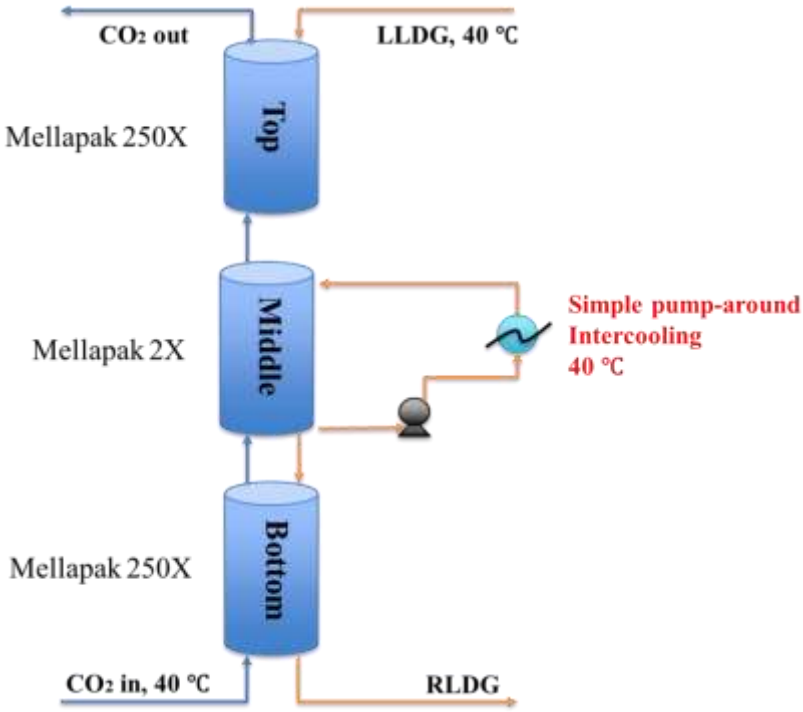

Figure 1: Simple pump-around intercooling

Based on Case 19 5 m PZ, Mellapak 2X was chosen for the middle pump-around section and Mellapak 250X was chosen for the top and bottom sections. Simple pump-around intercooling around the middle section was first tested with 23.4% CO_2 inlet concentration, 95% removal, and 0.209 lean loading (Table 1). For Case 19-1, liquid feed flow rate (L) was first set at 1.1*L_{min} and the pump-around intercooling L_R/G was set at 5 mol/mol. For Case 19-2, L was increased to 1.2*L_{min} and the pump-around intercooling L_R/G was kept at 5 mol/mol. Then L was kept at 1.2*L_{min} and the pump-around intercooling L_R/G was increased to 10 mol/mol. Aspen Plus® calculated absorber results with optimized intercooling position are listed in Table 2.

Table 1: Case 19 input information

Case	CO_2 in (%)	Removal (%)	LLDG
19	23.4	95	0.209

Table 2: Absorber performance with simple pump-around intercooling with Mellapak 250X 2X 250X

Case	RLDG	L_R/G	L/L_{min}	Total Surface Area (1000*m^2)	Surface Area Fraction			Normalized Packing (sec*m^2/mol)
					Top	Mid	Bot	
19-1	0.368	5	1.1	1475.7	0.3	0.6	0.1	635

19-2	0.355	5	1.2	1316.8	0.3	0.6	0.1	567
19-3	0.363	10	1.2	1072.8	0.4	0.5	0.2	462

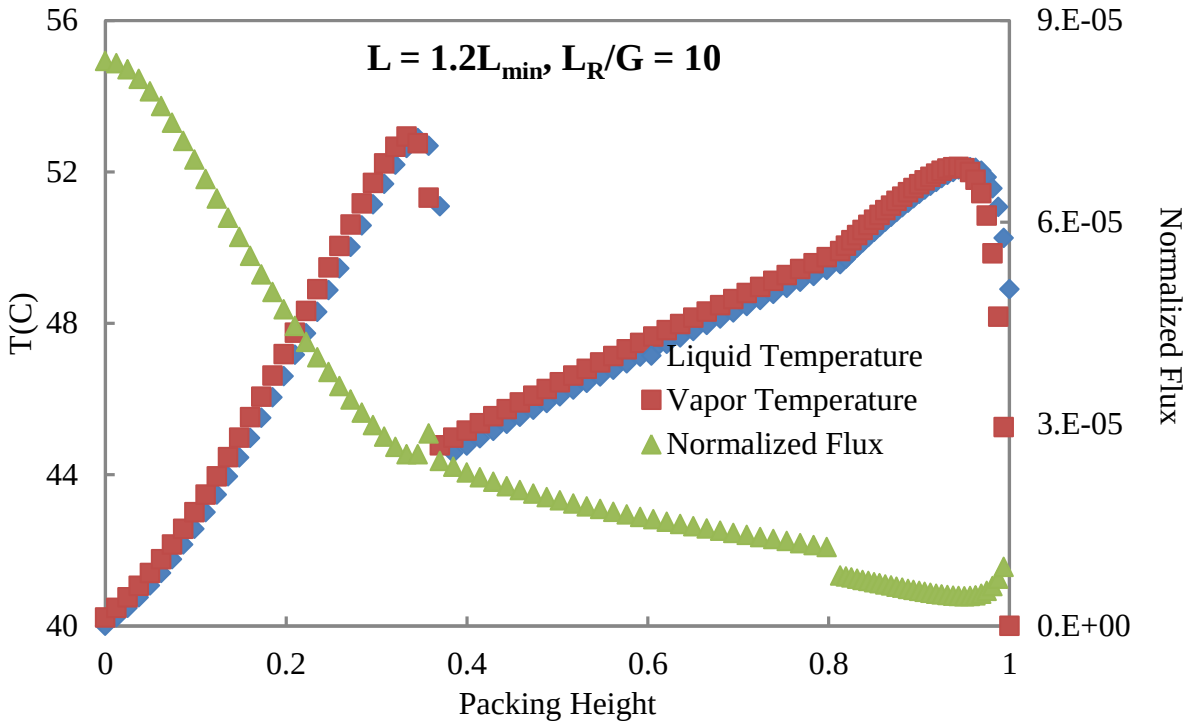

Figure 2: Normalized flux and temperature profile of Case 19-3

Table 2 shows that total surface area decreases in Case 19-2, suggesting that the absorber performs better at 1.2*L_{min}. When increasing the pump-around recycle rate, the total surface area is even lower (Case 19-3), suggesting that the absorber performs better at a higher lean solvent rate and a higher pump-around recycle rate. Figure 2 shows the liquid and vapor temperature as well as normalized flux along the column of Case 19-3. The simple pump-around intercooling cannot cool the gas and liquid to 40 °C, and the temperature bulge in the bottom section limits the mass transfer rate. More advanced intercooling is required to cool down the hot gas and liquid.

Absorber performance with advanced pump-around intercooling

Mellapak 250X/Mellapak 250X/Mellapak 250X

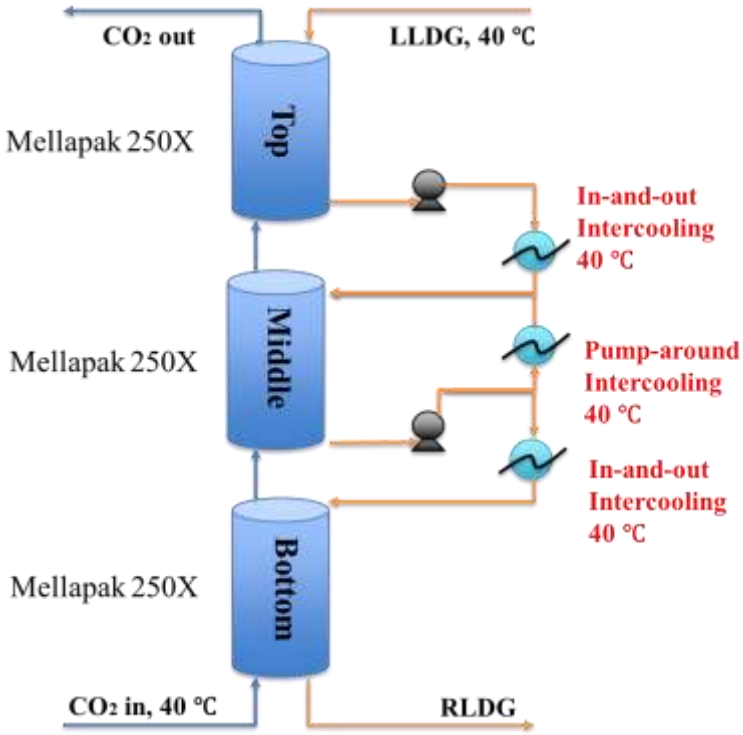

Figure 3: Advanced pump-around intercooling

Two in-and-out intercoolings are added above and below the pump-around intercooling, which is called advanced pump-around intercooling. To find out the best packing type for this intercooling configuration, Mellapak 250X was first tested. L/L_{min} was set at 1.1 and 1.2, and L_R/G was set at 10 mol/mol and 15 mol/mol. Aspen Plus® calculated absorber results with optimized intercooling position, which are listed in Table 3. The absorber liquid/gas temperature profile as well as normalized flux along the column of Case 19-4 are shown in Figure 4.

Table 3: Absorber performance with advanced pump-around intercooling with Mellapak 250X/250X/250X

Case	RLDG	L_R/G	L/L_{min}	Surface Area Fraction			Normalized Packing(sec*m^2/mol)	Flooding		
				Top	Mid	Bot		Top	Mid	Bot
19-4	0.415	10	1.1	0.26	0.50	0.20	946	0.45	0.70	0.51
19-5	0.398	10	1.2	0.32	0.43	0.21	670	0.44	0.70	0.50
19-6	0.418	15	1.1	0.26	0.50	0.19	991	0.40	0.70	0.45
19-7	0.400	15	1.2	0.32	0.43	0.20	703	0.40	0.70	0.45

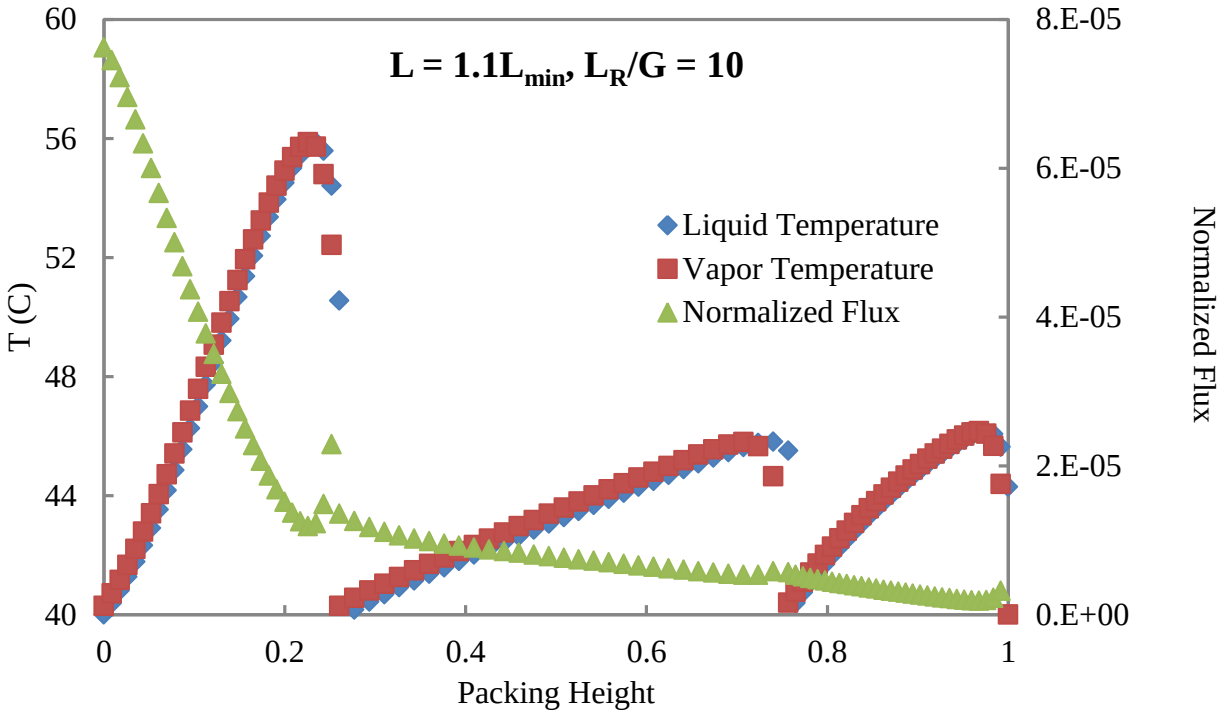

Figure 4: Normalized flux and temperature profile of Case 19-4

As shown in Table 3, rich loading of advanced pump-around intercooling cases is around 0.4, higher than that of simple pump-around cases, which results in better stripper energy performance. The absorber liquid/gas temperature profile suggests that the advanced pump-around intercooling can cool the gas and liquid to 40 °C before entering the next stage (Figure 4). Table 3 shows that for a fixed L_R/G, both the absorber normalized packing and L/L_{min} decrease with L/L_{min}. Absorber capital cost can be saved but stripper energy performance is worse. Table 3 also shows that when L_R/G increases from 10 to 15, absorber normalized packing increases slightly and flooding in the top and bottom section is less, suggesting that higher pump-around recycle rate is not always beneficial. Although a larger amount of solvent recycling improves the mass transfer rate, it is easier to cause flooding in the middle section, as a result of which the diameter becomes larger and normalized packing increases. In order to match the flooding along the column, packing with smaller surface area per volume should be used in the middle section.

Mellapak 250X/Mellapak 2X/Mellapak 250X

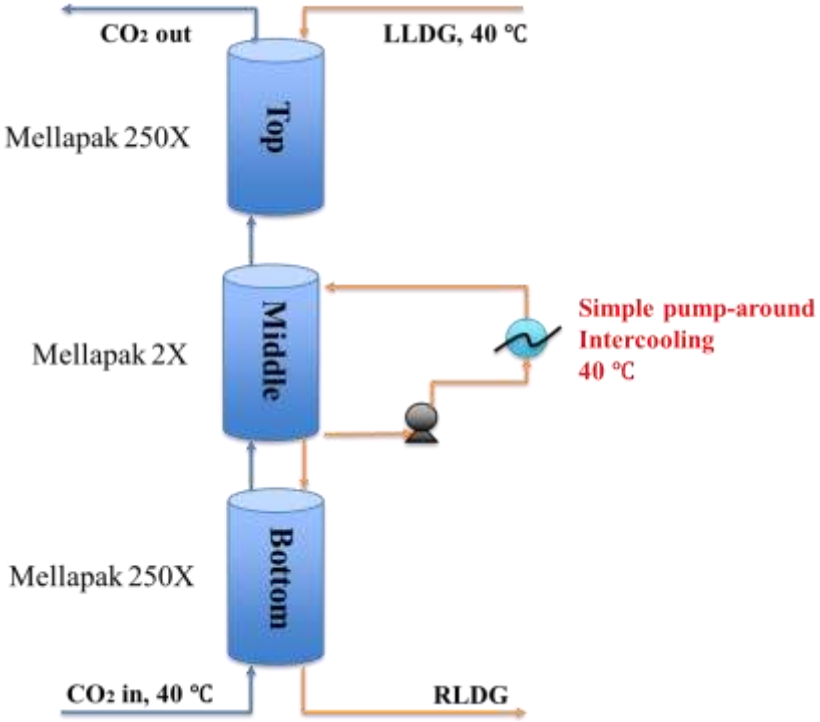

Figure 5: Advanced pump-around intercooling

Packing with smaller surface area per volume is less likely to cause flooding, as a result of which diameter can be reduced and flooding can be matched along the column. Mellapak 2X was used in the middle pump-around section. The liquid feed flow rate was chosen as $1.2*L_{min}$ and L_R/G was chosen as 10 mol/mol and 15 mol/mol. Aspen Plus® calculated absorber results with optimized intercooling position, as listed in Table 4.

Table 4: Absorber performance with advanced pump-around intercooling with Mellapak 250X/2X/250X

Case	RLDG	L_R/G	L/L_{min}	Surface Area Fraction			Normalized Packing(sec*m^2/mol)	Flooding		
				Top	Mid	Bot		Top	Mid	Bot
19-8	0.404	10	1.2	0.30	0.54	0.21	670	0.52	0.70	0.59
19-9	0.406	15	1.2	0.31	0.57	0.18	692	0.46	0.70	0.52

Table 4 shows that RLDG increases slightly and normalized packing remains the same after the packing modification, which will result in better stripper performance while maintaining same absorber capital cost. Flooding also becomes more balanced along the column.

Absorber economics with 5 m PZ and 5 m MDEA/5 m PZ

Calculation methods for absorber costing are based on Frailie (2014). Total costs related to the absorber include the costs of the column, intercoolers, and intercooler pumps. Absorber operating conditions with both 5 m PZ (Case 19-PZ) and 5 m MDEA/5 m PZ (Case 19-5) are listed in Table 5. The corresponding absorber costs are listed in Table 6. Both Case 19-PZ and Case 19-5 were simulated with normal LLDG.

Table 5: Absorber operating conditions with 5 m PZ and blend of 5 m MDEA/5 m PZ

Case Number	LLDG	RLDG	Lean Flow (kg/h)	IC Configuration	Packing Types	D (m)	H (m)
19-PZ	0.303	0.408	4310	In-and-out IC, Pump-around IC	250X 2X 250X	16.6	11.2
19-5	0.209	0.398	2078	Advanced Pump-around IC	250X 250X 250X	16.6	28.9

New target 23.4% CO_2	*Equipment Prices at 593 MWe*	Case 19-PZ	Case 19-MDEA/PZ (1.2L/min)	Case 19-MDEA/PZ (1.3L/min)
Intercooling Type		**In-and-out IC and PA IC**	**Advanced PA IC**	**Advanced PA IC**
Packing Type		**250X 2X 250X**	**250X 250X 250X**	**250X 2X 250X**
Costs of Absorber Column	**Sump + Mixing Length**	$62,074	$68,246	$61,199
	Flue Gas Inlet	$34,970	$37,339	$34,626
	Shell	$1,536,620	$2,518,753	$2,356,955
	Manholes (1/m Ht)	$23,810	$65,817	$64,988
	Ladders	$700	$1,934	$1,910
	Platforms and Handrails	$13,276	$14,140	$13,151
	Distributors	$3,626,151	$4,028,571	$3,569,055
	Packing	$3,286,289	$14,211,051	$11,068,948
	Water Wash	$5,029,090	$5,557,727	$4,954,164
	Total Cost	**$13,438,483**	**$26,163,845**	**$21,841,388**
Costs of Absorber Intercooling	**Total Cost**	**$2,740,859**	**$2,218,790**	**$2,218,790**
Costs of Absorber Intercooling Pumps	**Total Cost**	**$2,220,534**	**$2,476,750**	**$1,765,040**
Total Costs Related to Absorber	**Total Cost**	**$18,399,876**	**$30,859,385**	**$25,825,219**

Table 5 shows that 5 m MDEA/5 m PZ results in twice the delta loading and half of the lean solvent flow rate due to the high CO_2 capacity, but results in more than twice the amount of packing due to low absorption rate. Table 6 shows that the cost of the absorber column almost double due to the higher packing height, and cost of intercoolers and pumps remain the same.

Table 7: Total equipment costs with 5 m PZ and 5 m MDEA/5 m PZ

Equipment Prices at 593 MWe	Case 19-PZ ($)	Case 19-5 ($)
Inlet Gas Blower	$2,841,000	$2,841,000
Absorber	$13,438,483	$26,163,845
Absorber Intercooler	$2,740,859	$2,218,790
Absorber Intercooler Pump	$2,220,534	$2,476,750
Rich Amine Pump	$1,070,226	$535,113
Rich Amine Carbon Filter	$181,583	$102,325
Particulate Filter	$136,000	$136,000
Rich/Lean Amine Exchanger	$28,191,689	$13,051,708
Lean Solvent Cooler	$1,435,688	$652,585
Flash Tank	$736,454	$622,175
Packed Column	$1,076,927	$692,234
Steam Heater	$8,406,909	$7,846,374
Overhead Condenser	$522,068	$522,068
Overhead Accumulator	$30,160	$21,704
Compressors	$10,406,462	$9,961,213
Multistage Centrifugal Pump	$540,000	$540,000
Makeup Amine Tank	$345,000	$345,000
Makeup Amine Pump	$9,000	$9,000
Water Tank	$103,000	$103,000
Water Pump	$13,000	$13,000
Surge Tank	$989,238	$635,869
Lean PZ Pump	$667,468	$333,734
Reclaimer	$5,437,213	$2,603,081
Dehydration Unit	$1,966,000	$1,966,000
Total	$83,504,960	$74,392,568
Capture	$70,592,498	$61,925,355
Compression	$12,912,462	$12,467,213

Table 7 shows the total equipment costs with 5 m PZ and 5 m PZ/5 m MDEA. With the solvent blend, the stripper benefits a lot from the greater delta loading and lower lean solvent flow rate, but the lower absorption rate results in higher absorber costs. Total costs related to the absorber increase by 52% and total equipment costs go down by 10.9%.

Future work

Cases with over-stripping LLDG and higher L/L_{min} will be tested to lower the absorber packing height.

Conclusions

1. The advanced pump-around intercooling (with two in-and-out intercoolings added above and below) is more efficient than the simple pump-around intercooling. It can sufficiently cool down the gas and liquid to 40 °C before entering the next stage.

2. A higher pump-around intercooling recycle rate can decrease absorber packing height but will result in larger diameter due to flooding. In order to match the flooding along the column, packing with smaller surface area per volume should be used in the pump-around section.

3. 5 m MDEA/5 m PZ results in twice the delta loading and half of the lean solvent flow rate due to the high CO_2 capacity, but results in more than twice the amount of absorber packing due to low absorption rate.

4. When using 5 m MDEA/5 m PZ, total costs related to the absorber increase by 52% and total equipment costs go down by 10.9% compared with 5 m PZ.

References

Frailie PT. *Modeling of Carbon Dioxide Absorption/Stripping by Aqueous Methyldiethanolamine/Piperazine*. The University of Texas at Austin. Ph.D. Dissertation. 2014.

Stripper Performance and Equipment Costs Using 5 m PZ and MDEA/PZ and Design of Ammonia Purging System

Quarterly Report for July 1 – September 30, 2014

by Junyuan Ding

Supported by Membrane Technology and Research, Inc.,

and the DOE cooperative agreement DE-FE0013188

McKetta Department of Chemical Engineering

The University of Texas at Austin

October 31, 2014

Abstract

Previous work optimized stripping with 5 m piperazine (PZ) with rich loading from 0.37 to 0.43 mol CO_2/mol N. Advanced flash with warm rich bypass and cold rich exchanger bypass is used for stripping. The Independence model for PZ in Aspen Plus® was used to simulate the stripping performance.

In this quarter, stripping data for 24 cases, including heat duty, equivalent work, CO_2 output pressure, and optimal cold and warm rich bypass, were used to build a correlation with CO_2 rich and lean loading. The Second Law efficiency based on the ratio of stripping minimum work and total ideal work was introduced to explain the stripping work. The Second Law efficiency has a maximum value at a specific CO_2 loading.

In previous work, four cases whose inlet CO_2 concentration and CO_2 removal rate were given by MTR (Cases 13, 14, 18, and 19) were simulated based on absorber performance. Since 5 m MDEA/5 m PZ has a higher CO_2 capacity than 5 m PZ, Case 19-MDEA/PZ (rich loading of 0.398 mol CO_2/mol N and lean loading of 0.209 mol CO_2/mol N) using 5 m MDEA/5 m PZ was studied to reduce the heat duty, compared with Case 19 (rich loading of 0.411 mol CO_2/mol N and lean loading of 0.303 mol CO_2/mol N) using 5 m PZ. The base-case stripping configuration was the advanced flash with warm rich bypass and cold rich exchanger bypass. The Independence model for MDEA/PZ in Aspen Plus® was used to simulate the stripping performance. Equipment costs for Case 19 using 5 m PZ and 5 m MDEA/5 m PZ were both analyzed according to the economic part of the Frailie dissertation.

Ammonia purging design is required for amine scrubbing. Amine scrubbing may create an air quality problem by releasing ammonia. Some amine is converted to ammonia through oxidative or thermal degradation in the absorber and reboiler. Ammonia emits into air with the treated flue gas from the absorber, serving as a significant precursor of $PM_{2.5}$.

In this work, a top stripper and a reflux flow of the condensate over the stripper is used to concentrate ammonia and the rest is purged. Different reflux ratios are chosen to see the ammonia concentration and flowrate of the purge. 1 kg/1000 kg mass ratio of NH_3/H_2O is set for the ammonia amount. The base-case stripping configuration was the advanced flash with warm

rich bypass and cold rich exchanger bypass. The Independence model for PZ in Aspen Plus® was used to simulate the stripping performance.

1: Regression and the Second Law Efficiency of Stripper Performance using 5 m PZ

Introduction

A hybrid amine/membrane CO_2 capture model is being developed by combining a CO_2 membrane separator with the absorber/stripper. The membrane separator has been developed by Membrane Technology and Research, Inc. (MTR). The absorber and stripper performance is simulated using the Independence model for PZ in Aspen Plus®.

Due to the outstanding energy properties of aqueous PZ, including high CO_2 capacity, high thermal stability, moderately high viscosity, oxidative degradation resistance, and low volatility in CO_2-loaded solutions, it is a superior solvent for CO_2 capture by amine scrubbing. 5 m PZ solves the precipitation problem that the more viscous 8 m PZ causes in the solvent loop.

This work focuses on simulating the energy performance of CO_2 rich loading of 0.37, 0.40, and 0.43 mol/equiv PZ with 5 m PZ. Output CO_2 pressure, heat duty, compression work, pump work, and cold/warm rich bypass are recorded and calculated. For each CO_2 rich loading, there is an optimal lean loading, which requires the minimum equivalent work for CO_2 scrubbing.

If most of the gas were sent to the membrane unit, a large area of membrane would be needed to achieve efficient removal of the CO_2 into the air stream. This would be expensive, but would have the benefit that the concentration of CO_2 in the flue gas would increase to around 25%.

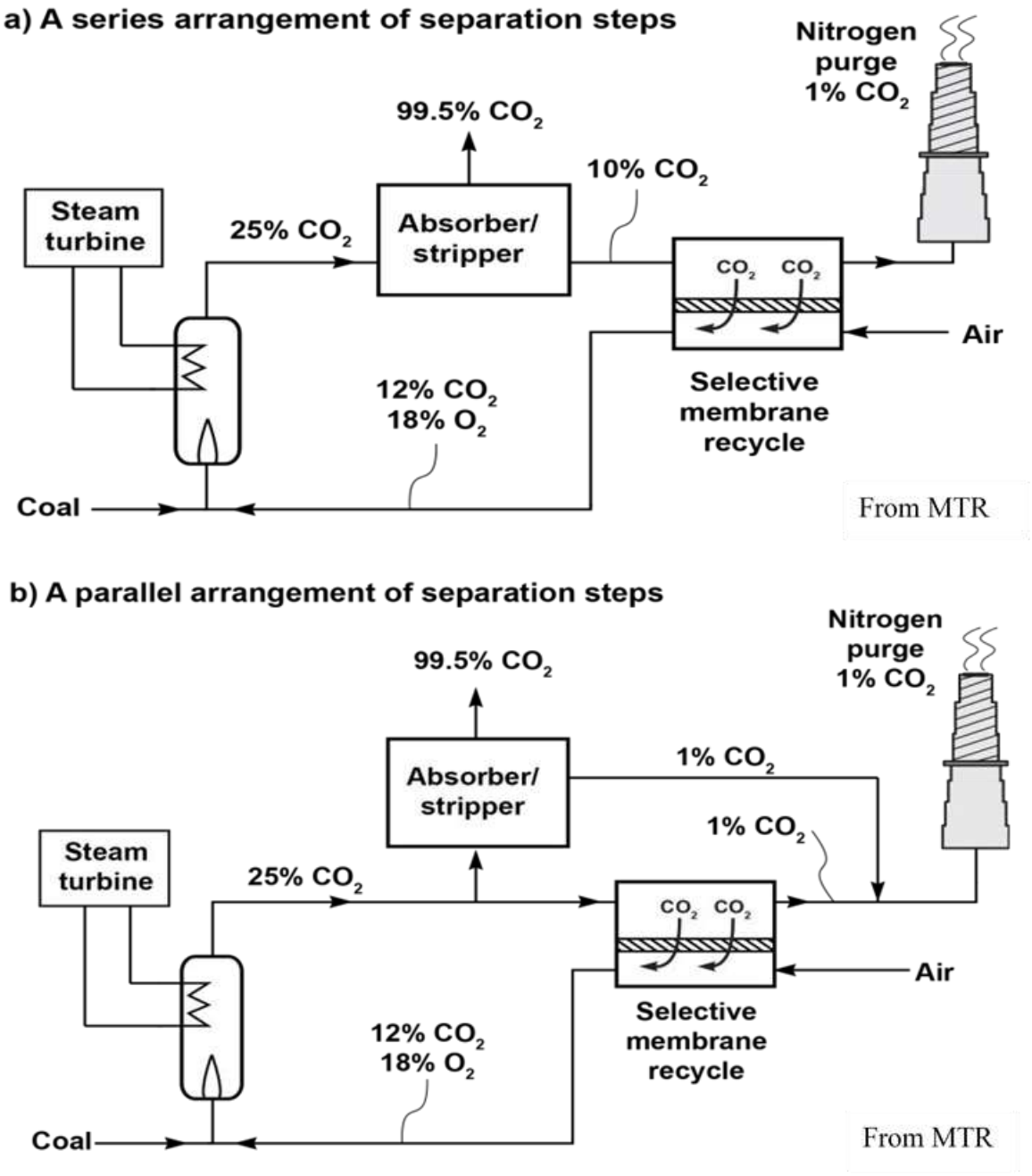

Figure 1: Two configurations of hybrid amine/membrane CO_2 capture model

Methods

Hybrid amine/membrane

The amine regeneration system for the hybrid amine/membrane process was simulated using the Independence model in Aspen Plus®. Figure 2 shows the advanced flash stripper configuration. All of these cases are simulated using 5 m PZ stripping at 150 °C, main exchanger LMTD = 5 °C, top exchanger LMTD = 20 °C, lean solvent output at 40 °C, and 150 bar CO_2 product.

When CO_2 rich loading and lean loading of the advanced flash stripper are given, the overall equivalent work will vary with the cold rich bypass and warm rich bypass. There is an optimal point where the equivalent work is minimized. The corresponding cold rich bypass and warm rich bypass is the optimal bypass for this specific CO_2 rich and lean loading. In order to distinguish this from the bypass at the optimal lean loading for each CO_2 rich loading, the former is described as "bypass" and the latter "optimal bypass".

Regression analysis in Excel is used to build the correlations of heat duty, equivalent work, CO_2 output pressure, optimal cold and warm rich bypass, and CO_2 rich and lean loading.

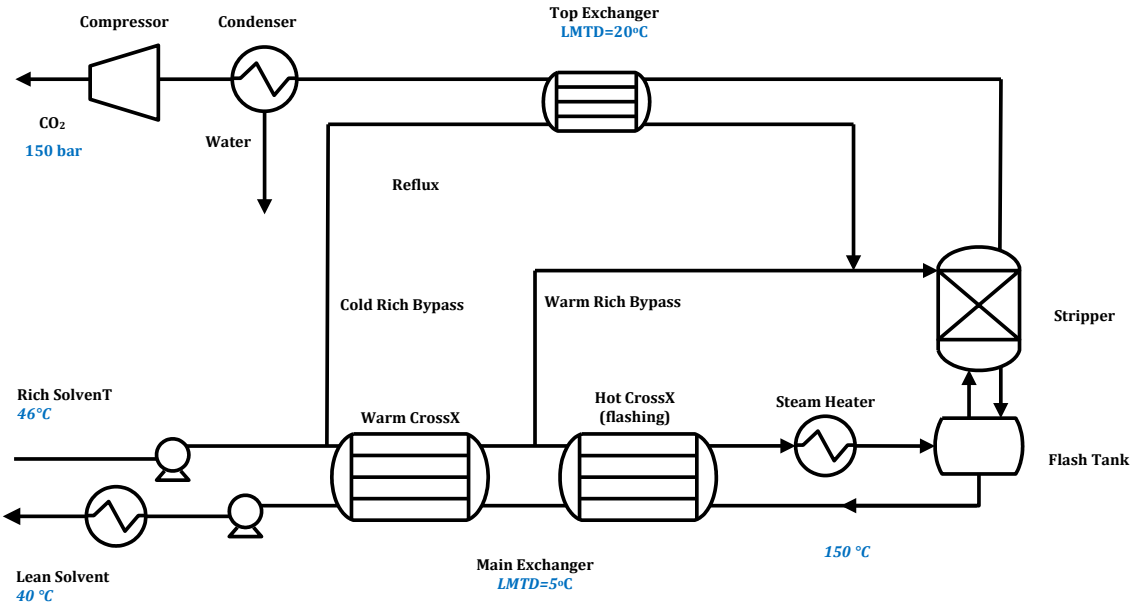

Figure 2: Stripping configuration using 5 m PZ

Equivalent Work Calculation

Equivalent work replaces heat duty as a more general metric of energy use than heat duty alone. It is defined as the sum of pump work, compression work, and heat work, as Equation 1 shows.

$$W_{eq}\,(\text{kJ/mol } CO_2) = W_{heat} + W_{pump} + W_{comp} \quad (1)$$

Heating work can be generated from the heat duty of the reboiler using Equation 2. A typical value of 90% is used for the turbine efficiency (η) and T_{sink} is taken as 313K.

$$W_{heat}\,(\text{kJ/mol } CO_2) = \eta\left(\frac{T_{source} + \Delta T - T_{sink}}{T_{source} + \Delta T}\right)Q_{reb} \quad (2)$$

Compression work can be approximated by Equation 3, which is typically assumed to be at a discharge pressure of 150 bar.

$$W_{comp}\,(\text{kJ/mol } CO_2) = \begin{cases} 4.572\ln\left(\frac{150}{P_{in}}\right) - 4.096 \cdots P_{in} \le 4.56 bar \\ 4.023\ln\left(\frac{150}{P_{in}}\right) - 2.181 \cdots P_{in} \ge 4.56 bar \end{cases} \quad (3)$$

Minimum Work

Minimum work is the total reversible work required considering the stripping process as a Carnot cycle. Minimum work can be estimated as $W_{min}\,(\text{kJ/mol } CO_2) = \Delta G = \Delta H - T\Delta S$.

In a real process, part of the work produced is consumed by irreversible operations, such as heat transfer in the cross exchanger, condenser, reboiler, etc. The Second Law efficiency, which is the ratio of minimum work to total ideal work, is chosen to reflect the utilization of energy. To estimate total ideal work the heat work, W_{heat}, is replaced by ideal heat work, $W_{heat,ideal}$, setting the turbine efficiency in Equation 2 to 1.0.

Process Safety

The stripper pressure should never exceed the pressure rating of the vessel. The stripper vessel will be equipped with a relief valve that will discharge the CO_2/amine mixture to a safe, low pressure point, probably the inlet to the absorber.

Results and Discussion

Regression analysis over a wider range of rich loading

Total equivalent work, heat duty, stripping pressure, warm rich bypass, and cold rich bypass for each case were regressed in Excel as a function of CO_2 rich loading and lean loading. Comparisons between simulation results and predicted values by regression are shown in Figures 3–7.

Figure 3 compares the total equivalent work for variable CO_2 rich loading. As CO_2 rich loading increases, the equivalent work requirement decreases for the same loading difference between rich and lean. Since CO_2 capacity becomes dominant at high lean loading, total equivalent work for all these rich loadings changes rapidly at high lean loading values and becomes flat at the low lean loading end. At all three minimum points, the loading difference between rich solvent and lean solvent is 0.14.

The expression of total equivalent work (Figure 3) by regression is:

$$W_{eq} = 39.4 + 101.0LLDG + 583.2LLDG^2 + 177.8RLDG^2 - 961.9RLDG * LLDG \quad (4)$$

RLDG represents rich loading and LLDG represents lean loading.

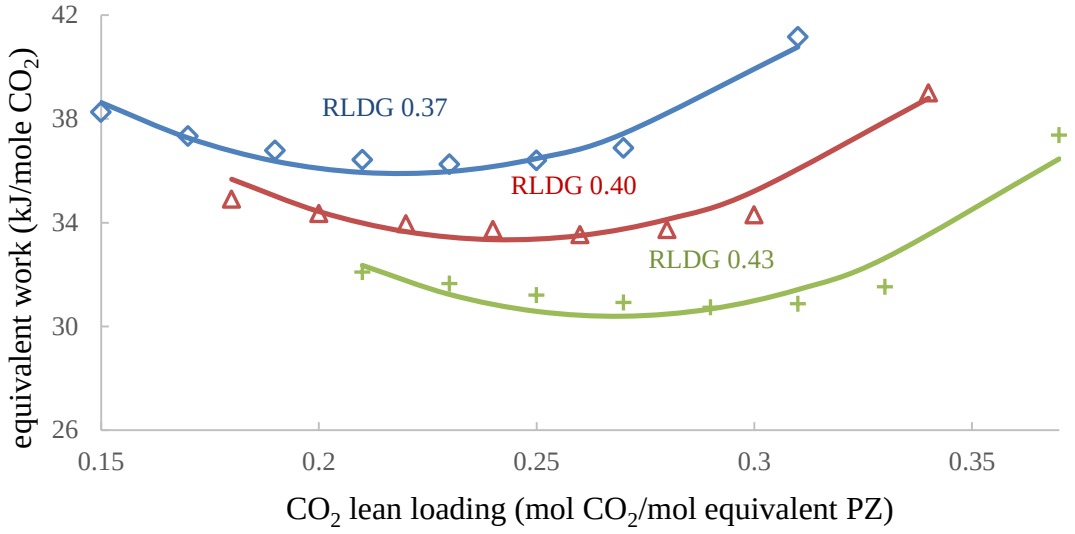

Figure 3: Equivalent work and its predicted value at different rich and lean loadings. Lines predicted by Equation 4.

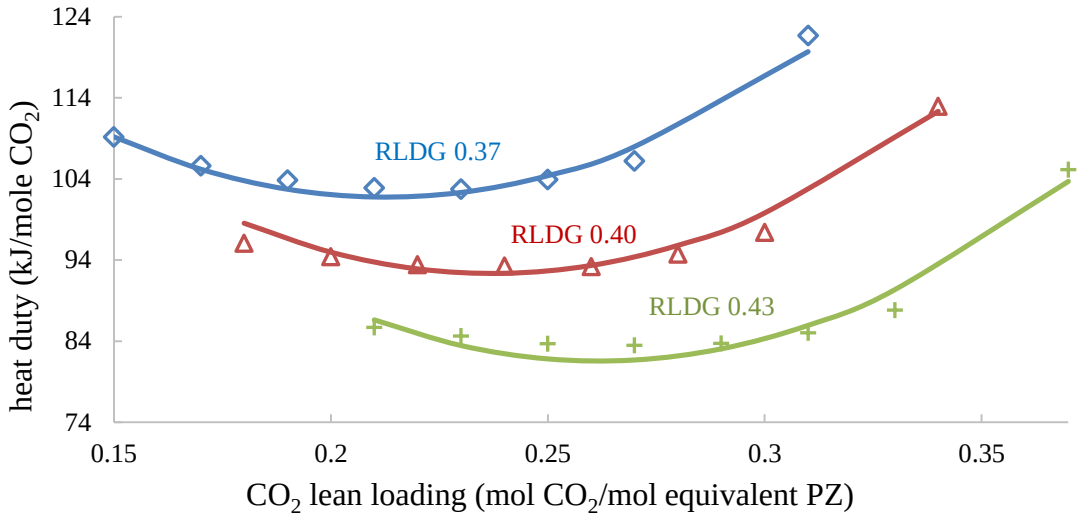

Figure 4: Heat duty and its predicted value at different rich and lean loadings. Lines predicted by Equation 5.

Heat duty of the reboiler is composed of sensible heat requirement, latent heat requirement, and stripping steam heat requirement. Heat work accounts for about 70% of the total equivalent work. Figure 5 shows the comparison of heat duty for variable CO_2 rich loading. Heat duty also

has its minimum value at a CO_2 loading difference of 0.14 mol CO_2/mol PZ. The sensible heat requirement dominates at high lean loading (low capacity). The stripping steam requirement dominates at low lean loading.

The expression of heat duty (Figure 4) by regression is:

$$Q = 119.1 + 342.2LLDG + 1891.5LLDG^2 + 497.7RLDG^2 - 3098.8RLDG * LLDG \quad (5)$$

Thermodynamically, the stripping pressure at 150 ^oC (Figure 5) depends only on the lean loading and is given empirically by:

$$\ln P = 6.6 - 5.9LLDG + 21.7LLDG^2 \quad (6)$$

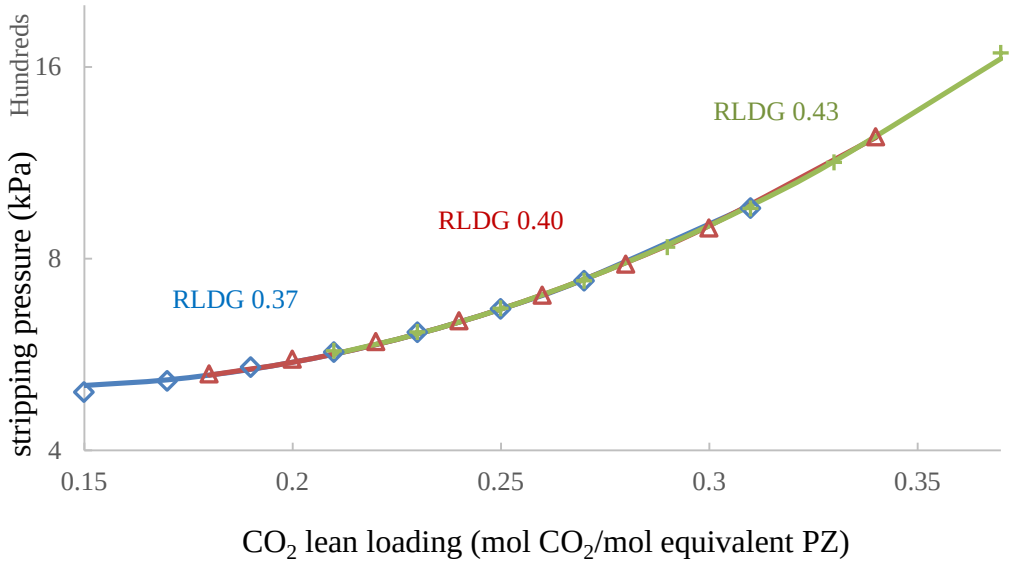

Figure 5: Stripping pressure and its predicted value at 0.37 to 0.40 rich loading. Bottom temperature = 150 ^oC. Lines predicted by Equation 6.

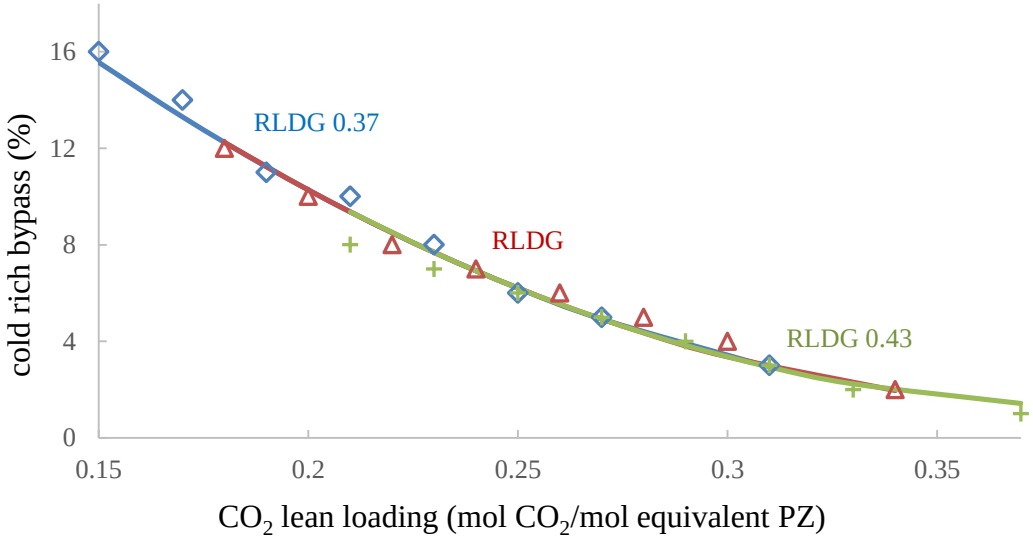

Figure: 6: Cold rich bypass. Lines predicted by Equation 7.

The optimal cold rich bypass (Figure 6) is not a function of rich loading and is given by:

$$CRBP = 0.38 - 1.91LLDG + 2.44LLDG^2 \quad (7)$$

As CO_2 lean loading increases, cold rich bypass plays a less important role in the advanced flash stripper, because for high CO_2 lean loading, less water is heated to the vapor phase, and so less steam stripping heat needs to be recovered by cold rich bypass. The cold rich bypass can be removed from the advanced flash stripper design when stripping very high CO_2 lean loading.

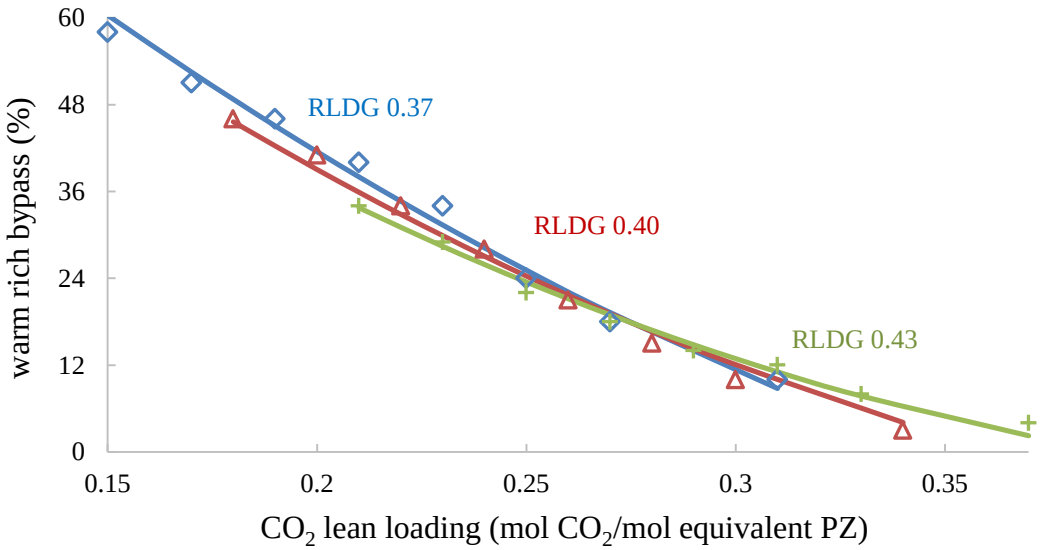

Figure 7: Optimum warm rich bypass in the advanced flash stripper with 5 m PZ. Lines predicted by Equation 8.

As Figure 7 shows, the expression of the optimal rich bypass is:

$$WRBP = 2.43 - 9.56LLDG + 4.98LLDG^2 - 3.00RLDG^2 + 1.09RLDG * LLDG \quad (8)$$

Warm rich bypass depends in large part on CO_2 lean loading, and changes in the same way that cold rich bypass does. It also depends on CO_2 rich loading. Warm rich bypass at low CO_2 rich loading decreases more rapidly with CO_2 lean loading than at high CO_2 rich loading. At low CO_2 lean loading, low CO_2 rich loading has a greater warm rich bypass. All the lines decrease and cross at the same point, CO_2 lean loading 0.27 mol/equivalent PZ. At high CO_2 lean loading, warm rich bypass with high CO_2 rich loading becomes higher than low CO_2 rich loading, but they all tend to zero. Combined with the profile of cold rich bypass, both warm rich bypass and cold rich bypass play less important roles in recovering energy at high CO_2 lean loading. In other words, at high CO_2 lean loading, the simple stripper is more economical than the advanced stripper because of the cross exchanger capital cost.

Similarly, optimal lean loading at each CO_2 rich loading and its corresponding stripping pressure, heat duty, total equivalent work, optimal cold rich bypass, and warm rich bypass are regressed as functions of rich loading:

$$OPTLLDG = RLDG - 0.14 \quad (9)$$

$$OPTQ = 223.95 - 337.07RLDG + 25.30RLDG^2 \quad (10)$$

$$OPTW_{eq} = 62.88 - 54.93RLDG - 46.13RLDG^2 \quad (11)$$

$$OPT \ln P = 8.03 - 12.51RLDG + 22.04LLDG^2 \quad (12)$$

$$OPTCRBP = 0.33 - 0.67RLDG \quad (13)$$

$$OPTWRBP = 6.88 - 30.00RLDG + 33.33RLDG^2 \quad (14)$$

The Second Law Efficiency

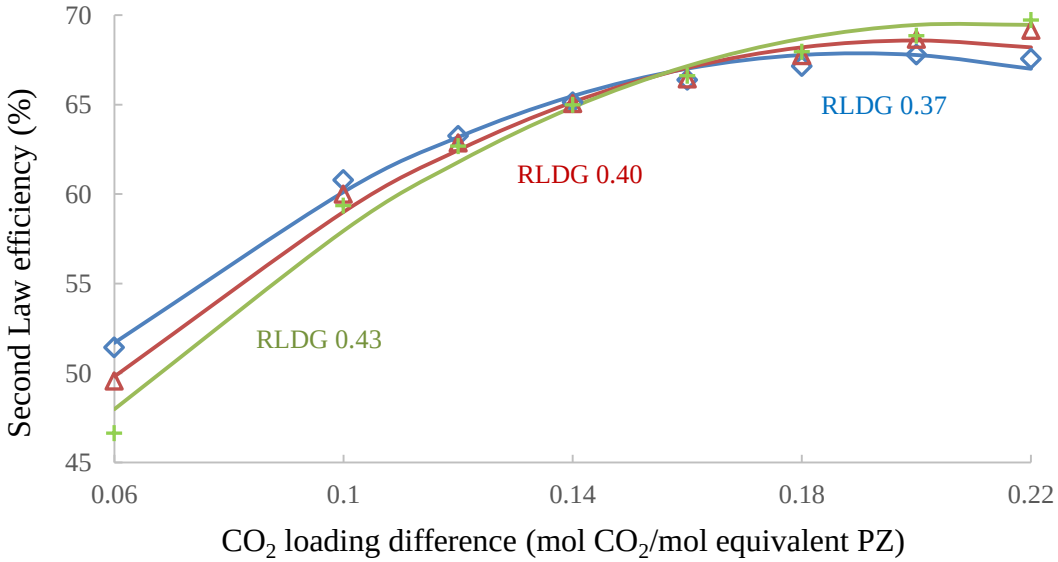

Figure 8: Second law efficiency of the advanced flash stripper with 5 m PZ. Marks calculated by W_{min} /$W_{total,ideal}$. Lines predicted by Equation 15.

Figure 8 shows the effective utilization of stripping energy represented by the Second Law efficiency. CO_2 loading difference (ΔLDG) is calculated by CO_2 rich loading minus CO_2 lean loading. The regressed expression for the Second Law efficiency is:

$$EFF = 0.76 - 1.27LLDG - 9.58LLDG^2 - 2.84RLDG^2 + 12.74RLDG * LLDG \quad (15)$$

The curves on Figure 8 at different rich loading cross at a ΔLDG of 0.14 mole CO_2/mol equivalent PZ, which is the same as that giving the optimum equivalent work. The variation of efficiency with lean loading may result in part from the contribution of rich pump work as shown in Figure 9. The role of the bypass flows may also change with rich loading and delta loading as shown in Figure 10.

At low ΔLDG (defined as CO_2 partial pressure irreversibility dominant part), the higher the CO_2 rich loading, the higher the CO_2 partial pressure. High CO_2 rich loading has high pump work requirement, as Figure 9 shows. The Second Law efficiency at high CO_2 rich loading is lower than that at low CO_2 rich loading at low ΔLDG. As the pump work for different CO_2 rich loadings decreases and becomes closer to each other with increasing CO_2 loading difference, it plays a less important role in the efficiency. As CO_2 loading difference goes up, efficiency of different CO_2 rich loading increases and become close to each other.

The efficiency at different CO_2 rich loadings splits after 0.14 mole CO_2/mol equivalent PZ loading difference. At high CO_2 loading difference (defined as sensible heat irreversibility dominant part), the Second Law efficiency of low CO_2 rich loading is lower than that of high CO_2 rich loading because lower CO_2 rich loading requires more bypasses, as Figure 10 shows. At high CO_2 loading difference, the steam stripping heat that must be recovered by rich solvent bypass is high. This leads to a corresponding higher irreversibility in cross exchanger and reboiler. The cross exchanger irreversibility has a stronger impact on low CO_2 rich loading. As a result, low CO_2 rich loading has lower Second Law efficiency at high CO_2 loading difference.

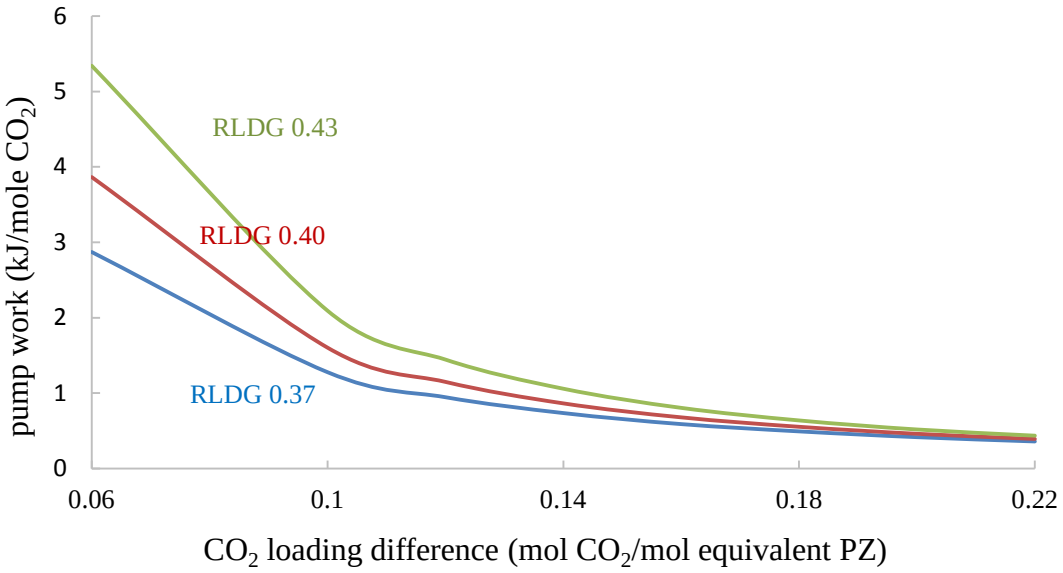

Figure 9: Pump work at variable CO_2 rich loading.

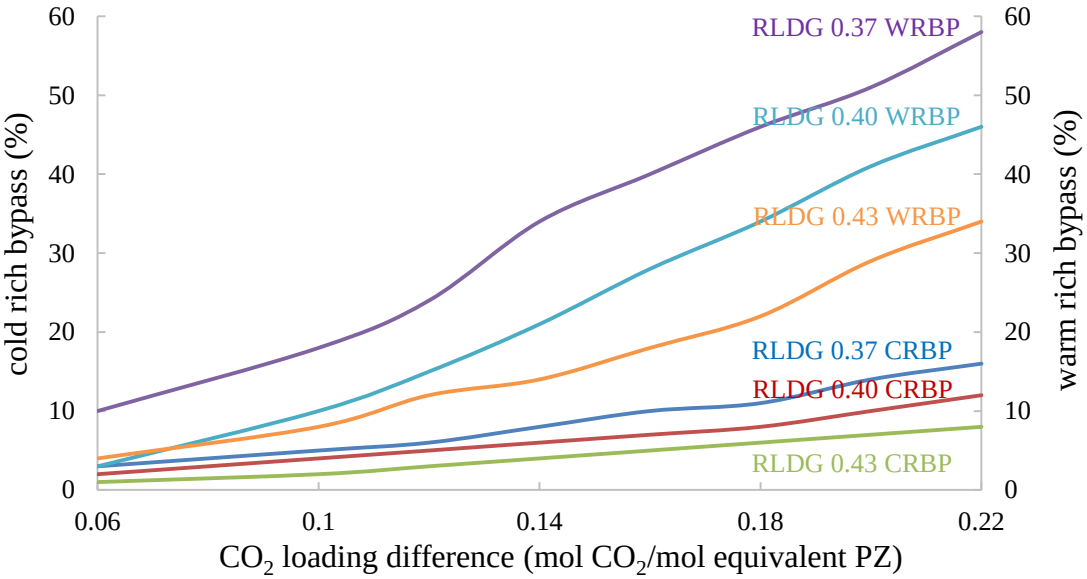

Figure 10: Cold and warm rich bypass for different CO_2 rich loading with CO_2 loading difference. The upper three lines are warm rich bypass presented on the right Y axis in %. The lower three lines are cold rich bypass presented on the left Y axis in %.

Due to the combined effect of pump irreversibility and cross exchanger irreversibility, there is a maximum efficiency with 0.37 mol/equivalent PZ CO_2 rich loading at 0.2 mol/equivalent PZ CO_2 loading difference (Figure 10). Since bypass has less impact at high CO_2 rich loading, the efficiencies of the other two CO_2 rich loadings are still increasing at 0.22 mol/equivalent PZ CO_2 loading difference, but tend to flatten out. They may reach maximum efficiency at higher CO_2 loading difference, where more energy recovery is required. If 5 m packing of the stripper is used instead of the current 2 m, the Second Law efficiency will be higher at the high loading difference area.

Conclusions

1. As the CO_2 rich loading varies from 0.37 to 0.43, the optimum lean loading occurs at a loading difference of 0.14 mol/equivalent PZ CO_2.

2. The minimum total equivalent work decreases from 36.2 kJ/mol CO_2 to 30.7 kJ/mol CO_2 as the rich loading increases from 0.37 to 0.43.

3. Heat duty, total equivalent work, stripping pressure, and bypasses are correlated as functions of CO_2 rich loading and lean loading.

$$Q = 119.1 + 342.2LLDG + 1891.5LLDG^2 + 497.7RLDG^2 - 3098.8RLDG * LLDG$$

$$W_{eq} = 39.4 + 101.0LLDG + 583.2LLDG^2 + 177.8RLDG^2 - 961.9RLDG * LLDG$$

$$\ln P = 6.6 - 5.9LLDG + 21.7LLDG^2$$

$$CRBP = 0.38 - 1.91LLDG + 2.44LLDG^2$$

$$WRBP = 2.43 - 9.56LLDG + 4.98LLDG^2 - 3.00RLDG^2 + 1.09RLDG * LLDG$$

4. The Second Law efficiency of the advanced flash stripper varies from 45 to 70% as the delta loading varies from 0.06 to 0.22. At the optimum delta loading of 0.14 the efficiency is 65%.

2: Stripper Performance and Equipment Costs Using 5 m MDEA/5 m PZ

Introduction

A hybrid amine/membrane CO_2 capture model is being developed by combining a CO_2 membrane separator with the absorber/stripper. The membrane separator has been developed by Membrane Technology and Research, Inc. (MTR). The absorber and stripper performance is simulated using the Independence model for PZ in Aspen Plus®.

Due to the high CO_2 capacity of MDEA/PZ, less solvent is regenerated for the same amount of CO_2 product. Stripping energy will be reduced by substituting 5 m MDEA/5 m PZ for 5 m PZ. Equipment cost is also expected to decrease because of the smaller lean/rich amine exchanger although a bigger stripper is required. The lower CO_2 loading limit for 5 m MDEA/5 m PZ is also higher than 5 m PZ, which means it is not as good as 5 m PZ for low CO_2 inlet concentration. The absorption rate of 5 m MDEA/5 m PZ is also lower than 5 m PZ. So the capital cost of the absorber will increase since the required packing height increases.

Methods

Hybrid amine/membrane

The amine regeneration system for the hybrid amine/membrane process was simulated by the Independence model in Aspen Plus®. The advanced flash stripper configuration was used and stripping conditions for 5 m MDEA/5 m PZ are the same as those for 5 m PZ except at 120 °C.

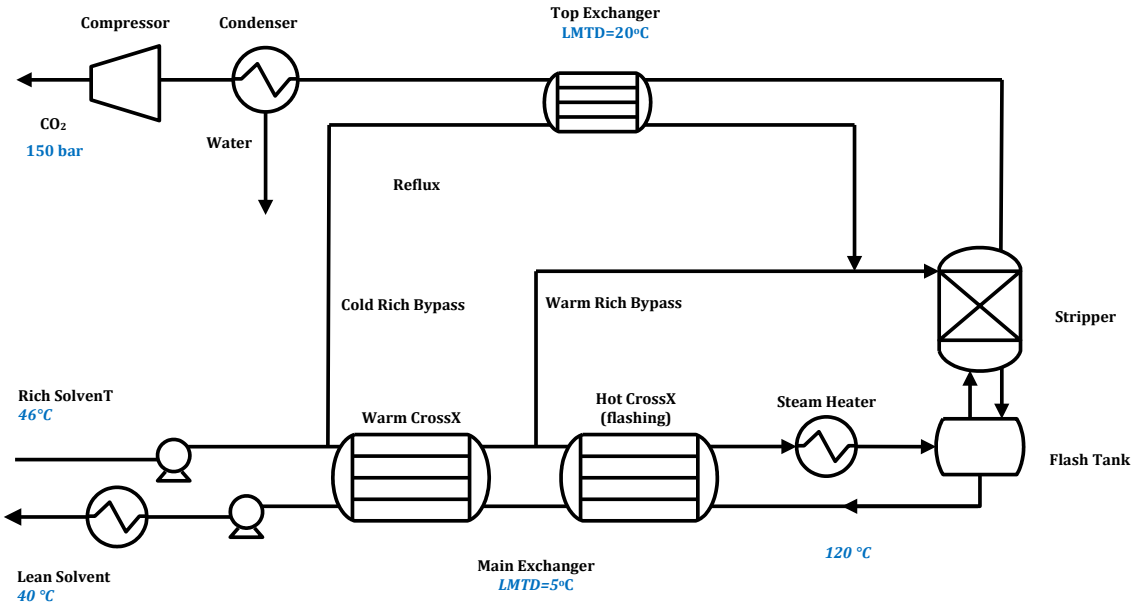

Figure 11: Stripping configuration using 5 m MDEA/5 m PZ.

Equivalent Work Calculation

Equivalent work replaces heat duty as a more general metric of energy use than heat duty alone. It is defined as the sum of pump work, compression work, and heat work, as Equation 1 shows.

Heating work can be generated from the heat duty of the reboiler using Equation 2.

Compression work can be approximated by Equation 3.

Results and Discussion

Stripper Performance Using 5 m MDEA/5 m PZ (Case 19-MDEA/PZ)

Table 1: Comparison of stripper performance using 5 m PZ and MDEA/PZ

Solvent	5 m PZ	5 m MDEA/5 m PZ
CO_2 rich loading	0.411	0.398
CO_2 lean loading	0.303	0.209
L/G (mass)	10.3	5.4
Pressure (bar)	8.66	2.84
Cold rich bypass (%)	4	10
Warm rich bypass (%)	9	24
Equivalent work	33.24	32.41
Heat duty	93.14	94.71
Cold rich bypass (%)	4	9
Warm rich bypass (%)	10	24

Table 1 compares the energy performance of Case 19 using 5 m PZ and the blended solvent. At the same CO_2 partial pressure, L/G and stripping pressure are much lower for blended solvent. As a result, compression work is a little higher and pump work is much lower. The total equivalent work of 5 m MDEA/5 m PZ is lower than that of 5 m PZ.

Table 2: Purchased Equipment Cost of Case 19 using 5 m PZ and 5 m MDEA/5 m PZ are these colors intentional

Description	Case 19	Case 19-MDEA/PZ
Inlet Gas Blower	2,841,000	2,841,000
Absorber	15,228,000	26,164,000
Absorber Intercooler	2,871,000	2,219,000
Absorber Intercooler Pump	2,334,000	2,477,000
Rich Amine Pump	970,000	535,000
Rich Amine Carbon Filter	173,000	115,000
Particulate Filter	136,000	136,000
Rich/Lean Amine Exchanger	25,842,000	8,875,000
Lean Solvent Cooler	1,305,000	783,000
Stripper	707,000	936,000
	1,014,000	688,000
Steam Heater	8,082,000	8,081,000
Overhead Condenser	522,000	653,000
Overhead Accumulator	31,000	30,000
Compressors	10,044,000	10,103,000
Multistage Centrifugal Pump	540,000	540,000
Makeup Amine Tank	345,000	345,000
Makeup Amine Pump	9,000	9,000
Water Tank	103,000	103,000
Water Pump	13,000	13,000
Surge Tank	931,000	632,000
Lean MEA Pump	605,000	334,000
Reclaimer	4,915,000	2,579,000
Dehydration Unit	1,966,000	1,966,000
Total	**81,528,000**	**71,157,000**
Capture	**68,978,000**	**58,548,000**
Compression	**12,550,000**	**12,609,000**

Table 2 shows the purchased equipment costs of Case 19 using 5 m PZ and 5 m MDEA/5 m PZ of 593 MWe based on Frailie spreadsheet (2014). For the stripper, the cost centers are the steam heater, compressors, and reclaimer. Total equipment costs of blended solvent is 13% lower than that of 5 m PZ. The main two changes are on the main exchanger and reclaimer, due to lower solvent flow rate caused by higher CO_2 capacity. Compressors cost just a little higher while the compression work increases a lot.

But both cases using 5 m PZ and 5 m MDEA/5 m PZ are using main exchanger LMTD of 5 ℃, which is not their optimum LMTD. Energy performance and equipment costs will be different from these two tables when using their optimum LMTD.

Conclusions

1. The energy cost of using MDEA/PZ is lower than using 5 m PZ. For Case 19, equivalent work using 5 m MDEA/5 m PZ (32.41 kJ/mol CO_2) is less than using 5 m PZ (33.24 kJ/mol CO_2).

2. The capital cost of Case 19 using MDEA/PZ ($ 71,157,000) is less than using PZ ($ 81,528,000).

3: Model design of Ammonia Purging System

Introduction

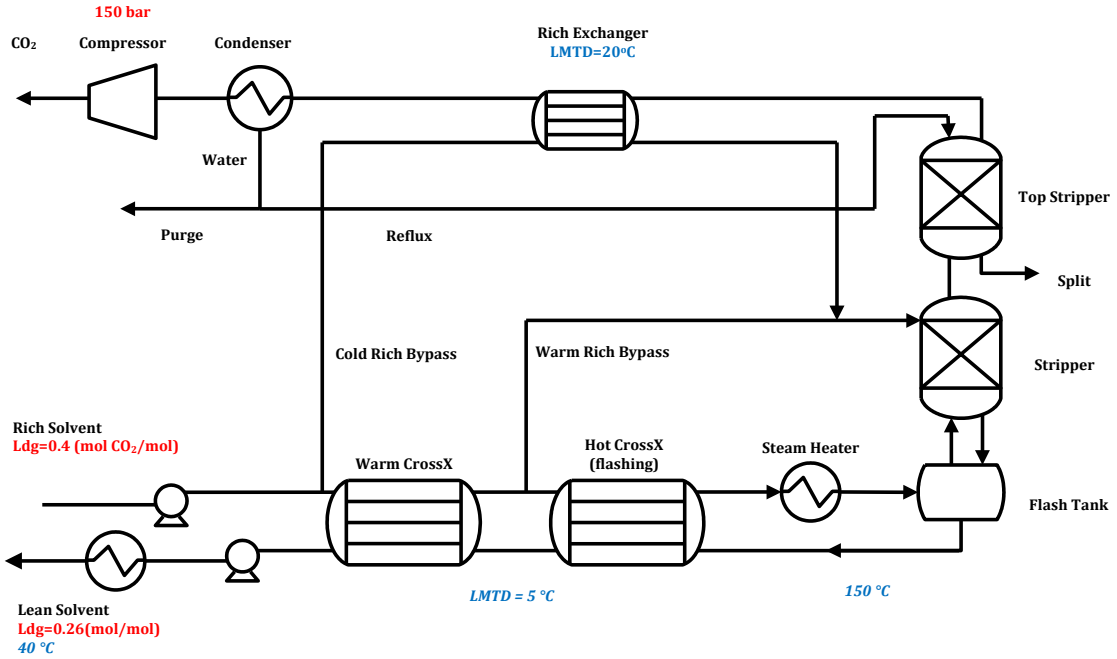

Figure 12: Initial Configuration of the ammonia purging system.

Figure 12 shows the configuration of the ammonia purging system. A top stripper is added above the flash stripper. The vapor coming out from the flash stripper goes up across the top stripper, top heat exchanger, and condenser. The vapor out from the condenser is compressed to 150 bar. The condensate coming down from the condenser is separated into two parts. One part is sent back to the top of the top stripper, serving as feeding liquid. The other part is purged. The reflux ratio is defined as the flowrate ratio of the reflux over the whole condensate. The liquid coming out from the bottom of the top stripper at high temperature is also sent away. An applicable way to save the energy it carries and the large amount of water in it is to send it to a cross heat exchanger and then to the water wash. As the reflux ratio goes up, ammonia and CO_2 concentration in the reflux loop increases. On the other hand, as more condensate is used for reflux, the amount of the purged flow sent out of the system is reduced. Compared with previous advanced flash stripper without reflux, total amount of CO_2 captured and NH_3 removed is increased. An optimum reflux ratio can be found to have the best value of mol NH_3/mol CO_2 removed.

CO_2 rich loading of 0.4 mol/mol equivalent PZ and lean loading of 0.26 mol/mol equivalent PZ stripping with 5 m PZ is chosen as the base case.

Methods

Adding ammonia component

Two reactions with ammonia occur in the amine scrubbing system.

$$NH_3 + HCO_3^- \leftrightarrow NH_2COO^- + H_2O \quad (16)$$

$$NH_3 + PZH^+ \leftrightarrow NH_4^+ + PZ \quad (17)$$

Properties of NH_3, NH_4^+ are in the data bank of Aspen Plus®. The equilibrium coefficient of Equation 16 is set by:

$$\ln (K_{eq}) = -4.5834 + 2900/T \quad (18)$$

New components were added into Aspen Plus® using the methods of Sherman (2013).

Process Safety

The stripper pressure should never exceed the pressure rating of the vessel. The stripper vessel will be equipped with a relief valve that will discharge the CO_2/amine mixture to a safe, low pressure point, probably the inlet to the absorber.

Results and Discussion

Table 3 shows the comparison of the purged amount and concentration of CO_2 and ammonia under different reflux ratio and non-reflux. With the increasing reflux ratio from 0.8 to 1.0, total CO_2 removed from the output vapor of the stripper has a minimum value at reflux ratio of 0.85. But in terms of CO_2 in both purge flow and the output vapor, the amount of CO_2 removed decreases with the reflux ratio, and are all higher than without reflux/purge. In the purge, total amount of NH_3 and of CO_2 both have maximum value at reflux ratio of 0.85 while the mole fraction of total ammonia increases with the reflux ratio.

Table 3: ammonia purge under different reflux ratio and non-reflux

reflux ratio	0.8	0.85	0.9	0.95	1	non-reflux/purge
purged total NH_3 (mol/s)	14.41	16.32	13.51	6.42	0	-
purged total CO_2 (mol/s)	14.47	16.36	13.53	6.43	0	-
mole fraction of purged total NH_3 (%)	0.160	0.255	0.344	0.344	0.347	-
treated CO_2 (vapor)(kg/s)	60.92	60.76	60.87	61.15	61.25	60.95
total CO_2 removed (kg/s)	61.55	61.49	61.46	61.43	61.25	60.95
kg purge/ton CO_2 treated	36.80	30.51	21.18	10.01	0	-
mol NH_3/mol CO_2 treated	0.0104	0.0118	0.0098	0.0046	0	-
split H_2O (kg/s)	8.17	8.93	9.24	9.63	9.20	8.49 (condensate)
mole fraction of split total NH_3 (%)	0.0054	0.0059	0.0090	0.0162	0.0276	0.0176 (condensate)
mole fraction of split total CO_2 (%)	0.0059	0.0062	0.0081	0.0126	0.0199	0.0206 (condensate)
temperature of output vapor (℃)	106.1	102.1	97.5	96.2	95.9	119.3
temperature of split (℃)	114.1	114.7	113.2	109.8	106.6	-

With a large amount of the condensate sending back for reflux, the steam stripping heat is expected to be recovered from the split flow instead of the output vapor by changing the top V/L heat exchanger to an L/L heat exchanger. This is because the temperature of split flow with reflux is much higher than the output vapor. The split flow with reflux substitute the condensate without reflux/purge to serve as a better source of water wash. Compared with condensate in previous design without reflux/purge, the split flow has a higher amount of water and lower concentration of both NH_3 and CO_2. The new configuration is shown in Figure 13.

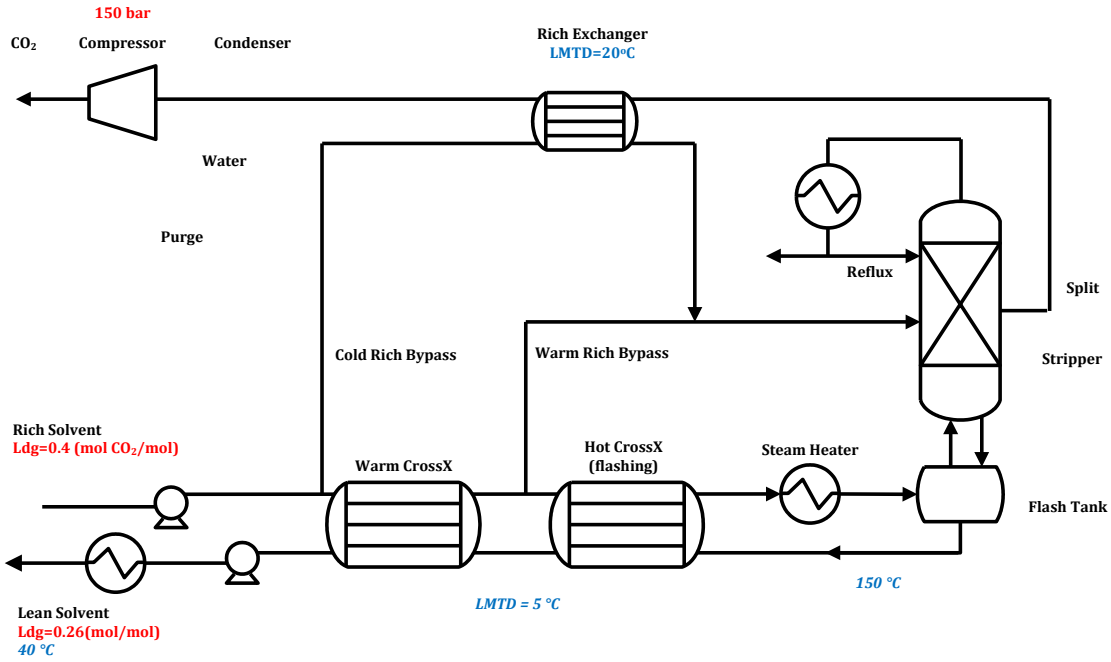

Figure 13: Final Configuration of the ammonia purging system.

Figure 14 shows the mole fraction of total NH_3 and mole amount of CO_2 and total NH_3 in the purge. The mole amount of CO_2 and NH_3 in the purge are almost the same. They are at their top at a reflux ratio of 0.85 (16.36 mol/s of total CO_2 and 16.32 mol/s of total NH_3). The mole fraction of total ammonia in purge increases with the reflux ratio.

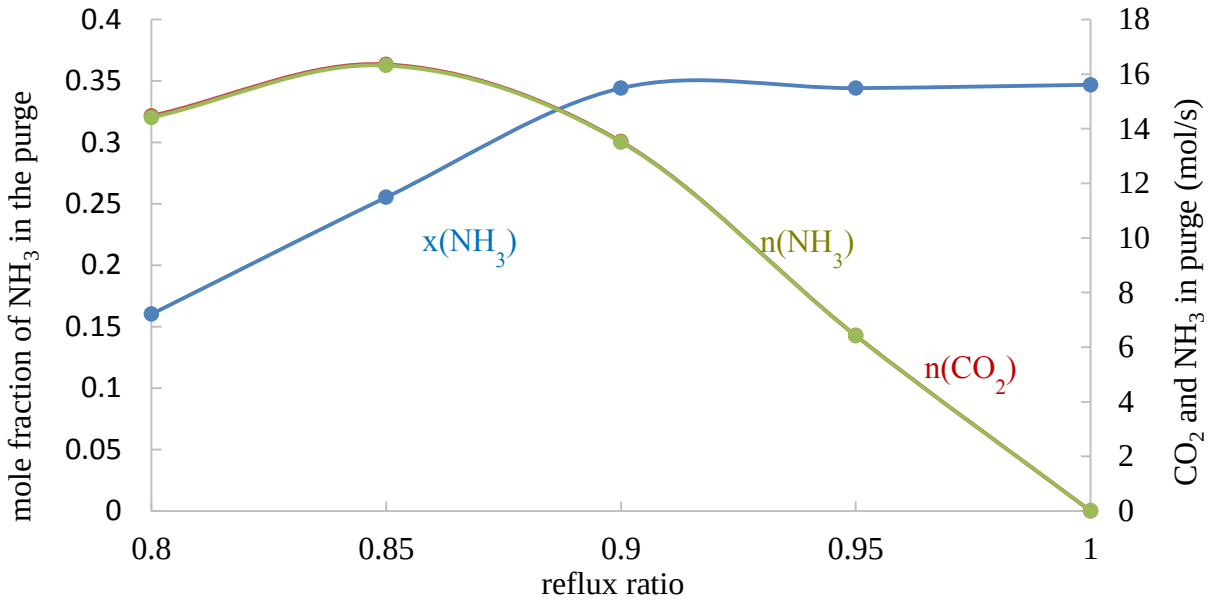

Figure 14: mole fraction of NH_3 and mole amount of NH_3 and H_2O in the purge.

Figure 15 shows mole fraction and amount of NH_3 in the purge normalized by CO_2 removed. The amount of CO_2 removed is based on the output vapor sent to the compressor. As reflux ratio increases from 0.8 to 1, the normalized purge's flow rate decreases from 36.8 kg/ton CO_2 removed to 0, and the increase of the NH_3 mole fraction in the purge slows down. There is a peak value of the normalized amount of NH_3 in purge (0.0118 mole NH_3/mole CO_2 removed) around 30.5 kg purge/ton CO_2 removed. At that point the normalized mole fraction of NH_3 in purge is decreasing rapidly. The appropriate range of reflux ratio for ammonia purging is in the range of 0.85 to 0.93.

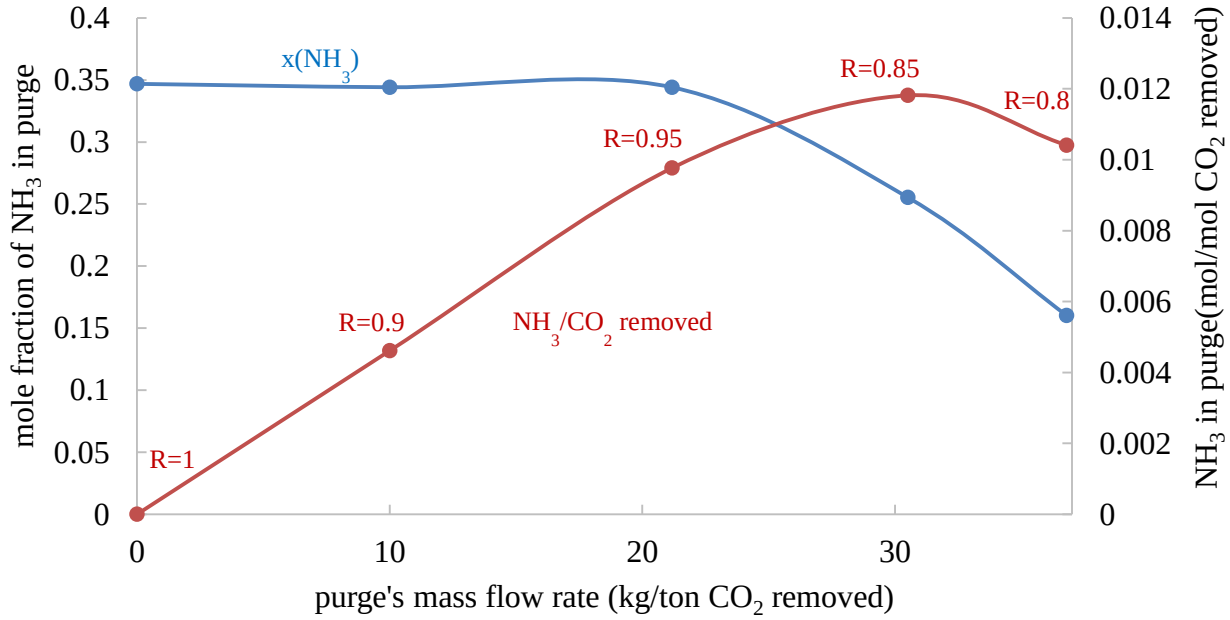

Figure 15: mole fraction and normalized amount of NH_3 in purge.

Conclusions

Adding reflux and purge can separate ammonia from the amine scrubbing system efficiently. As reflux ratio increases from 0.8 to 1, the mole fraction of NH_3 in the purge increases from 0.160 to 0.347. The normalized amount of NH_3 in purge has a peak value (0.0118 mole NH_3/mole CO_2 removed) at 30.5 kg purge/ton CO_2 removed.

Future Work

1. Optimize stripper performance using 5 m MDEA/5 m PZ.

2. Develop the ammonia purging model based on amine degradation rate and ammonia emission standard.

References

Rochelle GT et al. "CO_2 Capture by Aqueous Absorption, Second Quarterly Progress Report 2014." Texas Carbon Management Program. The University of Texas at Austin. 2014.

Merkel TC, Lin H, Wei X. "Power plant post-combustion carbon dioxide capture: An opportunity for membranes." Membrane Technology and Research, Inc. *J Membr Sci.* 2010;359: 115-125.

Frailie PT. *Modeling of Carbon Dioxide Absorption/Stripping by Aqueous methyldiethanolamine/Piperazine.* The University of Texas at Austin. Ph.D. Dissertation. 2014.

Freeman B, Hao P, Baker R, Kniept J, Chen E, Ding J, Zhang Y, Rochelle GT. "Hybrid membrane-absorption CO_2 capture process." Presented at GHGT-12, Austin, United States, October 6th, 2014.

Madan T. *Modeling of Stripper Configurations for CO_2 Capture using Aqueous Piperazine*. The University of Texas at Austin. M.S. Thesis. 2011.

Lin Y-J, Madan T, Rochelle GT. "Regeneration with Rich Bypass of Aqueous Piperazine and Monoethanolamine for CO_2 Capture." *IECR.* 2014;53:4067–4074.

Xu Q. *Thermodynamics of CO_2 Loaded Aqueous Amines.* The University of Texas at Austin. Ph.D. Dissertation. 2011.

Freeman SA. *Thermal Degradation and Oxidation of Aqueous Piperazine for Carbon Dioxide Capture.* The University of Texas at Austin. Ph.D. Dissertation. 2011.

Van Wagener DH. *Stripper Modeling for CO_2 Removal Using Monoethanolamine and Piperazine Solvents.* The University of Texas at Austin. Ph.D. Dissertation. 2011.

Packing characterization: hydraulic and mass transfer results overview

Quarterly Report for July 1 – September 30, 2014

by Chao Wang

Supported by the Carbon Management Project,

Process Science and Technology Center

and Frank Seibert

Separations Research Program

The University of Texas at Austin

October 31, 2014

Abstract

In this quarter, a review of hydraulic and mass transfer results containing all 14 packings measured in this work was presented. The experimental results serve as Chapter 4 of the Ph.D. dissertation. The effects of liquid superficial velocity (u_L), gas superficial velocity (u_G), packing surface area (a_P), and packing corrugation angle (θ) on hydraulic properties and mass transfer performance were explored. In general, pressure drop increases steadily with gas flow rate (F-factor) to the power of 1.6–1.9. The pressure drop increases by 30% from dry condition to a liquid load of 5 gpm/ft^2 (12 m^3/m^2*h), and increases slightly with increasing liquid flow rate. The liquid hold-up increases slightly with gas flow rate in the pre-loading region, and increases sharply with gas flow rate in the loading region until flood. Liquid hold-up increases with liquid flow rate at the constant gas flow rate. Both pressure drop and liquid hold-up increase with packing surface area and decrease with packing corrugation angle.

The effective mass transfer area increases with liquid velocity to the 0.15 power and is essentially independent of gas velocity. The fractional effective area decreases as packing surface area increases because of the inefficient wetting in the higher specific surface area packings. Rivulets, ripples, and droplets provide additional mass transfer area in lower specific surface area packings. The effective mass transfer area is not a function of packing corrugation angle.

The liquid film mass transfer coefficient (k_L) is a function of liquid velocity and independent of gas velocity. Conversely, the gas film mass transfer coefficient (k_G) is a function of gas velocity and independent of liquid velocity. The k_L increases with liquid velocity (u_L) to the power of 0.5–0.77 for all packings in this work. The k_G increases with liquid velocity (u_G) to the power of 0.43–0.76 for all packings in this work. Summaries of k_L and k_G are shown in Figures 4.27 and 4.28 of the attached Chapter 4.

Packing geometries have similar effects on k_L and k_G. Both k_L and k_G increase as packing surface area increases and decrease as corrugation angle increases.

A dissertation chapter (Chapter 4) follows, which includes all experimental results.

Future Work

Next quarter, work will be focused on other chapters of the dissertation. In Chapter 5, studies on packing geometries are conducted to quantify the effects of packing surface area (a_P) and corrugation angle (θ) on k_L and k_G. A new concept, the Mixing Points Density (M), is introduced to represent the geometry effects. Three mass transfer correlations will be developed. In Chapter 6, an economic study on the effects of operation condition and packing selection on absorber total cost will be conducted. The optimum operation condition and packing for amine scrubbing CO_2 absorber will then be given.

Lab Safety issues

1. Steel reinforced gloves are required to prevent being cut when handling sheet metal structured packings.
2. Chemical resistant lab gloves are required when handling a strong base such as NaOH used in effective area measurement, and toxic chemicals such as toluene in k_L measurement. After runs, NaOH should be neutralized before draining.
3. A gas mask with respirator is required when changing SO_2 bottles.

Attached Chapter

Chapter 4: Packed Column Results

4.1 Hydraulic

4.1.1 General overview

The packing hydraulic characteristics (pressure drop and liquid hold-up) were determined prior to the mass transfer measurements. The air/water system was used in the hydraulic tests. The gas flow factor (F_G) was chosen as the independent variable since it is theoretically meaningful (Bernoulli equation) and allows for the incorporation of temperature effects (via gas density).

The pressure drop results for Sulzer Mellapak^{TM} 250Y (MP250Y), a standard structured packing with surface area of 250 m^2/m^3, are shown in Figure 4.1. The dry pressure drop increases with gas F-factor to the power of 1.6–1.9. Theoretically, the power should be around 2 based on Bernoulli equation. However, the friction loss reduces the power slightly. Pressure drop increases by 30–40% when irrigated with 5 gpm/ft^2 (12 m^3/m^2*h) liquid flow (compared with dry pressure drop), and increases slightly (5–10%) as liquid flow rate keeps increasing. In the pre-loading region, irrigated pressure drop increases steadily with gas flow rate to the power of 1.6–2.0, which is similar to the dry pressure drop curve. In the loading region, pressure drop increases dramatically with gas flow rate until flood. The power of pressure drop on F-factor increases from 2.0 to 10.0 in the loading region.

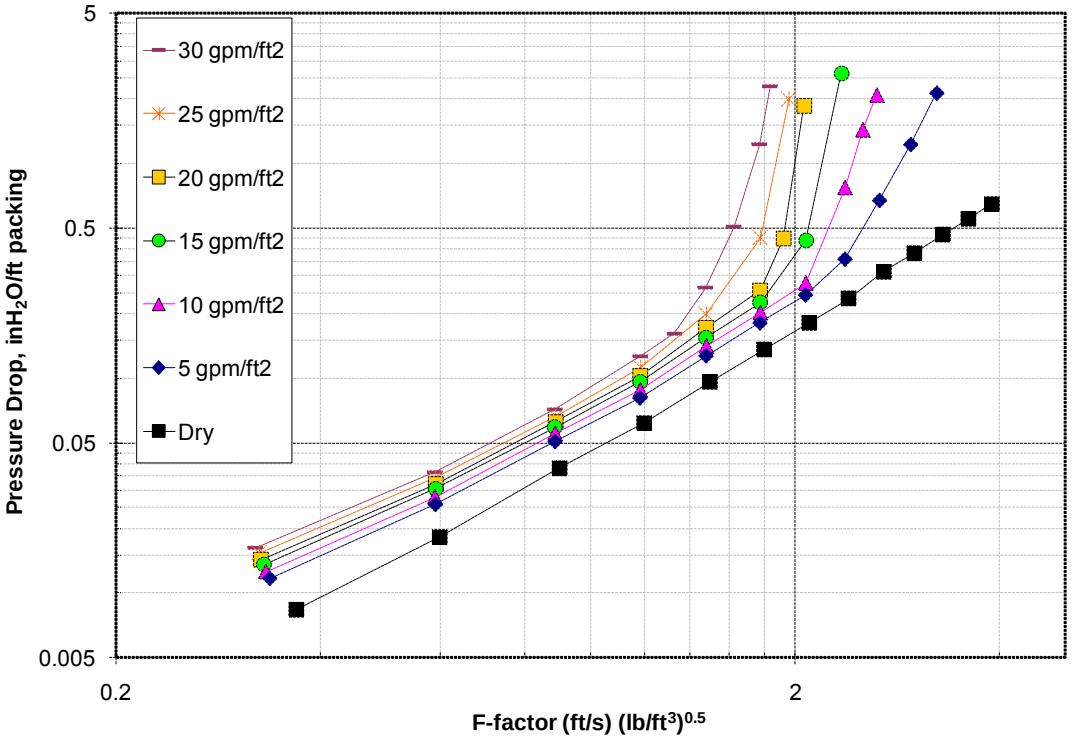

Figure 4.1. Pressure drop results for MP250Y

The liquid hold-up characteristics for Mellapak 250Y are shown in Figure 4.2. Liquid fractional hold-up is the ratio of liquid volume in the packing to the packing void volume. In the pre-loading region, liquid hold-up increases slightly with gas flow rate because the gas and liquid have limited interaction in this region. In the loading region, liquid hold-up increase slightly with gas flow rate until the loading where it increases sharply. The interaction between gas and liquid is quite intensive in the loading region. For a fixed gas rate, the liquid hold-up increases with liquid flow rate. In the pre-loading region, the liquid hold-up for this packing is between 3–13%, which is within the expected magnitude (1–15%).

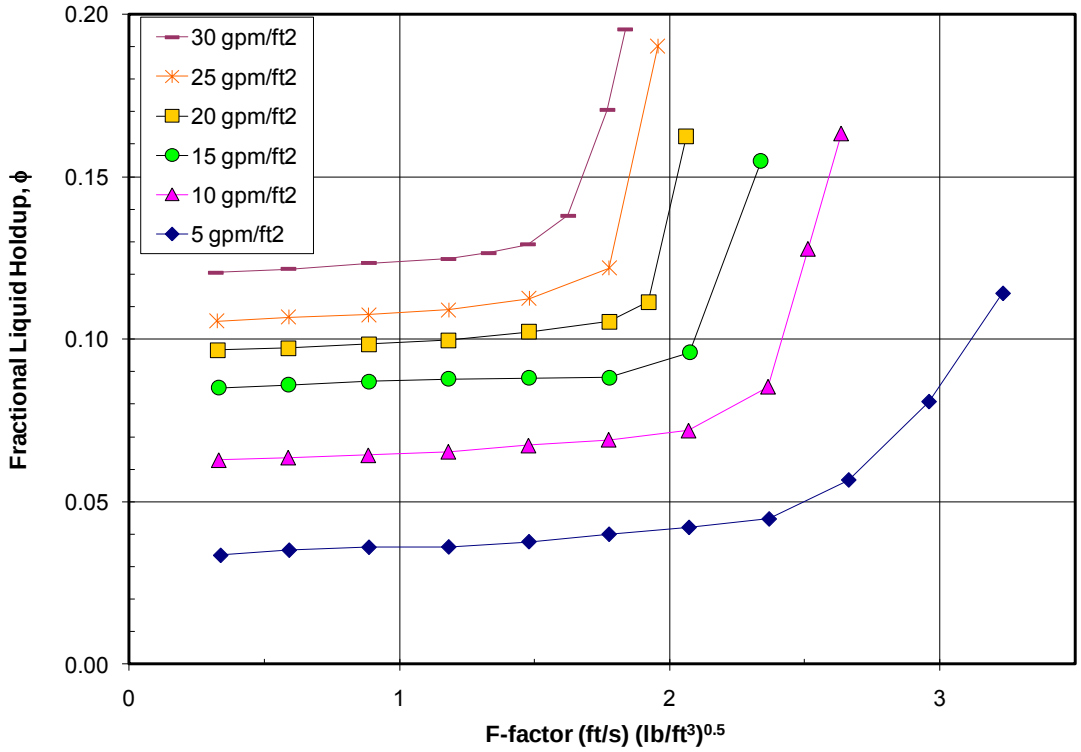

Figure 4.2. Liquid hold-up results for MP250Y

4.1.2 Effect of Packing Surface Area

The dry pressure drop data for four packings with specific area ranging from 125 to 500 m^2/m^3 (Mellapak 125Y, 250Y and GT-PAK™ 350Y, 500Y) are compared in Figure 4.3. Dry pressure drop can be correlated as a function of F-factor (F_G):

$$(DP/Z)_{dry} = C * F_G^n \qquad (4\text{-}1)$$

For each packing, the exponent n varies in a small range (1.75 to 1.88) while the constant C varies with packing specific area (a_P). The dry pressure drop can be expressed by a normalized correlation:

$$\frac{(DP/Z)_{dry}}{a_P} = 0.12 * F_G^{1.81} \qquad (4\text{-}2)$$

Equation (4-2) compares well with the correlation by Tsai (2010) shown in Equation (4-3):

$$\frac{(DP/Z)_{dry}}{a_P} = 0.125 * F_G^{1.84} \qquad (4\text{-}3)$$

There is a very small difference in the constant and the exponent which is expected considering experimental error and the difference of the database.

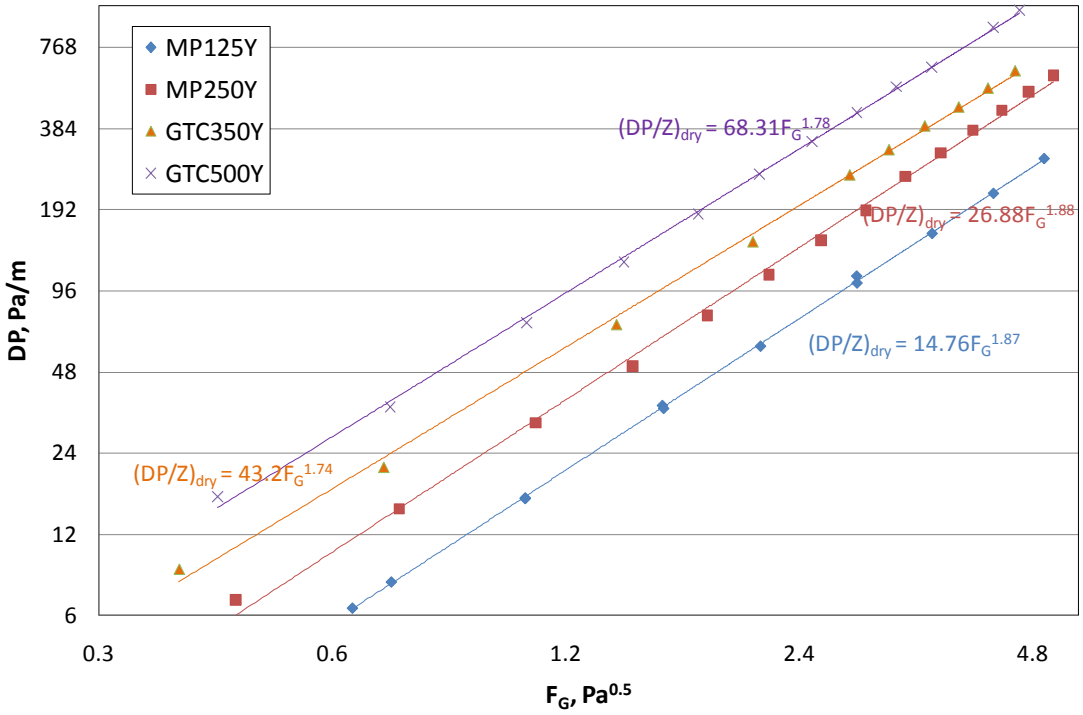

Figure 4.3. Dry pressure drop comparison

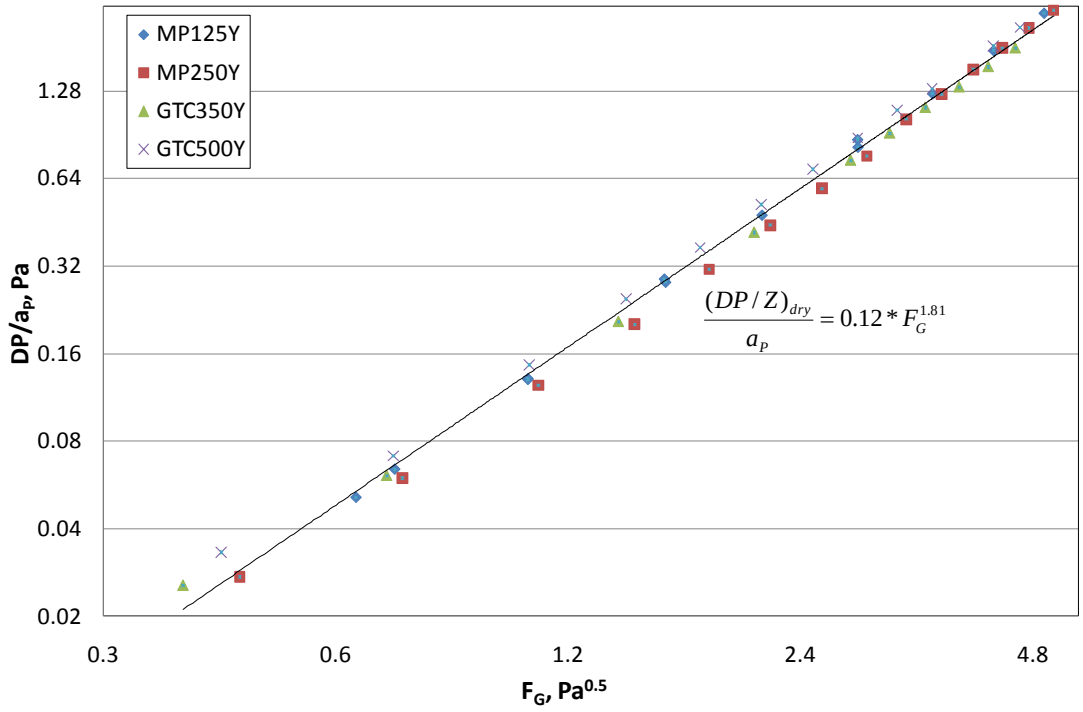

Figure 4.4. Normalized dry pressure drop

Irrigated pressure drop data (liquid flow rate at 24.4 m^3/m^2*h or 10 gpm/ft^2) are shown in Figure 4.5. The data are normalized by dividing pressure drop of packing MP250Y at the same condition. For each packing, normalized pressure drop is quite stable till flood. The capacity difference between the packings is shown, with MP500Y exhibiting a much earlier onset to flooding (F_G ~ 1.7 $Pa^{0.5}$) compared to MP125Y (F_G ~ 3.9 $Pa^{0.5}$). In the preloading region, the normalized pressure drop increases with packing specific area (MP125Y ~ 0.68, MP250Y ~ 1.45, GT-PAK™ 350Y~ 2.08, GT-PAK™ 500Y ~ 4.31), but the ratio is not constant. For high surface area packing, the value is higher than expected since resistance for gas and liquid flow is much higher.

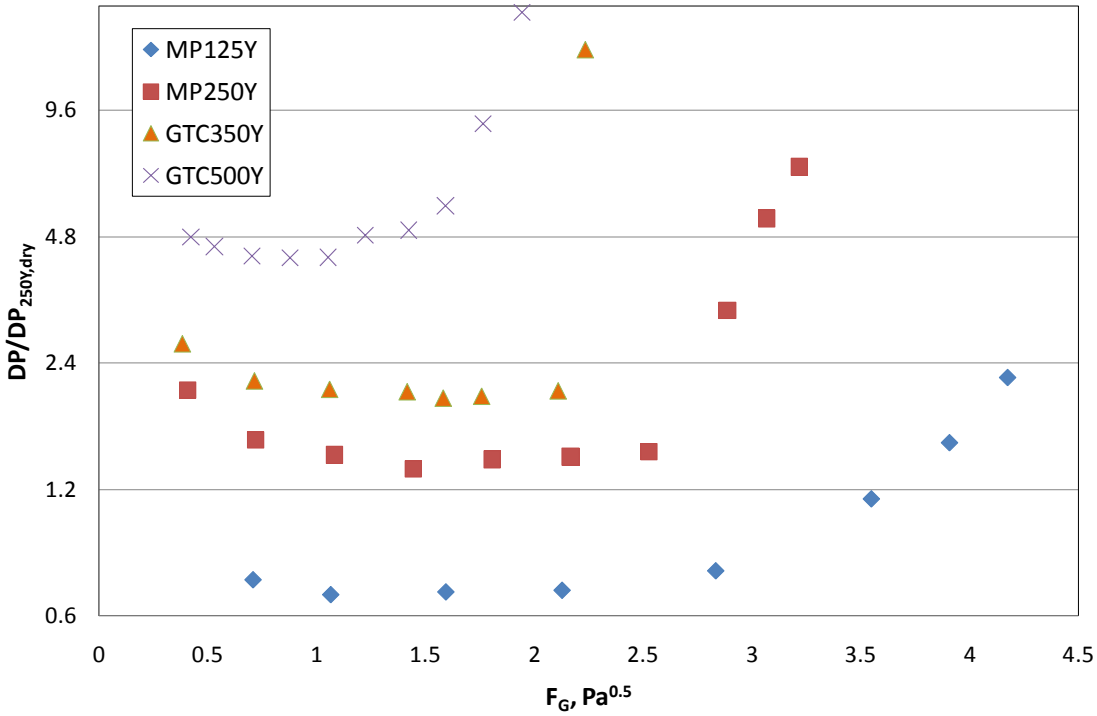

Figure 4.5. Normalized irrigated pressure drop at liquid load of 24.4 m^3/m^2*h

A comparison of liquid hold-up of these four packings is shown in Figure 4.6. The capacity difference between packings is also evident in this plot (MP125Y the largest capacity and GT-PAK™ 500Y the smallest capacity). Liquid hold-up increases with packing specific area but the relative value decreases (MP125Y ~ 3%, MP250Y ~ 6%, GT-PAK™ 350Y ~ 8%, GT-PAK™ 500Y ~ 9%). There are two reasons for this. One, the larger surface area packing is packed more intensively with higher resistance for liquid flowing down than smaller surface area packing which is why liquid hold-up increases with packing surface area. Two, the larger surface area packing has less void space for liquid to fill which is why the increasing ratio decreases.

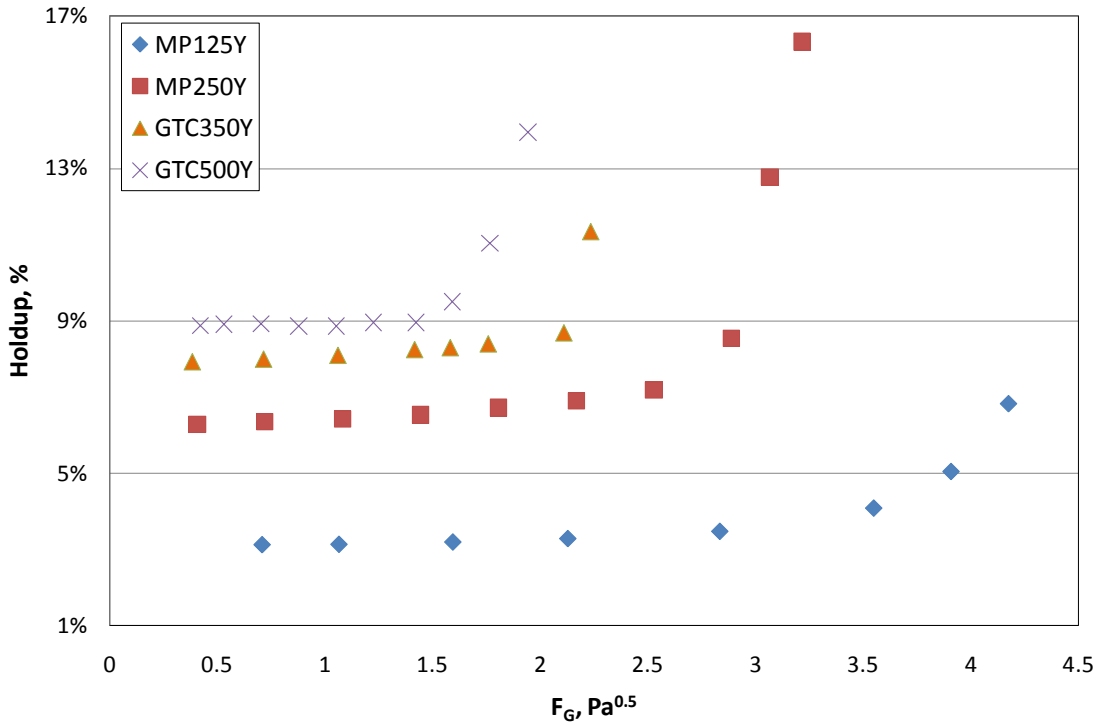

Figure 4.6. Liquid hold-up comparison at liquid load of 24.4 m^3/m^2*h

4.1.3 Effect of Packing Corrugation Angle

Besides the packing specific area, another factor that will influence the hydraulic performance of the packing is the corrugation angle. Figure 4.7 shows the normalized dry pressure drop of two pairs of packing: MP250Y/X and GT-PAK^{TM} 350Y/Z. An increase in the corrugation angle will result in a significant reduction in pressure drop. A 51% pressure drop reduction is observed for the MP250X relative to MP250Y and 64% from GT-PAK^{TM} 350Y to 350Z. The ratio is also maintained in the irrigated conditions (24.4 m^3/m^2*h or 10 gpm/ft^2) as shown in Figure 4.8 where pressure drop is reduced by 60% from MP250Y to MP250X and 68% from GT-PAK^{TM} 350Y to 350Z. A larger increase in corrugation angle also causes a larger reduction in fractional liquid hold-up, though the difference is not as significant. Liquid hold-up comparisons of MP250Y/X and GT-PAK^{TM} 350Y/Z are shown in Figure 4.9. Similar with pressure drop, liquid hold-up decreases as packing corrugation angle increases.

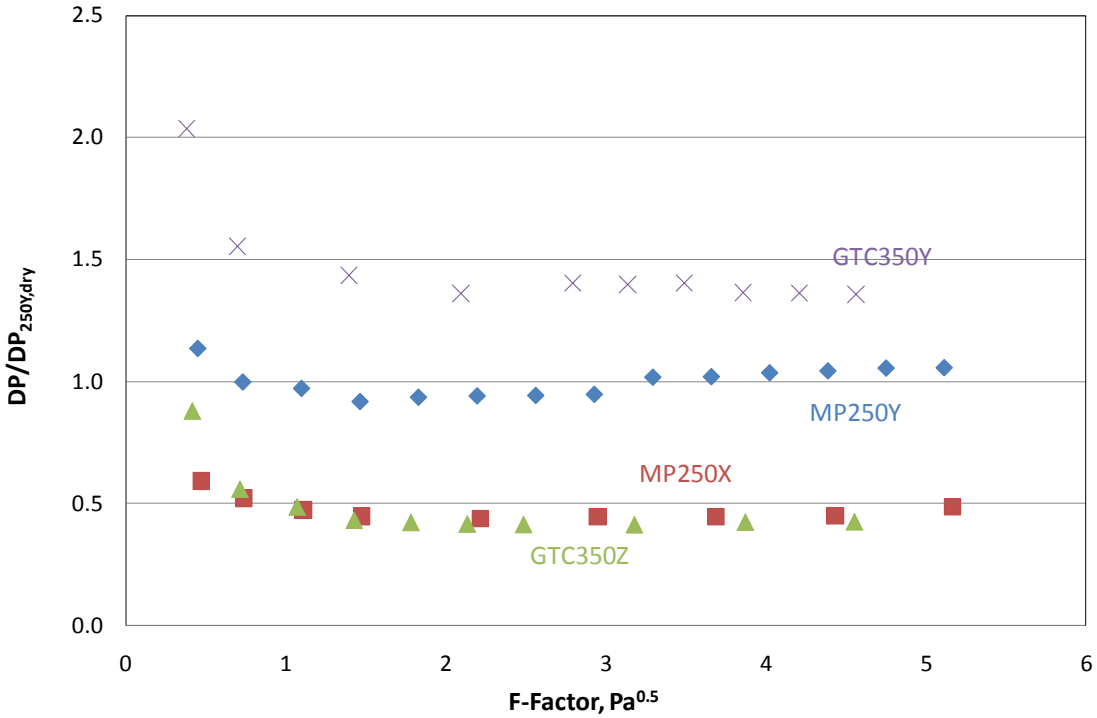

Figure 4.7. Normalized dry pressure drop of MP250Y/X, GT-PAK™ 350Y/Z

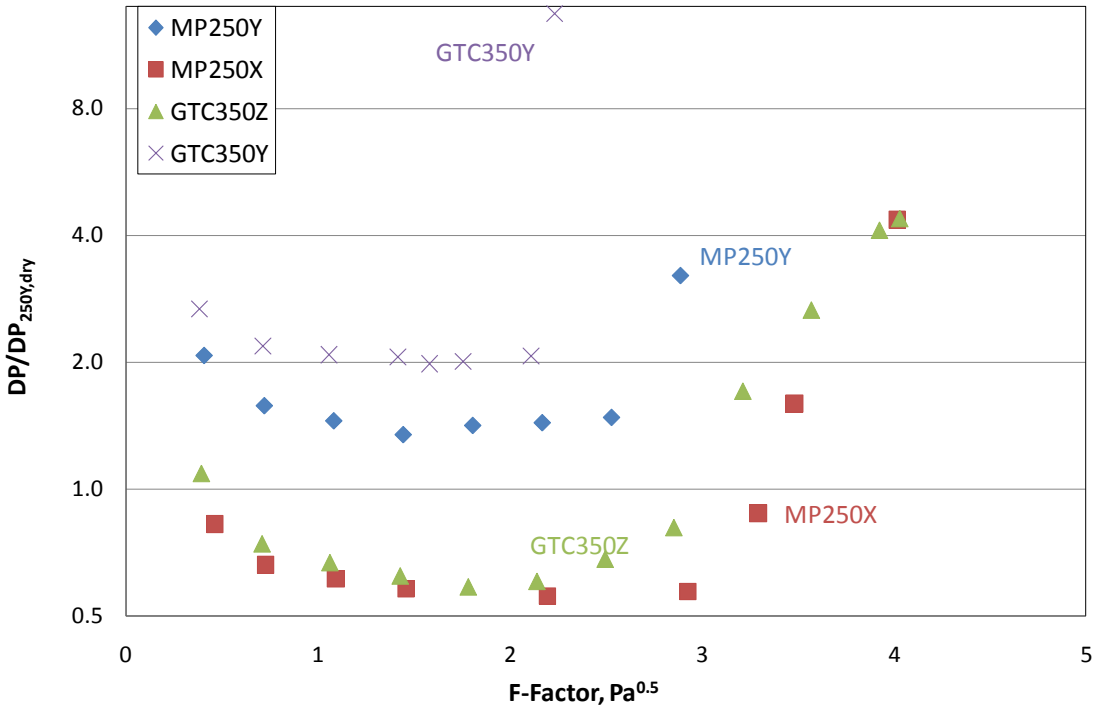

Figure 4.8. Normalized irrigated pressure drop of MP250Y/X, GT-PAK™ 350Y/Z at a liquid load of 24.4 m^3/m^2*h (10 gpm/ft^2)

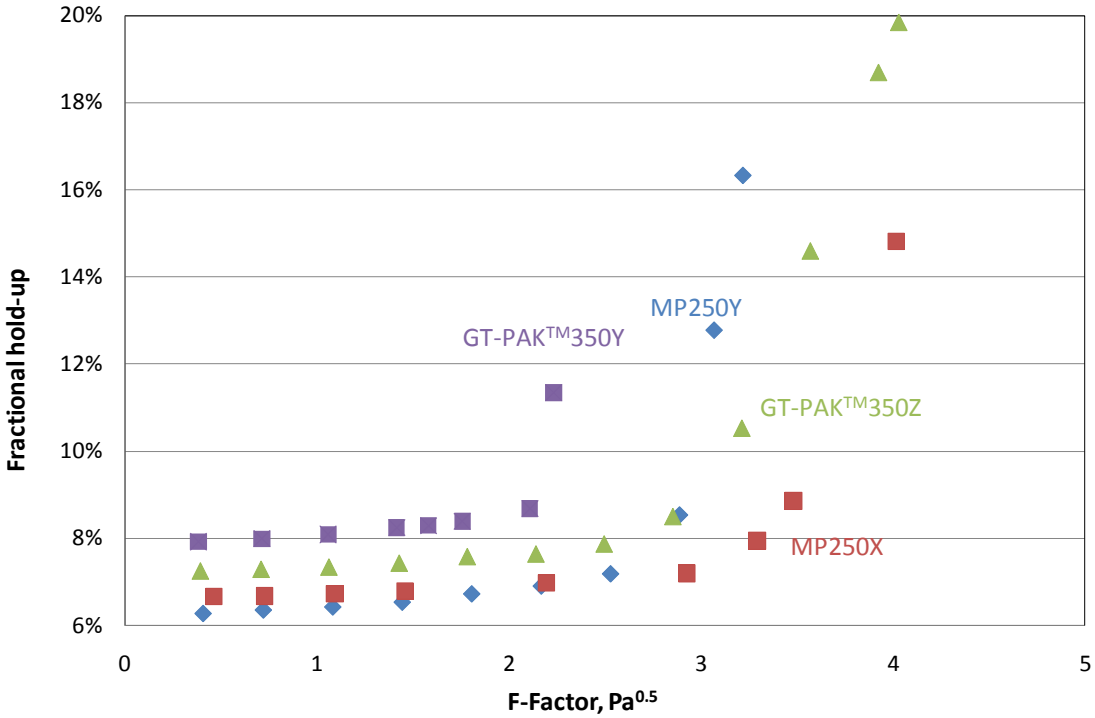

Figure 4.9. Liquid hold-up of MP250Y/X, GT-PAK™ 350Y/Z at a liquid load of 24.4 m^3/m^2*h (10 gpm/ft^2)

4.1.4 Effect of Packing Nominal Size (Random packing)

Several random packings were also studied in this work. For random packings, nominal size is the equivalent packing diameter that can describe the packing piece. Larger nominal size packings have a higher void fraction and thus smaller specific area per volume. Figure 4.10 illustrates nominal size influence on dry pressure drop. Three packings with different nominal sizes are compared. The characteristics are listed in Table 4.1. with a with larger surface area structured packings, the lower void fraction and larger resistance for liquid and gas flow promote a higher pressure drop. Normalized pressure drop increases as a ratio of packing specific area (RSR#0.7 ~ 1.2, RSR#0.5 ~ 3.0, RSR#0.3 ~ 4.1). Irrigated pressure drop follows this trend (Figure 4.11) but the ratio is higher.

The fractional liquid hold-up characteristics are compared in Figure 4.12. Liquid hold-up decreases as nominal size increases (packing specific area decreases). Packing capacity increases as nominal size increases. However, the difference between RSR#0.3 and #0.5 is not quite significant.

Table 4.1. Characteristics of Raschig Super Rings

	Nominal size	Void fraction	Specific area, a_P
	mm	%	m^2/m^3
RSR#0.3	15	96	315
RSR#0.5	20	97	250
RSR#0.7	25	98	180

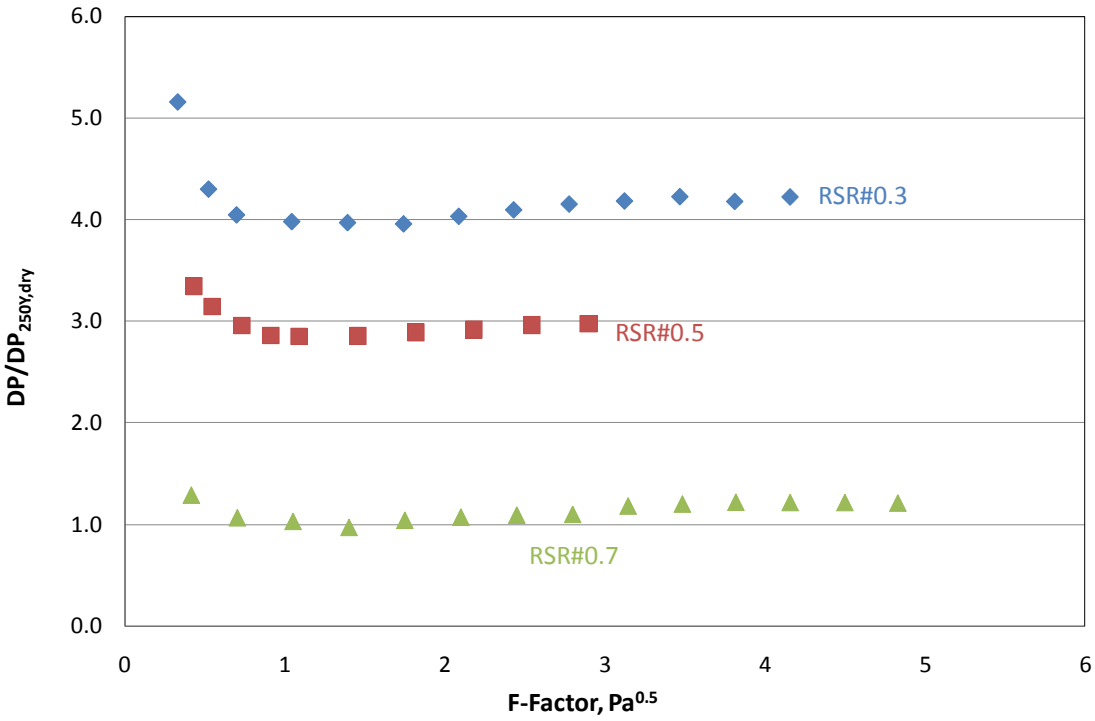

Figure 4.10. Normalized dry pressure drop of RSR#0.3, #0.5, #0.7

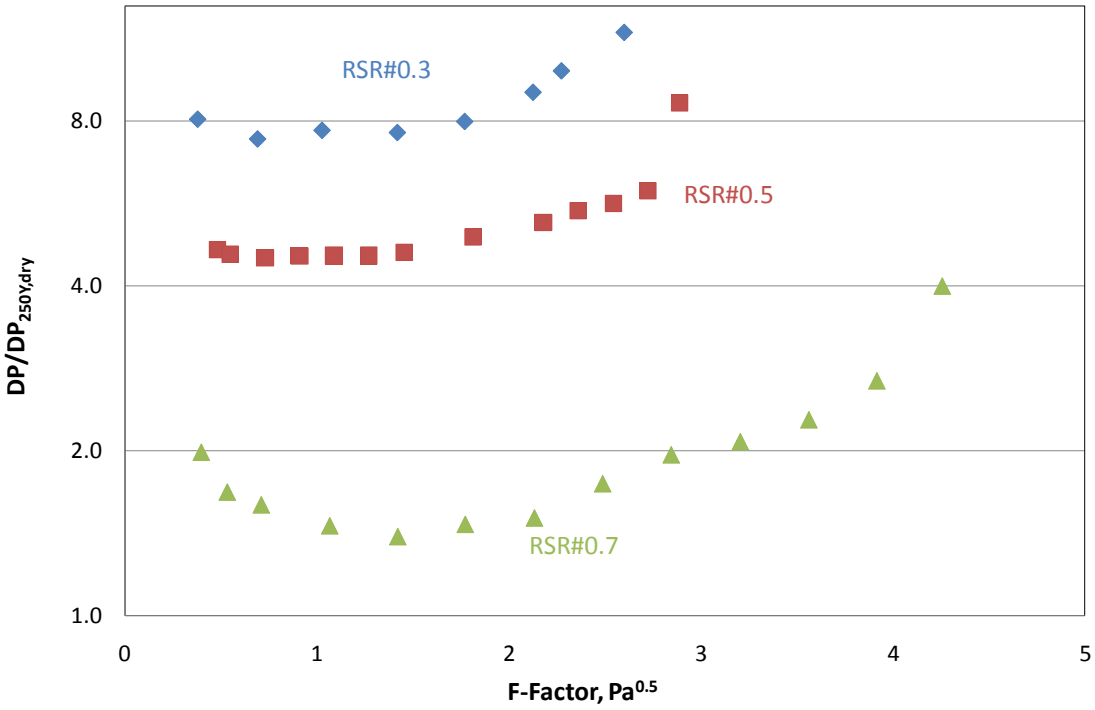

Figure 4.11. Normalized irrigated pressure drop of RSR#0.3, #0.5, #0.7 at liquid load of 24.4 m^3/m^2*h (10 gpm/ft^2)

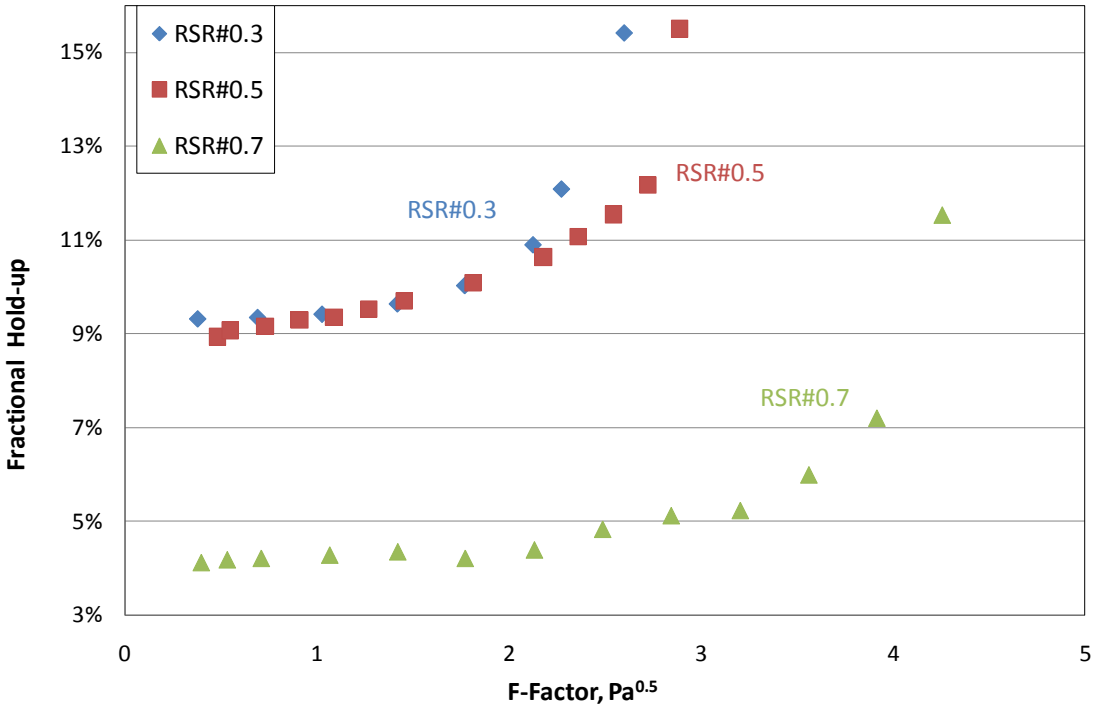

Figure 4.12. Fractional liquid hold-up of RSR#0.3, #0.5, #0.7

4.2 Mass Transfer Area

4.2.1 Effect of Gas and Liquid velocities

The first mass transfer property explored is the effective packing mass transfer area (effective area). Figure 4.13 shows the effective area measured at different gas and liquid velocities for MP250Y. The effective area increases with liquid velocity to 0.15 power for all gas velocities. The effective area increases by about 9% when gas velocity increases from 0.59 m/s to 1.48 m/s, and increases by 2–3% as gas velocity keeps increasing until flood. All other packings show similar results, where the effective area is a function of liquid velocity and a slight function of gas velocity.

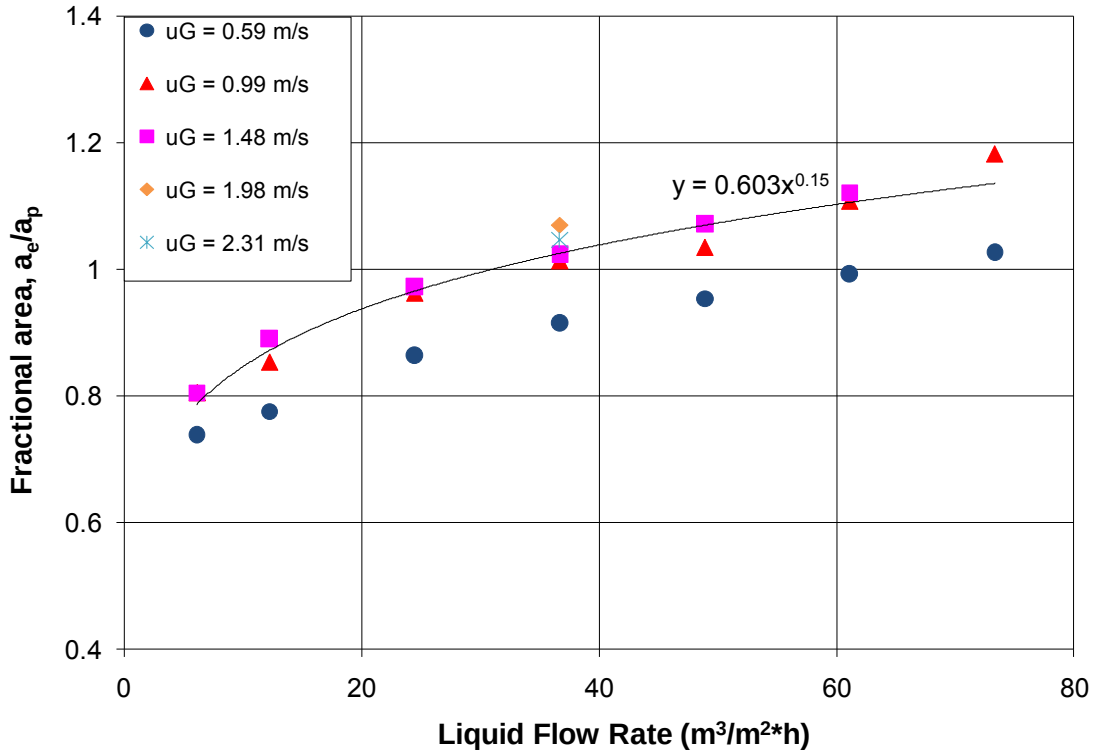

Figure 4.13. Fractional effective area of MP250Y

4.2.2 Effect of Packing Surface Area

The effective area of four structured packings with identical corrugation angles (45 degree) and surface area ranging from 125 to 500 m^2/m^3 are compared in Figure 4.14. The gas velocity is 0.99 m/s (300 ACFM) for all packings. Every packing shows an increase in effective area with increasing liquid load which confirms the conclusion in the previous section. At the same liquid load, the effective area increases with packing surface area. However, the effective area increases at a smaller ratio than the packing surface area increases. The effective area of 250Y is 43% greater than 125Y, which is less than the 50% difference between the surface areas. The effective area of 500Y is 14% greater than 350Y which is less than the 30% surface area difference. The phenomenon of lower specific surface area packing providing higher fractional effective area is illustrated in Figure 4.15. Rivulets, ripples, and droplets formation between the sheets, those mass-transfer-enhancing film instabilities (Henriques de Brito, 1994), are easily formed in coarser packings with high void fraction. End effects and wall effects could also have a relative higher impact on coarser packings. Finer packings such as 350Y and 500Y could be more subject to maldistribution and insufficient wetting, causing a relative lower fractional effective area.

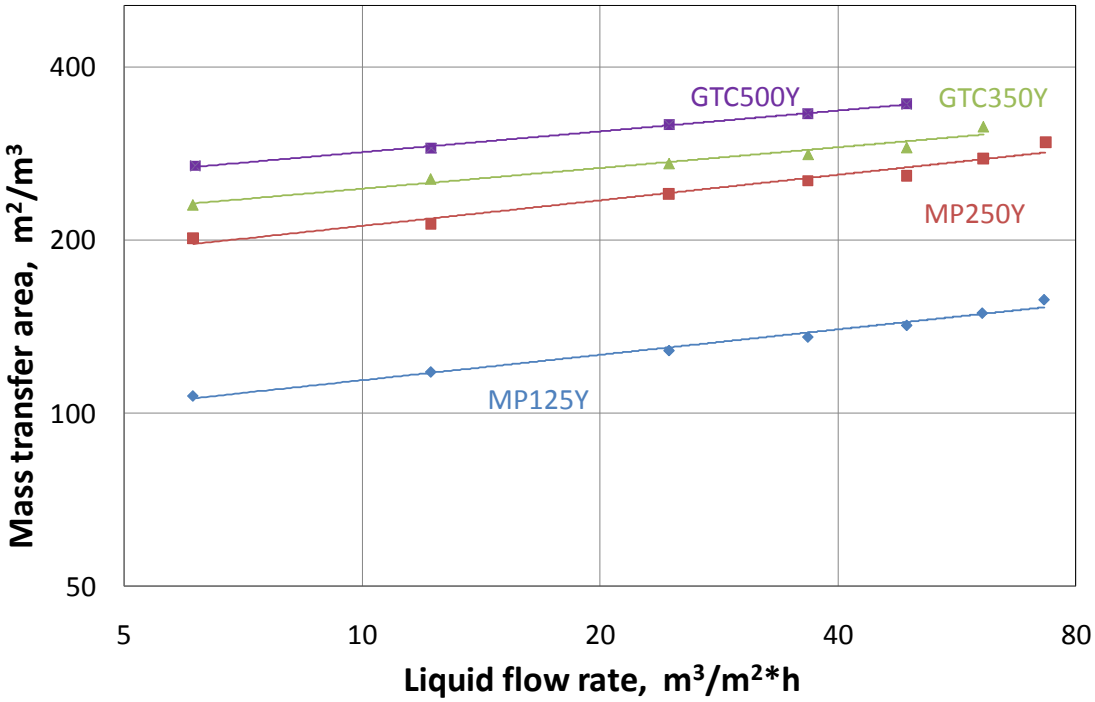

Figure 4.14. Mass transfer area comparison between 125Y, 250Y, 350Y, 500Y

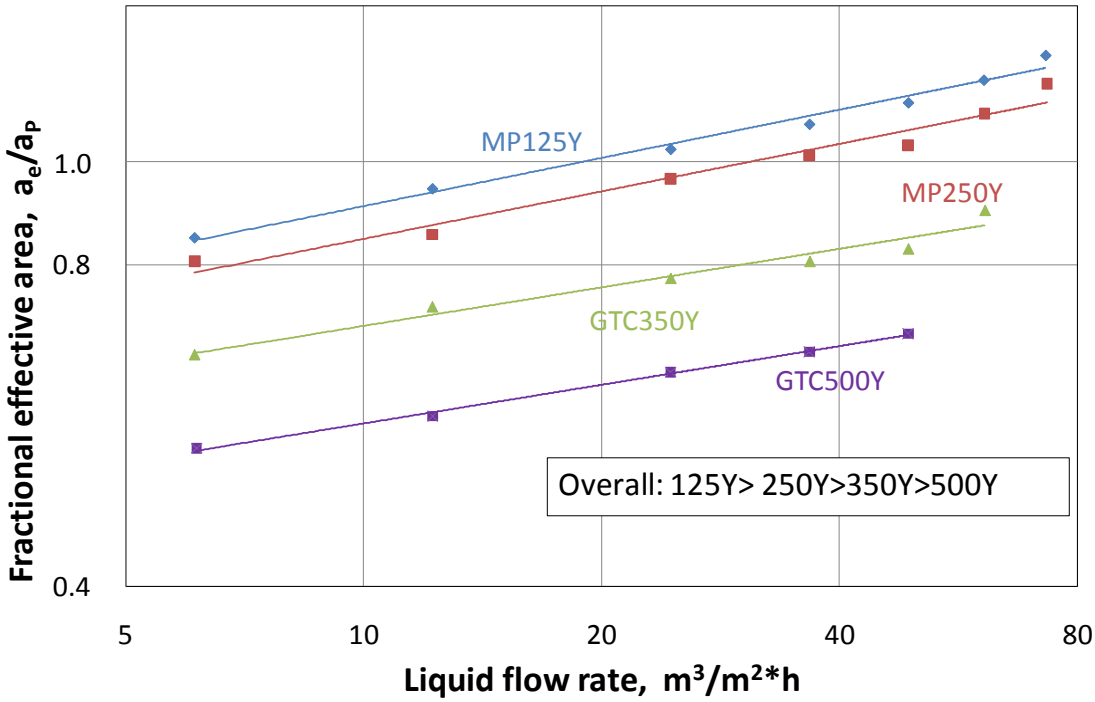

Figure 4.15. Fractional effective area comparison between 125Y, 250Y, 350Y, 500Y

4.2.3 Effect of Packing Corrugation Angle

The effective areas of MP250Y and 250X are compared in Figure 4.16. MP250X has an equivalent specific surface area and geometric structure except for its higher corrugation angle (60 degrees) relative with MP250Y (45 degrees). The solid dots are experimental data measured at all three gas velocities (0.6 m/s, 0.99 m/s, 1.48 m/s) and the solid lines are trend lines of experimental data. The measured effective area of MP250Y is 6% higher than MP250X. However, this difference is insufficient to distinguish from the experimental error. These two packings are assumed to have the same effective area.

A similar conclusion is also reached in the comparison between GT-PAK™ 350Y/Z (Figure 4.17). These two packings have an equivalent surface area and geometric structure except for the corrugation angle. GT-PAK™ 350Y has a 45-degree corrugation angle while 350Z has a 70-degree angle. The difference of measured effective area between these two packings is 7%, which is still within the 10% experimental noise range.

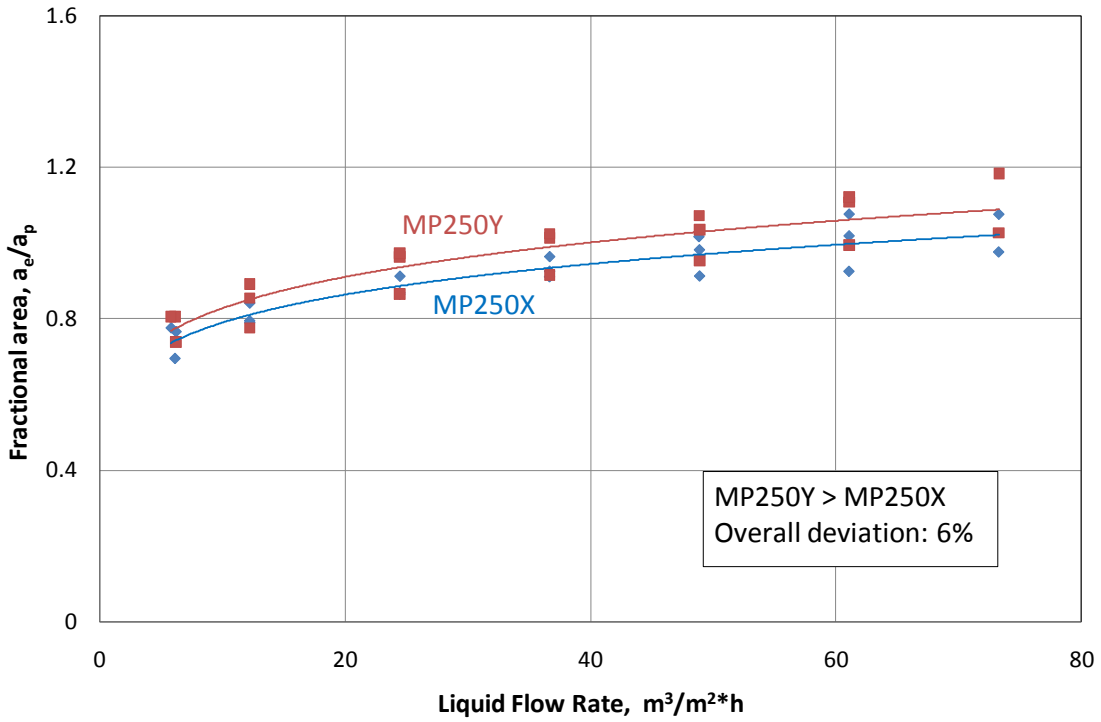

Figure 4.16. Fractional effective area comparison between MP250Y/X

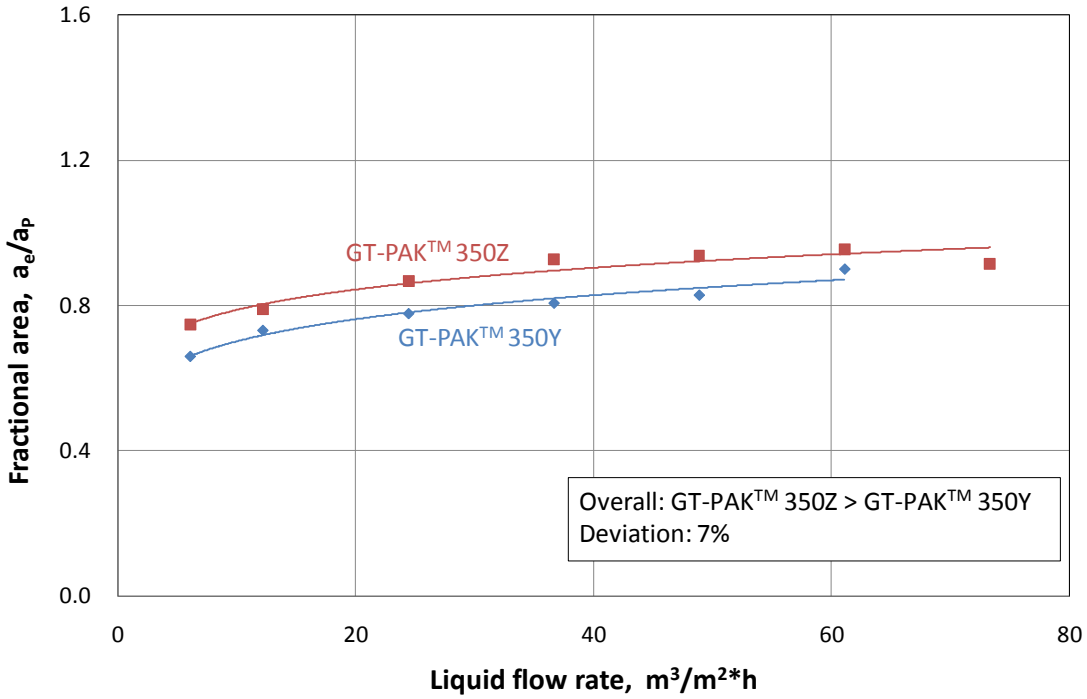

Figure 4.17. Fractional effective area comparison between GT-PAK™ 350Y/Z

The conclusion that the corrugation angle has little impact on the effective area was also confirmed by a previous University of Texas researcher (Tsai, 2010). It is believed that effective area is determined by the wettability of the packing surface. Thus, the effective area would be influenced by: (1) the surface tension which determines the contact angle of liquid and packing surface; and (2) the liquid phase Reynolds number which determines the liquid flow pattern. Other factors such as gas velocity, liquid viscosity, and packing corrugation angle would not have a significant impact on effective area. The effective area model is composed by these influencing factors and will be further discussed in Chapter 5.

4.2.4 Effect of Packing Nominal Size (Random packing)

The effective areas of three Raschig Super Rings (RSR#0.3, 0.5, 0.7) with different nominal sizes are compared in Figure 4.18. The effective area increases as packing nominal size decreases (packing surface area increases). Similar to structured packing, the effective area of Raschig Super Rings increases at a smaller ratio than the surface area increases. The effective area of RSR#0.3 is 11% greater than RSR#0.5, which is less than the 19% difference between the surface areas. The effective area of RSR#0.5 is 6% higher than RSR#0.7, which is less than the 28% surface area difference. Considering fractional effective area, the large nominal size packing (RSR#0.7) has a larger fractional area than small nominal size packing (RSR#0.5, 0.3), as shown in in Figure 4.19. Mass-transfer-enhancing film instabilities such as rivulets, ripples, and droplets which form easily between the sheets in large nominal size packing contribute to the mass transfer area.

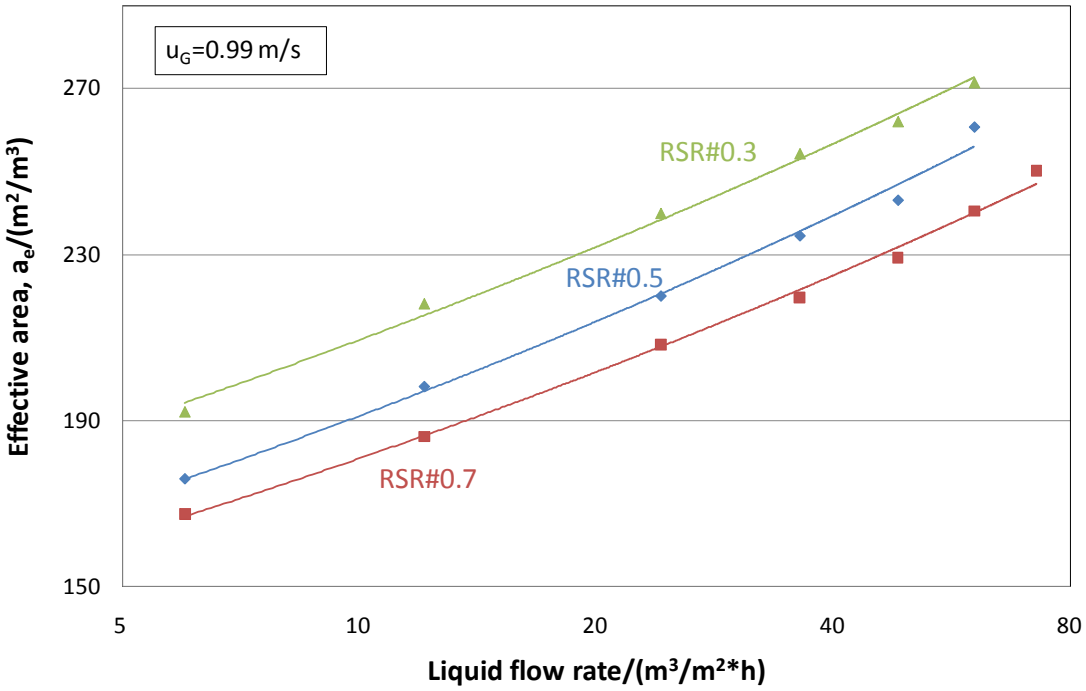

Figure 4.18. Effective area comparison between RSR#0.3, 0.5, 0.7

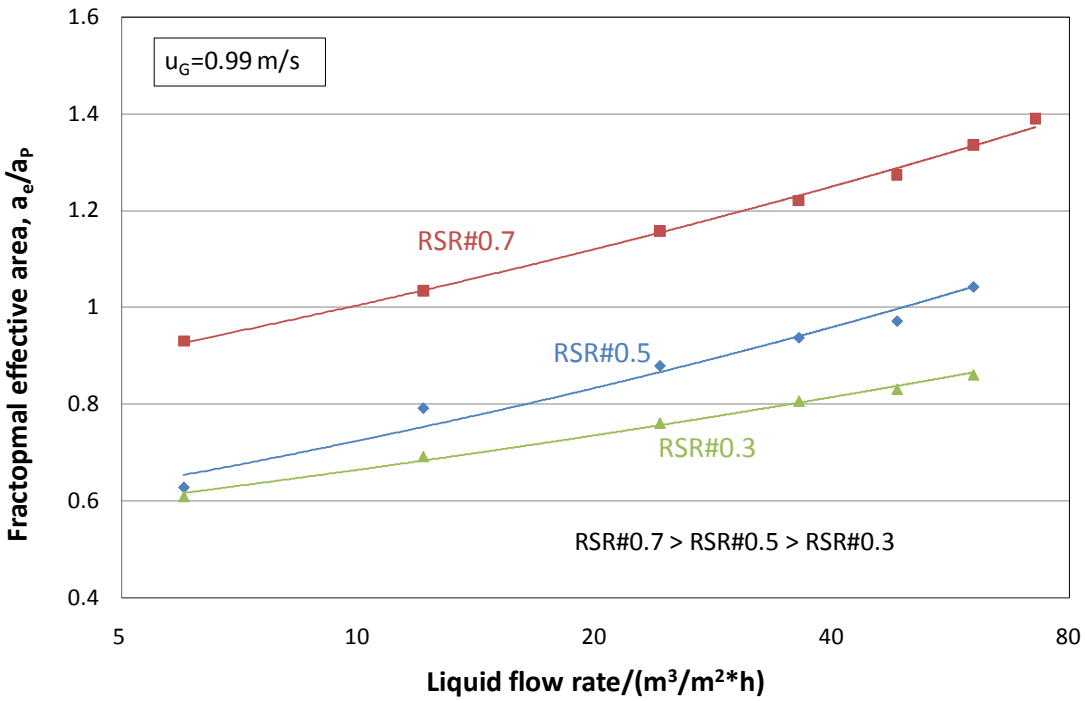

Figure 4.19. Fractional effective area comparison between RSR#0.3, 0.5, 0.7

4.2.5 Effective area summary

The effective area results are summarized in Figure 4.20 at moderate liquid and gas flow rate (0.99 m/s for gas velocity and 24.4 m/h for liquid velocity). In this work, three types of packings were measured: structured packing (blue points), hybrid packing (green points), and random packing (red points). For all packings, the fractional effective area decreases with packing surface area (decreasing ratio distinct between packing types). For structured packings, the fractional effective area barely changes with packing corrugation angle. The solid line in Figure 4.20 shows the area model developed in this work, which will be discussed in Chapter 5.

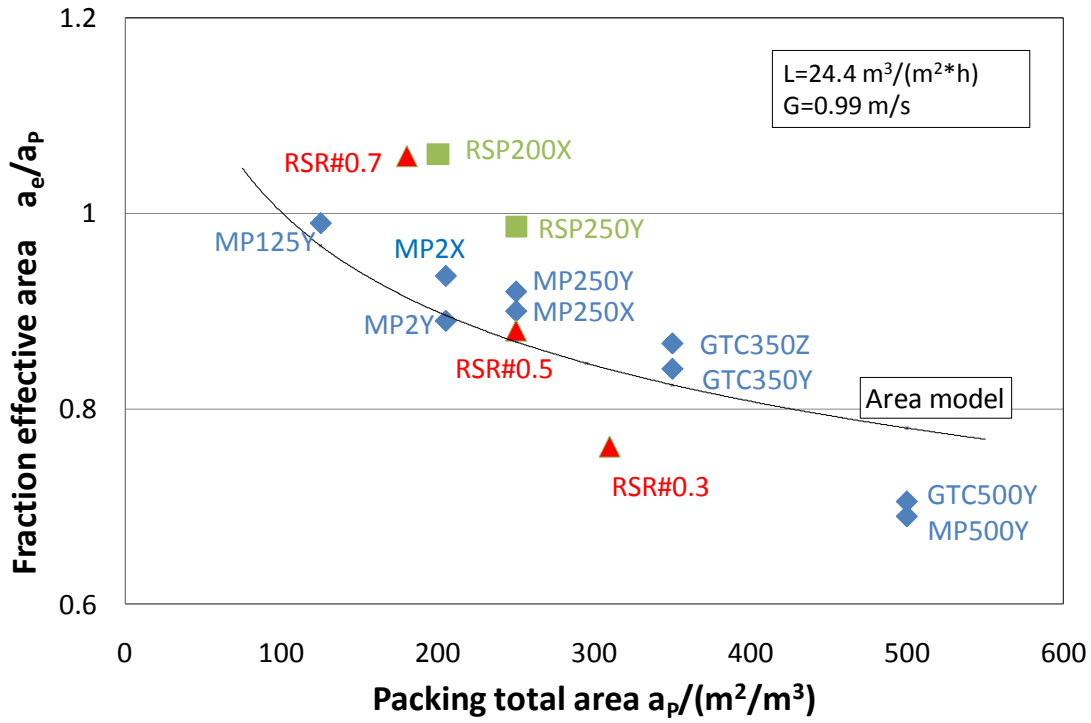

Figure 4.20. Fractional effective area summary

4.3Liquid and Gas Film mass transfer coefficients (k_L and k_G)

4.3.1 Effect of Gas and Liquid velocities

Figure 4.21 shows the liquid film mass transfer coefficient measured at different gas and liquid velocities for GT-PAK™ 350Y. The liquid film mass transfer coefficient (k_L) increases with liquid velocity to 0.71 power. The effective area increases about 2% when gas velocity increases from 0.59 m/s to 0.99 m/s, and increases by 3% from 0.99 m/s to 1.48 m/s. All other packings show similar results: that liquid film mass transfer coefficient is a function of liquid velocity and essentially independent of gas velocity.

Figure 4.22 shows the gas film mass transfer coefficient for MP250Y. The gas film mass transfer coefficient (k_G) increases with gas velocity to 0.61 power while it barely changes with liquid velocity. For safety, environmental, and cost concerns, only a few data points were repeated at different liquid velocities to minimize unnecessary SO_2 scrubbing experiments.

Results show that k_L is only a function of liquid velocity and k_G is only a function of gas velocity. It is because k_L relates to the mass transfer in the bulk liquid phase, and it should not

be influenced by the gas flow. As for k_G, it should only be influenced by the turbulence in the bulk phase of gas, and not be influenced by the liquid flow.

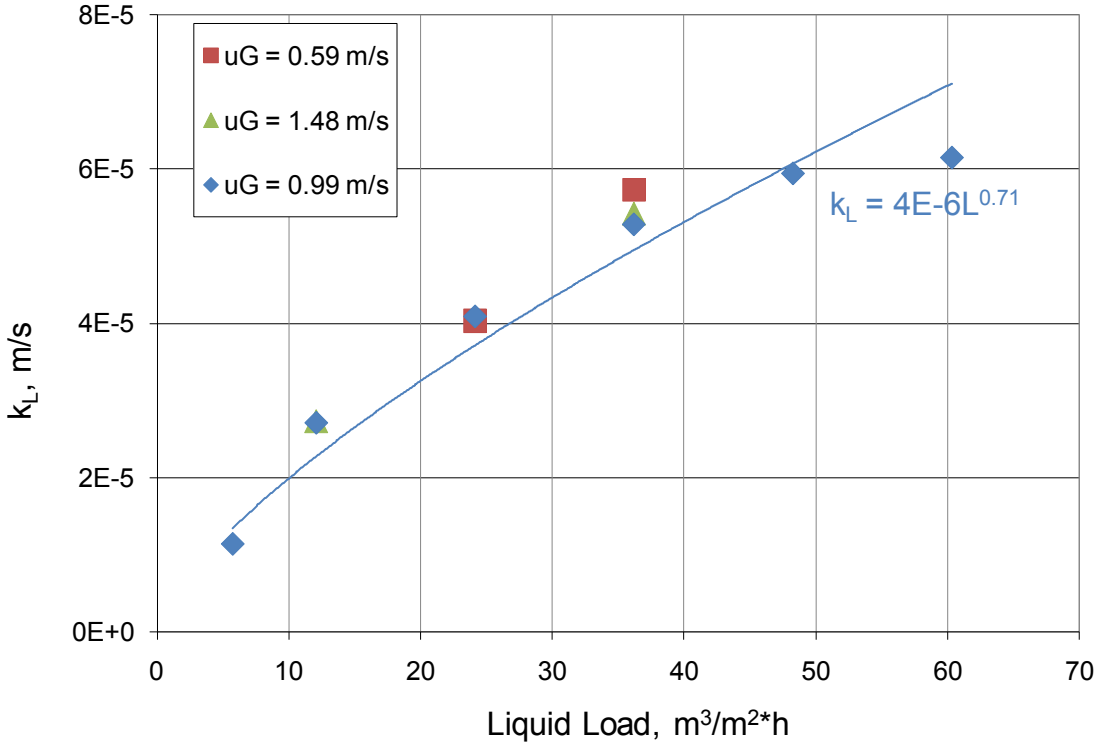

Figure 4.21. Liquid film mass transfer coefficient of GT-PAK™ 350Y

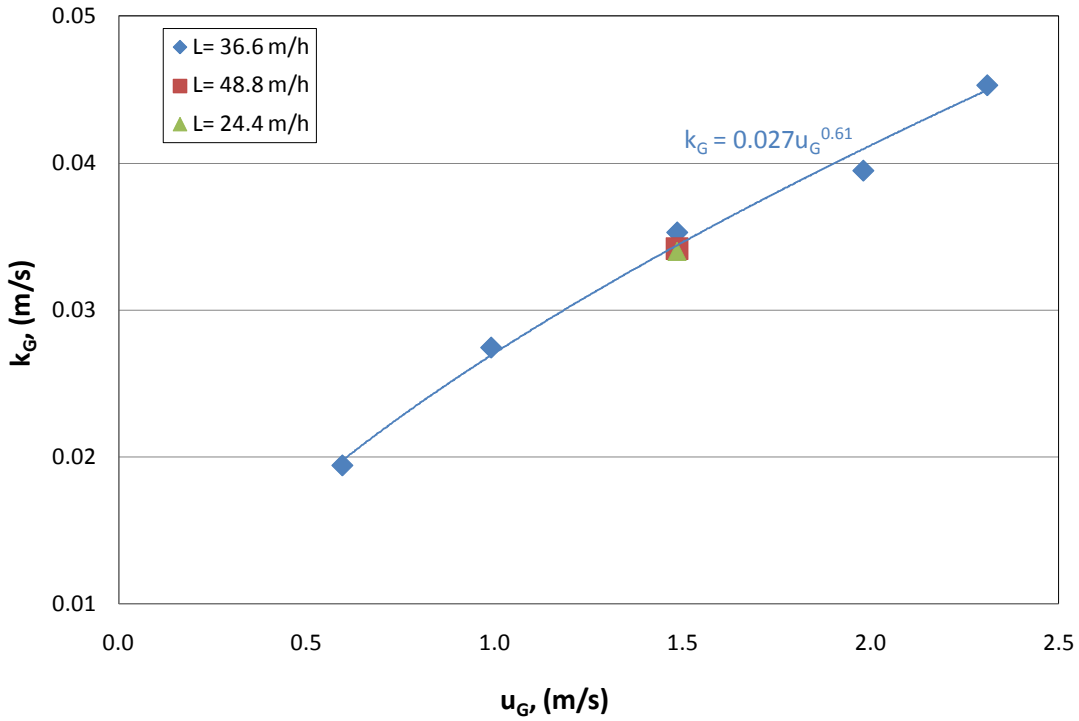

Figure 4.22. Gas film mass transfer coefficient of MP250Y

4.3.2 Effect of Packing Surface Area

Liquid film mass transfer coefficients of packings with same corrugation angle (45 degrees) but different surface area (250, 350, 500 m^2/m^3) are compared in Figure 4.23. For all packings, the k_L value increases with liquid velocity which is consistent with the conclusion in Section 4.3.1. At the same gas and liquid flow rate, the k_L value increases as surface area increases. In general, the k_L value of 500Y is 33% higher than 350Y, and the k_L value of 350Y is 21% higher than 250Y. These differences are higher than the anticipated experimental error of 10%.

A similar conclusion is found when comparing the gas film mass transfer coefficient of packings with different surface areas (Figure 4.24). At similar gas and liquid flow rates, the k_G value of 500Y is 23% higher than 350Y, and the k_G value of 350Y is 22% higher than 250Y. The difference between 250Y and 125Y is negligible (only 3%) since there could be extra bubbles, ripples creating mass transfer in the low specific area packing like 125Y.

In general, both k_L and k_G increase with surface area. This tendency is also true for random packings (Section 4.3.5). To understand this phenomenon, the packing geometry is studied and a new concept is proposed in Section 4.3.4.

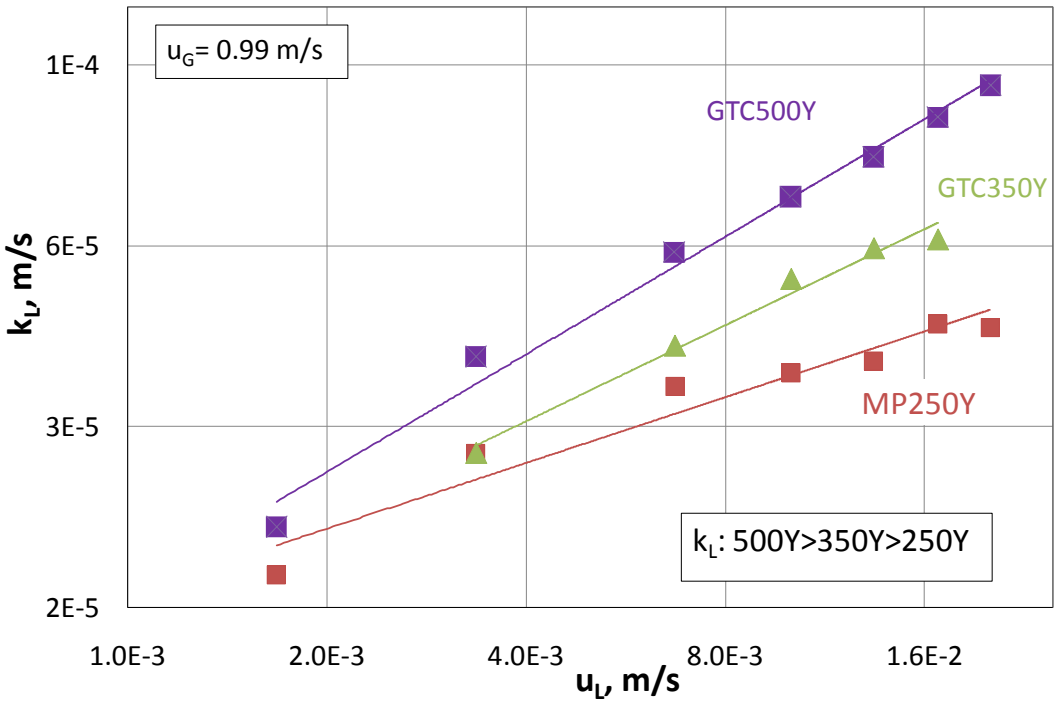

Figure 4.23. k_L comparison between 250Y, 350Y, 500Y

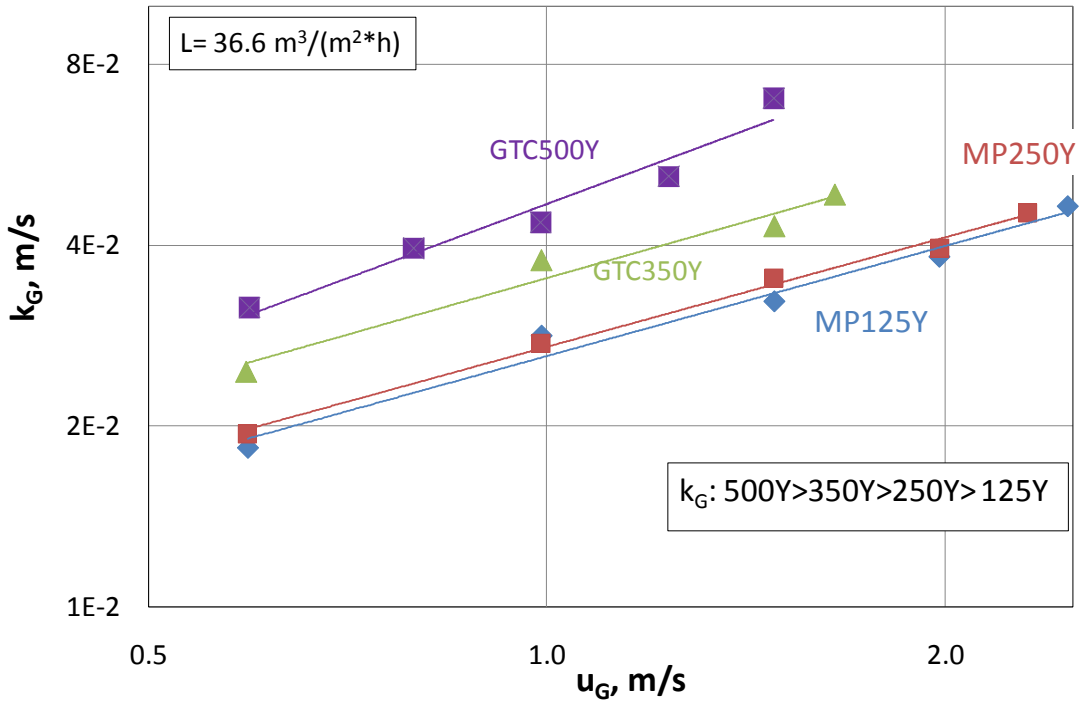

Figure 4.24. k_G comparison between 125Y, 250Y, 350Y, 500Y

4.3.3 Effect of Packing Corrugation Angle

The liquid film and gas film mass transfer coefficients (k_L and k_G) for two packings with the same surface area but different corrugation angles (GT-PAK™ 350Y and 350Z) are compared in Figure 4.25 and Figure 4.26. At the same liquid and gas flow rate, both k_L and k_G increase as corrugation angle decreases from 70 degrees to 45 degrees (350Z to 350Y). The mass transfer coefficient difference between these two packings is between 25% and 35%, which is not negligible. This result is consistent with previous work. Olujic and Fair (2000) reported that Montz B1-250 (45°) had a 20% lower HETP than Montz B1-250.60 (60). Rocha et al. (1996) also predicted the 45° packing to have 15 to 20% greater gas and liquid film mass transfer coefficients than the 60° packing based on distillation data measured by the Separations Research Program at The University of Texas. Considering the previous result where the effective mass transfer area is independent of corrugation angle, it can be interpreted that the increase in the HETP from 60° packing to 45° packing is entirely attributable to a higher mass transfer coefficient.

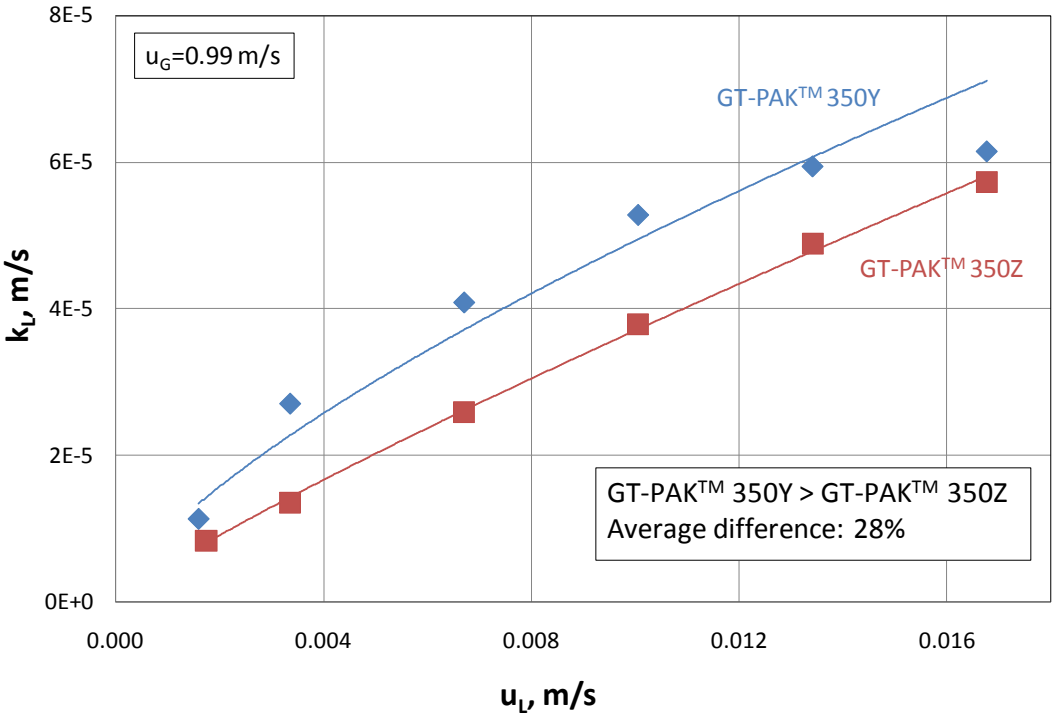

Figure 4.25. k_L comparison between GT-PAK™ 350Y and 350Z

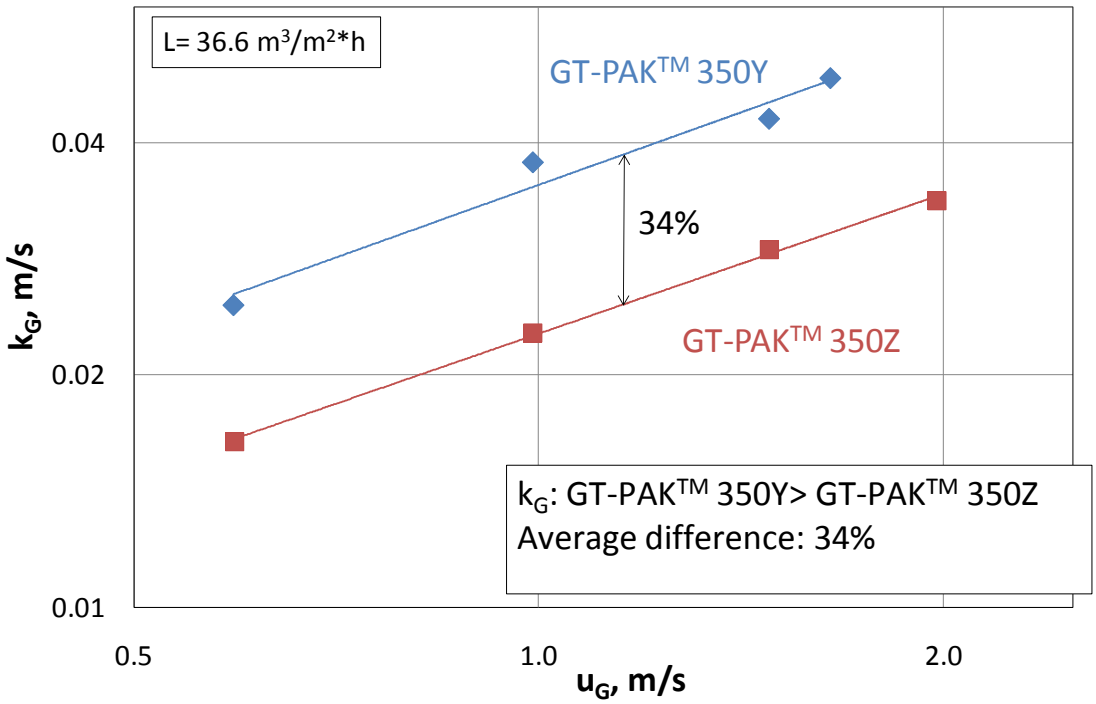

Figure 4.26. k_G comparison between GT-PAK™ 350Y and 350Z

4.4 Conclusions

In this chapter, the effects of operating conditions and packing geometries on hydraulic properties and mass transfer performance were explored. The pressure drop increases steadily with gas flow rate (F-factor) to the power of 1.6–1.9. The pressure drop increases by 30% from dry condition to a liquid load of 5 gpm/ft^2 (12 m^3/m^2*h), and increases slightly with increasing liquid flow rate. The liquid hold-up increases slightly with gas flow rate in the pre-loading region, and increases sharply with gas flow rate in the loading region until flood. Liquid hold-up increases with liquid flow rate at the constant gas flow rate. Both pressure drop and liquid hold-up increase with packing surface area and decrease with packing corrugation angle.

The effective mass transfer area increases with liquid velocity to the 0.15 power and is essentially independent of gas velocity. The fractional effective area decreases as packing surface area increases because of the inefficient wetting in the higher specific surface area packings. Rivulets, ripples, and droplets also provide additional mass transfer area in lower specific surface area packings. The effective mass transfer area is not a function of packing corrugation angle.

The liquid film mass transfer coefficient (k_L) is a function of liquid velocity and independent of gas velocity. Oppositely, the gas film mass transfer coefficient (k_G) is a function of gas velocity and independent of liquid velocity. The k_L increases with liquid velocity (u_L) to the power of 0.5–0.77 for all packings in this work. The k_G increases with liquid velocity (u_G) to the power of 0.43–0.76 for all packings in this work. Summaries of k_L and k_G are given in Figures 4.27 and 4.28.

Packing geometries have similar effects on k_L and k_G. Both k_L and k_G increase as packing surface area increases and decrease as corrugation angle increases. In the next chapter, studies on packing geometries are conducted to understand this phenomenon.

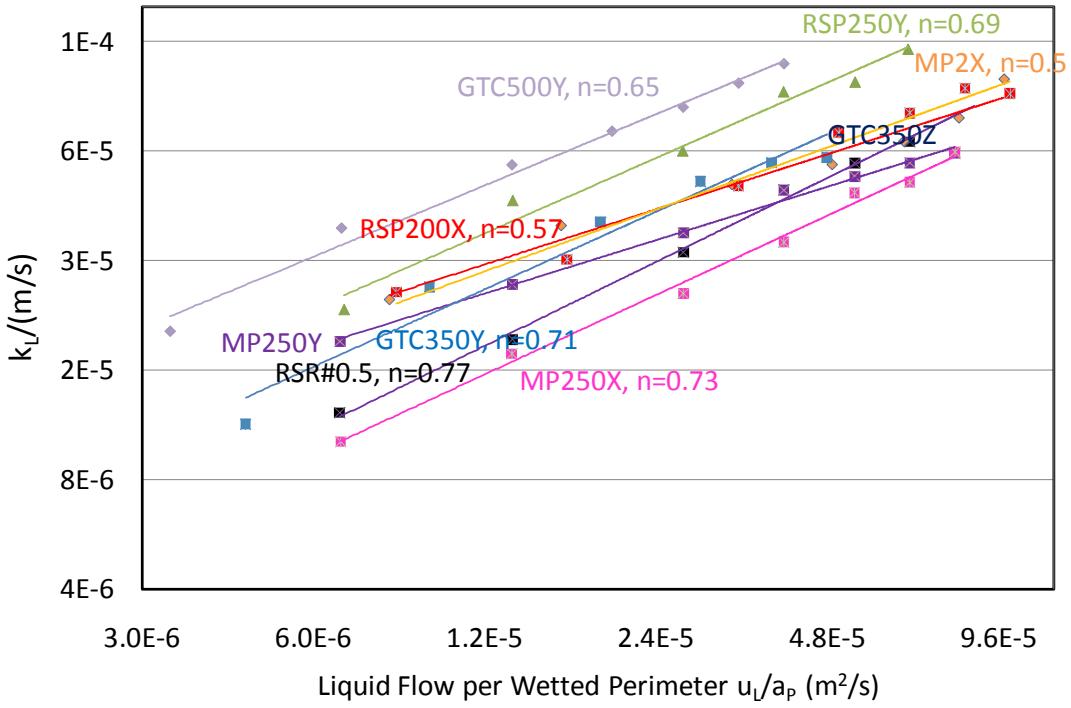

Figure 4.27. Liquid film mass transfer coefficient (k_L) summary

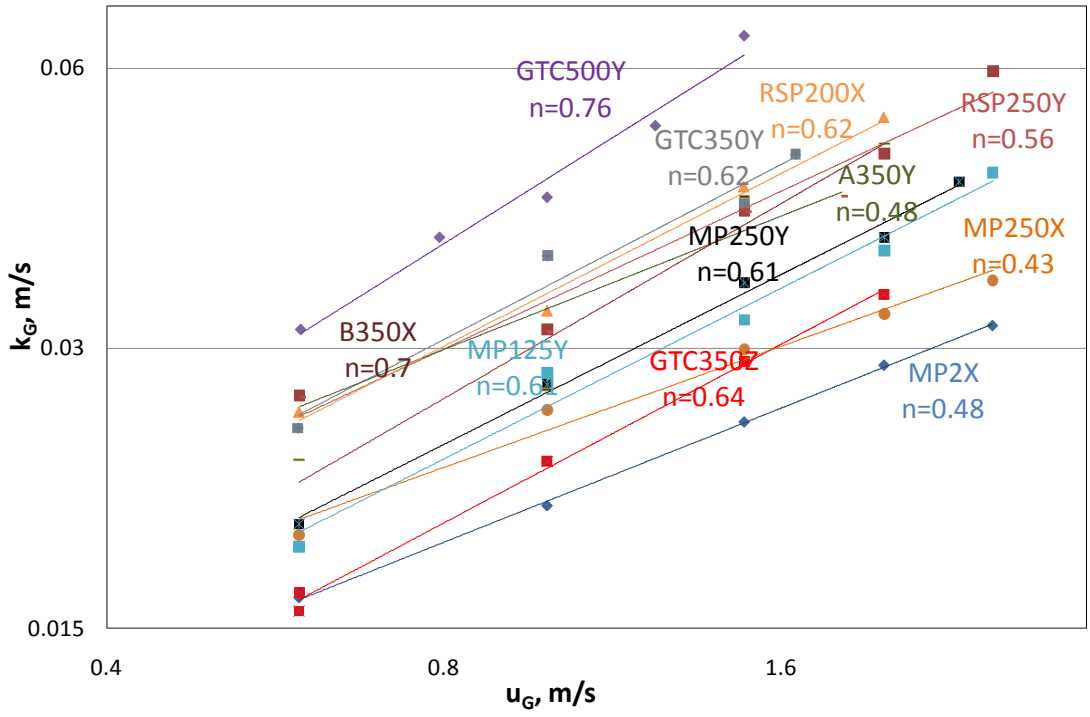

Figure 4.28. Gas film mass transfer coefficient (k_G) summary

Effect of liquid viscosity on the liquid film mass transfer coefficient in packed columns

Quarterly Report for July 1 – September 30, 2014

By Di Song

Supported by the Texas Carbon Management Program

and the

Process Science and Technology Center

The University of Texas at Austin

October 31, 2014

Abstract

In this quarter, a model of surface tension (σ) for NaOH/H_2O/glycerol was built based on literature data. A modified correlation for liquid flow rate (L) of the rotameter in the wetted wall column (WWC) was built, introducing corrected terms for liquid viscosity (μ_L). Based on the updated data for L, surface depletion of each WWC case was calculated, and surface-depletion correction was made to part of the k_g' data. Models of the overall reaction rate constant (k_{Alk}) were built based on empirical data for k_g'. A paper for GHGT-12 was completed summarizing the previous work.

Introduction

Packed columns are important for separation processes including post-combustion CO_2 capture. Since the amine solvent used for CO_2 scrubbing may have a viscosity significantly greater than water, it is important to know how μ_L affects k_L in the column. Few of the existing k_L (k_La) correlations provide satisfactory predictions for the influence of μ_L (Rochelle et al., 2013). This project aims to build a reliable k_L correlation to predict the effect of μ_L on k_L. The overall plan for the project is summarized in previous reports (Rochelle et al., 2014a).

Results

For future measurement of a_e, a model of σ for H_2O/glycerol (Equations 1 & 2) was built based on literature data (Takamura et al., 2012). Ions up to 0.7 N have minimal effect on σ, according to the authors. Literature and calculated values are shown in Figure 1.

$$\sigma_m = \sigma_w + (0.058T - 8.6)w_g \quad (1)$$

$$\sigma_w = 71.7 - 0.0145(T - 30) \quad (2)$$

where:

σ_m = surface tension of H_2O/glycerol (10^{-3} N/m);
σ_w = surface tension of H_2O (10^{-3} N/m);
w_g = weight fraction of glycerol;
T = temperature (°C).

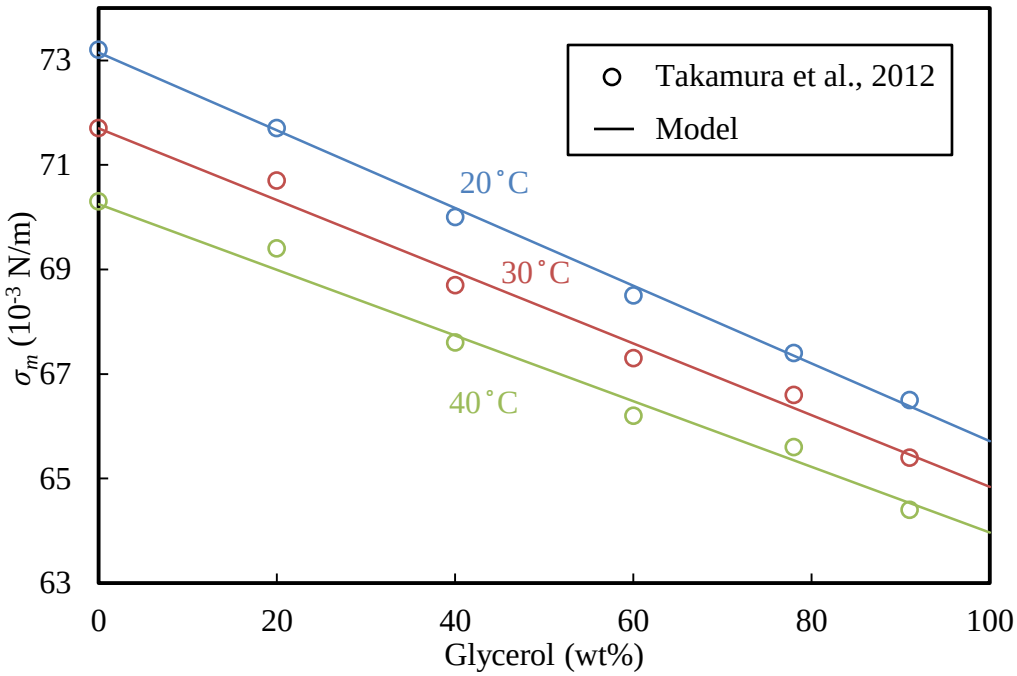

Figure 1: Literature and calculated values of σ for H_2O/glycerol

The correlation developed by Cullinane (2005) has been used by previous researchers (Chen, 2011; Tsai, 2010) to calculate L for the WWC (Equation 3). However, since the ball float in the rotameter is not immune to μ_L, the correlation is no longer accurate for highly viscous liquid (e.g., the correlation overpredicts L by 10 times for 80 wt % glycerol solution at 24 °C). A modified correlation has been built with μ_L correction terms (Equation 4).

$$L = (0.45x - 0.29) \cdot \sqrt{\frac{7.83-\rho_{L,T_{ref}}}{(7.83-0.99)\rho_{L,T_{ref}}}} \cdot \sqrt{\frac{7.83-\rho_L^2}{7.83-\rho_{L,T_{ref}}^2}} \quad (3)$$

$$L = (10.9x - 14.9) \cdot \sqrt{\frac{7.83-\rho_{L,T_{ref}}}{(7.83-0.99)\rho_{L,T_{ref}}}} \cdot \sqrt{\frac{7.83-\rho_L^2}{7.83-\rho_{L,T_{ref}}^2}} \cdot (-0.02\mu^2 + 1.8\mu + 6.3)^{-1.4} \quad (4)$$

where:

L = liquid flow rate (cm^3/s);
x = rotameter reading;
ρ = liquid density (g/cm^3);
T_{ref} = standard temperature of 25 °C;
μ = liquid viscosity (cP).

With the corrected data for L, surface depletion of alkalinity can be calculated with greater accuracy. For liquid with high glycerol concentration (> 80 wt %), it was found that the depletion ratio can be as high as 40% in the worst-case scenario. Within one set of k_g' measurements, the higher the partial pressure of CO_2, the more severe the depletion, which explains the non-zero-intercept problem reported previously (Rochelle et al., 2014b). Correction

of alkalinity surface depletion (Equation 5) was made to k_g' for solutions with high glycerol concentration (> 80 wt %). After the correction, data for k_g' no longer have the non-zero intercept problem (see Figure 2).

$$N'_{CO_2} = N_{CO_2}\sqrt{\frac{1}{1-depletion\%}} \tag{5}$$

where:

N_{CO2} = CO_2 flux (mol·s/cm^2);

N'_{CO2} = CO_2 flux after correction of alkalinity surface depletion (mol·s/cm^2).

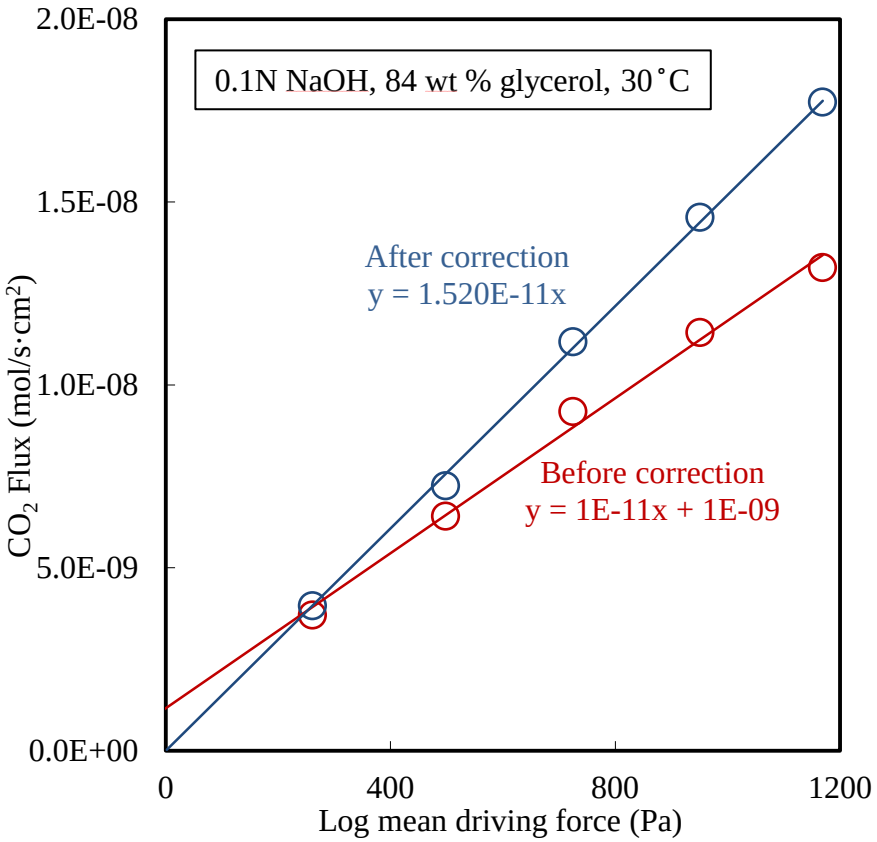

Figure 2: Example of alkalinity surface depletion correction for k_g'

The following equilibrium/reactions are believed to take place in CO_2/NaOH/H_2O/glycerol:

$$Glycerol + OH^- \overset{K_T}{\leftrightarrow} Glycerol^- + H_2O \tag{R1}$$

$$CO_2 + 2OH^- \xrightarrow{k_{OH-}} CO_3^{2-} + H_2O \tag{R2}$$

$$CO_2 + 2Glycerol^- + H_2O \xrightarrow{k_{Gly^-}} CO_3^{2-} + 2Glycerol \tag{R3}$$

k_{Alk} can be determined from empirical k_g' by Equation 6, based on which models have been built (Equations 7–10) to calculate k_{Alk}. Concentrations of hydroxide and glycerol anion can be calculated by Equations 11 & 12, which are derived from material balance of R1–R3.

Parameters of the model are summarized in Table 1. Calculated k_{Alk} and k_{Alk} determined from empirical k_g' are shown in Figure 3.

$$k_{Alk} = \frac{(k_g' H_{CO_2})^2}{[Alk] D_{CO_2}} \tag{6}$$

$$K_T = exp\left(A_1 - \frac{B_1}{T} + C_1[Alk] + D_1[Gly]_T\right) \tag{7}$$

$$k_{OH^-} = exp\left(A_2 - \frac{B_2}{T} + C_2[Alk] + D_2[Gly]_T\right) \tag{8}$$

$$k_{gly^-} = exp\left(A_3 - \frac{B_3}{T} + C_3[Alk] + D_3[Gly]_T\right) \tag{9}$$

$$k_{Alk} = \frac{[OH^-]}{[Alk]} k_{OH^-} + \frac{[Gly^-]}{[Alk]} k_{gly^-} \tag{10}$$

$$[Gly^-]^2 - \left\{[Gly]_T + \frac{1}{K_T} + [Alk]\right\}[Gly^-] + [Alk][Gly]_T = 0 \tag{11}$$

$$[OH^-] = [Alk] - [Gly^-] \tag{12}$$

Table 1: Parameters in Equations 7–9

Subscript	A	B	C	D
1	-9.26	-2400	19.0	-0.43
2	22.7	6037	1.16	0.10
3	20.2	4575	-12.5	0.15

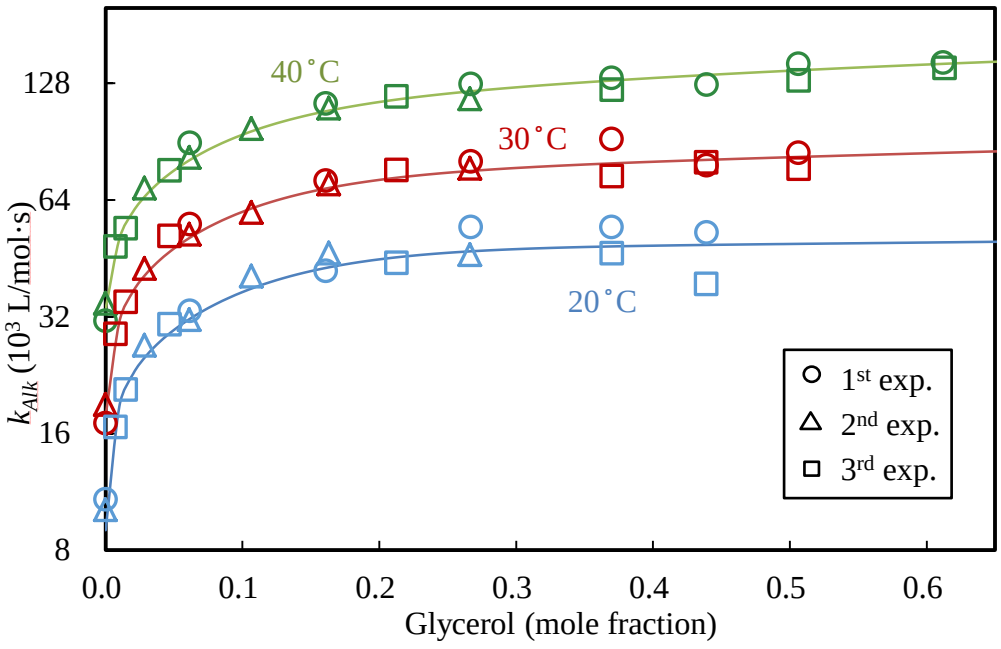

Figure 3: Calculated k_{Alk} and k_{Alk} determined from empirical k_g'

Discussion

The k_{Alk} model needs modification when k_g' data with elevated hydroxide concentration are obtained.

Safety Issues

1. Hard hats are required for experiments outside the control room.
2. Alkaline solvents (NaOH) should be neutralized to pH 6–10 before disposal.
3. A gas mask with respirator is required when handling volatile and toxic chemicals.
4. Steel reinforced gloves are required when handling sheet metal structured packing.
5. During WWC experiments, special caution should be taken to keep the reaction chamber pressure constant by adjusting the gas flow rate and needle valve. A too high pressure may cause leakage or failure of glass tubes.

Conclusions

A model of σ for NaOH/H_2O/glycerol was built based on literature data. A modified correlation for liquid flow rate (L) of the rotameter in the wetted wall column (WWC) was built introducing corrected terms for liquid viscosity (μ_L). Based on the updated data for L, surface depletion of each WWC case was calculated, and surface-depletion correction was made to part of the k_g' data. Models of overall reaction rate constant (k_{Alk}) were built based on empirical data for k_g'.

Future Work

1. Conduct WWC experiments with higher NaOH concentration (0.4 M).
2. Start the a_e measurement in the pilot packed column.

References

Chen X. *Carbon Dioxide Thermodynamics, Kinetics, and Mass Transfer in Aqueous Piperazine Derivatives and Other Amines*. The University of Texas at Austin. Ph.D. Dissertation. 2011.

Cullinane JT. *Thermodynamics and Kinetics of Aqueous Piperazine with Potassium Carbonate for Carbon Dioxide Absorption*. The University of Texas at Austin. Ph.D. Dissertation. 2005.

Rochelle GT et al. "CO_2 Capture by Aqueous Absorption, Third Quarterly Progress Report 2013." Texas Carbon Management Program. The University of Texas at Austin. 2013.

Rochelle GT et al. "CO_2 Capture by Aqueous Absorption, First Quarterly Progress Report 2014." Texas Carbon Management Program. The University of Texas at Austin. 2014a.

Rochelle GT et al. "CO_2 Capture by Aqueous Absorption, Second Quarterly Progress Report 2014." Texas Carbon Management Program. The University of Texas at Austin. 2014b.

Takamura K, Fischer H, Morrow NR. "Physical properties of aqueous glycerol solutions." *J Pet Sci Eng*. 2012;98–99(0):50–60.

Tsai RE. *Mass Transfer Area of Structured Packing*. The University of Texas at Austin. Ph.D. Dissertation. 2010.

Kinetic Modelling of 4 m 2MPZ/4 m PZ and 4 m AMP/2 m PZ

Quarterly Report for July 1 – September 30, 2014

by Brent Sherman

Supported by the Texas Carbon Management Program

and the Carbon Capture Simulation Initiative

McKetta Department of Chemical Engineering

The University of Texas at Austin

October 31, 2014

Abstract

The kinetics of two different piperazine (PZ) blends were regressed: 4 m 2-methylpiperazine (2MPZ)/4 m PZ and 4 m 2-amino-1-propanol (AMP)/2 m PZ. For each, wetted wall column (WWC) flux data covering a wide loading and temperature range were regressed using activity-based kinetics. The pseudo-first-order rate constants show that the fastest reaction for 2MPZ/PZ is the formation of $PZ(COO^-)_2$ catalyzed by free 2MPZ, and for AMP/PZ it is the formation of $AMPCOO^-$ catalyzed by free AMP. While this is reasonable for the AMP/PZ system, it is suspicious for the 2MPZ/PZ system as the formation of $PZCOO^-$ catalyzed by free PZ should be the fastest. Further, the rate-based absorber model with kinetics could not be converged for 2MPZ/PZ due to an unreasonable 2MPZ zwitterion activity coefficient. While a working process model was achieved by removing zwitterion reactions, this model underpredicts the mass transfer of CO_2.

Introduction

This work has four goals: rigorous thermodynamic and kinetic models; a generic amine modeling method; viscosity process effects; and economic evaluation. Developing more rigorous models enables the creation of a generic amine modeling method. The aim of the method is to streamline model development, shortening the time to a process model. Process performance can be evaluated from an economic standpoint with special interest paid to viscosity effects.

A process model requires both a thermodynamic and a kinetic model. This past quarter the kinetics of two systems were modeled: 4 m 2MPZ/4 m PZ and 4 m AMP/2 m PZ. The thermodynamic model for each is complete (Sherman et al., 2014; Li et al., 2014). Process modeling using the 2MPZ/PZ model revealed underlying flaws in the 2MPZ thermodynamic model that necessitate repeating the regression of the 2MPZ subsystem. Using these kinetic models, the dominant reactions of the systems can be established. Determining the dominant reactions elucidates the most important parameters.

CCSI Activities

There are two parallel uncertainty quantification (UQ) efforts in CCSI. One is focused on upgrading the MEA model Phoenix. The other is focused on the 2MPZ system. Over the summer, the parameters governing the amine volatility of 2MPZ in unloaded solution were varied systematically using Latin hypercube sampling. These samples were run using Aspen V7.3 with Turbine, a CCSI product for running thousands of Aspen Plus® cases. Preliminary results are shown in the Appendix.

Modeling Methods

4 m 2MPZ/4 m PZ

Table 1: Reaction set for 4 m 2MPZ/4 m PZ. Kinetic reactions are numbered.

Stoichiometry	Reaction
$PZCOO^- + H_2O + CO_2 \leftrightarrow HPZCOO + HCO_3^-$	1
$2MPZCOO^- + H_2O + CO_2 \leftrightarrow H2MPZCOO + HCO_3^-$	2
$2\ PZCOO^- + CO_2 \leftrightarrow PZ(COO^-)_2 + HPZCOO$	3
$PZCOO^- + 2MPZ + CO_2 \leftrightarrow PZ(COO^-)_2 + 2MPZH^+$	4
$PZCOO^- + 2MPZCOO^- + CO_2 \leftrightarrow PZ(COO^-)_2 + H2MPZCOO$	5
$PZ + 2MPZ + CO_2 \leftrightarrow PZCOO^- + 2MPZH^+$	6
$2\ PZ + CO_2 \leftrightarrow PZCOO^- + PZH^+$	7
$2\ 2MPZ + CO_2 \leftrightarrow 2MPZCOO^- + 2MPZH^+$	8
$2MPZ + PZ + CO_2 \leftrightarrow 2MPZCOO^- + PZH^+$	9
$2\ 2MPZCOO^- + CO_2 \leftrightarrow 2MPZ(COO^-)_2 + H2MPZCOO$	10
$2MPZCOO^- + 2MPZH^+ \leftrightarrow H2MPZCOO + 2MPZ$	eq.
$2MPZ + HCO_3^- \leftrightarrow 2MPZH^+ + CO_3^{-2}$	eq.
$2MPZ + PZH^+ \leftrightarrow 2MPZH^+ + PZ$	eq.
$PZCOO^- + PZH^+ \leftrightarrow HPZCOO + PZ$	eq.

Table 1 shows the reaction set used, where kinetic reactions are numbered and equilibrium reactions are denoted as "eq." The equilibrium reactions are calculated from Equation 1,

$$K_{eq,j} = \frac{\Delta G_j^0}{RT} \tag{1}$$

where R is the universal gas constant, T is temperature, and G_j^0 is the Gibbs free energy. Each kinetic reaction is represented as a forward-reverse pair of reactions. The forward reaction rate is calculated using Equation 2,

$$r = k a_{Am} a_{CO_2} a_B \tag{2}$$

where k is the reaction rate constant, a_i is the activity of the ith component. k is calculated using Equation 3,

$$k = k_0 \exp\left[\frac{-E_A}{R}\left(\frac{1}{T} - \frac{1}{T_{ref}}\right)\right] \tag{3}$$

where k_o is the reaction pre-exponent, E_A is the activation energy, and T_{ref} is the reference temperature taken as 40 °C. The corresponding reverse rate k_o and E_A are backcalculated from the reaction equilibrium of Equation 1. This method of matching power-law equations has been called into question as it does not approach the correct equilibrium (Mathias et al., 2014). This is not anticipated to be a problem as the kinetics are exclusively used with 20 °C. The user subroutine method used by Mathias will still be explored as it obviates the need for a separate calculation.

As with any reacting system, diffusion can play a role. Here, the diffusion of amine-products is accounted for using Equation 4,

$$D_{Am-Prod} = D_0 \left(\frac{T}{T_{ref}}\right)^{\alpha} \left(\frac{\mu}{\mu_{ref}}\right)^{\beta} \tag{4}$$

where D_0 is a pre-factor in m^2/sec, α is the temperature dependence, and β is the viscosity dependence. The experimental loading is adjusted up to 10% of the loading range corresponding to P^*_{CO2} = 0.5–5 kPa. For further details on the kinetic modeling method used, see Frailie (2014).

The data fit are the thirty-two extreme absorption and desorption CO_2 fluxes N_{CO_2} from the WWC (Chen, 2011). The temperatures range from 40 to 100 °C with four loadings ranging from lean to rich.

Ideally, a model should reduce down to its submodels, meaning that the 2MPZ/PZ model reduces to a PZ or a 2MPZ model. However, owing to the previously documented discrepancy in CO_2 parameter values, this model does not (Rochelle et al., 2014). In an ideal case, the only available kinetic parameters would be cross terms. Those are reactions 4, 5, 6, and 9 of Table 1. However, as the ability to reduce the 2MPZ submodel is precluded, those parameters are also available. One parameter of the pure 2MPZ model was changed, that of reaction 10. The cross term kinetic parameters were initially equated to those of PZ.

4 m 2MPZ/4 m PZ Modification

When using the 4 m 2MPZ/4 m PZ model for process modeling, the absorber did not converge. This is another case where the wetted wall column (WWC) model converges, but an actual absorber does not work properly. In the previous case of 8 m 2MPZ, the absorber converged but was desorbing CO_2 (Rochelle et al., 2012). To troubleshoot that system, the kinetics were redone from scratch. The root cause was never fully determined.

Here, the root cause was determined by examining the process parameters and the underlying thermodynamic and kinetic parameters. As the WWC model had converged and the absorber process model used the same thermodynamic and kinetic parameters, process parameters were suspected.

The typical convergence procedure for an absorber is to give Aspen Plus® a good initial guess. This is done by setting the absorber to rate-based with a reaction set consisting of the same reactions as the 2MPZ/PZ system but with zeros for k_o and E_A. This is converged, then the proper reaction set is used in the top few stages. Once this converges, the rest of the absorber stages are set to the same non-zero reaction set, making the absorber a true process model.

This procedure did not work. In an effort to converge the model, many things were tried, such as varying the number of stages, decreasing the height of packing, changing the mass transfer or interfacial area or holdup correlations, increasing the granularity of initializing the reaction set, increasing the L/G ratio, and changing the homotopy values. These all proved unsuccessful, ruling out process parameters as the source of the problem and leaving the thermodynamic and kinetic parameters.

As the kinetic model depends on the thermodynamic model, it is not possible to isolate the kinetic parameters from the thermodynamic parameters. To troubleshoot the kinetics, reactions were selectively deleted. After deleting reactions 5 and 10, the absorber converged, and the departure of the forward-reverse power-law reaction equilibria from the true thermodynamic reaction equilibria were examined. Ideally, the following relationship holds true:

$$K_{eq,j} = \frac{\Delta G_j^0}{RT} = \frac{k_f}{k_r} \tag{5}$$

In practice, the second equality of Equation 5 only holds from 40 to 60 °C, because $\frac{k_f}{k_r}$ does not account for the temperature dependence of the activity coefficients. All of the reactions involving the zwitterion showed they diverged furthest from the equality of Equation 5.

Figure 1 shows the three reactions involving the zwitterion (2, 5, and 10) along with one other reaction. As the kinetic equilibrium is calculated from the thermodynamic equilibrium at 40 and 60 °C, the equilibria match (i.e., the second equality of Equation 5 holds). Moving outside the 40–60 °C range, the two equilibria diverge (i.e., the second equality becomes less true). The divergence is typically less than that of reaction 1 shown in Figure 1. The extreme divergence of the zwitterion reactions shows that the activity coefficient temperature behavior is too complex to be captured by the power-law equilibrium (Mathias et al., 2014).

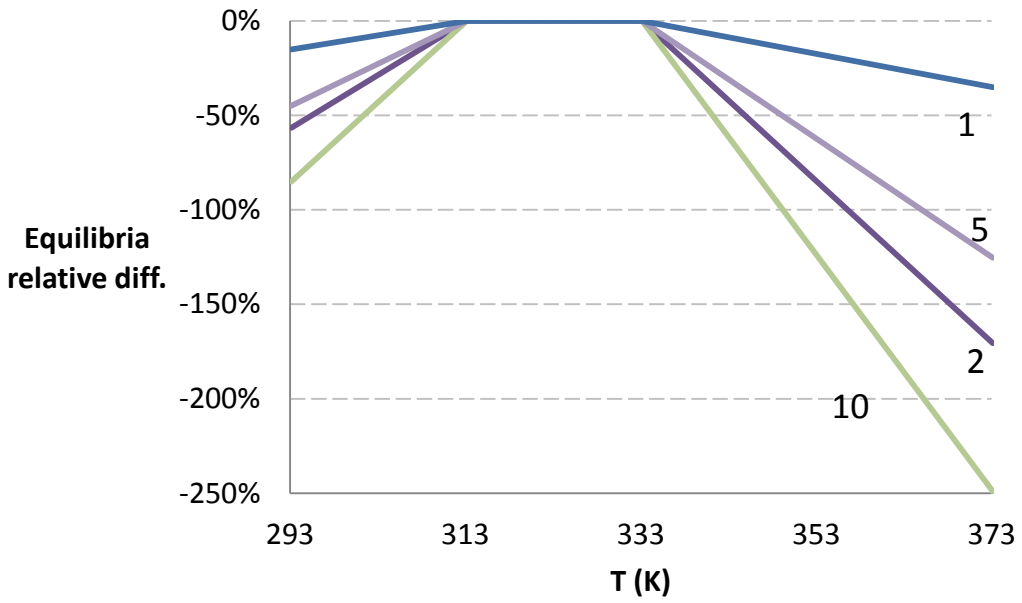

Figure 1: The top four equilibrium discrepancies for 2MPZ/PZ reactions of Table 1

This divergence led to an examination of the temperature dependence of the 2MPZ zwitterion activity coefficient ($\gamma_{H2MPZCOO}$). Figure 2 shows that the temperature dependence for H2MPZCOO is twice that of HPZCOO. This indicates that the problem lies with the activity coefficients calculated by the thermodynamic model. In the operational loading range of 0.3 to 0.4 mol CO_2/mol alk, the temperature dependence of $\gamma_{H2MPZCOO}$ is four times that of γ_{HPZCOO}.

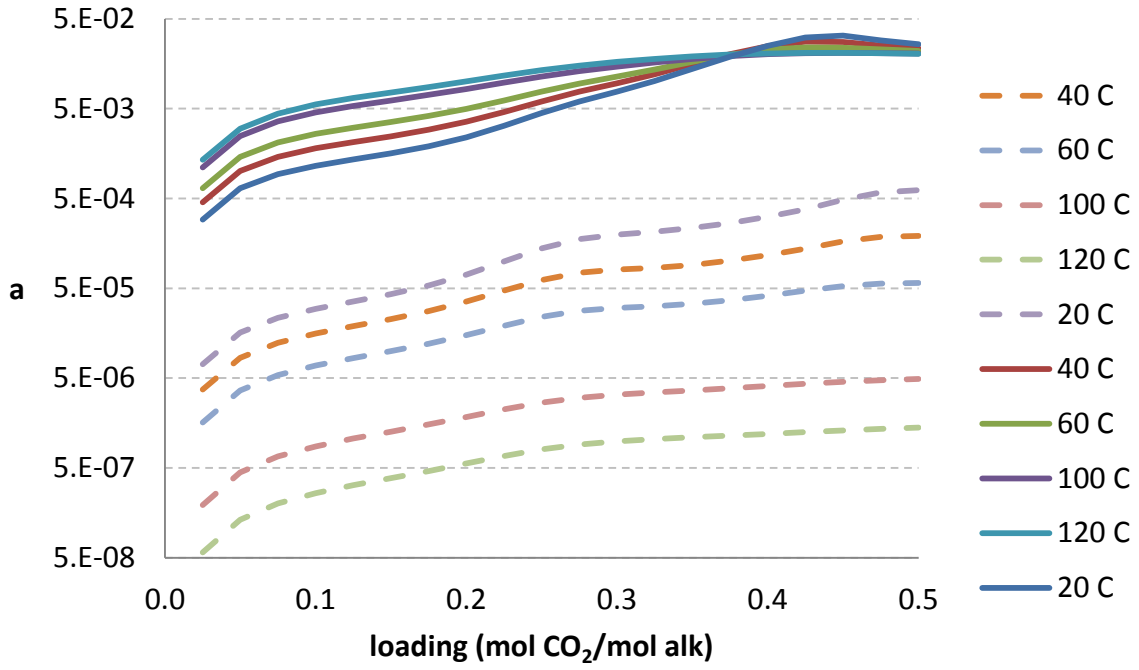

Figure 2: Activity coefficient temperature behavior of H2MPZCOO (dashed) and HPZCOO (solid)

Since the absorber is operating between 40 and 60 °C, where the equilibria agree, the problem must lie in that temperature range. Figure 3 shows the activity coefficients of the species involved in the 2MPZ zwitterion reactions at 40 °C. $\gamma_{H2MPZCOO}$ is two orders of magnitude below the analogous PZ species, and exhibits a minima and stronger loading dependence than γ_{HPZCOO}.

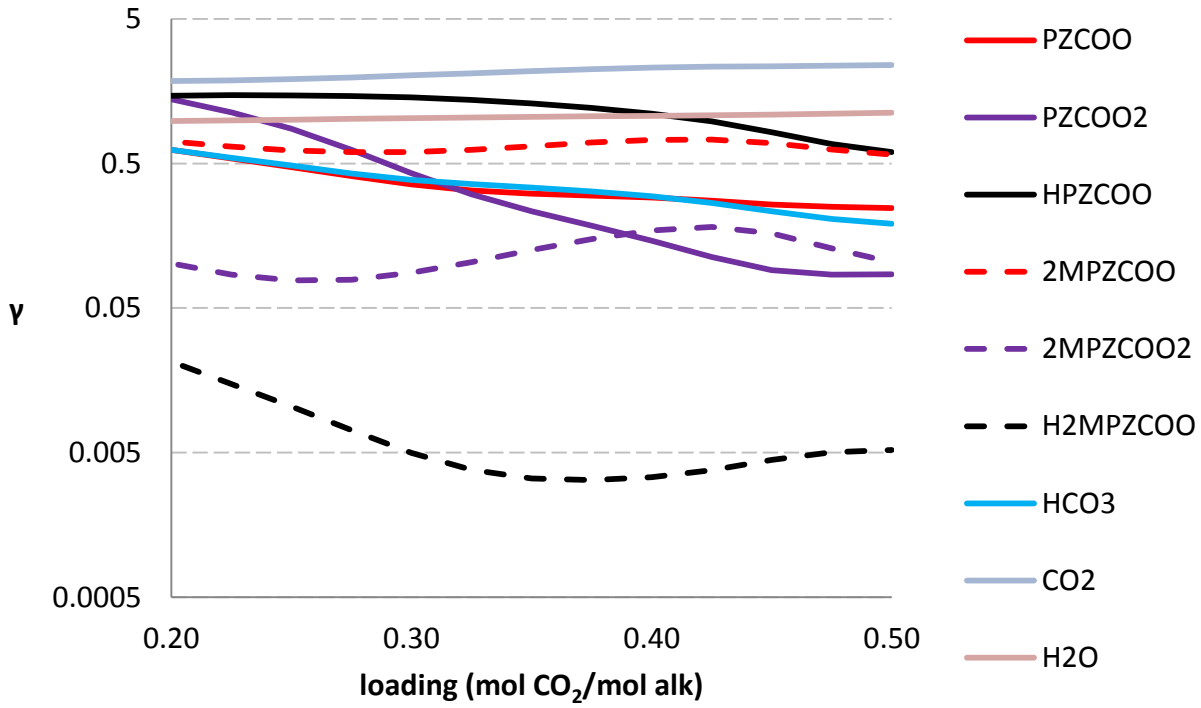

Figure 3: Activity coefficients at 40 °C for species of reactions 2, 5, and 10

The cause of the absorber process model failing to converge is the poor $\gamma_{H2MPZCOO}$ behavior propagating through the kinetic model. To remedy this, $\gamma_{H2MPZCOO}$ needs to be redone. A temporary fix was made by removing reactions 5 and 10. All kinetic and diffusivity parameters were left as is.

4 m AMP/2 m PZ

Figure 4 compares two sets of AMP NMR data from one author that are contradictory (Ciftja et al., 2014; Ciftja et al., 2011). As the new data are more comprehensive than the older data, the Gibbs free energy of aqueous formation and the enthalpy of aqueous formation were regressed again.

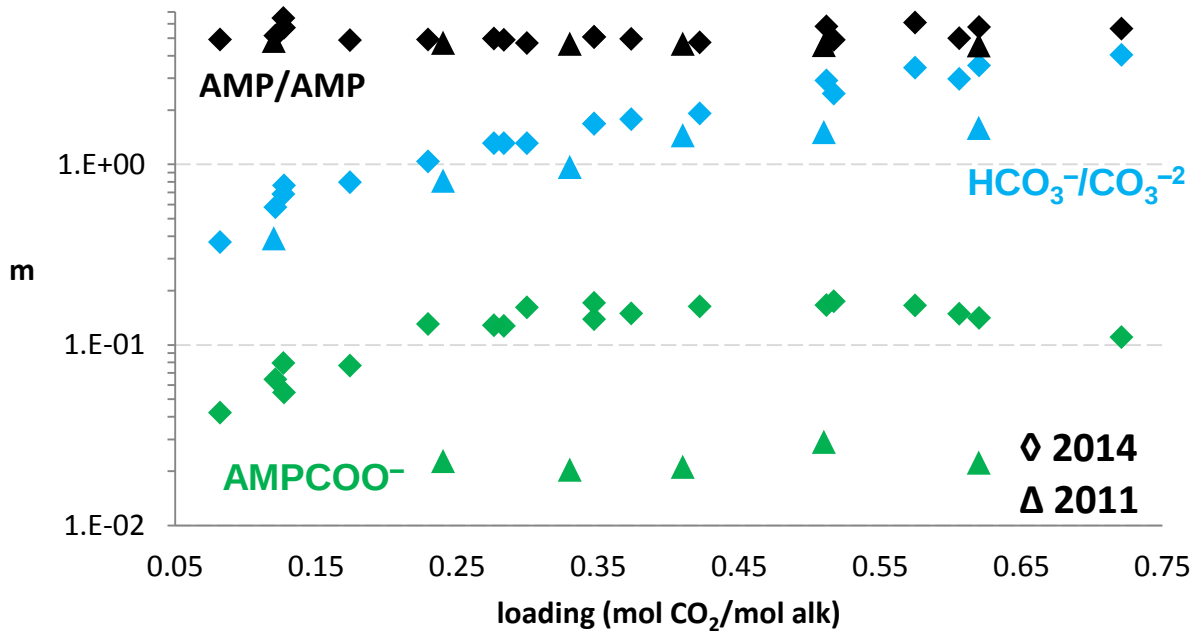

Figure 4: New and old Ciftja NMR data for 4.8 m AMP. Data are from Ciftja (Ciftja et al., 2014, 2011).

The viscosity and density are regressed before kinetics. These hydraulic properties were fit using Equations 6 and 7, which are similar to previous work (Frailie, 2014).

$$\frac{\mu_{AMP+PZ}}{\mu_{H2O}} = exp\begin{Bmatrix}[(ax_{AMP} + bx_{PZ} + c)T + dx_{AMP} + ex_{PZ} + f] \\ * [(gx_{AMP} + hx_{PZ} + iT + j)\alpha + 1] * \frac{x_{AMP+PZ}}{T^2}\end{Bmatrix} \quad (6)$$

a–j are parameters, α is loading (mol CO_2/mol alk), and x_i is the mass fraction.

$$\rho_{AMP+PZ} = x_{H_2O}\rho_{H_2O} + x_{AMP}(aT + b) + x_{PZ}(cT + d) + x_{CO_2}(eT + f) \quad (7)$$

a–f are parameters, and x_i is the mole fraction.

Viscosity is regressed using least-squares minimization in Excel to match available data (Rochelle et al., 2012b).

No loaded density data are available for this system. Using the same parameters from loaded MDEA/PZ produced unsatisfactory results, so unloaded AMP data were used to fit parameters *a* and *b* (Xu et al., 1991; Chan et al., 2002). The other parameters were set to give the expected trend with loading.

With viscosity and density correlated, the kinetics were modeled using the approach outlined for 2MPZ/PZ. Table 2 shows the reaction set used.

Table 2: 4 m AMP/2 m PZ reaction set

Stoichiometry		*Reaction*
$PZCOO^- + H_2O + CO_2$	$\leftrightarrow HPZCOO + HCO_3^-$	1
$AMP + H_2O + CO_2$	$\leftrightarrow AMPH^+ + HCO_3^-$	2
$2\ PZCOO^- + CO_2$	$\leftrightarrow PZ(COO^-)_2 + HPZCOO$	3
$PZCOO^- + AMP + CO_2$	$\leftrightarrow PZ(COO^-)_2 + AMPH^+$	4
$PZ + AMP + CO_2$	$\leftrightarrow PZCOO^- + AMPH^+$	5
$2\ PZ + CO_2$	$\leftrightarrow PZCOO^- + PZH^+$	6
$2\ AMP + CO_2$	$\leftrightarrow AMPCOO^- + AMPH^+$	7
$AMP + HCO_3^-$	$\leftrightarrow AMPH^+ + CO_3^{-2}$	eq.
$AMP + PZH^+$	$\leftrightarrow AMPH^+ + PZ$	eq.
$PZCOO^- + PZH^+$	$\leftrightarrow HPZCOO + PZ$	eq.

Results and Discussion

4 m 2MPZ/4 m PZ

Fitting the CO_2 flux (N_{CO_2}) resulted in the kinetic parameters shown in Table 3 and the diffusion parameters shown in Table 4. In Table 3, all reactions involving only PZ have the same value as Independence (Frailie, 2014). In Table 4, the $D_{Am-Prod}$ is adapted to each system by changing the reference viscosity to the mid-range loading viscosity at 40 °C. While the raw temperature dependence α is the same across systems, the β is different. For 2MPZ/PZ, the exponential on μ is set to −1. This helped remove bias with loading, as viscosity changes with loading.

Table 3: Regressed reaction parameters for 4 m 2MPZ/4 m PZ

Stoichiometry		k_o *(kmol/s-m^3)*		E_A *(10^4 J/mol)*	
		forward	reverse	fwd	rev
$PZCOO^- + H_2O + CO_2$	$\leftrightarrow HPZCOO + HCO_3^-$	2.20E+04	9.74E+01	4.90	7.37
$2MPZCOO^- + H_2O + CO_2$	$\leftrightarrow H2MPZCOO + HCO_3^-$	2.62E+06	4.28E+05	9.80	17.5
$2\ PZCOO^- + CO_2$	$\leftrightarrow PZ(COO^-)_2 + HPZCOO$	2.76E+10	2.63E+05	1.42	8.93
$PZCOO^- + 2MPZ + CO_2$	$\leftrightarrow PZ(COO^-)_2 + 2MPZH^+$	1.00E+10	9.51E+04	6.98	16.6
$PZCOO^- + 2MPZCOO^- + CO_2$	$\leftrightarrow PZ(COO^-)_2 + H2MPZCOO$	2.76E+12	2.49E+09	1.42	14.1
$PZ + 2MPZ + CO_2$	$\leftrightarrow PZCOO^- + 2MPZH^+$	2.04E+10	6.44E+04	1.42	8.77
$2\ PZ + CO_2$	$\leftrightarrow PZCOO^- + PZH^+$	2.04E+10	6.44E+04	1.42	8.51
$2\ 2MPZ + CO_2$	$\leftrightarrow 2MPZCOO^- + 2MPZH^+$	1.45E+10	4.50E+04	1.42	8.93
$2MPZ + PZ + CO_2$	$\leftrightarrow 2MPZCOO^- + PZH^+$	9.00E+10	1.68E+05	0.457	7.95
$2\ 2MPZCOO^- + CO_2$	$\leftrightarrow 2MPZ(COO^-)_2 + H2MPZCOO$	2.76E+10	6.67E+08	1.42	12.1

Table 4: Regressed $D_{Am\text{-}prod}$ parameters of Equation 4

Parameter	*2MPZ/PZ*	*PZ/MDEA*	*AMP/PZ*	*Units*
D_o	4.00E-10	2.26E-10	4.00E-10	m^2/sec
α	-2.58	-2.58	-2.58	—
β	-1	-1.45	-2	—
T_{ref}	313.15	313.15	313.15	K
μ_{ref}	13.7	15.5	5.73	cP

Figure 5 shows the kinetic fit versus temperature. The scatter decreases with increasing temperature. There is a tendency to overpredict desorption and to underpredict absorption. When the filled and open points overlap, the equilibrium at that point is accurately represented. When the two points do not overlap, absorption or desorption is predicted despite zero driving force. Adjusting the loading brings the absorption-desorption points into agreement. When these points do not agree, the loading has been adjusted to the ±10% of operational loading limit. Fitting the data between 40 and 60 °C is most important, as the absorber operates in this range. Fitting the higher temperature data is done using the diffusion parameters of Table 4.

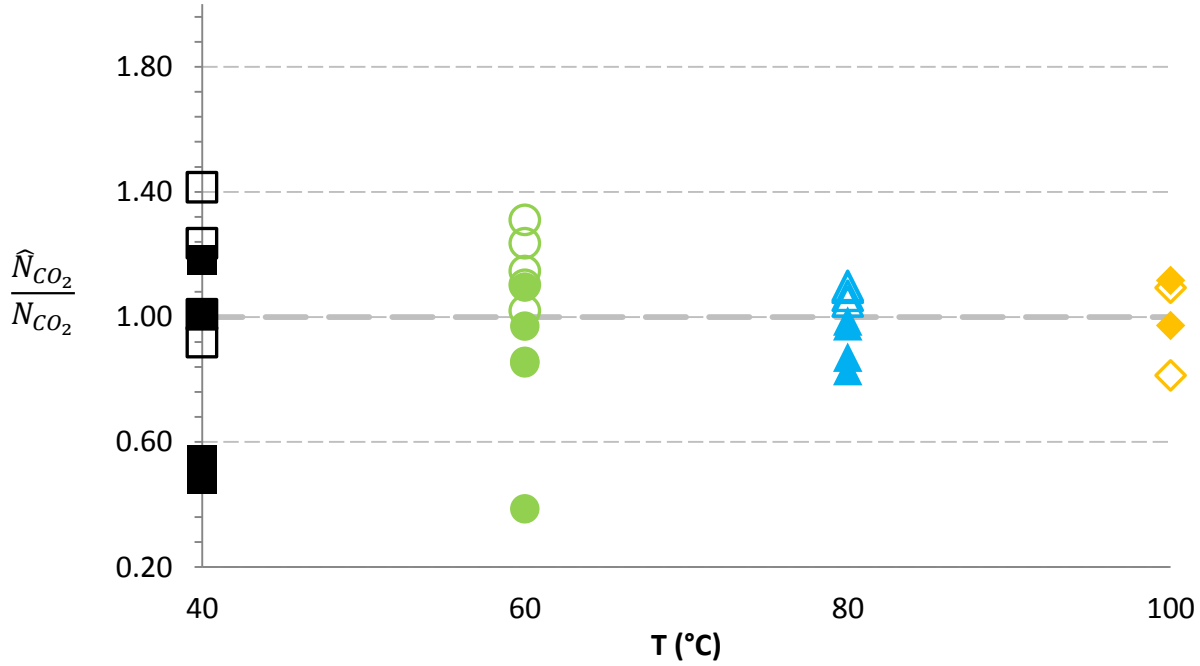

Figure 5: Kinetic fit for 4 m 2MPZ/4 m PZ. Data are from Chen (2011). Filled points are absorption; open desorption.

The data from Figure 5 are replotted against loading in Figure 6. There is a slight bias towards overprediction as loading increases. The two pairs of points at the rich end show a large equilibrium discrepancy.

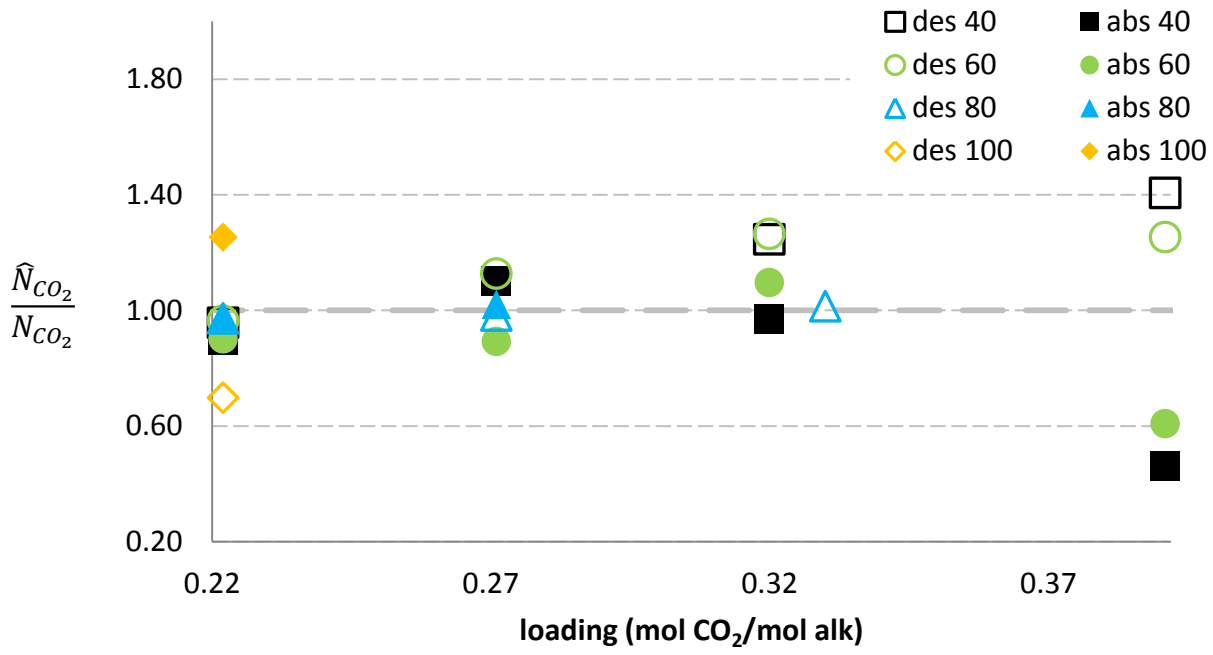

Figure 6: Kinetic fit for 4 m 2MPZ/4 m PZ. Data are from Chen (2011).

Figure 7 shows the pseudo-first-order reaction rate constant of each kinetic reaction as calculated by Equation 8,

$$k_1 = k a_{Am} a_B \tag{8}$$

where k is the reaction rate constant, and a_i is the activity of the ith component. The fastest reaction is the formation of PZ dicarbamate, which is counter-intuitive. The formation of PZ carbamate ought to be the fastest, but it is the third fastest at the lean loading end. The formation of bicarbonate catalyzed by PZ carbamate is the slowest, while the comparable reaction catalyzed by 2MPZ carbamate has similar rates to the carbamate reactions. These should have similar rates due to their similar pK_a values.

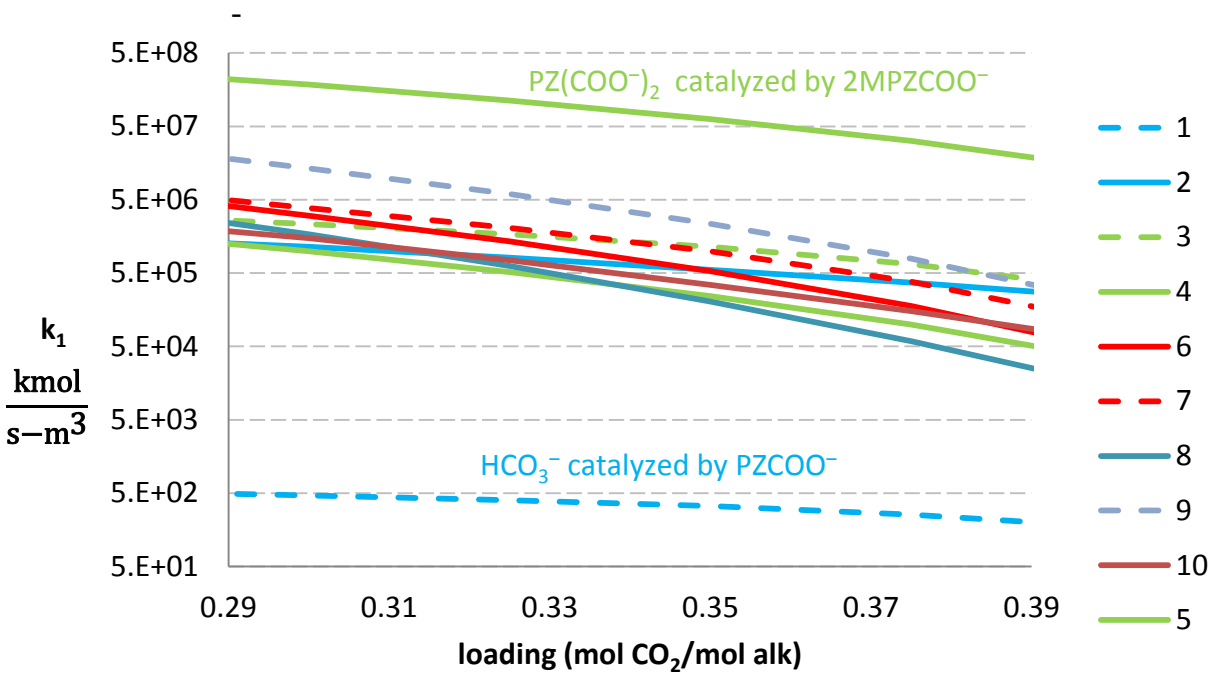

Figure 7: k_1 4 m 2MPZ/4 m PZ kinetic reactions. The number corresponds to Table 1. Dashed lines are catalyzed by PZ species; solid by 2MPZ.

4 m 2MPZ/4 m PZ Modification

After removing the two H2MPZCOO reactions the kinetic fit is shown in Figures 8 and 9.

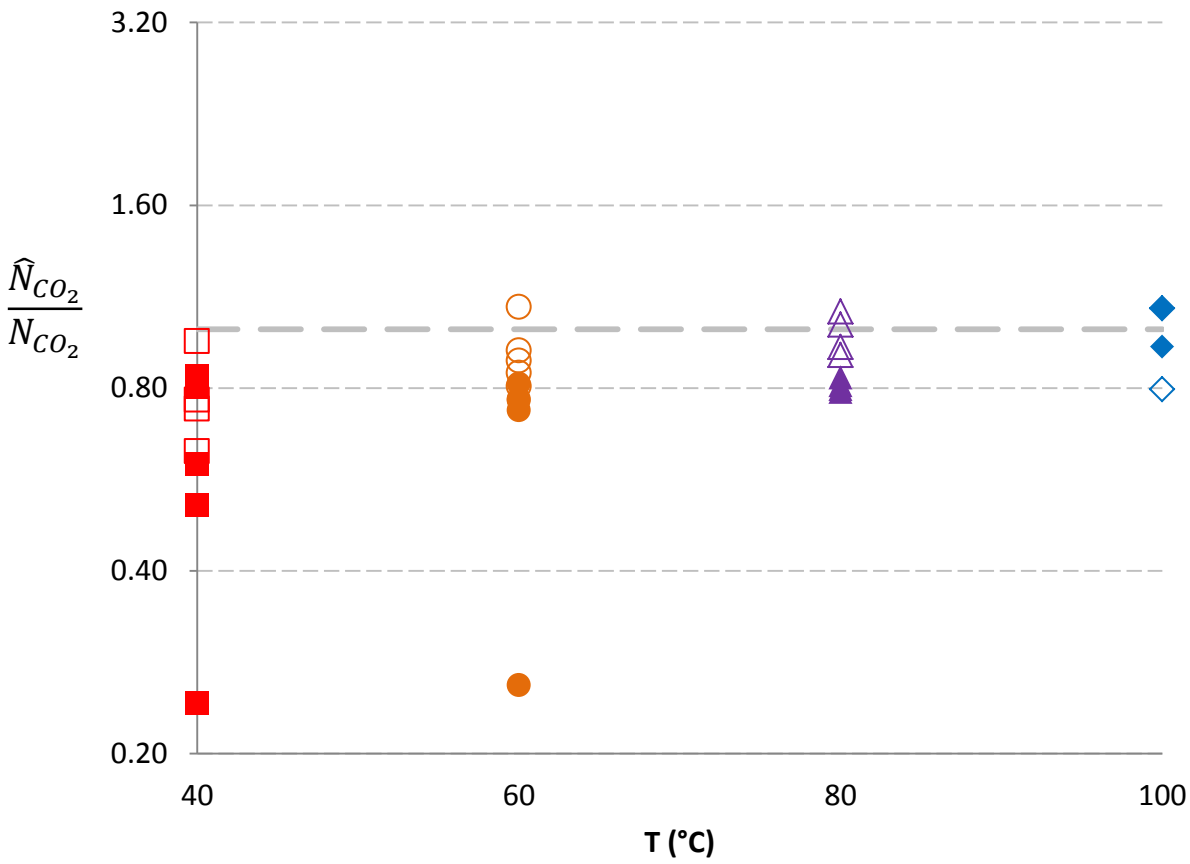

Figure 8: 4 m 2MPZ/4 m PZ kinetic fit without reactions 5 and 10. Data are from Chen (2011).

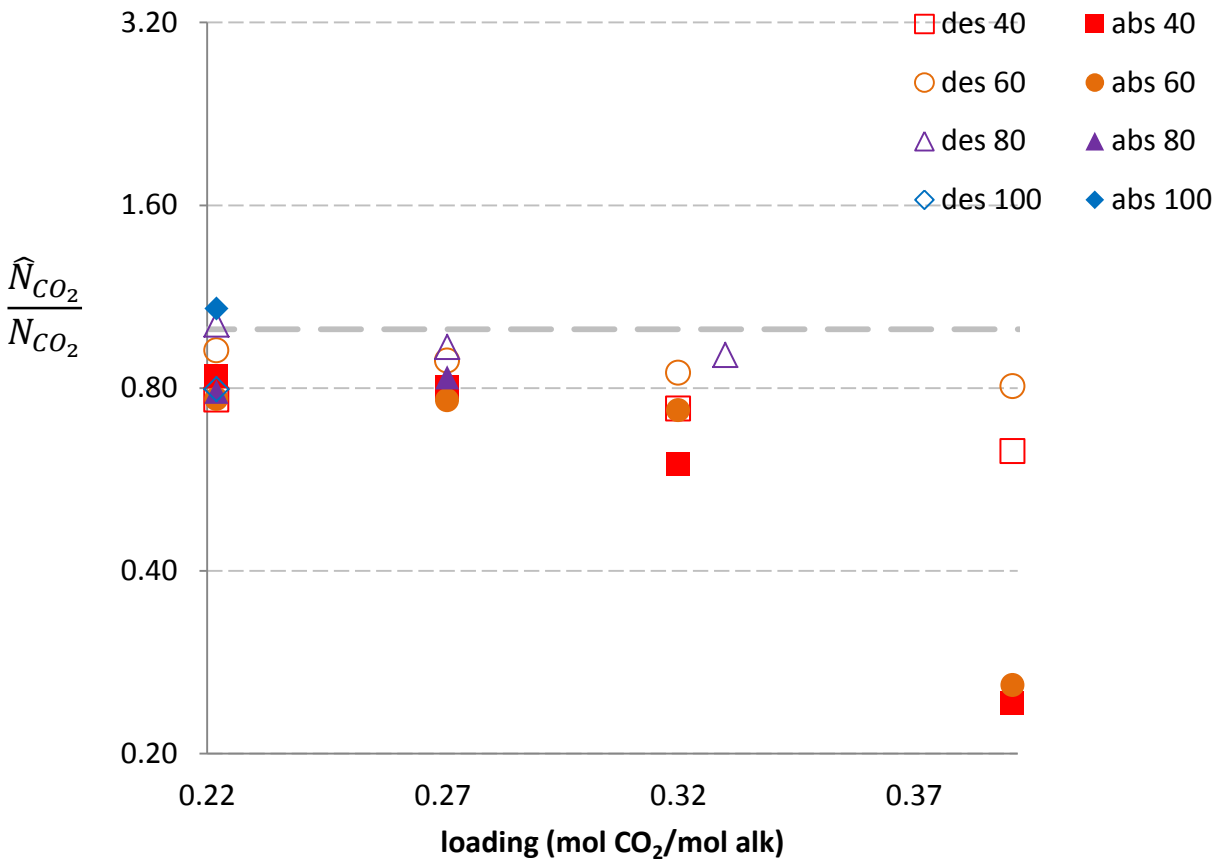

Figure 9: 4 m 2MPZ/4 m PZ kinetic fit without reactions 5 and 10. Data are from Chen (2011).

As expected, the model now tends to underpredict. There is a pronounced trend towards underprediction with increasing loading, and at 40 °C the model always underpredicts compared to the prior results of Figures 5 and 6. This short term solution is insufficiently accurate for process modeling. In order to fix this problem, the 2MPZ thermodynamic model needs to be redone.

4 m AMP/2 m PZ

Updating the AMP carbamate parameters to match current data (Ciftja et al., 2014) resulted in the values of Table 5 and the fit of Figure 10. These compare favorably to the values used by the built in Aspen Plus® AMP model.

Table 5: AMP carbamate parameters.

Source	ΔG_0^o *(10^8 J/kmol)*	ΔH_0^o *(10^8 J/kmol)*
Aspen Plus®	-4.56	-2.86
this work	-4.58	-7.50

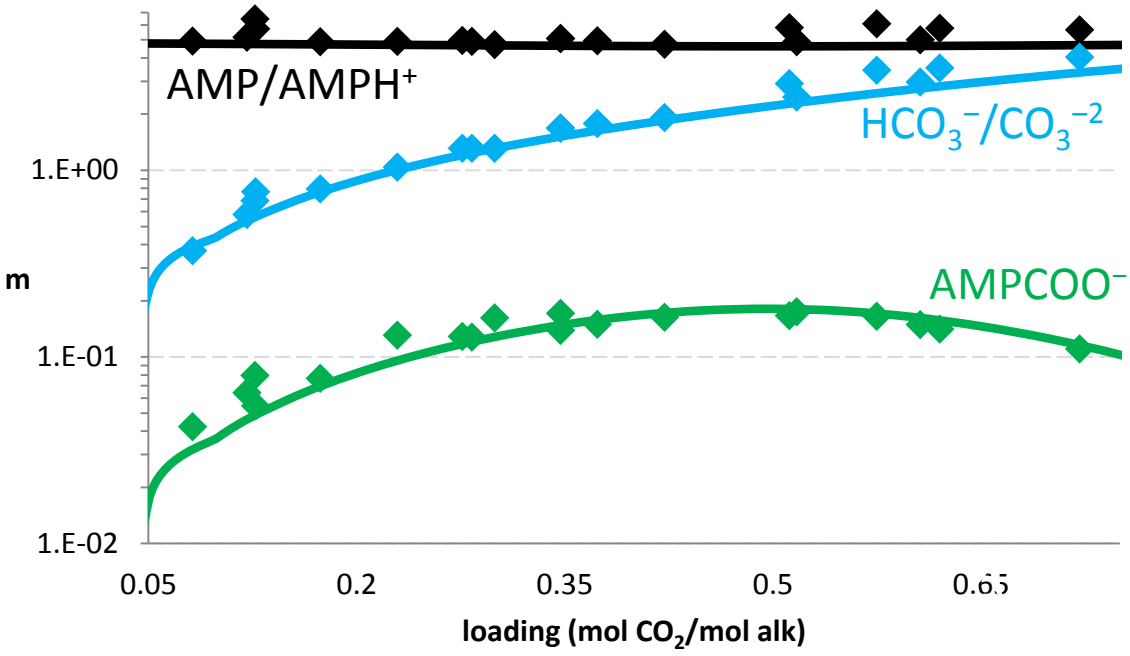

Figure 10: Fit of 4.8 m AMP data at 25 °C. Points are data, lines prediction (Ciftja et al., 2014).

The parameters used to fit the viscosity in Equation 6 are shown in Table 6. In the resulting fit shown in Figure 11, the data is best fit at 40 °C, with underpredictions at 20 °C and overpredictions at 60 and 80 °C.

Table 6: 4 m AMP/ 2m PZ viscosity parameters for Equation 6

Parameter	*Value*	*Parameter*	*Value*
a	912	f	5.40
b	1890	g	0.001472
c	968	h	1.74
d	1.39E-05	i	-0.00781
e	1.20	j	3.71

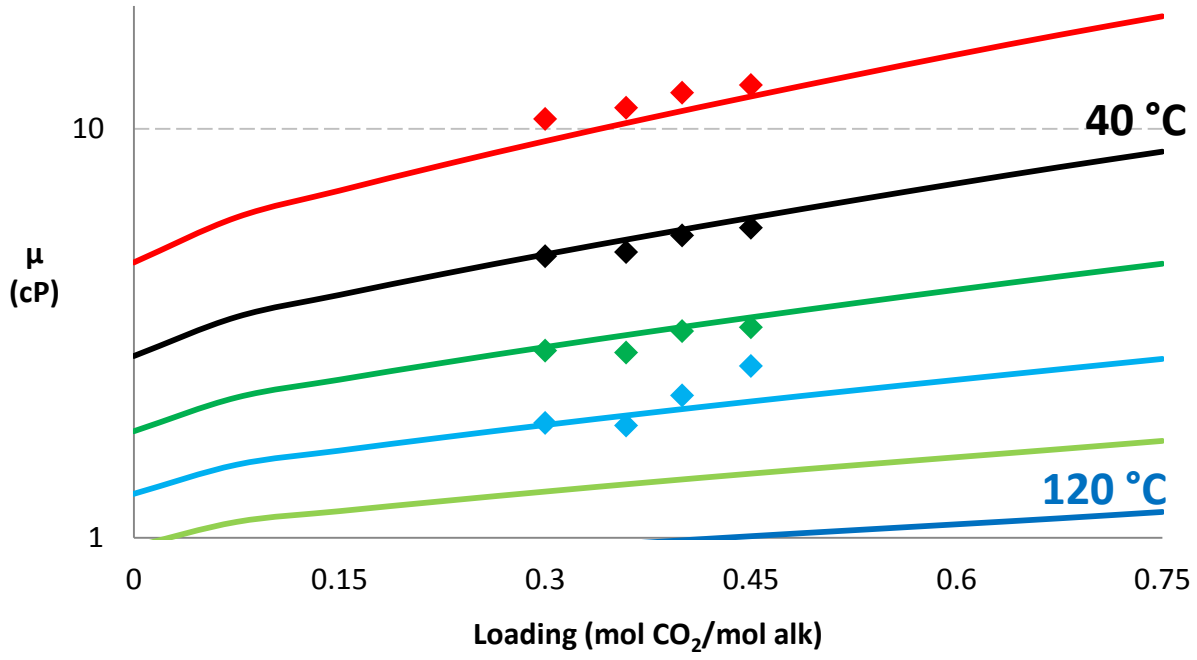

Figure 11: 4 m AMP/2 m PZ viscosity fit. Points are data from Li (Rochelle et al., 2012b); lines are model predictions at 20 °C intervals.

Table 7 shows the resulting parameters for Equation 7. The predictions in Figure 12 show the expected behavior. The impact of density on the model is minimal, so this level of uncertainty is acceptable.

Table 7: AMP/PZ density parameters for Equation 7

Parameter	*Value*
a	-2.00
b	1240
c	-0.00256
d	1300
e	2.00
f	1000

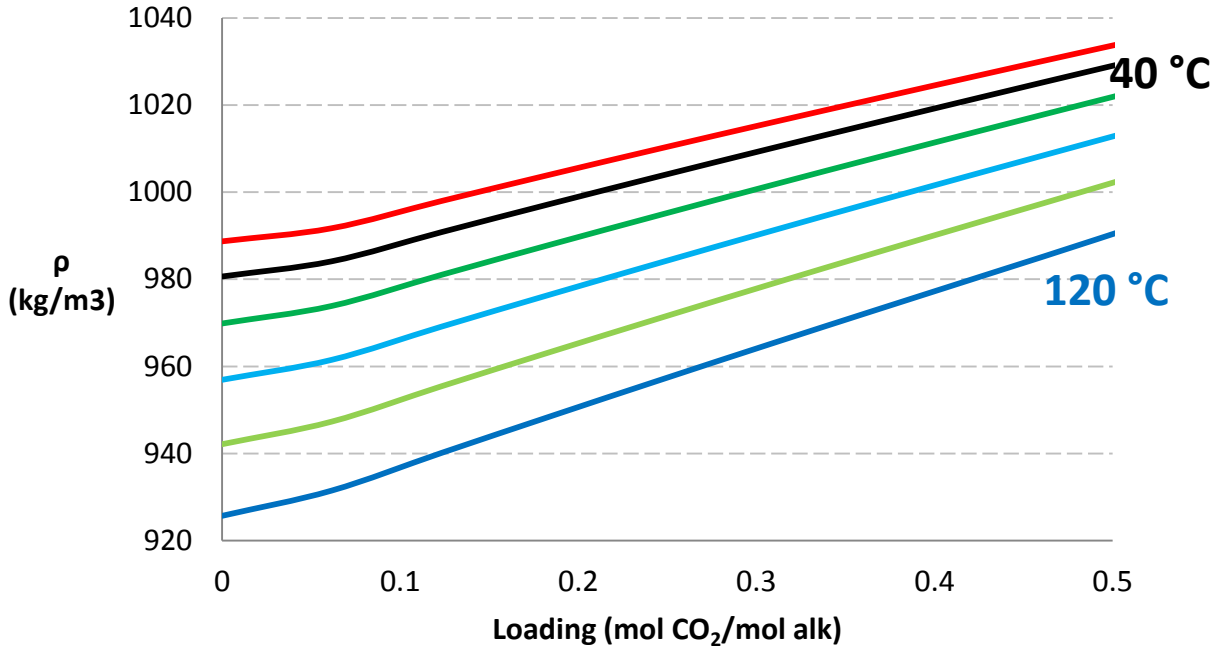

Figure 12: 4 m AMP/2 m PZ density predictions at 20 °C intervals

Table 8 shows the kinetic parameters, while Table 4 shows the diffusivity parameters. The reactions involving AMP in Table 8 shows that the k_0 is greater than the analogous PZ equation. While the pKa of AMP may explain the higher rates for the reactions where AMP serves as a base, the steric hindrance should make the formation of AMP carbamate slower than that of PZ carbamate. These parameters may be biased due to the greater concentration of AMP than PZ.

Table 8: 4 m AMP/ 2m PZ kinetic parameters

Reaction	k_o *(kmol/s-m^3)*		E_a *(J/mol)*	
	forward	reverse	fwd (10^2)	rev (10^4)
$PZCOO^- + H_2O + CO_2 \leftrightarrow HPZCOO + HCO_3^-$	2.20×10^4	97.4	490	7.37
$AMP + H_2O + CO_2 \leftrightarrow AMP^+ + HCO_3^-$	2.20×10^6	3.37×10^3	41.3	6.98
$2\ PZCOO^- + CO_2 \leftrightarrow PZ(COO^-)_2 + HPZCOO$	2.76×10^{10}	2.63×10^5	142	8.93
$PZCOO^- + AMP + CO_2 \leftrightarrow PZ(COO^-)_2 + AMP^+$	2.14×10^{11}	1.81×10^6	9.77	11.7
$PZ + AMP + CO_2 \leftrightarrow PZCOO^- + AMP^+$	2.39×10^{12}	6.74×10^6	9.76	9.44
$2\ PZ + CO_2 \leftrightarrow PZCOO^- + PZH^+$	2.04×10^{10}	4.27×10^4	142	8.51

2 AMP + CO_2 ↔ $AMPCOO^-$ + AMP^+	2.04×10^{12}	4.23×10^{8}	342	11.5

The resulting fit is shown in Figures 13 and 14. The 100 °C absorption point does not have the same order of magnitude driving force as the 100 °C desorption point, which partially explains the large discrepancy. In general, the model tends to underpredict.

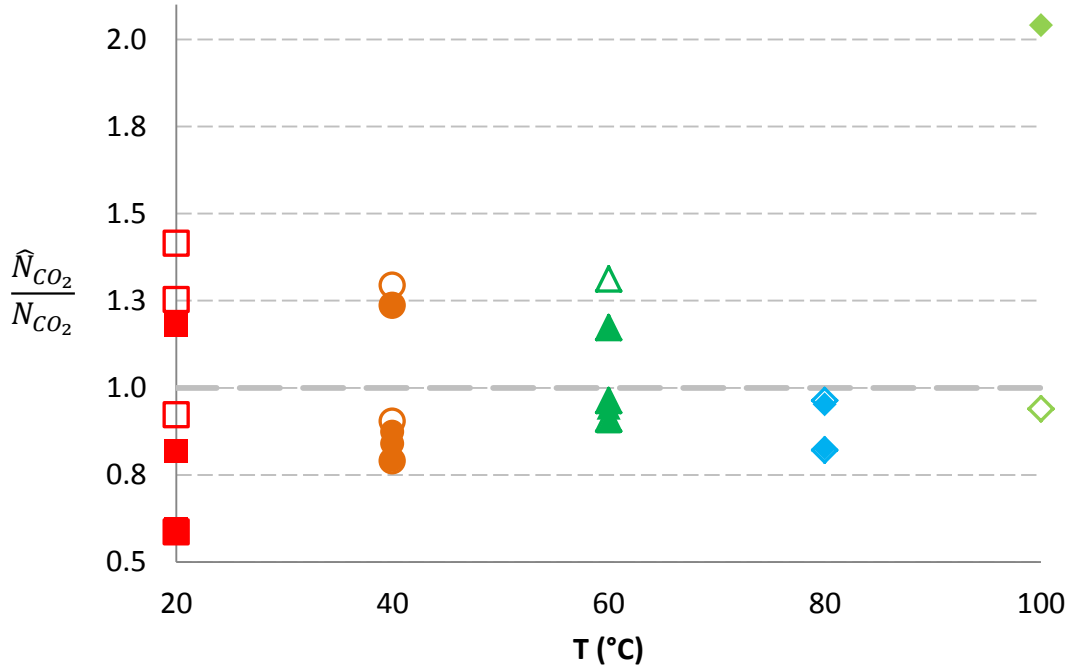

Figure 13: 4 m AMP/2 m PZ kinetic fit with filled points being absorption and open points desorption. Data are from Rochelle et al. (2013).

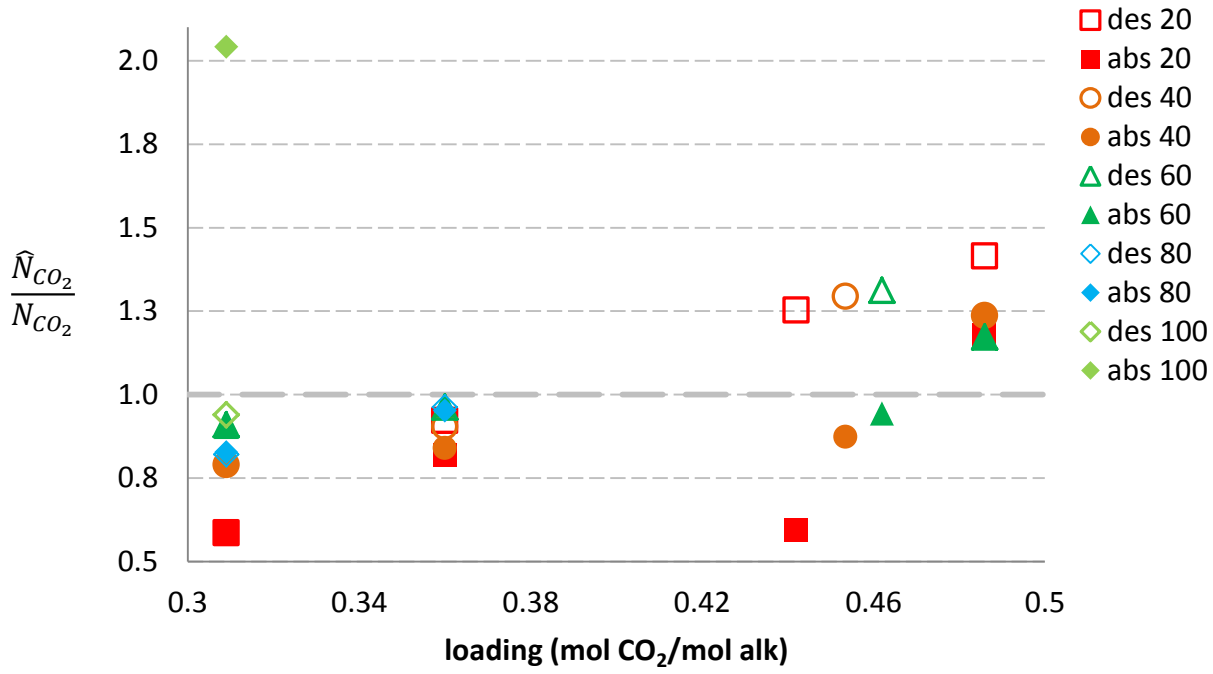

Figure 14: 4 m AMP/2 m PZ kinetic fit. Data are from Rochelle et al. (2013).

Figure 15 shows the forward rate k_1 as calculated by Equation 8. The pure PZ reactions are dashed. Comparing the AMP carbamate reaction (7) to the PZ carbamate reaction (6) shows that the PZ reaction decreases twice as fast as the AMP reaction. This could be due to the concentration of PZ being half that of AMP. As with 2MPZ/PZ, the formation of PZ dicarbamate is very fast (5). This seems to be more of an artifact than a physically significant result.

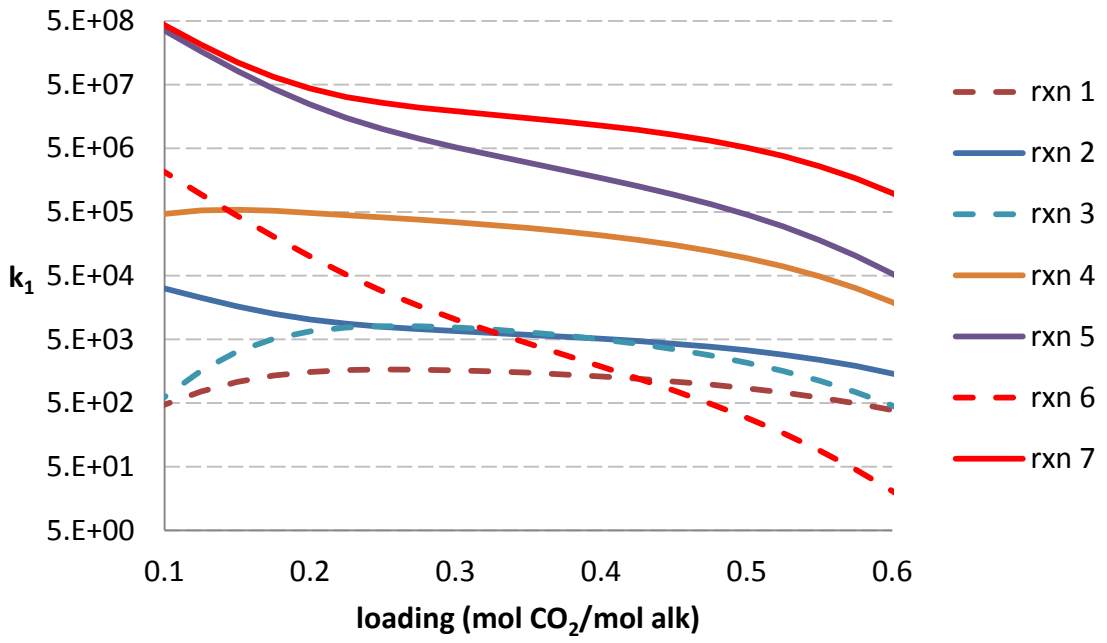

Figure 15: k_1 for AMP/PZ reactions of Table 2. Pure PZ reactions are dashed.

Conclusions

1. The lower pKa of AMP leads to faster reaction rates for reactions catalyzed by AMP rather than PZ.
2. The thermodynamic 2MPZ model does not accurately represent the activity coefficient of the 2MPZ zwitterion. This inaccuracy precludes process modeling.
3. Using updated 4.8 m AMP NMR data gives the same aqueous Gibbs free energy of formation as the Aspen Plus® model.
4. Counterintuitively, the formation of PZ dicarbamate catalyzed by either 2MPZ or AMP is one of the fastest reactions.

Future Work

Immediate objectives are:

- incorporating new AMP/PZ viscosity data (Fu et al., 2014);
- changing to MATLAB for viscosity and density regression to give confidence intervals on parameters;
- regressing 5 m PZ/2.3 m AMP kinetic data;
- converting an Excel heat exchanger model to a USER2 Aspen Plus® model;
- using a user subroutine to force the agreement of the thermodynamic and kinetic equilibrium.

Long term objectives are:

- redoing the regression of 2MPZ parameters to improve activity coefficient behavior and to use a common databank as Independence;
- studying steric hindrance in the AMP and 2-PE systems.

References

Chan C, Maham Y, Mather AE, Mathonat C. "Densities and volumetric properties of the aqueous solutions of 2-amino-2-methyl-1-propanol, n-butyldiethanolamine and n-propylethanolamine at temperatures." *Fluid Phase Equilib*. 2002;198:239–250.

Chen X. *Carbon Dioxide Thermodynamics, Kinetics, and Mass Transfer in Aqueous Piperazine Derivatives and Other Amines*. The University of Texas at Austin. Ph.D. Dissertation. 2011.

Ciftja AF, Hartono A, Svendsen HF. "Experimental study on carbamate formation in the AMP–CO_2–H_2O system at different temperatures." *Chem Eng Sci*. 2014;107:317–327. doi:10.1016/j.ces.2013.12.028.

Ciftja AF, Hartono A, da Silva EF, Svendsen HF. "Study on carbamate stability in the Amp/CO_2/H_2O system from ^{13}C-NMR spectroscopy." *Energy Proc*. 2011;4:614–-620.

Frailie PT. *Modeling of Carbon Dioxide Absorption/Stripping by Aqueous Methyldiethanolamine/Piperazine*. Ph.D. Dissertation. 2014.

Li H, Frailie PT, Rochelle GT, Chen J. "Thermodynamic modeling of piperazine/2-aminomethylpropanol/CO_2/water." *Chem Eng Sci*. 2014;117:331–341.

Mathias PM, Gilmartin JP. "Quantitative Evaluation of the Effect of Uncertainty in Property Models on the Simulated Performance of Solvent-Based CO_2-Capture." Presented at *GHGT-12*, Austin, TX. Oct 5–9, 2014.

Rochelle GT et al. "CO_2 Capture by Aqueous Absorption, Second Quarterly Progress Report 2012. Luminant Carbon Management Program. The University of Texas at Austin. 2012.

Rochelle GT et al. "CO_2 Capture by Aqueous Absorption, Second Quarterly Progress Report 2013." Texas Carbon Mangement Program. The University of Texas at Austin. 2013.

Sherman B, Frailie PT, Le L, Salta N, Rochelle GT. "Thermodynamic and Kinetic Modeling of Piperazine/2-Methylpiperazine." Presented at *GHGT-12*, Austin, TX. Oct 5–9, 2014.

Xu S, Otto FD, Mather AE. "Physical properties of aqueous AMP solutions." *J Chem Eng Data*. 1991;36(1):71–75.

Appendix

This appendix contains the poster presented at the September Industrial Advisory Board meeting.

CCSI September 2014 IAB Meeting Poster

CCSI™ Solvent Model Development and Calibration with 2MPZ

Carbon Capture Simulation Initiative

Brent Sherman, **K. Sham Bhat**, **Kayode Ajayi**, Gary T. Rochelle

Background

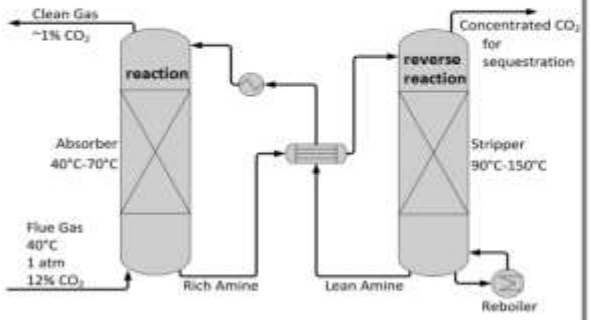

2-methylpiperazine (2MPZ) + piperazine (PZ)

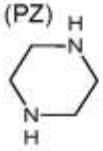

- fast rates (65% > $k'_{g,avg}|_{MEA}$)
- high capacity (79% > ΔC_{MEA})
- wide solubility window

Methods

- Aspen Plus®
- thermodynamic: eNRTL
- kinetics: activity-based
- regress data sequentially

Data	
amine volatility	
pK_a	
CO_2 solubility	WWC, P_T
density	
viscosity	
flux (WWC)	

$$r = k\prod_i a_i$$

$$k = k_0 \exp\left[\left(\frac{-E_A}{R}\right)\left(\frac{1}{T}-\frac{1}{T_{ref}}\right)\right]$$

$$D_{Am} = -4.0E^{-10}\frac{m^2}{s}\left(\frac{T}{T_{ref}}\right)^{-2.6}\left(\frac{\mu}{0.0137\text{Pa}-\text{s}}\right)^{-1.0}$$

Model Fit

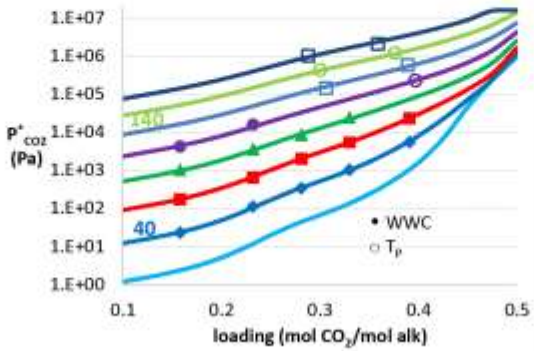

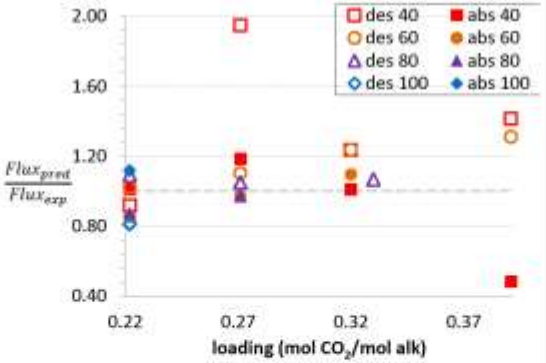

TxCMP

Contact: brentjsherman@utexas.edu

Uncertainty Quantification

- Possible uncertainty due to Henry's constant and NRTL parameters.
- Default parameter values given large weight.
- Calibrate Aspen model to amine volatility data using Bayesian methods.
- Large space filling parameter design to emulate model with minimal uncertainty.
- Will expand UQ methods to analyze other solvent data including up to 80 parameters.

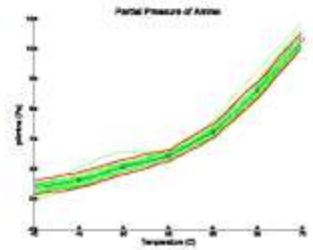

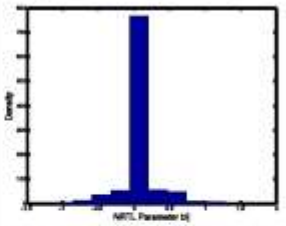

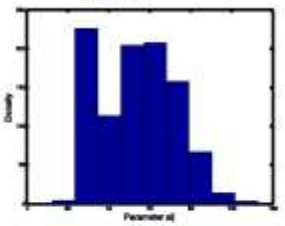

Conclusions

- Kinetic model fit with 19 parameters, thermo fit with 40.
- Calibration approach- uncertainty while assigning weight to defaults.
- Reducing model solver failures.

NETL · Berkeley Lab · Lawrence Livermore National Laboratory · Los Alamos National Laboratory EST. 1943 · Pacific Northwest National Laboratory · U.S. Department of Energy

Time Scale Analysis of Amine Scrubbing

Quarterly Report for July 1 – September 30, 2014

by Matthew S. Walters

Supported by the Texas Carbon Management Program

McKetta Department of Chemical Engineering

The University of Texas at Austin

October 31, 2014

Abstract

The process dynamics of amine scrubbing exhibit time scale multiplicity as a result of significant material and energy recycle. A low-fidelity model of the process has been developed using lumped parameters, approximate thermodynamics, and adjustable heat and mass transfer coefficients. The material states of the low-fidelity model were demonstrated to be in non-standard singularly perturbed form. In this model form, only the stripper vapor mole fractions evolve exclusively on the slow time scale; all other variables have both fast and slow components. A coordinate transform using the total liquid material hold-ups can be used to explicitly separate the slow and fast dynamics. This work has been presented at the GHGT-12 conference. The system model was demonstrated to be ill-conditioned based on the eigenvalues of the linear system.

Introduction

A linearized model can help give insight into the properties of a full nonlinear system. The nonlinear model of the system is given in Equation 1:

$$\dot{\boldsymbol{x}} = f(\boldsymbol{x}, \boldsymbol{u}, \boldsymbol{d}) \tag{1}$$

where:

$\boldsymbol{x} \in \mathbb{X} \subset \mathbb{R}^n$ is the state vector,
$\boldsymbol{u} \in \mathbb{U} \subset \mathbb{R}^m$ is the input vector,
and $\boldsymbol{d} \in \mathbb{D} \subset \mathbb{R}^p$ is the disturbance vector.

The nonlinear model can be linearized about a nominal operating point, giving the linear model shown in Equation 2:

$$\dot{\boldsymbol{x}} = \boldsymbol{A}(\boldsymbol{x} - \boldsymbol{x_0}) + \boldsymbol{B}(\boldsymbol{u} - \boldsymbol{u_0}) + \boldsymbol{\omega}(\boldsymbol{d} - \boldsymbol{d_0}) \tag{2}$$

where:

$$\boldsymbol{A} = \left.\frac{\partial f}{\partial x}\right|_{\boldsymbol{x}=\boldsymbol{x}_0, \boldsymbol{u}=\boldsymbol{u_0}, \boldsymbol{d}=\boldsymbol{d_0}}$$

$$\boldsymbol{B} = \left.\frac{\partial f}{\partial u}\right|_{\boldsymbol{x}=\boldsymbol{x}_0, \boldsymbol{u}=\boldsymbol{u_0}, \boldsymbol{d}=\boldsymbol{d_0}}$$

$$\boldsymbol{\omega} = \frac{\partial f}{\partial d}\Big|_{\boldsymbol{x}=\boldsymbol{x}_0,\boldsymbol{u}=\boldsymbol{u}_0,\boldsymbol{d}=\boldsymbol{d}_0}$$

and $(\boldsymbol{x_0}, \boldsymbol{u_0}, \boldsymbol{d_0})$ is the nominal point.
The matrix **A** is known as the system matrix and provides information about the stability and conditioning of the process. The conditioning of a system is a measure of how much the outputs change when a small perturbation is introduced. Systems that experience large changes in process outputs from small perturbations are said to be ill-conditioned (Baldea & Daoutidis, 2012).

Results

The low-fidelity nonlinear model was linearized, and the response of the absorber liquid mole fractions from the linear model is compared to the nonlinear model in Figure 1. It is clear that the linear model closely tracks the nonlinear model in the region close to the nominal operating point.

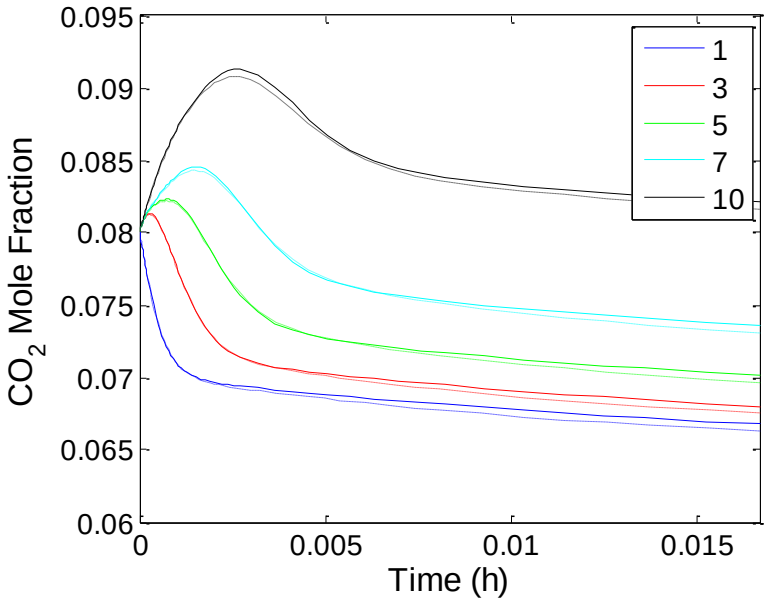

Figure 1: Response of absorber liquid mole fractions at select stages to perturbation in initial conditions for the linear (solid) and nonlinear (dashed) models.

The eigenvalues of the linear model are plotted in Figure 2. The real parts of the eigenvalues span several orders of magnitude, as seen in the plot.

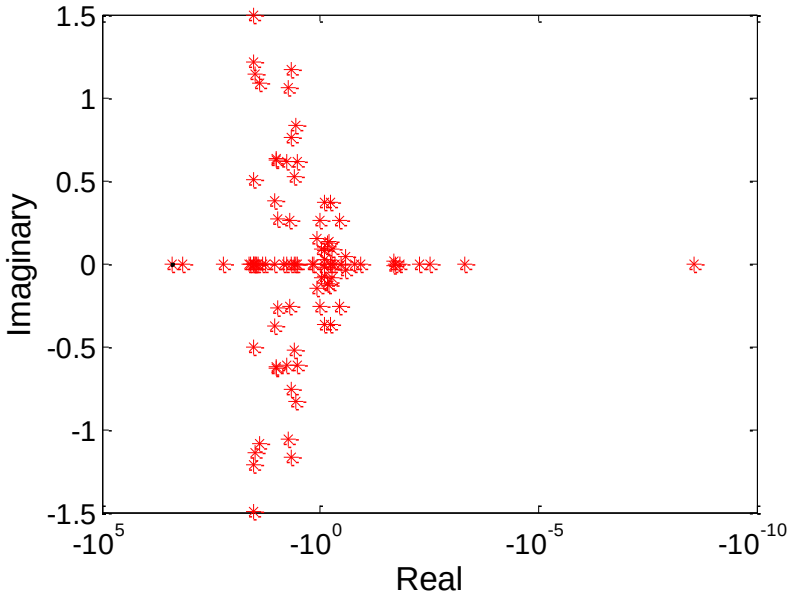

Figure 2: Eigenvalues of the linearized system.

Discussion

The eigenvalues of the system matrix represent the reciprocal of time constants that occur in the process. The condition number, defined in Equation 3 in terms of the maximum and minimum eigenvalues (λ_{max} and λ_{min}), is a measure of the conditioning of a system.

$$CN = \frac{|\lambda_{max}|}{|\lambda_{min}|} \tag{3}$$

A well-conditioned system has a condition number close to unity, implying that all the time constants are of the same order of magnitude. Conversely, an ill-conditioned system has a large condition number. The amine scrubbing system is ill-conditioned with a condition number of $\sim 10^{11}$. Ill-conditioned systems present control challenges and can exhibit oscillatory behavior in the process variables (Baldea & Daoutidis, 2012). This is unacceptable from an equipment protection and process safety viewpoint. For example, oscillations in pressure can wear out pump and heat exchanger seals and lead to leaking hazardous amine solvent. An effective control strategy to address the time scale multiplicity present in amine scrubbing will be considered in future work.

Conclusions

- The amine scrubbing process has a fast time scale associated with large recycle flowrates and a slow time scale associated with small feed and product flowrates.
- The linear system model is ill-conditioned because it has a large condition number.
- An effective control strategy should take into consideration the different time scales that occur in the process.

Future Work

- Compare a reduced order model of the slow dynamics to the full order model of the system.
- Test a model-based controller using the reduced model on the low-fidelity model in MATLAB®.
- Test a model-based controller using the reduced model on the medium-fidelity model in gPROMS®.

References

Baldea M, Daoutidis P. *Dynamics and Nonlinear Control of Integrated Process Systems*. New York, Cambridge University Press. 2012.

Topics on Amine Degradation

Quarterly Report for July 1 – September 30, 2014

by Omkar Namjoshi, Daniel Hatchell, and Hanbi Liu

Supported by the Texas Carbon Management Program

McKetta Department of Chemical Engineering

The University of Texas at Austin

October 31, 2014

Overview

Three papers were prepared and presented at the GHGT-12 conference. These are included as attachments to the quarterly report.

The first paper, "Thermal Degradation of PZ-Activated Tertiary Amines and Hindered Amines," presented thermal degradation rate measurements for a range of PZ-activated tertiary amines at an initial loading of 0.23 mol CO_2/mol alkalinity and an initial concentration of 5 m PZ/5 m tertiary amine, as well as PZ-activated hindered amines at an initial loading of 0.23 mol CO_2/mol alkalinity and an initial concentration of 1.33 m PZ/2.67 m hindered amine. These rate measurements were interpreted in the context of maximum stripping temperatures (T_{MAX}). PZ-activated tertiary morpholines were found to be the most stable solvent class, with T_{MAX} values greater than 150 °C. PZ-activated acyclic tertiary amines without methyl groups were of an intermediate stability, with T_{MAX} values between 130 and 140 °C. PZ-activated acyclic tertiary amines with at least one methyl group were stable below 130 °C. Acyclic PZ-activated hindered amines had stability temperatures ranging from 128 °C to 147 °C, with the least stable acyclic hindered amines having the greatest number of hydroxyl groups. Cyclic PZ-activated hindered amines had stability temperatures below 130 °C.

The second paper, "Thermal Degradation of Linear Amines," presented thermal degradation rate measurements for a range of linear diamines and alkanolamines with an initial concentration of 10 m alkalinity (5 m alkalinity for hexamethylenediamine) and an initial loading of 0.4 mol CO_2/mol alkalinity. Increasing amine chain length between the amino function and the end amino or hydroxyl function decreased the initial rate of thermal degradation and increased the activation energy of thermal degradation. Ethylenediamine was found to be the most corrosive amine tested, whereas propylenediamine was the least corrosive.

The third paper, "Oxidative Degradation of Diamines and Structural Derivatives," presented oxidative degradation rate measurements for a range of linear diamines and alkanolamines with an initial concentration of 10 m alkalinity (5 m alkalinity for hexyamethylenediamine) and an initial loading of 0.4 mol CO_2/mol alkalinity and in the presence of 0.4 mM Fe, 0.2 mM Mn, 0.1 mM Ni, and 0.05 mM Cr. Propylenediamine and monopropanolamine were found to be

oxidatively stable and did not show any appreciable oxidative degradation, whereas all amines tested lost about 80% of their mass after 2 weeks.

Conclusions

1. PZ-activated tertiary morpholines were found to be the most stable solvent class, with T_{MAX} values greater than 150 °C.
2. PZ-activated acyclic tertiary amines without methyl groups were of an intermediate stability, with T_{MAX} values between 130 and 140 °C.
3. PZ-activated acyclic tertiary amines with at least one methyl group were stable below 130 °C.
4. Acyclic PZ-activated hindered amines had T_{max} from 128 °C to 147 °C, with the least stable acyclic hindered amines having the greatest number of hydroxyl groups.
5. Cyclic PZ-activated hindered amines had T_{max} below 130 °C.
6. Increasing amine chain length between the amino function and the end amino or hydroxyl function of linear amines decreased the initial rate of thermal degradation and increased the activation energy of thermal degradation.
7. Ethylenediamine was found to be the most corrosive amine tested, whereas propylenediamine was the least corrosive.
8. Propylenediamine and monopropanolamine were found to be oxidatively stable and did not show any appreciable oxidative degradation, whereas all amines tested lost about 80% of their mass after 2 weeks.

Future Work

Future work will focus on finalizing a rigorous kinetic model for the degradation of MDEA and PZ in the presence of H^+.

Aerosol Mitigation in CO_2 Capture

Quarterly Report for July 1 – September 30, 2014

by Steven Fulk

Supported by the Texas Carbon Management Program

and DOE/URS contract DE-FE0005654

McKetta Department of Chemical Engineering

The University of Texas at Austin

October 31, 2014

Acknowledgement

This material is based on work supported in part by the Department of Energy under Award Number DE-FE0005654.

Disclaimer

Abstract

Work completed this quarter is divided between this report and a manuscript prepared for the GHGT-12 conference (appended to this report).

In the GHGT-12 work, inlet aerosols of variable (0.5 m PZ and 0.05 vol % H_2SO_4) composition were generated by vaporizing a metered liquid stream kept at 1 mL/min sucked through an eductor by a preheated (310 ºC) motive N_2 stream at 1.035 SCFM. The solvent flowrate (6–36 GPH), inlet CO_2 concentration (0–8 vol %), and the inlet solvent temperature (40 and 50 ºC) were changed independently and the outlet PZ concentration was measured using FTIR.

The baseline outlet gas CO_2 and PZ concentrations relative to the solvent (0.9 m PZ) flowing at 12 GPH were 110.4 and 2.8 ppmv, respectively. Injection of PZ and H_2SO_4 aerosols increased the outlet PZ value to 65 and 6.5 ppmv, respectively.

Increasing the inlet concentration of CO_2 to 4 vol % doubled the measured PZ in the exhaust gas under PZ aerosol load; however, further increase of CO_2 produced very minor relative changes. PZ seems to be inversely related to inlet CO_2 concentration in the case of H_2SO_4 aerosols.

Changes to the solvent flowrate had far greater impact on the exhaust rate of amine. PZ decreased from 75 to 20 ppmv when the solvent rate was reduced from 36 to 6 gpm for the PZ aerosol case in the presence of no inlet CO_2. Solvent rate was found to have the opposite behavior for the H_2SO_4 aerosol case; PZ emissions increased from 6 to 20 ppmv as the solvent rate was increased from 6–36 GPH. Similar behavior was found during multivariable (CO_2 and flowrate) studies, though the absolute changes in measured PZ were much smaller.

Finally, PZ emissions were found to have a reciprocal relationship to inlet solvent temperature for the PZ aerosol case. No clear trend was observed during H_2SO_4 aerosol testing.

In this document, LVI flow measurements and a new multi-point FTIR sampling system were tested. The LVI flow rate and vacuum level were verified against vendor data and matched closely to the Air-Vac HAVR093SS eductor. The multi-point FTIR sampling system flow rate was measured for variable inlet throttling. The flow rate for both sample lines (10’ and 30’) was 8.9 and 6.3 SLPM at 70% throttle between 25–60 Hz. The flow rate for both sample lines (10’ and 30’) was 6.6 and 5.3 SLPM at 90% throttle between 25–60 Hz.

Introduction

Volatile emissions are a primary concern for CO_2 capture plants using amine scrubbers. Emissions constitute increased economic expense through solvent loss as well as being a source of potentially hazardous environmental pollutants. Compounds found in treated flue gas include contaminants from thermal degradation and oxidation as well as combustion byproducts. Degradation and reaction products have a wide range of toxicity and biodegradation characteristics, which potentially represent unacceptable emissions; as a result, recent work has focused on estimating volatile losses and assessing their toxicological impact.

Volatile emissions can be reduced through the use of a water wash – an absorber column using recycled water as a solvent. Design considerations for water wash systems include liquid distribution methods to adequately wet packing with low liquid rates, and balancing water in the absorber/stripper system by adjusting the total volatile concentration in the wash water. Water wash columns have relatively flat efficiency profiles, meaning the removal efficiency is not a strong function of either the gas or liquid flowrates or the operating temperature.

Emissions with Aerosols

Recent pilot plant measurements have shown that normal water wash columns are ineffective at controlling volatile loss of amine and other pollutants due to the presence of aerosols. In 2011, MHI presented pilot test results for both KS-1™ and MEA which showed that emissions were proportional to inlet SO_3 concentration (MHI, 2012). Amine levels exiting the wash section were 0.4–23.2 ppmv and 0.8–67.5 ppmv for KS-1™ and MEA, respectively, for 0–3 ppmv inlet SO_3. Aerosols were visibly present at the direct-contact cooler (DCC) and wash outlets. At the Maasvlakte pilot plant, TNO and SINTEF jointly tested a 30 wt % MEA CO_2 capture unit with a downstream water wash complete with online gas and aerosol phase sampling (TNO, 2012; SINTEF, 2012). Excessive emissions were observed; aerosols, not physical entrainment, were responsible for the increase. Lithium and rubidium carbonate (Li_2CO_3, Rb_2CO_3) tracers in the

solvent and wash loops verified negligible entrainment. A Brownian demister unit (BDU) was installed downstream from the wash section, which reduced emissions to previously simulated levels, indicating the bulk of emissions were contained in the droplet phase. Mean droplet diameters (d_{Drop}) were measured using light extinction coefficients and ranged from 0.76–7.88 μm at the BDU inlet and 0.2–1.74 μm at the outlet. The quality of the inlet flue gas and the absolute temperature of the absorber influenced the emission rate. More recently, a baseline study using MEA at NCCC in Wilsonville, Alabama saw higher amine emissions than expected (NCCC, 2012). The number of absorber beds (2–3), intercoolers (0–2), and inlet SO_3 concentration (1.8 and 3.2 ppmv) were varied as part of a parametric test on the emission rate. It was concluded that carryover was proportional to inlet SO_3 and also to the concentration of MEA in the wash water. Emissions were inversely related to absorber temperature. In all studies, aerosols increased emissions roughly 1–2 orders of magnitude.

It is clear from pilot plant observations and emission studies that removing aerosols is a key part of reducing possible solvent release from amine-based CO_2 capture plants. The failure of conventional wash columns and the potential financial impact of particle collectors necessitate fundamental research to identify more practical means of controlling emissions for large-scale processes. Understanding interconnectivities of the bulk CO_2 removal process operating conditions and aerosol dynamics can provide the insight required to either design or operate a system with the intention of suppressing droplet growth; or conversely, to condition aerosols for easier removal.

Safety

The FTIR and peripheral equipment are maintained at 180 °C to prevent condensation inside the analyzer. The surface temperature of fittings and any metal tubing used for connections present potential burn hazards when in operation. Any heated transition or connection should be insulated to prevent contact burns. Insulation also prevents cold spots, which can lead to condensation. Leather work gloves should always be worn when working with FTIR lines and fittings to prevent burns.

All lines that directly connect to heated fittings must be Teflon® to prevent melting and gas loss from the process. Melted tubing can lead to hazardous gas release. Tubing should be confirmed to be of Teflon® grade or higher prior to use with the FTIR.

Aerosol Growth Column (AGC)

An updated P&ID of the AGC is shown in Figure 1–Figure 3 below. Changes and calibration data performed during this quarter are detailed below.

LVI

The carrier gas (N_2) flow rate into the LVI system was measured by a direct-read Key Instruments MR3A06SVVT rotameter with Viton® o-ring seals and a glass float (ρ_{float} = 2.53 g/mL). The rated accuracy is ± 5% of full-scale (60 SCFM). The rotameter was installed upstream of the pressure regulator in the LVI enclosure and just downstream of an isolation valve on the N_2 supply line. The flow rate reading was compensated for density using the pressure and temperature at the outlet of the rotameter body by using Equation (1). Equation (1) assumes that the gas density follows ideal gas law and that the density of both the reference gas and the process gas are negligible compared to the rotameter float. Conversion from standard

conditions to actual conditions was done by dividing Equation (1) by the ratio of the process-to-standard gas density, yielding Equation (2). The supply pressure was measured at 100 psig and the temperature assumed to be ambient at 21 ºC. Standard conditions were specified as 14.696 psia and 20 ºC by Key Instruments.

$$Q_G(\text{ACFM}) = Q_{STD}(\text{SCFM}) \sqrt{\frac{P^{STD}}{P^G} \cdot \frac{T^G}{T^{STD}} \cdot \frac{MW_{STD}}{MW_G}} \tag{1}$$

$$Q_G(\text{SCFM}) = Q_{STD}(\text{SCFM}) \sqrt{\frac{P^G}{P^{STD}} \cdot \frac{T^{STD}}{T^G} \cdot \frac{MW_G}{MW_{STD}}} \tag{2}$$

The flow rate into the LVI system is choked because of the eductor nozzle diameter. Therefore, the flow rate through the eductor body should follow a linear relationship to the inlet set pressure controlled by the inlet pressure regulator. Equation (3) shows the calculation for the mass flow rate of an ideal compressible gas. The flow rate at different operating temperature can be calculated as shown in Equation (4).

$$\dot{m} = C_D A P_0 \sqrt{\frac{1}{RT_0} \gamma \left(\frac{2}{\gamma+1}\right)^{\frac{\gamma+1}{\gamma-1}}} \tag{3}$$

$$\dot{m}(T_2) = \dot{m}(T_1) \sqrt{\frac{T_1}{T_2}} \tag{4}$$

where:

γ = C_p/C_v

C_p = Constant pressure heat capacity

C_v = Constant volume heat capacity

C_D = Discharge coefficient

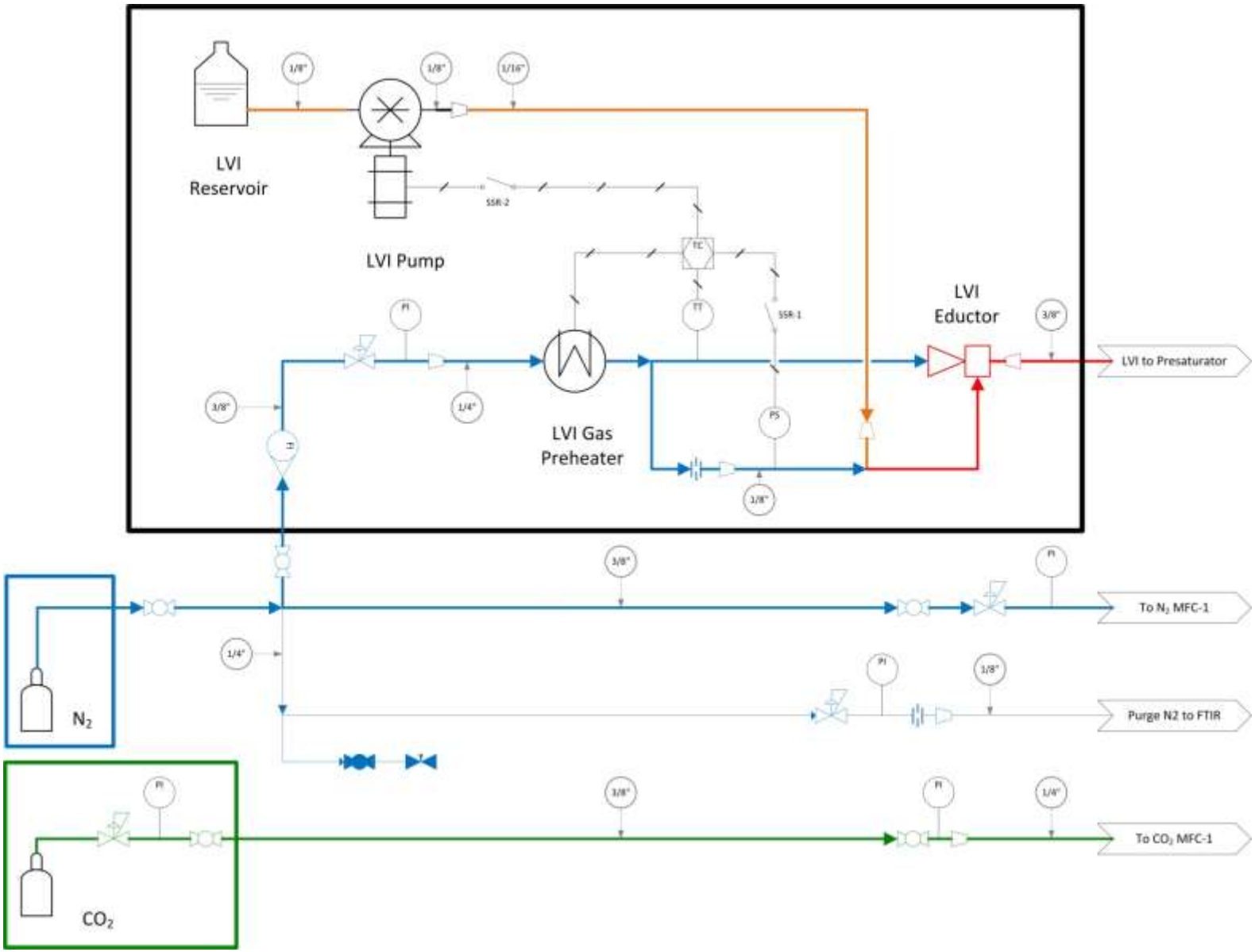

Figure 1: Aerosol Growth Column P&ID Sheet #1

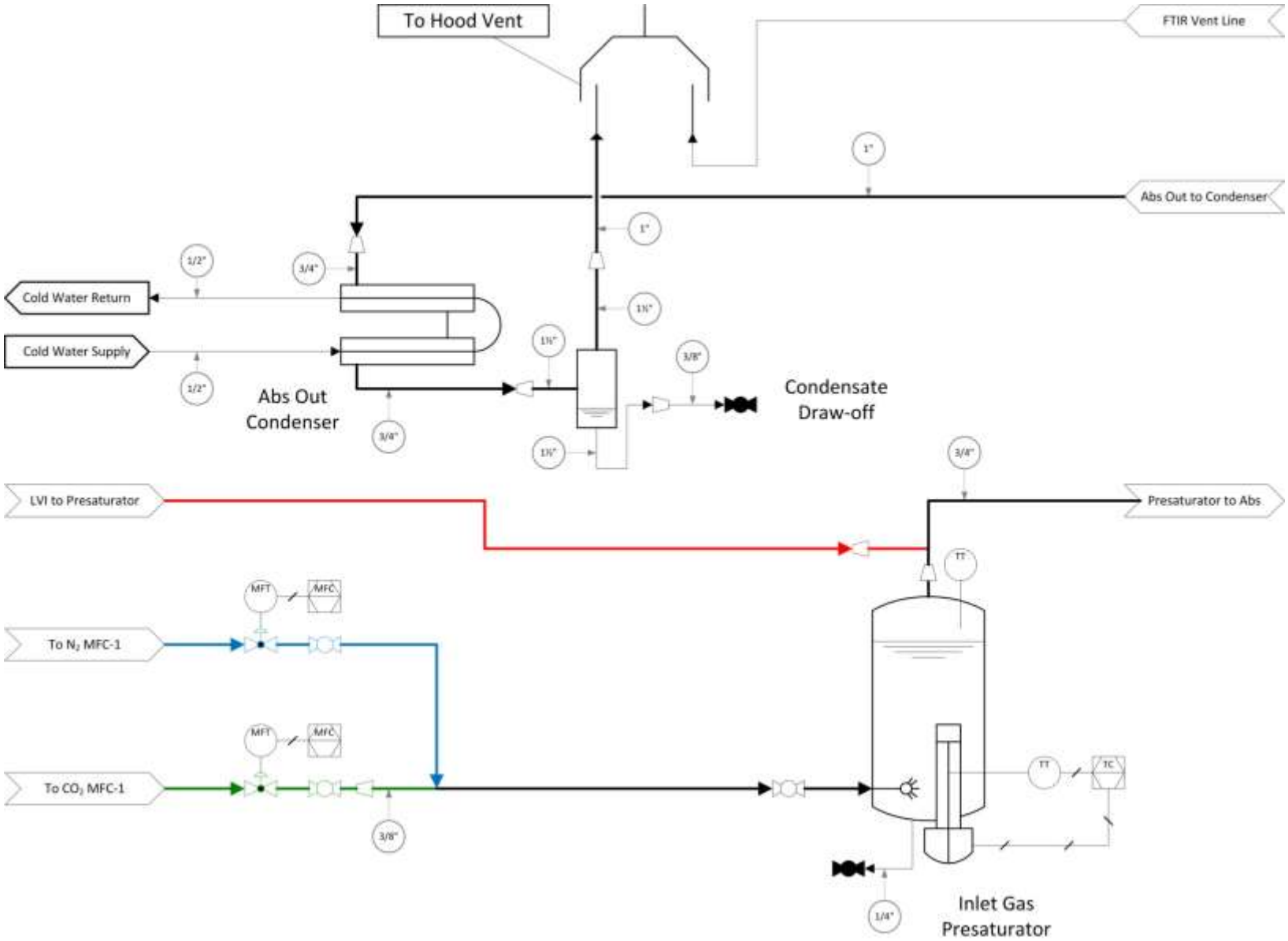

Figure 2: Aerosol Growth Column P&ID Sheet #2

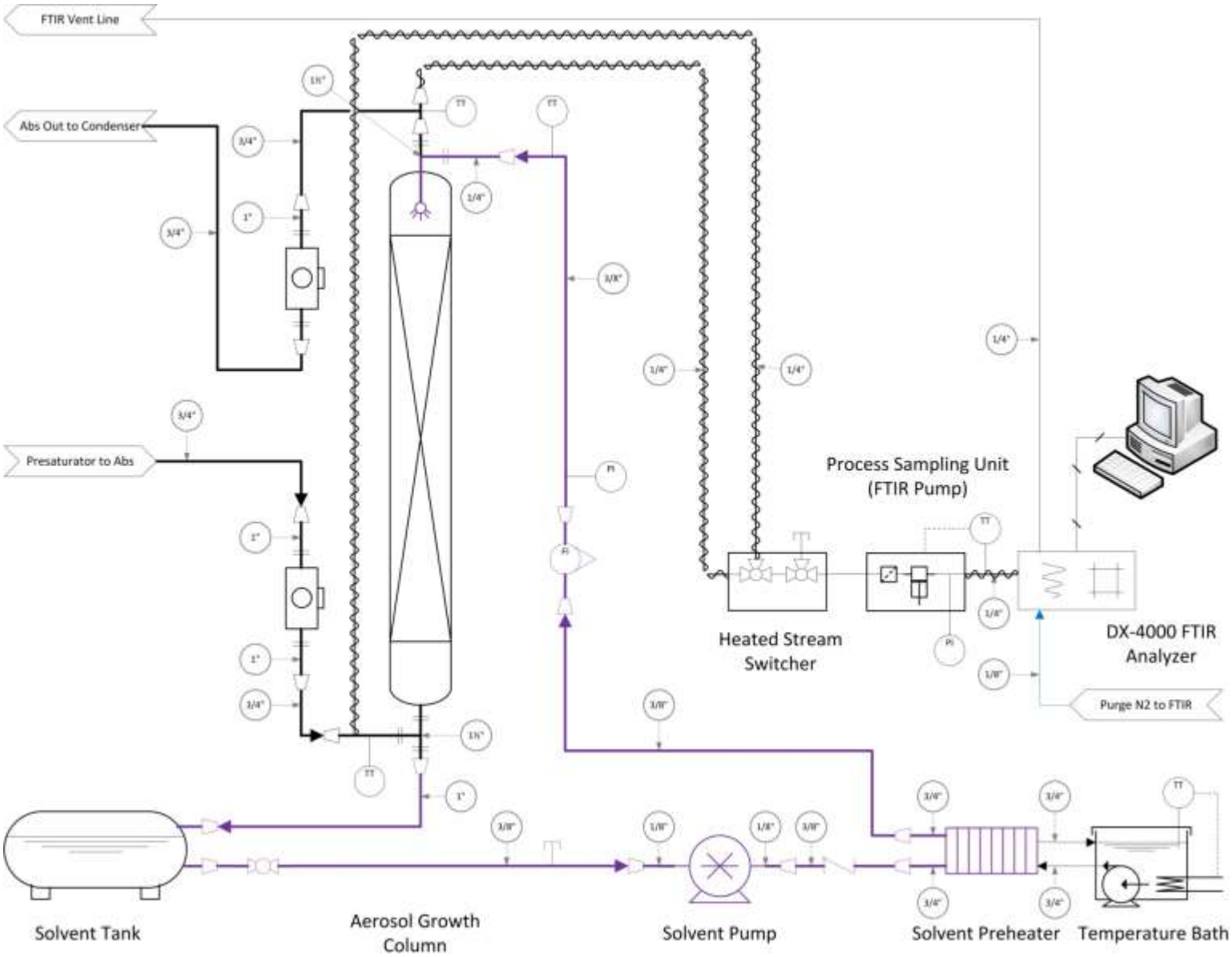

Figure 3: Aerosol Growth Column P&ID Sheet #3

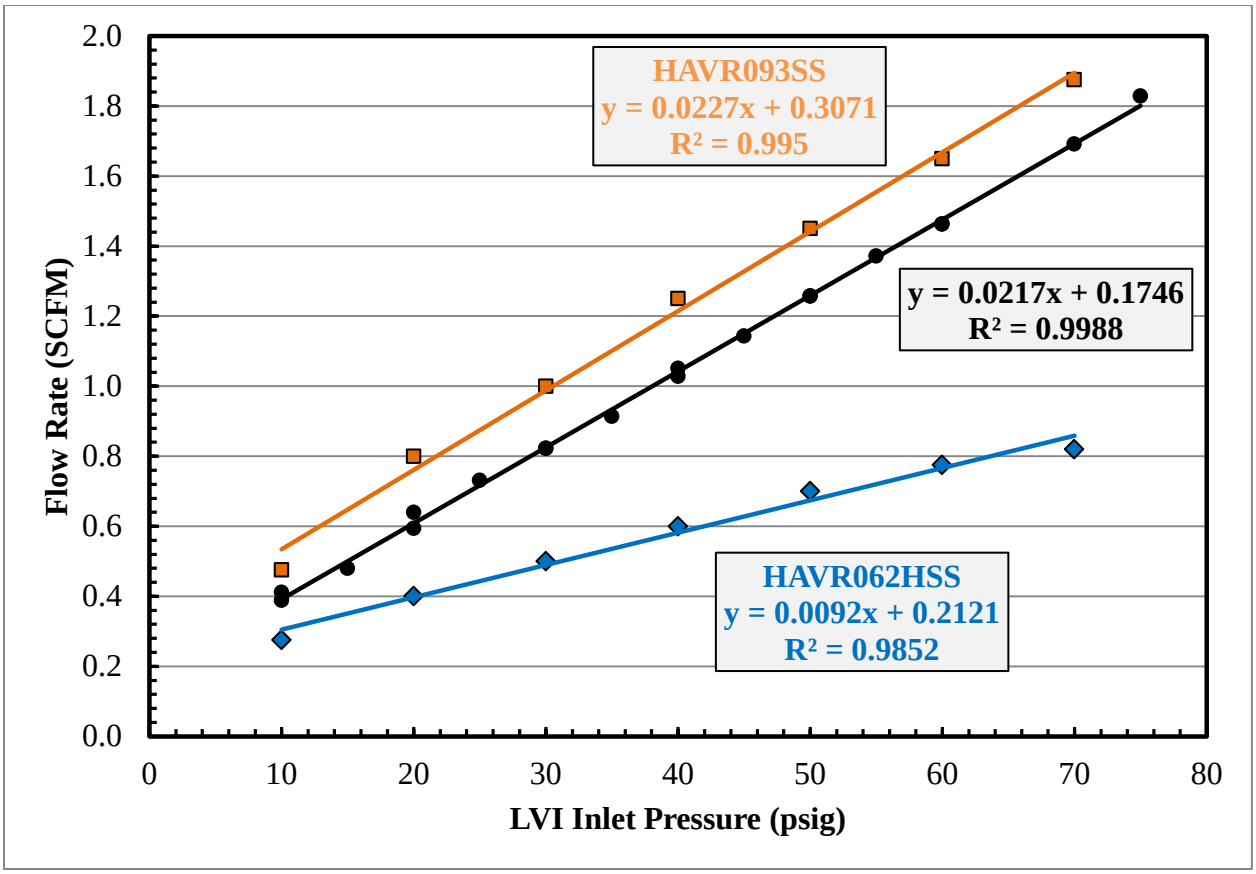

Figure 4: Measured LVI carrier gas flow rate compared to manufacturer data. The measured flow rate was compensated for density using P = 100 psig and T = 21 ºC.

Figure 4 shows the compensated flow rate through the LVI and the digitized curves for two eductor bodies; Air-Vac HAVR062SS is the flow body specified in the LVI manual and Air-Vac HAVR093SS is the next larger eductor design. The measured flow rate through the LVI matches the slope of the HAVR093SS curve to within 5%. It was discovered after disassembling the LVI that the actual eductor was indeed the HAVR093SS, not the HAVR062SS as specified. The decrease in flow rate can be attributed to several sources: (1) the eductor body and nozzle were coated with Dursan® coating to prevent corrosion, and (2) compounding error from the rotameter, pressure, and temperature measurements.

The eductor vacuum was measured using the vacuum gauge mounted in the LVI enclosure. Figure 5 shows the comparison between the measured vacuum plotted against manufacturer data. The HAVR093SS and the HAVR062SS eductor models share the same vacuum curve. Deviations at low inlet pressure are due to: (1) lower volumetric flow rates at a given inlet pressure, and (2) the increase in absolute measurement error of the vacuum gauge. The deviations at higher inlet pressure are likely due to leakage in the vacuum line; the vacuum line was connected to the LVI pump, though leakage around the pump shaft seal at high vacuum levels has been observed.

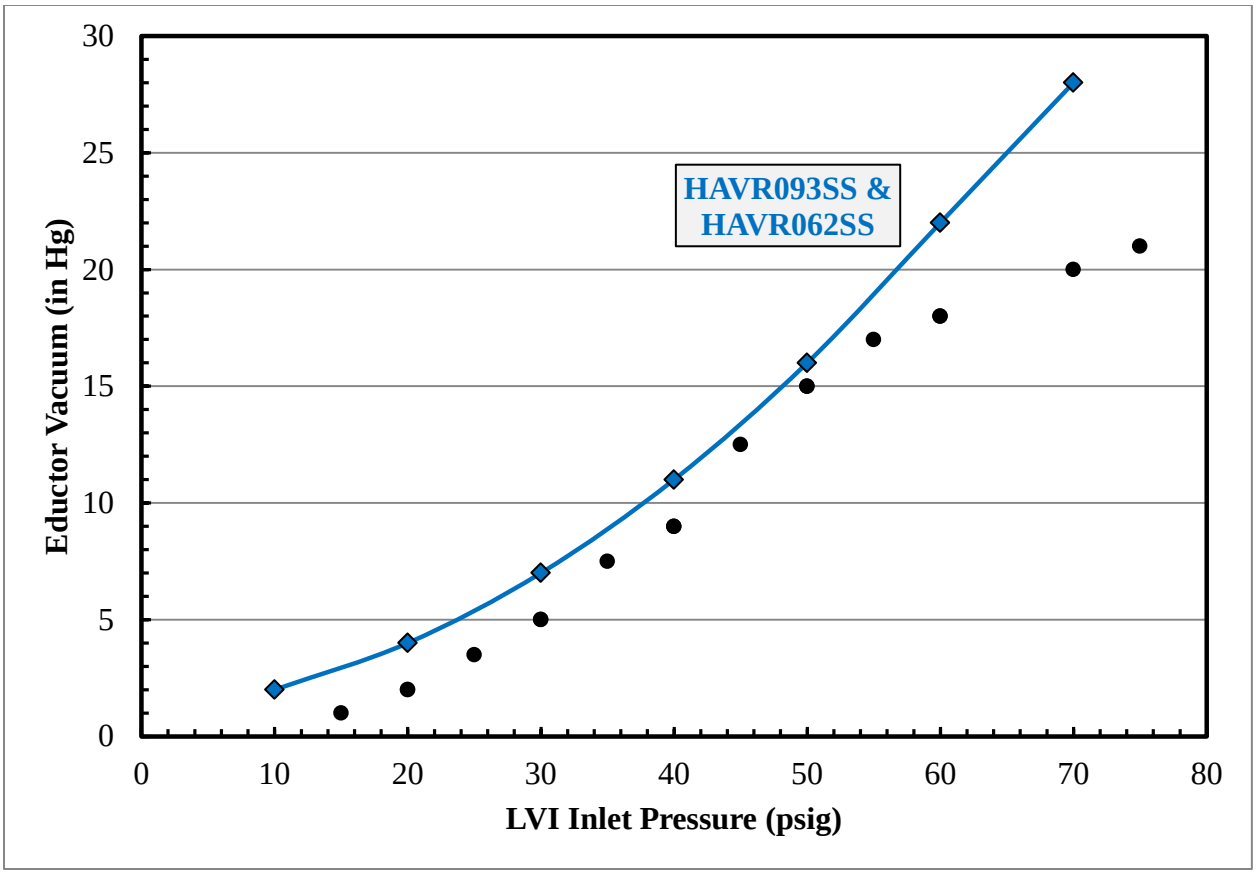

Figure 5: Measured LVI eductor vacuum compared to manufacturer data

FTIR

The FTIR and peripherals were relocated outside the AGC walk-in hood. The heated FTIR lines were re-routed to pass overhead across a strut channel rack, hung from the vent hood using swivel beam clamps. Moving the FTIR out of the hood space eliminates tripping hazards due to the heated lines.

The heated line name-plate current draw is 15.7A; therefore, a 20A rated temperature controller and circuit were required. A NEMA 5-20p power cord and K-type thermocouple extension wire were cup-soldered to a female 7-pin Hirschmann™ connector. The thermocouple reading should not be affected by the soldered joint, provided the soldered joint temperature is the same as the internal cold-reference junction in the temperature controller. An 18" adapter line was made to minimize the distance between the temperature controller and the soldered joint.

The two FTIR sampling lines (10' and 30' long) were connected to a heated stream switcher box containing two, three-way valves to select and isolate the FTIR lines. The stream switcher is temperature-controlled to 180 ºC and is connected to a temperature controller using a 4-pin Amphenol power line and a K-type thermocouple.

An SS-1RS4-SH needle valve was added inside the heated stream switcher box to throttle the new rack-mount FTIR pump to establish a flow rate of less than 10 SLPM at full drive speed

(60 Hz). The new FTIR pump is a 0.5 HP Baldor Super-E Model M35J302P862 motor with an Air Dimensions, Inc. Dia-Vac-R181 heated diaphragm vacuum pump head controlled by a Baldor Drives VS1ST 0.5 HP AC variable speed drive (VSD). Figure 6 shows the flow rate measured by two 5 SLPM rotameters connected in parallel as a function of the needle valve stroke position and the VSD frequency at room temperature. The flow path upstream of the pump included the FTIR lines, the heated stream switcher box, a 3' jumper line, and the FTIR pump heated filter. Downstream of the FTIR pump, the flow path included another 3' jumper line, the FTIR cell, and a 1/4" tube line to the rotameters (approximately 3').

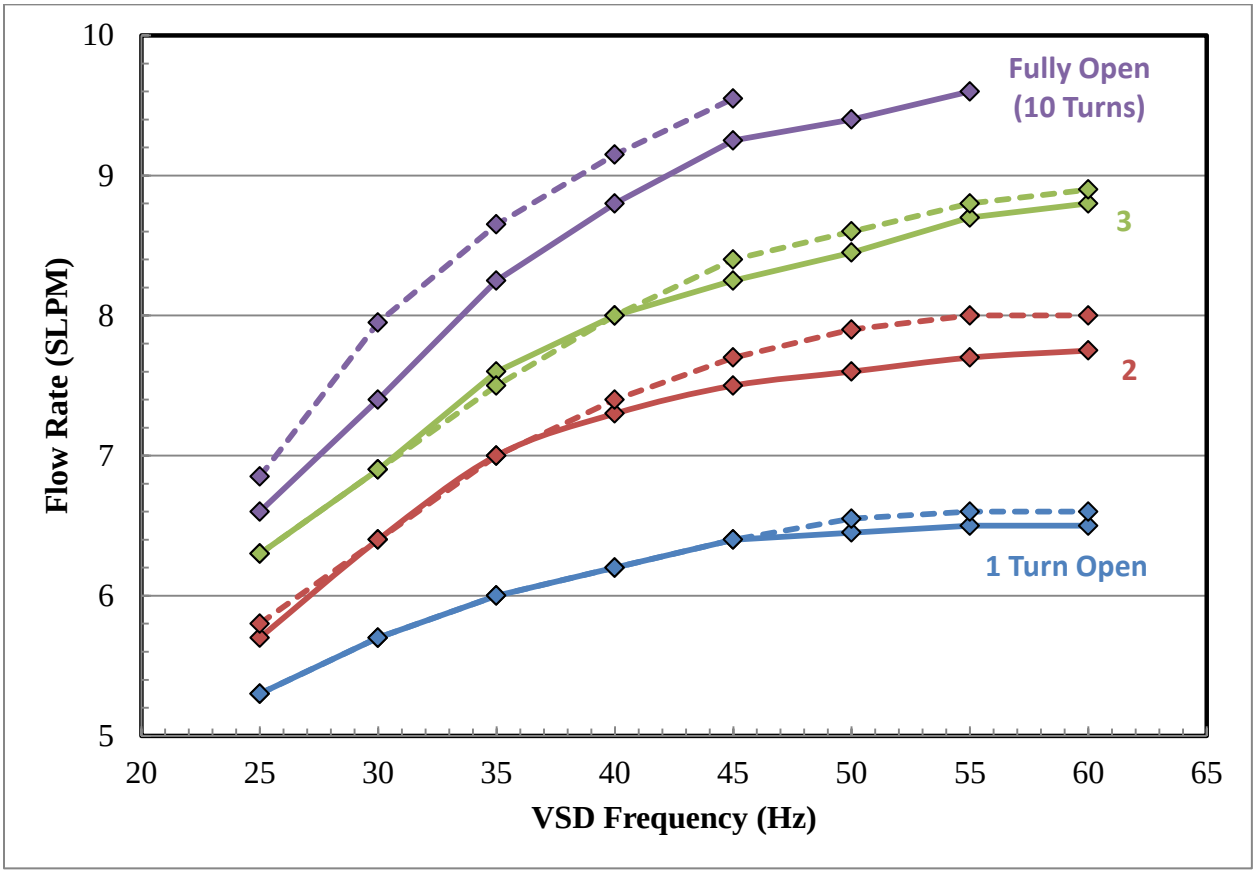

Figure 6: Flow curve for the new FTIR sampling system with varying throttle valve stroke position. The solid and dashed lines are for the 10' and 30' FTIR lines, respectively.

The pressure drop across the FTIR lines is nearly identical. The IDs of the lines are 0.153" and 0.123" for the 30' and 10' lines, respectively. Pressure drop calculations using the correct IDs at the measured flow rates confirm equivalent pressure drop even though the line lengths are different by a factor of three.

The FTIR sampling system will be operated at 180 ºC, which will increase the pressure drop of the system; therefore, a valve position of 4 turns open will be used to maintain a flow rate under 10 SLPM at full drive speed.

Conclusions

Experimental achievements are summarized below:

- A multi-point, heated sampling system for FTIR analysis was built and tested for a new rack-mounted CX-4000 FTIR system.
- LVI carrier gas flow rate measurement was added and validated against vendor data.

Future Work

The AGC solvent PZ concentration will be increased incrementally from 0.3 m to 8 m and further CO_2 capture/LVI tests will be performed. Liquid samples will be analyzed to track loading and H_2O balance.

References

Fulk SM, Rochelle GT. "Quantification of Total Piperazine Emissions by FTIR Under Variable Bench-Scale Absorber Conditions." Presented at *GHGT-12*, Austin, TX. Oct 5–9, 2014.

Mitsubishi Heavy Industries (MHI). "Amine Emission Control Technology of KM CDR Process™." Presented at the Amine Workshop in Palo Alto, California. August 16, 2011.

National Carbon Capture Center (NCCC). "National Carbon Capture Center: Post Combustion." Presented at the 2012 NETL CO_2 Capture Technology Meeting. July 10, 2012.

Netherlands Organization for Applied Scientific Research (TNO). "Emission Reducing Technologies Aerosols." Presented at UTCCS-1 in Austin, TX. January 25, 2012.

Rochelle GT et al. "CO_2 Capture by Aqueous Absorption, Fourth Quarterly Progress Report 2013." Texas Carbon Management Program. The University of Texas at Austin. 2014.

SINTEF. "Emission Studies at the Maasvlakte CO_2 Capture Pilot Plant." Presented at UTCCS-1 in Austin, TX. January 25, 2012.

Aerosol Observation and Separation in Amine-Based CO_2 Capture

Quarterly Report for July 1 – September 30, 2014

by Matt Beaudry

Supported by the Texas Carbon Management Program

McKetta Department of Chemical Engineering

The University of Texas at Austin

October 31, 2014

Abstract

Amine emissions in aerosol form have been observed as a significant problem for amine-based CO_2 capture plants. Unarrested soot and hydrolyzed SO_3 condense in the absorber while collecting amine. Conventional water wash columns are ineffective at removing the amine once it is captured in the aerosols. While Brownian diffusion units have proven to be fairly effective at reducing amine emissions, cyclonic separators offer the potential for improved capture performance with a simpler system at a lower cost. A swirl tube cyclonic separator has been designed and will be implemented in both the Aerosol Growth Column and the PRC Pilot Plant. The flexibility of the design will allow for capture of aerosols at controllable sizes. Another aerosol sampling system has been designed to utilize centrifugal forces to control the size of particles sampled by FTIR analysis. It is hoped that this will provide similar data to the PDI with more robust and less expensive equipment.

Introduction

Aerosols and Emissions

The emission of volatile compounds is a major concern at CO_2 capture facilities utilizing amine scrubbing. Amine solvent lost through the overhead of absorber columns not only represents an environmental and safety hazard, but also has undesirable economic implications. Amine losses can occur via three different processes: through the gas phase as a function of vapor pressure in the absorber column, liquid entrainment as the gas velocity increases, and as a mist composed of aerosols. Losses through the gas phase can be mitigated with the use of a water wash. Liquid entrainment can be reduced by designing the column to use a gas velocity that prevents the entrainment of liquid droplets.

Aerosol formation in absorber columns occurs when SO_3 is present in the incoming flue gas. The SO_3 hydrolyzes to H_2SO_4 in the humid atmosphere of the absorber. From there, aerosols in absorber columns can grow via two different mechanisms: heterogeneous or homogeneous nucleation. Heterogeneous nucleation occurs in the presence of soot or fly ash particulate. Growth occurs as the aerosol collects sulfuric acid, water, and amine. This is the dominant aerosol growth mechanism in most industrial processes (Mertens, 2013), especially for strong

acids besides H_2SO_4 (Schaber, 1995). Khakharia et al. reported that amine emissions were more heavily influenced by soot concentrations at lower soot and SO_3 concentrations, but increasing the SO_3 concentration relative to the soot content significantly increased the amine emissions.

Homogeneous nucleation of aerosols occurs exclusively between molecules of the condensable components (Mertens, 2013). This is a very rapid process, occurring within a second of the sulfuric acid hydrolyzation (Wix, 2010). As the SO_3 content in the flue gas increases, this becomes the more dominant mechanism for aerosol growth. Homogeneous nucleation is heavily influenced by the saturation degree, given by Equation 1 (Schaber, 1995).

$$S_i = P_i / P_i^e(T, y_i) \quad (1)$$

Where S_i is the degree of saturation, P_i is the partial pressure of the condensable component, and $P_i^e(T, y_i)$ is the equilibrium partial pressure as a function of temperature and gas phase concentration. Heterogeneous nucleation requires a low degree of saturation at an S_i value of approximately 1.0, while homogeneous nucleation needs a S_i value closer to 4.0 (Sinanis, 2008). The saturation degree is a local phenomenon in homogeneous nucleation. Saturation levels are at a maximum close to the surface of an aerosol and reduce to equilibrium levels as the distance from the droplet surface increases (Wix, 2010).

Aerosol Collection

Research conducted by MHI utilized demister units that operate under Brownian diffusion principles (MHI, 2011). Brownian diffusion is the seemingly random motion of particles in a fluid field that is a result of their impact with the high velocity atoms that the field is composed of. Demister units in amine-based CO_2 capture plants pass the gas discharge from the water wash through a system of mesh screens. These screens collect aerosol particles along their random Brownian diffusion pathways, thus preventing their emission to the atmosphere. MHI found that a demister unit significantly reduced amine emissions without reducing gaseous ammonia emissions, indicating that the majority of amine losses were due to retention in aerosols.

Demister units provide one possible means for aerosol removal. Another option is the use of cyclonic separators, which operate by using centrifugal forces to separate particles from a fluid stream. This technology was outlined in the report from last quarter (Rochelle, 2014). These devices are frequently used in agricultural and coal processing industries, and are relatively easy to implement, thanks to their simple design and absence of moving parts.

Two important parameters in designing cyclonic separators are the cut size and the steepness of the cut curve. These parameters are most heavily influenced by the velocity of the gas inside the separator, and the diameter of the gas outlet. The cut size refers to the cutoff collection size for the separator. If a cyclonic separator has a cutoff size of 1 μm, this means that particles 1 μm and larger will be collected, while smaller particles will pass through the system. The steepness of the cut curve determines the effectiveness of the separator. A sharp cut curve indicates that the separator collects almost all particles above the designed cut size, while a soft cut curve is more lenient on the collection of larger particles. For the purposes of these experiments, a sharper cut curve is preferred.

Safety

The sulfuric acid aerosols generated in the LVI are very hazardous. These aerosols can cause chemical burns on contact with the skin as well as posing an inhalation hazard. Contact with these aerosols must be mitigated. The piping and unit operations downstream of the LVI are constructed of corrosion resistant materials and should be checked for leaks prior to operation. The AGC is operated indoors inside of a walk-in fume hood to minimize the risk of sulfuric acid exposure for those operating the apparatus. Proper personal protection equipment, and the training on how to use it, is essential for everyone while operating the equipment.

Experimental Methods

Aerosol Collection

An aerosol collection system is designed for use with both the Aerosol Growth Column (AGC) and the PRC Pilot Plant. Flexibility of the design is of utmost importance. As outlined in last quarter's report, a swirl tube type cyclonic separator will be utilized. This is shown in Figure 1.

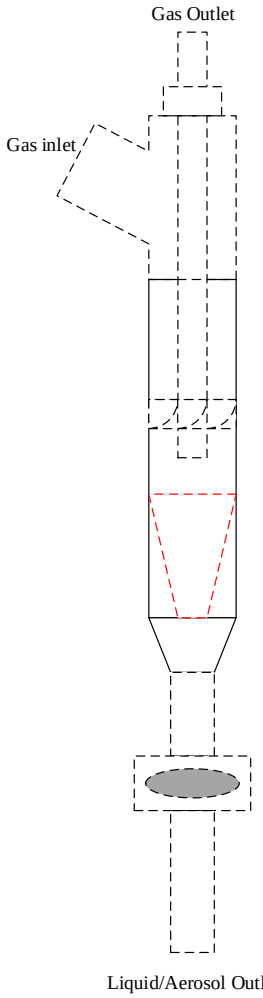

Figure 1: Side view of swirl tube apparatus

The swirl tube itself has an outer diameter of approximately 5.72 cm and a total length of 130 cm. The long length is to allow for flow stabilization before entering the vaned section of the swirl tube, and for the variation of cyclone length. The length of the cyclone affects the efficiency of the separator, as it controls the location of the vortex point. The vortex point is the point at which the gas flow changes rotational direction (Gao, 2010). Much of the entrained aerosol is released at this location, which should be at the bottom of the cyclone. If the cyclone is too long, the vortex point will form on the cyclone wall and can re-entrain separated aerosols; if it is too short it inhibits the formation of the vortex point and results in minimal particle separation. The ideal cyclone length is based on the gas velocity and the aerosol loading. The outer shell of the swirl tube will be constructed from transparent acrylic glass, to allow visual confirmation of the cyclonic separator performance.

The vanes will have an entry angle in line with the flow and the tube body, and an exit angle of 30°. A removable cone insert, indicated by the red dashes in Figure 1, will be fabricated to test the effect this has on separator performance. Hsu et al. (2014) reported an improvement in efficiency in cyclonic separators with a cone, though this has yet to be observed for swirl tubes.

The system will be capable of collecting aerosols of varying sizes. One of the key parameters for determining cut size in this design is the diameter of the vortex finder, or the gas outlet. This system is designed to use ¼", ½", and ¾" steel Swagelok piping. Combined with varying the total gas flow rate, this will allow for the collection of particles at any cut size between 1 and 5 μm.

Finally, a length of tubing at the bottom of the separator will serve as a collection point for the captured aerosols. This will be equipped with a float valve that will control the amount of fluid in the tubing. The length of tubing between the bottom of the separator and the float valve can be varied to determine an optimal length. A longer length can reduce re-entrainment of collected aerosols, but at the expense of a reduced velocity and slight increase in pressure drop (Qian, 2006).

It will be beneficial to test the effectiveness of other aerosol removal devices with the Aerosol Growth Column apparatus. Comparing the performance of swirl tubes to that of other aerosol capture devices, such as demisters and Brownian Diffusion candles, will provide valuable information on the capabilities of each technology. Figure 2 presents the process flow diagram, provided by Steven Fulk, for the AGC system with a replaceable spool piece for different aerosol capture devices.

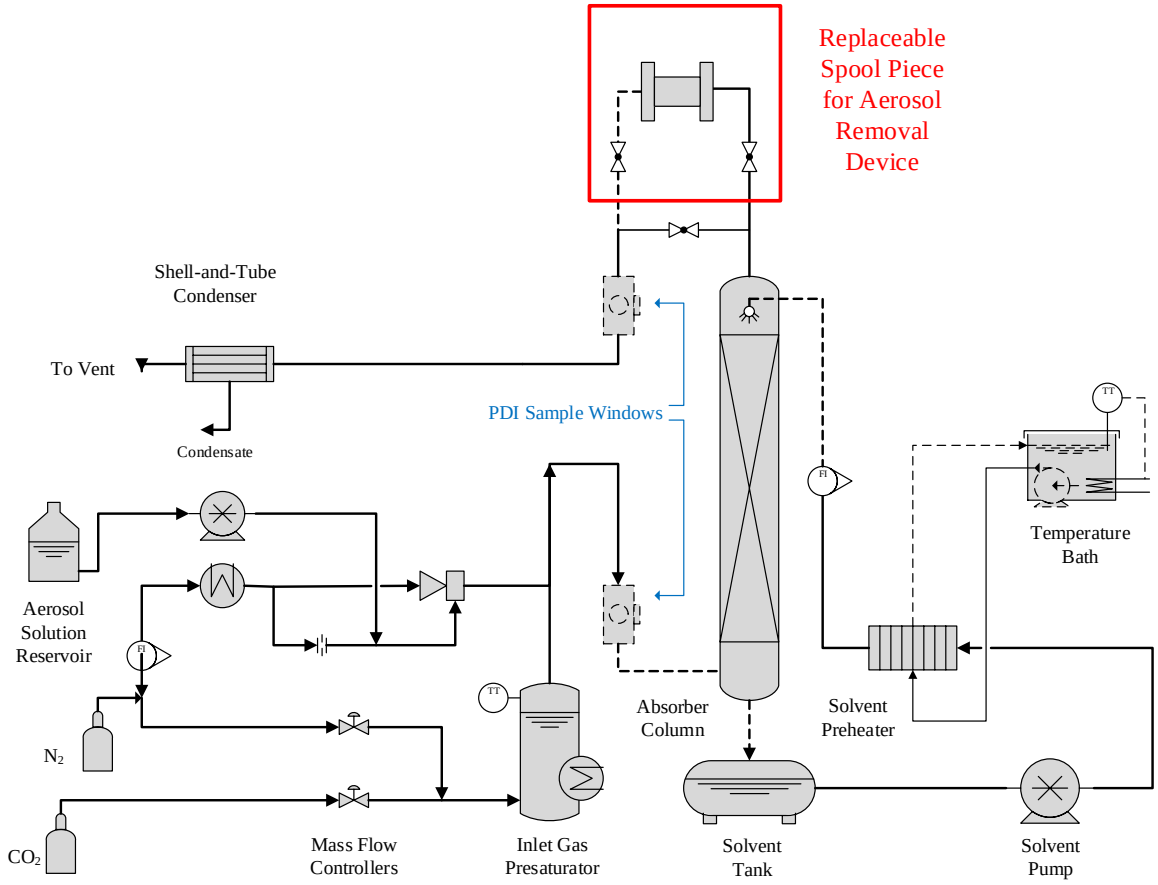

Figure 2: PFD of AGC apparatus with capability to configure to different aerosol capture devices

Aerosol Observation

The effectiveness of the swirl tubes will be evaluated with a Fourier Transform Infrared Spectrometer (FTIR) and a Phase Doppler Interferometer (PDI). The PDI operates by intersecting two lasers at an angle through a small, well-defined volume. A particle that passes through this volume scatters light that is collected by an optical receiver, which uses a phase-Doppler type analysis to determine particle sizes and concentration. The FTIR will be used to quantify the amount of amine that is captured in the aerosols at varying points in the system. Obtaining FTIR samples before and after the swirl tube will determine how successful the swirl tube is at capturing the amine-laden aerosols. An FTIR probe will be placed at the same location as the PDI window downstream of the absorber column, as seen in Figure 2. By utilizing the bypass around the replaceable spool piece for the aerosol removal device, the concentrations of the components both entering and leaving the aerosol removal devices can be determined. If precise enough data from the FTIR and PDI are captured, a mass balance can be calculated across the aerosol removal device to potentially determine an exact composition of the aerosols.

Phase Doppler Interferometers are very expensive and fragile pieces of equipment, an unfortunate combination. A device is required that can perform a similar analysis without the unnecessary risks of an expensive breakdown. The goal is to develop a piece of equipment that utilizes varying centrifugal force to remove aerosols of different sizes. This can be coupled with FTIR analysis, along with precise knowledge of the aerosol composition, to determine the size range of aerosols produced in a given process. An outline of the design is presented in Figure 3. This is based on a device described by Prado, who used similar equipment to study the effect of liquid entrainment through sieve trays in distillation columns (Prado, 1986)

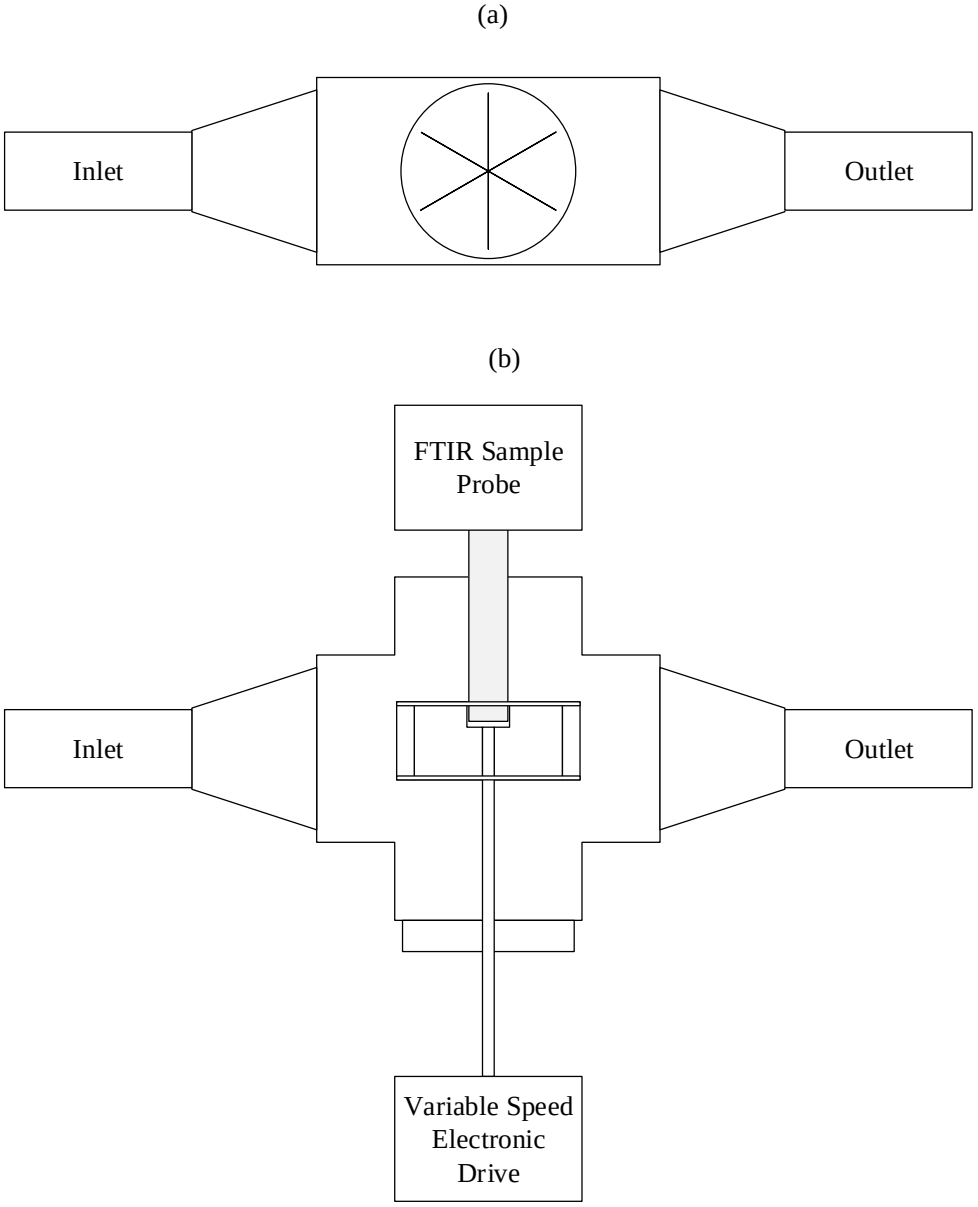

Figure 3: Schematic of (a) side view and (b) top view of centrifugal sampling device

The device will be placed downstream of the absorber column, where the replaceable spool piece is located in Figure 2. A piping cross will form the shell of the device, with the aerosol-laden vapor entering and leaving through the inlet and outlet, as labeled in Figure 3. An FTIR sample

probe will enter the cross perpendicular to the fluid flow, directly across from a variable speed electronic drive coupled to a paddle wheel-type fan. Fluid will enter the sample probe tip at a location inside the paddle wheel. By varying the speed of rotation of the paddle wheel, the size of aerosols sampled can be varied. At slower speeds, small and large aerosols are both allowed to enter the FTIR probe tip. As the speed increases, the larger aerosols are contacted by the paddle wheel and blocked from entering the probe tip due to their greater momentum compared to the smaller aerosols. It is hoped to link a rotational speed to the cutoff size of aerosols blocked from entering the probe. These data will be coupled with FTIR analysis to reduce the necessity of the PDI system and its associated expenses.

Discussion

Effective aerosol collection from absorber outlet streams should be possible with the use of swirl tubes. Minimal pressure drop is expected across these cyclonic separators. The magnitude of the pressure drop is dependent on the aerosol concentration, and varying the amount of aerosol produced in the Aerosol Growth Column or the pilot plant may result in an increased pressure drop across the swirl tube. Current calculations indicate that pressure drop should not be severe enough to negatively affect performance of the Aerosol Growth Column or the PRC Pilot Plant. It is believed that combining this technique with FTIR analysis will be a cost effective method for capturing and characterizing aerosols.

A simpler and more robust aerosol size sampling system is preferable, due to the high costs and low durability of the PDI. A centrifugal sampling system has been designed, and will be constructed and tested next quarter. If a strong correlation can be made between the PDI results and the results from this device, the PDI may no longer be necessary.

Future Work

The goal of this project is to determine the effectiveness of cyclonic separators, or more specifically swirl tubes, and other capture devices for removing aerosols from the outlet stream of an amine-based CO_2 capture plant. Next quarter, construction of the swirl tube itself will be completed. The PDI is scheduled to be received from Artium Technologies this quarter, and testing will begin on determining the effectiveness of the swirl tubes and other capture devices at removing aerosol particles from the Aerosol Growth Column. The centrifugal sampling device will also be implemented and tested in comparison to the PDI.

An eventual goal for the AGC is the addition of a water wash column downstream of the absorber column. This will more accurately simulate the operation of an amine-based CO_2 capture facility. A PFD of the proposed system is presented in Figure 4.

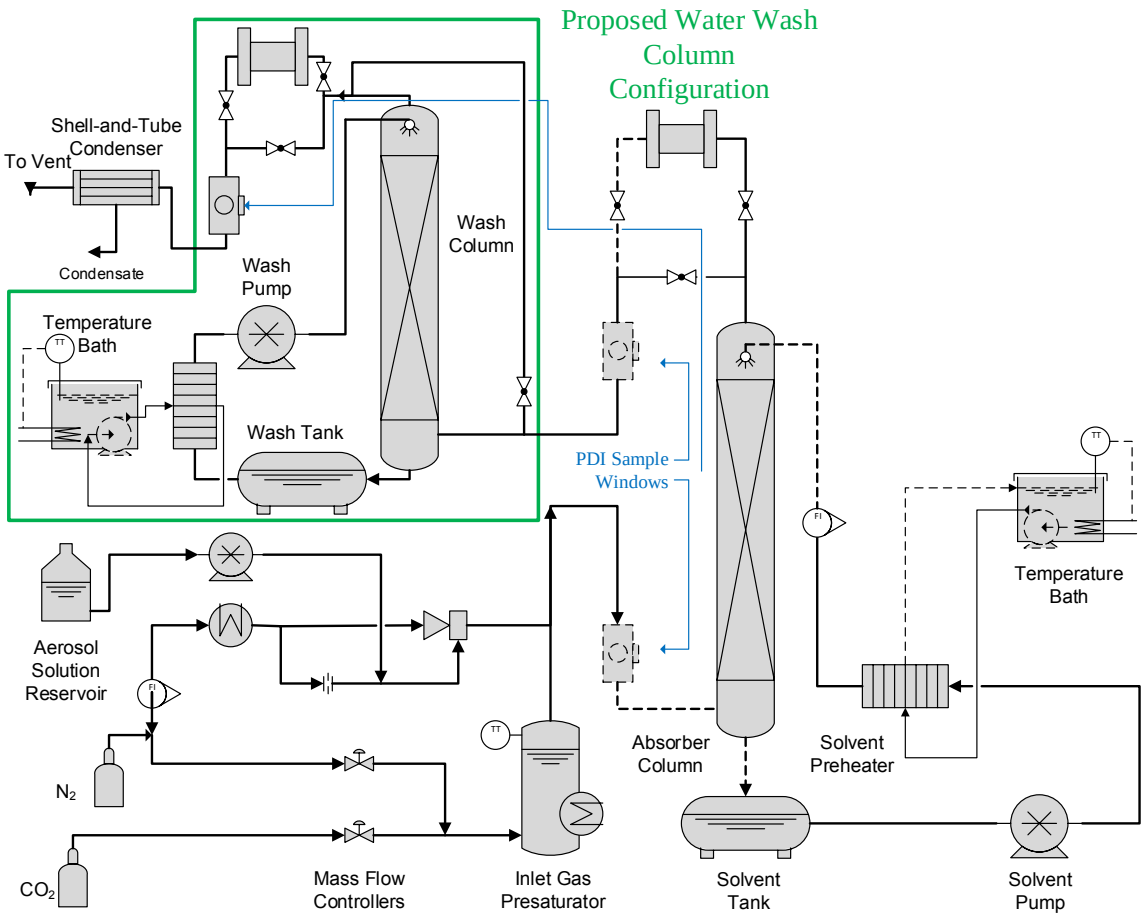

Figure 4: PFD of AGC apparatus with the proposed water wash system

PDI and FTIR sample points will be placed upstream of the absorber column and downstream of both the absorber column and water wash, which will allow for observation of aerosol formation and growth at all stages of the system. The water wash will be constructed in approximately the same fashion as the absorber column, and will include a wash water tank, heat exchanger, and pump. A bypass will allow for operation of the absorber column without the water wash. An additional replaceable spool piece will be located downstream of the water wash to test aerosol removal devices at this point.

Research will also be conducted on the viability of using a Condensation Particle Counter, (CPC), to aid in aerosol observation. The CPC will take a slipstream of aerosol laden vapor, expose it to saturation levels that cause the particles to grow exponentially, and then use optical light scattering methods to determine the aerosol density in the vapor. The CPC is a form of ex situ observation, which may result in changes to aerosol size and count density. If these changes can be minimized, a CPC may be a viable backup to the PDI measurements, at a lower cost.

References

Gao C, Sun G, Dong R, Fu S. “Characterizing the dynamic property of the vortex tail in a gas cyclone by wall pressure measurements” *Fuel Processing Tech*. 2010;91:921–926.

Hsu CW, Huang S, Lin C, Hsiao T, Lin W, Chen C. “An Experimental Study on Performance Improvement of the Stairmand Cyclone Design” *Aerosol and Air Quality Research*. 2014;14:1003–1016.

Khakharia P, Brachert L, Mertens J, Huizinga A, Schallert B, Schaber K, Vlugt T, Goetheer E. “Investigation of aerosol based emission of MEA due to sulphuric acid aerosol and soot in a Post Combustion CO_2 Capture process.” *Int J Greenhouse Gas Cont*. 2013;19:138–144.

Mertens J, Lepaumier H, Desagher D, Theilens ML . “Understanding ethanolamine (MEA) and ammonia emissions from amine based post combustion carbon capture: Lessons learned from field tests” *Int J Greenh Gas Cont*. 2013;13:72–77.

Mitsubishi Heavy Industries (MHI). “Amine Emission Control Technology of KM CDR Process™.” Presented at the Amine Workshop in Palo Alto, California. August 16, 2011.

Prado M. “The Bubble-to-Spray Transition on Sieve Trays: Mechanisms of the Phase Inversion”. Austin, The University of Texas at Austin, 1986.

Rochelle GT et al. "CO_2 Capture by Aqueous Absorption, Second Quarterly Progress Report 2014." Texas Carbon Management Program. The University of Texas at Austin. 2014.

Qian F, Zhang J, Zhang M. “Effects of the prolonged vertical tube on the separation performance of a cyclone” *J Haz Mater*. 2006;136:822–829.

Schaber K. “Aerosol formation in absorption processes” *Chem Eng Sci*. 1995;50:1347–1360.

Sinanis S, Wix A, Ana L, Schaber K. “Characterization of sulphuric acid and ammonium sulphate aerosols in wet flue gas cleaning processes” *Chem Eng Proc: Process Intensification*. 2008;47:22–30.

Wix A, Brachert L, Sinanis S, Schaber K. “A simulation tool for aerosol formation during sulphuric acid absorption in a gas cleaning process” *J Aerosol Sci*. 2010;41:1066–1079.

Amine Degradation in Pilot Plants

Quarterly Report for July 1 – September 30, 2014

by Paul T. Nielsen

Supported by the Texas Carbon Management Program

McKetta Department of Chemical Engineering

The University of Texas at Austin

October 31, 2014

Abstract

In a oxidation experiment using 4 m PZ in the HTOR degradation rig cycled from 40 °C to 150 °C, the rate of ammonia production, a major oxidation product, was approximately half that previously observed with 8 m PZ at similar conditions. The ammonia rate increased over the course of the experiment, and appeared to be tracking along with the accumulation of dissolved metal ions in solution. The metal ions may be participating in a free radical shuttling mechanism to oxidize the amine. A nitrogen bubble column designed to remove dissolved oxygen was partially effective, reducing ammonia generation by 20%. 0.24 moles of total formate were produced per mole of ammonia generated.

Degraded MEA solvent samples were analyzed from a 2-week campaign conducted at the NCCC pilot plant in June 2014. 55 mmol/kg of N-(hydroxyethyl)-glycine and 19 mmol/kg of formate accumulated during the campaign. No significant accumulation of nitrosamine was observed.

Samples were analyzed from a new vacuum reclaimer being tested at the Searles Valley Minerals Facility pilot plant operated by HTC in Trona, California, using 20 wt % MEA. The reclaimer waste typically contained 2 to 3 moles of MEA per mole of heat stable salt. The purified MEA product stream had no significant contamination.

Introduction

Amine solvents used in post-combustion CO_2 capture degrade via a combination of thermal degradation in the stripper and oxidation by the flue gas in the absorber, which typically contains between 5 and 12 vol % O_2. Dissolved oxygen can react to form peroxides and free radical carriers, which can be carried over to the heated stripper to further oxidize the amine. The most representative method of determining the rate of amine loss and types of products formed is a cyclic system combining the effects of both oxidation and high-temperature thermal degradation. This can only be accomplished in a bench-scale cyclic degradation apparatus or in a pilot plant.

In this quarter, a cyclic oxidation experiment was run on the HTOR apparatus to measure the oxidation rate of 4 m PZ and test an N_2 bubble column to remove dissolved oxygen from the solvent. In addition, samples were collected and analyzed from a pilot plant campaign conducted by Southern Company at the NCCC facility in Wilsonville, AL, and from a test of a new reclaimer design by HTC at the Searles Valley Minerals Facility in Trona, CA, both using MEA.

A poster was presented at the GHGT-12 conference in October, 2014, on the oxidation of PZ in the HTOR apparatus and pilot plants (included as an attachment to this report).

Experimental Methods

HTOR Apparatus

In this quarter, the bubble removal vessel used to prevent entrained gas from entering the high temperature section was modified into an N_2 bubble column to strip dissolved oxygen. A full description of the HTOR apparatus can be found in the attached paper and in the Ph.D. dissertation by Voice (2014).

Analytical Methods

A complete description of analytical methods used can be found in previous quarterly reports (Rochelle et al., 2014) and the dissertation by Freeman (2011); the TONO method can be found in Fine (2014).

Results and Discussion

HTOR10: 4 m PZ 40–150 °C

4 m PZ was oxidized in the HTOR apparatus for 220 hours. After an initial 24-hour baseline/leak test with the trim heater set to 40 °C, the trim heater oil bath temperature was raised to 150 °C. After allowing another day for the system to reach steady state, an initial liquid sample was taken and iron and manganese sulfate were added to the solvent. No chromium or nickel was added in this experiment. At 100 hours, a silicon-based antifoaming agent was added to reduce foaming in the oxidation reactor and bubble removal vessel. At 170 hours, N_2 sparging in the bubble removal vessel was started at a flow rate of 0.5–1 L/min. This was discontinued at the 200-hr due to buildup of solid PZ in the bubble removal vessel gas vent line, which increased pressure in the vessel and choked off the N_2 flow. At 220 hours, the apparatus was shut down for repairs.

Figure 1 shows the ammonia emitted during the entire experiment as measured by FTIR as well as the total accumulation of stainless steel metal (SSM) ions in solution. The solvent did not degrade sufficiently to accurately quantify PZ loss rate via cation IC or alkalinity titration. Previous experiments have shown 1 mole of ammonia is typically produced per mole of PZ oxidized, allowing the ammonia rate to be used as a proxy for the oxidation rate (Nielsen, 2014).

The ammonia rate did not settle to a steady state during the experiment, instead rising steadily. The total accumulation of stainless steel metal ions trended along with the increase in ammonia rate. The metal ions may be participating in a shuttling mechanism to oxidize the amine, thus increasing oxidation as the ions accumulate. This is contrary to previous theories in which metal ions serve as a catalyst of oxidation and therefore oxidation should not be a function of metal ion concentration (Voice, 2014). The similarity of the ammonia rate to the accumulation of dissolved metalshown in Figure 1 is most likely a coincidence. The HTOR has a total residence time of 9 minutes for the solvent to cycle through it. Therefore, only 0.15 moles of ammonia are produced per mole of dissolved metal ions per cycle.

N_2 sparging reduced the ammonia rate by approximately 20%. The bubble removal vessel contains metal packing in the bottom to break up entrained air bubbles, which limited the

operating depth of the sparger to approximately 5 cm. This most likely limited the amount of dissolved oxygen which could be stripped. After 30 hours of operation, both solvent and gas flow into the column had become erratic, and sparging was stopped. It was determined that the vapor line leaving the column had become clogged with solid PZ, leading to an increase in pressure in the vessel. In future operation, this line will be periodically washed with water or solvent to prevent buildup of precipitate.

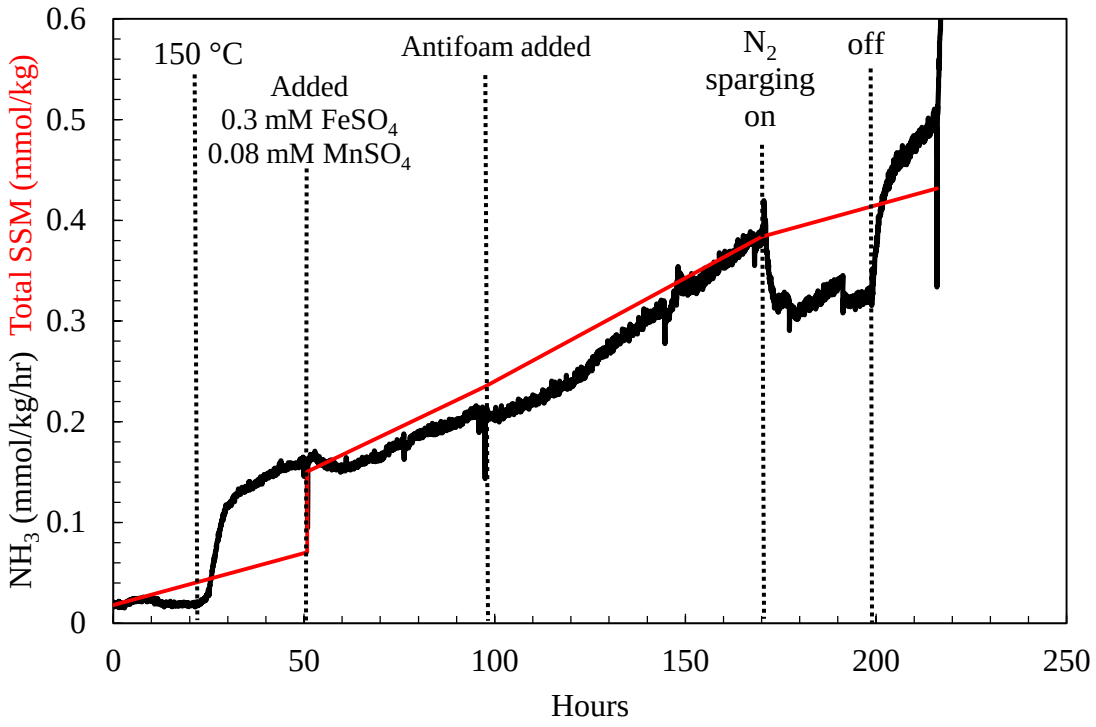

Figure 1: Ammonia emissions as measured by FTIR and total stainless steel metal ion accumulation as measured by ICP-OES during HTOR10 (7.5 L/min air + 0.5% CO_2, 0.2 L/min 4 m PZ cycled 40–150 °C, 1.9 L total solvent inventory)

Figure 2 shows the major oxidation products observed in the liquid phase, as well as the cumulative ammonia emitted as quantified by integrating the data from the FTIR. Ethylenediamine (EDA) was observed at the highest concentration. It appeared to be approaching a steady state by the end of the run. EDA is more volatile and more susceptible to oxidative and thermal degradation than PZ and should not be expected to exceed 100 mmol/kg. Total formate accumulated linearly at a rate of 0.23 moles per mole of ammonia produced.

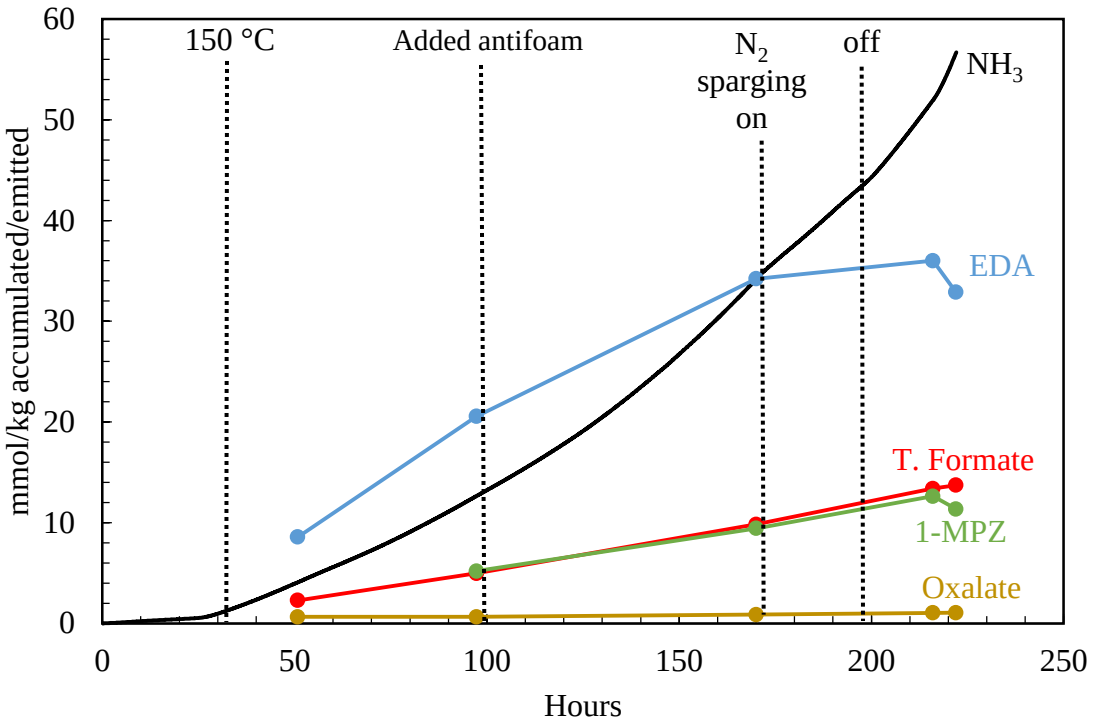

Figure 2: Cumulative ammonia and accumulation of oxidation products in HTOR10

Figure 3 shows the individual dissolved SSM ions in the solvent as quantified by ICP-OES. 0.3 mmol/kg of $FeSO_4$ and 0.08 mmol/kg of $MnSO_4$ was added early in the run. While the manganese appeared in full in the later samples, very little iron was observed throughout the run. Iron has been previously shown to be only slightly soluble in PZ solvent, and the solubility may be dependent on the presence of degradation products (Nielsen, 2014). No chromium or nickel was added artificially, thus the buildup of these metals was the direct result of corrosion of the apparatus, most likely the stainless steel cross exchanger and trim heater. The accumulation rate of nickel and chromium was about half that previously observed with 8 m PZ in the HTOR at 150 °C (Nielsen, 2014). The corrosion rate is most likely a function of amine concentration.

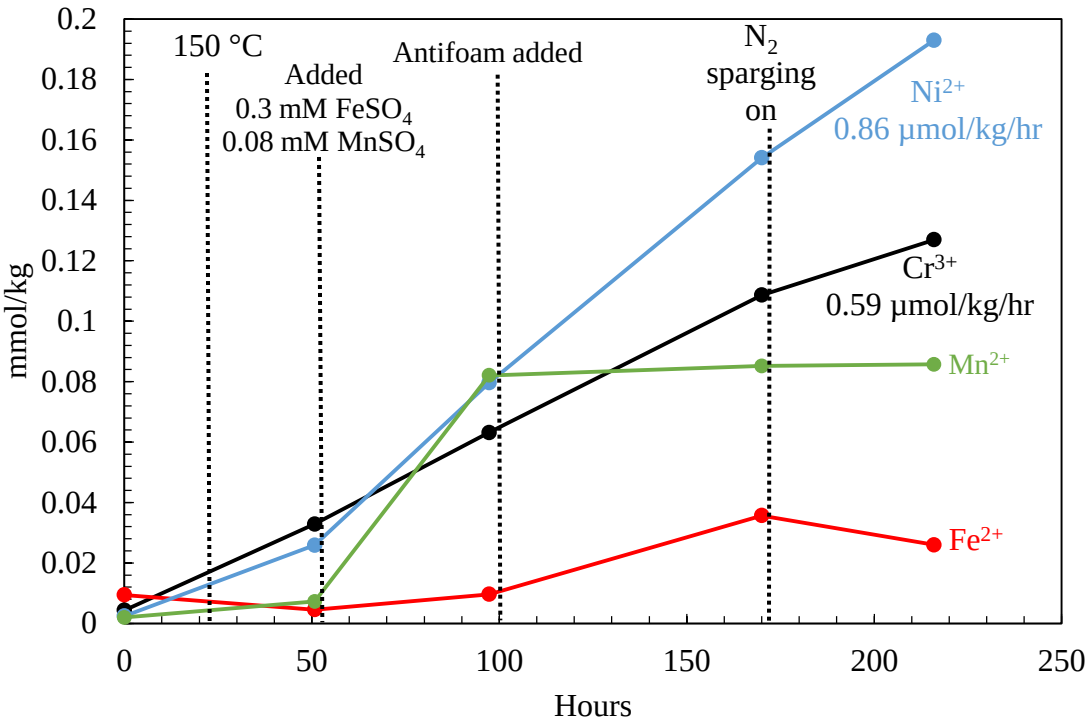

Figure 3: Accumulation of individual stainless steel metal ions in HTOR10

NCCC June 2014 MEA Campaign

Samples of 7 m MEA were collected and analyzed from a 2-week pilot plant campaign conducted by Southern Company at the NCCC facility in Wilsonville, AL. NCCC treats a 0.5 MW_e slipstream of coal flue gas from the neighboring coal-fired power plant. This campaign used a simple stripper at 120 °C to regenerate the solvent. The solvent inventory had been used in previous pilot plant campaigns and already contained some degradation products and contaminants. Samples of lean and rich solvent were collected in a 2-week time series. Figure 4 shows all quantified contaminants in the samples. N-Hydroxyethyl-glycine (HEGly) increased from 60 to 115 mmol/kg, and total formate increased from 18 to 37 mmol/kg. Most other contaminants follow a similar trend, with the exception of N-hydroxyethyl-ethylenediamine (HEEDA), the most significant thermal degradation product quantified, which stayed constant at less than 12 mmol/kg, indicating no significant thermal degradation occurred during the run. Sulfate and nitrate were also observed to accumulate from the absorption of SO_2 and NO_x from the flue gas. Iron was observed to increase linearly from 0.46 to 0.73 mmol/kg during the run. Nitrite and total nitrosamines as measured by the TONO titration method (Fine, 2014) were observed at less than 0.3 mmol/kg.

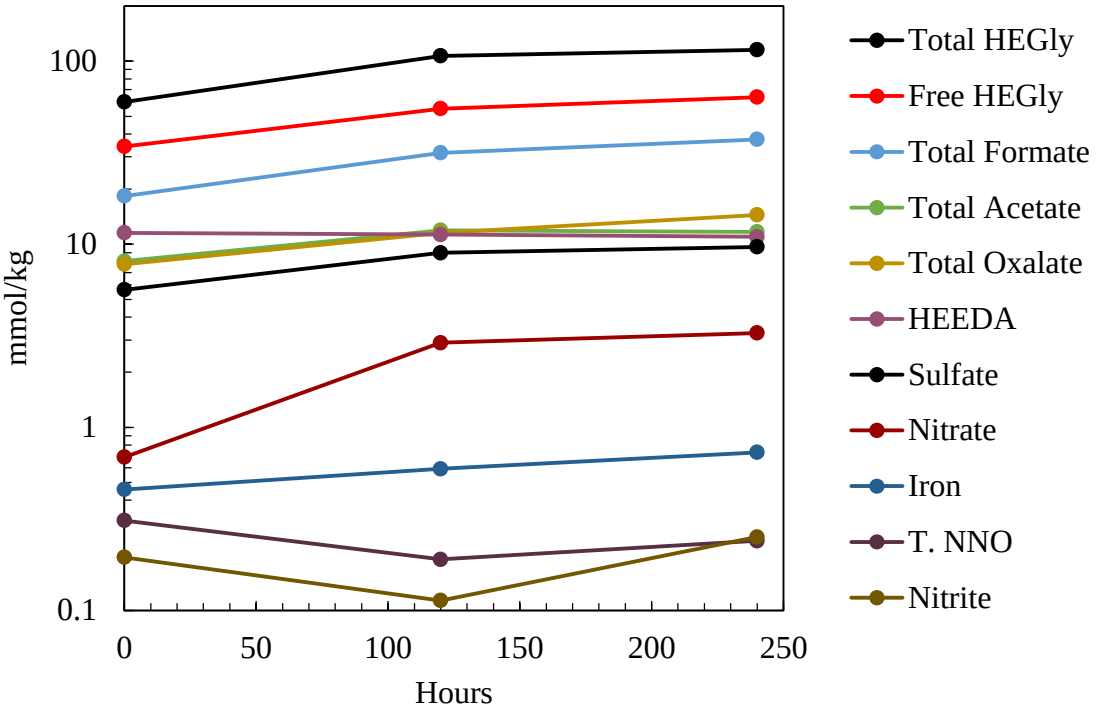

Figure 4: Accumulation of contaminants in MEA solvent during NCCC June 2014 campaign

HTC Solvent Reclaimer System Results

Samples were collected and analyzed from 3 runs of the HTC ΔReclaimer™, a vacuum reclaimer, conducted at the Searles Valley Minerals Facility in Trona, CA, which captures 800 ton/day CO_2 from a coal-fired power plant using 20 wt % MEA. Samples of degraded feed solvent, recovered product solvent, waste process fluid collected during the run, and the final waste sludge were analyzed. NaCl was added to the feed in varying amounts to simulate more heavily degraded solvent. The feed was also pretreated with either NaOH or Na_2CO_3 to reverse amides. Table 1 shows the average for each type of sample for each run. Detailed results from each sample are shown in Appendix A. A more detailed analysis of the experiment and reclaimer design can be found in the paper presented by El Moudir et al. at GHGT-12 (2014).

Table 1: Results of Reclaiming 20 Wt % MEA in the HTC ΔReclaimer™ System

	Run 1			Run 2			Run 3	
T (°F)	185 °F			185 °F			200 °F	
Recovery (%)	98%			95%			91%	
mol MEA/mol HSS in waste	2.9			1.7				
	Feed	Product (wt %)	Waste	Feed	Product (wt %)	Waste	Feed	Product (wt %)
Total Impurities	1.5			5.8			8.5	
Organic HSSs	0.23	0.02	1.3	0.26	0.02	1.4	0.21	0.02

Inorganic HSSs	1.5	0.004	4	2.1	0.01	16.9	2.8	0.004
HEGly	0.39		2.4	0.48	0.002	3.5	0.43	
Fe^{2+} (ppm)	5	0.3	13.6	7	0.1	66.4	4.8	0.1

Conclusions

- Ammonia production, and by proxy amine oxidation, increased along with the accumulation of stainless steel metals in solution with 4 m PZ in the HTOR.
- Ethylenediamine was the most significant oxidation product observed to accumulate in the PZ solvent during the HTOR experiment. It appeared to be reaching a steady state of 35 mmol/kg by the end of the run. 0.24 moles of total formate were produced per mole of ammonia emitted during the HTOR experiment. N-methyl-piperazine was also observed at a similar concentration to total formate.
- Removal of dissolved oxygen with N_2 sparging in a bubble column before the high temperature section of the HTOR reduced the ammonia rate by 20%. Improvements need to be made to the column design and operation before further testing can be done.
- In samples received from a pilot plant campaign conducted at NCCC in June using 7 m MEA, HEGly was the most significant degradation product quantified, at a concentration in excess of 1 wt % by the end of the campaign. Organic heat stable salts, chiefly formate, acetate, and oxalate, were observed in similarly high concentrations. No significant accumulation of thermal degradation or nitrosamines was observed.
- Reclaimer waste from a pilot-scale vacuum reclaimer contained 2 to 3 moles of MEA per mole of heat stable salt. MEA recovery decreased as the concentration of contaminants in the solvent feed was increased. No significant contaminants were observed in the reclaimed MEA product stream.

Future Work

In the next quarter, the HTOR apparatus will be upgraded with an improved N_2 bubbler column to increase liquid depth and improve the removal of dissolved oxygen. An electrical resistance corrosion probe will be added to the high temperature section and an oxidation/reduction potential probe will be added downstream of the high pressure/temperature section. All this will be tested with 5 m PZ solvent with and without the addition of Inhibitor 8, a nonvolatile thermally-stable free radical scavenger designed to be recoverable from reclaimer waste.

The effect of heat stable salts at concentrations up to 10 wt % on the viscosity of MEA and PZ solvents will be determined experimentally. This data will be used to model the decrease in heat and mass transfer coefficients and the expected consequences of such changes. Formate, acetate, propanoate, glycolate, oxalate, and nitrate will be studied in detail. In addition, the effect of up to 20% thermal degradation on viscosity will be determined.

A new thermal reclaimer, designed to treat up to 1 drum (42 gallons) of solvent per day, will be used to reclaim degraded pilot plant PZ solvent from the SRP (mildly degraded) and Tarong facilities (moderately degraded). Inhibitor 8 will be added to the SRP solvent before reclaiming, and then a method to recover the inhibitor from the reclaimer waste will be tested.

References

El Moudir W, Fairchild J, Aboudheir A. “HTC Solvent Reclaimer System at Searles Valley Minerals Facility in Trona, California.” Presented at GHGT-12, Austin, TX, October 5–9, 2014.

Fine NA, Nielsen PT, Rochelle GT. “Decomposition of Nitrosamines in CO_2 Capture by Aqueous Piperazine or Monoethanolamine.” *Environ Sci Technol*. 2014;48:5996–6002.

Freeman SA. *Thermal Degradation and Oxidation of Aqueous Piperazine for Carbon Dioxide Capture*. The University of Texas at Austin. Ph.D. Dissertation. 2011.

Nielsen PT, Voice AK, Rochelle GT. “Cyclic oxidation of Piperazine in bench and pilot scale CO_2 capture processes.” Presented at GHGT-12, Austin, TX, October 5–9, 2014. Rochelle GT et al. “CO_2 Capture by Aqueous Absorption, First Quarterly Progress Report 2014.” Texas Carbon Management Program. The University of Texas at Austin. 2014.

Voice AK. *Amine Oxidation in Carbon Dioxide Capture by Aqueous Scrubbing*. The University of Texas at Austin. Ph.D. Dissertation. 2013.

Appendix A: HTC ΔReclaimer™ Raw Data

Table A1: Results of alkalinity titration, cation IC, ICP-OES, and T. NNO analysis

			Titration	Cation IC			ICP-OES				T. NNO
Batch	Code	Type	T. Alkalinity mol/kg	MEA mol/kg	MEA wt %	MEA trimer mmol/kg	Fe mmol/kg	Cr mmol/kg	Ni mmol/kg	Mn mmol/kg	T. NOx mmol/kg
201405-1	18-1	treated feed lean	2.95		18.0		0.086	0.003	0.004	0.002	0.95
	18-2	feed lean	2.81		17.2		0.092	0.002	0.005	0.002	
	18-3	recovered 1	2.46		15.0		0.002	0.001	0.001	0.000	
	18-4	recovered 1 no CO2	2.38		14.5		0.003	0.002	0.001	0.000	
	18-5	process fluid		7.80	47.6	0.3	0.335	0.012	0.021	0.003	0.36
	18-6M	recovered 2	2.61		15.9		0.003	0.001	0.001	0.000	
201406-1	15-1	feed lean		2.90	17.7	0.1	0.125	0.003	0.004	0.002	1.17
	15-2	treated feed lean		2.72	16.6	0.1	0.110	0.002	0.003	0.002	
	15-3	recovered 1					0.002	0.001	0.001	0.000	
	15-4	process fluid		8.03	49.1	0.6	0.507	0.011	0.022	0.003	
	15-5	recovered 1 no CO2					0.004	0.002	0.001	0.000	
	16-1	recovered 2					0.003	0.001	0.002	0.000	
	16-2	waste		5.01	30.6	0.7	1.189	0.050	0.054	0.036	
201406-2	6-1	feed lean		2.70	16.5	0.1	0.089	0.003	0.004	0.002	1.12
	6-2	treated feed lean		2.54	15.5	0.0	0.079	0.004	0.004	0.002	
	6-3	recovered 1		2.42	14.8		0.005	0.003	0.002	0.001	
	6-4	feed without CO2		2.95	18.0	0.1	0.093	0.003	0.003	0.002	
	6-5	recovered 1 no CO2		2.44	14.9		0.006	0.003	0.001	0.001	
	4-1	recovered 2		1.73	10.6		0.006	0.003	0.001	0.001	
	W-2	waste	7.29	5.38	32.9	0.6	0.243	0.012	0.015	0.003	0.38
	W-1	process fluid		7.07	43.2	0.3	0.761	0.016	0.012	0.025	

Table A2: Results of Anion IC and HPLC-AA analysis

			Anion IC									HPLC (AA method)	
Batch	Code	Type	Formate mmol/kg	T. Formate mmol/kg	T. Acetate mmol/kg	T. Glycolate mmol/kg	Oxalate mmol/kg	T. Oxalate mmol/kg	Sulfate mmol/kg	Chloride mmol/kg	Nitrite mmol/kg	HEGly mmol/kg	T. HEGly mmol/kg
201405-1	18-1	treated feed lean	13.0	14.3	11.4	6.3	2.9	3.2	116.5	485.0	1.2	28.7	36.0
	18-2	feed lean	12.8	15.4	12.0	5.8	3.1	3.3	122.9	511.0	1.4	27.6	35.4
	18-3	recovered 1	0.4	1.1	0.2	1.7	0.8	1.9	0.4	1.2			
	18-4	recovered 1 no CO2	0.2	0.3	0.1	1.0	0.9	1.0	0.2	0.6			
	18-5	process fluid		56.8	56.4	22.6		17.2	142.1	1179.8			182.8
	18-6M	recovered 2	0.6	0.7	0.2	1.9	0.9	1.1	0.2	0.6			
201406-1	15-1	feed lean	15.9	20.3	15.5	5.6	3.5	4.0	110.2	289.5	1.3	44.4	40.1
	15-2	treated feed lean	15.3	17.2	14.3	5.2	3.2	3.6	94.7	249.5	1.1	36.9	34.9
	15-3	recovered 1	0.3	0.7	0.2	2.3	0.9	0.8	0.3	0.4	0.1		
	15-4	process fluid		84.4	79.5	23.9		17.8	23.4	959.0			275.9
	15-5	recovered 1 no CO2	0.2	0.2	0.1	0.8	0.9	0.9	0.2	0.5			
	16-1	recovered 2	0.3	0.8	0.2	2.4	0.9	0.9	0.2	0.5	0.2		
	16-2	waste	75.6	104.3	101.9	29.4		7.6	1178.2	1583.8	2.9	90.9	290.6
201406-2	6-1	feed lean	17.2	18.8	13.4	3.8	3.6	4.2	90.2	182.0	1.5	40.3	32.5
	6-2	treated feed lean	13.7	15.7	12.2	4.6	2.9	3.4	71.0	143.6	1.3	31.8	30.4
	6-3	recovered 1	0.1	0.3	0.1	1.0	0.9	0.9	0.3	0.5			
	6-4	feed without CO2	13.1	13.7	14.5	4.0	0.8	3.0	66.4	133.2	0.6	32.9	34.2
	6-5	recovered 1 no CO2	0.2	0.4	0.1	0.5	0.9	0.8	0.3	0.4			
	4-1	recovered 2	0.4	0.6	0.5	0.6	0.9	1.5	0.3	3.5		1.1	1.4
	W-2	waste	80.7	91.2	87.2	16.5	23.1	29.9	17.1	1080.6	0.3	136.7	202.3
	W-1	process fluid		43.0	38.9	15.2		12.7	935.5	403.4			92.4

NO_2 Absorption into Aqueous Amines and Sulfite

Quarterly Report for July 1 – September 30, 2014

by Nathan A Fine & Virbin Nath Sapkota

Supported by the Texas Carbon Management Program

McKetta Department of Chemical Engineering

The University of Texas at Austin

October 31, 2014

Abstract

Absorption of nitrogen oxides in aqueous amines

Nitric oxide (NO) and nitrogen dioxide (NO_2) were absorbed into aqueous amine to determine the absorbing species, the absorption kinetics, and the aqueous products at the ppm-level NO_x concentrations typical of flue gas from fossil fuel power plants. At flue gas conditions of 0.5–5 ppm of NO_2, absorption is dominated by free radical absorption of NO_2 as nitrite. NO_2 absorption kinetics are first order in NO_2 partial pressure, half order in free amine concentration, and fastest in methyldiethanolamine (MDEA). The reaction-enhanced liquid mass transfer coefficient for NO_2 absorption in 8 m piperazine (PZ) at absorber conditions is $9.7*10^{-7}$ mol/s·m^2·Pa, yielding 92% NO_2 absorption at a typical A/G of $3.3*10^6$ s·Pa·m^2/mol. Similarly, 9 m monoethanolamine (MEA) will absorb roughly 70% of the inlet NO_2 while 7 m MDEA/2 m PZ will absorb over 99% of the NO_2. Nitrite and nitrate are the main NO_x absorption products in MDEA with nitrite dominating at low NO_2 partial pressures. In PZ, the amine free radical formed during NO_2 absorption will react directly with NO to form n-nitrosopiperazine (MNPZ), or react with itself to form 2-piperazinol (2-PZOH). Typical nitrosamine yields in 5 m PZ are around 15% of total absorbed NO_x and can be halved with the addition of 200 mM Inhibitor A (Inh A), a free radical scavenger. Nitrate and nitramine are minor products of NO_x absorption, accounting for less than 5% of total absorbed NO_x.

NO_2 catalyzed sulfite oxidation

This quarter, rates of sulfite (SO_3^{2-}) oxidation during nitrogen dioxide (NO_2) absorption into sulfite solutions were measured using the high gas flow apparatus. The SO_3^{2-} absorbs NO_2 via a free radical mechanism that produces sulfite radical ($SO_3^{-}\cdot$) and nitrite. The radical then catalyzes SO_3^{2-} oxidation to form sulfate. Free radical scavengers such as thiosulfate can be added to suppress radical concentrations and inhibit sulfite oxidation. The effects of thiosulfate, sulfite, NO_2 absorption, temperature, and O_2 partial pressure were investigated. Under normal industrial conditions, oxidation is inverse half-order in thiosulfate, first order in sulfite, and half order in NO_2 absorbed. Sulfite oxidation shows little dependence on O_2 partial pressures above 5 kPa but has a strong dependence on O_2 at lower partial pressures. Oxidation from 20 °C to 65 °C was fit using the Arrhenius equation with an activation energy of 24.1 kJ/mol. The addition of 0.01 mM Fe increased oxidation rates by a factor of 3 compared to solutions with 0.01 mM EDTA added to chelate metals.

Nitrosamine Accumulation in Amine Scrubbing

Amine scrubbing is a mature and industrially proven method for carbon capture, but the amine solvents used can nitrosate in the desorber, forming hazardous, carcinogenic nitrosamines. In amine scrubbers, nitrosamine accumulation behaves as shown in Figure 1.

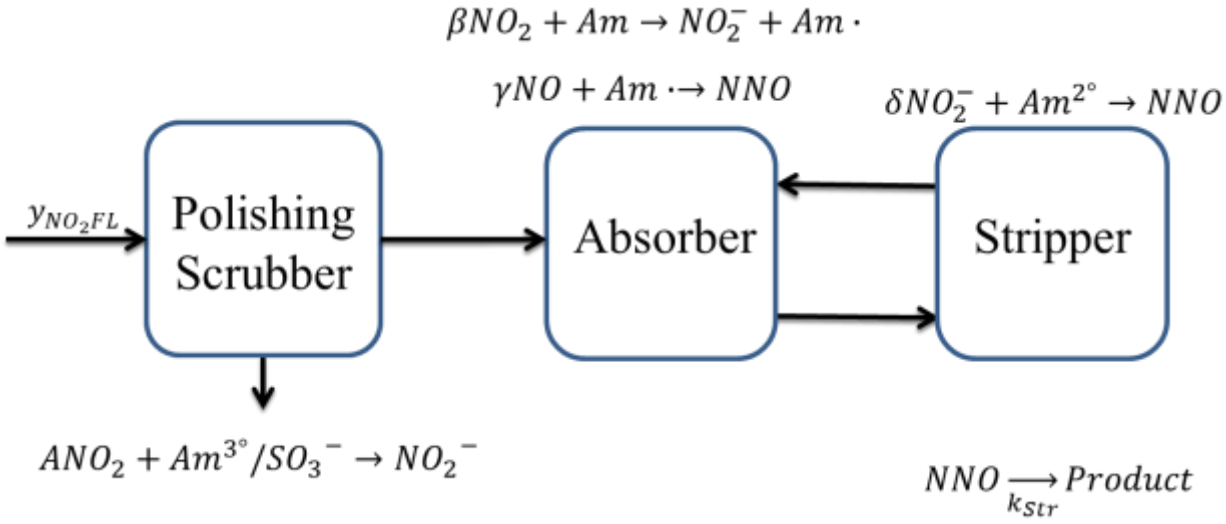

Figure 1: Nitrosamine Cycle

Flue gas containing NO_x, SO_x, and CO_2 gases enters a polishing scrubber where a fraction (A) of the NO_2 can be removed by reaction with sulfite or tertiary amine. The remaining NO_x then enters the absorber where a portion of the NO_2 (β) can be absorbed into the amine solution as nitrite. The NO can also be absorbed into solution (γ) by reacting with amine free radicals formed during NO_2 absorption. The rest of the NO_x will vent from the absorber along with the remaining scrubbed flue gas. Nitrite can also be formed from amine oxidation in solvents that are not oxidatively stable, such as MEA. The nitrite formed, from either NO_x absorption or amine oxidation, travels to the stripper where it can nitrosate a secondary amine with a yield of δ. This yield is determined by the concentration of secondary amines in the solution and their relative nitrosation rates compared to the principal amine. After nitrosating, the nitrosamines thermally decompose in the stripper sump, following pseudo-first-order nitrosation decomposition behavior with a pseudo-first-order rate constant, k_{str}. Nitrosamine sources from NO_x absorption and amine oxidation balance out with nitrosamine thermal decomposition, yielding a steady state nitrosamine concentration:

$$NNO_{Str} = \frac{(1-A)y_{NO_x}\frac{G}{L}\delta(\beta+2\gamma) + \delta k_{Ox}\tau_{Tot}}{k_{Str}\tau_{Str}} \quad (1)$$

This report focuses on inhibiting sulfite oxidation in a NaOH polishing scrubber in order to enhance NO_2 absorption in the prescrubber (A) and thus decrease the steady state nitrosamine concentration.

Sulfite Oxidation in Limestone and Sodium Hydroxide Scrubbing

Limestone slurry scrubbing is a common method for flue gas desulfurization. The process also removes NO_2, although it does not remove NO because of its limited solubility and reactivity. In the presence of gas phase O_2, the absorption of NO_2 is accepted as follows:

$$NO_2 + {SO_3}^{2-} \rightarrow {NO_2}^- + {SO_3}^- \cdot \quad (2)$$

$${SO_3}^- \cdot + O_2 \rightarrow {SO_5}^- \cdot \quad (3)$$

$${SO_5}^- \cdot + {SO_3}^{2-} \rightarrow {SO_4}^- \cdot + {SO_4}^{2-} \quad (4)$$

$${SO_4}^- \cdot + {SO_3}^{2-} \rightarrow {SO_3}^- \cdot + {SO_4}^{2-} \quad (5)$$

$$2{SO_3}^- \cdot \rightarrow {S_2O_6}^{2-} \quad (6)$$

Equation 2 was first outlined by Nash (1979) and Equations 3–5 were proposed by Huie and Neta (1984). These occur in the mass transfer boundary layer. The important implication is that for every mole of NO_2 absorbed, several moles of SO_3^{2-} can be consumed due to free-radical propagation. Because NO_2 absorption is first order in SO_3^{2-} (Shen, 1997), NO_2 absorption is strongly affected by sulfite oxidation. In a limestone slurry scrubber, SO_2 gas is absorbed into solution as SO_3^{2-}, which balances the SO_3^{2-} loss from oxidation until a steady state SO_3^{2-} concentration is reached.

Several factors affect the oxidation rate. Free radical scavengers, such as thiosulfate, can provide an alternative termination step to the free radical process, drastically reducing the amount of sulfite oxidized:

$$NO_2 + {SO_3}^{2-} \rightarrow {NO_2}^- + {SO_3}^- \cdot \quad (2)$$

$${SO_3}^- \cdot + O_2 \rightarrow {SO_5}^- \cdot \quad (3)$$

$${SO_5}^- \cdot + {S_2O_3}^{2-} \rightarrow {SO_5}^{2-} + {S_2O_3}^- \cdot \quad (7)$$

$${SO_5}^{2-} + {SO_3}^{2-} \rightarrow 2{SO_4}^{2-} \quad (8)$$

$$2{S_2O_3}^- \cdot \rightarrow {S_4O_6}^{2-} \quad (9)$$

Takeuchi studied the effects of other antioxidants, such as hydroquinone, phenol, ethanolamines, ethylene glycol monoethyl ether, glycine, EDTA, and acetic acid; all of these antioxidants slowed sulfite oxidation (Takeuchi et al., 1977). Changes in other process variables such as NO_2 flow, O_2 flow, initial sulfite concentration, metals, and temperature could affect the sulfite oxidation rate, to a lesser extent. Shen (1998) studied the absorption of NO_2 into sulfite and thiosulfate inhibited solutions and also investigated the effects of adding Fe^{2+}, chloride, and Ethylenediaminetetraacetic acid (EDTA) and quantified the effects of sulfite and oxygen concentrations and the presence of gas-phase SO_2 and O_2. However, all previous experimental work has focused on limestone slurry scrubbing conditions with relatively high inlet partial pressures of SO_2, slightly acidic solutions, and a high feed of metals from both the fly ash and

limestone. This experimental set expands the body of knowledge to include NaOH scrubbing conditions with lower SO_2 feed, basic solutions, and lower metals.

Methods

All of the experiments were run in the high gas flow apparatus (HGF) previously described (Sexton, 2008). The mixture of the sparging gas was controlled by a series of mass flow controllers. Dry air exited the mass flow controller and was passed through a temperature controlled hydrator to maintain water balance. NO_2 and NO gases were directly mixed with the hydrated air stream. The resulting gas stream was either sparged directly into the bottom of the HGF or put through a bypass.

Before solutions were loaded into the HGF, it was triply rinsed with deionized distilled water to remove any contaminants. The temperatures of the hydrator and HGF water baths were adjusted and allowed to reach a steady temperature. To evaluate the amount of absorbed NO_2, the exit gas streams were diluted by a dry air stream and fed into a chemiluminescent trace level NO_x analyzer (Fine et al., 2014).

The absorbing solution consisted of approximately 360 g of aqueous sulfite and thiosulfate in a 0.5 M $NaHCO_3$ buffer with EDTA added to chelate any trace metals. The initial solution was pH controlled to 9.2 by adding NaOH. During startup, the gas stream was set to HGF bypass mode while pouring the solution into the HGF. The gas stream was then sparged into the HGF for a short period in order to coat the walls of the HGF and ensure the solution was well mixed. The gas was set back to bypass mode and 1 ml of initial sample was taken from a sample port at the bottom of the HGF. The sample was immediately injected into 0.1g of 35 wt % formaldehyde to react any free sulfite remaining to methylsulfonic acid (MSA). MSA is stable at room temperature, allowing indirect sulfite analysis using anion chromatography.

Once the sample was taken, NO_2 concentration values from the trace level NO_x analyzer were recorded while in bypass mode. Then, the gas was set back to sparge into the HGF, and NO_2 values were recorded as soon as they stabilized at a new value. At predetermined time intervals, the sampling procedure was repeated to get a sulfite oxidation kinetics in the semi-batch process. A 50x dilution was performed on each sample generated, and the diluted samples were analyzed on the anion chromatographer.

Safety

Though this experiment has important implications for nitrosamine management, nitrosamines were not directly handled in this experiment. Most of the chemicals used in this experiment were safe to handle with standard laboratory practices with the notable exception of formaldehyde. Work with an open formaldehyde container was always done under a fume hood with the exit gas vented to the atmosphere. The sample vials were closed with slitted caps such that the formaldehyde could not escape, yet sample could be injected into the formaldehyde solution. When the formaldehyde container was not in use, it was always kept in the flammables cabinet.

Nitrogen oxides were the main hazardous gases. Stainless steel tubing was used with gases containing nitrogen oxides. All joints were checked for leaks before usage. Lines containing pressurized nitrogen oxides were depressurized nightly. The tanks containing nitrogen oxides are stored in a vented cabinet next to low-level NO_x sensors.

Results and Discussion

Table 1 gives overall results for the entire experimental set. A mixture of hydrated N_2, air, NO, and NO_2 gases was sparged through aqueous solutions containing compositions of sodium sulfite ($NaSO_3$), sodium thiosulfate (NaS_2O_3), sodium bicarbonate ($NaHCO_3$), and EDTA in the High Gas Flow apparatus (HGF). The sulfite and sulfate concentrations were measured at various times in the semi-batch process using anion chromatography. The decrease in the sulfite concentration over time was attributed to sulfite oxidation, and the time series was used to regress sulfite oxidation rate constants $k_{1\ obs}$ and $k_{0\ obs}$.

NO_2 flux was initially determined by using a chemiluminescent trace level NO_x analyzer to measure the difference between the concentration of NO_2 when the gas passed through the HGF and when it bypassed the HGF. Assuming no leaks, this difference in NO_2 concentration was the amount of NO_2 absorbed into solution. However, this method was not reliable at higher temperatures, when the sparging gas was over-saturated at room temperature. Having significant amounts of water vapor present in the streams presented a risk to the analyzer used in the experiment, which typically operates under ambient, unsaturated conditions. Instead, an empirical model regressed from NO_2 flux measurements at 20 °C was used to estimate NO_2 absorbed:

$$NO_2\ absorbed[=]\frac{mol}{kg_{sol}\cdot min}=\frac{\left(1-e^{-N_{og}}\right)y_{NO_2}\dot{V}}{m_{sol}}*\left[\frac{1\ mol}{22.4\ L}\right] \qquad (10)$$

$$\dot{V}=7.5\frac{L}{min}\ ,\ m_{sol}=0.36\ kg\ ,\ N_{og}=k_g{}'A=7.37\sqrt{\left[{SO_3}^{2-}\right]}$$

This model assumes that NO_2 flux is controlled by mass transfer with fast reaction in the liquid boundary layer and minimal impact from the diffusion of reactants and products. The model fit all the NO_2 flux data measured at 20 °C for inhibited solutions. However, NO_2 flux into uninhibited solutions was noticeably slower due to high sulfite depletion at the gas-liquid interface, so NO_2 flux measured by the NO_x analyzer was used in place of the model. Similar slow rates of aerobic NO_2 absorption into uninhibited sulfite solutions have been reported in the literature (Shen, 1997; Takeuchi et al., 1977). The amount of SO_3^{2-} oxidized per mole of NO_2 absorbed (R) was calculated at a normalized SO_3^{2-} concentration of 0.040 mol/kg. High values imply that a single NO_2 molecule catalyzes large amounts of sulfite oxidation. In Experiments 6–8 when the effect of SO_3^{2-} was examined, the R value is shown for the initial concentration of SO_3^{2-} instead of the normalized 0.040 mol SO_3^{2-}/kg. The calculated R value was determined using Equation 11 and a simple least-squares regression with the prefactor and activation energy as free parameters; the effect of iron and O_2 partial pressure were not regressed.

$$R_{Calc}=R_o\sqrt{\frac{5\ ppm}{\left(1-e^{-N_{og}}\right)y_{NO_2}}}*\frac{[{SO_3}^{2-}]}{\sqrt{[S_2O_3]}*\sqrt{0.064\frac{mol}{kg}}}*\exp\left[\frac{-E_a}{R}\left(\frac{1}{293K}-\frac{1}{T}\right)\right] \qquad (11)$$

$$R_o[=]\frac{mol\ {SO_3}^{2-}{}_{ox}}{mol\ {NO_2}_{Abs}}=59.0 \qquad E_a=24.1\ kJ/mol$$

Many of the various species were changed independently during separate experiments, but in all of the following: the total gas flow rate was kept at 7.5 SLPM, the volume of solution introduced to the HGF was constant, 0.5 M $NaHCO_3$ was added to maintain a buffered solution, NaOH was

added to buffer to pH = 9.2, and 0.02 mM EDTA was added to chelate any metal impurities. Additionally, a base case was picked to compare all of the variations in the different independent conditions. The base case solution has initial concentrations of 0.040 mol/kg Na_2SO_3 and 0.025 mol/kg $Na_2S_2O_3$. The temperature of the HGF was held at 20 °C, and the gas contained 5 ppm NO_2 in hydrated air diluent.

Table 1: NO_2 Catalyzed Sulfite Oxidation Results

Exp. #	Sulfite (mM)	Thiosulfate (mM)	Temperature (°C)	Oxygen (%)	NO_2 (ppm)	$k_{1\,obs}*10^3$ (1/min)	$k_{0\,obs}*10^3$ (mol/kg/min)	NO_2 Flux$*10^6$ (mol/kg/min)	$R_{obs}\left(\frac{{SO_3}^{2-}{}_{ox}}{NO_2\ Flux}\right)$	R_{calc}
1	40.2	25	20	21%	5	6.5	-	3.6	73.4	67.2
2*	44.3	0	20	21%	2	70.1	97.5	1.2	1751.7	-
3*	39.2	0	20	21%	5	110.8	154.1	3.0	1107.9	-
4*	33.8	0	20	21%	10	156.7	218.0	6.0	783.4	-
5	40.0	100	20	21%	5	3.4	-	3.6	37.9	33.6
6	7.2	25	20	21%	5	4.0	-	2.1	13.1	15.6
7	67.0	25	20	21%	5	7.0	-	3.9	119.4	107.0
8	135.6	25	20	21%	5	6.4	-	4.3	201.7	210.9
9	45.0	25	20	21%	2	3.7	-	1.4	102.9	106.2
10	53.9	25	20	21%	10	9.4	-	7.1	52.9	47.5
11*[+]	37.2	25	20	21%	5	18.4	-	3.6	207.0	67.2
12	45.2	25	35	21%	5	10.3	-	3.6	115.9	108.9
13	7.4	25	53	21%	5	15.0	-	2.2	175.5	183.3
14	33.9	25	64	21%	5	22.1	-	3.6	248.6	245.3
15*	41.6	25	20	10.2%	5	5.9	-	3.6	66.8	67.2
16*	48.2	25	20	5.1%	5	5.6	-	3.6	63.0	67.2
17*	49.1	25	20	2.0%	5	3.9	-	3.6	44.3	67.2

Highlighted cells represent the changes compared to the base case (Experiment 1).

*Experiments 2–4, 11, and 15–17 were not used to regress R_{Calc} .

[+]In Experiment 11, 0.1 mM Fe was added instead of 0.02 mM EDTA.

For Experiments 1 and 5–16, the rate law was assumed $\frac{d[{SO_3}^{2-}]}{dx} = k_{1\,obs}[{SO_3}^{2-}]$.

For Experiments 2–4, the rate law was assumed $\frac{d[{SO_3}^{2-}]}{dx} = k_{1\,obs}[{SO_3}^{2-}] + k_{0\,obs}$; measured NO_2 flux was used instead of Equation 10.

Uninhibited Aerobic NO_2 Absorption with Varying NO_2 Flow

The rates for uninhibited sulfite oxidation were quantified in solutions with no added thiosulfate The NO_2 flow rate was varied, but sulfite, temperature, and pH were kept constant at base case conditions. Three concentrations of NO_2 were tested: 2 ppm NO_2, 5 ppm NO_2, and 10 ppm NO_2, and each was given approximately 30 minutes to react (Figure 2).

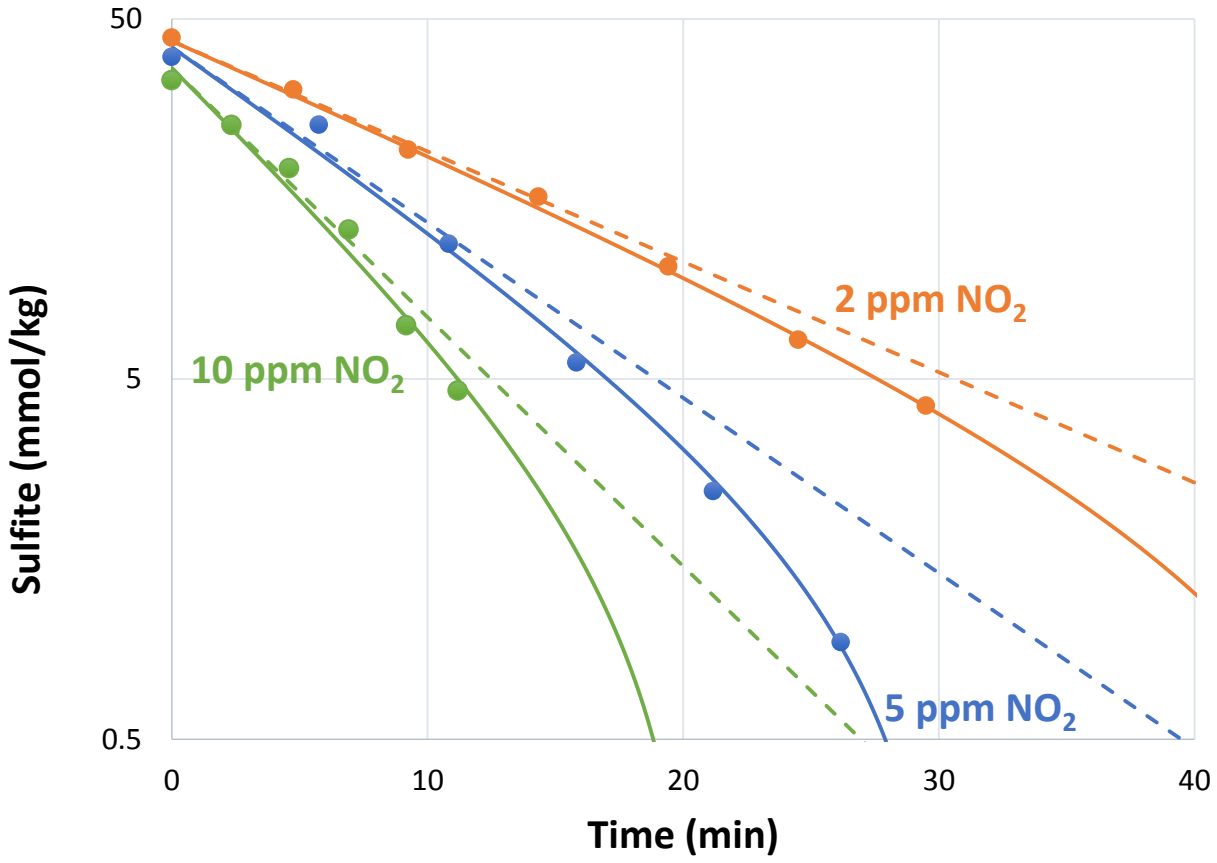

Figure 2: Uninhibited sulfite oxidation with varying NO_2 concentrations (Experiments 2–4)

The sulfite concentrations were fitted with the following rate law equation, graphed with solid lines above:

$$\frac{d[SO_3{}^{2-}]}{dx} = k_{1\,\mathrm{obs}}[SO_3{}^{2-}] + k_{0\,\mathrm{obs}} \tag{12}$$

The zeroth order term dominates at low concentrations of sulfite. The dashed line models pseudo-first-order oxidation:

$$\frac{d[SO_3{}^{2-}]}{dx} = k_1[SO_3{}^{2-}] \tag{13}$$

The observed oxidation only deviates significantly from the pseudo-first-order rate when the concentration of sulfite is below 5 mmol/kg. Thus, $k_{0\ obs}$ is only significant below 5 mmol/kg, and otherwise, oxidation behaves pseudo-first order in sulfite.

This also verifies the half-order relationship of NO_2 on sulfite oxidation. In all runs, proportional increases in NO_2 concentration result in half that proportional increase in the $k_{1\ obs}$ and $k_{0\ obs}$.

Additionally, increases in the concentration of NO_2 have a half-order effect on reducing the SO_3^{2-} oxidized/NO_2 absorbed ratio. From the 2 to the 5 ppm cases, the ratio dropped by a factor of 1.56, and from the 2 to 10 ppm cases, the ratio dropped by a factor of 2.22. However, the large ratios of sulfite oxidized/NO_2 absorbed would make an uninhibited system a poor absorber of NO_2 unless the inlet SO_2 concentration was very high.

Inhibited Aerobic NO_2 Absorption with Varying Thiosulfate Concentrations

The rates for inhibited sulfite oxidation were quantified in solutions with thiosulfate added at 0 mM, 25 mM, and 100 mM. Sulfite, temperature, pH, and gas composition and flow were kept constant at base case conditions. Data for the 0 mM run came from the 5 ppm uninhibited experiment and data for the 25 mM run were treated as the base case for all experiments (Figure 3).

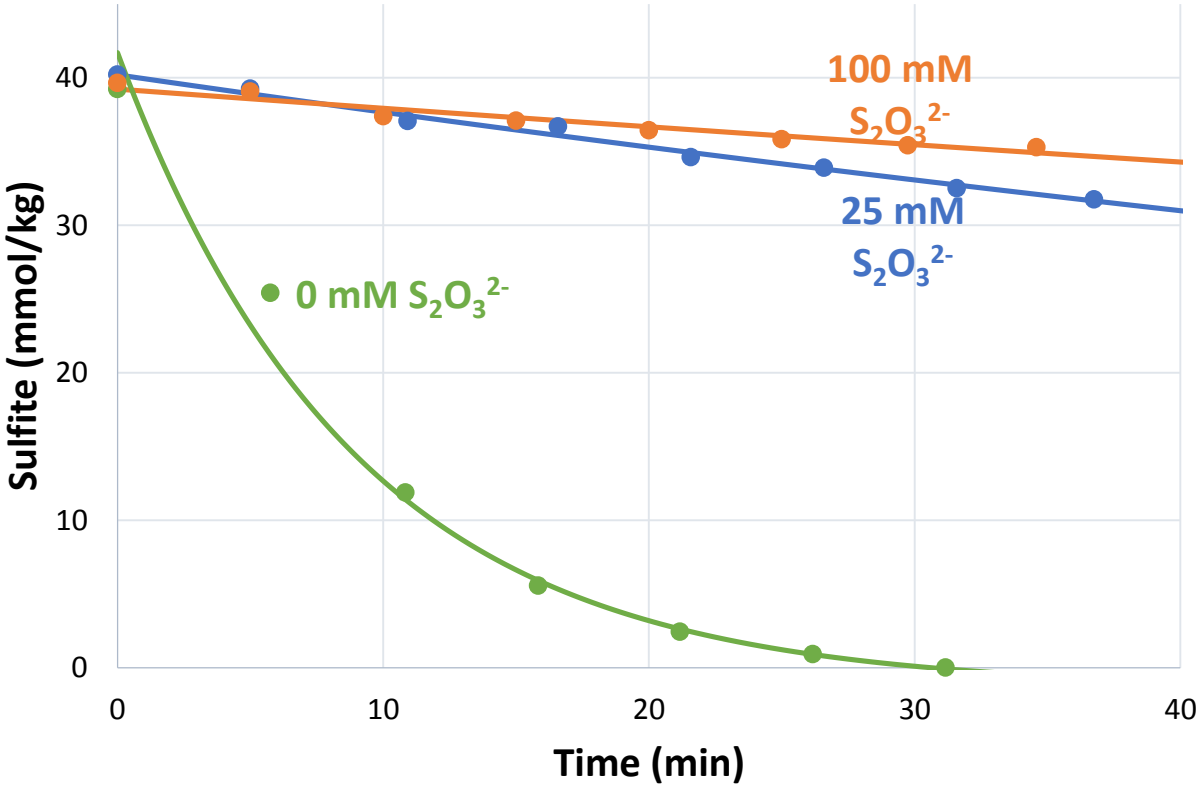

Figure 3: Sulfite oxidation with varying $S_2O_3^{2-}$ concentration (Experiments 1, 3, 5)

SO_3^{2-} for the 25 mM $S_2O_3^{2-}$ and 100 mM $S_2O_3^{2-}$ runs were fitted with Equation 12, because the sulfite remains much higher than 5 mmol/kg. The 0 mM $S_2O_3^{2-}$ results were modeled with Equation 13. Thiosulfate inhibited sulfate oxidation by an order of magnitude; this system is a much better absorber of NO_2 than an uninhibited system. Increasing thiosulfate from 25 mM to 100 mM decreased both the sulfite oxidation rate and SO_3^{2-} oxidized/NO_2 absorbed ratio by approximately a factor of 2. This half-order correlation in oxidation rates is corroborated in previous work (Shen, 1997).

Inhibited Aerobic NO_2 Absorption with Varying Sulfite Concentrations

Sulfite oxidation rates were quantified with sulfite of 7 mM, 40 mM, 65 mM, and 135 mM. Thiosulfate, temperature, pH, and gas composition and flow were kept constant at base case conditions. Data for 40 mM sulfite came from the base case.

The results for this group are summarized in Figures 4 & 5.

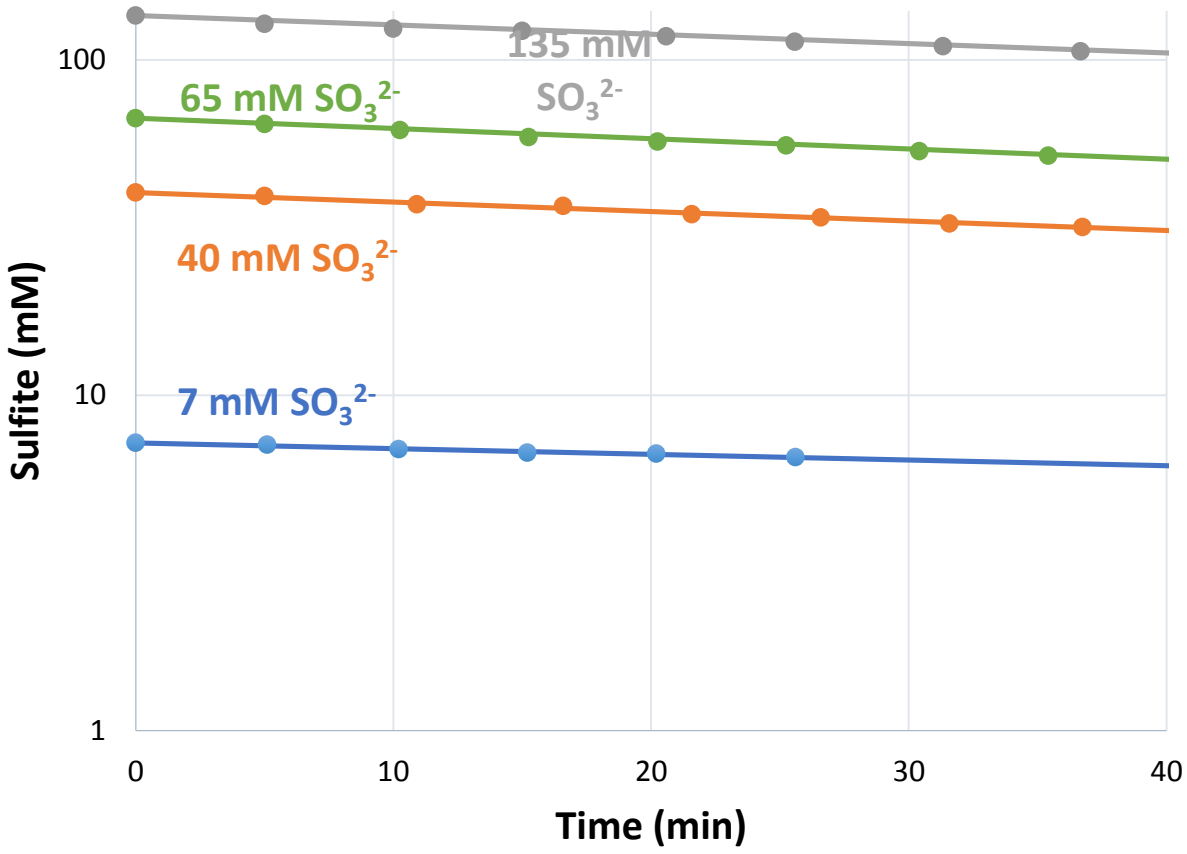

Figure 4: Sulfite oxidation with varying SO_3^{2-} (Experiments 1, 6, 7, 8)

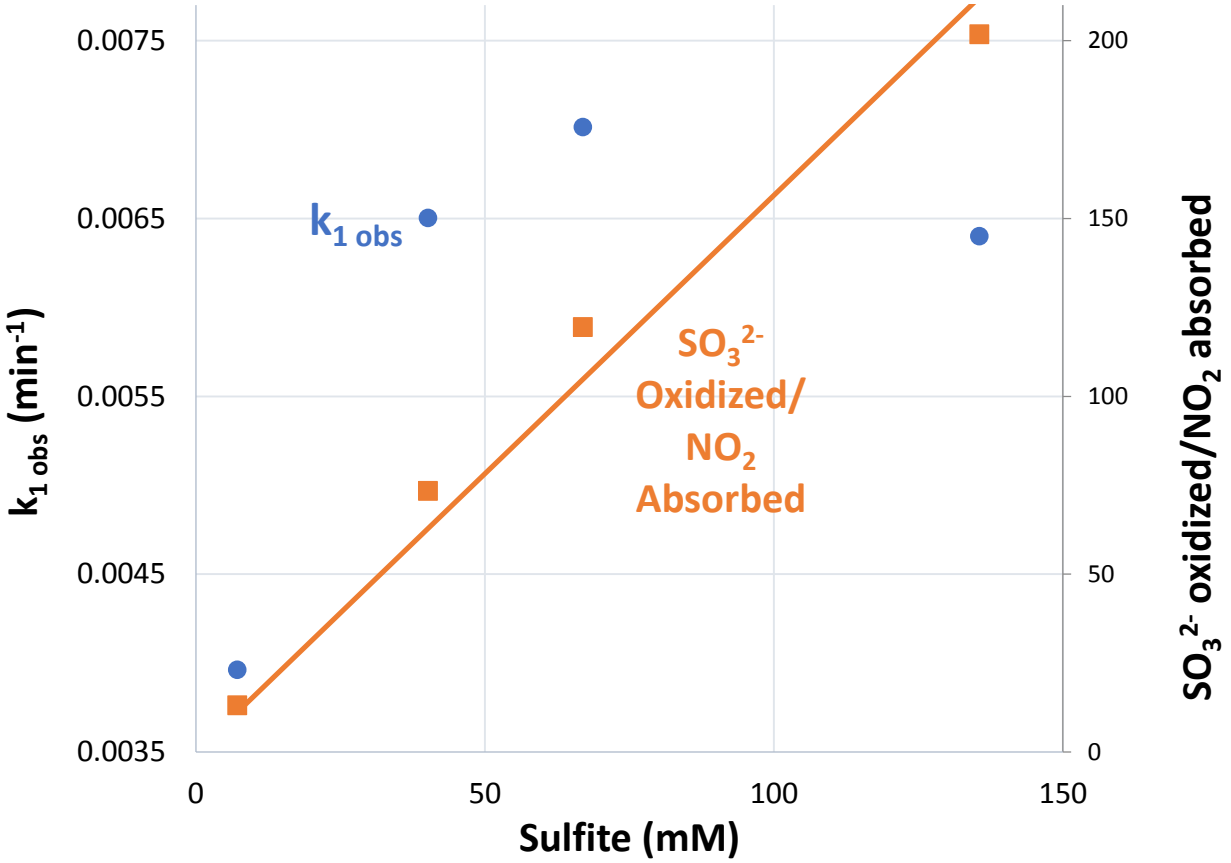

Figure 5: Sulfite oxidation with varying SO_3^{2-} (Experiments 1, 6, 7, 8)

The sulfite concentrations were fitted with Equation 13. Because Equation 12 assumes sulfite oxidation is pseudo-first order in sulfite, $k_{1\ obs}$ should be the same for all runs. However, the $k_{1\ obs}$ for the 7 mM SO_3^{2-} case is significantly lower than the rest. This is due to low NO_2 absorption in the low initial SO_3^{2-} concentration. Once normalized for NO_2 absorption, the ratio of the amount of SO_3^{2-} oxidized/NO_2 absorbed is first order in sulfite.

Inhibited Aerobic NO_2 Absorption with Varying NO_2 Flow

Sulfite oxidation rates were quantified with NO_2 concentrations of 2 ppm, 5 ppm (base case), and 10 ppm NO_2. Thiosulfate, sulfite, temperature, pH, and total gas flow were kept constant at base case conditions.

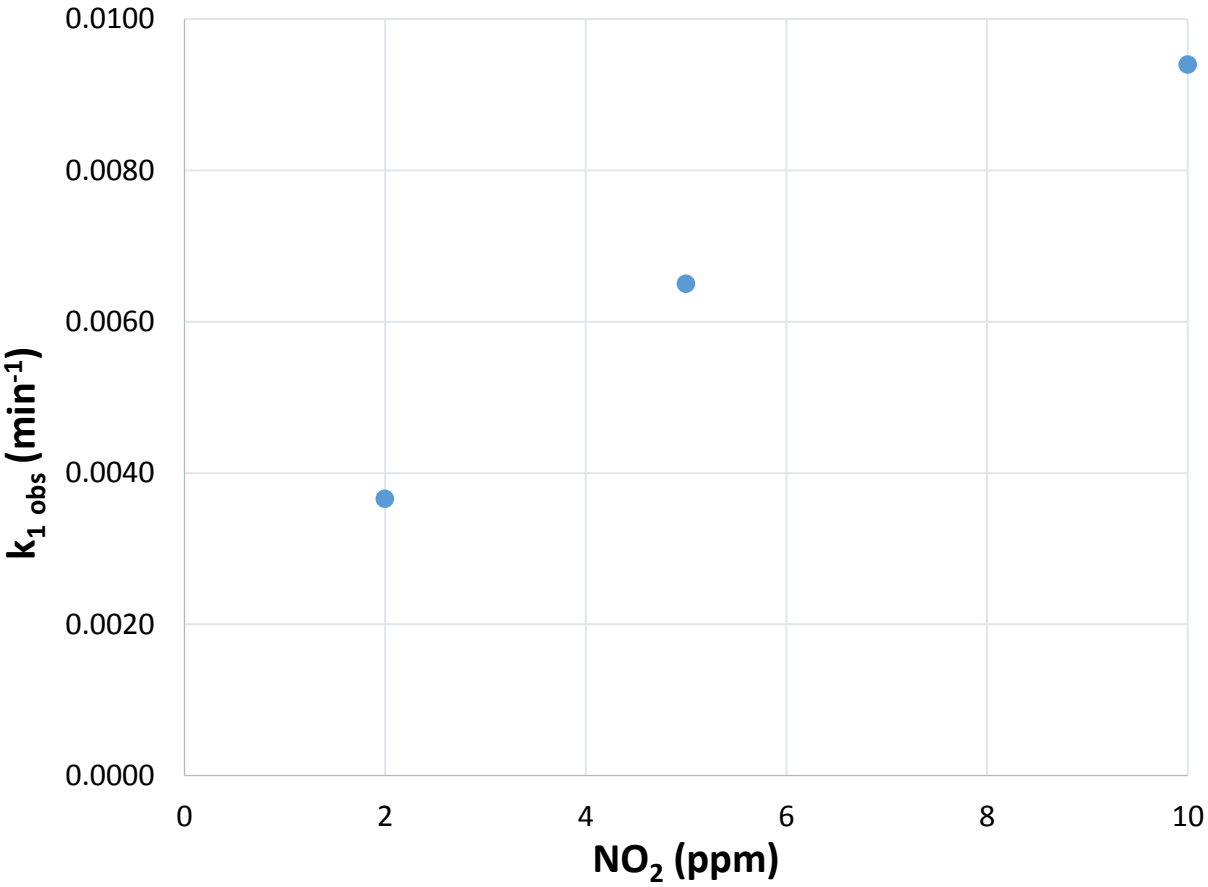

Figure 6: Inhibited sulfite oxidation with varying NO_2 concentration (Experiments 1, 9, 10)

The sulfite concentrations were fitted to Equation 13. Between the 2 ppm and 5 ppm cases, the $k_{1\ obs}$ increased by a factor of 1.78 while the concentration of NO_2 increased by a factor of 2.5, indicating half-order behavior. This half-order correlation is corroborated in previous work (Shen, 1997). However, the SO_3^{2-} oxidized/NO_2 absorbed ratio decreased by a factor of 1.63 while the NO_2 increased by a factor of 2.5, suggesting an inverse half-order relationship between NO_2 absorbed and the ratio. Shen showed that NO_2 absorption is first order in NO_2, but that SO_3^{2-} oxidation is half-order in NO_2. Increases in NO_2 partial pressures increase NO_2 absorption faster than they increase SO_3^{2-} oxidation. This has important implications for NO_2 absorbing applications; higher partial pressures of NO_2 are more efficiently removed with less sulfite loss per unit NO_2 absorbed, although the rate of sulfite oxidation does increase in the process.

Inhibited Aerobic NO_2 Absorption with Added Metals

Work done by Ulrich et al. (1986) indicates that Fe^{2+} is a powerful catalyst effective at $3 * 10^{-6}$ M. Sulfite oxidation rates were quantified with 0.01 mM Fe^{2+} and compared to the base case, which had 0.02 mM EDTA to chelate any background Fe^{2}. Thiosulfate, sulfite, temperature, pH, and gas flow and composition were kept constant at base case conditions. The addition of 0.01 mM Fe^{2+} increased the $k_{1\ obs}$ by a factor of 2.83, which contradicts earlier conclusions that metals did not have a significant effect on sulfite oxidation rates (Shen et al., 1998). Shen reported that metals such as Fe^{2+} are insignificant catalysts of sulfite oxidation in the presence of NO_2, however, his experiments were conducted with 200–1000 ppm NO_2, which catalyzes far more

sulfite oxidation than added metals do. The addition of iron, therefore, did not cause a significant increase in the oxidation rate in his experiments.

In contrast, work done by Ulrich indicates that Fe^{2+} is a powerful catalyst effective at background concentrations. However, those experiments were run without NO_2 absorption. The current results show the importance of adding chelating agents to the NaOH scrubber to limit oxidation. This is economically viable in NaOH scrubbing since most of the fly ash, a large source of metal ions, will effectively be captured upstream of the scrubber. Furthermore, the NaOH feed will have much lower levels of metals compared to the limestone feed for traditional flue gas desulfurization.

Inhibited Aerobic NO_2 Absorption with Varying Temperature

Sulfite oxidation rates were quantified with varied temperature between 20 °C and 65°C (Figure 7). Thiosulfate, sulfite, pH, and gas flow and composition were kept constant at base case conditions.

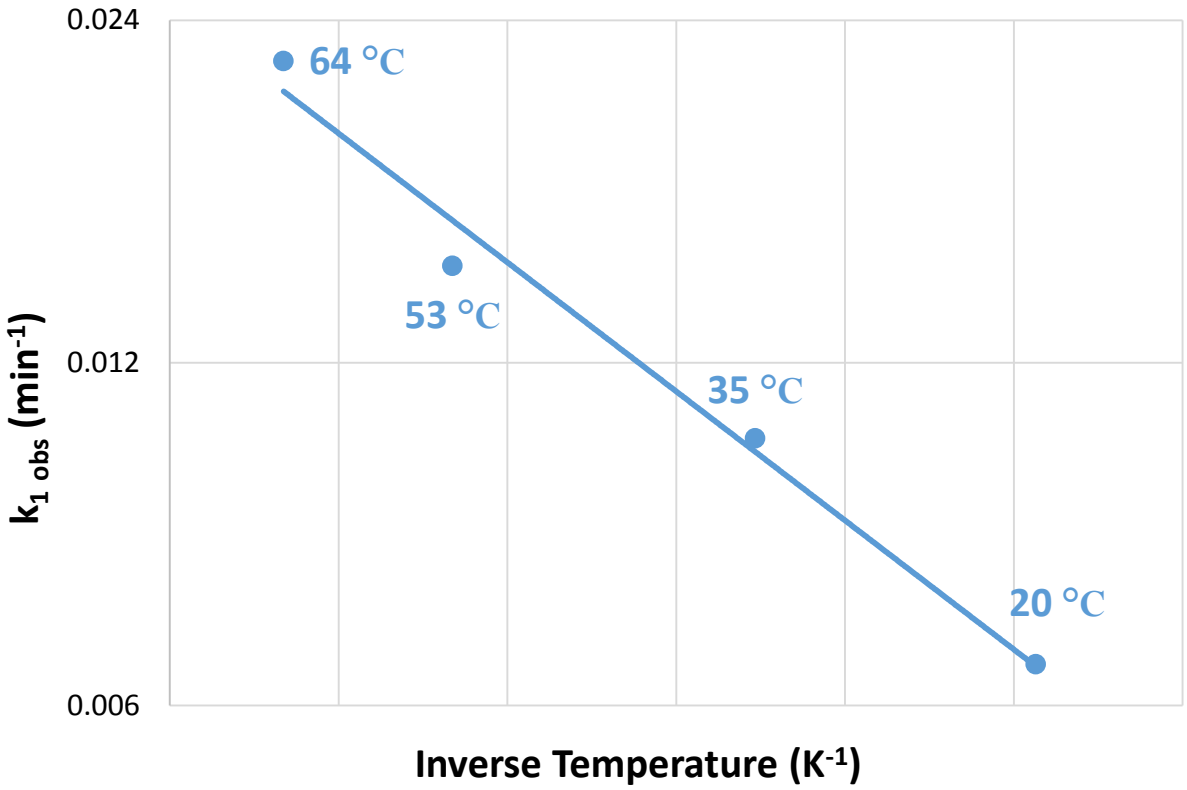

Figure 7: Sulfite oxidation with varying temperature (Experiments 12, 13, 14)

The linear relationship which appears in the graph of inverse temperature vs $k_{1\ obs}$ on a semilog scale follows the Arrhenius equation. The k_g for NO_2 absorption has almost no temperature dependence in this temperature range (Shen, 1997), so NO_2 flux was assumed to be constant. Since all other dependent variables for R were held constant, an apparent activation energy of 24.1 kJ/mol was regressed using Equation 14.

$$R = A * exp\left[\frac{-E_a}{R}\left(\frac{1}{293K} - \frac{1}{T}\right)\right] \quad (14)$$

Inhibited Aerobic NO_2 Absorption with Varying Oxygen Flow

Sulfite oxidation rates were quantified with oxygen concentrations of 21%, 10.2%, 5.1%, and 2%. Thiosulfate, sulfite, temperature, pH, and total gas flow were kept constant at base case conditions. Total gas flow was kept constant by blending air and N_2 to the desired O_2 concentration.

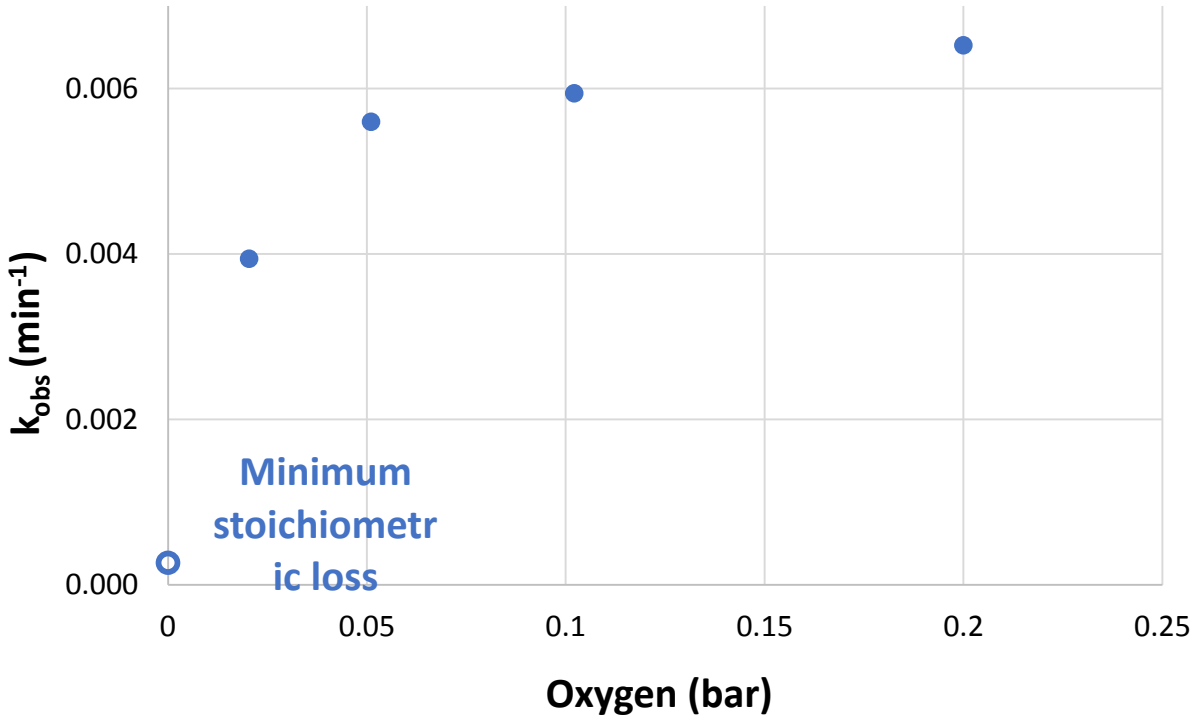

Figure 8: Sulfite oxidation with varying oxygen (Experiments 15, 16, 17)

Until O_2 partial pressure decreases below 5 kPa, O_2 does not have a very significant effect on $k_{1\ obs}$. This is due to the free radical species in the rate limiting step of the propagation. At high partial pressures of O_2, $SO_3^- \cdot$ oxidizes instantaneously in the boundary layer to form the $SO_5^- \cdot$ (Equation 3). The $SO_5^- \cdot$ then catalyzes oxidation until thiosulfate terminates the mechanism. At low O_2 partial pressures, the rate-limiting step occurs when $SO_3^- \cdot$ reacts with dissolved oxygen. Since $SO_3^- \cdot$ is present in solutions, thiosulfate can directly react with $SO_3^- \cdot$. Thus the relative concentrations of thiosulfate and dissolved oxygen become determining factors in the overall oxidation rate. The O_2 partial pressure in power generation applications will not affect sulfite oxidation since coal flue gas contains 5% O_2 and NGCC flue gas contains over 10% O_2.

Conclusions

NO_2 catalyzed sulfite oxidation

- An uninhibited sulfite system is not effective for NO_2 absorption. The ratio of SO_3^{2-} oxidized/NO_2 absorbed, is on the order of 1000.
- Thiosulfate drastically reduces sulfite oxidation; addition of 0.1M $S_2O_3^{2-}$ reduced $k_{1\ obs}$ by a factor of 33.

- Increasing sulfite does not affect $k_{1\ obs}$, but produces a first-order correlation between SO_3^{2-} oxidized/NO_2 absorbed and sulfite.
- Sulfite oxidation is half order in NO_2 and is removed more efficiently at higher partial pressures (SO_3^{2-} oxidized/NO_2 absorbed is inverse half order with NO_2).
- Iron and other metals can catalyze oxidation, but NO_2 catalysis is dominant.
- EDTA or a similar chelating agent should be added to chelate the metal ions; 0.01 mM Fe^{2+} has $k_{1\ obs}$ and SO_3^{2-} oxidized/NO_2 absorbed 2.8 times greater than 0.02 mM EDTA.
- Sulfite oxidation rates follow the Arrhenius law with an apparent activation energy of 24.1 kJ/mol.
- Oxygen concentrations do not have an effect on the oxidation rate until below roughly 5 kPa O_2.
- For common industrial applications, oxygen concentrations will not affect sulfite oxidation.

Absorption of nitrogen oxides in aqueous amines

A complete discussion on NO_x absorption into amine solutions can be found in the GHGT-12 paper, "Absorption of nitrogen oxides in aqueous amines." The main conclusions are summarized below for convenience.

NO_x Absorption Kinetics

- NO_x absorption at ppm levels of NO_x is dominated by the free radical absorption of NO_2.
- Free radical absorption of NO_2 is first order in NO_2 partial pressure and half order in free amine concentration.
- Absorption can be modeled as mass transfer with fast reaction in the pseudo-first-order regime.
- NO_2 absorption kinetics are fastest with tertiary amines and slowest with primary amines similar to ClO_2 free radical absorption into amines.
- 70–99% of NO_2 will absorb in amine scrubbers designed to capture 90% of CO_2; only 4% of NO_2 absorption can be attributed to hydrolysis.
- A prescrubber with an A/G of $1*10^6$ s·Pa·m^2/mol can scrub 90% of flue gas NO_2 with 0.17 m free MDEA.
- MDEA oxidation is not catalyzed by NO_2 absorption in the presence of air and stainless steel metals.

NO_x Absorption Products

- 10 ppm of NO_2 absorbs into 0.1 m MDEA with a 95% nitrite yield and a 5% nitrate yield.
- Nitrite yield is independent of NO and oxygen, proving that the absorption species is NO_2 directly instead of N_2O_3.
- NO_2 hydrolysis through N_2O_4 becomes the dominating absorption mechanism when NO_2 partial pressure is above 10 Pa (100 ppm at atmospheric pressure).
- Nitrosamine is less than 3% of total absorption product in 0.1 m MDEA.
- NO can be directly absorbed into amine solution by reacting with the free radical formed by NO_2 absorption.
- In PZ solution, NO absorption forms MNPZ with yields of 20–35% of total absorbed NO_x at 20 °C.
- PZ free radicals can also react with themselves or free radical scavengers to lower the yield to MNPZ.
- MNPZ yield is independent of amine concentration and loading, but yield increases as the ratio of NO_2:NO_x decreases.

- PZ free radicals can also react with themselves or with free radical scavengers to lower the MNPZ yield.
- Increasing absorption temperature from 20 °C to 60 °C decreases MNPZ yield by 60% due to the decreased solubility of NO.
- MNPZ yield at 40 °C in 5 m PZ with an NO_2:NO_x ratio of 1:10 is 17% with nitrite closing the mole balance.
- High temperature nitrosation from nitrite is the dominating mechanism for nitrosamine formation in amine scrubbing.

Future Work

Complete a techno-economic evaluation of NO_2 scrubbing with a thiosulfate-inhibited sodium sulfite.

References

Nash T. "The effect of nitrogen dioxide and of some transition metals on the oxidation of dilute bisulphite solutions." *Atmos Environ*. 1979;13(8):1149–1154.

Huie R, Neta P. "Chemical behavior of sulfur trioxide (1-)(SO_3-) and sulfur pentoxide (1-)(SO_5-) radicals in aqueous solutions." *J Phys Chem*. 1984;88(23):5665–5669.

Shen C. *Nitrogen Dioxide Absorption in Aqueous Sodium Sulfite*. The University of Texas Austin. Ph.D. Dissertation. 1997.

Takeuchi H, Ando M, Kizawa N. "Absorption of Nitrogen Oxides in Aqueous Sodium Sulfite and Bisulfite Solutions." *Ind Eng Chem Process Des Dev*. 1977;16(3):303–308. doi:10.1021/i260063a010.

Shen C, Rochelle G. "Nitrogen dioxide absorption and sulfite oxidation in aqueous sulfite." *Environ Sci Technol*. 1998;32(2):1994–2003.

Sexton AJ. *Amine Oxidation in CO_2 Capture Processes*. The University of Texas at Austin. Ph.D. Dissertation. 2008.

Fine NA, Nielsen PT, Rochelle GT. "Decomposition of nitrosamines in CO_2 capture by aqueous piperazine or monoethanolamine." *Environ Sci Technol*. 2014;48(10):5996–6002. doi:10.1021/es404949v.

Ulrich RK, Rochelle GT, Prada RE. "Enhanced Oxygen Absorption Into Bisulfphite Solutions Containing Transition Metal Ion Catalysts." *Chem Eng Sci*. 1986;41(8):2183–2191.

Shen C, Rochelle G. "Nitrogen dioxide absorption and sulfite oxidation in aqueous sulfite." *Environ Sci Technol*. 1998;32(2):1994–2003.

Ulrich RK, Rochelle GT, Prada RE. "Enhanced Oxygen Absorption Into Bisulfphite Solutions Containing Transition Metal Ion Catalysts." *Chem Eng Sci*. 1986;41(8):2183–2191.

Ion Exchange for Metals Removal from Amine Solutions

Quarterly Report for July 1 – September 30, 2014

by Kent Fischer

Supported by the Texas Carbon Management Program

McKetta Department of Chemical Engineering

The University of Texas at Austin

October 31, 2014

Abstract

Several experiments were conducted to test metals removal from amine solutions using an ion exchange resin. Amines tested include MEA, PZ, and a degraded PZ solution from a pilot plant. The resin tested was Amberlite IRC748i, a resin which shows promising selectivity for cations from high pH solutions. High metal selectivity is due to the very favorable complex formed between the resin functional group and strongly cationic metals. This report documents removal over time and selectivity of metals.

Introduction

Ion exchange chromatography

The ion exchange reaction is given below in Equation 1, where M is a metal and R_s represents an ion exchange resin. The resin used in these experiments is Amberlite IRC 748i, a resin manufactured by Rohm and Haas (subsidiary of Dow Chemical) and used for extraction of cations from chloralkali brines. This resin was selected for testing because its application suggests that the resin will perform well at high pH values such as those present in amine solutions.

$$M_{aq}^{2+} + 2R_s^{2-} \rightarrow [M \cdot 2R_s]^{2-} \qquad overall \qquad (1)$$

This ion exchange resin consists of a divinylbenzene/styrene copolymer backbone with aminodiacetic chelating functionality. As the resin is exposed to a PZ solution, all functional sites are flooded with the diprotonated PZ molecule, forming a coordination complex as shown in Equation 2. Protonated PZ is a large molecule, which prevents a strong complex from forming due to steric interactions between PZ and the resin functional group. This complex is expected to be weak and transient. Metals are present in low concentrations in the solution, but they bind much more strongly to the functional site on the resin. Thus, as the amine solution flows past the resin, the metals are removed from solution. The small, very cationic metals interact easily with the resin, allowing a complex to form between two functional groups and a cation. This likely forms an octahedral complex with coordination number 6, illustrated below in Equation 3. Confirmation of these three-dimensional structures would require X-ray crystallographic measurements, which are beyond the scope of this work. The structures below are provided only to suggest a possible explanation for the high selectivity of these resins for metals.

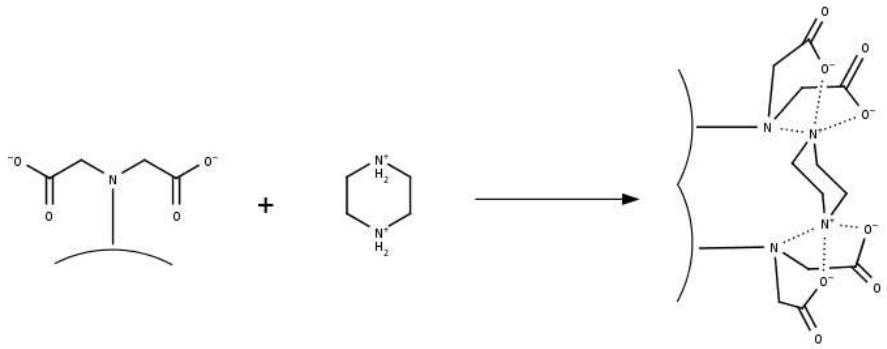

$2\ R^{2-} + H_2PZ^{2+} \rightarrow [R_2{\cdot}PZ]^{2-}$ *step I* (2)

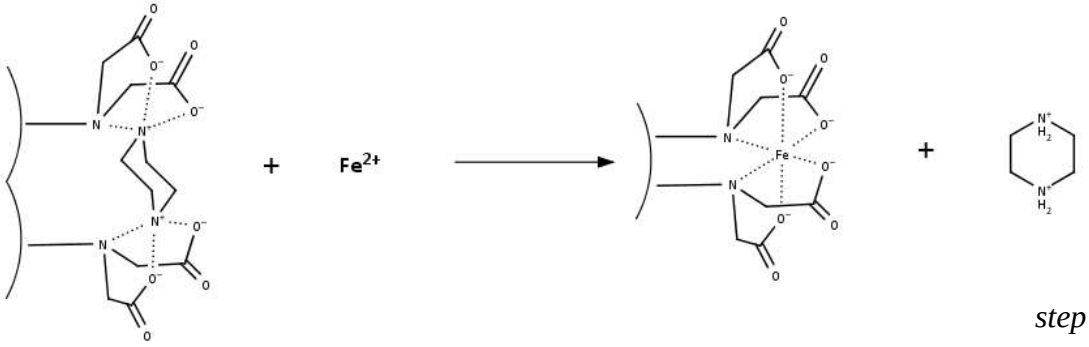

$[R_2{\cdot}PZ]^{2-} + Fe^{2+} \rightarrow [R_2{\cdot}Fe]^{2-} + H_2PZ^{2+}$ *step II* (3)

Experimental Methods

Several amine solutions were contacted with the ion exchange resin in a long glass column. Neat MEA and PZ were loaded with CO_2 and then had metals added as sulfate salts. In addition, an experiment was conducted using 8 m PZ from Pilot Plant 2, which is a heavily degraded pilot plant solution with a high metal content. The column is shown in Figure 1. Solution was put into the top of the glass column, then slowly pumped past the resin using a peristaltic pump. The solution was collected in 10 mL glass vials after passing through the column. After collection, the solution was analyzed for metals using ICP-OES.

The Amberlite resin was obtained from Dow Chemical Company and used in the Na^+ form. The properties of this resin are given below in Table 1. Amine was run through the column at 4–5 bed vol/hr. with a residence time of 700–800 seconds. These run characteristics are given below in Table 2.

Table 1: Properties of Ion Exchange Resins

	Amberlite IRC748i
Max Op. Temp.	90 °C
Total Exchange Capacity, min.	1.35 eq/L
Water Retention Capacity	60-65 %
Uniformity Coefficient	1.7 eq/G
Harmonic mean size	0.5-0.65 mm
Fines content	< 0.300 mm 1.0% max
Coarse beads	>1.100 mm 5.0% max
Physical forms	beige beads

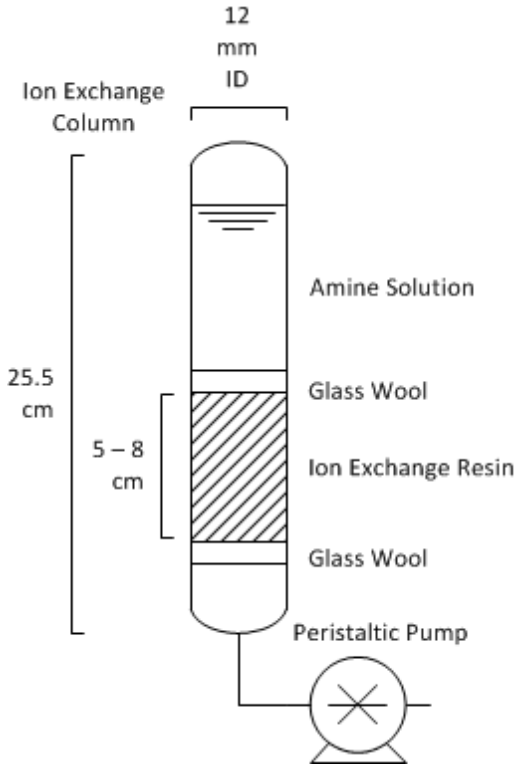

Figure 1: Metals removal column

Table 2: Operating Conditions for Ion Exchange Experiments

Solvent	Residence Time (s)	Flow Speed (BV/Hr)
Neat PZ	696	5.2
Neat MEA	861	4.2

Pilot Plant Amine used in column experiments

Pilot Plant 2 used flue gas from a coal-fired boiler with SCR and FGD. Pilot Plant 2 PZ was fully characterized by Nielsen, and his results are given below in Table 3 as the "PP2 Lit" value for reference. There is some deviation between these results and Nielsen's for PZ and metals, especially Fe.

Table 3: Preparation of "Low-Metals" Piperazine (mmol/kg solution)

	Ca	Co	Cr	Fe	Mg	Mn	Mo	Ni	Se	Piperazine
PP2 PZ	0.21	0.08	1.98	0.45	0.50	0.15	0.21	1.70	0.15	4134
PP2 Lit*	-	-	2.21	1.13	-	-	-	1.86	-	3546

*(Nielsen, 2012)

Safety

Regeneration of ion exchange resins is accomplished by running a dilute solution of acid through the columns. This is usually accomplished with dilute H_2SO_4. Care must be taken to avoid the use of concentrated acids as they can react with the ion exchange resin, causing decomposition of the matrix immobilizing the ion exchange agent. This can cause damage to the column and release of vapor, which could cause an acid spill. Nitric acid in particular is a powerful oxidizer, and it should not be used for resin regeneration due to the higher risk of resin damage. Personal protective equipment including safety glasses, a lab coat, and gloves must be worn while handling concentrated acids.

Results

The results for neat PZ are given below in Figures 2 and 3. Figure 2 shows removal of each metal over time, compared to the initial value. All values shown are from ICP-OES. Figure 3 shows metals removal at the end of the run, which extended to 16 bed volumes. From neat PZ, this resin showed high removal of Ni and Mn at 81% and 71%, respectively. The resin showed moderate removal of Fe and Cr, at 47% and 36%.

The results for neat MEA are given in Figures 4 and 5. Figure 4 shows removal of each metal over time, compared to the initial value. All values shown are from ICP-OES. Figure 5 shows metals removal at the end of the run, which extended to 14 bed volumes. From neat MEA, this resin showed high removals of Ni and Mn at 88% and 94%, respectively. The resin showed moderate removal of Fe, at 40%. The resin showed low Cr removal, at only 10%.

The results for Pilot Plant 2 PZ are given in Figures 6, 7, and 8. Figure 6 shows removal of major metals over time, and Figure 7 shows removal of minor metals over time during the same run. Figure 8 shows removal of metals at the end of the run, which extended to 15 bed volumes. This resin showed complete Ca, Mg, and Mn removal (100%). The resin showed moderate removal of Ni and Fe, at 52% and 43%. The resin showed low removal of Cr, Mo, Ni and Se.

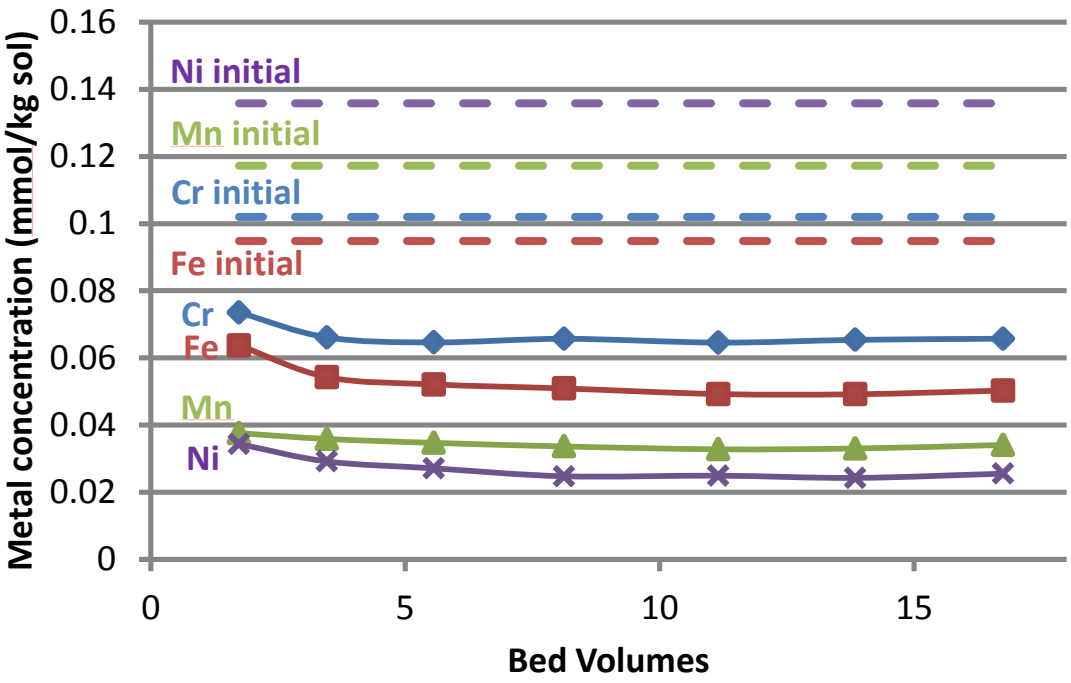

Figure 2: Amberlite IRC748I, 4 m neat PZ, α = 0.31

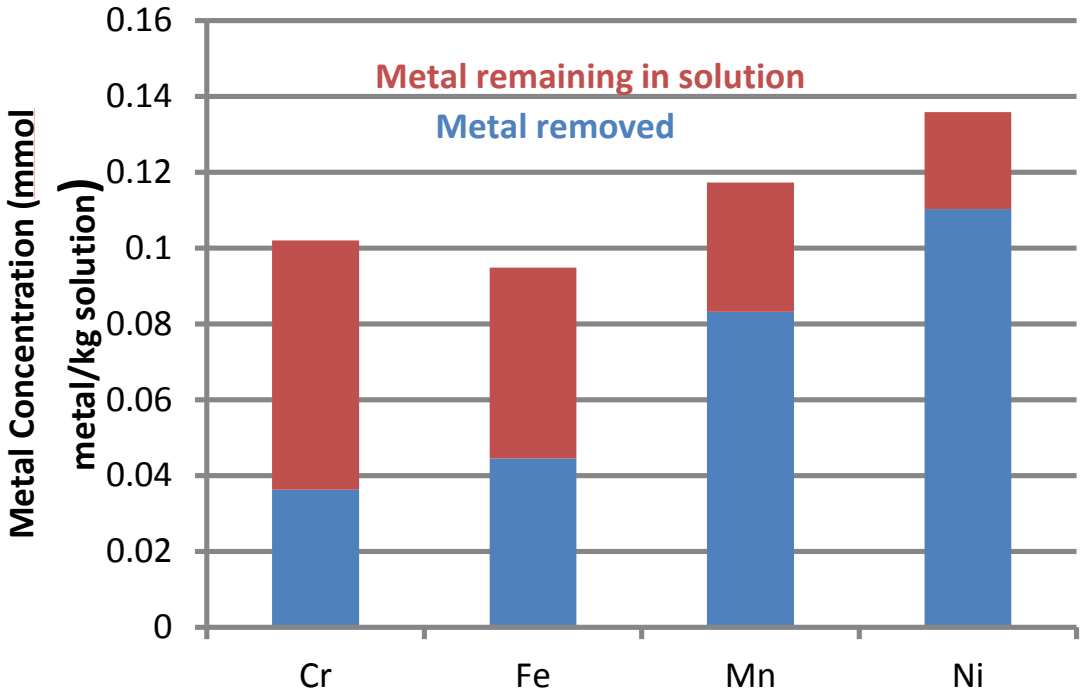

Figure 3: Amberlite IRC748I, 4 m neat PZ, α = 0.31

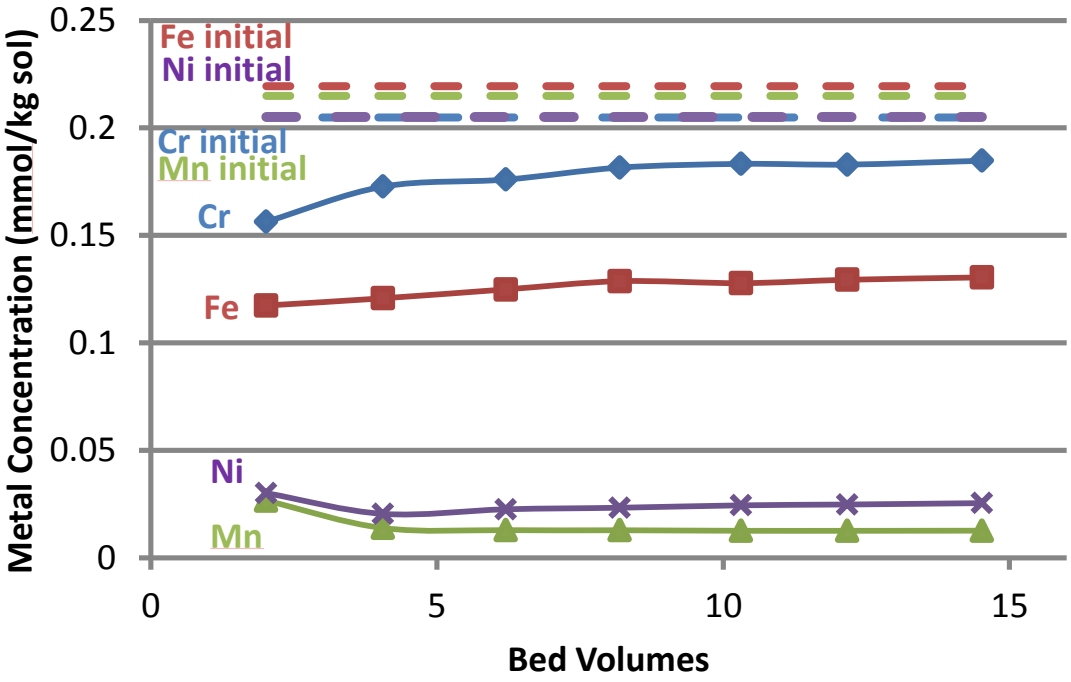

Figure 4: Amberlite IRC 748I, 4 m neat MEA, α = 0.22

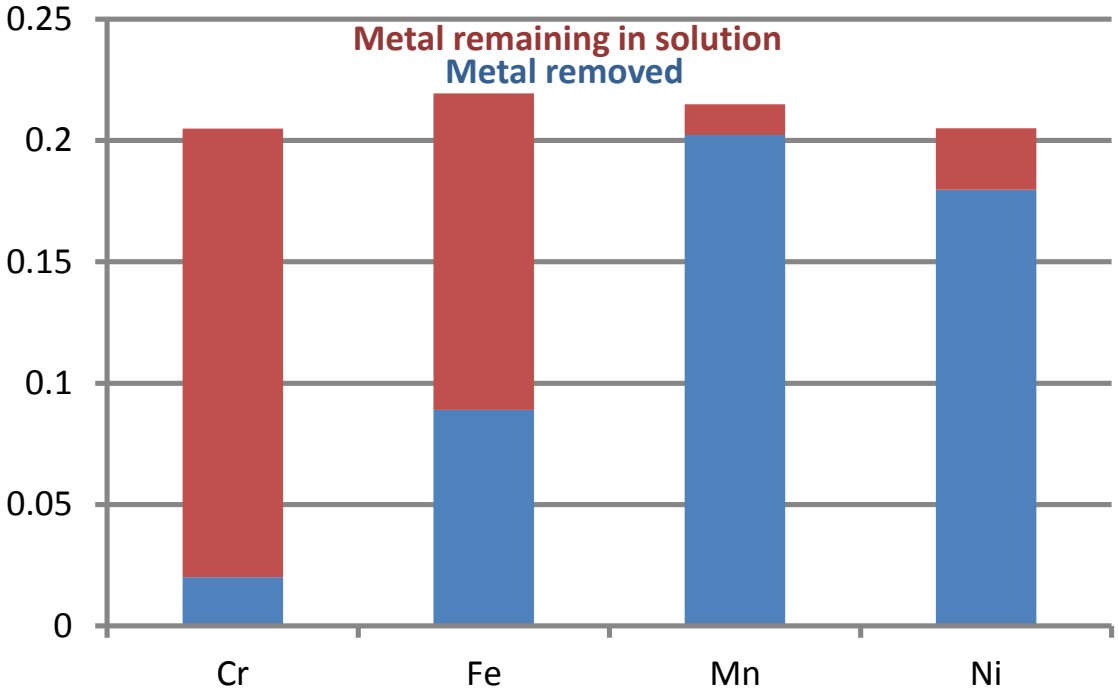

Figure 5: Amberlite IRC748I, 4 m neat MEA, α = 0.22

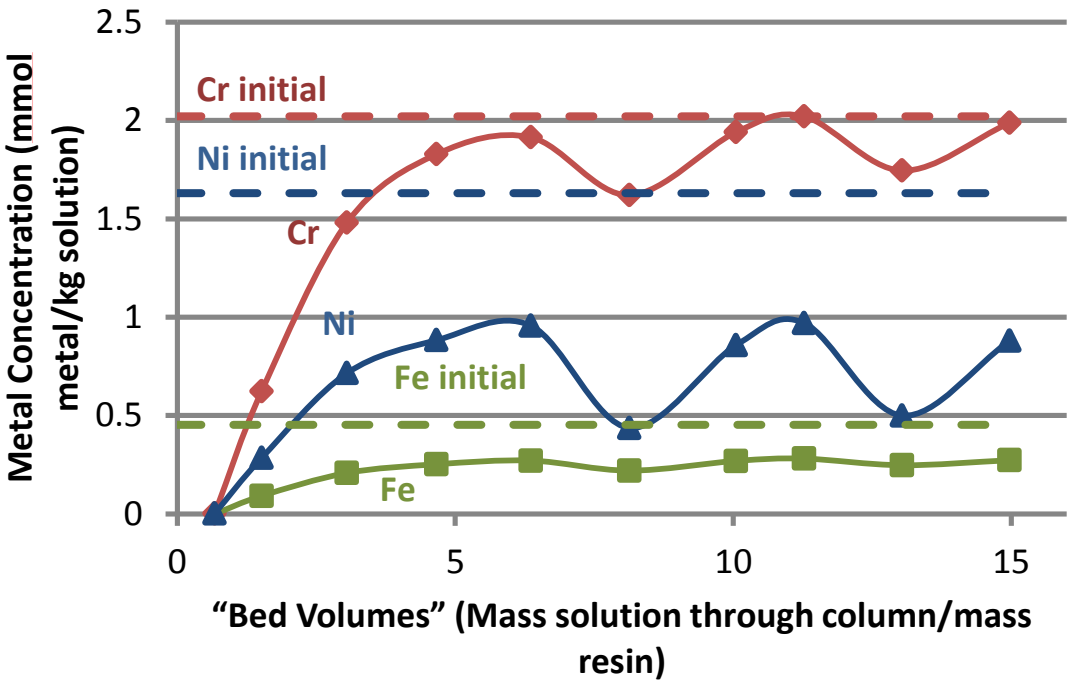

Figure 6: Amberlite IRC748I, PP2 PZ, major metals

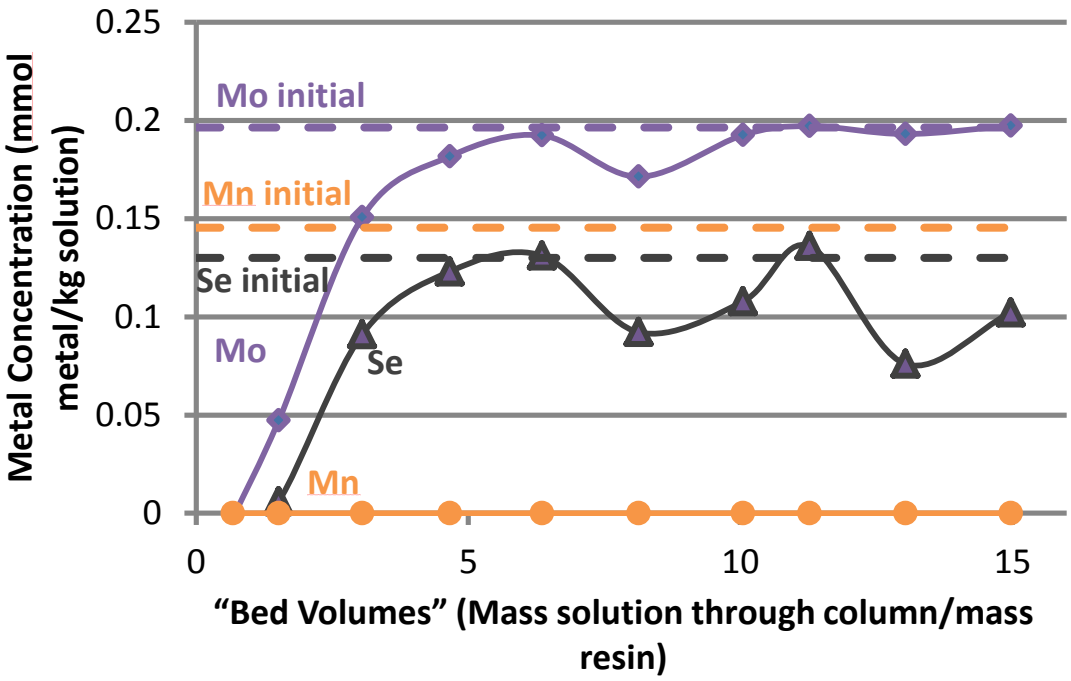

Figure 7: Amberlite IRC748I, PP2 PZ, minor metals

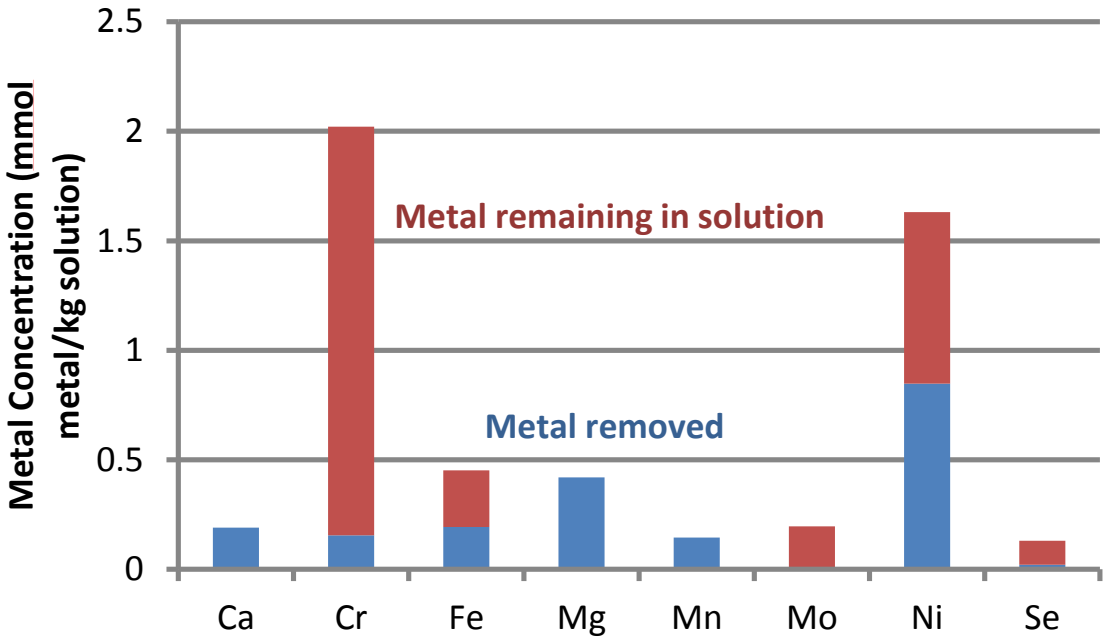

Figure 8: Amberlite IRC748I, PP2 PZ

Analytical Methods

ICP OES

All metals analysis was done by inductively coupled plasma optical emission spectroscopy using a Varian 710-ES instrument run in axial configuration. Wavelengths analyzed are given in Table 4. Results for each wavelength were averaged with other wavelengths for the same ion.

Table 4: Wavelengths Analyzed in ICP OES analysis (nm)

Ca	Ca	Ca	Co	Co	Co	Cr	Cr	Cr
393.366	396.847	422.673	228.615	230.786	238.892	205.560	206.158	267.716
Fe	Fe	Fe	Mg	Mg	Mg	Mn	Mn	Mn
234.350	238.204	259.940	279.553	280.270	285.213	257.610	259.372	260.568
Mo	Mo	Mo	Ni	Ni	Ni	Se	Se	Se
202.032	203.846	204.598	216.555	221.648	231.604	185.457	196.026	203.985

Cation Chromatography

The concentrations of PZ in Table 3 were determined using cation chromatography on a Dionex ICS2100 instrument. The solution was diluted to 10,000X and then eluted with methanesulfonic acid mixed with water. The eluent followed a gradient starting at 5.5 mM and ending at 38.5 mM methanesulfonic acid. The samples were eluted over an IonPac GC 17 guard column followed by an IonPac CS 17 analytical column. These columns contain ethylvinylbenzene cross-linked with 55% divinylbenzene resin.

Conclusions

From neat 4 m PZ, Amberlite 748i showed high removal of Ni and Mn at 81% and 71% respectively. The resin showed moderate removal of Fe and Cr, at 47% and 36%. Breakthrough of metals was not reached by about 16 bed volumes of amine. The initial concentrations of metals were Cr: 0.10 mM, Fe: 0.09 mM, Mn: 0.12 mM, and Ni: 0.14 mM.

From neat 4 m MEA, Amberlite 748i showed high removal of Ni and Mn at 88% and 94% respectively. In addition, the resin showed moderate removal of Fe, at 40%. Breakthrough of metals was not reached by about 14 bed volumes of amine. The initial concentrations of metals were Cr: 0.20 mM, Fe: 0.22 mM, Mn: 0.21 mM, and Ni: 0.21 mM.

From PP2 PZ, Amberlite 748i showed complete Ca, Mg, and Mn removal (100%). In addition, the resin showed moderate removal of Ni and Fe, at 52% and 43%. The resin showed low removal of Cr, Mo, Ni and Se. Breakthrough of Fe, Ni, and Mn was not reached by 15 bed volumes. The initial metal concentrations for stainless steel metals were Cr: 2.0 mM, Fe: 0.45 mM, Mn: 0.14 mM, and Ni: 1.6 mM.

References

Nielsen PT, Li L, Rochelle GT. "Piperazine degradation in pilot plants." *Energy Proc.* 2013;37:1912–1923.

Available online at www.sciencedirect.com

ScienceDirect

Energy Procedia 00 (2013) 000–000

Energy Procedia

www.elsevier.com/locate/procedia

GHGT-12

Pilot Plant Activities with Concentrated Piperazine

Eric Chen[a], Steven Fulk[b], Darshan Sache[b], YuJeng Lin[b], Gary T. Rochelle[b]*

[a]*Pickle Research Campus, The University of Texas at Austin, 10100 Burnet Rd., Bldg 133, R7100, Austin, TX, USA*
[b]*McKetta Department of Chemical Engineering, The University of Texas at Austin, 200 E. Dean Keeton St., C0400, Austin, TX 78712-1589, USA*

Abstract

Amine aerosol testing was conducted at the University of Texas at Austin CO_2 capture pilot plant using concentrated piperazine (3.7 molal) and high temperature flash with cold rich bypass (140 °C). Two methods of piperazine aerosols generation were tested: H_2SO_4 injection with a liquid vaporizer injector, and direct injection 20 ppm of SO_2 into the synthetic flue gas. A Phase Doppler Interferometer (PDI) analyzer from Artium Technologies was used to measure piperazine aerosol droplet sizes and distributions at the absorber gas outlet. A FTIR system with new upgraded heated probes was used to make measurements of total PZ concentrations at the absorber gas inlet and outlet. A manual sampling train method was used to provide secondary validation of FTIR and PDI measurements.

Selection and peer-review under responsibility of GHGT.

Keywords: CO_2 pilot plant; concentrated piperazine; amine aerosols; advanced flash stripper

1. Introduction

1.1. Concentrated Piperazine

Concentrated (30-40 wt %) piperazine (PZ) with advanced flash stripper regeneration is a second generation amine-based process for CO_2 capture [1]. 8 molal (m) PZ has double the CO_2 absorption rate and capacity of 7 m MEA. PZ also has a moderately high heat of absorption (70 kJ/mole) and is oxidatively and thermally stable, which should provide 10 to 20% better energy performance than 7 m MEA with thermal swing regeneration at 150 °C [2]. However, 8 m PZ has a limited operating range due to solid solubility issues encountered at both the lean and rich CO_2 loadings.

* Corresponding author. Tel.: +1-512-471-7230; fax: +1-512-471-7060.
E-mail address: gtr@che.utexas.edu

Selection and peer-review under responsibility of GHGT.

An alternative solvent that can circumvent some of the limitations of 8 m PZ and still retain its benefits is 5 m PZ. The use of 5 m PZ eliminates the solubility limitation on the rich CO_2 loading end and expands the lean solubility window relative to 8 m PZ (Fig. 1). 5 m PZ can be operated at a lower lean loading, which has been shown to provide better performance in the absorber. The absorption rate (k_g') of 5 m PZ is approximately 30 % higher than 8 m PZ which results in a significant reduction in the packing area requirement. It also has about the same equivalent work requirement as 8 m PZ (Table 1). The viscosity of 5 m PZ is 50 % less than 8 m PZ. However, in order to obtain the same CO_2 capacity as 8 m PZ, the L/G for 5 m PZ must be operated approximately 17 % higher. 5 m PZ can be operated at 150 °C, which permits regeneration of CO_2 at high pressures (6-8 bar).

An analysis for the annualized cost of regeneration has found that the optimum lean loading for 5 m PZ is 0.22 mol CO_2/mol alkalinity with a 7.5 °C LMTD for the cross-exchanger. For 8 m PZ, the optimum lean loading is 0.26 mol CO_2/mol alkalinity and 10 °C LMTD. Fig. 2 shows that the equivalent work at the optimum conditions of 5 m PZ and 8 m PZ is approximately the same. Therefore, there are inherent benefits with using 5 m PZ over 8 m PZ and other amine solvents.

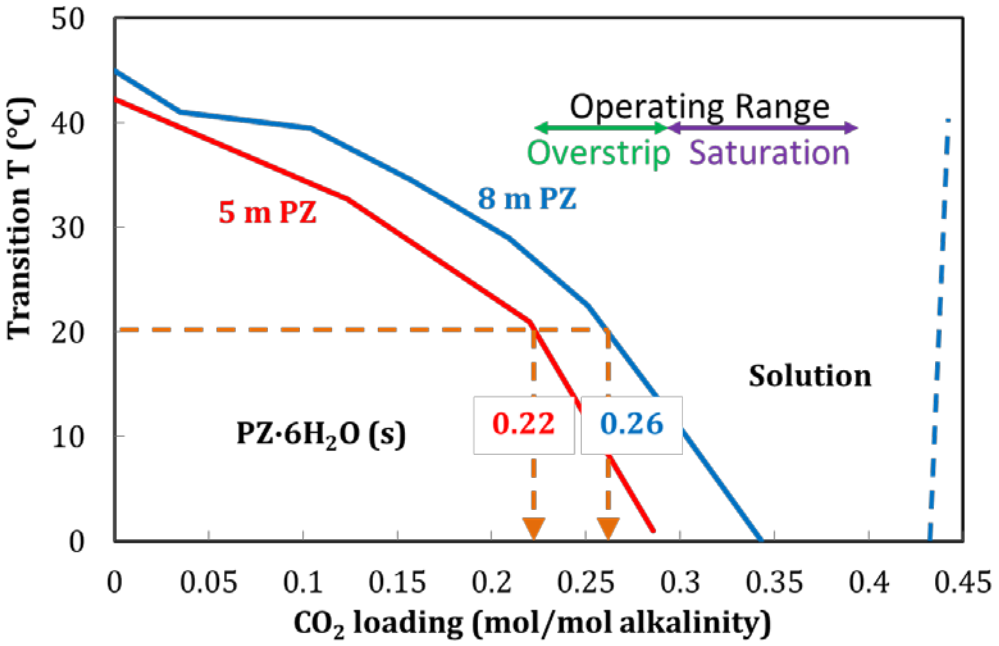

Fig. 1. Solubility window for 5 m and 8 m PZ.

Table 1. Performance data for 5 m PZ, 8 m PZ, 7 m MEA, 4 m AMP/2 m PZ, and 5 m MDEA/5 m PZ.

Parameter	5 m PZ	8 m PZ	7 m MEA	4 m AMP/ 2 m PZ	5 m MDEA/ 5 m PZ
$k_g'_{ave}$ x 10^7 (mol/s-Pa-m^2)	11.3	8.5	4.3	8.6	8.5
Viscosity (cP)	4	11	3	5	13
Capacity (mol CO_2/kg)	0.81	0.84	0.67	0.90	0.91
T_{max} (°C)	163	163	121	128	117
Lean Loading (mol CO_2/mol total alkalinity)	0.22	0.26	-	-	-
Rich Loading (mol CO_2/mol total alkalinity)	0.40	0.40	-	-	-
L/G (mol/mol)	3.03	2.55	-	-	-
Equivalent Work (kJ/mol CO_2)	36.0	36.3	-	-	-
Packing Required (m^2/mol CO_2)	126	298	-	-	-

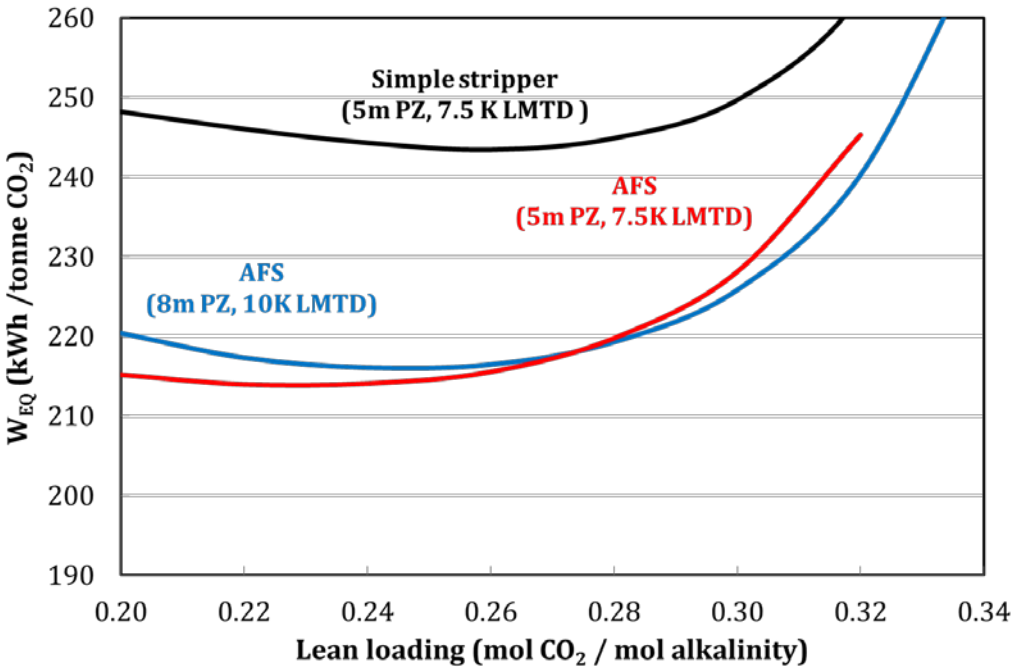

Fig. 2. Equivalent work comparison for 5 m PZ and 8 m PZ with the simple stripper and advanced flash stripper (AFS) configurations and cross exchanger LMTD approach temperatures.

1.2. SRP CO_2 Pilot Plant

The advanced flash stripper with cold and warm rich bypass builds on the technology developed from the two-stage flash and warm rich bypass configuration tested during a pilot plant campaign at the University of Texas of Austin Separation Research Program (SRP) in October 2011 (Fig. 3). The SRP pilot plant has a removal capacity of 3-6 tons of CO_2/day and uses synthetic flue gas consisting of CO_2 and air. The high temperature advanced flash stripping process at 150 °C exploits the high thermal stability of PZ and results in a much higher regeneration pressure (5-10 bar). A new configuration will integrate a gas-liquid heat exchanger to recover the heat from the overhead vapor by cross-exchanging it with the cold rich bypass stream. The advanced flash stripping process offers a smaller footprint, a more simple design, and lower capital costs than a conventional packed stripper column.

Fig. 4 shows the advanced intercooling configuration, which splits the liquid flow at the heat exchanger and returns a portion of the flow to the bottom packed bed and the remaining flow is recycled as spray to the top packed bed. The intercooling recycle flow rate can potentially be five times the solvent feed flow to the absorber column. This configuration maximizes the amount of intercooling and increases the amount of mass transfer area available for CO_2 absorption.

Fig. 3. SRP pilot absorber/stripper system with high temperature flash skid (bottom left).

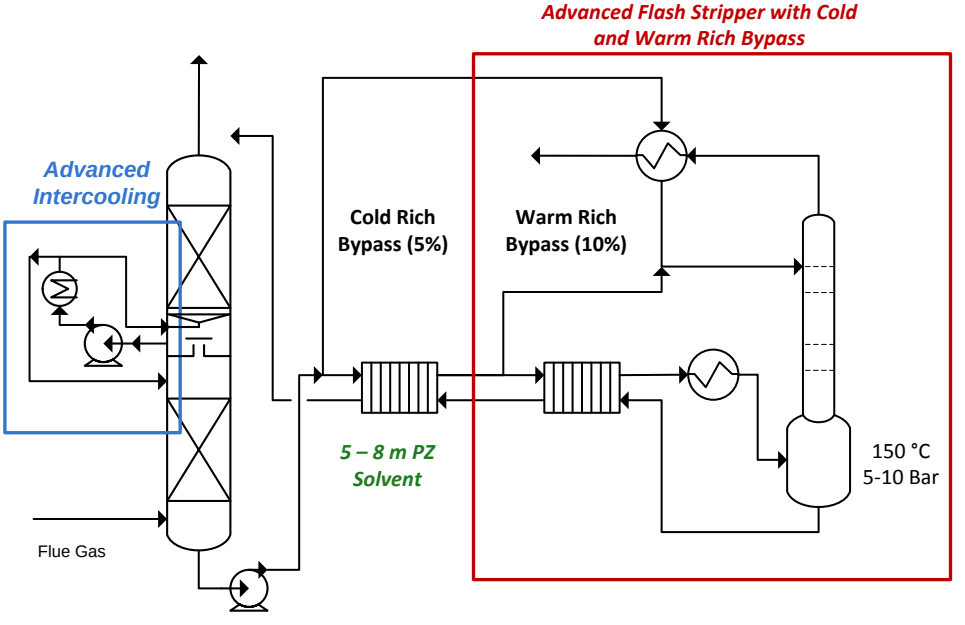

Fig. 4. Advanced flash stripper configuration.

1.3. Amine Aerosol Emissions

Elevated emissions of amines have been observed at several CO_2 capture pilot plants and attributed to amine aerosol formation. Absorber water wash systems traditionally used to address amine volatility are not effective for the removal of amine aerosols. Pilot and bench-scale studies have shown that SO_3 can become the nucleation site for the formation of amine aerosols. However, accurate measurements of amine aerosol droplet size and distributions is a challenge.

1.4. Past SRP Pilot Plant Testing

Testing at the pilot scale with concentrated PZ has been completed in five separate campaigns since 2008 at the SRP pilot plant, which has a CO_2 removal capacity of 3-6 tons/day (~0.1 MW) and consists of an intercooled absorber and simple stripper column. Both columns have an inner diameter of 0.43 m and each column is typically filled with 6.1 m of packing. The facility uses synthetic flue gas consisting of air and CO_2, which provides the flexibility to test at CO_2 concentrations for both coal (12 mol %) and gas (3 mol %). A new high temperature and pressure two-stage flash regeneration skid was designed, fabricated, and operated in 2010 and 2011 and successfully regenerated 8 m PZ at 150 °C and 14 bar.

1.5. Pilot Plant Objectives

The SRP pilot plant campaign conducted in November 2013 focused on the development of methods for generating, measuring, and capturing PZ aerosols. To facilitate this effort, a liquid vaporizer injector (LVI) was procured and used to generate H_2SO_4 aerosols for injection into the pilot absorber gas inlet duct. An SO_2 gas injection system was also tested as an alternative aerosol generation method. A Phase Doppler Interferometer (PDI) analyzer from Artium Technologies was used to measure PZ aerosol droplet sizes and distributions at the absorber gas outlet. A FTIR system with newly upgraded heated probes was used to make measurements of total PZ concentrations. Pilot plant testing was completed with 4 m PZ instead of 8 m PZ to evaluate performance differences with a lower viscosity and capacity solvent. The SRP absorber column was packed with 6.1 m of RSP 250 structured packing and operated with two intercooling configurations. The existing two-stage flash process was modified into a single-stage flash with cold rich bypass process and operated at 140 °C.

2. Pilot Plant Configuration

2.1. Pilot Plant Configuration and Modifications

The November 2013 pilot plant campaign was conducted with absorber intercooling and one-stage flash with cold rich bypass (Fig. 5). The absorber column was packed with 6.1 m of RSP 250 structured packing, divided into two 3.05 m sections by a chimney tray and redistributor (Table 1). Liquid from the top packed bed is collected by a chimney tray, cooled to 40 °C, and circulated to the intercooling loop.

The absorber column can be operated in two intercooling configurations: in-and-out intercooling and pump-around spray recycle intercooling. The pump-around configuration uses a spray nozzle to return the liquid solvent to the absorber column in between the chimney tray and bottom of the top packed bed. Liquid from the spray is eventually returned to the collector plate inventory. The liquid on the collector plate overflows through a weir in the middle of the chimney to the redistributor below. A liquid inventory of approximately 38 L is maintained. This configuration circulates liquid solvent up to two times the solvent feed flow rate and increases mass transfer area for CO_2 absorption. The absorber was operated with both modes of intercooling to determine its effect on aerosol emissions.

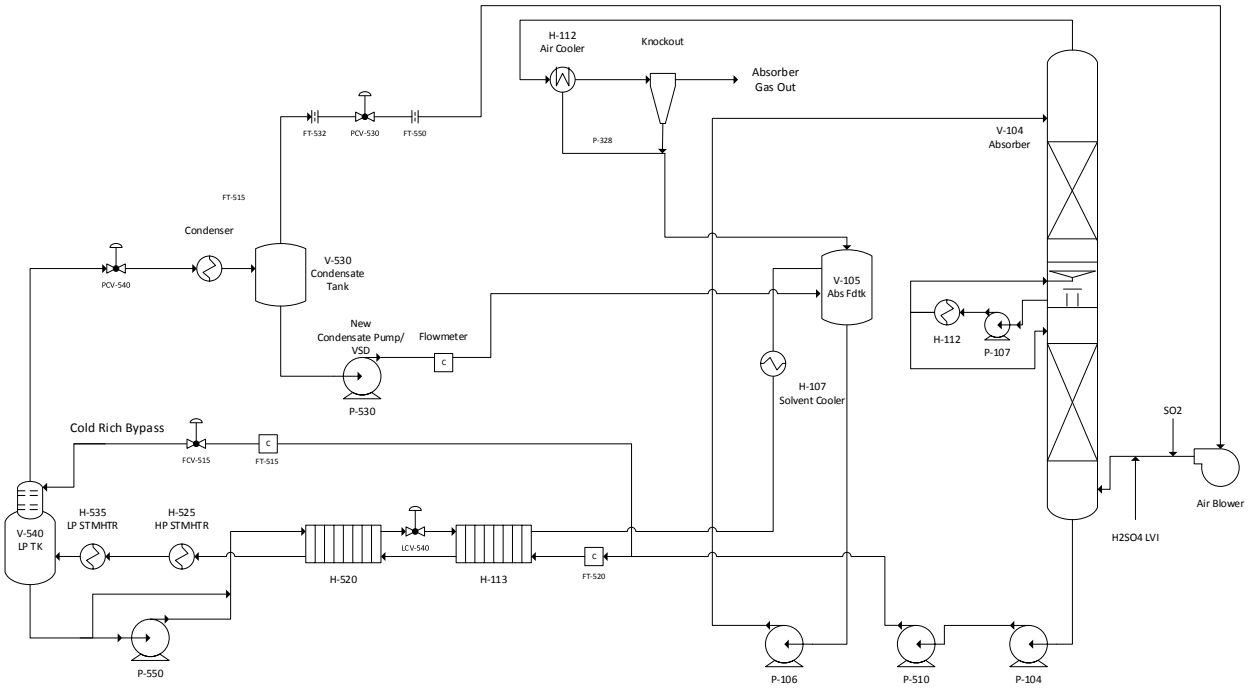

Fig. 5. Process flow diagram for SRP pilot plant integrated with the high temperature one-stage flash skid.

Table 2. Absorber column packing and liquid distributor specifications.

Packing	Absorber Top Distributor	Absorber Middle Distributor
RSP 250 Structured Packing	HC Perforated Pipe (SRP3C)	HC Trough Drip Tube
Two 3.05 m beds	Range: 1.8 – 5.5 m^3/hr	Range: 0.7 – 7 m^3/hr
250 m2/m3	3.7 pts/m^2	1.3 pts/m^2

2.2. Amine Aerosol Generation

The Liquid Vaporizer and Injector (LVI) by Air Quality Analytical, Inc. was used to generate H_2SO_4 aerosol at 1–5 ppmv in a 9.9 m^3/min stream using a solution of 10 vol % H_2SO_4 [3]. The vaporized acid was injected into the absorber inlet duct where it re-condensed as submicron H_2SO_4 mist on contact with the cold absorber feed gas. The acid was injected approximately 3 m upstream of the absorber gas inlet nozzle. The campaign also tested an alternative aerosol generation method where 2 mol % SO_2 gas mixture was injected into the flue gas to produce 10-25 ppmv of SO_2 in a 9.9 m^3/min gas stream. SO_2 was injected at the discharge of the gas blower, which is approximately 15 m away from the absorber column gas inlet.

2.3. Aerosol Measurements

Amine aerosol measurements were quantified using the following methods: FTIR, Phase Doppler interferometry (PDI), manual impinger-based measurements for amine concentrations, and manual impinger-based measurements for sulfuric acid concentrations using EPA Method 8. The samples were collected at three locations: absorber gas inlet, absorber gas outlet, and gas knockout tank outlet. FTIR and manual H_2SO_4 measurements were made at the absorber gas inlet (Fig. 6). FTIR, PDI, and manual amine measurements were made at the absorber gas outlet. A third FTIR measurement was made at the absorber gas knockout outlet, but a leak was detected and the sample point was removed from service.

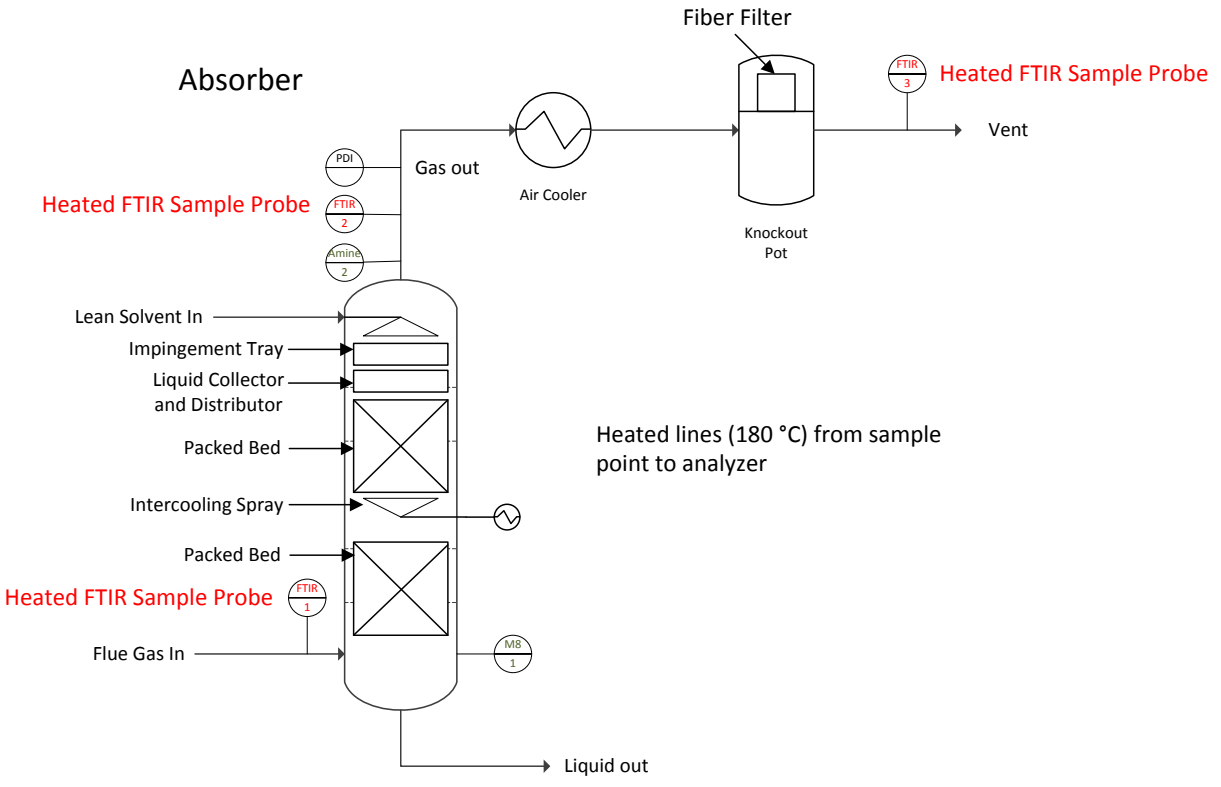

Fig. 6. Locations of FTIR, PDI, and manual sampling ports.

2.3.1. Absorber FTIR Gas Analysis

A Gasmet™ DX4000 portable FTIR spectrometer was used to analyze for H_2O, CO_2, PZ, NH_3 and SO_2 concentrations in the gas at the absorber inlet and outlet. The FTIR has a path length of 5 m and a wavenumber resolution of 8 cm^{-1}. The FTIR extractive system included heated probes with heated probe tubes and heated sample lines at each of the three sampling locations. A heated hot box with manual valves was used to switch between the three sample locations. All of the components of the sampling systems were maintained at 180 °C to prevent condensation and vaporize any aerosolized material. Heat tracing and insulation was installed on exposed transition tubing. The FTIR sample pump was installed downstream of the FTIR analyzer. For the pilot plant testing, all run data were signal averaged for 1 minute.

2.3.2. Phase Doppler Interferometry (PDI)

A demonstration Phase Doppler Interferometer (PDI) analyzer from Artium Technologies, Inc. was tested to determine droplet sizes and distributions. The PDI consisted of a transmitter, receiver, and data acquisition/processing box and was designed to make optical measurements through a windowed spool section. The Artium PDI was capable of measuring droplet diameters from 0.5–10 μm (Fig. 7). The sample gas from the absorber outlet duct was pulled through a pipe nozzle by a regenerative blower at a rate of 0.6 m^3/min, which approximated an isokinetic sample. The PDI optical window spool section was located less than one meter from the sample nozzle and upstream of the blower. The sample stream was pumped out of the regenerative blower back into the absorber outlet gas downstream of the sample point. Fig. 8 shows a simplified process flow diagram of the bypass sampling system.

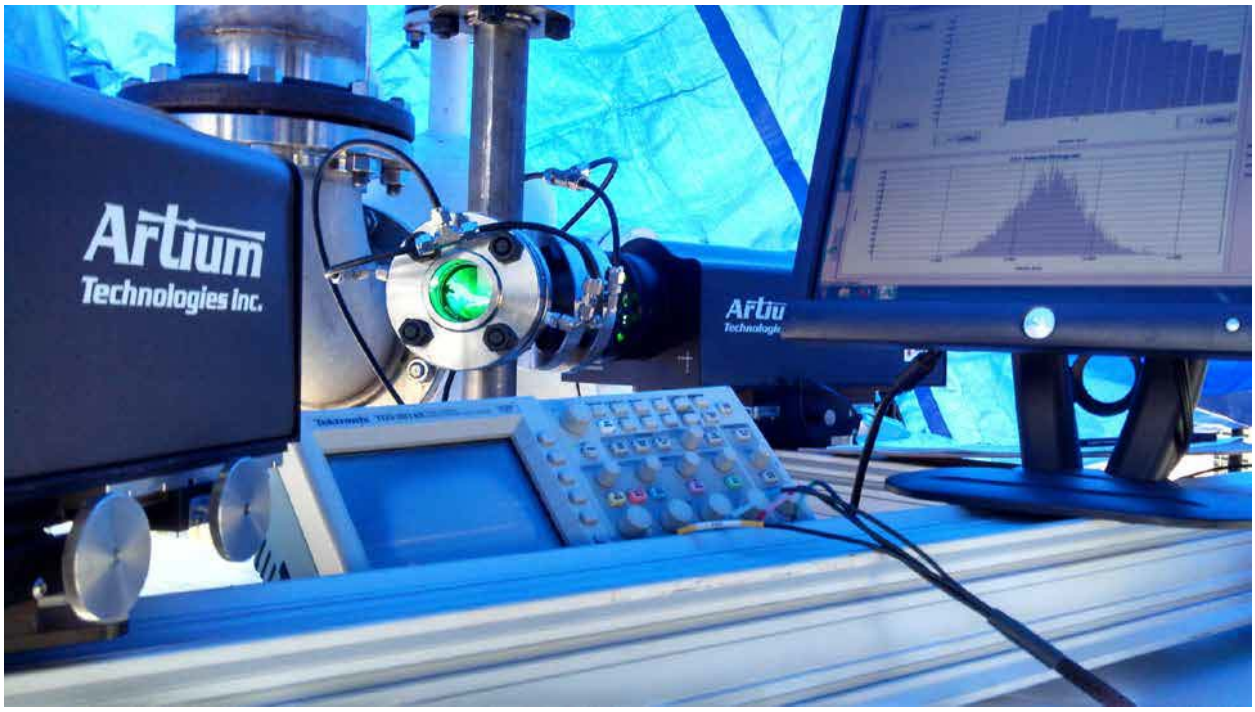

Fig. 7. PDI Instrument Installed at SRP.

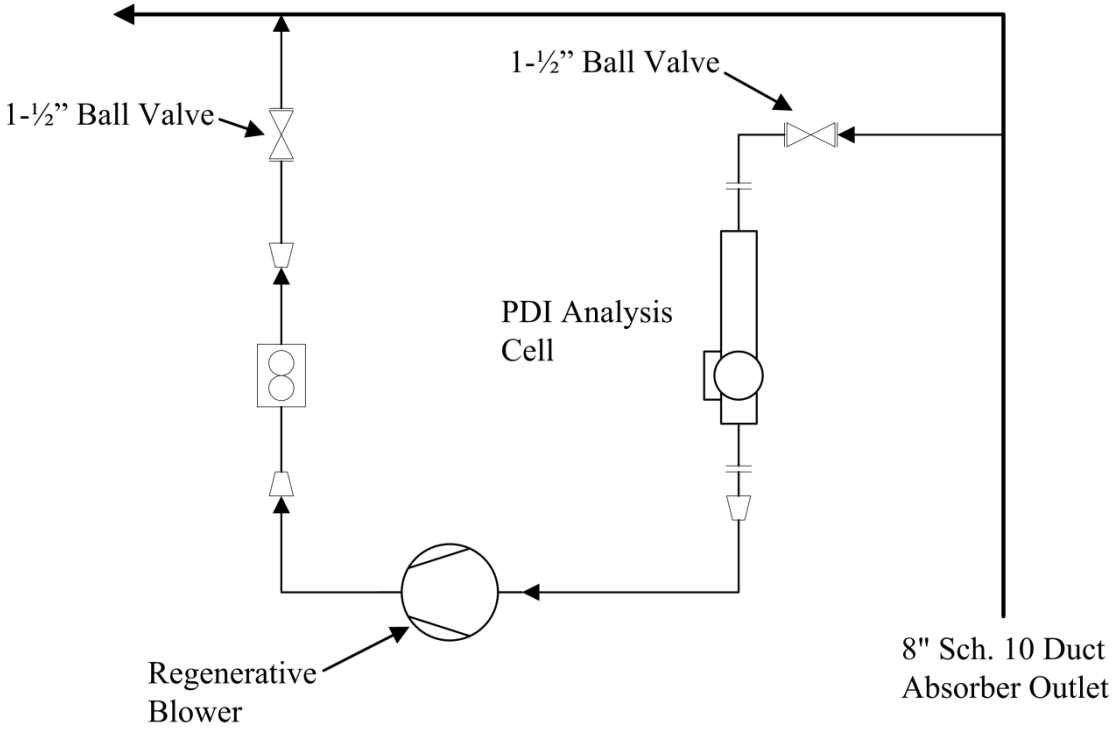

Fig. 8. PDI bypass sampling system process flow diagram.

2.3.3. Manual Measurement for Amine Concentration

Gas-phase amine concentrations at the absorber outlet were measured with a manual sampling method in which flue gas was pulled iso-kinetically through a glass probe maintained at 127 °C and then through a series of devices designed to collect both the aerosol and vapor-phase fractions of the amine emissions. The gas passed from the probe into a condenser coil that was maintained as cold as possible with ice water (8 °C on 11/21/13 and 2 °C on 11/22/13). The purpose of the condenser coil was to knock out aerosol particles by both condensation and impingement via the gas' tortuous path through the coil.

The coil was oriented vertically such that gas passed from top to bottom; an empty modified impinger (i.e., no impingement plate) was mounted at the coil exit to collect condensate; this was followed by an empty Greenburg Smith impinger (i.e., fitted with an impingement plate). The gas then passed through two Greenburg Smith impingers containing 0.1 N H_2SO_4; the purpose of these impingers was to collect any remaining gas-phase amine that penetrated the coil. The gas was then conditioned (dried with silica gel) so that sample volume could be measured.

Sample runs lasted thirty minutes. On completion of a sample run, the sampling train parts (probe, condenser, impingers, and connection pieces) were recovered with a 0.1 N H_2SO_4 rinse. The recovery of the sample train resulted in two fractions to be analyzed: (1) the probe, condenser, and empty impinger were recovered and analyzed together, and (2) the acid impinger was recovered and analyzed separately. The recovered fractions were analyzed for PZ concentration via cation chromatography. These concentrations were multiplied by the mass of liquid recovered to determine the mass of PZ in the recovered fraction. The total amine concentration in the flue gas was calculated by summing the amine mass recovered in the two fractions and then dividing by the volume of flue gas sampled.

The sampling train was designed to measure total gas-phase and aerosol amine emissions; it was not designed to distinguish between and quantify aerosol and gas-phase emissions. The contact of flue gas with condensed liquid in the condenser and empty impinger results in gas-phase amine being captured in the front end of the train.

2.3.4. EPA Method 8 for SO_2 and Sulfuric Acid Species

A modified version of EPA Method 8 was used to quantify sulfur dioxide and sulfuric acid emissions in the flue gas at the absorber inlet. In this method, gas is extracted from a sampling point in the inlet duct. The SO_2 and SO_3, including those fractions in any sulfuric acid mist, are captured in the sampling train, which consists of a Greenburg Smith impinger containing 80% isopropyl alcohol, a non-heated filter, a modified impinger containing 6% hydrogen peroxide, and a Greenburg Smith impinger containing 6% hydrogen peroxide. The sulfate content of the recovered train was measured by anion chromatography. Since there was no particulate matter in the flue gas, a heated filter was not used upstream of the sampling train.

2.4. Aerosol Capture

The aerosol mitigation effort has focused on strategies to grow the aerosol particles inside the absorber column and water wash in order to capture them with conventional droplet removal technologies such as impingement trays and sieve plates. An impingement tray was engineered in-house with some input from Dr. Frank Seibert and fabricated by a local machine shop. The impingement tray was designed to have 1.6 cm-of-H_2O of dry pressure drop and 1.9 cm-of-H_2O liquid pressure drop. The impingement tray consisted of three parts: demister, support ring, and sieve plate. The demister removes any entrained liquid as gas passes through the tray, and the demister is located approximately 1 m above the impingement tray to provide enough disengagement residence time for droplets to agglomerate on the demister.

The absorber feed pipe passes through a hole in the middle of the demister and is sprayed by a 180° spray nozzle outward to the absorber column walls. The liquid flows down the walls and then radially from the outside edge to the center of the impingement tray. An overflow weir on the tray proves a liquid level through which the absorber gas must pass. The liquid then overflows the weir and into the downcomer connected to the liquid distributor below. The impingement tray was fabricated but was not tested during the 2013 campaign.

3. Pilot Plant Results

3.1. Pilot Plant Performance

The November 2013 SRP pilot plant campaign evaluated 3.7 m PZ (24 wt %), one-stage flash with cold rich bypass, and absorber spray recycle intercooling. The campaign only lasted for two days because of ongoing issues with the LVI. Table 3 shows that operating conditions and performance of the pilot plant. The gas and liquid rates were constant for the duration of the campaign. However, although the absorber inlet gas rate was maintained at 9.9 m^3/min, the dramatic difference in ambient temperature resulted in different gas mass flow rates. This is reflected in the L/G (mass/mass) of 3.7–4.0. When the intercooling spray was turned off, the CO_2 removal decreased from 92% to 75%. The flash stripper was maintained at 140 °C and 4.5 bar, which was slightly lower than the typical 150 °C at which the PZ campaigns have operated in the past.

Table 3. November 2013 one-stage flash operating conditions (1 mol PZ = 2 mol total alkalinity).

Parameter	Value
PZ (wt %)	23.8 – 24.5
Lean loading (mol CO_2/mol total alkalinity)	0.22
Gas Rate (m^3/min)	10
L/G (mass/mass)	3.7 – 4.0
Intercooling (40 °C, column middle)	On/Off
CO_2 Removal (%)	75 – 92
Flash Stripper Pressure (bar)	4.5
Flash Tank Temperature (°C)	139
Absorber Packing	RSP 250

3.2. LVI H_2SO_4 Aerosol Generation

A liquid vaporizing injector used H_2SO_4 to generate PZ aerosols at the SRP pilot plant. Prior to installation at the plant, it was tested at the bench scale to verify performance. However, when the LVI was operated during the pilot plant campaign, it experienced intermittent operation as a result of corrosion. This resulted in the eductor plugging and subsequent shutdown of the LVI. The LVI was operable for a limited amount of time when the eductor was cleaned after each shutdown. The LVI was eventually abandoned and direct injection of SO_2 was tested as an alternative method for PZ aerosol generation. Table 4 shows the aerosols generation methods and sampling methods used in the November 2013 operations. The absorber was operated with the intercooling spray recycle and also without intercooling.

Even with intermittent operation, the LVI was operated long enough to demonstrate that PZ aerosols could be generated by the injection of sulfuric acid mist at the absorber inlet. Fig. 9 shows FTIR measurements that were made at the absorber gas outlet for PZ, H_2O, CO_2, and NH_3. The figure shows a net increase in PZ concentration during the two periods where the LVI was operated. The baseline concentration of 15 ppm increased up to 50–70 ppm during the two injections. The manual sampling method (URS-2) also confirmed the elevated PZ concentrations measured by the FTIR. Manual measurements via EPA Method 8 confirmed that no SO_X species were detected in the flue gas during LVI operation.

FTIR measurements were attempted at the knock-out tank outlet, but there appeared to be a leak in the line that could not be fixed during the test campaign. No data were reported from this sampling location.

Table 4. Aerosol generation and sampling matrix for November 2013 campaign.

Date	Start Time	End Time	Intercooling	Intercooling Mode	H_2SO_4 Injection	SO_2 Injection	FTIR	Manual Methods	PDI
11/21/13	9:30	11:15	ON	Spray	OFF	OFF	X		
11/21/13	11:15	11:40	ON	Spray	ON (Intermittent)	OFF	X		X
11/21/13	11:40	14:23	ON	Spray	OFF	OFF	X		
11/21/13	14:23	16:52	ON	Spray	ON (Intermittent)	OFF	X	URS-1 URS-2	X
11/22/13	9:40	13:40	OFF	–	OFF	OFF	X	URS-4 URS-5	
11/22/13	13:40	14:52	OFF	–	OFF	25 ppm	X	URS-7	
11/22/13	14:52	15:30	ON	Spray	OFF	25 ppm	X	URS-8	
11/22/13	15:30	16:45	ON	Spray	OFF	OFF	X		

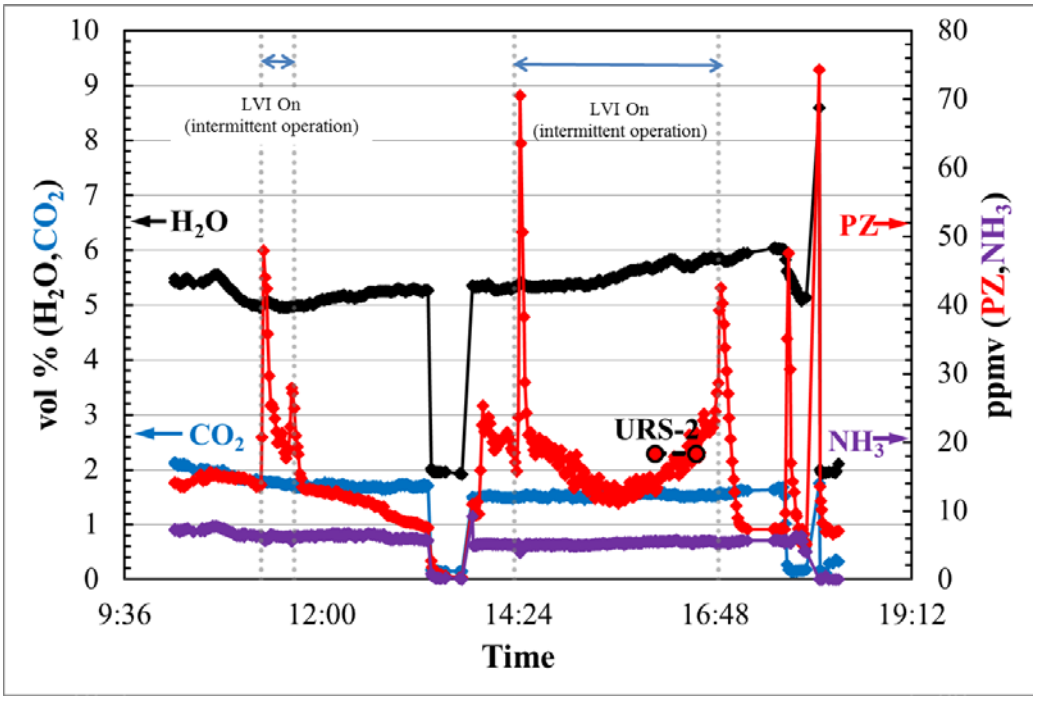

Fig. 9. FTIR (UT/SRP) and manual sampling (URS) data taken 11/21/13. Dashed lines with circle points are manual sampling PZ concentrations averaged over a 30-minute interval adjusted for moisture content. The LVI was in operation between the dotted gray lines.

3.3. SO_2 Aerosol Generation

Direct injection SO_2 gas was tested after it became apparent that the LVI would not be a reliable method for generating PZ aerosols. A rotameter was used to meter in 2 mol % SO_2 gas and obtain an approximate target concentration of 25 ppm in the flue gas. This was verified by absorber inlet FTIR measurements, which measured SO_2 concentrations of approximately 22.5 ppm on a wet basis (Fig. 10).

FTIR and manual measurements for PZ were made at the absorber gas outlet. Fig. 11 shows that with the injection of SO_2, the concentration of PZ increased, which indicated that PZ aerosols were generated. This increase in concentration at the absorber gas outlet was detected by both the FTIR and manual sampling methods (URS-7). During the second half of the SO_2 injection interval, the spray recycle intercooling was turned off and the PZ concentration decreased. Both FTIR and the manual sampling method (URS-8) confirmed the decrease. The figure also shows that the manual measurements (URS-4 and URS-5) were consistently higher than the FTIR measurements for PZ. The PZ analysis region overlapped the H_2O analysis region, and this may have contributed to some error in the PZ measurement.

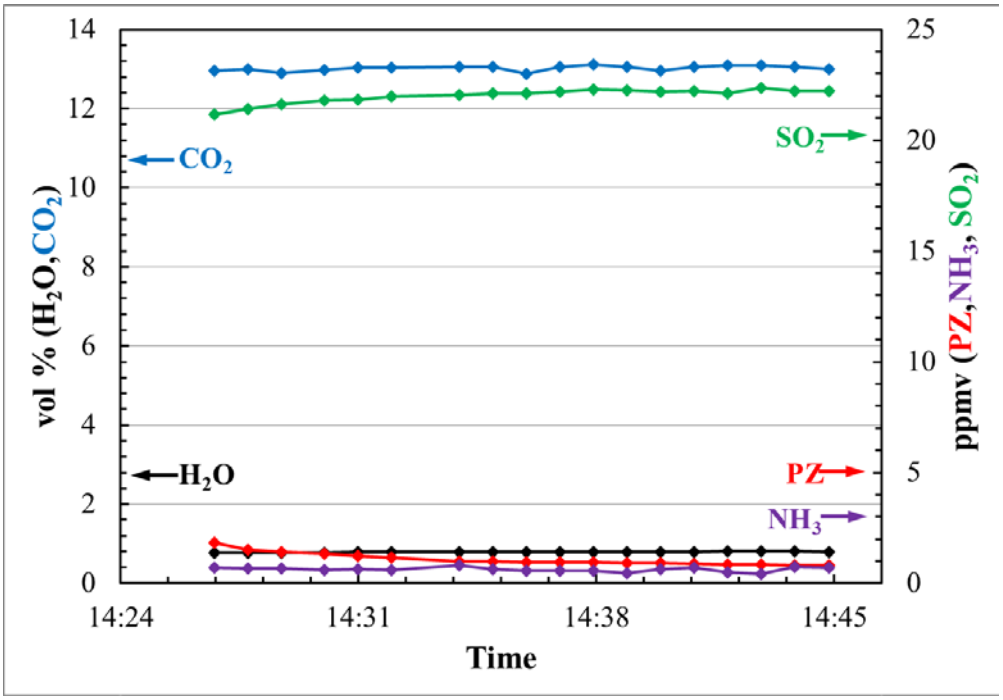

Fig. 10. FTIR analysis of SO_2 at the absorber inlet heated probe (11/22/13). SO_2 was injected at a target concentration of 25 ppmv.

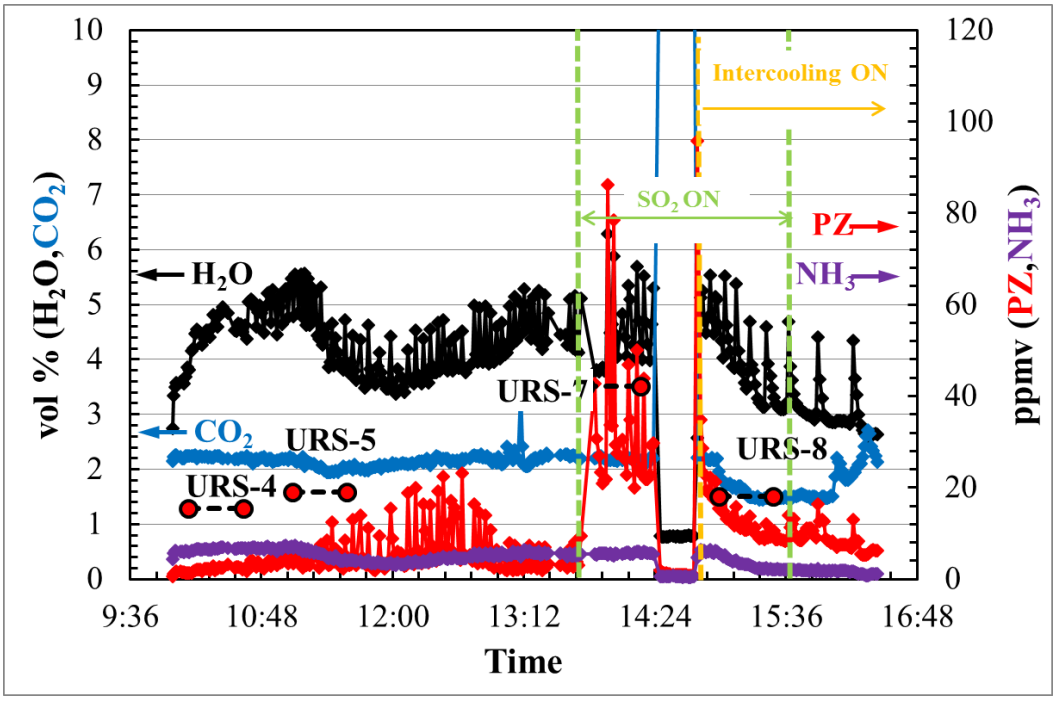

Fig. 11. FTIR (UT/SRP) and manual sampling (URS) data taken 11/22/2013. Dashed lines with circle points are manual sampling PZ concentrations averaged over a 30-minute interval adjusted for moisture content. SO_2 was injected during the period containing URS-7 and URS-8. The FTIR was switched to measuring the absorber inlet during the time period 14:24 through 14:45.

3.4. PDI Measurements

Prior to installation at the SRP absorber column gas outlet, the operation of the PDI was verified in the laboratory by spraying an atomized H_2O stream using an airbrush. After the PDI was installed at the absorber outlet gas duct, the airbrush test was repeated. The airbrush was used to verify that the optical configuration was measuring droplet sizes under 5 µm at high total concentrations. The total sample taken in a single measurement was fixed at 10,000 counts by the PDI software. The reported particle densities provide translation from probability distributions to absolute number distributions which can be used for mass balance calculations.

Even with the intermittent operation of the LVI aerosol generator, the PDI demonstrated that measurements of size distributions in highly dense (10^5 particles/cm^3) streams between 0.5 and 10 µm could be made. However, a drop-off at 0.5 µm is observed due to the sensitivity envelope of the PDI. Example histograms of the PDI from the SRP test campaign are shown in Fig. 12 and Fig. 13. The PDI data show that particle size distribution shifts to the right as the absorber temperature increases. The size distribution shifts to the right (indicating larger particles) when moving from Fig. 12 (15.5 °C) to Fig. 13 (38.5 °C). The steepness of the drop-off at 0.5 µm decreases as the absorber temperature increases due to the growth of the sub-0.5 µm particles into larger particles that were detected by the PDI.

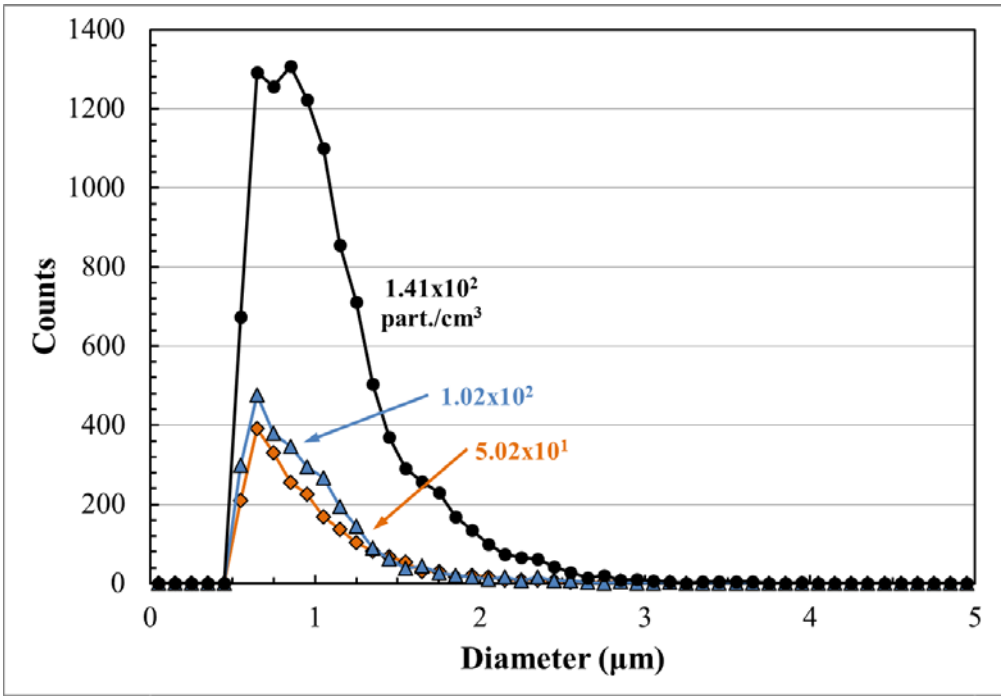

Fig. 12. Consecutive PDI analyses taken on 11/19/2013 starting at 08:27 at an H_2SO_4 injection rate of 1.5 mL/min. Absorber outlet temperature was 15.5 ℃ (10-min. average).

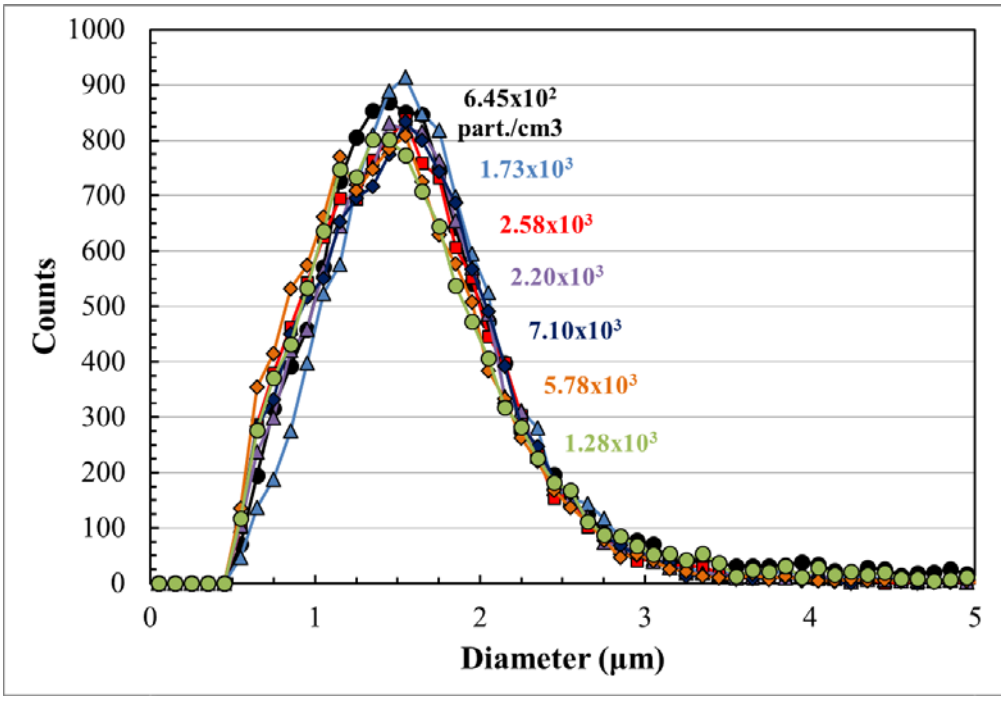

Fig. 13. PDI analyses taken on 11/21/2013 starting at 11:16 at an H_2SO_4 injection rate of 1.5 mL/min. Samples were not consecutive. Absorber outlet temperature was 38.5 ℃ (10-min. average).

3.5. Pilot Plant Data Reconciliation

Data from the pilot plant campaign at the J.J. Pickle Research Campus (PRC) were used to validate absorber models developed in Aspen Plus® within the Independence thermodynamic and kinetic framework. The model validation process included quantification of error in the pilot plant data and reconciliation of pilot results with model prediction by variation of global model correction factors. The error quantification and pilot plant data verification found that CO_2 and PZ component material balances closed within 95% confidence intervals, confirming internal consistency in the pilot data.

The two model parameters used to reconcile the November 2013 campaign were CO_2 lean loading and effective interfacial mass transfer area of the packing. The results indicated that a 7.3% correction in lean CO_2 loading or a 39% decrease in the packing mass transfer area enabled the model to match pilot plant mass and energy balance results (Table 5). Surprisingly, these results were consistent with the data reconciliation completed for the October 2011 campaign even though the pilot plant operating conditions were different (Table 6). The November 2013 campaign was conducted with 3.7 m PZ instead of 8 m PZ and used RSP 250 instead of GTC 350Z. RSP 250 has a dry mass transfer area of 250 m^2/m^3 and a corrugation angle of 45 degrees, whereas GTC 350Z has an area of 350 m^2/m^3 and a corrugation angle of 70 degrees.

One potential sources of bias may be the manual titrations for loading measurements completed for the pilot plant campaign or the bench-scale data used to develop the Aspen Plus® solvent model.

Table 5. Model Corrections Required for November 2013 and October 2011 PZ Pilot Plant Campaigns.

Parameter	Correction Factor: November 2013	Correction Factor: October 2011
CO_2 Correction	1.073 $\pm$ 0.013	1.075 $\pm$ 0.011
Interfacial Area	0.61 $\pm$ 0.01	0.74 $\pm$ 0.03
Interfacial Area (Corrected for different packing used)	0.74 $\pm$ 0.01	0.74 + 0.03

Table 6. Operating Conditions for the November 2013 and October 2011 Pilot Campaigns.

Campaign	November 2013	October 2011
Solvent Concentration (m)	3.6–3.75	7.2–7.9
Gas Rate (actual m^3/min)	9.9	9.9–19
Liquid Rate (m^3/hr)	2.7	2.7–3.9
Absorber Packing [Type/Sp. Area (m^2/m^3)/Angle]	Hybrid/250/Y	Structured/350/Z
Intercooling	Yes/No	Yes
Number of Runs	4	11

4. Conclusions

The 2013 SRP pilot plant campaign demonstrated 75 and 90% CO_2 removal with 3.7 m PZ and reliable operation with the modified single-stage flash with cold rich bypass. The gas rate was 9.9 m^3/min and the liquid to gas (L/G) ratio was 3.7–4.0 (mass/mass). Some issues with the reliable operation the LVI aerosol generator were identified. A Phase Doppler Interferometer (PDI) analyzer from Artium Technologies, Inc. was used to measure PZ aerosol droplet sizes and distributions at the absorber gas outlet. An FTIR system with new upgraded heated probes was used to make measurements of total PZ concentrations. Measurements by the PDI, FTIR, and manual stack sampling LVI all showed that PZ aerosols were formed when the LVI was operating properly. The results showed that PDI was able to measure aerosol droplets down to 0.5 microns, which was the limit of the demonstration unit that was used. A third

generation PDI instrument with a 0.1 micron resolution limit will be developed and tested in a future pilot plant campaign.

Acknowledgements

This work was supported by the CO_2 Capture Pilot Plant Program (C2P3), Texas Carbon Management Program (TxCMP), U.S. Department of Energy Award Number DE-FE0005654 and DE-FE0013188, Emerson Process Management, and Raschig-Jaeger Technologies.

The authors declare the following competing financial interest(s): One author of this publication consults for Southern Company and for Neumann Systems Group on the development of amine scrubbing technology. The terms of this arrangement have been reviewed and approved by the University of Texas at Austin in accordance with its policy on objectivity in research. The authors have financial interests in intellectual property owned by the University of Texas that includes ideas reported in this paper.

References

[1] G. T. Rochelle, E. Chen, S. A. Freeman, D. H. Van Wagener, Q. Xu and A. K. Voice, "Aqueous PZ as the new standard for CO2 capture technology," *Chem Eng J.*, vol. 171, no. 3, p. 725–733, 2011.

[2] S. Freeman, R. Dugas, D. Van Wagener, T. Nguyen and G. Rochelle, "Carbon dioxide capture with concentrated, aqueous piperazine," *International Journal of Greenhouse Gas Control*, vol. 4, no. 2, pp. 119-124, 2010.

[3] S. M. Fulk and G. T. Rochelle, "Quantification of total piperazine emissions by FTIR under variable bench-scale absorber conditions. Presented at GHGT-12, Austin, Texas, October 5-9, 2014," *Energy Procedia*, 2015.

Available online at www.sciencedirect.com

ScienceDirect

Energy Procedia 00 (2013) 000–000

Energy Procedia

www.elsevier.com/locate/procedia

GHGT-12

Optimization of stripping piperazine with variable rich loading

Junyuan Ding[a] Yu-Jeng Lin[a] Gary T. Rochelle[a] *

[a]*Department of Chemical Engineering, TheUniversity of Texas at Austin, 200 E. Dean Keeton St., C0400, Austin, TX 78712-1589, USA*

Abstract

Membrane Technology and Research, Inc. has proposed a hybrid system combining amine scrubbing with membrane technology to reduce energy cost. Previous studies of CO_2 absorption mainly focused on coal-fired flue gas with 12% CO_2. However, in the hybrid process, the CO_2 in the flue gas can be enriched to 20%. Natural gas turbines will have flue gas with as little as 3% CO_2. Based on the arrangement, the hybrid amine/membrane system provides a gas to the system that has double the CO_2 concentration of normal flue gas, reduces the volume of gas sent to the capture unit, or reduces the removal requirements for the capture unit.

The objective of this work is to minimize the total energy use of stripping concentrated piperazine (PZ) at rich loading when treating flue gas from 3 to 20% inlet CO_2. The base-case stripping configuration is the advanced flash stripper with warm rich bypass and cold rich exchanger bypass. . This configuration includes two split cross-exchangers in series, a convective steam heater, a smaller stripper column, a low residence time flash tank, and stripping at high temperature to produce CO_2 at 5 to 17 bar. Rich loading in 5 and 8 m PZ was varied from 0.37 to 0.43 mol CO_2/mol N. For each rich loading, lean loading was optimized to minimize the total equivalent work. The "Independence" model for PZ in Aspen Plus® was used to simulate the stripping performance.

Because 5 m PZ has a lower viscosity than 8 m PZ, it can achieve a reduced approach temperature in the cross exchanger. The total energy performance for 5 m PZ is practically the same as 8 m PZ, even though the capacity of 5 m PZ is lower. Significantly more energy is required to regenerate solvents with lower rich loading. As CO_2 rich loading increases, the equivalent work requirement decreases for the same loading difference between rich and lean.

Stripping data for 24 cases, including heat duty, equivalent work, CO_2 output pressure, and optimal cold and warm rich bypass were used to build a correlation with CO_2 rich and lean loading. The Second Law efficiency based on the ratio of stripping minimum work and total ideal work was introduced to make the most of stripping work. The Second Law efficiency has a maximum value at a specific CO_2 loading.

Keywords: advanced flsh stripper, total equivalent work, Second Law efficiency

1. Introduction

A hybrid amine/membrane CO_2 capture model is being developed by combining a CO_2 membrane separator with the absorber/stripper [1]. The membrane separator has been developed by Membrane Technology and Research, Inc. (MTR). The absorbing and stripping performance is simulated using the Independence model for PZ in Aspen Plus [2,3]®.

Due to the outstanding energy properties of aqueous PZ, including high CO_2 capacity, high thermal stability, moderately high viscosity, oxidative degradation resistance, and low volatility in CO_2-loaded solutions, it is a superior solvent for CO_2 capture by amine scrubbing. 5 m PZ solves the precipitation problem that the more viscous 8 m PZ causes in the solvent loop.

This work focuses on simulating the energy performance of CO_2 rich loading of 0.37, 0.40, and 0.43 mol/equiv PZ with 5 m PZ. Output CO_2 pressure, heat duty, compression work, pump work, and cold/warm rich bypass are recorded and calculated. For each CO_2 rich loading, there is an optimal lean loading which requires the minimum equivalent work for CO_2 scrubbing.

If most of the gas were sent to the membrane unit, a large area of membrane would be needed to achieve efficient removal of the CO_2 into the air stream. This would be expensive, but would have the benefit that the concentration of CO_2 in the flue gas would increase to around 25%.

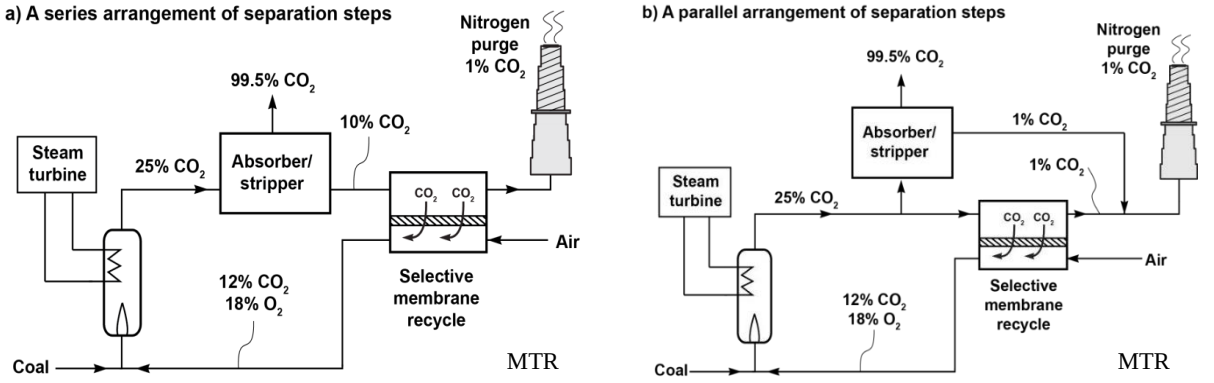

Fig. 1. Two configurations of hybrid amine/membrane CO_2 capture model: (a) a series arrangement of separation steps; (b) a parallel arrangement of separation steps [4].

There are two possible combination configurations of an absorption/stripper and a selective membrane recycle unit. Figure 1 (a) shows the series design. The stripper column does not have to regenerate very lean absorbent, and so needs less reboiler energy and the pressure of the column increases, which reduces the compression work. Figure 1 (b) shows the parallel arrangement, in which the CO_2 separation step treats about half of the total gas stream. The gas treated by the absorber is less in volume and has a higher loading difference, so the absorber and direct contact cooler can be much smaller. Reboiler duty will also decrease.

The advanced flash stripper with cold rich bypass and warm rich bypass offers better energy performance than the simple stripper [5]. A part of the CO_2 rich solvent goes through the upper cross exchanger to recover the stripping steam heat loss, as shown in Figure 2. The warm rich bypass split from the rich solvent between two cross exchangers mixes with the cold rich bypass, and then feeds into the flash stripper. The regenerated solvent coming down from the two strippers flows back across the two exchangers and serves as CO_2 lean solvent [6].

Aqueous PZ is a superior solvent for CO_2 capture by amine scrubbing. 8 m PZ was widely used in previous work, but with high CO_2 concentration flue gas protonated piperazine carbamate may precipitate in the rich end of the absorber column. 5 m PZ avoids this problem by dilution below the solid solubility. In addition, 5 m PZ has significantly lower viscosity than 8 m PZ, resulting in a greater heat transfer coefficient, reducing the capital cost of

the cross exchanger [7,8].

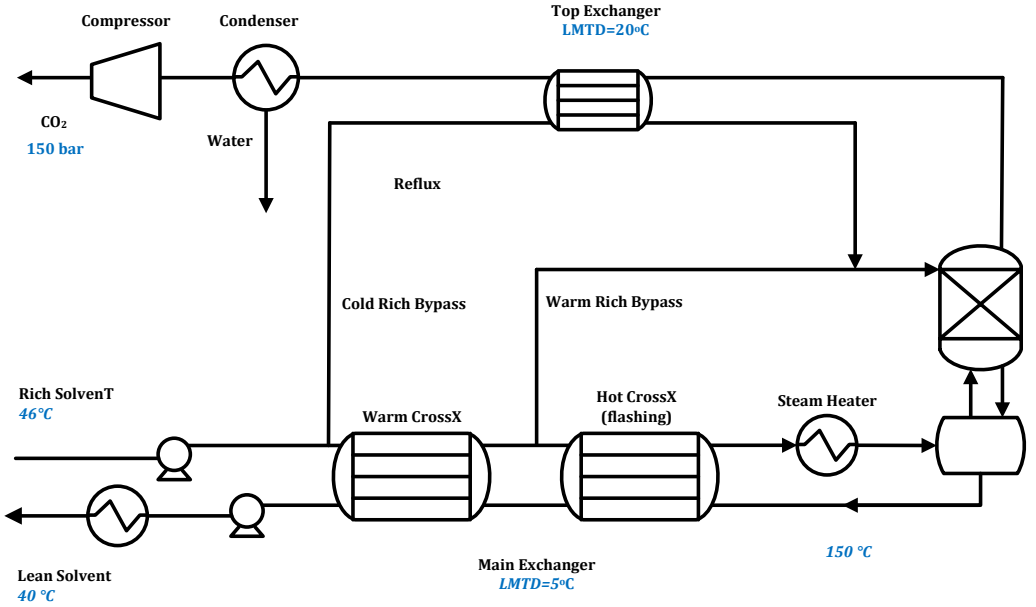

Fig. 2. Stripping configuration using 5 m PZ

2. Methods

2.1 Hybrid amine/membrane

The amine regeneration system for the hybrid amine/membrane process was simulated by the Independence model in Aspen Plus®. Figure 2 shows the advanced flash stripper configuration used. All of these cases are simulated using 5 m PZ stripping at 150 °C, main exchanger LMTD = 5 °C, top exchanger LMTD = 20 °C, lean solvent output at 40 °C, and 150 bar CO_2 product.

When CO_2 rich loading and lean loading of the advanced flash stripper are given, the overall equivalent work will vary with the cold rich bypass and warm rich bypass. There is an optimal point where the equivalent work is minimized. The corresponding cold rich bypass and warm rich bypass is the optimal bypass for this specific CO_2 rich and lean loading. In order to distinguish this from the bypass at the optimal lean loading for each CO_2 rich loading, the former is described as "bypass" and the latter "optimal bypass".

Regression analysis in Excel is used to build the correlations of heat duty, equivalent work, CO_2 output pressure, optimal cold and warm rich bypass, and CO_2 rich and lean loading.

2.2 Equivalent work calculation

Equivalent work replaces heat duty as a more general metric of energy use than heat duty alone. It is defined as the sum of pump work, compression work, and heat work, as Equation 1 shows.

$$W_{eq}\ (\text{kJ/mol } CO_2) = W_{heat} + W_{pump} + W_{comp} \quad (1)$$

Heating work can be generated from the heat duty of the reboiler using Equation 2. A typical value of 90% is used for the turbine efficiency (η) and T_{sink} is taken as 313K.

$$W_{heat}\ (\text{kJ/mol } CO_2) = \eta\left(\frac{T_{source} + \Delta T - T_{sink}}{T_{source} + \Delta T}\right)Q_{reb} \quad (2)$$

Compression work can be approximated by Equation 3, which is typically assumed to be at a discharge pressure of 150 bar [9].

$$W_{comp}\ (\mathrm{kJ/mol\,CO_2}) = \begin{cases} 4.572\ln(\frac{150}{P_{in}}) - 4.096 \cdots P_{in} \le 4.56bar \\ 4.023\ln(\frac{150}{P_{in}}) - 2.181 \cdots P_{in} \ge 4.56bar \end{cases} \quad (3)$$

2.3 Minimum work

Minimum work is the total reversible work required considering the stripping process as a Carnot cycle. Minimum work can also can be estimated as $W_{min}\ (\mathrm{kJ/mol\ CO_2}) = \Delta G = \Delta H - T\Delta S$.

In a real process, part of the work produced is consumed by irreversible operations, such as the cross exchanger, condenser, reboiler, and pump. The Second Law efficiency, which is the ratio of minimum work to total ideal work, is chosen to reflect the utilization of energy. To estimate total ideal work the heat work, W_{heat}, is replaced by ideal heat work, $W_{heat,ideal}$, setting the turbine efficiency in Equation 2 to 1.0.

3. Results and Discussion

3.1 Energy performance of the stripper

Table 1 shows the energy performance of the stripper using 5 m PZ at different CO_2 loadings. The energy consumption with high CO_2 rich loading is lower than that with low CO_2 rich loading.

For each rich loading, total energy performance changes with lean loading. At rich loading of 0.37 mol CO_2/mol PZ and lean loading of 0.23 mol CO_2/mol PZ, rich loading of 0.40 mol CO_2/mol PZ and lean loading of 0.26 mol CO_2/mol PZ, and rich loading of 0.43 mol CO_2/mol PZ and lean loading of 0.29 mol CO_2/mol PZ, the total equivalent work is the minimum for each rich loading. At these three minimum points, the loading difference between rich solvent and lean solvent are all 0.14 (Figure 3).

Table 1. Energy performance of stripper using 5 m PZ with stripping at 150 °C, main exchanger LMTD = 5 °C, top exchanger LMTD = 20 °C.

Rich loading (*mol CO2/mole PZ*)	Lean loading (*mol CO2/mole PZ*)	Total equivalent work (*kJ/mole CO_2*)	Heat duty (*kJ/mole CO_2*)	Stripping pressure (*kPa*)	Cold rich bypass (%)	Warm rich bypass (%)	Second law efficiency (%)
0.37	0.15	38.3	109.1	494	16	58	67.6
0.37	0.17	37.3	105.6	514	14	51	67.8
0.37	0.19	36.8	103.8	540	11	46	67.2
0.37	0.21	36.4	102.9	571	10	40	66.4
0.37	0.23	36.2	102.7	613	8	34	65.1
0.37	0.25	36.4	103.9	667	6	24	63.3
0.37	0.27	36.9	106.2	738	5	18	60.8
0.37	0.31	41.2	121.7	960	3	10	51.4
0.4	0.18	34.9	96.1	527	12	46	69.2
0.4	0.2	34.4	94.4	556	10	41	68.7
0.4	0.22	34.0	93.4	593	8	34	67.7
0.4	0.24	33.7	93.2	639	7	28	66.4
0.4	0.26	33.5	93.2	701	6	21	65.1
0.4	0.28	33.7	94.7	784	5	15	62.9
0.4	0.3	34.3	97.4	894	4	10	60.0

0.4	0.34	39.0	112.9	1243	2	3	49.6
0.43	0.21	32.1	85.7	573	8	34	69.7
0.43	0.23	31.7	84.6	613	7	29	68.9
0.43	0.25	31.2	83.7	668	6	22	68.0
0.43	0.27	30.9	83.5	739	5	18	66.6
0.43	0.29	30.7	83.7	834	4	14	65.0
0.43	0.31	30.9	85.0	959	3	12	62.7
0.43	0.33	31.5	87.8	1133	2	8	59.4
0.43	0.37	37.4	105.1	1683	1	4	46.7

As lean loading increases, CO_2 output pressure increases significantly and pump work increases with it (Figure 4). At the same time, the compression work required to compress CO_2 to 150 bar decreases. As the loading difference between rich and lean solvent decreases, the CO_2 capacity decreases and heat requirement increases. Also, as CO_2 partial pressure increases, the selectivity of CO_2 over water increases, which reduces the work requirement from steam stripping.

Due to these overall effects, an optimal point exists where the required work is minimized as a function of lean loading. This point is defined as the optimal CO_2 lean loading. The equivalent work of rich loading of 0.37 mol CO_2/mol PZ has a minimum value at CO_2 lean loading 0.23 mol/equivalent PZ. The equivalent work of rich loading of 0.40 mol CO_2/mol PZ has a minimum value at CO_2 lean loading 0.26 mol/equivalent PZ. The equivalent work of rich loading of 0.43 mol CO_2/mol PZ has a minimum value at CO_2 lean loading 0.29 mol/equivalent PZ.

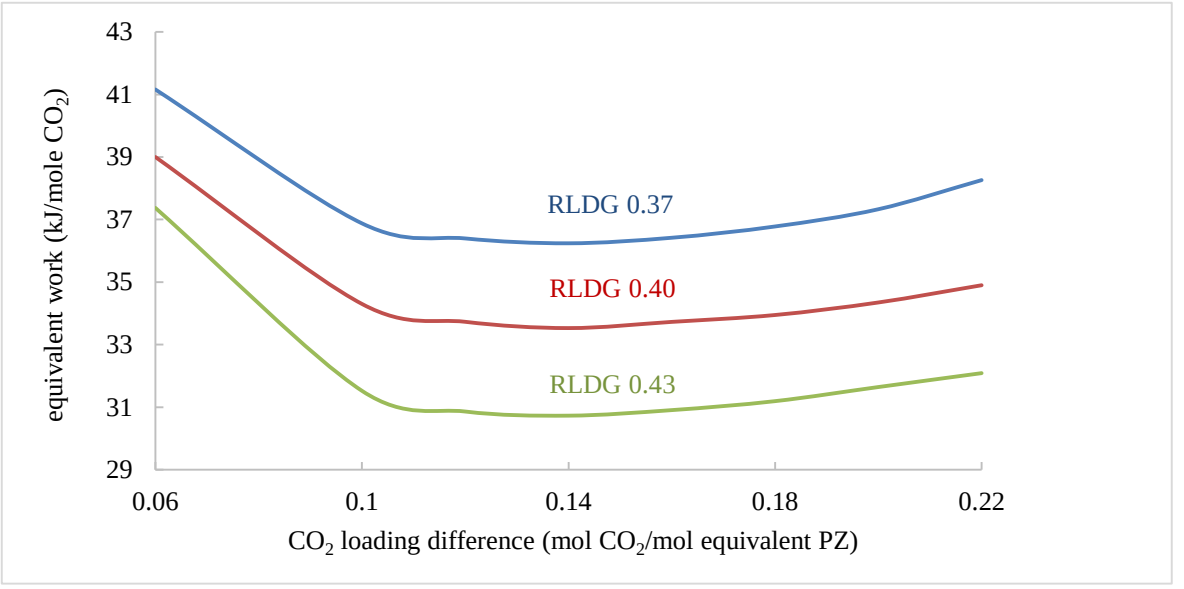

Fig. 3. Total equivalent work of the advanced flash stripper with 5 m PZ at different rich loadings. At a loading difference of 0.14 mol CO_2/mol PZ, the three different rich loadings have the minimum values of equivalent work.

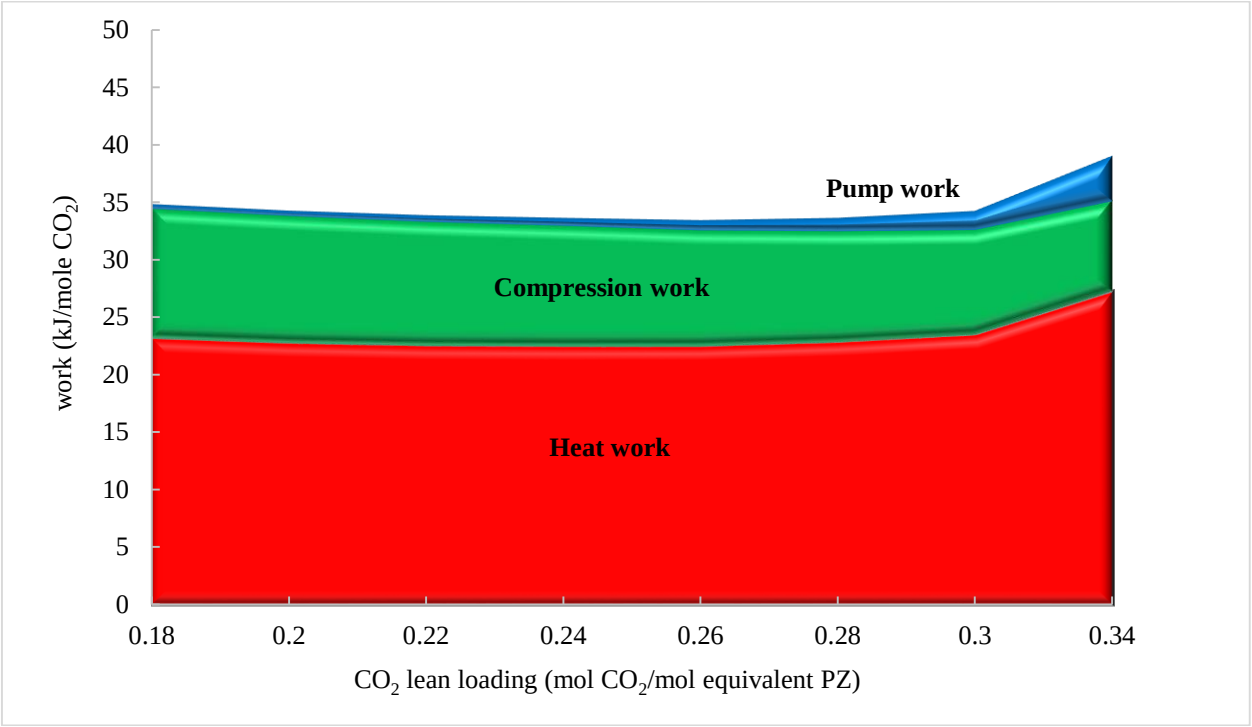

Fig. 4. Total equivalent work and its elements for CO_2 rich loading 0.4 mole/equivalent PZ (Optimal lean loading: 0.26 CO_2 mole/equivalent PZ).

3.2 Regression analysis over a wider range of rich loading

Total equivalent work, heat duty, stripping pressure, warm rich bypass and cold rich bypass for each case in Table 1 were regressed in Excel as a function of CO_2 rich loading and lean loading. Comparisons between simulation results and predicted values by regression are shown in Figures 5-9.

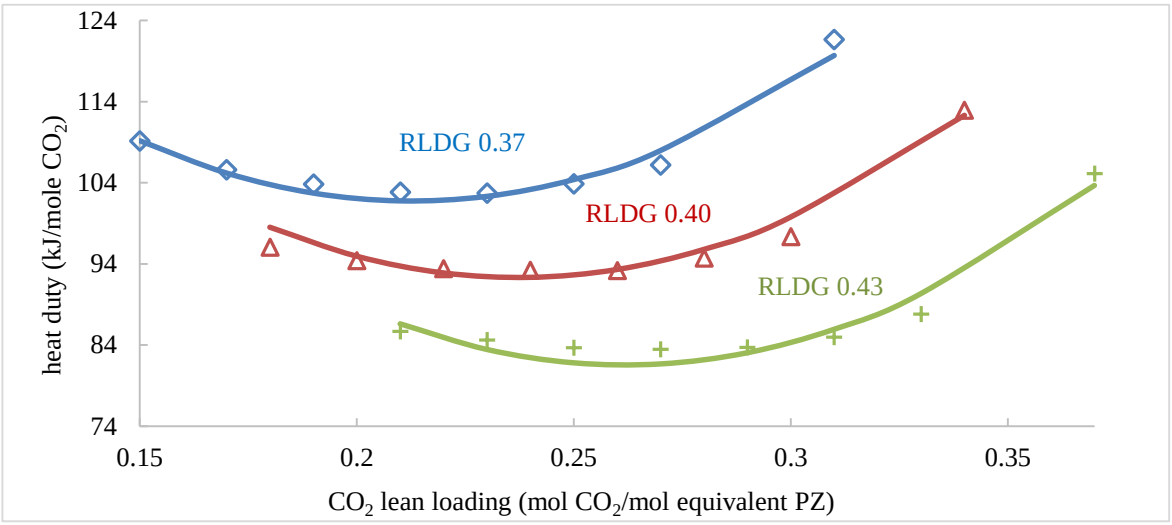

Fig. 5. Heat duty and its predicted value at different rich and lean loadings. Lines predicted by Eq 4.

Heat duty of the reboiler is composed of sensible heat requirement, latent heat requirement, and stripping steam heat requirement [2]. Heat work accounts for about 70% of the total equivalent work. Figure 5 shows the comparison of heat duty for variable CO_2 rich loading. Heat duty also has its minimum value at a CO_2 loading difference of 0.14 mol CO_2/mol PZ. The sensible heat requirement dominates at high lean loading (low capacity). The stripping steam requirement dominates at low lean loading.

The expression of heat duty (Figure 5) by regression is:

$$Q = 119.1 + 342.2LLDG + 1891.5LLDG^2 + 497.7RLDG^2 - 3098.8RLDG * LLDG \qquad (4)$$

RLDG represents rich loading and LLDG represents lean loading.

Figure 3 and Figure 6 compare the total equivalent work for variable CO_2 rich loading. As CO_2 rich loading increases, the equivalent work requirement decreases for the same loading difference between rich and lean. Since CO_2 capacity becomes dominant at high lean loading, total equivalent work for all these rich loadings changes rapidly at high lean loading values and becomes flat at the low lean loading end.

The expression of total equivalent work (Figure 6) by regression is:

$$W_{eq} = 39.4 + 101.0LLDG + 583.2LLDG^2 + 177.8RLDG^2 - 961.9RLDG * LLDG \qquad (5)$$

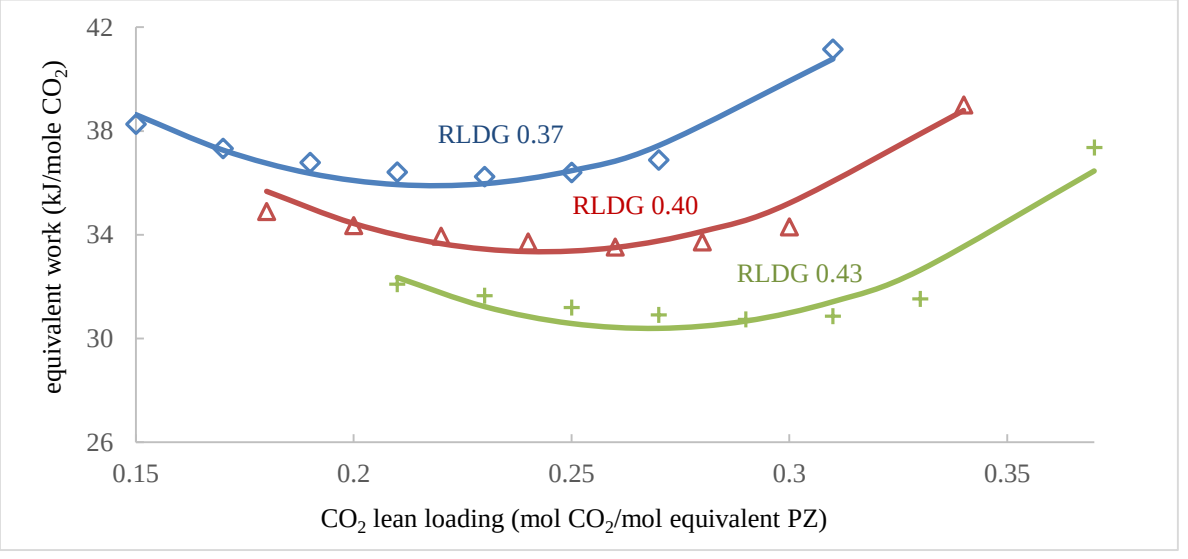

Fig. 6. Equivalent work and its predicted value at different rich and lean loadings. Lines predicted by Eq 5.

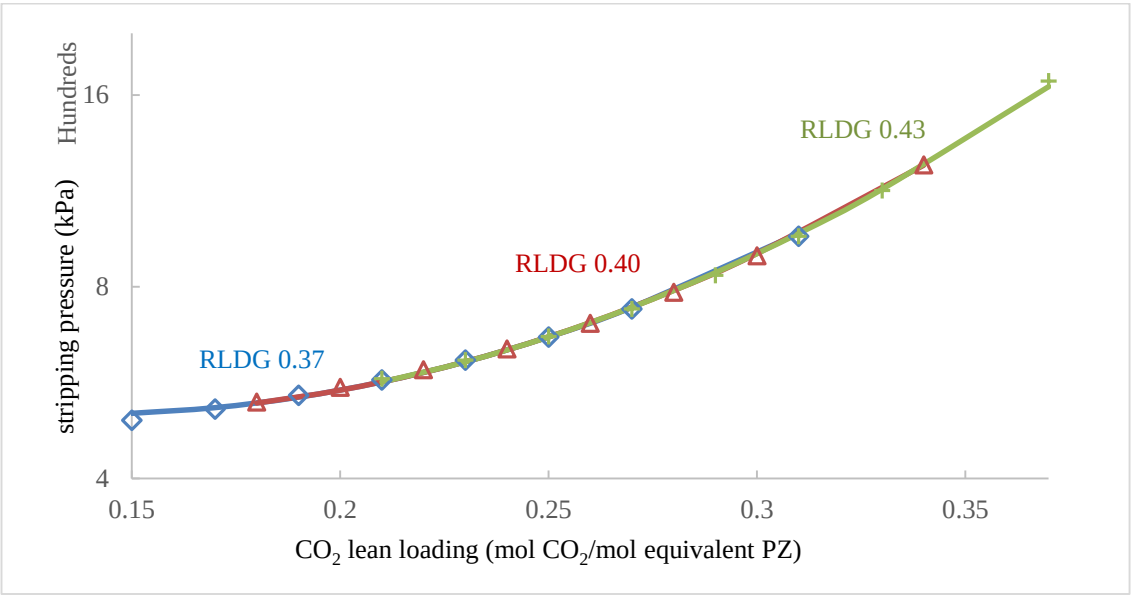

Fig. 7. Stripping pressure and its predicted value at 0.37 to 0.40 rich loading. Bottom T = 150 ºC. Lines predicted by Eq 6.

Thermodynamically, the stripping pressure at 150 ºC (Figure 7) depends only on the lean loading and is given empirically by:

$$\ln P = 6.6 - 5.9LLDG + 21.7LLDG^2 \qquad (6)$$

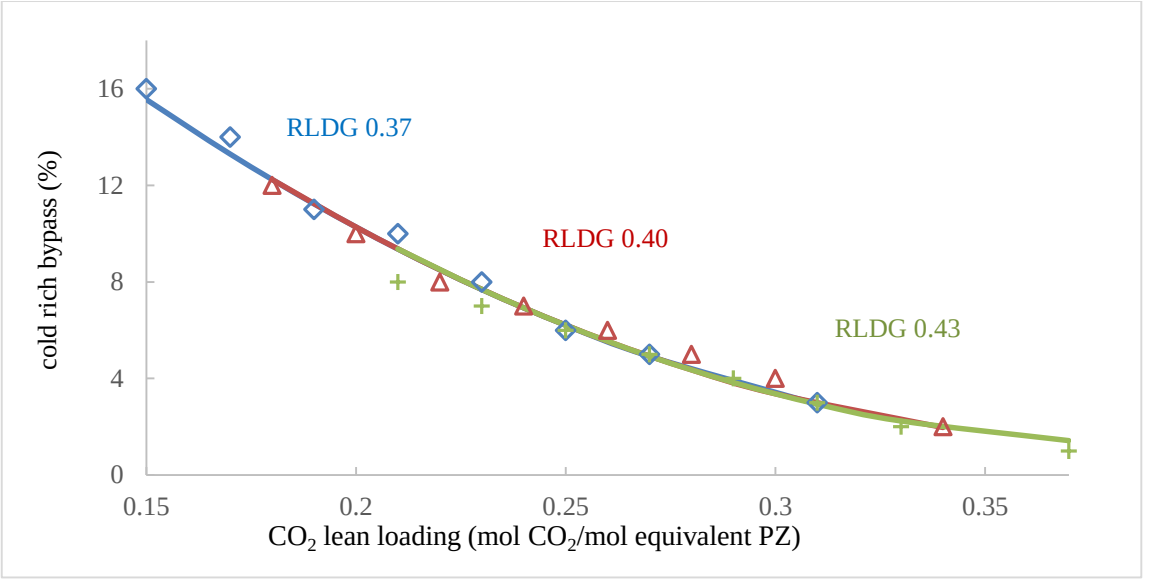

Fig. 8. Cold rich bypass. Lines predicted by Eq 7.

The optimal cold rich bypass (Figure 8) is not a function of rich loading and is given by:

$$CRBP = 0.38 - 1.91LLDG + 2.44LLDG^2 \qquad (7)$$

As CO_2 lean loading increases, cold rich bypass plays a less important role in the advanced flash stripper, because for high CO_2 lean loading, less water is heated to the vapor phase, and so less steam stripping heat needs to be recovered by cold rich bypass. The cold rich bypass can be removed from the advanced flash stripper design when stripping very high CO_2 lean loading.

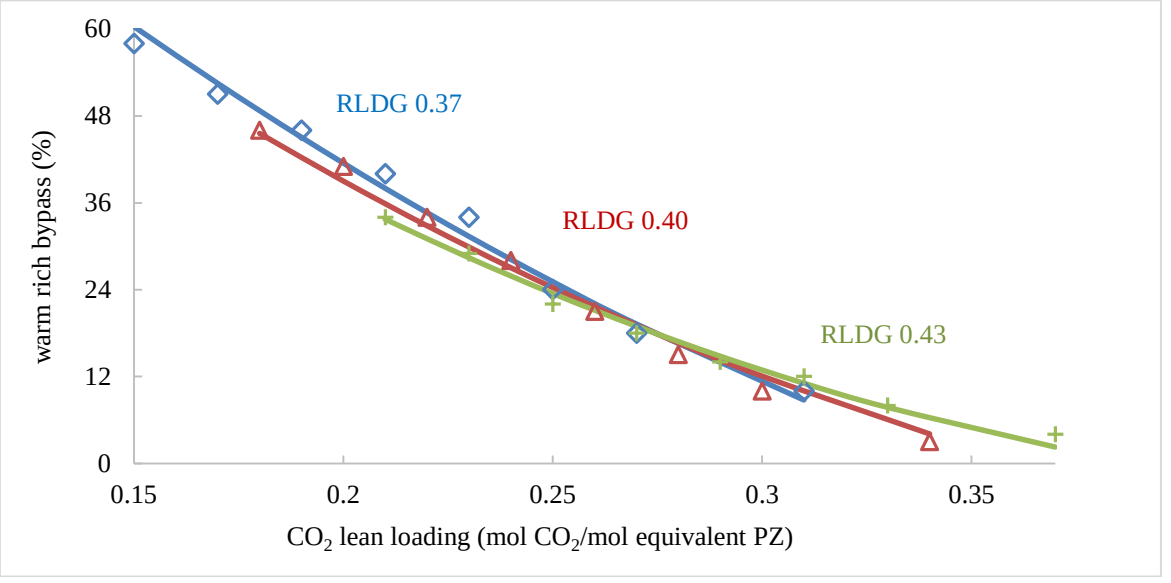

Fig. 9. Optimum warm rich bypass in the advanced flash stripper with 5 m PZ. Lines predicted by Eq 8.

As Figure 9 shows, the expression of the optimal cold rich bypass is:

$$WRBP = 2.43 - 9.56LLDG + 4.98LLDG^2 - 3.00RLDG^2 + 1.09RLDG * LLDG \quad (8)$$

Warm rich bypass depends in large part on CO_2 lean loading, and changes in the same way that cold rich bypass does. It also depends on CO_2 rich loading. Warm rich bypass at low CO_2 rich loading decreases more rapidly with CO_2 lean loading than that at high CO_2 rich loading. At low CO_2 lean loading, low CO_2 rich loading has a greater warm rich bypass. All the lines decrease and cross at the same point, CO_2 lean loading 0.27 mol/equivalent PZ. At the high CO_2 lean loading side, warm rich bypass of high CO_2 rich loading becomes higher than that of low CO_2 rich loading, but they all tend to zero. Combined with the profile of cold rich bypass, both warm rich bypass and cold rich bypass play less important roles in recovering energy at high CO_2 lean loading. In other words, at high CO_2 lean loading, the simple stripper is more economical than the advanced stripper because of the cross exchanger capital cost.

Similarly, optimal lean loading at each CO_2 rich loading and its corresponding stripping pressure, heat duty, total equivalent work, optimal cold rich bypass, and warm rich bypass are regressed as functions of rich loading:

$$OPTLLDG = RLDG - 0.14 \quad (9)$$

$$OPTQ = 223.95 - 337.07RLDG + 25.30RLDG^2 \quad (10)$$

$$OPTW_{eq} = 62.88 - 54.93RLDG - 46.13RLDG^2 \quad (11)$$

$$OPT \ln P = 8.03 - 12.51RLDG + 22.04LLDG^2 \quad (12)$$

$$OPTCRBP = 0.33 - 0.67RLDG \quad (13)$$

$$OPTWRBP = 6.88 - 30.00RLDG + 33.33RLDG^2 \quad (14)$$

3.3 The Second Law efficiency

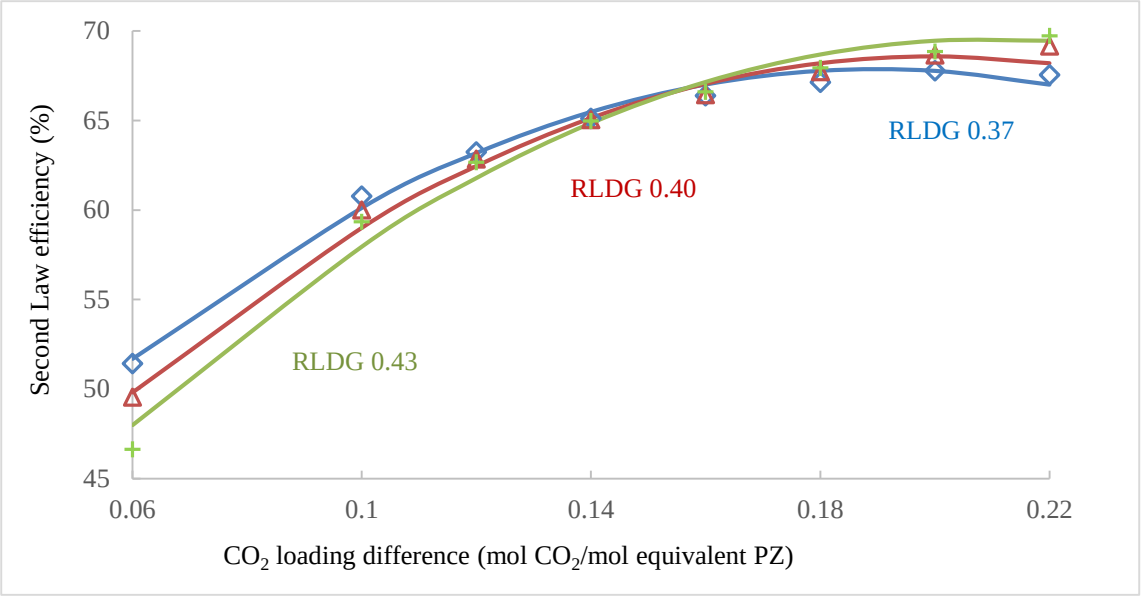

Fig. 10. Second law efficiency of the advanced flash stripper with 5 m PZ. Marks calculated by W_{min} /$W_{total,ideal}$. Lines predicte by Eq 15.

Figure 10 shows the effective utilization of stripping energy represented by the Second Law efficiency. CO_2 loading difference is calculated by CO_2 rich loading minus CO_2 lean loading. The values of the Second Law efficiency are shown in Table 1. The regressed expression for the Second Law efficiency is:

$$EFF = 0.76 - 1.27LLDG - 9.58LLDG^2 - 2.84RLDG^2 + 12.74RLDG * LLDG \quad (15)$$

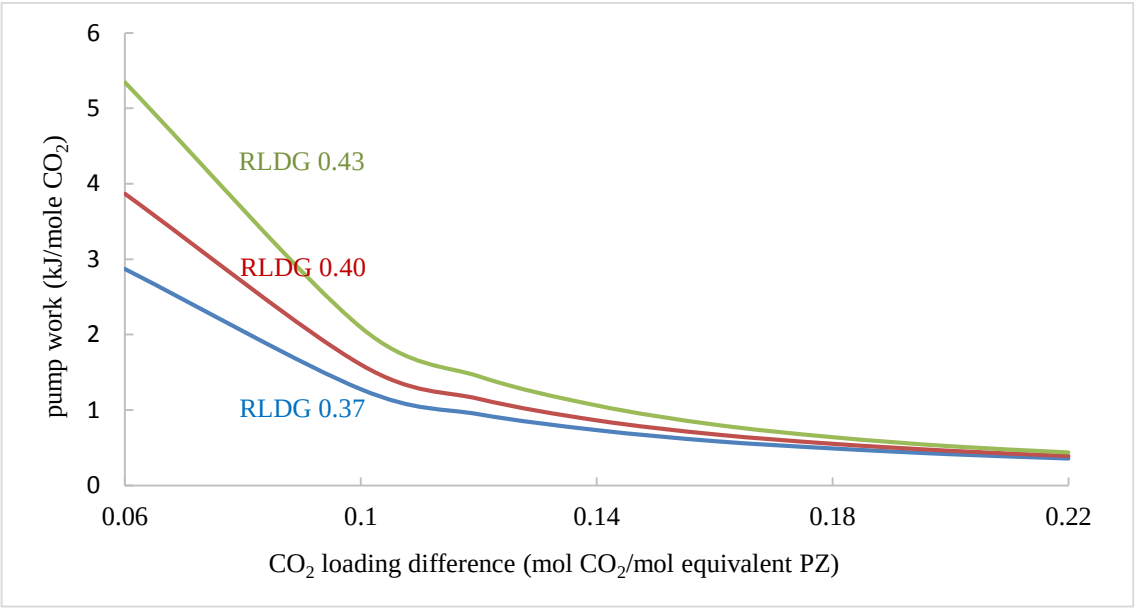

Fig. 11. Pump work at variable CO_2 rich loading changing

The curves on figure 10 at different rich loading cross at a CO_2 loading difference, 0.14 mole CO_2/mol equivalent PZ,

which is the same as that giving the optimum equivalent work. The variation of efficiency with lean loading may result in part from the contribution of rich pump work as shown in Figure 11. The role of the bypass flows may also change with rich loading and delta loading as shown in Figure 12.

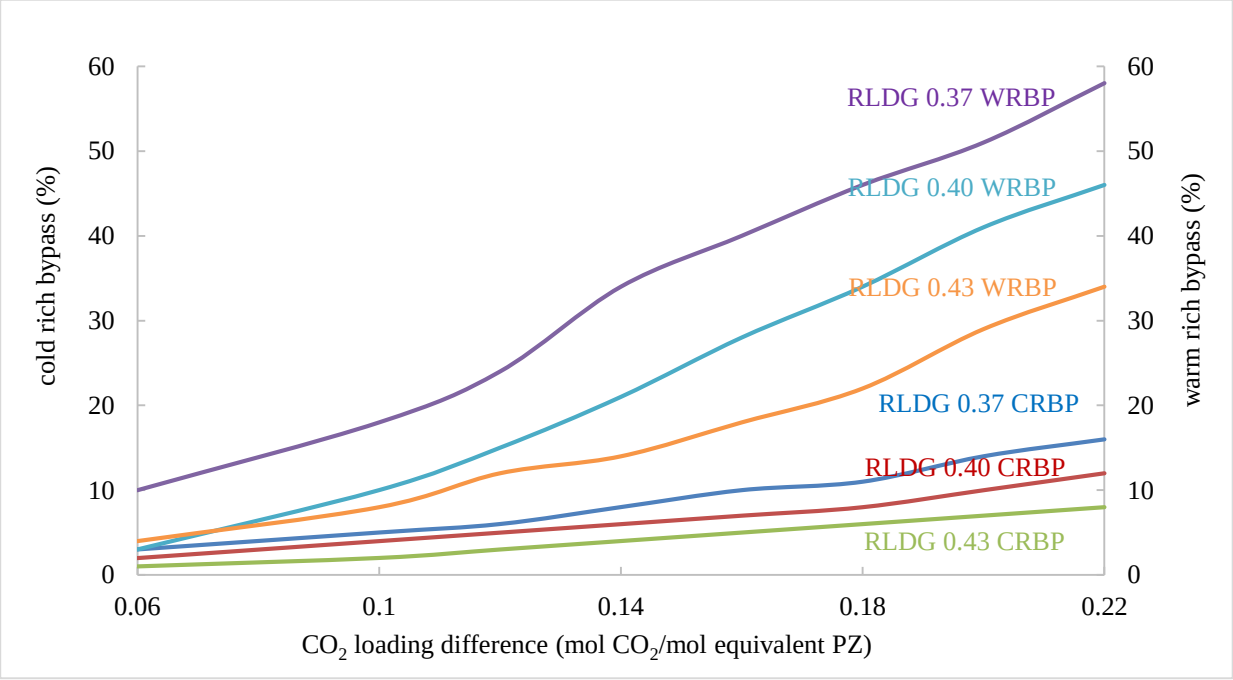

Fig. 12. Cold and warm rich bypass for different CO_2 rich loading changing with CO_2 loading difference. The upper three lines are warm rich bypass presented on the right Y axis in %. The lower three lines are cold rich bypass presented on the left Y axis in %.

Due to the combined effect of pump irreversibility and cross exchanger irreversibility, there is a maximum efficiency with 0.37 mol/equivalent PZ CO_2 rich loading at 0.2 mol/equivalent PZ CO_2 loading difference, as Figure 10 shows. Since bypass has less impact at high CO_2 rich loading, the efficiencies of the other two CO_2 rich loadings are still increasing at 0.22 mol/equivalent PZ CO_2 loading difference, but tend to flatten out. They may have maximum efficiency at higher CO_2 loading difference, where more energy recovery is required. If 5 m packing of the stripper is used instead of the current 2 m, the Second Law efficiency will be higher at the high loading difference area.

4. Conclusions

- As the CO_2 rich loading varies from 0.37 to 0.43, the optimum lean loading occurs at a loading difference of 0.14 mol/equivalent PZ CO_2 loading.
- The minimum total equivalent work decreases from 36.2 kJ/mol CO_2 to 30.7 kJ/mol CO_2 as the rich loading increases from 0.37 to 0.43.
- Heat duty, total equivalent work, stripping pressure, and bypasses are correlated as function of CO_2 rich loading and lean loading.

$$Q = 119.1 + 342.2LLDG + 1891.5LLDG^2 + 497.7RLDG^2 - 3098.8RLDG * LLDG$$

$$W_{eq} = 39.4 + 101.0LLDG + 583.2LLDG^2 + 177.8RLDG^2 - 961.9RLDG * LLDG$$

$$\ln P = 6.6 - 5.9LLDG + 21.7LLDG^2$$

$$CRBP = 0.38 - 1.91LLDG + 2.44LLDG^2$$

$$WRBP = 2.43 - 9.56LLDG + 4.98LLDG^2 - 3.00RLDG^2 + 1.09RLDG * LLDG$$

- The Second Law efficiency of the advanced flash stripper varies from 45 to 70% as the delta loading varies from 0.06 to 0.22. At the optimum delta loading of 0.14 the efficiency is 65%.

Acknowledgements

This paper is based in part on work supported by the Department of Energy under Award Number DE-FE0013188. The authors also acknowledge the financial support of the Texas Carbon Management Program.

The authors declare the following competing financial interest(s): One author of this publication consults for Southern Company and for Neumann Systems Group on the development of amine scrubbing technology. The terms of this arrangement have been reviewed and approved by the University of Texas at Austin in accordance with its policy on objectivity in research. The authors have financial interests in intellectual property owned by the University of Texas that includes ideas reported in this paper.

References

[1] Merkel TC, Lin H, Wei X. Power plant post-combustion carbon dioxide capture: An opportunity for membranes. Membrane Technology and Research, Inc.. *Journal of Membrane Science.* 2010;359: 115-125.

[2] Frailie PT. *Modeling of Carbon Dioxide Absorption/Stripping by Aqueous methyldiethanolamine/Piperazine.* Ph.D. Dissertation, The University of Texas at Austin: Austin, 2014.

[3] Zhang Y, Rochelle GT. Absorber Performance with High CO_2. The University of Texas at Austin. Presented at GHGT-12, Austin, United States, October 5-9, 2014.*Energy Procedia*, 2014.

[4] Freeman B, Hao P, Baker R. Hybrid membrane-absorption CO_2 capture process. Presented at GHGT-12, Austin, United States, October 5-9, 2014.*Energy Procedia*, 2014.

[5] Madan T. *Modeling of Stripper Configurations for CO_2 Capture using Aqueous Piperazine*. M.S. Thesis, The University of Texas at Austin: Austin, 2013.

[6] Lin Y-J, Madan T, Rochelle GT. Regeneration with Rich Bypass of Aqueous Piperazine and Monoethanolamine for CO_2 Capture. *Industrial & Engineering Chemistry Research.* 2014;53: 4067–4074.

[7] Xu Q. *Thermodynamics of CO_2 Loaded Aqueous Amines.* Ph.D. Dissertation, The University of Texas at Austin: Austin, 2011.

[8] Freeman SA. *Thermal Degradation and Oxidation of Aqueous Piperazine for Carbon Dioxide Capture.* Ph.D. Dissertation, The University of Texas at Austin: Austin, 2011.

[9] Van Wagener DH. *Stripper Modeling for CO_2 Removal Using Monoethanolamine and Piperazine Solvents.* Ph.D. Dissertation, The University of Texas at Austin: Austin, 2011.

Available online at www.sciencedirect.com

ScienceDirect

Energy Procedia 00 (2013) 000–000

Energy Procedia

www.elsevier.com/locate/procedia

GHGT-12

Thermodynamic modeling of aqueous piperazine/N-(2-aminoethyl) piperazine for CO_2 capture

Yang Du[a], Gary T. Rochelle[a,*]

[a]*McKetta Department of Chemical Engineering, The University of Texas at Austin, 200 E Dean Keeton St. Stop C0400, Austin, TX 78712-1589, USA*

Abstract

Aqueous piperazine (PZ) blended with N-(2-aminoethyl) piperazine (AEP) is an attractive solvent for CO_2 capture from coal-fired power plants. A rigorous thermodynamic model was developed in Aspen Plus® to predict properties of PZ/AEP/H_2O/CO_2, using the electrolyte-Nonrandom Two-Liquid (eNRTL) activity coefficient model. A sequential regression was performed to represent CO_2 solubility, speciation, and amine volatility data over operationally significant loading and temperature ranges. The model predicts a CO_2 cyclic capacity of 0.86 mol/kg (PZ + AEP + water) for 5 m PZ/2 m AEP, compared to 0.50 mol/kg for 7 m MEA and 0.86 mol/kg for 8 m PZ. The predicted heat of absorption is 75 to 85 kJ/mol CO_2 in the operating loading range (0.288–0.380 mol CO_2/mol alkalinity). Speciation for PZ/AEP/H_2O at various CO_2 loading and temperature was also predicted, from which behavior of CO_2 in the amine system was proposed.

Selection and peer-review under responsibility of GHGT.

Keywords: Piperazine; Aminoethylpiperazine; CO_2 capture; eNRTL; Modeling

1. Introduction

Amine scrubbing has shown the most promise for effective capture of CO_2 from coal-fired flue gas [1]. However, with traditional amine solvents such as monoethanolamine (MEA), the energy penalty for solvent regeneration and CO_2 compression is prohibitive. Concentrated piperazine (PZ) has been proposed as a better solvent for CO_2 capture from coal-fired flue gas, with a 10% energy benefit compared to MEA [2,3]. The application of concentrated PZ is

* Corresponding author. Tel.: 1-512-471-7230; fax: 1-512-471-7060.
E-mail address: gtr@che.utexas.edu

1876-6102
Selection and peer-review under responsibility of GHGT.

limited by its low solubility in water at low temperature and lean CO_2 loading [3]. Blending less concentrated PZ with its structural analog N-(2-aminoethyl) piperazine (AEP) remediates the precipitation issue while conserving the most desirable characteristics of concentrated PZ [4].

To predict the overall performance of this amine blend, it is necessary to develop a rigorous thermodynamic model which can accurately predict the thermodynamic properties, specifically vapor-liquid equilibrium (VLE), calorimetric properties, and chemical reaction equilibrium.

The thermodynamic properties of a variety of aqueous amine solutions for CO_2 absorption have been successfully modeled with the electrolyte-Nonrandom Two-Liquid (eNRTL) model as a thermodynamic framework. Austgen [5] used the eNRTL model developed by Chen and coworkers [6] to model the VLE of carbon dioxide over aqueous N-methyl-diethanolamine (MDEA), monoethanolamine (MEA), diethanolamine (DEA), and Diglycolamine® (DGA®). Posey [7] improved the Austgen models by studying the activity coefficient of the amines at infinite dilution. An activity-based PZ-H_2O-CO_2 model was developed by Hilliard [8] in Aspen Plus®. Frailie [9] extended Hilliard's model to represent various thermodynamic properties of more concentrated PZ solutions and identified this model as the Independence model.

In this work, a thermodynamic model for PZ-AEP-H_2O-CO_2 system was developed in Aspen Plus® based on the Independence model [9]. Unavailable model parameters were obtained by regressing experimental data, or by reference to the Independence model results for PZ. Amine volatility and CO_2 solubility data were used in regression. NMR measurements were used to validate the model prediction of aqueous speciation distribution. Heat of absorption for this solvent was predicted at operating conditions.

2. Thermodynamic framework

The thermodynamic model built for PZ-AEP-H_2O-CO_2 in this work is based on the model for PZ-H_2O-CO_2 ("Independence" model) developed by Frailie [9] in Aspen Plus®. Therefore, the basic thermodynamic framework is identical to the Independence model: using the eNRTL model for liquid phase behavior and the Soave-Redlich-Kwong (SRK) equation for gas phase behavior.

2.1. Aqueous-Phase Chemical Equilibrium

AEP is a tri-amine with primary, secondary, and tertiary amine groups in its structure, leading to various protonated and carbamate species. The third pKa of AEP was reported to be below 4 at 25–50 ℃ [10], while the normal pH value in CO_2-loaded amine solution at the rich loading is typically well above 8. Therefore, the amount of tri-protonated AEP is extremely small in loaded solutions and it is excluded from consideration in this work. Both the primary and secondary amino groups of AEP can connect with a carboxyl group, leading to two isomers of AEP carbamate. Table 1 lists potential species in PZ-AEP-H_2O-CO_2. For simplicity, protonated species are not listed. To differentiate the carbon nuclei with different electronic environments, they are numbered for different species present.

Table 1. Molecular structure of the compounds in CO_2-loaded PZ-AEP aqueous solutions

Name	Molecular Structure
AEP	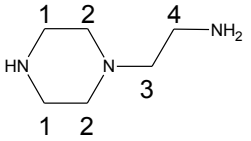

$AEPCOO^-$	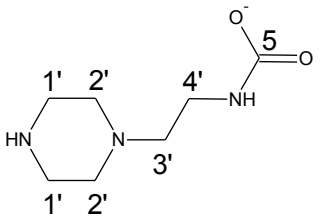
^-OOCAEP	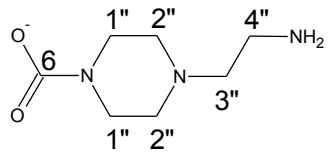
$AEP(COO^-)_2$	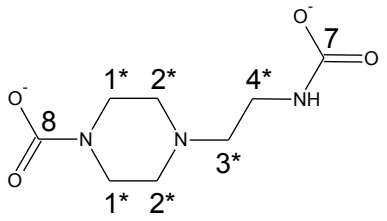
PZ	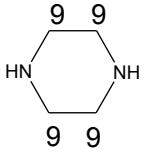
$PZCOO^-$	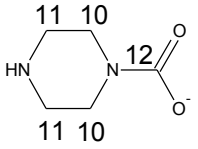
$PZ(COO^-)_2$	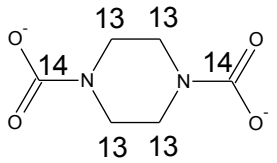
HCO_3^-/CO_3^{2-}	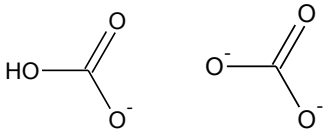

Besides the aqueous-phase chemical equilibrium reactions set up in the Independence model for PZ-H_2O-CO_2, the following reactions involving AEP species were used in this study.

$$AEP + H^+ \leftrightarrow AEPH^+$$

$$AEPH^+ + H^+ \leftrightarrow AEP(H^+)_2$$

$$AEPCOO^- + H^+ \leftrightarrow H^+AEPCOO^-$$

$$^-OOCAEP + H^+ \leftrightarrow {}^-OOCAEPH^+$$

$$H^+AEPCOO^- + H^+ \leftrightarrow (H^+)_2 AEPCOO^-$$

$$^-OOCAEPH^+ + H^+ \leftrightarrow (H^+)_2 AEPCOO^-$$

$$AEP(COO^-)_2 + H^+ \leftrightarrow H^+AEP(COO^-)_2$$

$$AEP + HCO_3^- \leftrightarrow AEPCOO^- + H_2O$$

$$AEP + HCO_3^- \leftrightarrow {}^-OOCAEP + H_2O$$

$$AEPH^+ + HCO_3^- \leftrightarrow H^+AEPCOO^- + H_2O$$

$$AEPCOO^- + HCO_3^- \leftrightarrow AEP(COO^-)_2 + H_2O$$

$$^-OOCAEP + HCO_3^- \leftrightarrow AEP(COO^-)_2 + H_2O$$

$$H^+AEPCOO^- + HCO_3^- \leftrightarrow H^+AEP(COO^-)_2 + H_2O$$

$$^-OOCAEPH^+ + HCO_3^- \leftrightarrow H^+AEP(COO^-)_2 + H_2O$$

AEP is an existing component in the Aspen Plus® databank. Other AEP-related species were added as new components. Following the treatment in the Independence model, AEP and zwitterions ($H^+AEPCOO^-$ and $^-OOCAEPH^+$) were modeled as Henry's components. Zwitterions were assigned an extremely low Henry's constant as they are expected to be non-volatile.

2.1.1. Reference state and units

In the Independence model, two different reference states are used depending on whether the species in consideration is a solvent or solute and the same treatment is followed in this work. The symmetric convention is applied for water as a solvent with the reference state as pure solvent at the system temperature and pressure:

$$\gamma_s \rightarrow 1 \text{ as } x_s \rightarrow 1 \quad (1)$$

The asymmetric convention was used for solutes (AEP, zwitterion, and ions) with the reference state as infinite dilution in water at the temperature and pressure of the system:

$$\gamma_i^* \rightarrow 1 \text{ as } x_i \rightarrow 0 \quad (2)$$

where γ_s is the symmetric activity coefficient of solvent and γ_i* the asymmetric activity coefficient of solutes.

2.1.2. Reaction equilibrium

The reaction equilibrium constant is expressed as follows:

$$K_j = \prod_i a_i^{\nu_{ij}} = \prod_i (x_i \gamma_i)^{\nu_{ij}} \quad (3)$$

where K_j is the equilibrium constant of reaction j on a mole fraction scale; a_i is the activity of component i; ν_{ij} is the stoichiometric coefficient of component i in reaction j; x_i and γ_i are the mole fraction and the activity coefficient of component i, respectively. The chemical equilibrium constant was determined from the Gibbs free energy change of the reaction.

$$-\ln K_j = \frac{\Delta G_j(T)}{RT} \quad (4)$$

where $\Delta G_j(T)$ is the Gibbs free energy change for reaction j at system temperature; $\Delta G_j(T)$ is defined as the difference between the Gibbs free energy of formation of the products and reactants at their reference state, $G_i(T)$, weighted by their stoichiometric coefficients.

$$\Delta G_j(T) = \sum_i v_{ij} G_i(T) \tag{5}$$

For solvents (water in this work), the Gibbs free energy of formation in their reference state (pure solvent) was calculated from that of ideal gas and the departure function:

$$G_s(T) = G_s^{ig}(T) + \Delta G_s^{ig \to l}(T) \tag{6}$$

The ideal gas Gibbs free energy of formation of the solvent was calculated from the following equation:

$$G_s^{ig}(T) = \Delta_f H_{s,298.15}^{ig} + \int_{298.15}^{T} C_{P,s}^{ig} dT - T \times \left(\frac{\Delta_f H_{s,298.15}^{ig} - \Delta_f G_{s,298.15}^{ig}}{298.15} + \int_{298.15}^{T} \frac{C_{P,s}^{ig}}{T} dT \right) \tag{7}$$

where $\Delta_f H_{s,298.15}^{ig}$ and $\Delta_f G_{s,298.15}^{ig}$ are ideal gas enthalpy of formation and ideal gas Gibbs free energy of formation of solvent s at 298.15 K, respectively, and $C_{P,s}^{ig}$ the ideal gas heat capacity of solvent *s*. The standard state thermodynamic properties of water ($\Delta_f H_{s,298.15}^{ig}$, $C_{P,s}^{ig}$, and $\Delta_f G_{s,298.15}^{ig}$) exist in the Aspen Plus® databank. The Gibbs free energy departure function for water was obtained from the ASME steam table. For molecular solutes (CO_2, AEP, and $H^+AEPCOO^-$), the Gibbs free energy in their reference state (infinite dilution in aqueous phase), $G_i^{\infty,aq}(T)$, was calculated from Henry's law:

$$G_i^{\infty,aq}(T) = G_i^{ig}(T) + RT \ln\left(\frac{H_{i,s}(T,P)}{P^{ref}} \right) \tag{8}$$

where $H_{i,s}(T,P)$ is the Henry's constant of molecular solute *i* in solvent *s* at system temperature T and pressure P; P^{ref} the reference pressure of 1 bar, and $G_i^{ig}(T)$ the ideal gas Gibbs free energy of formation of molecular solute *i*, which is calculated in the same way as for the solvent:

$$G_i^{ig}(T) = \Delta_f H_{i,298.15}^{ig} + \int_{298.15}^{T} C_{P,i}^{ig} dT - T \times \left(\frac{\Delta_f H_{i,298.15}^{ig} - \Delta_f G_{i,298.15}^{ig}}{298.15} + \int_{298.15}^{T} \frac{C_{P,i}^{ig}}{T} dT \right) \tag{9}$$

where $\Delta_f H_{i,298.15}^{ig}$ and $\Delta_f G_{i,298.15}^{ig}$ are ideal gas enthalpy of formation and ideal gas Gibbs free energy of formation of molecular solute *i* at 298.15 K, respectively, and $C_{P,i}^{ig}$ is the ideal gas heat capacity of molecular solute *i*.

$\Delta_f H_{i,298.15}^{ig}$, $\Delta_f G_{i,298.15}^{ig}$, and $C_{P,i}^{ig}$ of CO_2 and AEP exist in the Aspen Plus® databank. The difference of $\Delta_f H_{i,298.15}^{ig}$ and $\Delta_f G_{i,298.15}^{ig}$ between $H^+AEPCOO^-$/$^-OOCAEPH^+$ and the parent amine, AEP, were assumed to be the same as the difference between H^+PZCOO^- and PZ in the Independence model. These estimated values were used as initial guess in the regression of the data of CO_2 solubility in aqueous AEP solution, from which the final values of these parameters of $H^+AEPCOO^-$ and $^-OOCAEPH^+$ were obtained. $C_{P,i}^{ig}$ of $H^+AEPCOO^-$ and $^-OOCAEPH^+$ were estimated based on the ratio of their molecular weight to AEP. $C_{P,i}^{ig}$ of AEP, $H^+AEPCOO^-$, and $^-OOCAEPH^+$ were fixed in future regressions.

The Henry's constant, $H_{i,s}(T,P)$, was calculated from

$$H_{i,s}(T,P) = H_{i,s}(T,P_s^{*,l}) \exp\left(\frac{1}{RT} \int_{P_s^{*,l}}^{P} V_{i,s}^{\infty} dP \right) \tag{10}$$

where $H_{i,s}(T,P_s^{*,l})$ is the Henry's constant of molecular solute *i* in solvent *s* at system temperature T and the solvent vapor pressure; $P_s^{*,l}$ (obtained from the Antoine model), and $V_{i,s}^{\infty}$ the partial molar volume of molecular solute *i* at infinite dilution in solvent *s* at T and P (calculated from the Brelvi-O'Connell model [11] by using their critical properties). The Poynting pressure correction factor (the exponent term) accounts for the effect of pressure on Henry's constant, and is almost unity and can be ignored at low pressures. $H_{i,s}(T,P_s^{*,l})$ was calculated using the following correlation in Aspen Plus®:

$$\ln H_{i,s} = a_{i,s} + \frac{b_{i,s}}{T} + c_{i,s} \times \ln(T) + d_{i,s} \times T \tag{11}$$

The Henry's coefficients, $a_{i,s}$, $b_{i,s}$, $c_{i,s}$, $d_{i,s}$ of CO_2 in water are available in the Aspen Plus® databank, while the Henry's coefficients of AEP in water were obtained from regression of aqueous AEP volatility data.

For ionic solutes, the Gibbs free energy of formation in their reference state (infinite dilution in aqueous phase) at system temperature, $G_i^{\infty,aq}(T)$, were calculated from the enthalpy of formation and Gibbs free energy of formation in aqueous-phase infinite dilution at 298.15 K, and the heat capacity in aqueous-phase infinite dilution.

$$G_i^{\infty,aq}(T) = \Delta_f H_{i,298.15}^{\infty,aq} + \int_{298.15}^{T} C_{P,i}^{\infty,aq} dT - T \times \left(\frac{\Delta_f H_{i,298.15}^{\infty,aq} - \Delta_f G_{i,298.15}^{\infty,aq}}{298.15} + \int_{298.15}^{T} \frac{C_{P,i}^{\infty,aq}}{T} dT \right)$$
$$+ RT \ln\left(\frac{1000}{M_w} \right) \tag{12}$$

The term $RT\ln(1000/M_w)$ is added because $\Delta_f G_{i,298.15}^{\infty,aq}$, as reported in the literature, is based on molality scale, while $G_i^{\infty,aq}(T)$ is based on mole fraction scale. The standard state thermodynamic properties, $\Delta_f H_{i,298.15}^{\infty,aq}$, $\Delta_f G_{i,298.15}^{\infty,aq}$, and $C_{P,i}^{\infty,aq}$, for AEP-related ionic species are not available in the Aspen Plus® databank. The $\Delta_f H_{i,298.15}^{\infty,aq}$ and $\Delta_f G_{i,298.15}^{\infty,aq}$ of $AEPH^+$ and $AEP(H^+)_2$ were calculated from the protonation reactions of $AEPH^+$ and $AEP(H^+)_2$ measured by Pagano [10].

$$\Delta_f G_{AEPH^+,298.15}^{\infty,aq} = \Delta_f G_{AEP,298.15}^{\infty,aq} + \Delta_r G_i = \Delta_f G_{AEP,298.15}^{\infty,aq} - RT\ln K_{m,i} \tag{13}$$

$$\Delta_f H_{AEPH^+,298.15}^{\infty,aq} = \Delta_f H_{AEP,298.15}^{\infty,aq} + \Delta_r H_i \tag{14}$$

$$\Delta_f G_{AEP(H^+)_2,298.15}^{\infty,aq} = \Delta_f G_{AEPH^+,198.15}^{\infty,aq} + \Delta_r G_i = \Delta_f G_{AEP,298.15}^{\infty,aq} - RT\ln K_{m,i} \tag{15}$$

$$\Delta_f H_{AEP(H^+)_2,298.15}^{\infty,aq} = \Delta_f H_{AEPH^+,298.15}^{\infty,aq} + \Delta_r H_i \tag{16}$$

where $\Delta_r G_i$, $\Delta_r H_i$, and $K_{m,i}$ are Gibbs free energy change, enthalpy change, and molality scale protonation constants of a certain reaction; $\Delta_f G^{\infty,aq}_{AEP,298.15}$ and $\Delta_f H^{\infty,aq}_{AEP,298.15}$ are Gibbs free energy of formation and enthalpy of formation of AEP in aqueous-phase infinite dilution at 298.15 K, which can be obtained from Henry's law as follows:

$$\Delta_f G^{\infty,aq}_{AEP,298.15} = \Delta_f G^{ig}_{AEP,298.15} + R \times 298.15 \times \ln\left(\frac{H_{AEP,s,298.15}}{P^{ref}}\right) - RT\ln\left(\frac{1000}{M_w}\right) \tag{17}$$

$$\Delta_f H^{\infty,aq}_{AEP,298.15} = \Delta_f H^{ig}_{AEP,298.15} + R\,\frac{\partial \ln H_{AEP,H_2O}}{\partial\,(1/T)} \tag{18}$$

The term $RT\ln(1000/M_w)$ is subtracted because $\Delta_f G^{\infty,aq}_{i,298.15}$ in Aspen Plus® is based on molality scale, while $\Delta_f G^{ig}_{i,298.15}$ (as provided in the databank) is based on mole fraction scale. The conversion of equilibrium constants from molality scale to mole fraction scale can be found in Hilliard [8]. $\Delta_f G^{\infty,aq}_{i,298.15}$ and $\Delta_f H^{\infty,aq}_{i,298.15}$ of other AEP-related ions were initially estimated based on the assumption that the difference between AEP-related species is the same as the difference between corresponding PZ-related species. For example, we assume:

$$\Delta_f H^{\infty,aq}_{AEPCOO^-,298.15} - \Delta_f H^{\infty,aq}_{AEP,298.15} = \Delta_f H^{\infty,aq}_{PZCOO^-,298.15} - \Delta_f H^{\infty,aq}_{PZ,298.15}$$

and

$$\Delta_f H^{\infty,aq}_{AEP(COO^-)_2,298.15} - \Delta_f H^{\infty,aq}_{AEPCOO^-,298.15} = \Delta_f H^{\infty,aq}_{PZ(COO^-)_2,298.15} - \Delta_f H^{\infty,aq}_{PZCOO^-,298.15}$$

These values were used as an initial guess in the regression of the CO_2 solubility in aqueous AEP solution, from which the final value of these parameters was obtained. $C^{\infty,aq}_{P,i}$ of AEP was assumed to be the same as $C^{ig}_{P,i}$ of AEP, and then $C^{\infty,aq}_{P,i}$ of other AEP species was estimated based on the ratio of their molecular weight to AEP. $C^{\infty,aq}_{P,i}$ of all AEP species was fixed in future regressions.

2.2. Vapor-liquid phase equilibrium

Phase equilibrium governs the distribution of molecular species between the vapor and liquid phase. In the activity coefficient approach, the basic vapor-liquid equilibrium relationship for solvent is represented by:

$$\varphi^V_s y_s P = \gamma_s x_s P^{*,l}_s \exp\left(\frac{1}{RT}\int_{P^{*,l}_s}^{P} V^{*,l}_s dP\right) \tag{19}$$

where φ^V_s is the vapor phase fugacity coefficient of solvent s, γ_s the symmetric activity coefficient of solvent *s*, $P_s^{*,l}$ the solvent vapor pressure at system temperature, and $V^{*,l}_s$ the liquid pure component molar volume of solvent *s* calculated from the Rackett model. For molecular solutes, Henry's Law was used to determine vapor-liquid equilibrium:

$$\varphi^V_i y_i P = \gamma^*_i x_i H_{i,s}(T, P^{*,l}_s) \exp\left(\frac{1}{RT}\int_{P^{*,l}_s}^{P} V^{\infty}_{i,s} dP\right) \tag{20}$$

where γ^*_i is the symmetric activity coefficient of component *i*.

2.3. Vapor phase behavior

Vapor phase behavior was modeled using the Redlich-Kwong-Soave (RKS) equation of state:

$$P = \frac{RT}{V-b} - \frac{a}{V(V-b)} \tag{21}$$

T and P represent the temperature and pressure of the vapor phase and R represents the gas constant. The attraction between molecules and their size are represented in the equation by parameters a and b respectively, which are calculated from critical properties.

2.4. System non-idealities

Vapor phase non-idealities (fugacity) are calculated using the SRK equation of state. Liquid phase non-idealities (activity) are calculated using the eNRTL model [6]. The use of the eNRTL model in amine/acid gas systems has been described previously by Posey [7] and Frailie [9]. The basic postulate of this model is that the excess Gibbs energy of an aqueous electrolyte system can be written as the sum of three contributions: the NRTL term (related to the local ion-molecule, ion-ion, and molecule-molecule interactions that exist in the immediate neighborhood of any species), the PDH term (related to the long-range ion-ion interactions that exist beyond the immediate neighborhood of a central ionic species) and the Born term (accounts for the excess Gibbs energy of transfer from infinite dilution in the mixed solvent to infinite dilution in the aqueous phase).

$$g_i^{ex^*} = g_{PDH,i}^{ex^*} + g_{Born,i}^{ex} + g_{NRTL,i}^{ex^*} \tag{22}$$

Accordingly,

$$\ln \gamma_i = \ln \gamma_i^{PDH} + \ln \gamma_i^{Born} + \ln \gamma_i^{NRTL} \tag{23}$$

The adjustable parameters for the eNRTL model include the pure component dielectric constant coefficient, Born radius of ionic species, and NRTL parameters for molecule-molecule, molecule-electrolyte, and electrolyte-electrolyte pairs. The NRTL parameters are the nonrandomness factors and binary interaction parameters. Following the treatment for PZ in the Independence model, dielectric constants of AEP are assumed to be the same as MEA; ionic radii were assigned default values of 3 Å; the nonrandomness factor was fixed at 0.3 for molecule-molecule pairs and 0.2 for molecule-electrolyte and electrolyte-electrolyte pairs, and binary interaction parameters for electrolyte-electrolyte pairs were set to zero. Therefore, the only adjustable parameters of the eNRTL model in this work were binary interaction parameters for molecule-molecule pairs and for electrolyte-molecule pairs, as expressed in the following relationships as a function of temperature. Molecule-molecule binary interaction parameters:

$$\tau_{mm'} = A_{mm'} + \frac{B_{mm'}}{T} + C_{mm'} \ln(T) + D_{mm'} T \tag{24}$$

Electrolyte-molecule (or molecule-electrolyte) binary interaction parameters:

$$\tau_{x,y} = E_{x,y} + \frac{F_{x,y}}{T} \tag{25}$$

$$\tau_{x,y} = \tau_{ca,m} \text{ or } \tau_{m,ca} \tag{26}$$

Subscripts and indices of *m*, *c*, and *a* refer to molecules, cations, and anions, respectively. $\tau_{mm'}$, $\tau_{ca,m}$, and $\tau_{m,ca}$ can be obtained from the regression of amine volatility data and CO_2 solubility data.

The parameters used in this model are summarized in Table 2. All model parameters not mentioned in Table 1 were either from the Independence model or set to Aspen Plus® default values.

Table 2. Summary of model parameters

Parameters	Component	Source	Data for regression
$\Delta_f G^{ig}_{s,298.15}$	AEP	Aspen Plus® Databank	——
	$H^+AEPCOO^-$ / $^-OOCAEPH^+$	Regression	VLE and NMR for AEP-H_2O-CO_2
$\Delta_f H^{ig}_{s,298.15}$	AEP	Aspen Plus® Databank	——
	$H^+AEPCOO^-$/ $^-OOCAEPH^+$	Regression	VLE and NMR for AEP-H_2O-CO_2
$C^{ig}_{P,s}$	AEP	Aspen Plus® Databank	——
	$H^+AEPCOO^-$/ $^-OOCAEPH^+$	Ratio to $C^{ig}_{P,s}$ of AEP	——
$\Delta_f G^{\infty,aq}_{i,298.15}$	$AEPH^+$/$AEP(H^+)_2$	Pagano [10]	——
	Other AEP ions	Regression	VLE and NMR for AEP-H_2O-CO_2
$\Delta_f H^{\infty,aq}_{i,298.15}$	$AEPH^+$/$AEP(H^+)_2$	Pagano [10]	——
	Other AEP ions	Regression	VLE and NMR for AEP-H_2O-CO_2
$C^{\infty,aq}_{P,i}$	All AEP species	Ratio to $C^{ig}_{P,s}$ of AEP	——
Henry's constant	AEP/H_2O	Regression	Volatility of AEP
	$H^+AEPCOO^-$ / H_2O	Assumed same as H^+PZCOO^-/ H_2O	——
	$^-OOCAEPH^+$ / H_2O		
Dielectric constant	AEP	Assumed same as PZ	——
NRTL binary interaction parameters	AEP/H_2O	Regression	Volatility of AEP
	AEP cation, PZ anion/ H_2O PZ cation, AEP anion/ H_2O AEP cation, AEP anion/ H^+PZCOO^- PZ cation, PZ anion/ $H^+AEPCOO^-$ PZ cation, PZ anion/ $^-OOCAEPH^+$	Regression	VLE for PZ-AEP- H_2O-CO_2

3. Results and Discussion

3.1. Identification of ^{13}C NMR spectra

Quantitative ^{13}C NMR was used in this work to investigate the species distribution in AEP-H_2O-CO_2 and PZ-AEP-H_2O-CO_2, and validate the model prediction of speciation. Due to the rapid exchange rate of protons, a protonated/di-protonated species and the unprotonated counterparts cannot be differentiated by the NMR spectroscopy used in this study. Therefore the sum of these was quantified from the NMR spectra. Potential species in the PZ-AEP-H_2O-CO_2 system are listed in Table 1. The identification of NMR peaks in loaded 6 m AEP and 5 m PZ/2 m AEP is shown in Figure 1. Due to the long distance between the primary and secondary amino groups in AEP, the addition of a carboxyl group to a -NH_2 does not affect the chemical shift of the C on the other side. This led to the overlap of peaks from different species as shown in Figure 1.

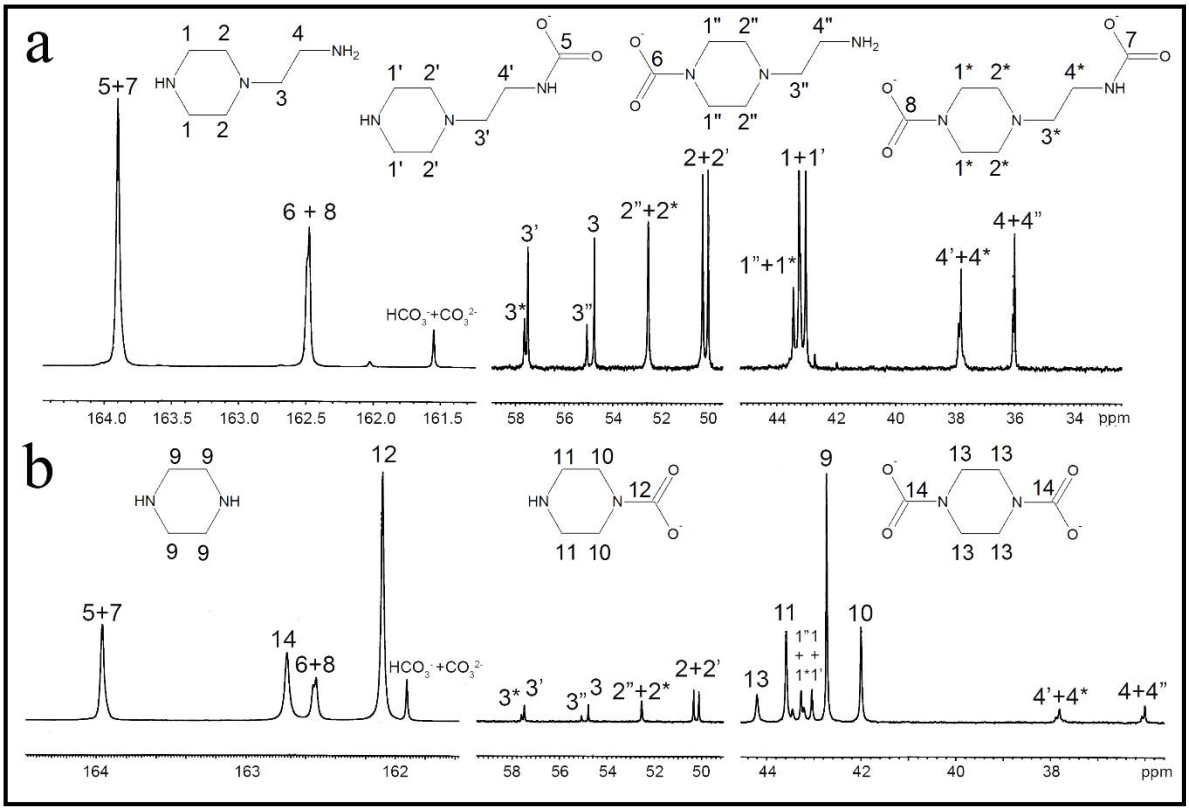

Fig. 1. ^{13}C NMR spectra for 6 m AEP (a) and 5 m PZ/2 m AEP (b) at 25 ℃ and CO_2 loading of 0.3

3.2. AEP-H_2O

The amine vapor pressure of 0.7 m and 5 m AEP from 40–70 ℃ has been measured in a stirred reactor coupled with a hot gas FTIR analyzer (Fourier Transform Infrared Spectroscopy, Temet Gasmet Dx-4000). The details of the experimental apparatus, procedure, and analytical methods were described by Nguyen [12]. The volatility data were regressed to determine Henry's constant coefficients of AEP in water (Equation 11) and molecule-molecule binary interaction parameters $\tau_{mm'}$ for the AEP/H_2O pair (Equation 24). The regression results are given in Table 3. All parameters concerning AEP/H_2O were held constant during subsequent regressions. After the regression, the model predicts the volatility of AEP well (Figure 2). The volatility of AEP was found to be just 1% of the volatility of aqueous PZ with similar alkalinity and no CO_2 loading, indicating a negligible amine loss owing to volatilization, but a potential difficulty with thermal reclaiming.

Table 3. Regressed parameters and standard error for AEP/H_2O regression

Parameter	Species	Value (SI units)	Standard deviation
$\tau_{mm'}$/1	H_2O/AEP	3.3	0.19
Henry/1	AEP/H_2O	36	1.5
Henry/2	AEP/H_2O	-10780	507

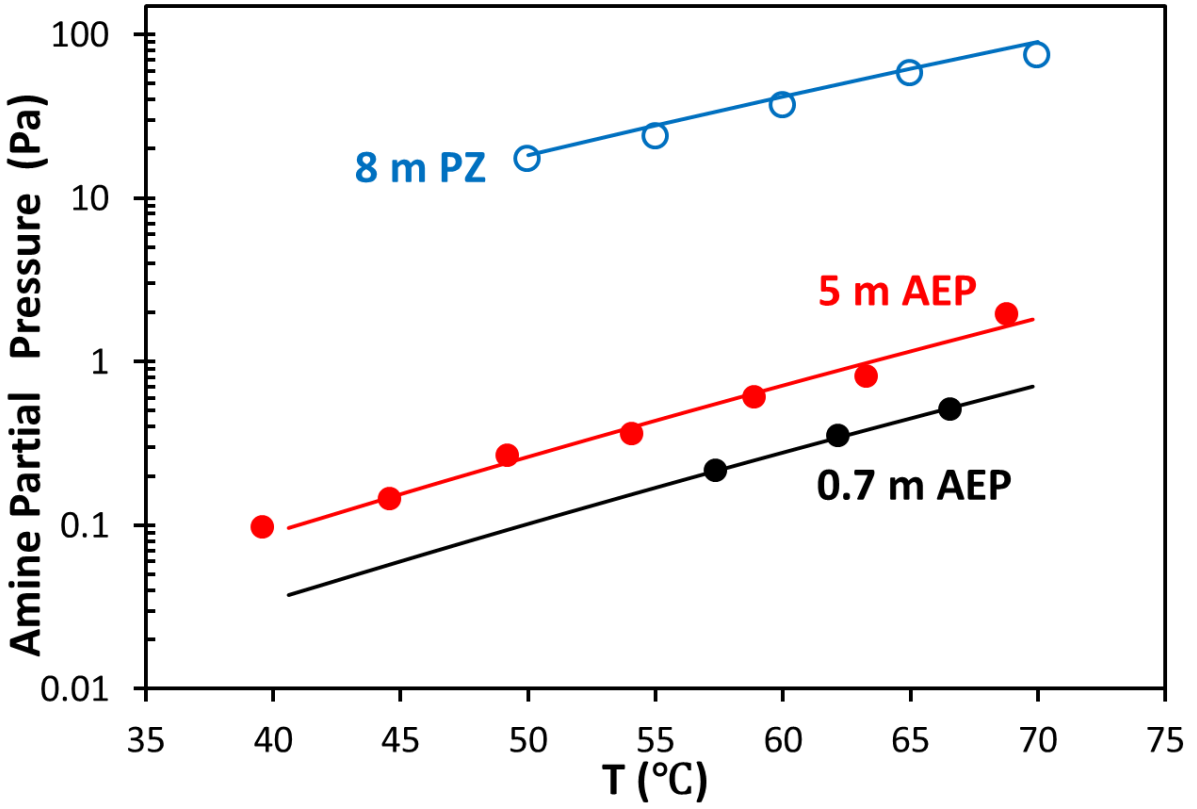

Fig. 2. AEP vapor pressure predicted by the model compared with experimental data, as well as data for 8 m PZ with no CO_2 loading [12]. Filled points: Experimental data; Solid lines: Model prediction from this work.

3.3. AEP-H_2O-CO_2

The vapor-liquid equilibrium (VLE) of CO_2 for 6 m AEP has been measured with a wetted wall column at temperatures up to 100 ℃ [12]. These CO_2 solubility data were used for data regression. After the initial regression of the VLE data the model did not predict the speciation. As Aspen Plus® is not configured to regress speciation data, the free energy of formation of AEP carbamate species was manually adjusted to fit the NMR speciation data at 25 ℃, and then standard enthalpies of formation were regressed again to get a better prediction of CO_2 solubility. This process was repeated to get a reasonable prediction for both CO_2 solubility and speciation (Figures 3 and 4). From the VLE prediction, the CO_2 cyclic capacity of this solvent is calculated as 0.71 mol/kg (AEP + water), using the following equation.

$$Capacity = \frac{(\alpha_{rich} - \alpha_{lean}) * mol\ \text{alkalinity}}{kg(\text{amine}+H_2O)} = \frac{mol\ CO_2}{kg} \quad (27)$$

where $\propto_{lean}$ and $\propto_{rich}$ are defined as the CO_2 loading with P_{CO2*} of 0.5 and 5 kPa at 40 ℃. The determined parameters are given in Table 4.

As noted previously, the original species and their protonated/di-protonated species cannot be differentiated in the NMR spectra, so they were quantified as a group in Figure 4. At CO_2 loading below 0.2 mol CO_2/mol alkalinity, $AEPCOO^-/H^+AEPCOO^-$ is the dominant CO_2 sink, followed by $^-OOCAEP/^-OOCAEPH^+$. At CO_2 loading above 0.25 mol CO_2/mol alkalinity, the fraction of CO_2 in the form of monocarbamate decreases with CO_2 loading, due to its conversion to AEP dicarbamate and HCO_3^-/CO_3^{2-}. The fraction of AEP dicarbamate as a CO_2 sink increases with CO_2

loading and becomes dominant at CO_2 loading above 0.37 mol CO_2/mol alkalinity. Although the fraction of HCO_3^-/CO_3^{2-} as a CO_2 sink keeps increasing with loading, it is not a dominant one at loading below 0.4 mol CO_2/mol alkalinity.

Figure 5 shows the detailed predicted speciation for 6 m AEP at 40 ℃. Free AEP decreases rapidly with CO_2 loading and is almost completely depleted at α = 0.3 mol/mol alkalinity. $AEPH^+$, $AEPCOO^-$, and ^-OOCAEP are the three major products in the lean loading range. As CO_2 loading increases to α = 0.35, the amount of $AEP(H^+)_2$, $H^+AEPCOO^-$, $^-OOCAEPH^+$, and $AEP(COO^-)_2$ is more and more significant. At α above 0.35, $AEP(H^+)_2$ and $H^+AEP(COO^-)_2$ are the two dominant species, followed by HCO_3^-. $(H^+)_2AEPCOO^-$, CO_3^{2-}, and free CO_2 are not significant species in the solution across the entire CO_2 loading range.

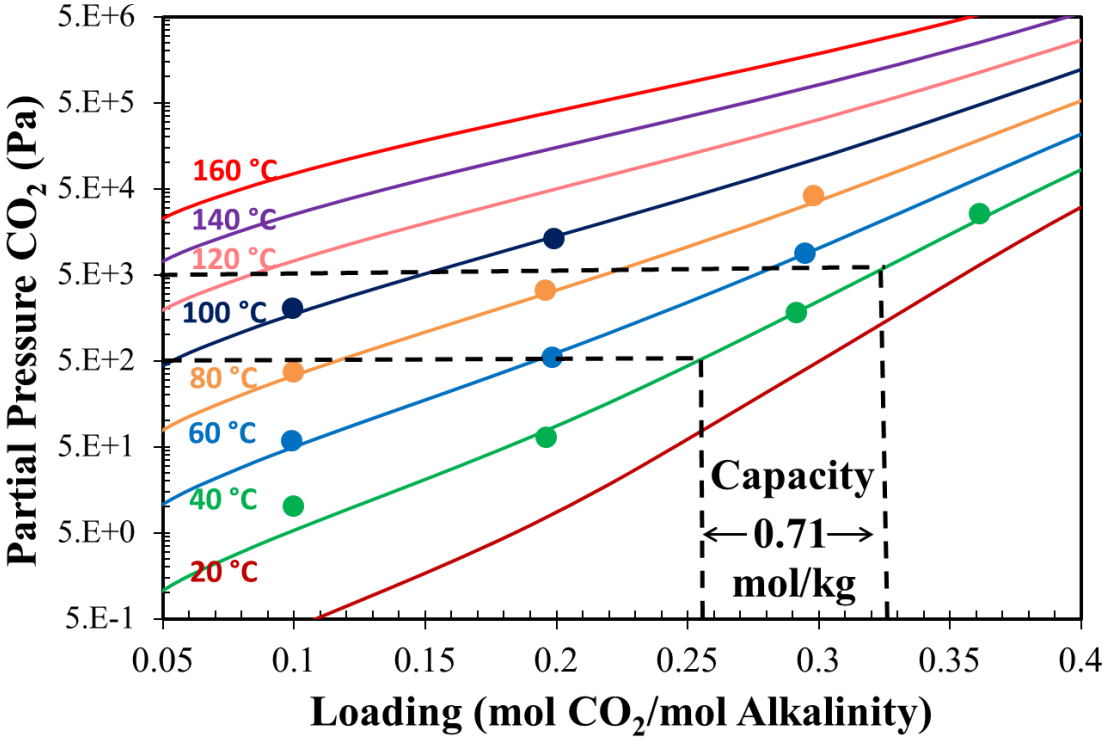

Fig. 3. Experimental measurement (points) [13] and Aspen Plus® predictions (lines) for VLE of loaded 6 m AEP solution between 20 ℃ and 160 ℃

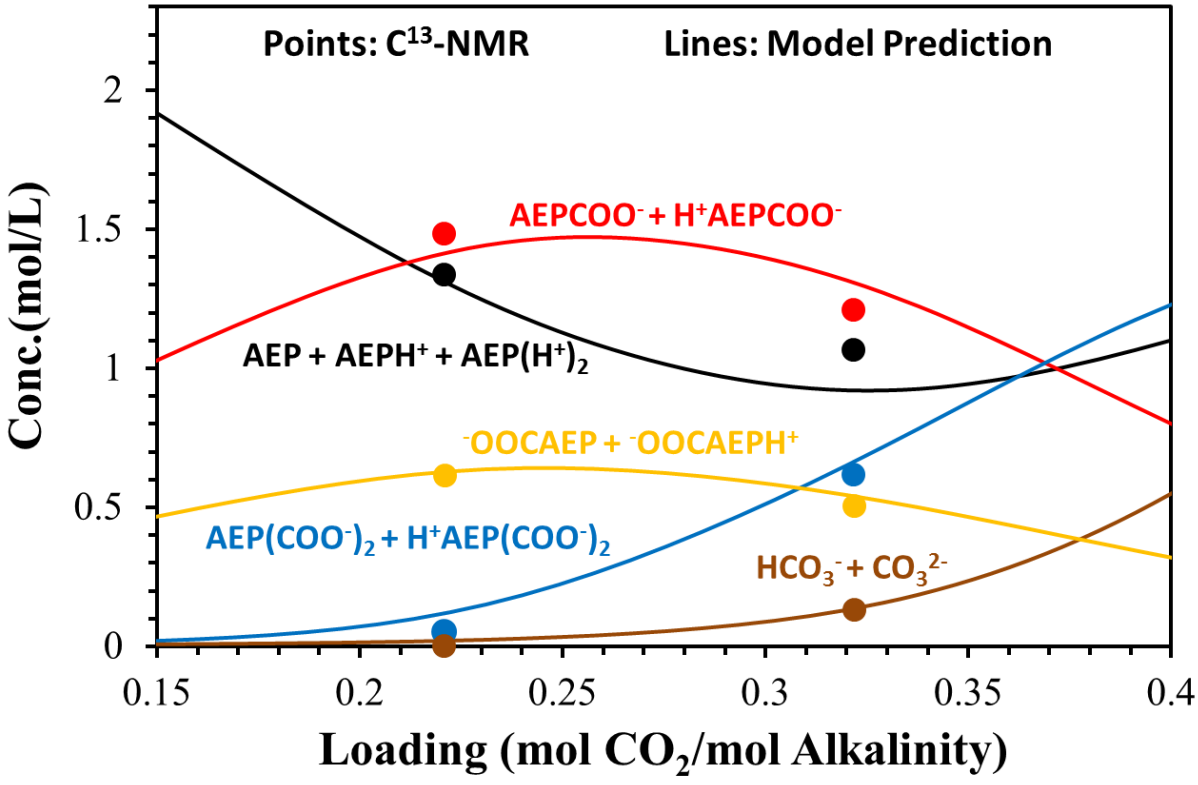

Fig. 4. ^{13}C speciation for 6 m AEP-CO_2-H_2O at 25 ℃

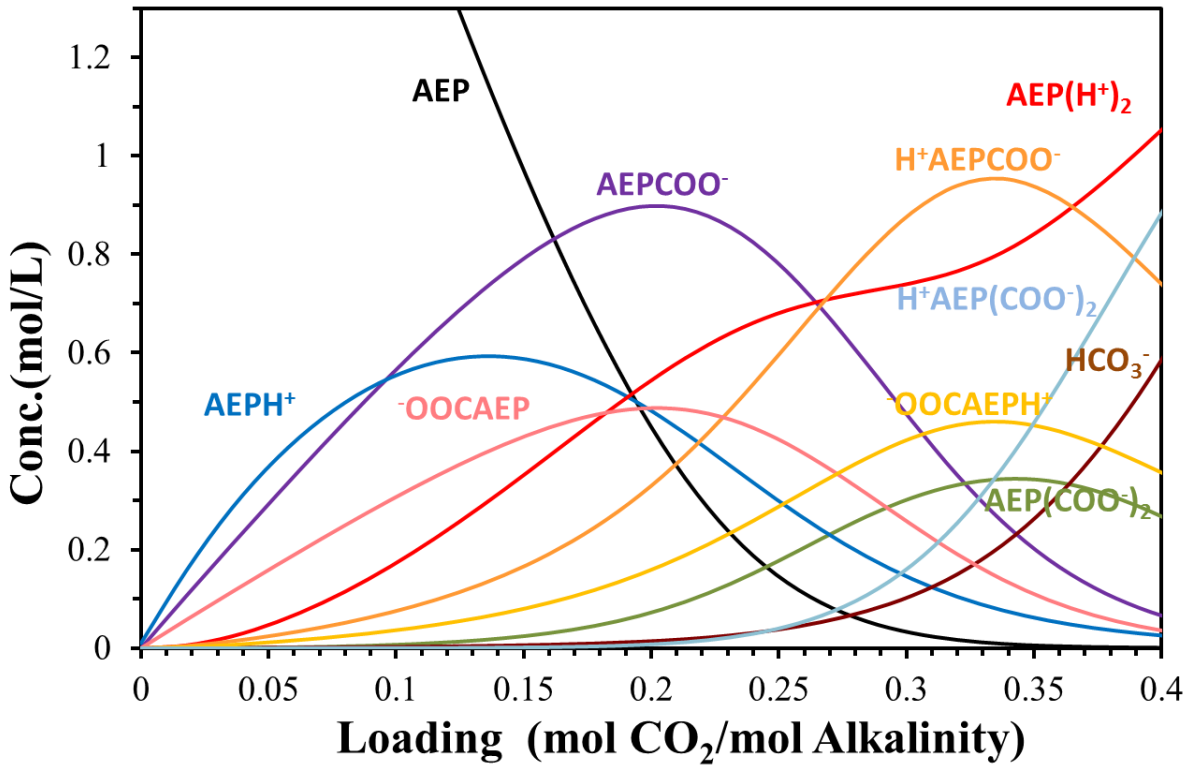

Fig. 5. Predicted speciation distribution for 6 m AEP-CO_2-H_2O at 40 ℃

Table 4. The adjusted parameters for 6 m AEP-CO_2-H_2O

Parameter	Species	Value (kJ/mol)
$\Delta_f G^{\infty,aq}_{i,298.15}$	$AEPCOO^-$	-99.9
	^-OOCAEP	-98.0
	$H^+AEP(COO^-)_2$	-501.5
$\Delta_f G^{ig}_{s,298.15}$	$H^+AEPCOO^-$	-93.5
	$^-OOCAEPH^+$	-91.2
$\Delta_f H^{\infty,aq}_{i,298.15}$	$AEPCOO^-$	-523.9
	^-OOCAEP	-515.8
	$H^+AEP(COO^-)_2$	-963.4
$\Delta_f H^{ig}_{s,298.15}$	$H^+AEPCOO^-$	-550.5
	$^-OOCAEPH^+$	-540.1

3.4. PZ/AEP/H_2O/CO_2

The VLE of CO_2 for 5 m PZ/2 m AEP from 20–160 ℃ was regressed to determine NRTL binary interaction parameters for molecule-electrolyte pairs, $\tau_{ca,m}$, including AEP cation, PZ anion/H_2O pairs; PZ cation, AEP anion/H_2O pairs; AEP cation, AEP anion/H^+PZCOO^- pairs; PZ cation, PZ anion/$H^+AEPCOO^-$ (Equation 25).

After regression, the VLE of CO_2 in 5 m PZ/2 m AEP is predicted well by the model (Figure 6), especially at the normal operating conditions of the absorber (40–60 ℃ and loading from 0.288–0.380). From the VLE prediction, the CO_2 cyclic capacity of this solvent is calculated as 0.86 mol/kg (PZ + AEP + water), compared to 0.50 mol/kg for 7 m MEA and 0.86 mol/kg for 8 m PZ. The higher CO_2 capacity leads to lower solvent flow rate for a specific CO_2 removal requirement, and thus less sensible heat demand for stripping. The regressed parameters are summarized in Table 5. The non-regressed or non-adjusted parameters used in this model are summarized in Table 6 (for non-temperature-dependence parameters) and Table 7 (for temperature-dependence parameters).

NMR measurement for 5 m PZ/2 m AEP at 25 ℃ was used to validate the prediction of speciation by this model. The prediction of the model is in good agreement with the experimental NMR measurements, except that the amount of AEP dicarbamate is underpredicted (Figure 7). $PZCOO^-/H^+PZCOO^-$ is the dominant CO_2 sink in the solution across the entire CO_2 loading range, followed by $AEPCOO^-/H^+AEPCOO^-$. The share of PZ dicarbamate as a CO_2 sink increases with CO_2 loading and becomes significant at rich CO_2 loading. The share of $OOCAEP/^-OOCAEPH^+$ and AEP dicarbamate as a CO_2 sink is not significant across the loading range, and the share of HCO_3^-/CO_3^{2-} is negligible.

Figure 8 shows the detailed predicted speciation for 5 m PZ/2 m AEP at 40 ℃. For simplicity, species with concentration below 0.1 mol/L across the entire loading range are not shown (including $AEPH^+$, $AEPCOO^-$, ^-OOCAEP, $AEP(COO^-)_2$, $H^+AEP(COO^-)_2$, and $(H^+)_2AEPCOO^-$). Free PZ and AEP decreases drastically with CO_2 loading and are almost completely depleted at α = 0.35 mol/mol alkalinity. PZH^+ and $PZCOO^-$ are the two major products in the lean loading range and reach their maximum at α = 0.3 and α = 0.2 mol/mol alkalinity, respectively. As CO_2 loading increases, the amount of H^+PZCOO^-, $H^+AEPCOO^-$, $PZ(COO^-)_2$, and $AEP(H^+)_2$ is more and more significant. HCO_3^- is not a significant species in the solution across the entire CO_2 loading range.

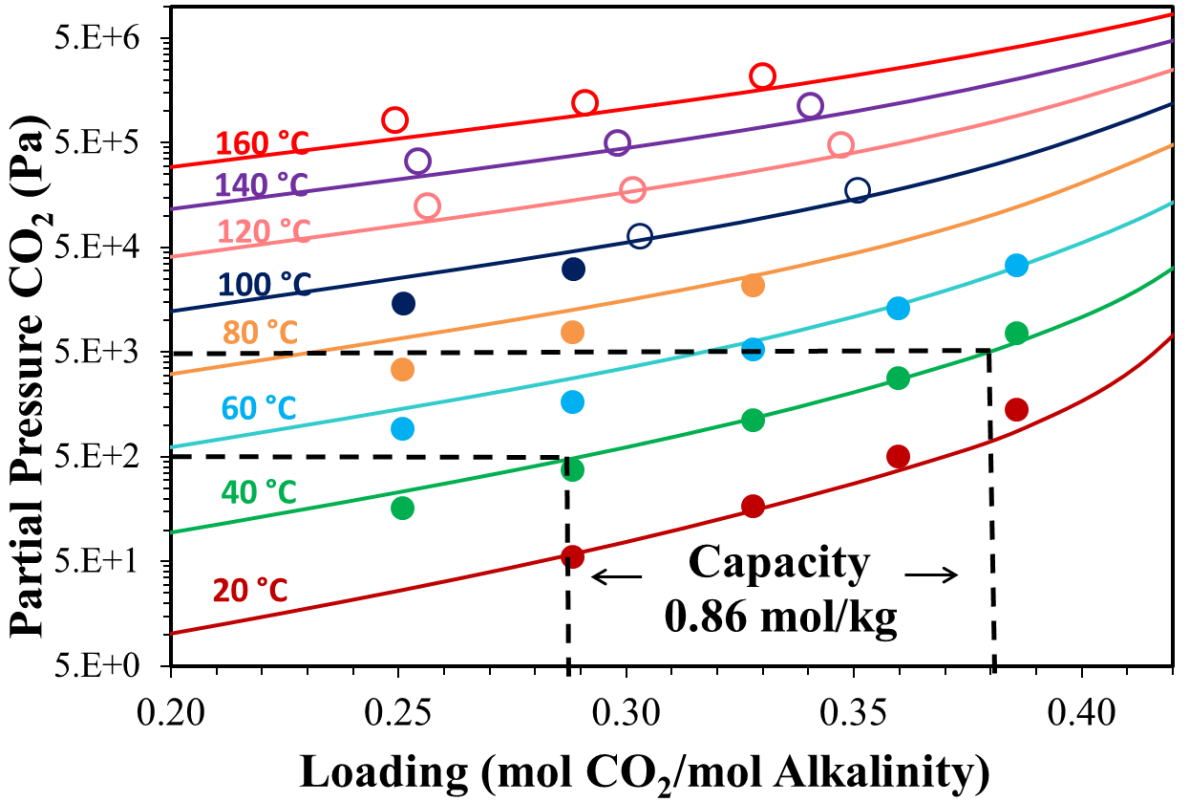

Fig. 6. Comparison of Aspen Plus® predictions (lines) and experimental data (points) for loaded 5 m PZ/2 m AEP between 20 ℃ and 160 ℃

Table 5: Regressed parameters and standard error

Parameter	Species		Value	Standard error	Default
$\tau_{ca,m}$	(PZH^+, $AEPCOO^-$)	H_2O	-6.08	25	-4
	(PZH^+,$^-$OOCAEP)	H_2O	-6.04	32	-4
	(PZH^+,$AEP(COO^-)_2$)	H_2O	-5.20	39	-4
	($AEP(H^+)_2$,$PZ(COO^-)_2$)	H^+PZCOO^-	-7.01	9	-2

Table 6: Summary of non-adjusted and non-temperature-dependence parameters used in this model

Parameter	Species	Value (kJ/mol)
$\Delta_f G_{i,298.15}^{\infty,aq}$	$AEPH^+$	210.4
	$AEP(H^+)_2$	162.2
	$(H^+)_2AEPCOO^-$	-30.4
$\Delta_f H_{i,298.15}^{\infty,aq}$	$AEPH^+$	-117.0
	$AEP(H^+)_2$	-160.0
	$(H^+)_2AEPCOO^-$	-601.1

Table 7: Summary of non-adjusted and temperature-dependence parameters used in this model

Comp.	Parameters			
	a	b	c	d
	Henry's constants (bar): $\ln H_{i,s} = a_{i,s} + \frac{b_{i,s}}{T} + c_{i,s} \times \ln(T) + d_{i,s} \times T$			
$H^+AEPCOO^-/H_2O$	-20	0	0	0
$^-OOCAEPH^+/H_2O$	-20	0	0	0
	Ideal gas heat capacity(J/kmol-K): $C_{P,i}^{ig} = a_i + b_i \times T + c_i \times T^2 + d_{i,s} \times T^3$			
$H^+AEPCOO^-$	-54909	1289	-0.96	0.00029
$^-OOCAEPH^+$	-54909	1289	-0.96	0.00029
	Aqueous Infinite Dilution Heat Capacity(J/kmol-K): $C_{P,i}^{\infty,aq} = a_i + b_i \times T + c_i \times T^2 + d_{i,s} / T$			
$AEPH^+$	-40709	956	-0.71	0.00021
$AEP(H^+)_2$	-40709	956	-0.71	0.00021
$AEPCOO^-$	-54909	1289	-0.96	0.00029
^-OOCAEP	-54909	1289	-0.96	0.00029
$AEP(COO^-)_2$	-68794	1615	-1.20	0.00036

$H^+AEP(COO^-)_2$	-68794	1615	-1.20	0.00036
$(H^+)_2AEPCOO^-$	-54909	1289	-0.96	0.00029

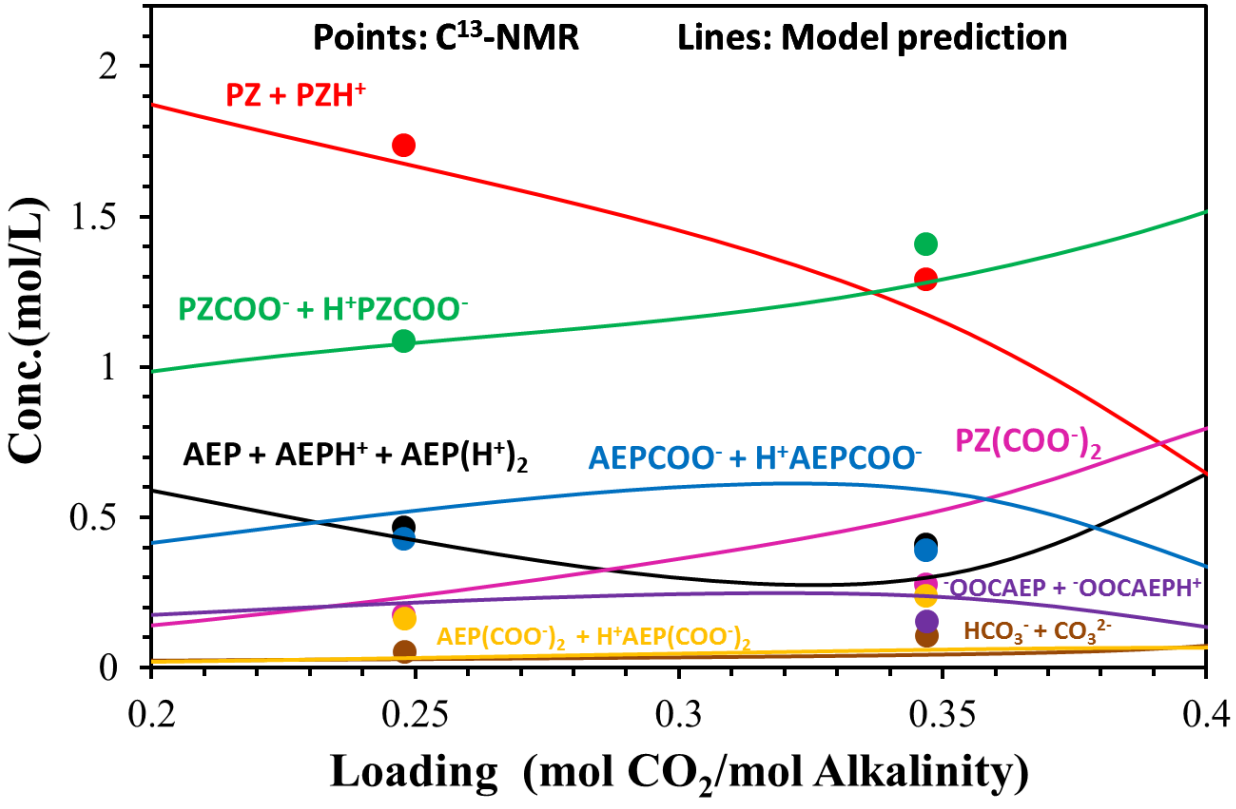

Fig. 7. Speciation validation for 5 m PZ/2 m AEP

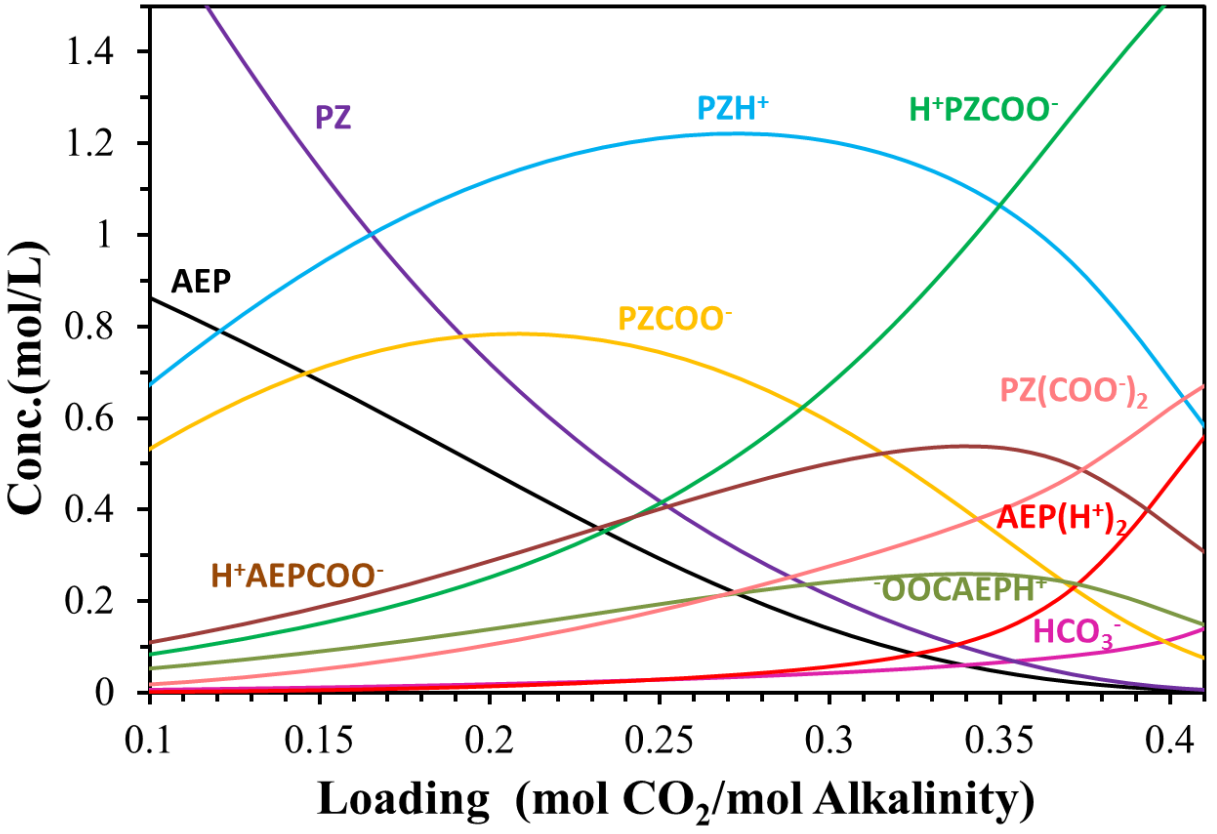

Fig. 8. Predicted speciation distribution for 6 m AEP-CO_2-H_2O at 40 ℃

3.5. Heat of absorption prediction

The predicted heat of absorption for 6 m AEP and 5 m PZ/2 m AEP is shown in Figures 9 and 10. At 40 ℃ the heat of absorption of 6 m AEP is about 50–70 kJ/mol CO_2 in the operating loading range (0.255–0.325) and the heat of absorption of 5 m PZ/2 m AEP is around 75–85 kJ/mol CO_2 in the operating loading range (0.288–0.380). The decrease of heat of absorption with loading is due to the production of HCO_3^- at rich loading, which gives a low enthalpy reaction between CO_2 and H_2O. Heat of absorption predictions in Aspen Plus® can be calculated using the calorimetric method and the Gibbs-Helmholtz equation. The use of these two methods to calculate heat of absorption has been described previously by Frailie [9]. In this model, these two methods give slightly inconsistent results of $H_{abs\text{-}CO2}$ at rich loading. The slight discrepancy of prediction is thought to be due to the inaccuracy of the calorimetric method.

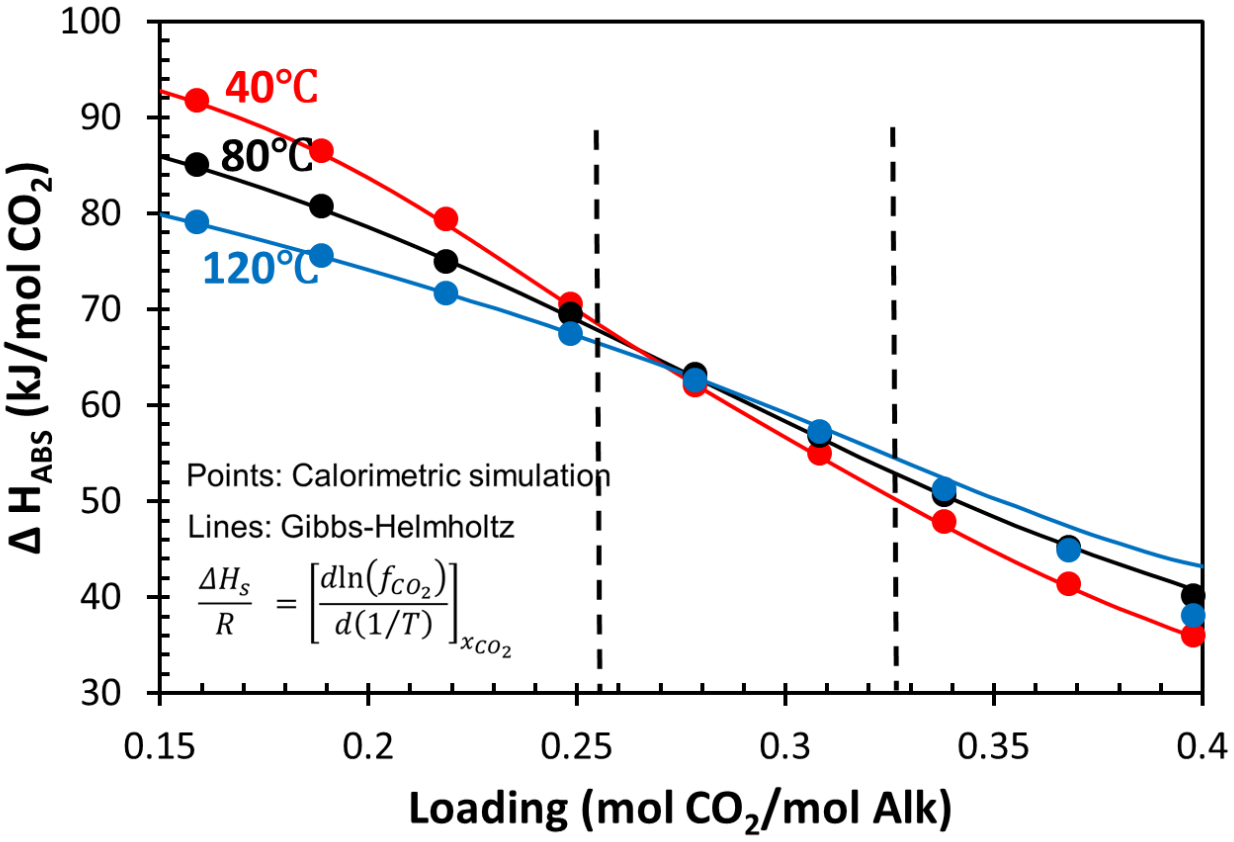

Fig. 9. Aspen Plus® model predictions of heat of absorption for 6 m AEP using Gibbs-Helmholtz (points) and calorimetric (lines) calculations

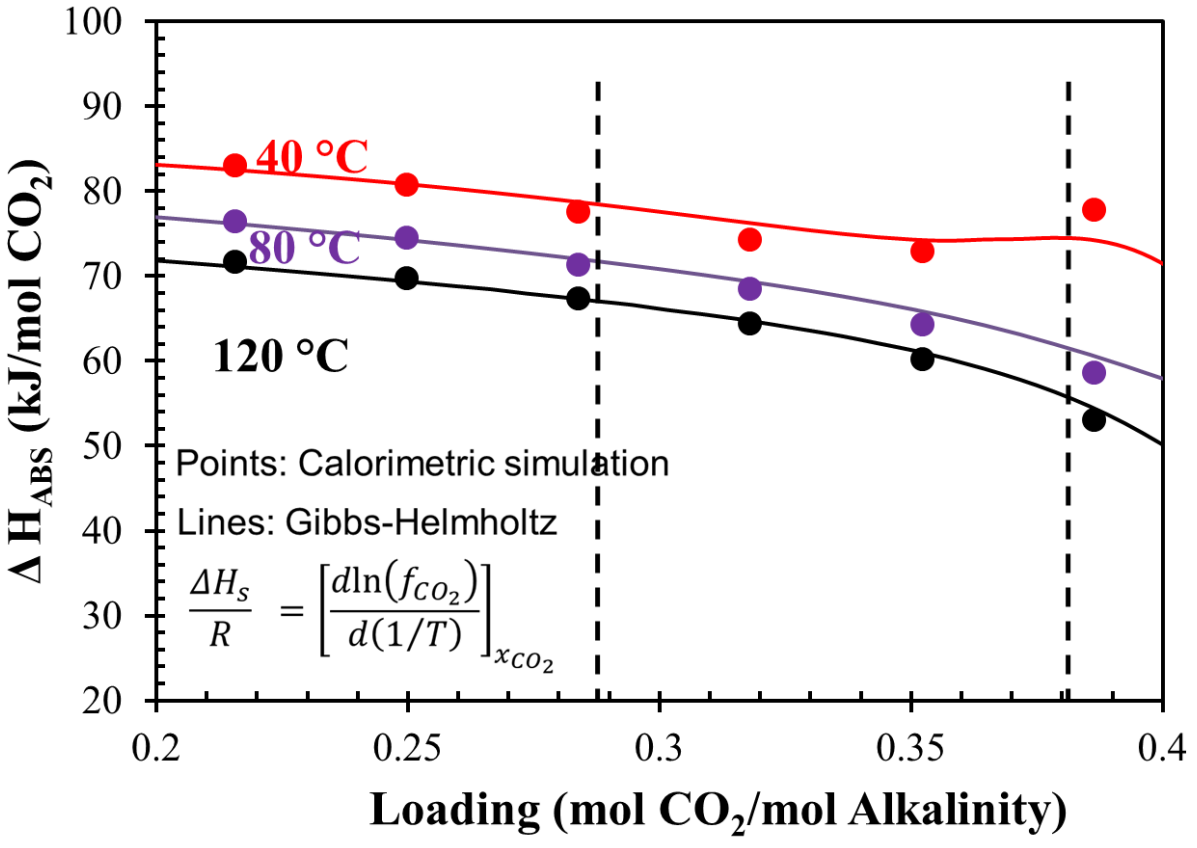

Fig. 10. Aspen Plus® model predictions of heat of absorption for 5 m PZ/2 m AEP using Gibbs-Helmholtz (points) and calorimetric (lines) calculations

Conclusions

A thermodynamic model was developed for PZ-AEP-H_2O-CO_2 in the framework of the eNRTL model by sequential data regression. The prediction for CO_2 solubility and speciation is in good agreement with the experimental data. From the VLE prediction, the CO_2 cyclic capacity of 6 m AEP is 0.71 mol/kg (AEP + water) and the CO_2 cyclic capacity of 5 m PZ/2 m AEP is 0.86 mol/kg (PZ + AEP + water).

Speciation prediction from the model shows that in AEP-H2O-CO2, at lean loading, AEPCOO-/H+AEPCOO- is the dominant CO_2 sink, followed by $^{-}$OOCAEP/$^{-}$OOCAEPH^{+}. The share of AEP dicarbamate as a CO_2 sink increases with CO_2 loading and becomes dominant at rich CO_2 loading. The share of HCO_3^-/CO_3^{2-} as a CO_2 sink is not significant at loading below 0.4 mol CO_2/mol alkalinity. For 6 m AEP, free AEP is depleted at α = 0.3 mol/mol alkalinity. AEPH^{+}, AEPCOO^{-}, and $^{-}$OOCAEP are the three major products in the lean loading range. As CO_2 loading increases to α = 0.35, the amount of AEP(H^{+})$_2$, H^{+}AEPCOO^{-}, $^{-}$OOCAEPH^{+}, and AEP(COO^{-})$_2$ is more and more significant. At α above 0.35, AEP(H^{+})$_2$ and H^{+}AEP(COO^{-})$_2$ are the two dominant species, followed by HCO_3^-. (H^{+})$_2$AEPCOO^{-}, CO_3^{2-}, and free CO_2 are not significant species in the solution across the entire CO_2 loading range.

Heat of absorption for 6 m AEP and 5 m PZ/2 m AEP decreases with CO_2 loading, due to the production of HCO_3^- at rich loading. At 40 ℃ the heat of absorption of 6 m AEP is about 50–70 kJ/mol CO_2 at operation loading range (0.255–0.325) and the heat of absorption of 5 m PZ/2 m AEP is around 75–85 kJ/mol CO_2 at operation loading range (0.288–0.380).

Acknowledgements

The authors acknowledge the financial support of the Texas Carbon Management Program.

The authors declare the following competing financial interest(s): One author of this publication consults for Southern Company and for Neumann Systems Group on the development of amine scrubbing technology. The terms of this arrangement have been reviewed and approved by the University of Texas at Austin in accordance with its policy on objectivity in research. The authors have financial interests in intellectual property owned by the University of Texas that includes ideas reported in this paper.

References

[1] Rochelle GT. Amine Scrubbing for CO_2 Capture. Science 2009;325(5948):1652–54.

[2] Rochelle GT, Chen E, Freeman SA, Van Wagener DH, Xu Q, Voice AK. Aqueous piperazine as the new standard for CO_2 capture technology. Chem Eng J 2011;171(3):725–33.

[3] Freeman SA, Dugas RE, Van Wagener DH, Nguyen T, Rochelle GT. Carbon dioxide capture with concentrated, aqueous piperazine. Int J Greenh Gas Con 2010;4(2):119–24.

[4] Du Y, Li L, Namjoshi O, Voice AK., Fine NA., Rochelle GT. Aqueous Piperazine/N-(2-Aminoethyl) Piperazine for CO_2 Capture. Energy Proc 2013; 37: 1621–38.

[5] Austgen DM. A Model of Vapor-Liquid Equilibria for Acid Gas-Alkanolamine-Water Systems. The University of Texas at Austin. Ph.D. Dissertation. 1989.

[6] Chen C.-C, Bokis CP, and Mathias PM. A Segment-Based Excess Gibbs Energy Model for Aqueous Organic Electrolyte Systems. AIChE J 2001;47:2593.

[7] Posey ML. Thermodynamic Model for Acid Gas Loaded Aqueous Alkanolamine Solutions. The University of Texas at Austin. Ph. D. Dissertation. 1996.

[8] Hilliard MD. A Predictive Thermodynamic Model for an Aqueous Blend of Potassium Carbonate, Piperazine, and Monoethanolamine for Carbon Dioxide Capture from Flue Gas. The University of Texas at Austin, Austin, TX, 2008.

[9] Frailie PT, Plaza JM. Modeling piperazine thermodynamics. Energy Proc 2011;4:35–42.

[10] Pagano JM, Goldberg DE, Fernelius WC. A Thermodynamic study of homopiperazine, piperazine, and N-(2-aminoethyl)-piperazine and their complexes with copper(II) ion. J Phys Chem 1961;65:1062–64.

[11] Brelvi SW, O'Connell JP. Corresponding States Correlations for Liquid Compressibility and Partial Molar Volumes of Gases at Infinite Dilution in Liquids. AIChE J 1972:18:1239–43.

[12] Nguyen T. Amine Volatility in CO_2 Capture. The University of Texas at Austin. Ph. D. Dissertation. 2013.

[13] Chen X, Rochelle GT. Aqueous piperazine derivatives for CO_2 capture: Accurate screening by a wetted wall column. Chem Eng Res Des 2011;89(9):1693–710.

Available online at www.sciencedirect.com

ScienceDirect

Energy Procedia 00 (2013) 000–000

Energy Procedia

www.elsevier.com/locate/procedia

GHGT-12

Absorption of nitrogen oxides in aqueous amines

Nathan A. Fine[a], Gary T. Rochelle[a]*

[a]*The University of Texas at Austin, Department of Chemical Engineering, 200 E Dean Keeton St. Stop C0400, Austin, TX 78712-1589*

Abstract

Nitric oxide (NO) and nitrogen dioxide (NO_2) were absorbed into aqueous amine to determine the absorbing species, the absorption kinetics, and the aqueous products at the ppm-level NO_x concentrations typical of flue gas from fossil fuel power plants. At flue gas conditions of 0.5-5 ppm of NO_2, absorption is dominated by free radical absorption of NO_2 as nitrite. NO_2 absorption kinetics are first order in NO_2 partial pressure, half order in free amine concentration, and fastest in methyldiethanolamine (MDEA). The reaction-enhanced liquid mass transfer coefficient for NO_2 absorption in 8 m piperazine (PZ) at absorber conditions is $9.7*10^{-7}$ mol/s·m^2·Pa, yielding 92% NO_2 absorption at a typical A/G of $3.3*10^6$ s·Pa·m^2/mol. Similarly, a 9 m monoethanolamine (MEA) solvent will absorb roughly 70% of the inlet NO_2 while a 7 m MDEA/2 m PZ solvent will absorb over 99% of the NO_2. Nitrite and nitrate are the main NO_x absorption products in MDEA with nitrite dominating at low NO_2 partial pressures. In PZ, the amine free radical formed during NO_2 absorption will react with NO to directly form n-nitrosopiperazine (MNPZ) or react with itself to form 2-piperazinol (2-PZOH). Typical nitrosamine yields in 5 m PZ are around 15% of total absorbed NO_x and can be halved with the addition of 200 mM Inhibitor A, a free radical scavenger. Nitrate and nitramine are minor products of NO_x absorption, accounting for less than 5% of total absorbed NO_x.

Selection and peer-review under responsibility of GHGT.

Keywords: nitrosamine; NO_x absorption; amine scrubbing; nitrite

* Corresponding author. Tel.: +1-512-471-7230; fax: +1-512-471-7060
E-mail address: gtr@che.utexas.edu

Selection and peer-review under responsibility of GHGT.

1. Introduction

1.1 Nitrosamine accumulation in amine scrubbing

Amine scrubbing is an efficient and proven method for carbon capture, but as a chemical process, it has the potential to form toxic byproducts such as nitrosamines [1,2]. Figure 1 gives a proposed sequence of processes that determine nitrosamine accumulation in amine scrubbing. Flue gas containing nitrogen oxides (NO_x) enters a polishing scrubber where a fraction (A) of the NO_x can be removed via reaction with sulfite or tertiary amine [3–5]. The remaining NO_x then enters the absorber where a portion of the nitrogen dioxide (NO_2) can absorb into the amine solution as nitrite (β). The NO can also absorb into solution via reaction with the amine radical to directly form the nitrosamine (γ) [6,7]. The rest of the NO_x will vent from the absorber along with the scrubbed flue gas. Amine oxidation is another source of nitrite in amine solvents that are not oxidatively stable such as monoethanolamine (MEA) [8,9]. Nitrite from NO_x absorption and amine oxidation will then travel to the stripper where it can nitrosate a secondary amine with a yield of δ. The yield is determined by the concentration of secondary amines in the solvent and their relative nitrosation rates compared to the principal amine [10,11]. After nitrosation, the nitrosamine will thermally decompose in the stripper sump according to a pseudo-first-order nitrosamine decomposition rate constant (k_{str}) [12,13]. Nitrosamine sources from NO_x absorption and amine oxidation will balance out with nitrosamine thermal decomposition to yield a steady-state nitrosamine concentration (Equation 1). This work focuses on NO_x absorption into aqueous amines, which is important for NO_x removal in the polishing scrubber (A) and NO_x absorption in the absorber (β and γ).

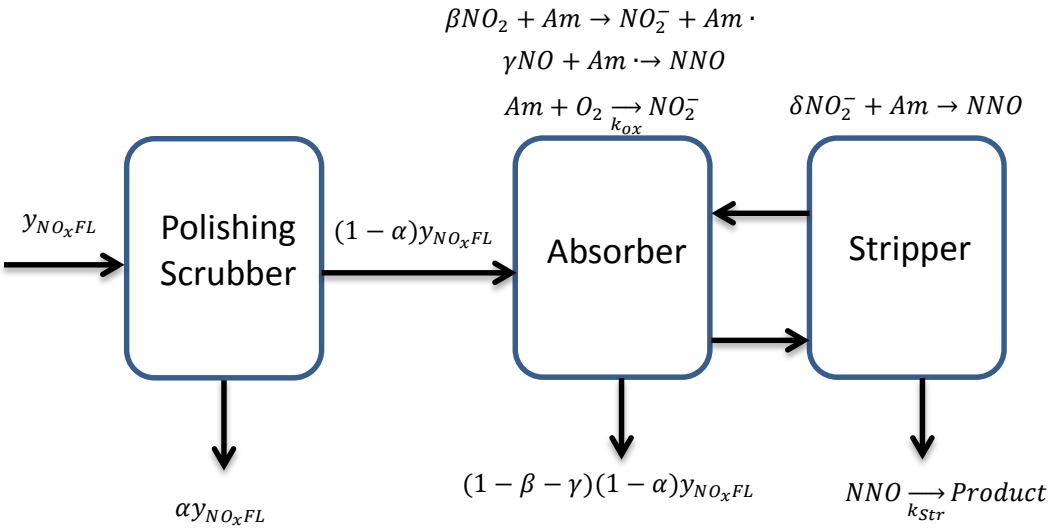

Figure 1: Nitrosamine Accumulation in Amine Scrubbing

$$NNO\ Steady\ State = \frac{(1-A)y_{NO_x}\frac{G}{L}(\delta\beta+\gamma)+\delta k_{Ox}\tau_{Tot}}{k_{Str}\tau_{Str}} \quad (1)$$

1.2 NO_x absorption into aqueous solutions

NO_x absorption at high concentrations has been heavily studied for the manufacturing of nitric acid [14]. With NO_x concentrations at approximately 10% by volume, NO_x absorption is dominated by the molecular absorption of dinitrogen trioxide (N_2O_3), and dinitrogen tetraoxide (N_2O_4). Absorption of N_2O_4 is pH independent above a pH of 5 since the pK_a of HNO_3 is low enough that it is completely dissociated in solution. However, the absorption of N_2O_3 depends on basicity due to the speciation of HNO_2 in the boundary layer. The fastest absorption rates are above a pH of 7 where HNO_2 is also completely dissociated in the boundary layer [15]. The equilibria for N_2O_3 and N_2O_4 are both second order in NO_x. Thus as NO_x concentration decreases, N_2O_3 and N_2O_4 comprise a decreasing proportion of the total NO_x. Even after accounting for the greater solubility of N_2O_3 and N_2O_4, only 0.2% of total absorbed NO_x at the gas-liquid interface exists as N_2O_3 or N_2O_4 at flue gas conditions compared to 66% during nitric acid manufacturing (Table 1).

Table 1: NO_x speciation under nitric acid manufacturing and flue gas conditions T = 25 °C, P = 1 Bar
Equilibria and Henry's coefficients from Patwardhan et al. [15]

Species	Henry's constant (M/Pa)	Concentration in equilibrium with 10% NO_x, 0.5% NO_2 (M)	Concentration in equilibrium with 100 ppm NO_x, 5 ppm NO_2 (M)
NO	1.84E-08	1.7E-04	3.6E-08
NO_2	1.18E-07	2.9E-05	1.7E-07
N_2O_3	5.92E-06	1.5E-04	1.5E-10
N_2O_4	1.38E-05	2.3E-04	2.3E-10

Due to the low concentration of N_2O_3 and N_2O_4, research for NO_x absorption at flue gas conditions has focused on the free radical absorption of NO_2. Sulfite, bisulfite, and sulfide all absorb NO_2 directly, greatly enhancing absorption at low NO_x levels [3,5]. Amines also enhance NO_x absorption with tertiary amines offering the highest absorption rates [4]. Nitrosamines have been shown to form during NO_x absorption into amine solutions at alkaline conditions [7,16–18]. At high NO_x concentrations, this can be attributed to the absorption of N_2O_3 and N_2O_4, two strong nitrosating agents [19]. However, Challis et al. theorize that at low NO_x concentrations and low amine concentrations, nitrosation is more likely to occur through free radical absorption of NO_2 followed by amine radical reaction of NO (Figure 2).

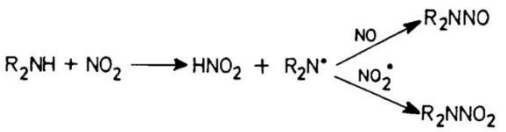

Figure 2: Series reaction to form nitrosamine [7]

2. Experimental Methods

2.1 Wetted Wall Column Apparatus

The mass transfer of NO_2 into amine solutions was measured using the wetted wall column (WWC) previously described by Dugas [20]. Briefly, a hydrated gas containing NO_2 contacts an amine solution over a known surface area. NO_2 concentration at the inlet and outlet of the wetted wall column are measured using a hot-gas FTIR [9]. The reaction enhanced liquid mass transfer coefficient (k_g') can then be

determined using the rate-based equation for NO_2 flux with a log mean partial pressure driving force (Equations 2-4).

$$N_{NO_2} = K_g * P_{NO_2\,LM} = \frac{G_{WWC} * (y_{NO_2\,in} - y_{NO_2\,out})}{A_{WWC}} \quad (2)$$

$$P_{NO_2\,LM} = \frac{P_{NO_2\,in} - P_{NO_2\,out}}{ln\left(\frac{P_{NO_2\,in}}{P_{NO_2\,out}}\right)} \quad (3)$$

$$\frac{1}{K_g} = \frac{1}{k_g} + \frac{1}{k_g'} \quad (4)$$

Conditions for the inlet gas stream are shown below (Table 2). The total solvent inventory for the WWC is approximately 2 L, which allows for lengthy experiment times without appreciable accumulation of absorption products that might interfere with rate measurements.

Table 2: WWC Gas Stream Conditions

Condition		Range
Temperature	(°C)	20–40
Pressure	(psig)	20–40
Flow Rate	(SLPM)	2-7
NO_2	(ppm)	50–300
H_2O	(%)	2.3-7.4
CO_2	(%)	0–4
N_2	(%)	76-98

2.2 High Gas Flow Apparatus

The WWC is ill-suited to measure aqueous products from NO_x absorption because of its large inventory, so the high gas flow contactor (HGF) previously described by Sexton [8] was repurposed to measure the reaction products of NO_x absorption. Briefly, a hydrated gas containing NO_x is sparged through 0.35 L of amine solvent (Table 3). NO_x concentration at the inlet and outlet of the HGF are measured using a hot-gas FTIR. The liquid is sampled by first setting the gas to bypass and then withdrawing 1 mL of sample through a septum. Absorption yields are determined by comparing reaction products to the overall mass balance of absorbed NO_x (Equation 5).

Table 3: HGF Gas Stream Conditions

Condition		Range
Temperature	(°C)	20–60
Pressure		Atmospheric
Flow Rate	(SLPM)	7.5
NO_2	(ppm)	10–150
NO	(ppm)	0-100
H_2O	(%)	2-20
CO_2	(%)	0.5-6
N_2 or Air	(%)	74-98

$$[NO_{2_{Abs}}] = \frac{PG_{HGF}}{RT} * m_{Sol} * (y_{NO_2\,in} - y_{NO_2})t \quad (5)$$

2.3 Aqueous Sample Analysis

Amines are analyzed using cation chromatography as described by Namjoshi et al. [21]. Nitrite and nitrate are analyzed using anion chromatography as described by Nielsen et al. [22]. N-nitrosopiperazine (MNPZ) is analyzed using high pressure liquid chromatography [12] and 2-piperazinol (2-PZOH) is analyzed using a dinitrophenylhydrazine (DNPH) derivitization method [13].

3. Results

Table 4 gives all the results for wetted wall column experiments. NO_2 absorption is modeled as a fast reaction in the liquid boundary layer with the pseudo-first-order assumption. NO_2 hydrolysis is assumed to be second order in NO_2 partial pressure while NO_2 absorption in amine is assumed to be first order.

Table 4: NO_2 absorption kinetics in the WWC

Solution	CO_2 Loading	T (°C)	$k_g' * 10^7$ (mol m^{-2} s^{-1} Pa^{-1})
0.001 M NaOH	0	20	$0.13\sqrt{P_{NO_2}}$
0.001 M NaOH	0	40	$0.11\sqrt{P_{NO_2}}$
5 m MEA	0.48	20	1.6
5 m MEA	0.48	40	1.9
9 m MEA	0.38	40	3.0
9 m MEA	0.48	20	1.9
9 m MEA	0.48	40	2.0
8 m PZ	0.26	40	13.7
8 m PZ	0.32	20	7.2
8 m PZ	0.32	40	9.7
8 m PZ	0.39	40	8.0
0.40 m MDEA	0	20	36.9
0.40 m MDEA	0	40	41.3
0.056 m MDEA	0	20	11.8
0.056 m MDEA	0	40	22.7
0.023 m MDEA	0	20	7.5
0.023 m MDEA	0	40	9.7

3.1 NO_2 Hydrolysis

Under basic conditions NO_2 absorbs into water as (N_2O_4), which then forms nitrite and nitrate (Equations 6a & 6b). Using film theory, the solution for NO_2 flux is given by Equation 7. Gas side mass transfer resistance can be ignored due to the relatively slow reaction kinetics.

$$2NO_2 \leftrightarrow N_2O_4 \tag{6a}$$

$$N_2O_4 + 2OH^- \rightarrow NO_2^- + NO_3^- + H_2O \tag{6b}$$

$$N_{NO_2} = P_{NO_2}\sqrt{\frac{2k_{H_2O}D_{N_2O_4}P_{NO_2}}{3H_{N_2O_4}{}^2}} = C_1 * P_{NO_2}{}^{3/2} = k_g' * P_{NO_2} \tag{7}$$

The flux of NO_2 into 0.001 M NaOH was measured from 2-30 Pa NO_2 at 20 °C and 40 °C. Flux as a function of NO_2 partial pressure was regressed using Equation 7 with C_1 as a free parameter. The data agrees well with the literature even though the experiments were run at different partial pressures and on different apparatuses (Figure 3). The experiment was attempted at 60 °C, but the results drastically over-predicted k_g'. This is most likely due to water condensation in the lines directly after the WWC, which provides extra surface area for NO_2 absorption.

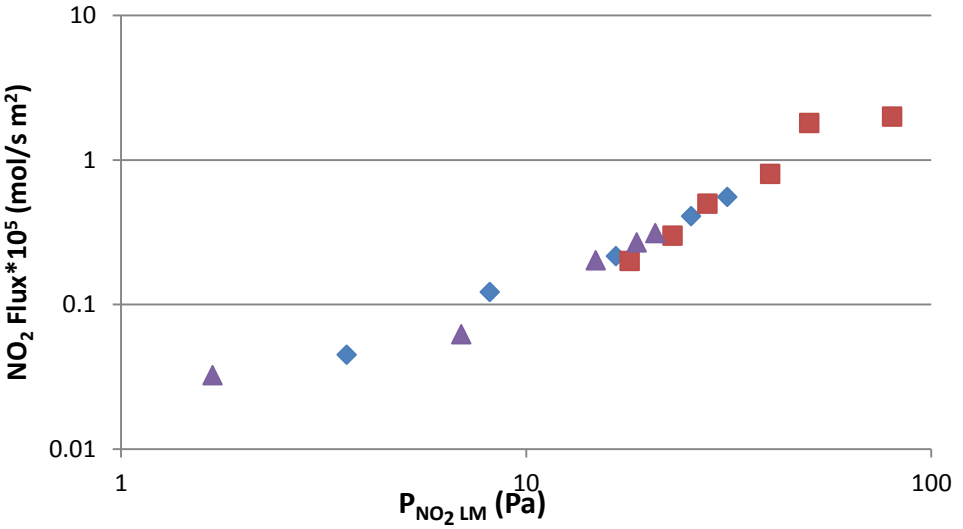

Figure 3: NO_2 Hydrolysis on the WWC at 20 °C (blue diamonds) and 40 °C (purple triangles) compared to NO_2 hydrolysis using the stirred cell at 25 °C [3] (red squares)

3.2 NO_2 Absorption into Amines during CO_2 Capture

NO_2 flux was measured in the wetted wall column at partial pressures ranging from 1–15 Pa. The gas side mass transfer coefficient (k_g) was measured with NO_2 absorption into 5.8 m methyldiethanolamine (MDEA), which has negligible liquid mass transfer resistance. The value for k_g is $25.2*10^7 \frac{mol}{m^2\, s\, Pa}$, approximately 40% higher than the k_g predicted for the wetted wall column under these conditions [23,24]. NO_2 flux into amine solutions is linear with respect to NO_2 partial pressure and passes through zero, suggesting that NO_2 absorption is dominated by first-order free radical absorption under experimental conditions (Figure 4).

The free radical absorption of NO_2 as nitrite is hypothesized to be first order in free amine, leading to a half-order amine dependence for the liquid mass transfer coefficient (Equation 8).

$$k_g' = \sqrt{\frac{k_{Am}[Am]_{Free} D_{NO_2}}{{H_{NO_2}}^2}} \tag{8}$$

The k_g' for NO_2 absorption into dilute MDEA is approximately half-order in total MDEA as hypothesized, and k_g' also increases with increasing free amine in piperazine (PZ) and MEA (Figure 5). However, k_g' flattens out at higher PZ loadings, suggesting that other PZ species such as PZH^+ and $PZCOO^-$ could also absorb NO_2. Finally, k_g' increases with increasing order of amines similar to the free radical absorption of ClO_2 in amines [2].

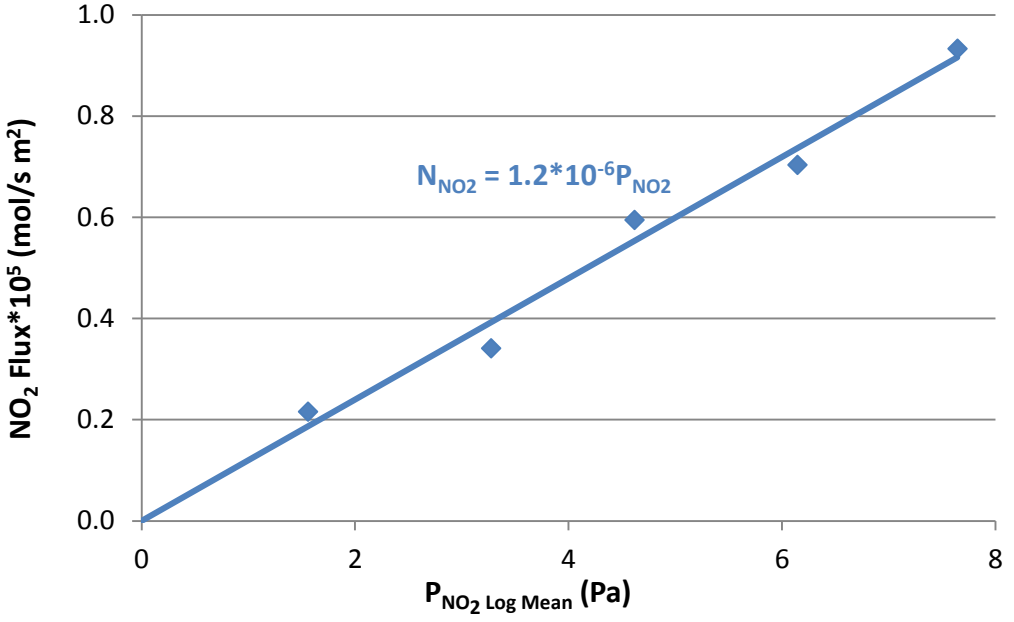

Figure 4: NO_2 Absorption into 0.05 m MDEA at 20 °C

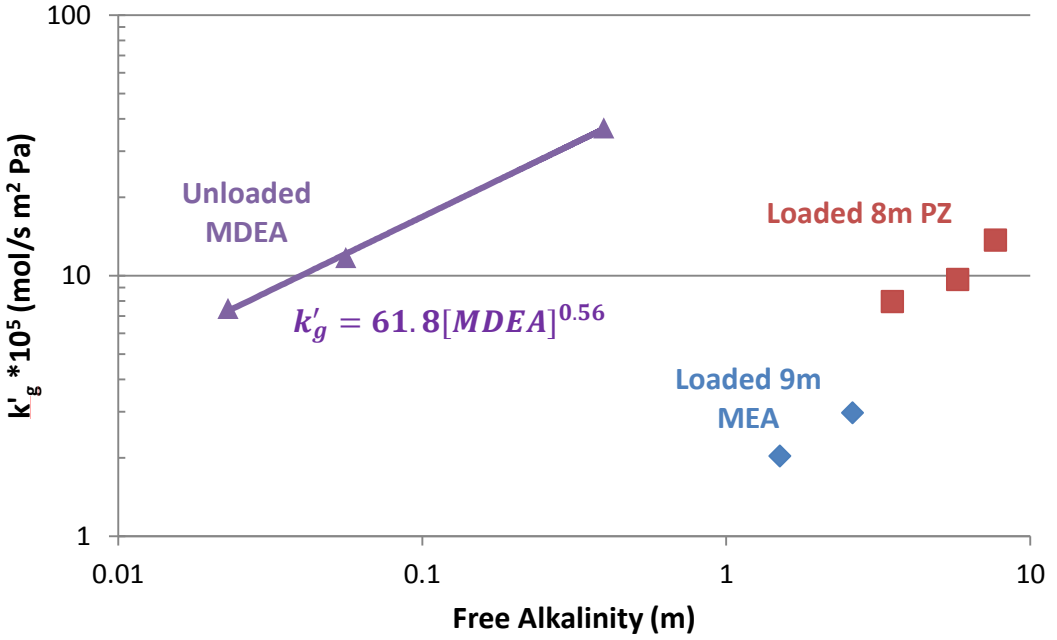

Figure 5: Dependence of k_g' on amine order and amine concentration, T = 40 °C

The fraction of NO_2 absorbed during CO_2 scrubbing can be estimated from the mass transfer coefficients and total wetted area of a typical amine scrubber (Equations 9 & 10). A typical MEA absorber designed for 90% CO_2 capture will absorb roughly 70% of inlet NO_2, PZ will absorb roughly 90% and MDEA/PZ will absorb over 99%. NO_2 hydrolysis can only account for 4% of total NO_x absorption (Table 5).

$$\frac{NO_{2\ absorbed}}{NO_{2\ Flue}} = (1 - e^{-N_{OG}}) \quad (9)$$

$$\mathrm{N_{OG}} = \frac{\mathrm{K_G} * \mathrm{A}}{\mathrm{G}} \quad (10)$$

Table 5: NO_2 absorbed in typical amine scrubbers

Solvent	A/G (m^2 s Pa/mol)	K_g (mol/m^2 s Pa)	NO_2 Absorbed (%)
9 m MEA	$4.3*10^6$	$3.0*10^{-7}$	73
8 m PZ	$2.6*10^6$	$9.7*10^{-7}$	92
7 m MDEA/2 m PZ	$2.6*10^6$	k_g limited	>99
Water at 2 ppm NO_2	$2.6*10^6$	$0.16*10^{-7}$	4

3.3 NO_x Absorption into MDEA

Tertiary amines are promising candidates for scrubbing NO_2 in a polishing scrubber before it reaches the absorber. Since NO does not absorb into solution by itself, one needs only to scrub the NO_2 to reduce the available nitrite, and ultimately reduce nitrosamine accumulation. Given a polishing scrubber with an A/G of $1.0*10^6$ s·Pa·m^2/mol, 90% NO_2 absorption could be achieved with k_g' = $23.0*10^{-5}$ mol/s·Pa·m^2. Figure 5 shows that this could be achieved with 0.17 m free MDEA in the polishing scrubber. Previously, sodium sulfite was studied for scrubbing NO_2 from flue gas. However, in aerobic environments sulfite catalytically oxidizes, drastically decreasing free sulfite in the boundary layer. The oxidation can decrease the rate of NO_2 absorption by 40% compared to an oxygen-free environment, necessitating the use of oxidation inhibitors [3]. In comparison, tertiary amines are oxidatively stable at low temperatures, so there is no expected penalty for NO_x absorption in a relatively high oxygen environment.

Hydrated N_2 gas with 60 ppm NO_2 was absorbed into a solution of 0.1 m MDEA at 20 °C for 2 hours using the HGF. The samples were extracted periodically and analyzed for nitrite and nitrate using anion chromatography. Nitrite and nitrate increased linearly with absorbed NO_2 (Figure 6) and together accounted for all of the absorbed NO_2. The same samples were analyzed for MDEA and methylaminoethanol (MAE) using cation chromatography. MDEA decomposition was not catalyzed by NO_2 absorption in the anaerobic environment with only 1.1 moles of MDEA decomposing for every mole of NO_2 absorbed. MAE is the only quantified amine product from NO_2 absorption, accounting for 67% of the decomposed MDEA (Figure 7). The experiment was repeated with air as the diluent and metal catalysts added to the amine solution, but there was no change in NO_x absorption products or MDEA decomposition rate.

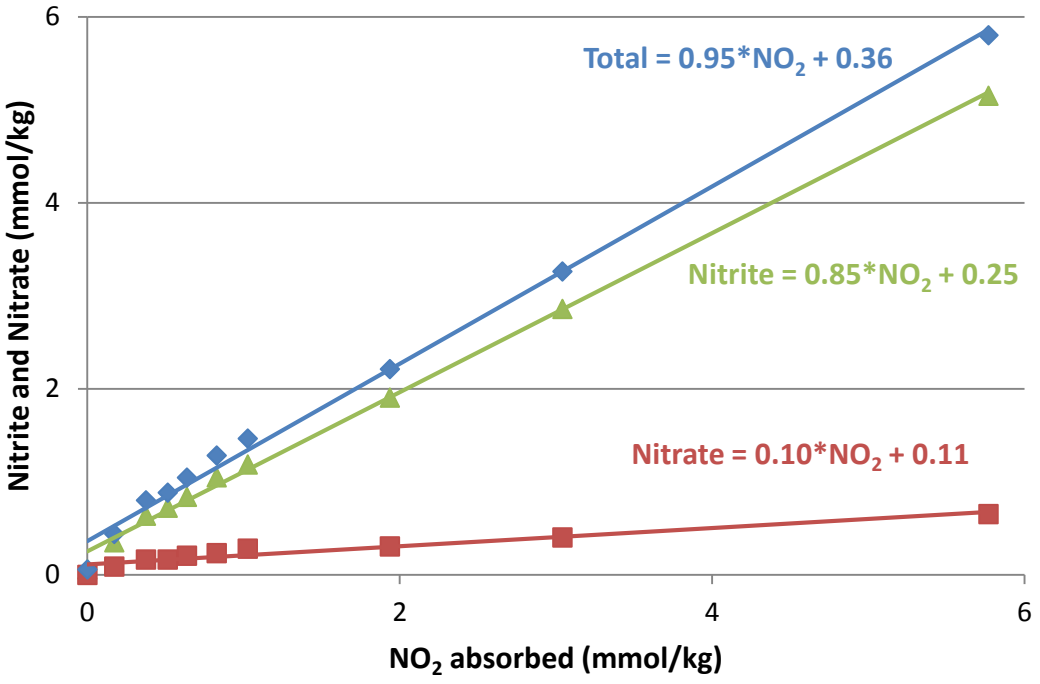

Figure 6: Nitrite and nitrate from NO_2 absorption into 0.1 m MDEA with 60 ppm NO_2 in hydrated N_2; T = 20 °C.

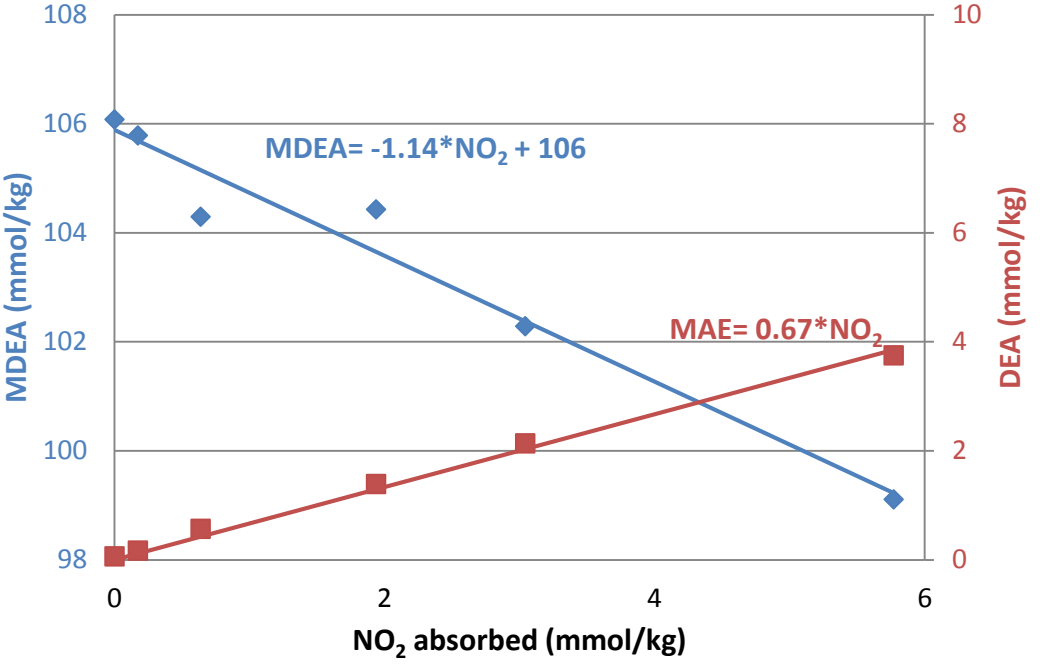

Figure 7: Amine products from NO_2 absorption into 0.1 m MDEA with 60 ppm NO_2 in hydrated N_2; T = 20 °C.

For a set of experiments NO_2 partial pressure was allowed to vary from 4 ppm to 144 ppm. Absorption products increased linearly with absorbed NO_2, and the data was linearly regressed with the slope representing the yield. The mole balance closed with an average of 97% of the total absorbed NO_x accounted for in the aqueous phase. Thus nitrosamine formed in MDEA could account for at most 3% of total absorbed product. Under similar conditions, Dai et al. reported that less than 1% of NOx absorbed in MDEA formed nitrosamine [16]. At very low concentrations of NO_2 almost all of the NO_2 absorbed as nitrite, which is consistent with free radical absorption of NO_2. As the concentration of NO_2 increased, the yield to nitrate increased, which shows the growing importance of NO_2 hydrolysis at high NO_2 concentrations (Figure 8). Both NO and oxygen had very little effect on the overall absorption products, proving that N_2O_3 is not an important absorption species under experimental conditions. A similar result with nitrite yield unaffected by NO concentration was obtained by Dai et al. in morpholine solution [25].

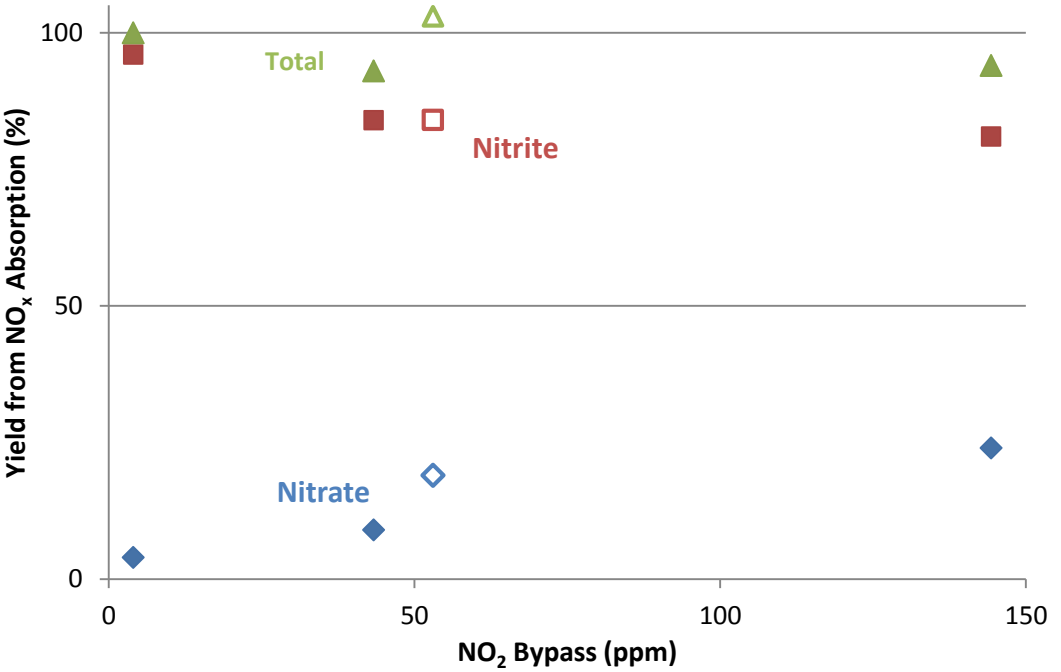

Figure 8: Nitrate and nitrite in 0.1 m MDEA, T = 20 °C (Closed points: NO_2 in N_2; Open Points: NO_2 with 200 ppm NO in air).

3.4 NO_x absorption into unloaded 1 m PZ

Unlike the radicals formed during NO_2 absorption in MDEA, the PZ radical can directly react with NO to form a stable nitrosamine. Previous research has shown that secondary amines will yield the highest nitrosamine concentrations during NO_x absorption [16] with nitrosamine yields of 6±2% of total absorbed NO_x in PZ at absorber conditions. The HGF was again used to study NO_x absorption products in 1 m PZ at 20 °C. All experiments were performed with 100 ppm NO and NO_2 varying from 10 to 100 ppm. MNPZ, nitrite, and nitrate were all proportional to total absorbed NO_x and together closed the mole balance within 4% (Figure 9). Nitrosamine yield varied from 20% to 35% of the total absorbed NO_x with no dependence on oxygen in the gas (Figure 10). Nitrosamine yield decreases with increasing NO_2 partial pressure, most likely due to the free radical termination step. At high concentrations of NO_2, there are more free radicals formed in the boundary layer. These can react with each other to form 2-PZOH with a second-order

dependence on free radical concentration (Equation 11). As the NO_2 partial pressure decreases, the free radical concentration decreases, and the radical is more likely to terminate by reacting with NO to yield MNPZ (Equation 12). The free radicals may also react with NO_2 to form the nitramine (Equation 13). However, nitramine concentration has been shown to be much lower than nitrosamine concentration [26] because NO_2 reacts quickly with the amine and is thus at a much lower concentration throughout the reaction boundary layer.

$$2PZ\cdot + H_2O \rightarrow PZ + 2PZOH \quad (11)$$

$$NO + PZ\cdot \rightarrow MNPZ \quad (12)$$

$$NO_2 + PZ\cdot \rightarrow PZNO_2 \text{ (minor)} \quad (13)$$

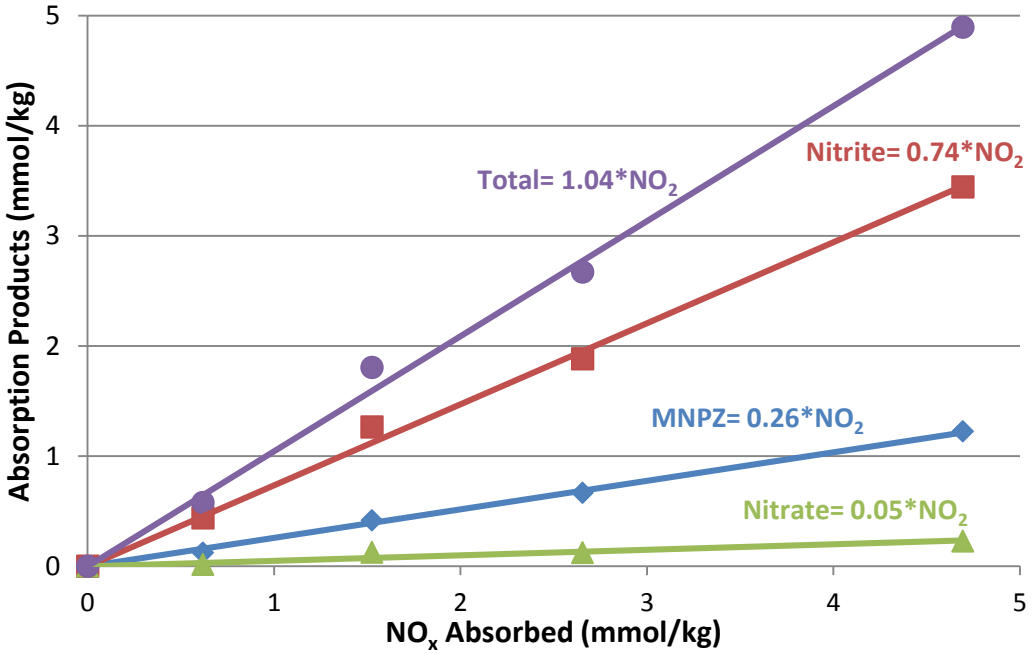

Figure 9: NO_x absorption products in 1 m PZ with 40 ppm NO_2, 100 ppm NO in hydrated N_2; T = 20 °C.

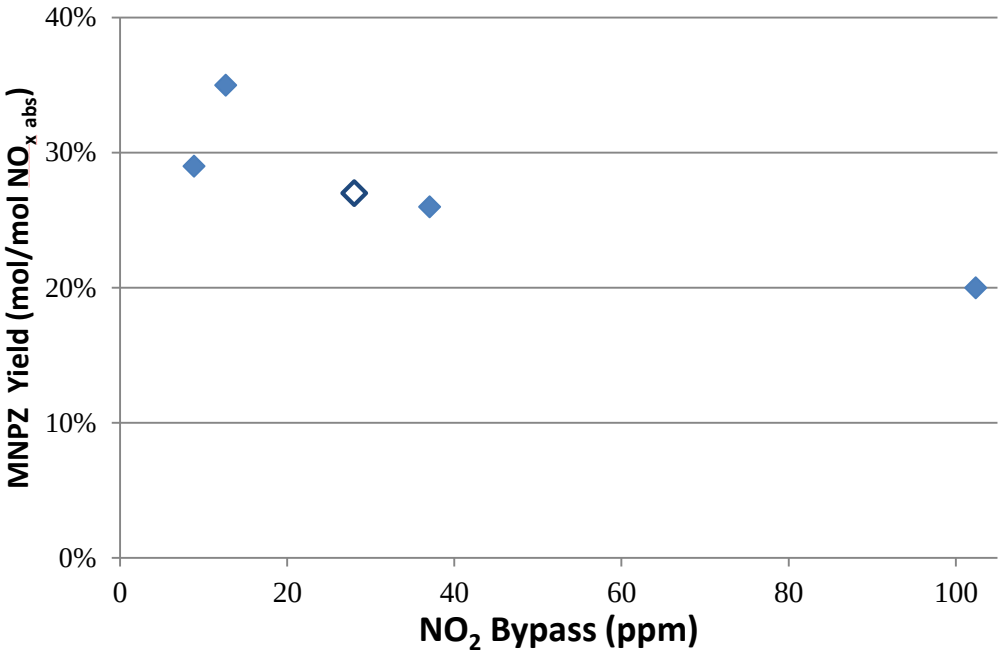

Figure 10: MNPZ yield in 1 m PZ with 100 ppm NO and varied NO_2 in hydrated N_2 (solid points) or air (open point); T = 20 °C.

3.5 NO_x Absorption into loaded 5 m PZ

A standard gas composition of 10 ppm NO_2 and 100 ppm NO in hydrated N_2 was sparged through loaded 5 m PZ to more closely simulate absorber conditions. MNPZ yield is independent of CO_2 loading and amine concentration as expected from the hypothesized termination mechanisms (Equations 14–16). Nitrosamine yield decreases drastically from 27% to 7% as temperature increases from 20 °C to 60 °C, possibly due to the decreased solubility of NO at higher temperatures (Figure 11). At 40 °C, nitrosamine yield is 17% which is roughly triple the nitrosamine yield found by Dai et al. at the same temperature. However, Dai et al. sparged with an NO_2:NO_x ratio of 1:2 [16], which favors termination as 2-PZOH instead of MNPZ.

One experiment was analyzed for 2-PZOH using the DNPH derivitization method. Although 2-PZOH concentrations were close to the quantification limit, it is clear that 2-PZOH increases with increasing absorbed NO_x (Figure 12). Since the stoichiometry of Equation 14 predicts 1 mol of 2-PZOH for every two moles of self-terminating amine radicals, the obtained yield of 65% is higher than expected. The high yield could possibly be explained by poor quantification of 2-PZOH at such low concentrations.

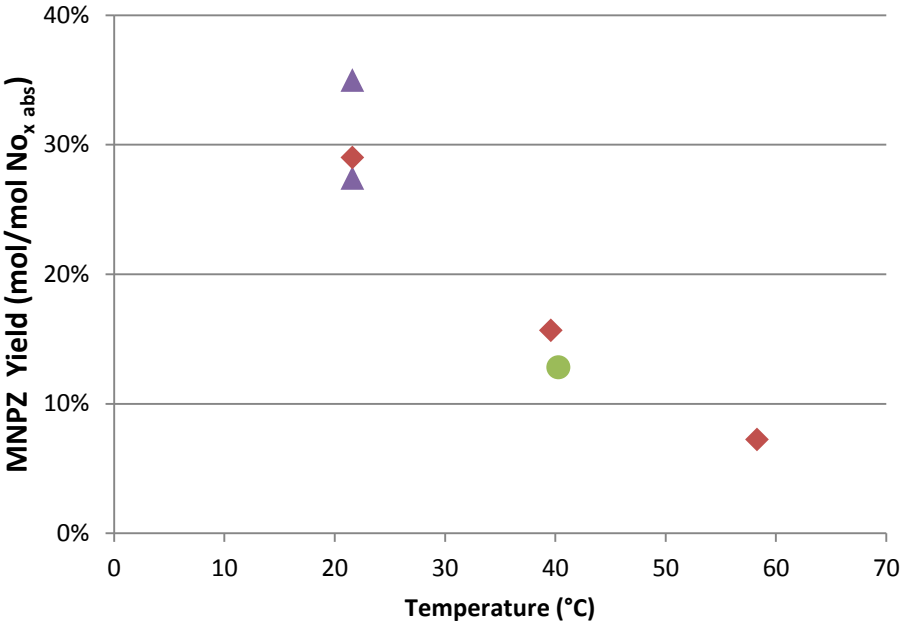

Figure 11: MNPZ yield in PZ with 10 ppm NO_2 and 100 ppm NO in hydrated N_2 for 5 m PZ α = 0.3 (red diamonds), 5 m PZ α = 0.15 (green circle) and 1 m PZ α = 0 (purple triangles).

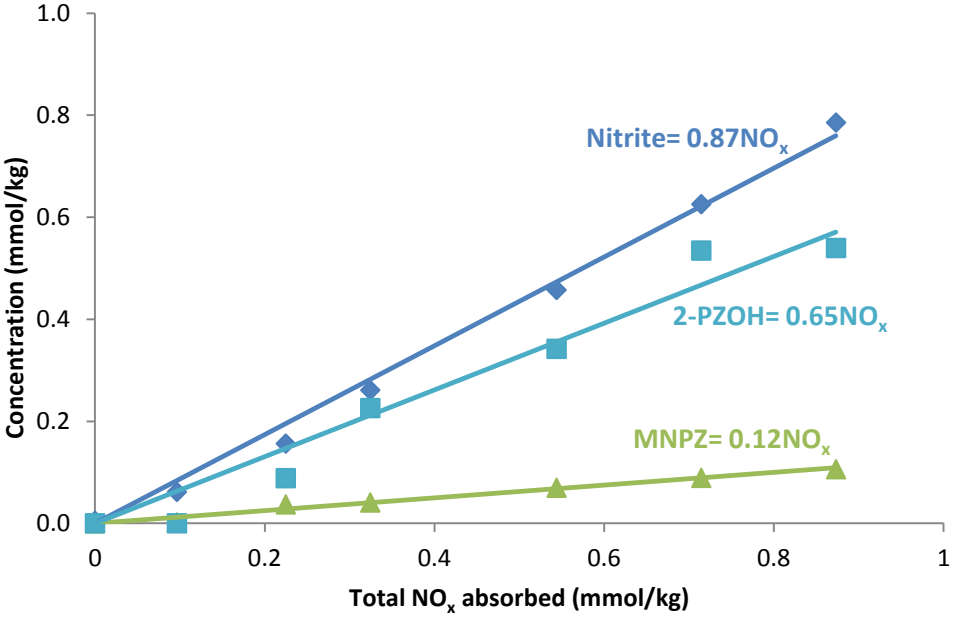

Figure 12: 2-PZOH accumulation from NO_x absorption in PZ; 10 ppm NO_2 and 100 ppm NO in hydrated N_2; 5 m PZ with α = 0.15 at 40 °C.

Two experiments were also performed with Inhibitor A (Inh A), a proprietary oxidative inhibitor that works as a free radical scavenger. As the concentration of Inh A increases, more of the PZ radical terminates by reacting with the scavenger instead of the NO. This decreases the MNPZ yield from 17% to 8% as Inh A increases from 0 to 200 mmol/kg (Figure 13). However, even though the MNPZ yield in the absorber decreases by 50%, this only has a minimum effect on the steady-state nitrosamine concentration since the absorbed nitrite will go on to nitrosate PZ under stripper conditions.

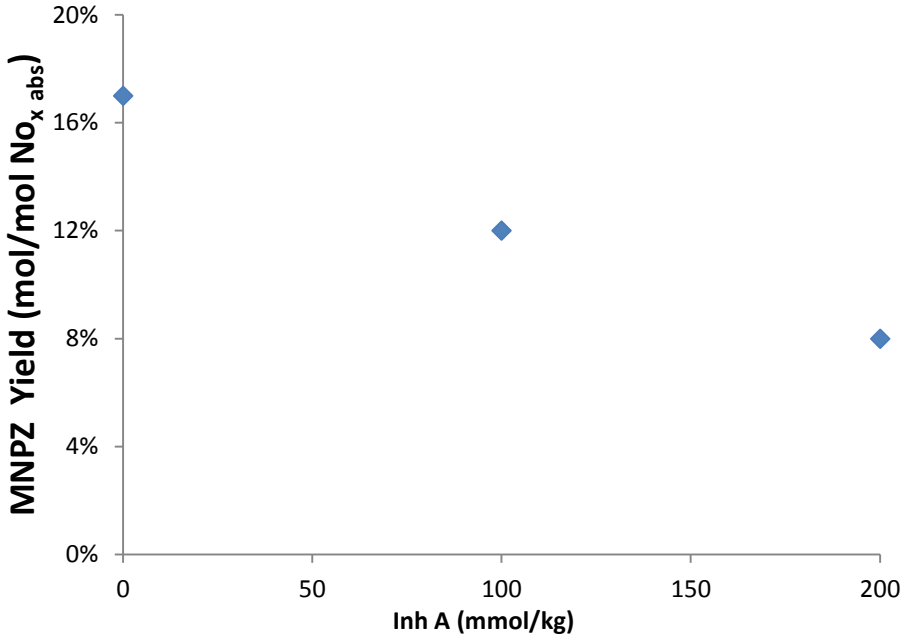

Figure 13: MNPZ yield with addition of Inh A; 10 ppm NO_2 and 100 ppm NO in hydrated N_2; 5 m PZ with α = 0.3; T = 40 °C,

4. Conclusions

4.1 NO_x Absorption Kinetics

- NO_x absorption at ppm levels of NO_x is dominated by the free radical absorption of NO_2.
- Free radical absorption of NO_2 is first order in NO_2 partial pressure and half order in free amine concentration.
- Absorption can be modeled as mass transfer with fast reaction in the pseudo-first-order regime.
- NO_2 absorption kinetics are fastest with tertiary amines and slowest with primary amines similar to ClO_2 free radical absorption into amines.
- 70–99% of NO_2 will absorb in amine scrubbers designed to capture 90% of CO_2; only 4% of NO_2 absorption can be attributed to hydrolysis.
- A prescrubber with an A/G of $1*10^6$ s·Pa·m^2/mol can scrub 90% of flue gas NO_2 with 0.17 m free MDEA.
- MDEA oxidation is not catalyzed by NO_2 absorption in the presence of air and stainless steel metals.

4.2 NO_x Absorption Products

- 10 ppm of NO_2 absorbs into 0.1 m MDEA with a 95% nitrite yield and a 5% nitrate yield.
- Nitrite yield is independent of NO and oxygen, proving that the absorption species is NO_2 directly instead of N_2O_3.
- NO_2 hydrolysis through N_2O_4 becomes the dominating absorption mechanism when NO_2 partial pressure is above 10 Pa (100 ppm at atmospheric pressure).
- Nitrosamine is less than 3% of total absorption product in 0.1 m MDEA.
- NO can directly absorb into amine solution by reacting with the free radical formed by NO_2 absorption.
- In PZ solution, NO absorption forms MNPZ with yields of 20–35% of total absorbed NO_x at 20 °C.
- PZ free radicals can also react with themselves or free radical scavengers to lower the yield to MNPZ.
- MNPZ yield is independent of amine concentration and loading, but yield increases as the ratio of NO_2:NO_x decreases.
- PZ free radicals can also react with themselves or with free radical scavengers to lower the MNPZ yield.
- Increasing absorption temperature from 20 °C to 60 °C decreases MNPZ yield by 60% due to the decreased solubility of NO.
- MNPZ yield at 40 °C in 5 m PZ with an NO_2:NO_x ratio of 1:10 is 17% with nitrite closing the mole balance.
- High temperature nitrosation from nitrite is the dominating mechanism for nitrosamine formation in amine scrubbing.

Acknowledgements

This work was supported by the Texas Carbon Management Program at the University of Texas at Austin.

The authors declare the following competing financial interest(s): One author of this publication consults for Southern Company and for Neumann Systems Group on the development of amine scrubbing technology. The terms of this arrangement have been reviewed and approved by the University of Texas at Austin in accordance with its policy on objectivity in research. The authors have financial interests in intellectual property owned by the University of Texas that includes ideas reported in this paper

This article was developed under STAR Fellowship Assistance Agreement No. FP917625-01-0 awarded by the U.S. Environmental Protection Agency (EPA). It has not been formally reviewed by EPA. The views expressed in this article are solely those of Nathan Fine and EPA does not endorse any products or commercial services mentioned in this article.

Appendix A. Table of uncommon abbreviations and symbols

Abbreviation	Description	Unit
NO_x	Nitrogen oxides	-
NO	Nitrogen monoxide	-
NO_2	Nitrogen dioxide	-
A	Fraction of NO_x absorbed in prescrubber	mol $NO_{x\ abs}$/mol $NO_{x\ flue}$
β	Fraction of NO_2 absorbed as nitrite	mol $NO_{2\ abs}$/mol $NO_{2\ flue}$
γ	Fraction of NO absorbed as nitrosamine	mol $NO_{\ abs}$/mol $NO_{\ flue}$

δ	Yield of nitrosamine from nitrite	mol NNO/mol nitrite
MEA	Monoethanolamine	-
k_{str}	Pseudo-first order decomposition of nitrosamine	s^{-1}
τ_{Str}	Residence time of the stripper	s
$\frac{G}{L}$	Ratio of molar flow rate of flue gas to volumetric flow rate of solvent.	mol flue gas/ L solvent
k_{ox}	Apparent rate of oxidation to nitrite	M/s
τ_{Tot}	Residence time of total scrubber	s
$NNO\ Steady\ State$	Steady state concentration of nitrosamine	M
NNO	Generic nitrosamine	-
$Am\cdot$	Amine radical formed from NO_2 absorption	-
N_2O_3	Dinitrogen trioxide	-
N_2O_4	Dinitrogen tetraoxide	-
WWC	Wetted wall column	-
N_{NO_2}	Molar flux of NO_2	mol/s m^2
K_g	Overall mass transfer coefficient of NO_2	mol/s m^2 Pa
$P_{NO_2\ LM}$	Log mean average of the partial pressures of NO_2 into and out of the WWC	Pa
G_{WWC}	Gas flow rate across the WWC	mol/s Pa
A_{WWC}	Wetted area of the wetted wall column	m^2
k_g	Gas side mass transfer coefficient	mol/s m^2 Pa
$k_g{}'$	Overall liquid side mass transfer coefficient	mol/s m^2 Pa
HGF	High Gas Flow apparatus	-
$[NO_{2_{Abs}}]$	Total NO_2 absorbed into solution	mmol/kg solution
G_{HGF}	Gas flow rate across the WWC	L/min
m_{Sol}	Mass of absorbing solution	kg
$y_{NO_2\ in}$	Mole fraction of NO_2 into the HGF	mol NO_2/mol gas
$y_{NO_2\ out}$	Mole fraction of NO_2 out of the HGF	mol NO_2/mol gas
t	Total time sparged	min
MNPZ	N-nitrosopiperazine	-
2-PZOH	2-piperazinol	-
DNPH	Dinitrophenylhydrazine	-
k_{Am}	Rate constant for NO_2 reaction with amine	$M^{-1}s^{-1}$
D_{NO_2}	Diffusivity of NO_2 in amine solution	cm^2/s
H_{NO_2}	Henry's constant for NO_2 in amine solution	Pa m^3/mol
MDEA	Methyldiethanolamine	-
PZ	Piperazine	-
N_{OG}	Overall number of transfer units	-
A/G	Wetted area per gas flow rate	m^2 s Pa/mol
MAE	Methylaminoethanol	mol/kg H_2O
$PZNO_2$	1-Nitropiperazine	-

References

[1] Strazisar BR, Anderson RR, White CM. Degradation Pathways for Monoethanolamine in a CO_2 Capture Facility. Energy & Fuels 2003;17:1034–9.
[2] Rochelle GT, Bishnoi S, Chi S, Dang H, Santos J. Research Needs for CO_2 Capture from Flue Gas by Aqueous Absorption/Stripping. Austin, Texas; 2001 Report No.: DE-AF26-99FT01029.
[3] Shen C. Nitrogen Dioxide Absorption in Aqueous Sodium Sulfite [PhD Thesis]. Austin, Texas: The University of Texas at Austin; 1997.
[4] Mimura T, Shimojo S, Mitsuoka S. Process for Removing Carbon Dioxide and Nitrogen Oxides from Combustion Gases. 5648053, 1997.
[5] Takeuchi H, Ando M, Kizawa N. Absorption of Nitrogen Oxides in Aqueous Sodium Sulfite and Bisulfite Solutions. Ind Eng Chem Process Des Dev 1977;16:303–8.
[6] Nedospasov AA. Is N_2O_3 the main nitrosating intermediate in aerated nitric oxide (NO) solutions in vivo? If so, where, when, and which one? J Biochem Mol Toxicol 2002;16:109–20.
[7] Challis BC, Kyrtopoulos SA. Nitrosation under alkaline conditions. J Chem Soc Chem Commun 1976;21:877–8.
[8] Sexton AJ. Amine Oxidation in CO_2 Capture Processes [PhD Thesis]. Austin, Texas: The University of Texas at Austin; 2008.
[9] Voice AK. Amine Oxidation in Carbon Dioxide Capture by Aqueous Scrubbing [PhD Thesis]. Austin, Texas: The University of Texas at Austin; 2013.[10] Fine NA, Goldman MJ, Rochelle GT. Nitrosamine Formation in Amine Scrubbing at Desorber Temperature. Environ Sci Technol 2014;48:8777–83.
[11] Goldman MJ, Fine NA, Rochelle GT. Kinetics of N-nitrosopiperazine formation from nitrite and piperazine in CO_2 capture. Environ Sci Technol 2013;47:3528–34.
[12] Fine NA, Rochelle GT. Thermal decomposition of n-nitrosopiperazine. Energy Proc 2013;37:1678–86.
[13] Fine NA, Nielsen PT, Rochelle GT. Decomposition of nitrosamines in CO_2 capture by aqueous piperazine or monoethanolamine. Environ Sci Technol 2014;48:5996–6002.
[14] Pradhan MP, Joshi JB. Absorption of NO_x gases in plate column: Selective manufacture of sodium nitrite. Chem Eng Sci 2000;55:1269–82.
[15] Patwardhan JA., Joshi JB. Unified model for NO_x absorption in aqueous alkaline and dilute acidic solutions. AIChE J 2003;49:2728–48.
[16] Dai N, Mitch WA. Influence of Amine Structural Characteristics on N-Nitrosamine Formation Potential Relevant to Postcombustion CO_2 Capture Systems. Environ Sci Technol 2013;47:13175–83.
[17] Chandan PA, Remias JE, Neathery JK, Liu K. Morpholine nitrosation to better understand potential solvent based CO_2 capture process reactions. Environ Sci Technol 2013;47:5481–7.
[18] Jackson P, Attalla M. N-Nitrosopiperazines form at high pH in post-combustion capture solutions containing piperazine: a low-energy collisional behaviour study. Rapid Commun Mass 2010;24:3567–77.
[19] Douglass M, Kabacoff B. The chemistry of nitrosamine formation, inhibition and destruction. J Soc Cosmet Chem 1978;606:581–606.
[20] Dugas R. Carbon dioxide absorption, desorption, and diffusion in aqueous piperazine and monoethanolamine. The University of Texas at Austin, 2009.
[21] Namjoshi O, Rochelle GT. Thermal degradation of PZ-promoted tertiary amine blends for CO_2 capture: comparison of structure effects and process conditions on degradation rate. Int J Greenh Gas Control *Manuscript Submitted*.
[22] Nielsen PT, Li L, Rochelle GT. Piperazine degradation in pilot plants. Energy Proc 2013;37:1912–23.
[23] Pacheco MA. Mass Transfer, Kinetics and Rate-based Modeling of Reactive Absorption. The University of Texas at Austin, 1998.
[24] Bishnoi S. Carbon Dioxide Absorption and Solution Equilibrium in Piperazine Activated Methyldiethanolamine [PhD Thesis]. Austin, Texas: The University of Texas at Austin; 2000.
[25] Dai N, Mitch WA. Effects of Flue Gas Compositions on Nitrosamine and Nitramine Formation in Postcombustion CO_2 Capture Systems. Environ Sci Technol 2014;48:7519–26.

[26] Dai N, Shah AD, Hu L, Plewa MJ, Mckague B, Mitch WA. Measurement of Nitrosamine and Nitramine Formation from NO_x Reactions with Amines during Amine-Based Carbon Dioxide Capture for Postcombustion Carbon Sequestration. Environ Sci Technol 2012;46:9793–801.

Available online at www.sciencedirect.com

ScienceDirect

Energy Procedia 00 (2013) 000–000

Energy Procedia

www.elsevier.com/locate/procedia

GHGT-12

Quantification of gas and aerosol-phase piperazine emissions by FTIR under variable bench-scale absorber conditions

Steven M. Fulk[a] and Gary T. Rochelle[a]*

[a]*The University of Texas at Austin, McKetta Department of Chemical Engineering, Texas Carbon Management Program, 200 E Dean Keeton St. Stop C0400, Austin, TX 78712-1589 USA*

Abstract

Recent pilot-scale CO_2 capture plants have found that amine condensation onto seed nuclei results in very high amine emissions which are very difficult to characterize and control using traditional aerosol removal techniques. Modeling and experiments have shown significant potential to efficiently capture high density, submicron particles in packed columns by adjusting contactor operating conditions. This study presents the influence of operating conditions on total (gas and aerosol) emissions of piperazine (PZ) measured by hot-gas Fourier Transform Infrared Spectroscopy (FTIR) from a bench-scale CO_2 absorber with RSR-0.3 random packing using 0.9 m PZ. Aerosols were created by vaporizing and quickly condensing 0.5 m PZ and 0.05 vol % sulfuric acid (H_2SO_4). PZ was inversely proportional to solvent temperature and flowrate, but increased independent of the inlet CO_2 with PZ/H_2O seed nuclei. PZ emissions were proportional to flowrate and inversely related to inlet CO_2 concentration for H_2SO_4/H_2O condensation nuclei.

Selection and peer-review under responsibility of GHGT.

Keywords: Emission measurement; aerosols; operating conditions; FTIR; piperazine

* Corresponding author. Tel.: +1-512-471-7230; fax: +1-512-471-7060.
E-mail address: gtr@che.utexas.edu

Selection and peer-review under responsibility of GHGT.

1. Introduction

1.1. Emissions from CO_2 Capture Plants

Acid gas removal by absorption/stripping using aqueous amine solvents has been successfully used on an array of industrially relevant applications for many decades. Recently, amine scrubbing has been identified as a crucial piece of technology in the portfolio of CO_2 abatement strategies designed to address climate change. The simplicity of chemically reversible separation of CO_2 has led to significant and fruitful studies involving process optimization by selecting amine solvents which change the thermodynamic and hydraulic performance of the absorber and stripper unit operations in an effort mitigate the drawbacks of a direct-contact, thermal-swing system: energy performance, capital cost, and environmental impact. Proper characterization of solvent performance at the bench-scale has facilitated the construction of numerous thermodynamic and kinetic process models which provide the tools to accurately predict process performance and capital cost of many combinations of solvents and process configurations. However, the omission of pollutants from modeling activities and other complexities of real-life application of these systems can lead to severe degradation of performance, as well as unacceptable emissions by a variety of mechanisms.

Traditional aqueous solvents used to capture CO_2 are continuously exposed to contaminants in the incoming flue gas. In the case of post-combustion carbon capture (PCCC), those pollutants include gaseous combustion byproducts such as O_2 (3-5 vol %), SO_x, NO_x, and HCl, post-treatment slippage from selective catalytic reduction (NH_3), flue gas desulfurization ($CaCO_3$ and $CaSO_4$), and mercury removal (activated carbon), as well as particulate matter (PM) produced from sublimation of vaporous heavy metals, ash shedding, heterogeneous and homogeneous nucleation, and cenosphere/bursting mechanisms [1]. In addition to inlet impurities, continuous thermal cycling of solvent (40-150 ºC) during the capture/release steps serves to diminish performance through thermal degradation. Out of all the possible pathways for emissions to occur, recent works have identified amine aerosol as not only the dominant emission pathway, but one of the most difficult to measure and to control with wash columns or other conventional countermeasures.

1.2. Previous Aerosol Measurements

Amine-containing aerosols can originate from a variety of sources: physical entrainment of solvent, homogeneous nucleation of amine with other gaseous species, and heterogeneous nucleation/condensation on preformed nuclei such as hygroscopic PM, and most importantly, H_2SO_4 mist formed by reaction and subsequent condensation of SO_3 and H_2O. Several studies have quantified the impact of H_2SO_4 mist and PM on the loss rate of amine in addition to characterizing the particle size distributions and concentrations using a variety of measurement techniques.

A review of aerosol literature in PCCC pilot plants and at the bench-scale shows that very low levels of inlet SO_3 and soot/PM can create seed nuclei on the order of a few nanometers in size at very high densities (10^6-10^8 particles/cm^3) which lead to excessive amine carryover in absorber exhaust [2, 3, 4]. Kamijo et al. show that 0-3 ppmv of SO_3 can produce 0.4-23.2 ppmv and 0.8-67.5 ppmv for KS-1^{TM} and MEA solvents, respectively [5]. High amine emissions due to aerosol carryover was also confirmed during CO_2 capture tests at Maasvlakte where detailed characterization of the particle phase was attempted using a combination of light extinction measurements, an Aerodynamic Particle Sizer (APS), an Electrical Low Pressure Impactor (ELPI), and the installation of a high efficiency droplet capture device called the Brownian Demister Unit (BDU) [6, 7]. The Sauter mean droplet diameter (D_{32}) at top of the absorption tower before to the BDU was reported to be 0.76-7.88 μm and decreased to 0.2-1.74 μm at the BDU outlet.

A more recent set of papers from Brachert, Mertens, and Khakharia detailing collaborative aerosol studies at the Karlsruhe Institute of Technology (KIT) clearly verified the direct influence of H_2SO_4 mist as well as soot/PM on the amine slippage rate while providing both inlet and outlet droplet size distribution measurements using the extractive ELPI sampling technique and a condensation particle counter (CPC) in combination with FTIR. Most importantly, it was found that soot concentrations of 10^6 particles/cm^3 and H_2SO_4 mist at a density of 10^8 particles/cm^3 resulted in 200 (74) and 600-1100 (223-409) mg/Nm^3 (ppmv) of MEA emissions, respectively [3],

and that the average seed nuclei grew from a few nanometers entering the absorber to nearly 1 μm at the outlet [2, 4]. Droplet growth was further verified by changing the dilution rate to the ELPI sampling train and observing the shifting size distribution.

Aerosol measurements from pilot plants and smaller-scale tests thus far have demonstrated the clear need to reduce PCCC emissions resulting from inlet condensation nuclei. Though many solutions currently exist, including high density fiber filters and inertial separation methods, the associated pressure drop likely precludes their use in full-scale CO_2 capture facilities. Research in this area must find more cost-effective strategies of capturing aerosols in CO_2 capture units.

1.3. Aerosol Abatement by Growth and Capture

Several aerosol researchers have pointed to efficient aerosol removal in packed columns by heterogeneous nucleation (condensation) [8, 9, 10]. By effectively selecting operating conditions, they argue, and experimentally confirm, that high degrees of supersaturation can be achieved which can "activate" aerosol growth and subsequent capture in randomly packed columns. The degree of supersaturation, and the influence of operating conditions, is characterized by the ratio of heat and mass transfer rates, given by the Lewis number. Heidenreich and co-authors demonstrated that high concentrations (10^6 particles/cm^3) of submicron particles of variable starting composition can be efficiently collected using a two-stage cascade counter-current contactor by increasing the temperature difference between the inlet fluids. In PCCC research, previous modeling of heat and mass transfer of aerosols in CO_2 capture systems have arrived at similar conclusions [11]. It was theorized that by altering the operating conditions or design of the CO_2 capture plant, aerosol capture may be facilitated by condensational growth or evaporative shrinking. Cascaded column designs to remove aerosols through growth conditioning could be readily incorporated into existing water wash towers.

Pilot plant measurements done by Mertens et al. have found similarly conclusive, quantitative linkages between operation of CO_2 capture plants and amine emissions [12]. In the study by Mertens and colleagues, MEA, PZ, and 2-amino-2-methyl-1-propanol (AMP), were measured using FTIR, flame ionization detection (FID), and a manual sampling technique employing a combination of impingers and adsorbents under different steady-state operating conditions. The study showed that amine emissions were positively correlated to the temperature difference across the water wash and negatively correlated to the inlet CO_2 concentration. Their conclusions indicate a strong influence of enthalpy on emissions; however, complex interactions of reaction enthalpy and solvent vapor pressure depression due to CO_2 loading.

The imbalance in rates of heat and mass transfer leads to greater supersaturation in gas-liquid contactors. The creation of supersaturation through influential operation handles can lead to emissions reductions strategies without resorting to costly countermeasures.

1.4. Work Objectives

This work seeks to reduce gaseous and amine aerosol emissions from CO_2 capture plants using aqueous amine solvents by investigating the influential process factors including: (1) inlet CO_2 content, (2) solvent flowrate, and (3) inlet solvent temperature. A newly constructed apparatus capable of simulating CO_2 capture using a dilute PZ solvent in the presence of aerosols will be presented. Gas-phase FTIR measurements will clearly demonstrate the effect of operating conditions, most notably the solvent rate, on PZ emissions. The findings of this work can further facilitate better emission reduction strategies from PCCC systems.

2. Experimental Methods

An experimental apparatus, analogous to a randomly packed amine-based CO_2 absorber, was constructed with the capability of generating and measuring aerosols as well as performing simultaneous gas-phase composition measurements at multiple sampling points under variable process conditions relevant to CO_2 capture absorbers and water wash columns. Figure 1 shows a simplified process flow diagram of the experimental apparatus.

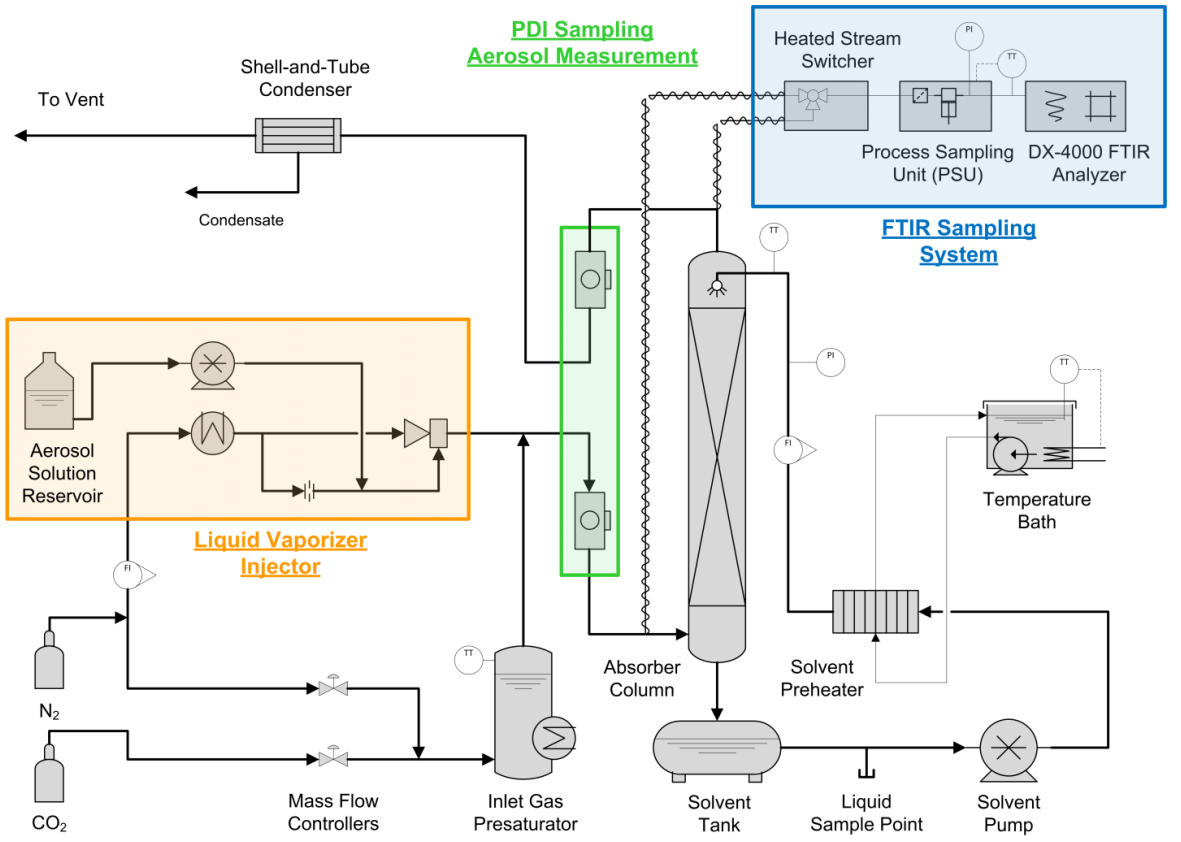

Figure 1: Process flow diagram of the Aerosol Growth Column (AGC), the Liquid Vaporizer and Injector (LVI) aerosol generator, and FTIR sampling system.

2.1. Aerosol Growth Column (AGC)

The absorber column built for this study, referred to as the AGC, is a randomly packed CO_2 absorber with a temperature controlled, recirculated solvent.

The inlet gas is made up of a mixture of N_2, taken from a large dewar, and Bone dry, Gr. 3.0 CO_2 (Airgas® CDBD200) regulated using a Y11-N245D320, CGA320 regulator. The N_2 supply is split following an isolation valve into three streams used for the absorber gas supply, the LVI gas supply, and FTIR maintenance, background, and calibration. The N_2 flowrate to the absorber is controlled by an analog 100 SLPM Brooks 5851 I-Series mass-flow controller connected to an NI 9265 4-ch, 20 mA current output module and an NI 9203 8-ch, 20 mA current input module. Connection is made with a 15 pin D-Sub cable at the controller side and crimp pin connections at the NI module side. The NI modules are connected to a cDAQ-9174 USB chassis which is controlled by a user-built LabVIEW™ application with interactive GUI via a laptop and USB 2.0 connection. The flowrate of CO_2 is controlled by a 15 SLPM Brooks 5850 I-Series mass-flow controller using the same NI modules and chassis.

The N_2/CO_2 gas stream is bubbled though a presaturator to approximately maintain H_2O balance within the absorber column. The presaturator for the AGC is constructed of 6” 304SS Sch. 10 pipe with #150 flanges. Temperature is controlled with a screw-plug immersion heater with a relayed temperature controller. The head-space temperature is logged with a separate K-type thermocouple connected to a 4-ch ± 80 mV NI-9211 module. The inlet gas is sparged into the presaturator by a 3/8” straight tube with small drilled holes. The total liquid height in the saturator is maintained at over 20”.

A hot gas mixture delivered by the LVI is mixed with the saturated process gas at the outlet of the presaturator in a 3/4" stainless steel tee fitting. Rapid cooling downstream of the LVI/process gas mixing point produces homogenous nuclei prior to entering the absorber column. The aerosol carrying gas is introduced into a flanged tee at the bottom of the column below the packing supports.

The absorption section of the AGC is constructed out of a 1½" 304SS Sch. 10 pipe with flanged ends. Removable lugs and a mesh screen support up to 6' of packing. The packing used in this study was RSR-0.3 random packing.

Solvent is drawn from a 16 gal SS tight-head drum (The Cary Company 26B6SS) by a Micropump® A-mount suction shoe pump head controlled by a Cole Parmer Console Drive. The flowrate is measured by a rotameter (Omega FL46302). The inlet solvent temperature is controlled by cross exchange with recirculated H_2O provided by a Lauda ECO E4G temperature bath. The cross exchanger is a Thermal Transfer Systems AN14-20H plate-and-frame heat exchanger. Solvent is delivered above the packing using hollow-cone spray nozzles (Kyser and Associates 1/4A-316SS2 & 1/4A-316SS-5) connected to a tapped blind flange. The solvent temperature is measured at the flange using a K-type thermocouple. CO_2-rich liquid drains through a 1" inner diameter (ID) gravity drain line back into the solvent tank.

The inlet and outlet gas composition can be sampled and analyzed by FTIR using the Process Sampling Unit (PSU) and heated stream switcher. The PSU consists of a heated filter and a heated Teflon® diaphragm pump. The heated stream switcher is a heated enclosure with 3-way valves which can alternately sample up to three FTIR locations. FTIR sample points are constructed from 3/4" threaded pipe tees reduced to 1/4" tubing connection using reducer bushings and Swagelok® adapters. FTIR connections are always insulated using glass wool and connections made to the process are heat-traced with heat tape controlled by AC Variable Autotransformers (variac). Variacs are typically set to 35% of full voltage (120V).

Outlet gas from the absorber runs through a counter-current, pipe-and-tube condenser fed with cooling water to knock out H_2O and amine. The cooled gas leaving the exchanger is sent to a 2" pipe tee to reduce the velocity such that condensate and large entrained droplets will be collected and drain to the condensate collection point located at the bottom of the column.

A liquid sampling port consisting of a 3/8" Swagelok® tee with a 12.7 mm OD RESTEK® BTO Septa is located at the inlet of the solvent pump. Liquid samples are drawn using a 2 mL syringe and are transferred to 4 mL (1 dr.) amber vials for subsequent analysis.

2.2. Liquid Vaporizer and Injector (LVI)

The LVI was designed by Air Quality Analytical, Inc. to produce H_2SO_4 aerosol up to 5 ppmv in a 350 ACFM (pilot-scale) gas stream. The LVI blends hot gas (310 ºC) with a metered stream (FMI RH00 pump and FMI VS200 controller) of liquid in an eductor (Air-VAC HAVR062HSS) body. The flowrate of the eductor motive fluid (N_2) is controlled by a pressure regulator and is measured using a rotameter adjusted for the supply pressure of 100 psig.

The vaporized material is introduced into the cold, main process gas stream where condensation occurs. Given a high enough supersaturation level, the vaporized liquid should form small, homogeneous aerosol nuclei.

The LVI controls and liquid reservoir (500 mL G45 amber bottle) are contained in a Hoffman 19" x 16" x 14" enclosure. The eductor, air preheater, and tubing are housed in a Wigman 10" x 8" x 4" steel enclosure with a 3/8" 316SS bulkhead outlet fitting. The Wigman enclosure is stuffed with several layers of internal closed-cell silicone foam insulation. The power, control, pressure, and liquid lines between the two enclosures are wrapped in a 15' woven umbilical line.

2.3. Analytical methods

2.3.1. FTIR

Low resolution FTIR is a powerful quantification tool used to measure species concentrations in the gas or vapor phase. Individual components are distinguished by their absorption of light over a range of particular wavenumbers in the mid-infrared (IR) region (500-4000 cm^{-1}). IR absorption causes molecular vibrations and rotations which are

unique to the structure and bond strength of a particular molecule. IR absorption bands can be used in combination with the Beer-Lambert law to quantify individual species present in complex, multicomponent sample matrices. Absorption is assumed to be proportional to concentration; reference (calibration) spectra for each individual component are multiplied by a scalar and summed across the measured IR range to reproduce the gross spectra measured by the FTIR.

The specific hardware used in this work is the Gasmet^{TM} DX4000 portable FTIR spectrometer. The path length is 5 m and the wavenumber resolution is 8 cm^{-1}. Peripheral equipment including heated sample lines, the heated stream switcher, and the PSU is maintained at 180 °C to prevent condensation during transport and analysis. Calcmet^{TM} software is used for chemometric analysis. Compensations for pressure and temperature on the total gas concentration are made using the onboard cell sensors.

Sample flow is kept at 2-12 SLPM by the PSU connected to the inlet of the FTIR cell. The flowrate to the FTIR optical purge line is kept at 0.1 SLPM by a pressure regulator and a Bird Precision critical orifice (0.004" ID).

Table 1 displays the analysis regions used in this work.

Table 1: IR absorption ranges for compositional analysis using Calcmet^{TM} chemometric software.

Component	Range 1 (cm^{-1})	Range 2 (cm^{-1})	Range 3 (cm^{-1})	# of Ref. Spectra
H_2O	2475 - 2600	3050 - 3375	--	7
CO_2	910 - 1015	2165 - 2240	2550 - 2750	6
PZ	2475 - 2540	2680 - 2900	--	11

3. Results and Discussion

The solvent used in this study was gravimetrically prepared by mixing 3 kg of PZ with 10 gallons of tap H_2O to produce a roughly 0.9-1.0 molal (m, moles/kg H_2O) solution. The initial solvent PZ concentration and CO_2 loading produced an initial P^*_{CO2} of 110.4 ppmv and P^*_{PZ} of 2.8 ppmv at 40 ºC as measured by FTIR.

The following section details total PZ emissions measurements at the AGC outlet under variable conditions using the solvent described above in the presence of injected aerosol.

3.1. Aerosol Injection and Emissions

The LVI affords a unique opportunity to study aerosols of various starting composition. Liquid solutions containing semi-volatile, and low-volatility species can be vaporized and recondensed as homogeneous aerosols provided a large enough supersaturation during cooling and mixing with the process gas. The LVI also allows for tracers to be added to the aerosol phase such that the partitioning between the gas, droplet, and solvent can be measured.

In this work, two different LVI solutions were used to create inlet aerosol: (1) 0.5 m PZ and (2) 0.05 vol % H_2SO_4. The LVI N_2 flowrate for all experiments was 1.035 SCFM produced by an eductor inlet pressure of 60 psig which created a vacuum level of 20 in Hg at the eductor suction. The LVI liquid flowrate was set to 1.0 mL/min for all cases. Table 2 shows the composition produced for both the PZ and H_2SO_4 aerosol cases. These streams were mixed with a constant process gas flowrate of 20 SLPM that was saturated to H_2O at 40 ± 1 ºC.

The presaturator and inlet solvent temperature was set to 40 ºC throughout all experiments, even when the solvent temperature was increased.

Reported inlet CO_2 concentrations are calculated by summing the output of the N_2 and CO_2 mass-flow controller outputs, adjusting for H_2O assuming saturation at the measured presaturator head-space temperature using DIPPR correlations [13], and renormalized to the total flowrate produced by mixing the LVI and saturated process gas. No condensation between the LVI/process gas mixing point and the inlet of the absorber was assumed because no appreciable liquid was ever observed in that line experimentally.

Table 2: LVI composition produced using 0.5 m PZ and 0.05 vol % H_2SO_4, respectively. The LVI product gas is mixed with the process gas (20 SLPM) which is saturated to H_2O at 40 ºC.

Component	Unit	PZ Aerosol	H_2SO_4 Aerosol
N_2	vol %	95.7	95.6
H_2O	vol %	4.3	4.4
PZ	ppmv	383	--
H_2SO_4	ppmv	--	7.5

3.1.1. Effect of inlet CO_2

The inlet CO_2 concentration was varied between 0-8 vol % during both the PZ and H_2SO_4 aerosol experiments. Figure 2 and Figure 3 show inlet CO_2, outlet CO_2, H_2O, and PZ, and the solvent flowrate. The steady state PZ concentration for the PZ and H_2SO_4 aerosol case was 50-75 and 5-7 ppmv, respectively. The dashed gray lines indicate when the LVI pump was either connected (LVI On) or disconnected (LVI Off). The dead volume in the LVI liquid line causes a response lag of about 3 minutes.

At a solvent rate of 12 GPH and 4 vol % inlet CO_2, PZ jumped from 50 to 100 ppmv for the PZ aerosol case. Further increases in CO_2 concentration appear to cause very small relative differences in outlet PZ measured during PZ aerosol injection. The large, CO_2 concentration independent change in PZ may be attributable to changes in the nucleation environment where an acid (CO_2) and a base (PZ) can fully react and condense in a humid environment. Alternatively, the low concentration of PZ in the solvent may not be supplying sufficient vapor pressure to create large enough saturation changes to cause observable aerosol growth even with the exothermic absorption of CO_2 increasing the solvent temperature. High solvent rates of 6-18 GPH, corresponding to a liquid-to-gas ratio (L/G) of 9.5-28.4 mol/mol, would also dampen any temperature bulging, and consequently saturation changes in the column.

Under identical conditions, but with H_2SO_4 injection, PZ shows less clear behavior. Though PZ initially increases by about 17% as CO_2 is increased from 0 to 4 vol %, an additional doubling of CO_2 to 8 vol % causes a 17% decrease in PZ. Once the solvent flowrate and CO_2 concentrations are lowered from 12 to 6 GPH and 8 to 4 vol %, respectively, outlet PZ increased from 3.5 to 5.5 ppmv. When the inlet CO_2 is turned off, PZ returns to the baseline of 6 ppmv.

Amine emissions respond to the inlet CO_2 concentration depending on the nuclei composition. FTIR measurements showed a near doubling of the outlet PZ when CO_2 was introduced into the AGC for PZ seed nuclei; aerosols produced from H_2SO_4 did not exhibit this behavior. However, emissions do appear to be inversely proportional to CO_2, though the absolute change was quite small in these tests. The predicted effect of CO_2 on aerosol growth is likely dampened under these conditions, i.e., high solvent rates and low solvent concentrations. Further exploration using a more concentrated solvent and lower L/G is required.

3.1.2. Effect of L/G

L/G was varied in this study between 9.5-57.0 mol/mol. Figure 4 and Figure 5 show the effect of L/G changes independent of inlet CO_2 concentrations for the PZ and H_2SO_4 aerosol cases, respectively.

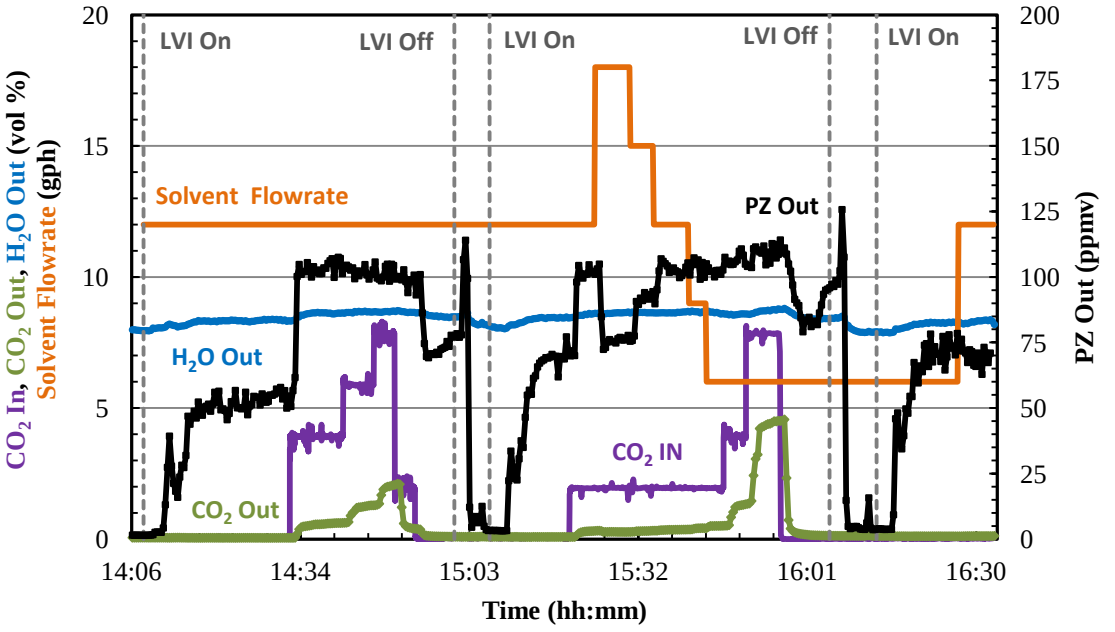

Figure 2: Absorber outlet emissions under PZ aerosol load in response to changing solvent flowrate and inlet CO_2 concentration. Outlet PZ increases sharply with CO_2, but is not correlated to the concentration. PZ is inversely related to solvent rate. Inlet solvent T is 40 ºC

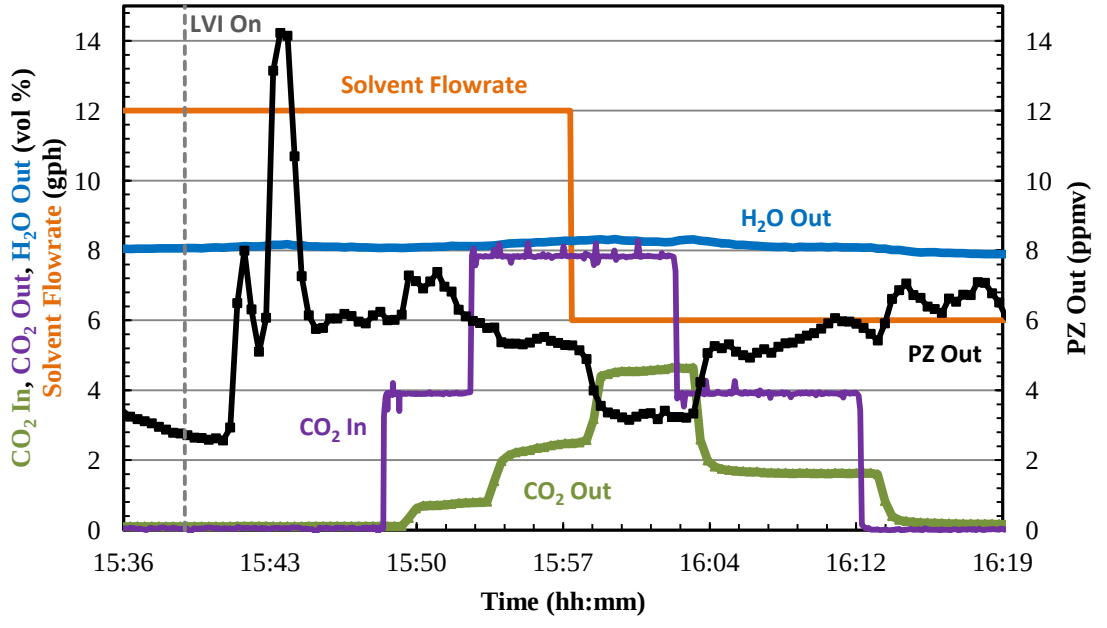

Figure 3: Absorber outlet emissions under H_2SO_4 aerosol load in response to changing solvent flowrate and inlet CO_2 concentration. Outlet PZ shows a weak, inverse correlation to CO_2 concentration and is positively correlated to solvent flowrate. Inlet solvent T is 40 ºC.

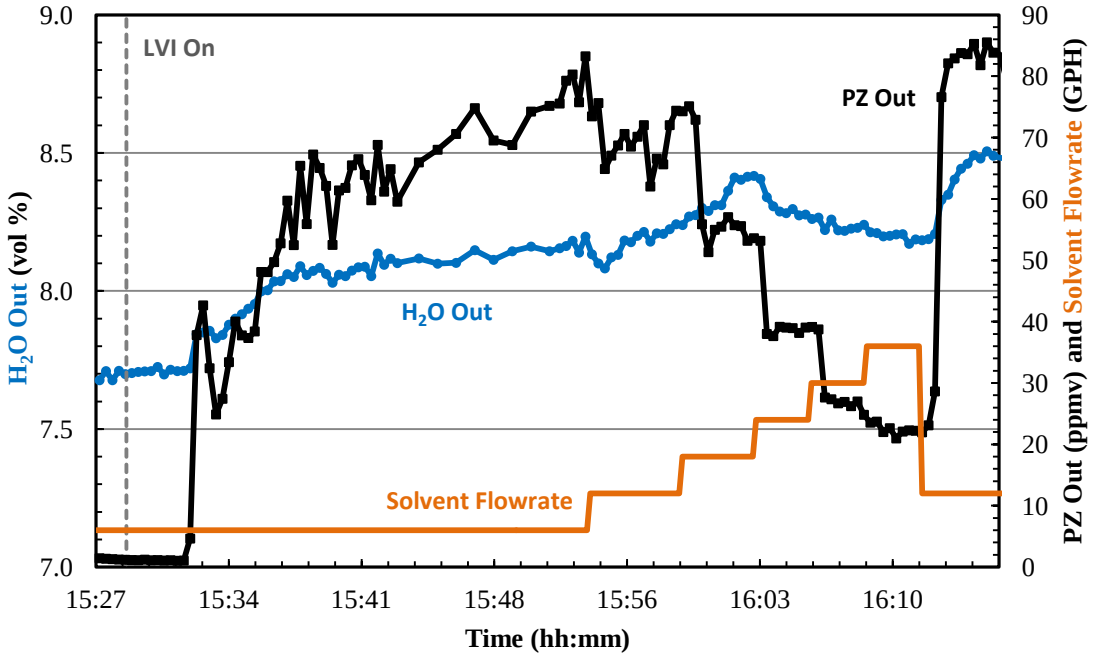

Figure 4: Absorber outlet emissions under PZ aerosol load in response to changing solvent flowrate. Outlet PZ is inversely proportional to the solvent rate. L/G varies from 9.5-57.0 mol/mol. Inlet solvent T is 40 ºC.

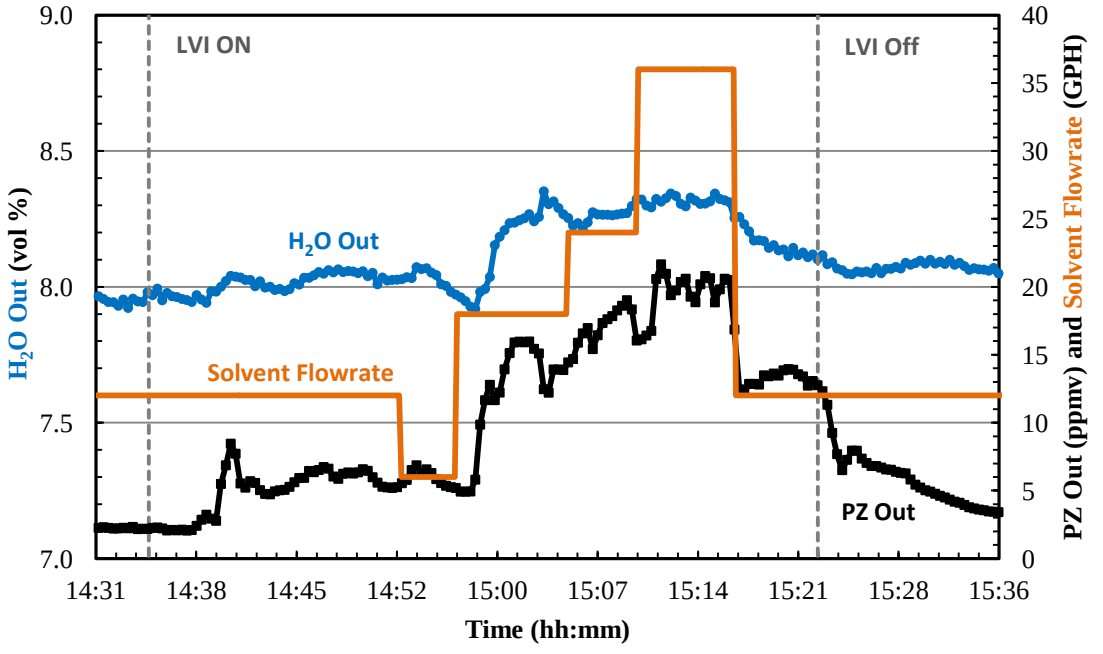

Figure 5: Absorber outlet emissions under H_2SO_4 aerosol load in response to changing solvent flowrate. Outlet PZ is proportional to the solvent rate. L/G varies from 9.5-57.0 mol/mol. Inlet solvent T is 40 ºC.

Stepwise decrease in solvent rate significantly reduces the outlet PZ measured during PZ aerosol injection experiments. Figure 4 shows that PZ decreases in a proportional fashion. Though this behavior was seen during the variable CO_2 experiments, the degree of reduction in PZ is not nearly as high. A mass balance using the LVI and process gas compositions leads to a total (gas and aerosol) PZ concentration of 231 ppmv. Since the baseline PZ measured at the AGC outlet is 50-75 ppmv, the AGC column is absorbing PZ, as well as possibly capturing PZ-containing aerosol with an efficiency of 67.5-78.4 %. It is therefore possible that increasing the solvent rate provides more absorption capacity and greater collection of PZ. In the case of the CO_2 experiment (Figure 2), PZ is not scrubbed with such high efficiency when the solvent rate is increased. CO_2 may be serving to sequester PZ inside the aerosols through reaction. Modeling work has shown that for even conservative CO_2 absorption rates, the absorption rate of CO_2 into amine-containing aerosols is very fast and that the aerosol phase is at a much higher CO_2 loading than the solvent, and therefore has a much lower P^*_{PZ} than the solvent. Fast reaction of CO_2, be it during nucleation or upon entering into the absorber, would prevent favorable partitioning of PZ towards the solvent. The CO_2 rich aerosol would then only respond to very large changes in driving forces created by CO_2 absorption at very low liquid rates, or large temperature differences between the inlet gas and liquid.

Figure 5 shows that H_2SO_4 aerosol has opposite behavior compared to PZ aerosols on varying the inlet solvent rate, though the measurement is less clean. Creation of supersaturation might explain the inverse relationship between solvent rate and PZ emissions. The inlet gas is about a 1.5:1 mixture of gases at 310 and 40 ºC that cools due to heat loss in the system prior to entering the absorber; therefore, it is expected that the inlet gas temperature is higher than the inlet solvent at 40 ºC. If the solvent temperature is raised, then the temperature difference across the column is minimized. Conversely, if the flowrate of the colder solvent is increased, the temperature gradient would be steeper, and cause higher degrees of supersaturation, and consequently more aerosol growth.

L/G affects outlet PZ emissions to a much higher degree than CO_2 for both aerosol cases investigated. Without size distribution measurements of the aerosols, differentiation of absorption and aerosol behavior is nearly impossible, though comparing the H_2O curves to that of PZ does provide some perspective. The outlet FTIR measurement, in the absence of aerosol generation, closely approximates saturated solvent conditions. The variability in these measurements is atypical of system control and heater oscillations. Further, the near parallel behavior of H_2O and PZ indicates that the majority of the measured PZ is in the aerosol phase.

3.1.3. Effect of temperature

The final operation variable explored in this study was the inlet solvent temperature. The temperature was increased from 40 to 50 ºC without changing the solvent flowrate and in the absence of CO_2.

Figure 6 and Figure 7 show the change in outlet PZ for the PZ and H_2SO_4 aerosol cases, respectively. PZ emissions dropped by 20% for the PZ aerosol case; distinct trends for the H_2SO_4 aerosols are indistinguishable. Increasing the solvent temperature decreases PZ absorption in the solvent as well as reducing the temperature gradient across the AGC. The PZ absorption or solvent washing and the supersaturation or aerosol growth mechanisms should influence the outlet PZ in opposing directions. Looking back at Figure 4, the H_2O curve increases with solvent flowrate, which would be consistent with the aerosol growth mechanism, but then decreases at higher flowrates, which is consistent with the absorption mechanism. It is possible that both mechanisms are occurring simultaneously, or in the best case, are starting to be captured in the packing.

Results at the time of this study are inconclusive on the effect of solvent temperature on outlet emissions. Particle size distribution measurements are needed to make valid conclusions.

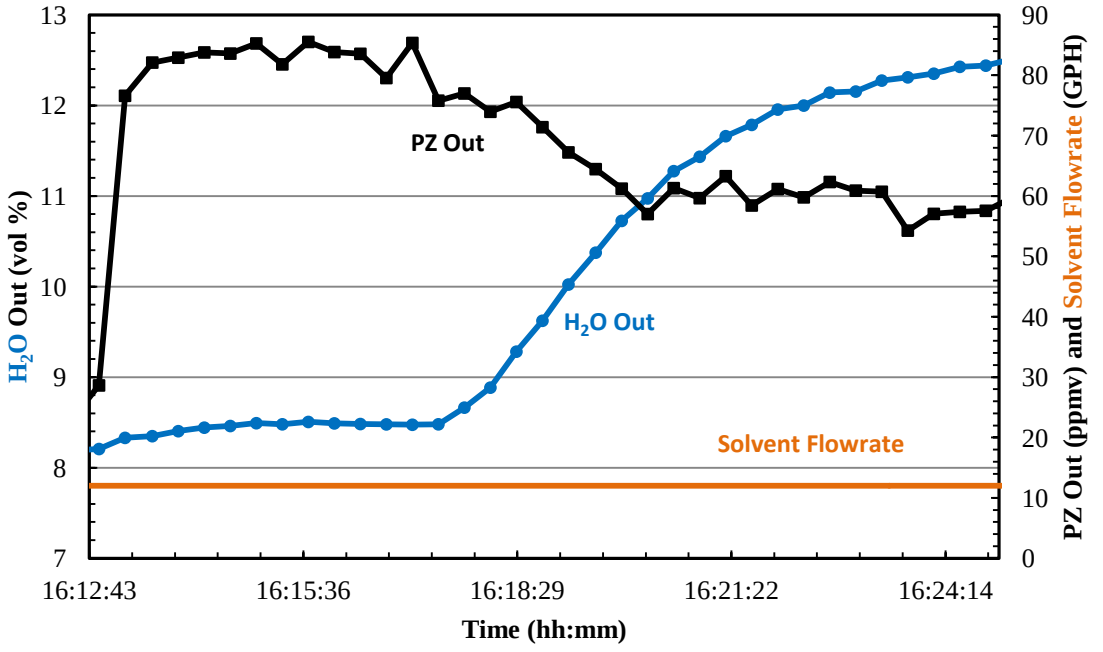

Figure 6: Absorber outlet emissions under PZ aerosol load in response to changing the solvent inlet temperature from 40 to 50 ºC. Outlet PZ is inversely proportional to the solvent temperature.

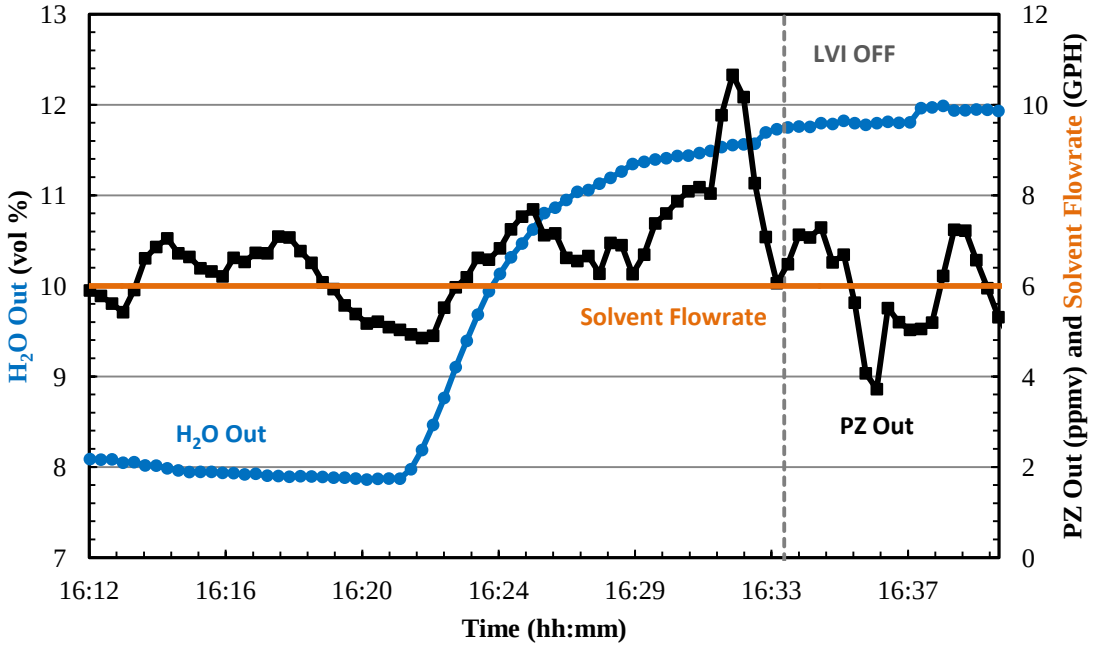

Figure 7: Absorber outlet emissions under H_2SO_4 aerosol load in response to changing the solvent inlet temperature from 40 to 50 ºC.

4. Conclusions

A new experimental apparatus was constructed to measure the effects of operating conditions of CO_2 absorbers using aqueous amine solvents on total (aerosol and gas-phase) emissions. Inlet aerosols of variable (0.5 m PZ and 0.05 vol % H_2SO_4) composition were generated by vaporizing a metered liquid stream kept at 1 mL/min sucked through an eductor by a preheated (310 ºC) motive N_2 stream at 1.035 SCFM. The solvent flowrate (6-36 GPH), inlet CO_2 concentration (0-8 vol %), and the inlet solvent temperature (40 and 50 ºC) were changed independently and the outlet PZ concentration was measured using FTIR.

The baseline outlet gas CO_2 and PZ concentrations relative to the solvent (0.9 m PZ) flowing at 12 GPH was 110.4 and 2.8 ppmv, respectively. Injection of PZ and H_2SO_4 aerosols increased the outlet PZ value to 65 and 6.5 ppmv, respectively.

Increasing the inlet concentration of CO_2 to 4 vol % doubled the measured PZ in the exhaust gas under PZ aerosol load; however, further increase of CO_2 produced very minor relative changes. PZ seems to be inversely related to inlet CO_2 concentration in the case of H_2SO_4 aerosols.

Changes to the solvent flowrate had far greater impact on the exhaust rate of amine. PZ decreased from 75 to 20 ppmv when the solvent rate was reduced from 36 to 6 gpm for the PZ aerosol case in the presence of no inlet CO_2. Solvent rate was found to have the opposite behavior for the H_2SO_4 aerosol case; PZ emissions increased from 6 to 20 ppmv as the solvent rate was increased from 6-36 GPH. Similar behavior was found during multivariable (CO_2 and flowrate) studies, though the absolute changes in measured PZ were much smaller.

Finally, PZ emissions were found to have a reciprocal relationship to inlet solvent temperature for the PZ aerosol case. No clear trend was observed during H_2SO_4 aerosol testing.

Future experiments with higher solvent concentrations should increase the effect of CO_2 interaction with the droplet phase, leading to cleaner distinction of the effects of solvent rate and inlet gas composition. The addition of droplet size analysis and particle counting will allow separation of total emissions into their respective phase contributions.

Acknowledgements

This material is based on work supported in part by the Department of Energy under Award Number DE-FE0005654.

This report was prepared as an account of work sponsored by an agency of the United States Government. Neither the United States Government nor any agency thereof, nor any of their employees, makes any warranty, express or implied, or assumes any legal liability or responsibility for the accuracy, completeness, or usefulness of any information, apparatus, product, or process disclosed, or represents that its use would not infringe privately owned rights. Reference herein to any specific commercial product, process, or service by trade name, trademark, manufacturer, or otherwise does not necessarily constitute or imply its endorsement, recommendation, or favoring by the United States Government or any agency thereof. The views and opinions of authors expressed herein do not necessarily state or reflect those of the United States Government or any agency thereof.

The authors acknowledge the financial support of the Texas Carbon Management Program.

The authors declare the following competing financial interest(s): One author of this publication consults for Southern Company and for Neumann Systems Group on the development of amine scrubbing technology. The terms of this arrangement have been reviewed and approved by the University of Texas at Austin in accordance with its policy on objectivity in research. The authors have financial interests in intellectual property owned by the University of Texas that includes ideas reported in this paper

References

[1] Damle AS, Ensor DS, Ranade MB. Coal Combustion Aerosol Formation Mechanisms: A Review. *Aerosol Sci. Tech.*, 1981;1:119-133.

[2] Brachert L, Mertens J, Khakharia P, Schaber K. The Challenge of Measuring Sulfuric Acid Aerosols: Number Concentration and Size Evaluation Using a Condensation Particle Counter (CPC) and an Electrical Low Pressure Impactor (ELPI+). *J. Aerosol Sci.*, 2014;67:

21-77.

[3] Khakharia P, Brachert L, Mertens J, Huizinga A, Schallert B, Schaber K, Vlugt TJ, Goetheer E. Investigation of Aerosol Based Emission of MEA due to Sulphuric Acid Aerosol and Soot in a post-combustion CO_2 Capture Process. *Int. J. Greenh. Gas Control*, 2013;19:138-144.

[4] Mertens J, Brachert L, Desagher D, Thielens M, Khakharia P, Goetheer E, Schaber K. ELPI+ Measurements of Aerosol Growth in an Amine Absorption Column. *Int. J. Greenh. Gas Control*, 2014;23:44-50.

[5] Kamijo T. Amine Emission Control Technology of KM CDR Process, Palo Alto, CA: EPRI, 2011.

[6] da Silva EF, Kolderup H, Hjarbo KW, Mejdell T, Huizinga A, Tuinman I, Zahlsen K, Vernstad K, Hyldbakk A, Holton T, Kvamsdal HM, van Os P, Goetheer E, Khakharia P. Emission Studies at the Maasvlakte CO_2 Capture Plant, Austin, TX, 2012.

[7] van der Gjip S, Huizinga A, Kester L, Khakharia P, Tuinman I, P. van Os P, Goetheer E. Emission Reducing Technologies: Aerosols, Austin, TX, 2012.

[8] Heidenreich S, Vogt U, Büttner H, Ebert F. A Novel Process to Separate Submicron Particles from Gases - A Cascade of Packed Columns. *Chem. Eng. Sci.*, 2000;55:2895-2905.

[9] Calvert S, Englund H. Handbook of Air Pollution Technology. New York, New York: Wiley; 1984, p. 236.

[10] Johannessen T, Christensen J, Simonsen O, Livbjerg H. The Dynamics of Aerosols in Condensational Scrubbers. *Chem. Eng. Sci.*, 1997;52:2541-2556.

[11] Fulk SM, Rochelle GT. Modeling Aerosols in Amine-Based CO2 Capture. *Energy Proc.*, 2013;37:1706-1719. Kyoto, Japan, 2013.

[12] Mertens J, Knudsen J, Thielens M, Andersen J. On-line Monitoring and Controlling Emissions in Amine post-combustion Carbon Capture: A Field Test. *Int. J. Greenh. Gas Control*, 2012;6:2-11.

[13] BYU DIPPR. "BYU DIPPR: Thermophysical Properties Laboratory," Provo.

[14] National Carbon Capture Center (NCCC), National Carbon Capture Center: post-combustion, 2012.

[15] Schaber K, Körber J, Ofenloch O, Ehrig R, Deuflhard P. Aerosol Formation in Gas-Liquid Contact Devices - Nucleation, Growth, and Particle Dynamics. *Chem. Eng. Sci.*, 2002;57:4345-4356.

[16] Reist PC. Aerosol Science and Technology. 2nd ed. New York, New York: McGraw-Hill, Inc.; 1993.

[17] Seinfeld JH, Pandis SN. Atmospheric Chemistry and Physics: From Air Pollution to Climate Change. New York, New York: John Wiley & Sons, Inc.; 1998.

[18] Kulkarni P, Baron PA, Willeke K. Aerosol Measurement: Principles, Techniques, and Applications. 3rd ed. Hoboken, New Jersey: John Wiley & Sons, Inc.; 2011.

Available online at www.sciencedirect.com

ScienceDirect

Energy Procedia 00 (2013) 000–000

Energy Procedia

www.elsevier.com/locate/procedia

GHGT-12

Thermal degradation of linear amines

Daniel Hatchell, Omkar Namjoshi, Kent Fischer, Gary T. Rochelle*

Abstract

This paper investigates the thermal degradation of eight linear amines loaded with CO_2 and H^+. The degradation rate of these amines tends to decrease with chain length. Hexamethylenediamine, the diamine with the longest chain, was found to be the most thermally resistant of the eight amines under CO_2 loading. Putrescine was the only amine under acid loading that was not thermally stable, suggesting that the reaction mechanism is initiated by H^+. Ethylenediamine, 2-(2-aminoethoxy)ethanamine, hexamethylenediamine, and Diglycolamine® reach a thermodynamic equilibrium with their degradation products. Ethylenediamine was also found to be the most corrosive amine tested.

Selection and peer-review under responsibility of GHGT.

Keywords: Thermal Degradation; Amines

1. Introduction

Thermal solvent degradation is important when selecting an appropriate amine for a carbon capture system. Solvents resistant to thermal degradation can be used at higher temperatures and consequently higher energy efficiency. It is necessary to understand the rate kinetics and associated mechanisms involved with thermal degradation to determine how an amine solvent will behave over time when subjected to high temperatures in the stripper. The purpose of this study is to present and analyze rate data of the thermal degradation of selected amines. This paper also investigates thermally induced corrosion and its connection to formate generation.

* Corresponding author. Tel.: 512-471-7230; fax: 512-471-7060.
E-mail address: gtr@che.utexas.edu

Selection and peer-review under responsibility of GHGT.

The amines in this study belong to two functional groups: linear diamines, which contain two amino groups, and linear alkanolamines, which contain an amino group and a hydroxyl group. Amines with variable carbon chain lengths were selected to establish the effect of chain length on degradation rate. This paper examines the following linear amines: 1,2-diaminoethane (EDA), propane-1,3-diamine (PDA), and butane-1,4-diamine (DAB), 2-(2-aminoethoxy)ethanamine (BAE), hexane-1,6-diamine (HMDA), 2-aminoethanol (MEA), 2-aminopropanol (MPA), and 2-(2-aminoethoxy)ethanol (DGA®). These compounds and their structures are listed in Table 1.

Table 1. List of amines examined

Amine Name	Abbreviation	Amine Structure
1,2-diaminoethane	EDA	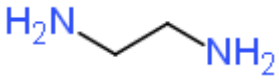
propane-1,3-diamine	PDA	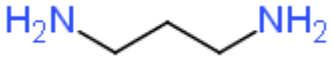
butane-1,4-diamine / putrescine	DAB	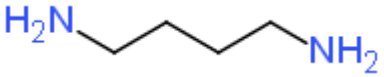
2-(2-aminoethoxy)ethanamine	BAE	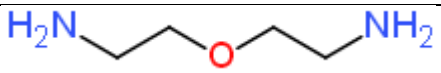
hexane-1,6-diamine	HMDA	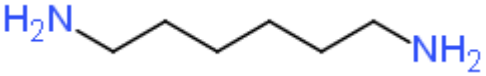
2-aminoethanol	MEA	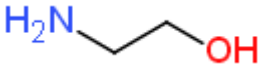
3-aminopropanol	MPA	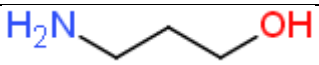
2-(2-aminoethoxy)ethanol	DGA®	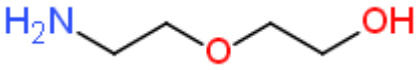

Some studies in the literature discuss the mechanisms of diamine and alkanolamine degradation. Work by Davis suggests that MEA degrades by a rate-limiting ring-closing reaction of the carbamate to form 2-oxazolidone[1]:

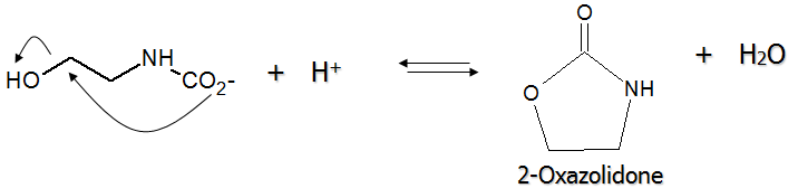

Fig. 1. MEA carbamate ring-closes to form 2-Oxazolidone

Work by Zhao predicts analogous rate-limiting steps for the degradation of EDA and PDA to form cyclic ureas [2]:

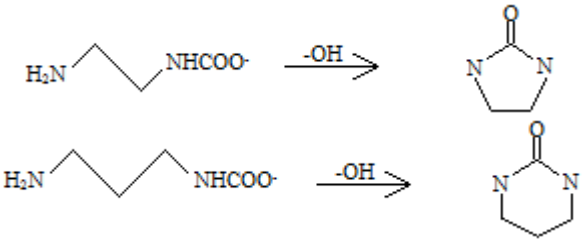

Fig. 2. EDA and PDA ring-close to form cyclic ureas.

MPA and PDA are expected to form similar cyclic products with stable six-membered rings. Larger molecules such as DAB are thought to eliminate the amino group and form a six-membered ring [3]:

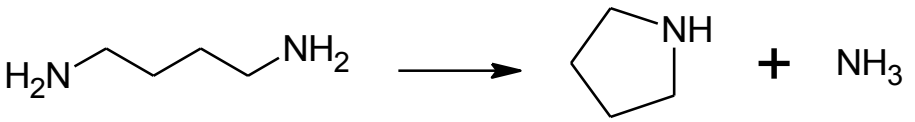

Fig. 3. Proposed degradation pathway of acidified putrescine to form pyrrolidine. CO_2 serves as an acidifying catalyst and not a reactant.

Thermal degradation rate data exist for EDA, DAB and MEA; these literature data are compared with the data gathered for this paper in the results section.

2. Experimental Methods

The CO_2-loaded amine solutions were prepared with an initial amine concentration of 10 m alkalinity and loaded with 0.4 mol CO_2/mol alkalinity. CO_2-loaded HMDA, and all acid-loaded experiments, were prepared with an initial amine concentration of 5 m alkalinity. The acid-loaded experiments had an initial loading of 0.2 mol H^+/mol alkalinity. 4 ml of each CO_2-loaded solution and 4.5 ml of each acid-loaded solution was placed inside 3/8" Swagelok® stainless steel cylinders with volumes of 4.5 ml. These cylinders were sealed and heated to the given temperature (135 °C, 150 °C, or 165 °C) in a convection oven. Cylinders were removed at predetermined intervals and promptly cooled in a refrigerator to halt any further thermal degradation.

After all cylinders had been removed from the oven and refrigerated, they were opened and the contents diluted by a factor of 10000 for analysis by cation chromatography (Dionex ICS-2100). Each series of amine was removed after 700 to 800 hours of heating. The dissolved products in these diluted samples were separated in a Dionex CS17 column and the relative quantities of each were plotted in a chromatograph. The concentrations of dissolved compounds in the analyzed solutions could be calculated by comparison to a known standard. The analytical and experimental techniques are similar to Freeman [4]. Degraded samples of PDA and BAE were heated to around 60 ^oC before diluting to melt any remaining solids.

Formate and metals concentration data were obtained for samples of EDA, PDA, DAB, and BAE degraded in the 150 ^oC series. Formate was determined for the first, fourth, and twelfth (last) samples to cover the entire range of degradation. These samples were hydrolyzed and subsequently analyzed by anion chromatography to obtain concentration data. Metals concentrations were measured for the twelfth, most degraded sample of the series to compare the amines in the cylinders in their most corroded state.

3. Results

All eight of the listed amines were degraded at 165 °C with a CO_2 loading of 0.4. Figures 4 and 5 plot the concentrations of these amines over time.

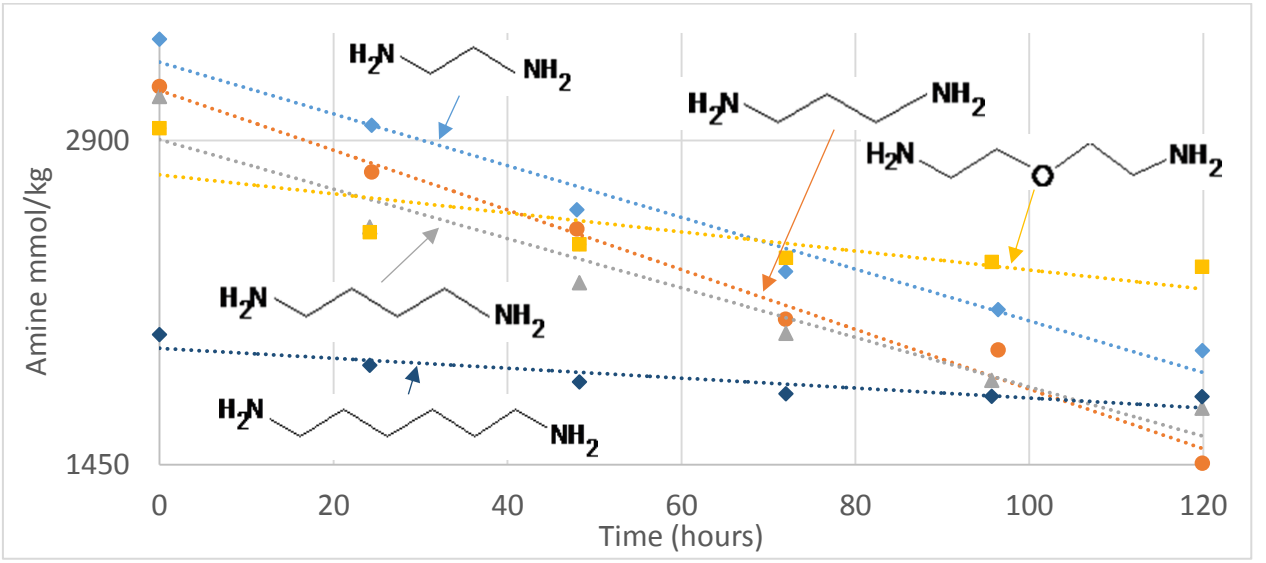

Fig. 4. 5 m EDA, 5 m PDA, 5 m DAB, 5 m BAE, and 2.5 m HMDA degraded at 165 °C at 0.4 CO_2 loading. BAE appears to reach equilibrium with the degradation products.

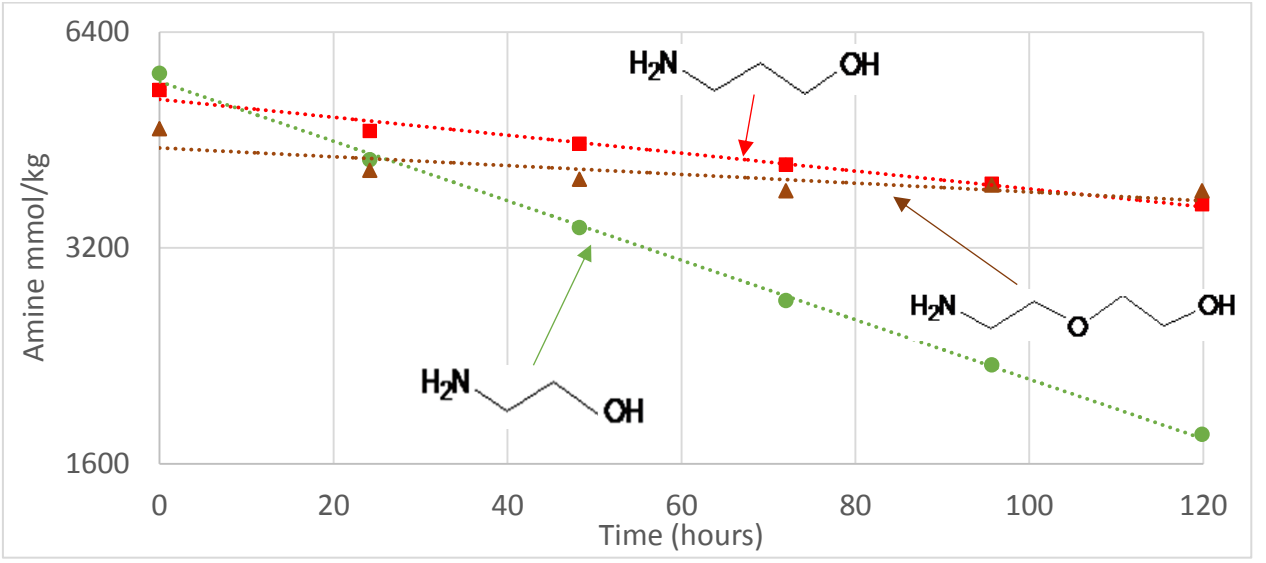

Fig. 5. 10 m MEA, 10 m MPA, and 5 m DGA® degraded at 165 °C at 0.4 CO_2 loading. DGA® appears to reach equilibrium with the degradation products.

DAB, MEA, and MPA follow close exponential fits, suggesting a first-order degradation mechanism. PDA and HMDA also appear to follow first-order fits, although to less certainty. DAB, BAE, and DGA® do not show a strong first-order reaction rate but are fitted to an exponential trend line for the purpose of comparison. BAE and DGA® appear to be reaching equilibrium by the second data point at 24 hours, so the initial rate constants estimated for these amines are likely inaccurate. Table 2 lists the first-order rate constants in units of hr^{-1} of each amine for this 165 °C experiment and for each successive temperature.

Table 2. First-order rate constants (hr^{-1}) for degradation reactions and associated activation energies (kJ/mol). The "eq" header indicates that the amine reached equilibrium with its degradation products. Amines are ordered by degradation rate at 165 °C.

Amine	165 °C (CO_2 = 0.4)	165 °C (Acid = 0.2)	150 °C (CO_2 = 0.4)	135 °C (CO_2 = 0.4)	Activation Energy (kJ/mol)
10 m MEA	0.00956	n/a	0.00270	0.00086	120
5 m PDA	0.00639	0.00069	0.00147	0.00036	140
5 m EDA	0.00553	0.00142	0.00287[eq]	0.00056[eq]	110
5 m DAB	0.00529	0.00457	0.00097	0.00030	140
5 m BAE	0.00515[eq]	0.00016	0.00105[eq]	0.00022[eq]	160
10 m MPA	0.00288	n/a	0.00080	0.00019	130
5 m DGA®	0.00262[eq]	n/a	0.00131[eq]	0.00014[eq]	150
2.5 m HMDA	0.00173	n/a	0.00069[eq]	0.00007[eq]	160

Structurally analogous amines tend to degrade more slowly as chain length increases, based on the 165 °C data. This is consistent across the diamines (EDA degrading the most quickly, HMDA degrading the most slowly) and the alkanolamines (MEA degrades the fastest, followed by MPA and then DGA®).

Figure 6 shows the degradation of EDA, PDA, DAB and BAE at an initial concentration of 0.2 mol H^+/mol alkalinity.

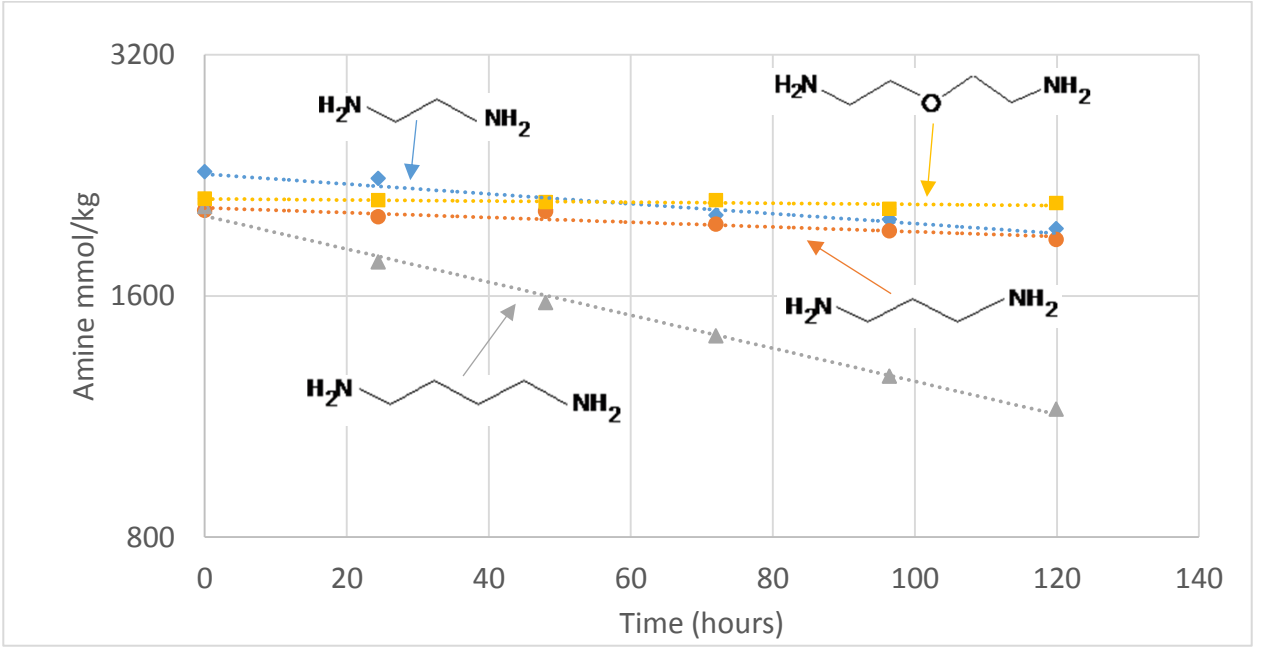

Fig. 6. Amines degraded at 165 °C at 0.2 H^+ loading. DAB maintains a similar degradation rate in acid conditions but the other three amines slow down significantly.

EDA, PDA, and BAE all degrade much more slowly under acidified conditions. The rate constants are tabulated in Table 2. The rate constant for EDA drops from 0.00553 hr^{-1} to 0.00142 hr^{-1}, for PDA from 0.00639 hr^{-1} to 0.00069 hr^{-1}, and for BAE from 0.00515 hr^{-1} to 0.00016 hr^{-1}. The degradation rate constant of DAB drops much less,

from 0.00529 hr^{-1} to 0.00457 hr^{-1}. This small change compared to the other three amines suggests that DAB degrades by some mechanism that does not incorporate CO_2 into the final degradation product. This would be consistent with the reaction proposed in Figure 3.

This mechanism involves the protonation of an amino group and subsequent attack on the alpha carbon by the other, non-protonated amino group of the DAB molecule. The molecule ring-closes to form pyrrolidine and eliminates an ammonia molecule. EDA and PDA do not appear to degrade as significantly under acid loading, and more likely follow reactions that combine with CO_2 to form a cyclic urea, as in Figure 2.

BAE hardly degrades at all under acid loading but has too long a chain to form a cyclic urea by the above mechanism.

Figures 7 and 8 plot the degradation of the eight amines at 150 °C at 0.4 loading of CO_2.

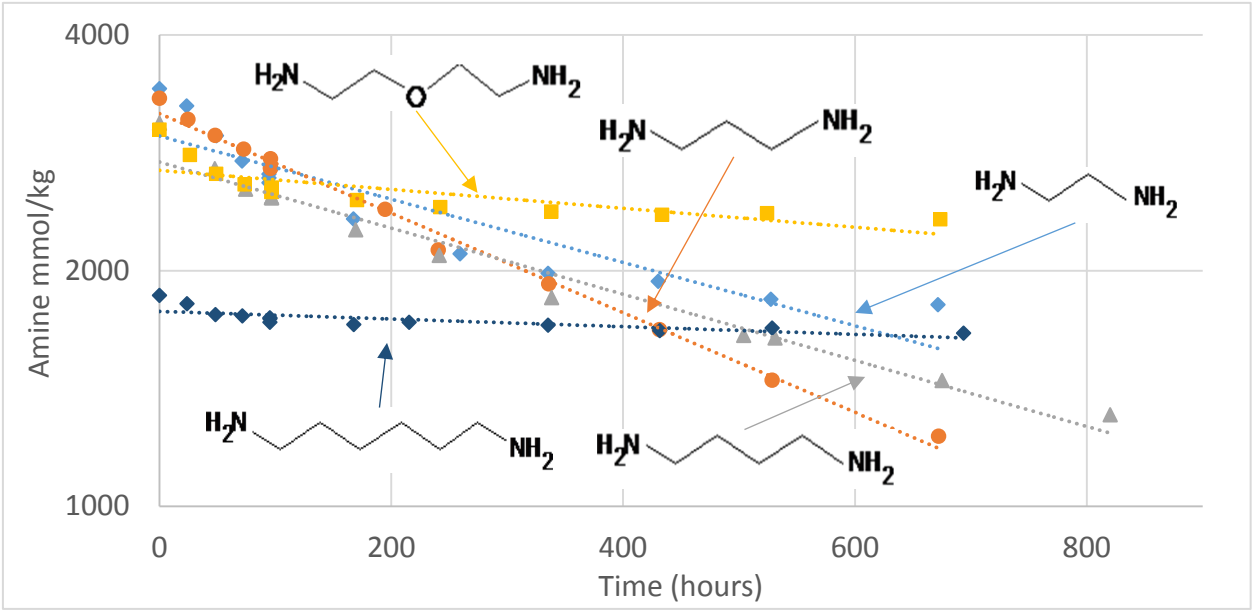

Fig. 7. 5 m EDA, 5 m PDA, 5 m DAB, 5 m BAE, and 2.5 m HMDA degraded at 150 °C at 0.4 CO_2 loading. BAE and HMDA appear to reach equilibrium with the degradation products. The rate of EDA degradation also appears to slow down significantly by 600 hours.

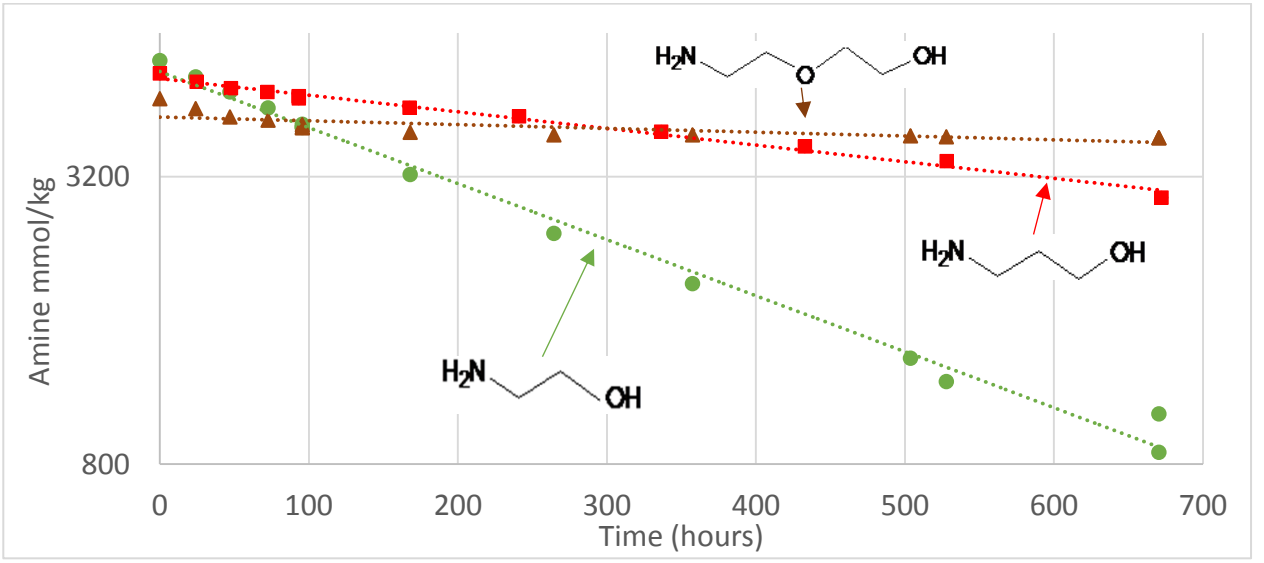

Fig. 8. 10 m MEA, 10 m MPA, and 5 m DGA® degraded at 150 °C at 0.4 CO_2 loading. DGA® appears to reach equilibrium with the degradation products.

BAE and HMDA reach equilibrium at around 100 hours at 150 °C, using more concentration measurements than the study at 165 °C and consequently revealing the initial degradation rate behavior in more detail. EDA and PDA appear to follow first-order behavior, although the degradation rate of EDA slows down around 300 hours. The rate behavior of HMDA and BAE is not as clear, and DAB seems to react by some mechanism greater than first order. MEA and MPA follow convincing first-order rate behavior but DGA® appears to equilibrate by 100 hours. The rate constants or initial rate constants are listed in Table 2.

Figures 9 and 10 plot the degradation of the eight amines at 135 °C at a CO_2 loading of 0.4.

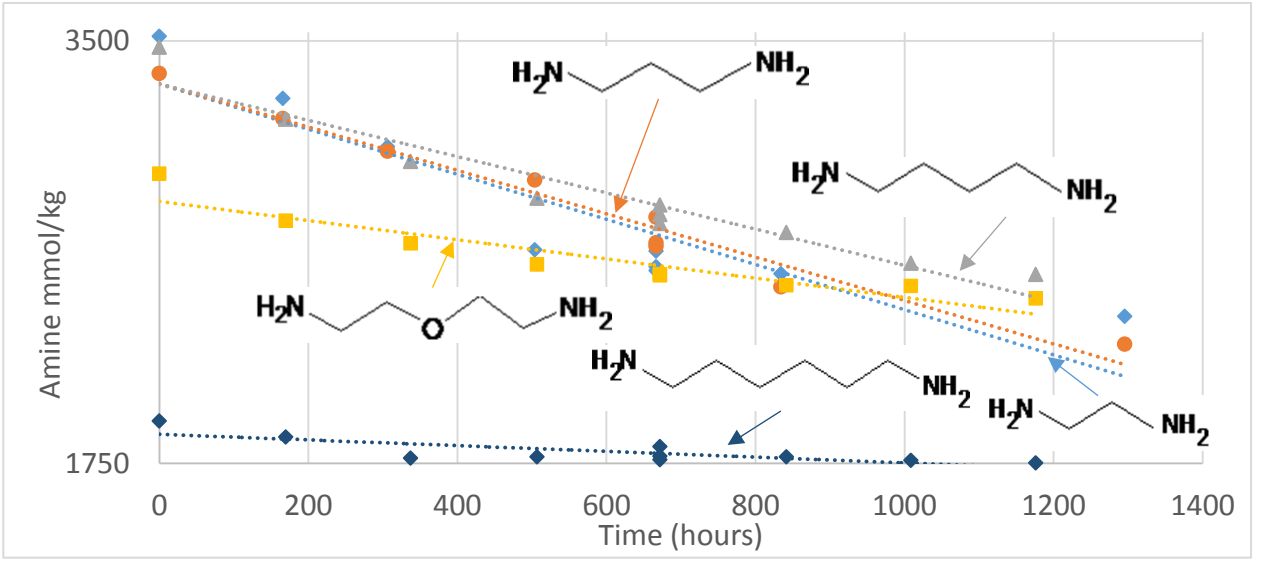

Fig. 9. 5 m EDA, 5 m PDA, 5 m DAB, 5 m BAE, and 2.5 m HMDA degraded at 135 °C at 0.4 CO_2 loading.

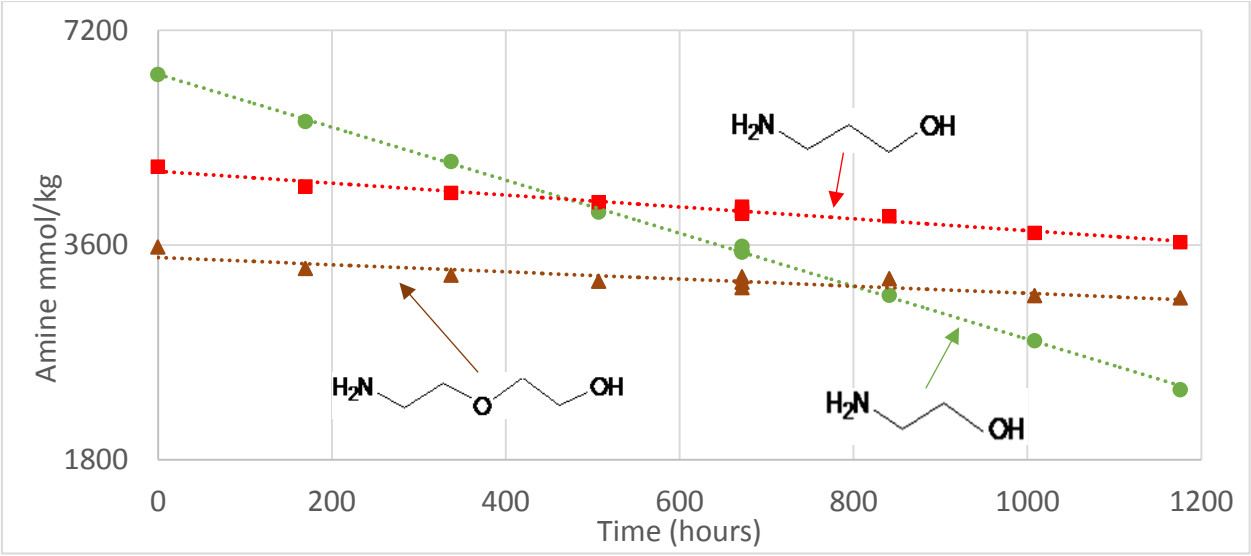

Fig. 10. 10 m MEA, 10 m MPA, and 5 m DGA® degraded at 135 °C at 0.4 CO_2 loading.

The degradation trends for all eight amines at 135 °C are generally comparable to the trends at 150 °C. EDA, BAE, DGA®, and HMDA all show signs of equilibrium with the degradation products by 500 hours. PDA, MEA, and MPA follow first order behavior. DAB again appears to degrade at some rate greater than first order.

Activation energies were calculated from the degradation rate constants over all three temperatures. This analysis gives activation energies of 110 kJ/mol for EDA, 140 kJ/mol for PDA, 140 kJ/mol for DAB, 160 kJ/mol for BAE, 160 kJ/mol for HMDA, 120 kJ/mol for MEA, 130 kJ/mol for MPA, and 150 kJ/mol for DGA®. These activation energies are also listed above in Table 2. Activation energy appears to increase with chain length for a given functional group.

Figure 11 compares the rate constant data of MEA, EDA and DAB with existing data by Davis (MEA), Zhou (EDA), and Namjoshi (DAB) [1,2,5].

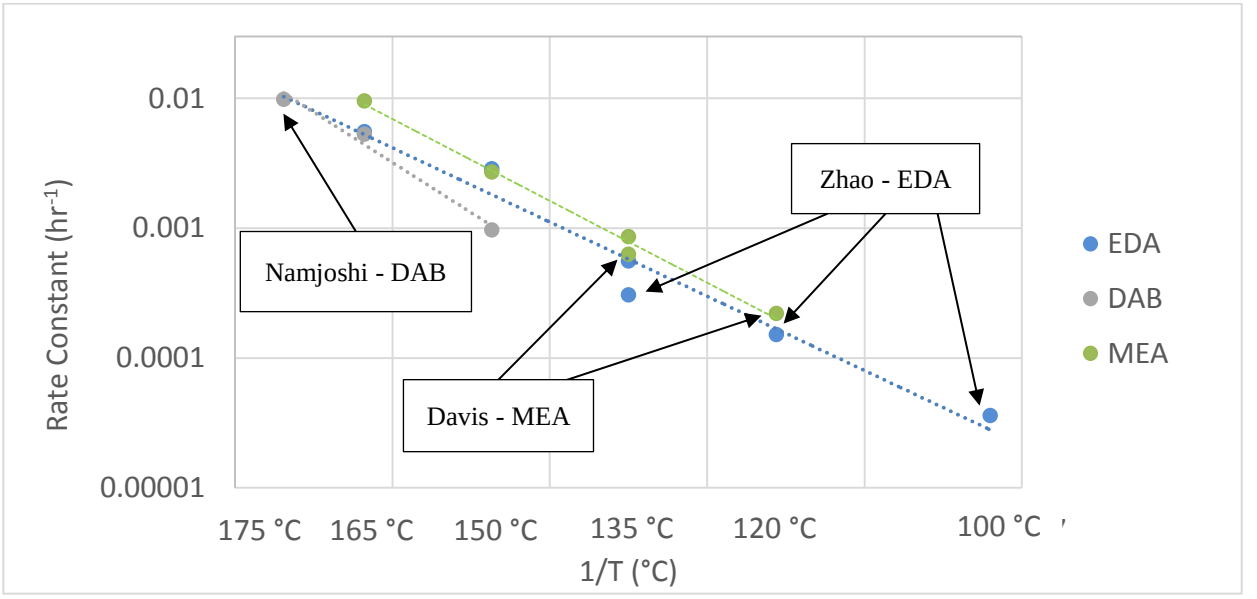

Fig. 11. Degradation rate constants of MEA, EDA, and DAB at 0.4 CO_2 loading in six temperatures across four studies. Davis uses 11 m MEA; Zhou uses 8 m EDA; Namjoshi uses 8 m DAB; this work uses 10 m MEA, 5 m EDA, and 5 m DAB.

The two data points by Davis measure the degradation rate constants of 11 m MEA at 135 °C and 120 °C with a CO_2 loading of 0.4. The work by Zhou studied the degradation of 8 m EDA at 135 °C, 120 °C, and 100 °C with a CO_2 loading of 0.4. The data point from Namjoshi comes from the degradation of 8 m DAB at 175 °C with a 0.4 CO_2 loading. These experiments used different initial concentrations for the amines than used in this paper; however, the calculated first-order rate constant is concentration independent so the initial concentration does not matter. The recalculated activation energy of MEA is 120 kJ/mol, equal to the original calculation; the recalculated EDA activation energy is 110 kJ/mol, also equal to the original calculation; the recalculated DAB activation energy is 150 kJ/mol compared with 140 kJ/mol. Assuming that the effect on degradation by molality is minimal, this comparison shows relatively consistent data across the three studies.

It was found that the concentration of formate and dissolved metals increased over time as some amines degraded in the metal cylinders. Figure 12 plots the concentration of formate in the samples of EDA, PDA, DAB, and BAE as they degrade at 150 °C at 0.4 CO_2 loading.

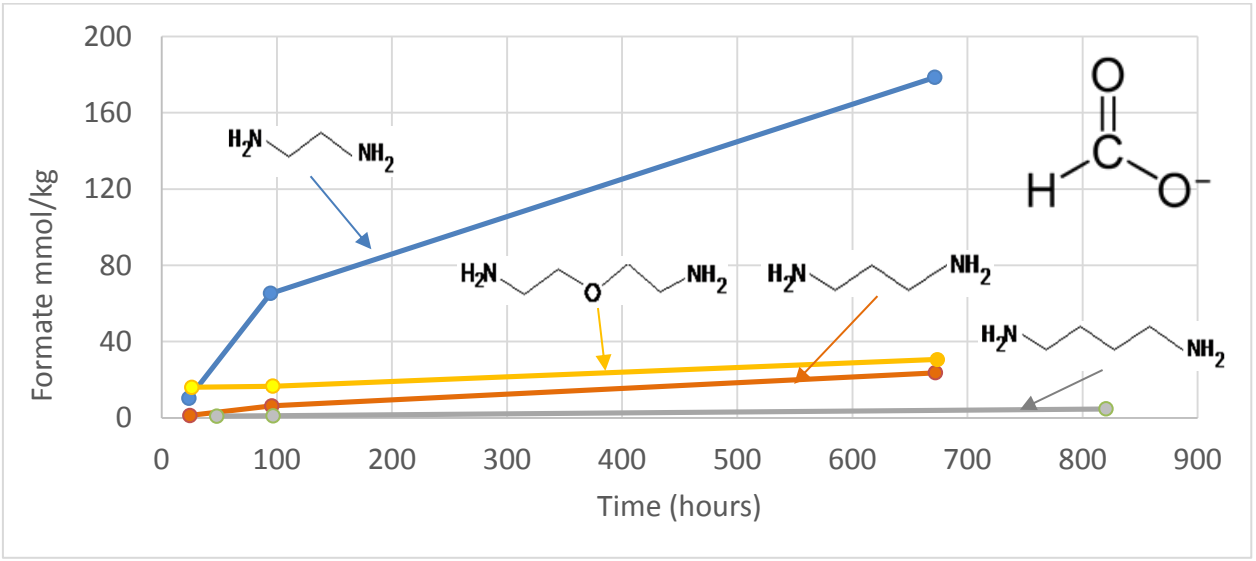

Fig. 12. Total formate generation in degraded 5 m EDA, 5 m PDA, 5 m DAB, and 5 m BAE. Samples degraded at 150 °C with CO_2 loading of 0.4.

Figure 13 displays the concentrations of chromium, nickel, manganese, and iron in the last of the degraded samples from the 150 °C series (this corresponds to 670 hours of degradation for EDA, PDA, and DAB, and 810 hours of degradation for BAE).

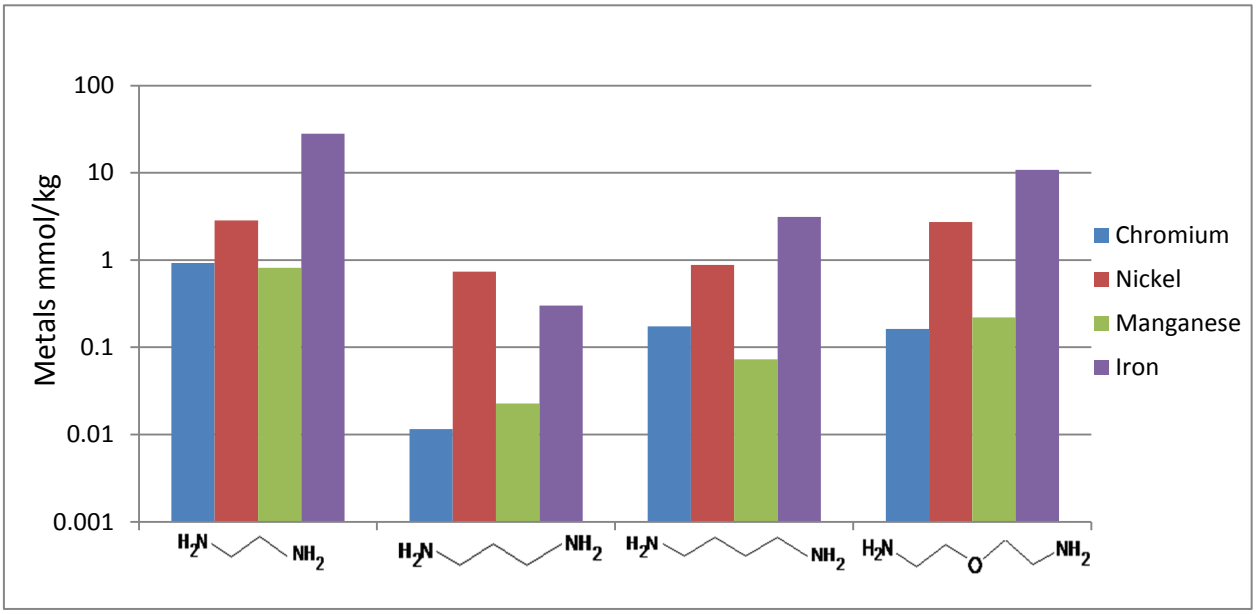

Fig. 13. Concentration of metals in the twelfth (last) amine sample of 150 °C, 0.4 CO_2 loading degradation series. Metals and formate are most prominent in EDA.

These two plots reveal a correlation in the concentration of heat-stable salts in solution and the concentration of corroded metals. EDA is especially corrosive and generates a large amount of formate while degrading, while DAB and PDA contain significantly less formate and metals in the degraded solution. These results have implications in

oxidative degradation. Metals are known to catalyze the oxidative degradation of certain amines [6]. It is unknown whether the generation of heat-stable salts drives corrosion or if dissolved metals catalyze heat-stable salt formation. Describing this relationship may lead to a better understanding of how to identify compounds resistant to corrosion and oxidation.

4. Conclusions

- Amines tend to be more thermally stable with increasing chain length. At 135 °C, diamine stability increases directly from HMDA (most stable) to EDA (least stable). This trend is present at 150 °C and 165 °C, but is not perfectly consistent. Alkanolamines behave similarly; MEA is less stable than MPA which is less stable than DGA® at 135 °C and 165 °C. The trend is again present at 150 °C but is not completely consistent.
- The following degradation activation energies were calculated for 0.4 CO_2 loading: 10 m MEA = 120 kJ/mol, 5 m PDA = 140 kJ/mol, EDA = 110 kJ/mol, 5 m DAB = 140 kJ/mol, 5 m BAE = 160 kJ/mol, 10 m MPA = 130 kJ/mol, 5 m DGA® = 150 kJ/mol, 2.5 m HMDA = 160 kJ/mol.
- DAB degrades at roughly the same rate with 0.2 acid loading compared to 0.4 CO_2 loading. EDA, PDA and BAE degrade significantly more slowly under the acidified conditions. EDA, PDA and BAE therefore require CO_2 to rapidly degrade at the concerned temperatures; DAB does not.
- BAE and DGA® consistently reach equilibrium with the degradation products. EDA and HMDA reach equilibrium at lower temperatures. At 165 °C, BAE and DGA® concentrations equilibrate after 24 hours. At 150 °C, BAE, HMDA and DGA® all equilibrate after 100 hours and EDA degradation begins to slow after 300 hours. EDA, BAE, HMDA, and DGA® degradation also appear to equilibrate after 500 hours at 135 °C.
- 5 m EDA is the most corrosive amine tested and generates the most formate at 150 °C (178.6 mmol/kg). Corrosion and formate generation are correlated and tend to occur simultaneously in degrading amines.

References

[1] Davis, J.D. *Thermal Degradation of Aqueous Amines Used for Carbon Dioxide Capture*. The University of Texas at Austin. Ph.D. Dissertation 2009.

[2] Zhou S, Chen X, Nguyen T, Voice AK, Rochelle GT. "Aqueous Ethylenediamine for CO_2 Capture." *ChemSusChem*. 2010;3(8):913–918.

[3] Lepaumier H, Martin S, Picq D, Delfort B, Carrette P-L. "New Amines for CO_2 Capture. III. Effect of Alkyl Chain Length between Amine Functions on Polyamines Degradation." *Ind. Eng. Chem. Res.* 2010;49:4553–4560.

[4] Freeman SA. *Thermal Degradation and Oxidation of Aqueous Piperazine for Carbon Dioxide Capture.* The University of Texas at Austin. Ph.D. Dissertation. 2011.

[5] Namjoshi O, Li L, Du Y, Rochelle GT. "Thermal Degradation of Piperazine Blends with Diamines." *Energy Proc.* 2013;37:1904–1911.

[6] Rochelle GT Et al. Second Quarterly Progress Report 2014." Texas Carbon Management Program. The University of Texas at Austin. 2014.

Available online at www.sciencedirect.com

ScienceDirect

Energy Procedia 00 (2013) 000–000

Energy Procedia

www.elsevier.com/locate/procedia

GHGT-12

Optimization of Advanced Flash Stripper for CO_2 Capture using Piperazine

Yu-Jeng Lin,[a] Gary T. Rochelle[a]*

[a]*McKetta Department of Chemical Engineering, The University of Texas at Austin, 200 E. Dean Keeton St,. C0400, Austin, TX 78712-1589*

Abstract

CO_2 capture from coal-fired power plants using amine scrubbing typically incurs a 20–30% energy penalty. The major energy requirements are the reboiler duty for solvent regeneration and the compression work for CO_2 sequestration. The advanced flash stripper using 8 m PZ was proposed, which recovers the stripping steam heat by employing cold and warm rich bypasses. The objective of this work is to quantify the benefits of the advanced regeneration system as energy and capital cost.

The advanced flash stripper saves 10% total equivalent work that includes heat duty work, compression work, and pumping work compared to the simple stripper. From the economic analysis, it was found that the compressor and the cross exchangers are the two major capital costs of the regeneration system. By considering the cost of the main heat exchangers, the temperature approaches and pressure drops of the cross exchanger and the steam heater were optimized. The optimum LMTD of the cross exchanger is around 10 K, which saves 8% regeneration cost compared to the base case with 5 K. The annualized regeneration cost of the advanced flash stripper is \$31/tonne CO_2 at the optimum lean loading 0.20, providing 15% cost savings compared to the base case simple stripper (5 K cross exchanger LMTD).

Selection and peer-review under responsibility of GHGT.

Keywords: Process design; Aspen Plus®; amine scrubbing

1. Introduction

In post-combustion CO_2 capture using amine scrubbing (Figure 1), steam usage for solvent regeneration and CO_2 compression work are the main contributors to the energy requirement. Implementing CO_2 capture incurs a 20–30% penalty on electricity output for a typical coal-fired power plant [1].

Alternative stripper configurations could improve energy efficiency significantly compared to a simple stripper. Van Wagener [2,3] emphasized the importance of increasing process reversibility by introducing more complex configurations including multi-stage flash, cold rich bypass, and an interheated column. Van Wagener showed that

Selection and peer-review under responsibility of GHGT.

the interheated stripper offers the best energy savings. Piperazine (PZ) is a new standard solvent [4] that provides higher reaction rate, capacity, and thermal stability than the conventional solvent, monoethanolamine (MEA). The energy performance compared to MEA has been demonstrated [3].

Loss of stripping steam vapor from the regenerator is one of the reasons that the simple stripper is inefficient. When the stripper is operated at 120–150 °C, water in the rich solvent is vaporized and emitted with CO_2 from the top of stripper. The proposed advanced flash stripper [5] applies cold and rich bypasses to recover the stripping steam heat, providing better energy savings than the interheated stripper. The CO_2 lean loading (mol CO_2/mol alkalinity) is the most important process operating parameter that determines the vapor-liquid equilibrium and regeneration capacity. The optimum lean loading has been investigated for MEA and PZ [5], however, only energy performance was considered. Besides reboiler duty, compression work and pump work should be considered. Capital cost should be included to determine optimum design conditions.

In this work, the advanced flash stripper using 8 m PZ has been modeled using Aspen Plus®. Total equivalent work is used as an indicator of energy performance that includes reboiler duty work, pump work, and compression work. The capital cost will be estimated for the regeneration system. The regeneration cost, including energy and capital cost, will be used to determine the optimum lean loading.

2. Process descriptions

2.1. Simple stripper

The simple stripper shown in Figure 1 is the base case. The cold rich solvent is heated by the hot lean solvent in the cross exchanger and then sent to the top of stripper. The reboiler provides the sensible heat, the heat of CO_2 desorption, and the vaporization heat of water. The hot lean solvent from the reboiler is returned to the absorber through the cross exchanger. The hot CO_2 vapor from the top of the stripper is cooled to 40 °C in the overhead condenser with loss of the latent heat of the excess water vapor.

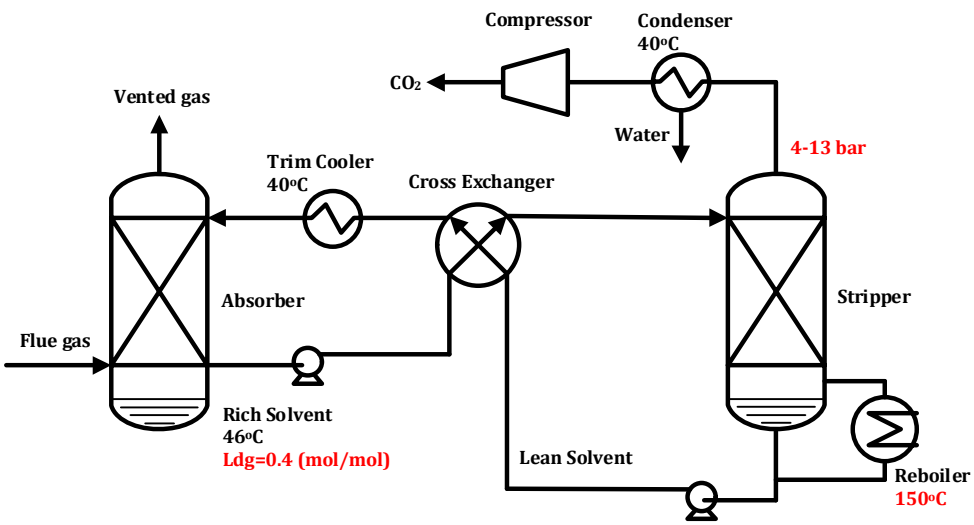

Figure 1. Amine scrubbing with simple stripper

2.2. Advanced flash stripper

Figure 2 shows the advanced flash stripper with warm rich bypass and cold rich bypass. In this configuration, the rich exchanger is used to preheat the cold rich solvent by hot CO_2 vapor coming out of the stripper. A portion of the

cold rich solvent obtains latent heat of steam from the stripped vapor. Warm rich bypass is extracted between two cross exchangers and fed to the top of the stripper after mixing with cold rich bypass. The temperature was selected as the bubble point temperature at the stripper operating pressure. The rest of the rich solvent is heated by a steam heater and fed into the bottom of the flash stripper. The reboiler in a typical stripper is replaced by a convective steam heater and a flash vessel. Only part of the rich solvent countercurrently contacts vapor in the flash stripper. Since the convective steam heater has less solvent hold-up and residence time, it will minimize thermal degradation.

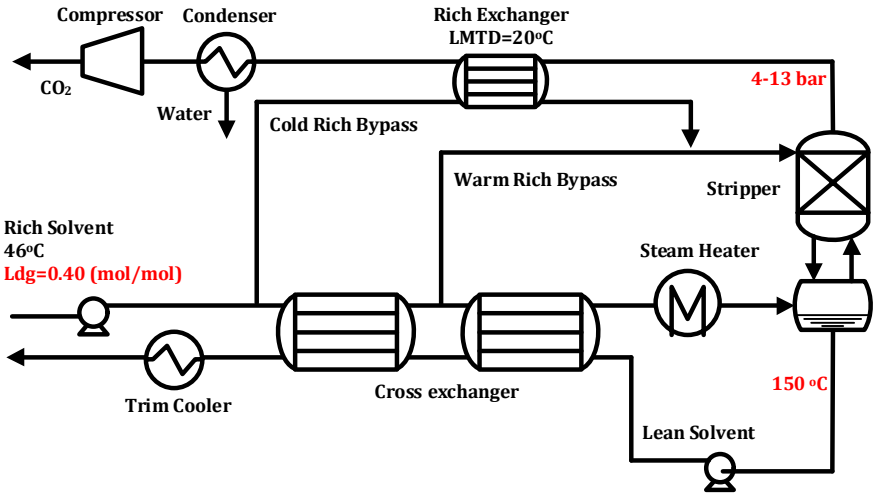

Figure 2. Advanced flash stripper

2.3. Multi-stage compressor

The inlet pressure of the compressor train is determined by the stripper pressure, which is dependent on the system lean loading and reboiler temperature. To sequester the CO_2 underground, the target pressure of the compressor has to be at least above its supercritical pressure, 74 bar. To replace the pressure loss during transportation, 0.4–0.5 bar/km is required. In this work, the target pressure is 150 bar. When the CO_2 is in the supercritical phase such that its density is similar to liquid, the difference between a pump and a compressor for the compression task disappears and becomes a question of density rather than phase. The supercritical pump is suggested for the last stage when the density is above 500 kg/m^3 [6].

To decrease the pipeline diameter, aftercooling can be applied to increase CO_2 density and reduce volume flow rate [7]. In this work, the aftercooler that cools CO_2 is employed before the supercritical pump to attain a density suitable for pumping and to reduce the pump work from reduced volume flow rate. The density of CO_2 increases dramatically with temperature around the critical region. The aftercooling temperature is specified as 30 °C to obtain the major density increase.

For a coal-fired power plant with 593 MW gross output, the CO_2 volume flow rate is around 140,000 ft^3/min at 1 bar [8]. A centrifugal compressor with intermediate pressure ratio and large capacity has been suggested for CO_2 capture [9].

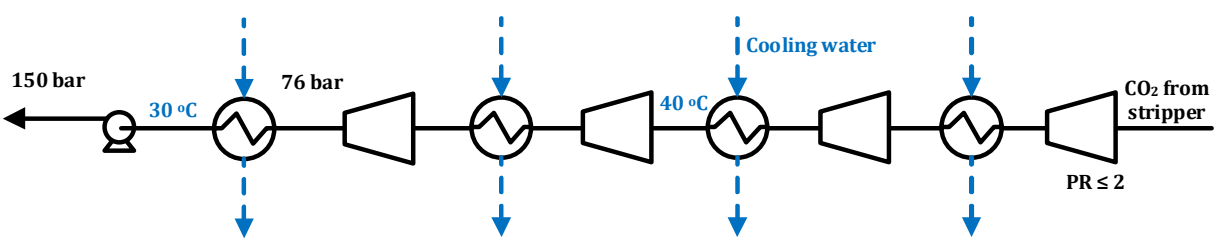

Figure 3. Multi-stage compressor with supercritical pump

3. Methods

3.1. Process specifications

The process specifications used in the simulations are shown in Table 1. Since the absorber is not included, a split flow sheet was used, with typical rich solvent conditions such as loading and temperature fixed as inputs.

This work simulates the solvent regeneration process, with the exception of the absorber, as shown in Figures 1 and 2. Simulation results were obtained from Aspen Plus® version 7.3. The Electrolyte Non-Random Two-Liquid (e-NRTL) property method was used. For the gas-liquid contacting separator unit, Aspen Plus® RateSep™ provides a rigorous rate-based model for heat and mass transfer using a non-equilibrium approach, applying two-film theory. The thermodynamic and kinetics model used for PZ in this work was "Independence" [10]. The model has been regressed in Aspen Plus® with experimental data including amine volatility, heat capacity, CO_2 solubility, and amine pKa over a range of amine concentration and CO_2 loading.

The multi-stage compressor was also modeled in Aspen Plus®. Since only CO_2 and water are presented, the Benedict-Webb-Rubin-Starling (BWRS) thermodynamic model was used. The multi-stage compressor will compress the CO_2 from the stripper pressure to 76 bar that includes 2 bar of net positive suction head (NPSH), and the supercritical pump will pressurize the supercritical CO_2 to 150 bar. The maximum pressure ratio of the compressor at each stage is specified as 2 due to high molecular weight.

Table 1. Stripper specifications

Solvent	8 m PZ
Process modeling tool	Aspen Plus® v7.3
Thermodynamic model	Independence
Packing type	2 m Mellapak standard 250X
Regeneration temperature (^oC)	150
Rich loading (mol CO_2/mol alk)	0.4
Rich solvent temperature (^oC)	46
Cross exchanger LMTD (^oC)	5
Rich exchanger LMTD (^oC)	20

Table 2. Multi-stage compressor specifications

Process modeling tool	Aspen Plus® v7.3
Thermodynamic model	BWRS
Maximum pressure ratio/stage	2
Compressor polytropic efficiency (%)	86
Intercooling temperature (^oC)	40
Aftercooling temperature (^oC)	30
Supercritical pump efficiency (%)	65
Multi-stage compressor outlet P (bar)	76
Final target P (bar)	150

3.2. Energy cost

Total equivalent work is used to account for the electricity penalty due to the steam extraction from the power plant, which is a more useful metric than reboiler duty alone. As Equation 1 shows, the equivalent work consists of pump work, compression work, and heat duty work. The pump is required to move the solvent from the absorber to the pressure of the stripper. The heat duty work is obtained from reboiler duty by multiplying by turbine efficiency and Carnot cycle efficiency (Equation 2). The turbine efficiency is set to a typical value of 90%. The compression work shown in Equation 3 is regressed using the configuration in Figure 3 from Aspen Plus® in the range of inlet pressure from 1 to 20 bar.

$$W_{eq}\left(\frac{kJ}{mol\ CO_2}\right) = W_{Heat} + W_{pump} + W_{comp} \tag{1}$$

$$W_{Heat} = 90\%\left(\frac{T_{steam} - T_{sink}}{T_{steam}}\right) Q_{reb} \tag{2}$$

$$W_{comp}\left(\frac{kJ}{mol\ CO_2}\right) = -3.48\ln(P_{in}) + 14.85,\ \ 1 < P_{in}(bar) < 20 \tag{3}$$

3.3. Capital cost

The purchased equipment cost (PEC) of unit operations were obtained either from vendor quotes or empirical correlations, and then scaled to 2014 cost level. Techno-economic analysis for CO_2 capture process have been studied by Frailie [10], who concluded that the total annualized capital cost can be calculated from PEC by Equation 4. The scaling factor α converts PEC to total capital cost and the annualizing factor β annualizes cost. The α includes direct cost, indirect cost, and working capital. The β takes into account return on investment (10%), taxes (35% of return on investment), depreciation, and maintenance (2–3%). The α and β are recommended as 5 and 0.2, respectively.

$$Total\ annualized\ capial\ cost\left(\frac{\$}{yr}\right) = \alpha \times \beta \times \mathrm{PEC}(\$) \tag{4}$$

3.4. Optimization of main heat exchangers

In the amine scrubbing process, the capital cost of the cross exchanger is one of the cost centers since the heat transferred from the hot lean solvent to the cold rich solvent is about 4–5 times the heat input to the reboiler/steam heater. The temperature approach and the pressure drop are the most important design parameters for the heat exchangers.

The pressure drop through the heat exchangers can be used to enhance the heat transfer coefficient, which reduces heat exchanger area but increases pumping cost. A pump for the lean solvent is not necessary when the stripper pressure is sufficient to get the solvent through the cross exchangers, the trim cooler and the absorber. The pressure drop of the trim cooler and the absorber is assumed as 1 bar and 3 bar, respectively. With the optimization, a lean solvent pump is possibly added when it is worth to save the capital cost of the cross exchanger by increasing pressure drop. To determine the temperature approach of the cross exchanger, the tradeoffs involve the capital cost and the steam cost of the reboiler/steam heater. The costs associated with the optimization of the main heat exchangers are summarized in Table 3. The decision variables include the pressure drop and the temperature approach of the cross exchanger and reboiler/steam heater.

Table. 3. Capital and energy cost associated with the optimization of main heat exchangers.

	Main heat exchanger cost	
	Cross exchanger	Steam heater/reboiler
Capital cost	Plate and frame exchanger	Shell and tube exchanger

Energy cost	Pump	Pump
	Pumping cost	Pumping cost
	-	Steam cost

4. Results and discussions

4.1. Optimization of heat exchangers

The pressure drop and the temperature approach of the cross exchangers and the steam heater/reboiler were optimized. Figure 4 shows the main exchanger cost of the advanced flash stripper with varied log mean temperature difference (LMTD), which is the parameter that has the greatest effect on the cost. The pressure drop and the steam temperature for each point are optimized. Three representative lean loadings are shown. The optimum LMTD is around 10 K in the range of optimum lean loading. From lean loading 0.32 to 0.26, the cost savings come from the improved capacity, but diminishing returns can be seen when the lean loading decreases further. The cost is less sensitive to LMTD at lower loading since the size of the cross exchanger is relatively small.

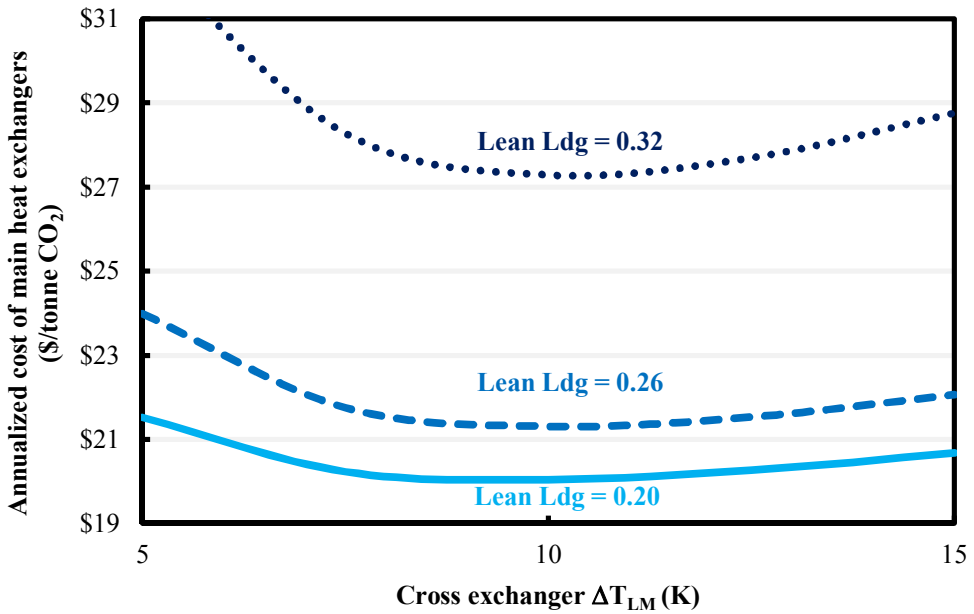

Fig. 4. Annualized cost of main heat exchangers of the advanced flash stripper with varied cross exchanger LMTD; optimum pressure drops; optimum steam temperature.

4.2. Total equivalent work and energy cost

The total equivalent work of the simple stripper and the advanced flash stripper is shown in Figure 5. Compared to the simple stripper, the energy saving of the advanced flash stripper is 10%, which is mostly derived from the recovery of stripping steam heat. The improvement is more significant at low loading because more stripping steam comes out with the CO_2 vapor. Figure 5 also shows the total equivalent work with 5 and 10 K cross exchanger LMTD. The energy performance is always better when a tighter temperature approach is employed. Less reboiler duty is required to heat the solvent to 150 ^{o}C when the temperature of the rich solvent coming into the stripper is higher by using a small LMTD, however, the capital cost of the cross exchanger is prohibitive compared to the energy savings.

The total equivalent work is converted to energy cost by using $100/MWh levelized cost of electricity (LCOE). Figure 6 shows the distribution of the energy cost with varied lean loading. The steam usage accounts for about 2/3 of total energy consumption. Both pumping work and compression work are driven by the stripper pressure. The pumping work increases faster when the lean loading is above 0.30 due to the low capacity, which offsets a part of benefits from the compression work when the stripper is operated at high pressure.

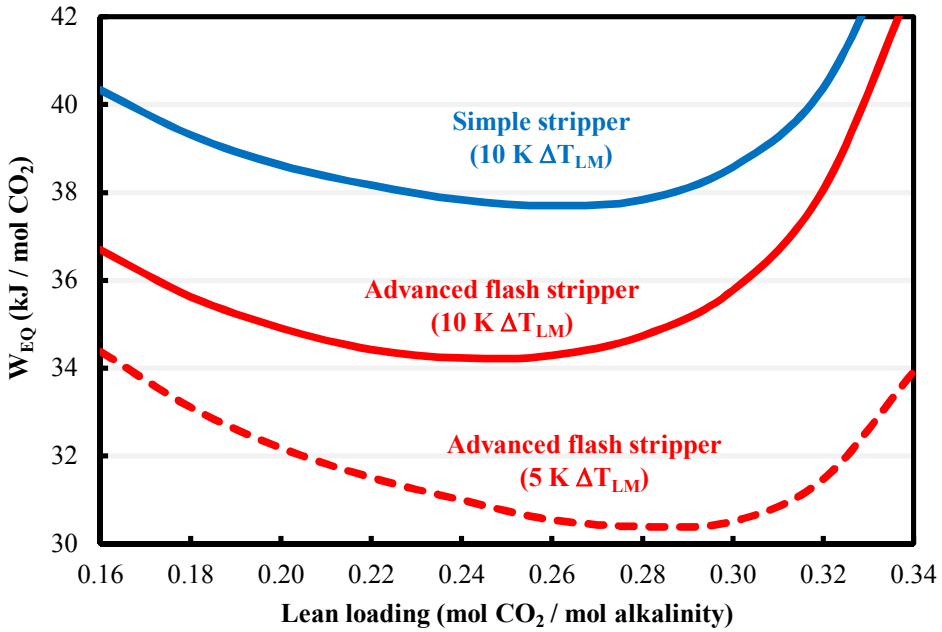

Fig. 5. Total equivalent work of simple stripper and advanced flash stripper at varied 5 and 10 K cross exchanger LMTD.

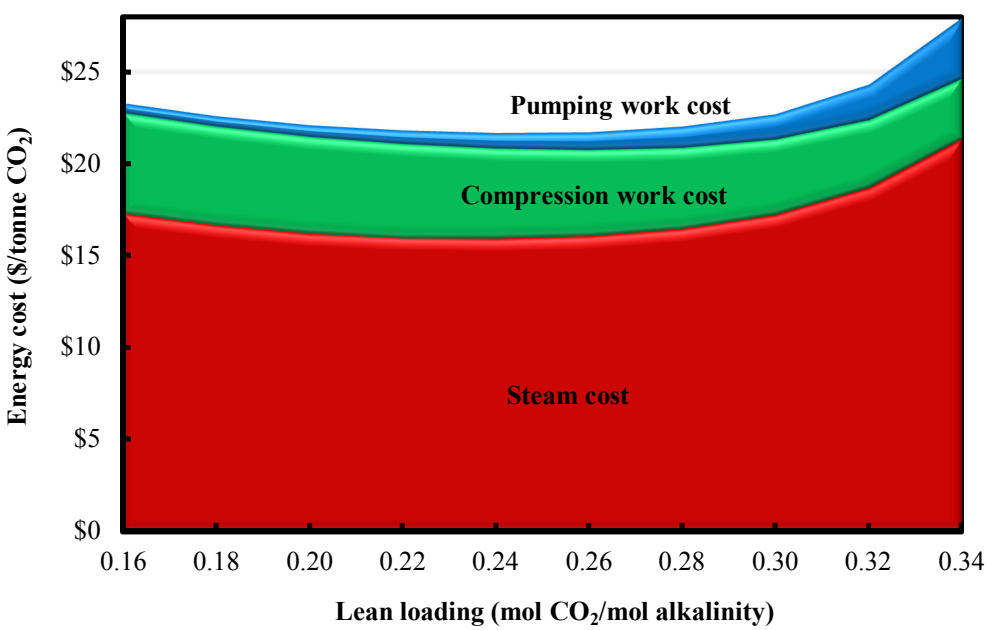

Fig. 6. Energy cost of the advanced flash stripper; LCOE = $100/MWh

4.3. Capital cost

The capital cost of the advanced flash stripper is presented with varied lean loading (Figure 7). The compressor and the cross exchange are the two major costs. The compressor cost is mainly affected by the stripper pressure. A discontinuity of increasing compressor cost is observed between lean loading 0.18 and 0.20, where the compressor train needs an extra stage to attain the target pressure of 150 bar. The capital cost of the cross exchanger is driven by the capacity and is most sensitive when the lean loading changes. The capital cost of the rich exchanger reflects the amount of the stripping steam recovered. Generally, at high lean loading range, the capital cost is dominated by the cross exchanger, but with decreasing lean loading, the compressor cost starts to take over.

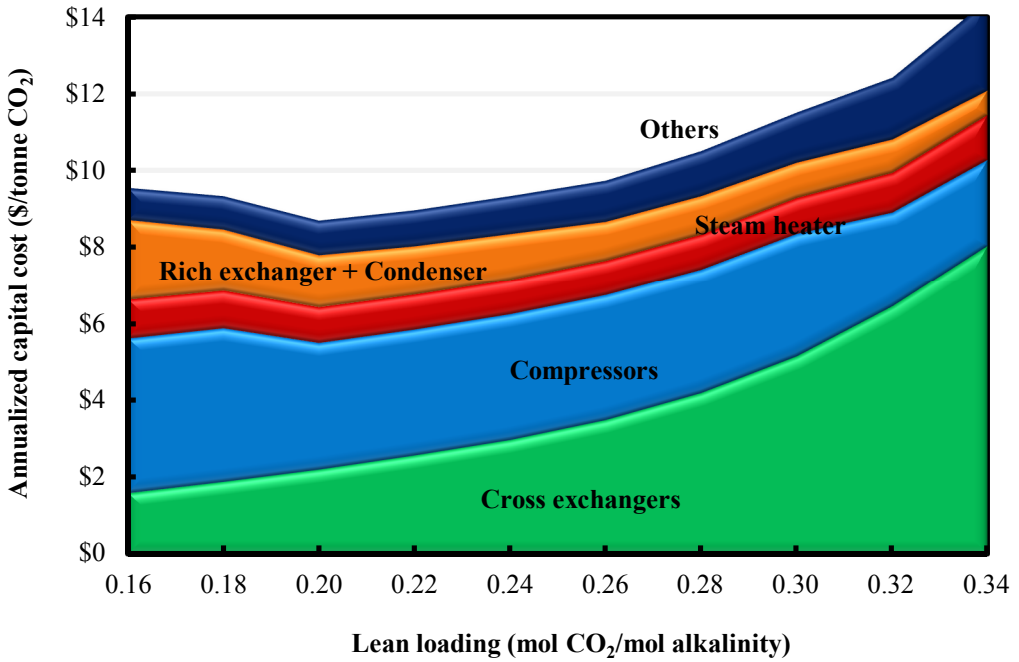

Fig. 7. Annualized capital cost of the advanced flash stripper

4.4. Lean loading optimization

The regeneration cost includes the energy cost and the capital cost shown in Figures 6 and 7. Figure 8 compares the simple stripper with and without the heat exchanger optimization. A typical cross exchanger LMTD, 5 K is arbitrarily chosen as the base case without optimization. The optimum case saves \$3/tonne CO_2, an 8% improvement compared to the base case. The results confirm the importance of heat exchanger design in the amine scrubbing process.

By applying the advanced flash stripper, the total regeneration cost improves 7% further, which mainly comes from the lower energy requirement. The optimum lean loadings for both the simple stripper and the advanced flash stripper are around 0.20, lower than the optimum that only the energy performance is considered (Figure 5), but is close to the optimum of the capital cost (Figure 7). Even though the energy cost accounts for 2/3 of the regeneration cost, the capital cost is more sensitive with varied lean loading. The low capacity at high lean loading reduces both energy and capital cost, so the optimum is forced to lower lean loading until the compression cost and the heat loss of stripping steam dominate. The results demonstrate that the advanced flash stripper provides the lowest regeneration cost even though process complexity increases.

With 8 m PZ a lean loading of 0.20 may not be operationally attractive because of the potential precipitation of $PZ.6H_2O$ solid at upset conditions or during shutdown when the solvent cools below 40°C. This possibility may

require additional capital cost to heat trace lines and provide other means to recover from an upset. Alternate solvents may also be considered that provide the same performance as 8 m PZ without precipitation at the optimum lean loading.

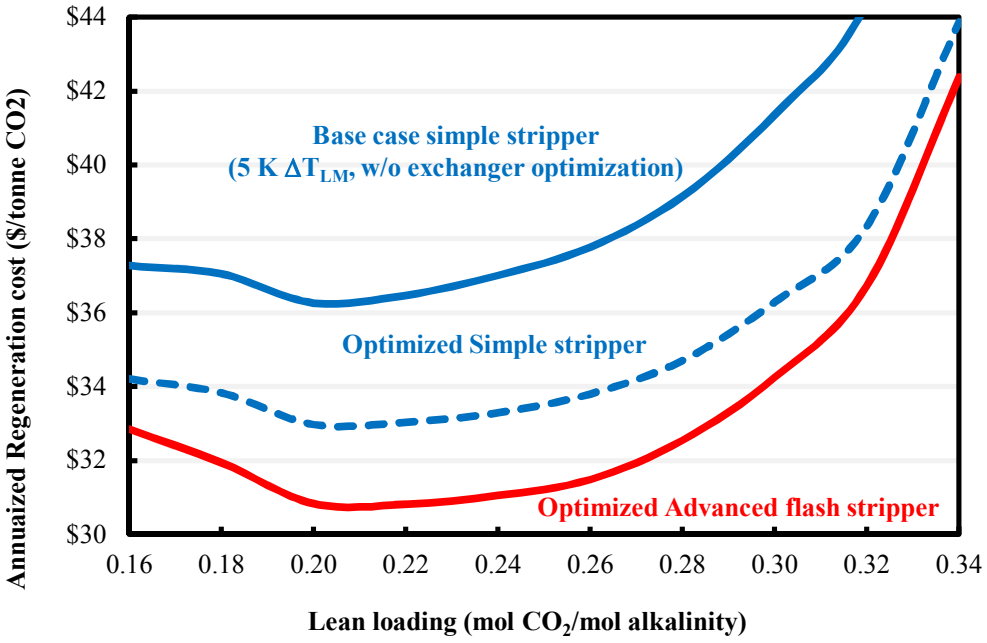

Fig. 8. Comparison of regeneration cost between the simple stripper and the advanced flash stripper

5. Conclusions

The advanced flash stripper that recovers the stripping steam heat by the cold and warm bypasses was proposed, which provides 30.4 kJ/mol CO_2 total equivalent work, giving 10% energy savings compared to the simple stripper. Besides the energy performance, the capital cost of regeneration was also evaluated. From the optimization of the main heat exchangers, the optimum LMTD of the cross exchanger is around 10 K. The compressor and the cross exchanger account for over 50% of the capital cost of regeneration. Combining the energy cost and the capital cost, the regeneration cost of the advanced flash stripper is \$31/tonne CO_2 at the optimum lean loading 0.20, providing 15% and 7% cost savings over the base case simple stripper (5 K cross exchanger LMTD) and optimized simple stripper, respectively.

References

[1] Rochelle GT. Amine scrubbing for CO_2 capture. Science 2009;325:1652–4.
[2] Van Wagener DH, Rochelle GT. Stripper configurations for CO_2 capture by aqueous monoethanolamine. Chem Eng Res Des 2011;89:1639–46.
[3] Van Wagener DH. Stripper Modeling for CO_2 Removal Using Monoethanolamine and Piperazine Solvents. Ph.D. Dissertation. The University of Texas at Austin, 2011.
[4] Rochelle GT, Chen E, Freeman SA, Van Wagener DH, Xu Q, Voice AK. Aqueous piperazine as the new standard for CO_2 capture technology. Chem Eng J 2011;171:725–33.
[5] Lin Y-J, Madan T, Rochelle GT. Regeneration with Rich Bypass of Aqueous Piperazine and Monoethanolamine for CO_2 Capture. Ind Eng Chem Res 2014.
[6] Bergamini L, Vescovo C, Milone F. Centrifugal pumps for CO_2 applications. Proc Twenty-Seventh Int Pump User Symp, 2011, p. 45–9.
[7] Moore J, Nored M. Novel concepts for the compression of large volumes of Carbon Dioxide. Proc ASME Turbo Expo Power Land, Sea Air, 2008.
[8] NETL. Cost and Performance Baseline for Fossil Energy Plants Volume 1: Bituminous Coal and Natural Gas to Electricity. 2010.
[9] Suri R. CO_2 Compression for Capture-Enabled Power Systems. University of Waterloo, 2007.

[10]Frailie PT. Modeling of Carbon Dioxide Absorption/Stripping by Aqueous Methyldiethanolamine/Piperazine. The University of Texas at Austin, 2014.

Available online at www.sciencedirect.com

ScienceDirect

Energy Procedia 00 (2013) 000–000

Energy Procedia

www.elsevier.com/locate/procedia

GHGT-12

Oxidative degradation of amine solvents for CO_2 capture

Hanbi Liu[a], Omkar A. Namjoshi[a], Gary T. Rochelle[a]*

[a]*McKetta Dept of Chemical Engineering, University of Texas at Austin, 200 E Dean Keeton St., MC C0400, Austin, TX 78712-1589*

Abstract

The oxidative degradation of diamines was measured in a stirred reactor at 70 ℃, 98kPa O_2, and 2kPa CO_2. Amines studied include ethylenediamine (EDA), propylenediamine (PDA), 1,4-diaminobutane (putrescine), hexamethylenediamine (HMDA), propanolamine (MPA), Diglycolamine® (DGA®), and bisaminoethyl ether (Jeffamine EDR-104®). Amine solutions with an initial concentration of 10 m alkalinity, an initial loading of 0.4 mol CO_2/mol alkalinity, and an initial metals concentration of 0.4 mM Fe, 0.2 mM Mn, 0.1 mM Ni, and 0.05 mM Cr were oxidatively degraded. The purpose of these experiments was to study the structural effect of diamines on their degradation rates.

At high metals concentration of 4 mM Fe, 2 mM Mn, 1 mM Ni, and 0.5 mM Cr, PDA does not show signs of significant degradation. This is also true for PDA at the normal metal concentration of 0.4 mM Fe, 0.2 mM Mn, 0.1 mM Ni, and 0.05 mM Cr. PDA was tested with antifoam and it did not show measurable degradation. EDA degradation follows zeroth order kinetics with a rate constant of 9.79 mmol/kg-hr and is likely mass transfer controlled. Putrescine degradation follows first order kinetics with a rate constant of 0.00104 1/hr and is likely kinetically controlled at experimental conditions. The degradation of HMDA follows first order kinetics with rate constant k = 0.01/hr. The degradation of bisaminoethyl ether follows first order kinetics with rate constant k = 0.023/hr. DGA® degradation also follows first order kinetics with rate constant k = 0.008/hr. HMDA, Jeffamine EDR-104®, and DGA® degradation are all kinetically controlled. MPA showed negligible degradation after 260 hours of run time. There was no significant degradation observed for PDA with normal and high metals concentration in previous experiments.

Selection and peer-review under responsibility of GHGT.

* Corresponding author. Tel.: 1-512-471-7230; fax: 1-512-471-7060.
E-mail address: gtr@che.utexas.edu

Selection and peer-review under responsibility of GHGT.

Keywords: Oxidative Degradation; Amines

1. Introduction

Oxidative degradation of amine solvent is a major source of solvent loss in flue gas carbon capture and mainly occurs in the absorber. The products of oxidative degradation have yet to be completely identified, and it is important to understand degradation mechanisms and the environmental impact of degradation products.

Previous studies on oxidative degradation by Voice, Goff, Zhou and Sexton focused on MEA degradation, oxygen mass transfer, and catalysts [1-4]. They found that Fe (II or III) and Cu (I) are potent catalysts, as are Mn and Cr. Voice found Ni to have no effect on oxidation while Sexton classifies it as a catalyst. They also screened amines for their degradation behaviors at absorber condition—putrescine, hexamethylenediamine (HMDA), and monopropanolamine (MPA) are resistant to oxidation while ethylenediamine (EDA), Jeffamine EDR-104®, and diglycolamine® (DGA®) are susceptible to oxidation. Voice concluded that tertiary amines, rings, hindered amines and those with no alpha hydrogen are likely to resist oxidation.

Following previous work, this study focuses on screening amines based on their structure and looking for correlation between amine structure and oxidative degradation behavior.

2. Experimental Methods

Solutions were prepared gravimetrically. The target amine concentration was 10 m alkalinity and the target CO_2 loading was 0.4 mol CO_2/mol alkalinity.

A schematic of the low gas flow apparatus is shown below. The apparatus is identical to the LGF reactor used by Voice [1] and approximates conditions in the absorber. Carbon dioxide and oxygen were passed through two calibrated mass flow controllers to maintain a reactor pressure of 98 kPa O_2 and 2 kPa CO_2, and the jacketed glass reactor was charged with approximately 350 ml of amine solution. The reactor head was sealed with a Teflon® cap. The O_2/CO_2 mixture was saturated with water before being fed to the reactor through the Teflon® cap. The reactor was agitated at 1400 rpm and maintained at 70 ℃.

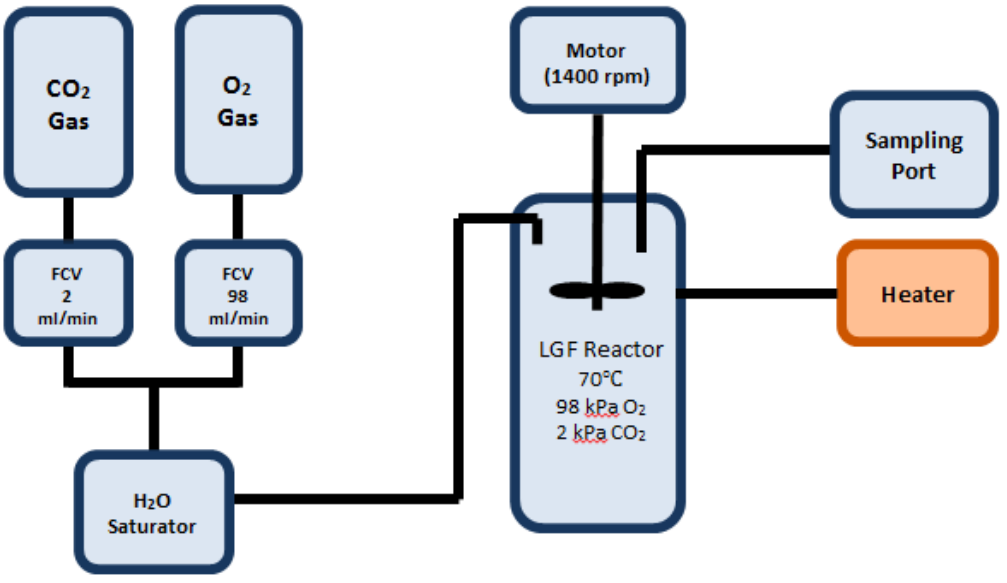

Fig. 1. Low gas flow oxidation apparatus

The water balance was maintained by adding water each time a sample was removed to make up for water loss through evaporation. Table 1 lists a sampling schedule that was generally followed for each experiment. The amines tested in this study included 1,4-diaminobutane (putrescine), ethylenediamine (EDA), 1,3-diaminopropane (PDA), hexamethylenediamine (HMDA), propanolamine (MPA), Diglycolamine® (DGA®), and bisaminoethyl ether (Jeffamine EDR-104®). The structures of these amines are listed in Table 2.

Table 1. General sampling schedule of oxidation experiments

Sample number	Time since start of experiment
1	At starting time
2	1 day
3	2 day
4	3 days
5	4 to 5 days
6	6 to 7 days
7	9 to 10 days
8	13 to 14 days

Table 2. Diamines tested in the LGF

Amine Name	Abbreviation	Structure
Ethylenediamine	EDA	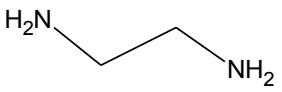
1,3-diaminopropane	PDA	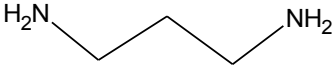
1,4-diaminobutane	Putrescine	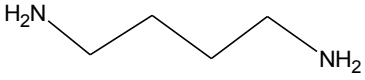
Hexamethylenediamine	HMDA	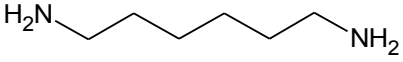
Propanolamine	MPA	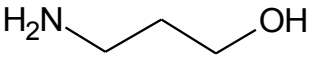
Diglycolamine®	DGA®	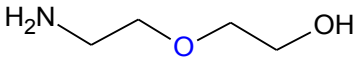

Bisaminoethyl ether Jeffamine EDR-104®

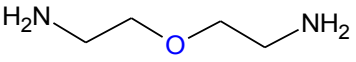

Cation chromatography was used to analyze for parent amine concentrations and degradation by-product concentrations; samples were diluted by a factor of 10000, and the separation was carried out using a Dionex CS17 column. Anion chromatography was used to qualitatively analyze for formate salts and nitrite. Samples were first hydrolyzed using concentrated sodium hydroxide and then diluted by a factor of 100. The separation was carried out using a Dionex AS15 column. The analytical methods are identical to those of Voice [1].

3. Results

Figure 2 shows the degradation of PDA with high and low metals. The amine concentrations are calculated based on cation chromatography results. PDA does not show significant degradation and the fluctuations are likely noise caused by water balance adjustments. A considerable amount of foam formed at the gas-liquid interface in both experiments. As a result, PDA was tested again with antifoam to study whether foaming on the solution surface is hindering oxygen diffusion into the bulk solution and hindering oxidation. Approximately 1 ml of antifoam was added to the PDA solution together with the metals at the start of the experiment, and as data in Figure 2 show, antifoam did not alter the degradation behavior of PDA.

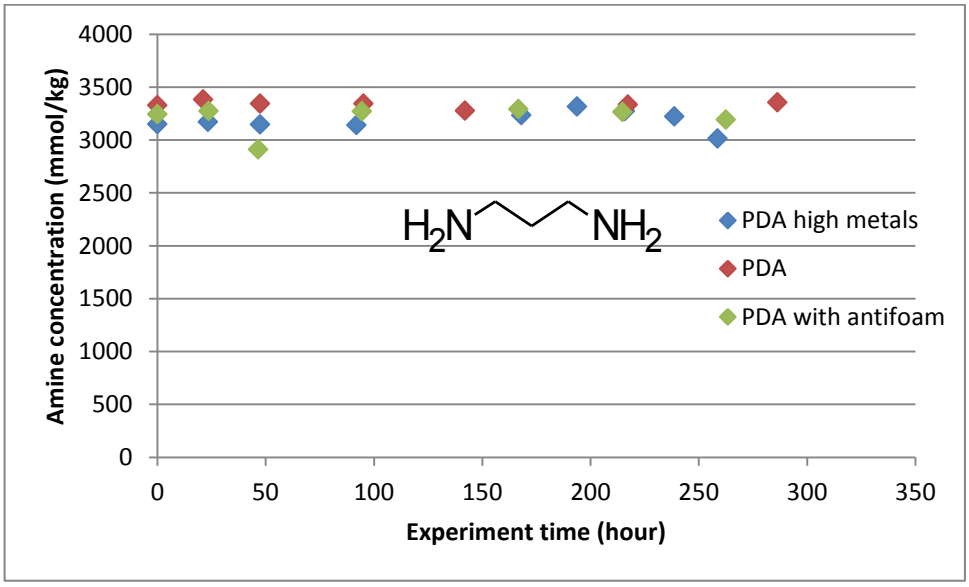

Figure 2. Oxidation of 5 m PDA. 70 ℃, 98 kPa O_2, 2 kPa CO_2, 100 ml/min gas flow, 1400 rpm.

The concentration of heat stable salts for PDA with antifoam is shown in Figure 3. The concentration is almost zero, indicating that almost no oxidative degradation took place.

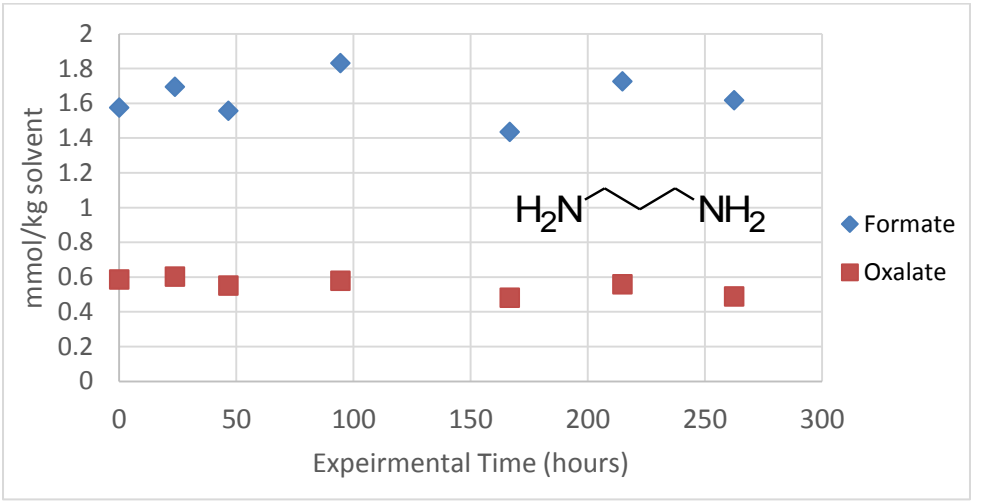

Figure 3. Total formate and total oxalate in oxidation of 5 m PDA. 70 ℃, 98 kPa O_2, 2 kPa CO_2, 100 ml/min gas flow, 1400 rpm.

The degradation of EDA follows zeroth order behavior with a rate constant of 9.79 mmol/kg-hr while degradation of putrescine follows first order behavior with a rate constant of 0.0104 1/hr. These data are summarized in Figures 4 and 5.

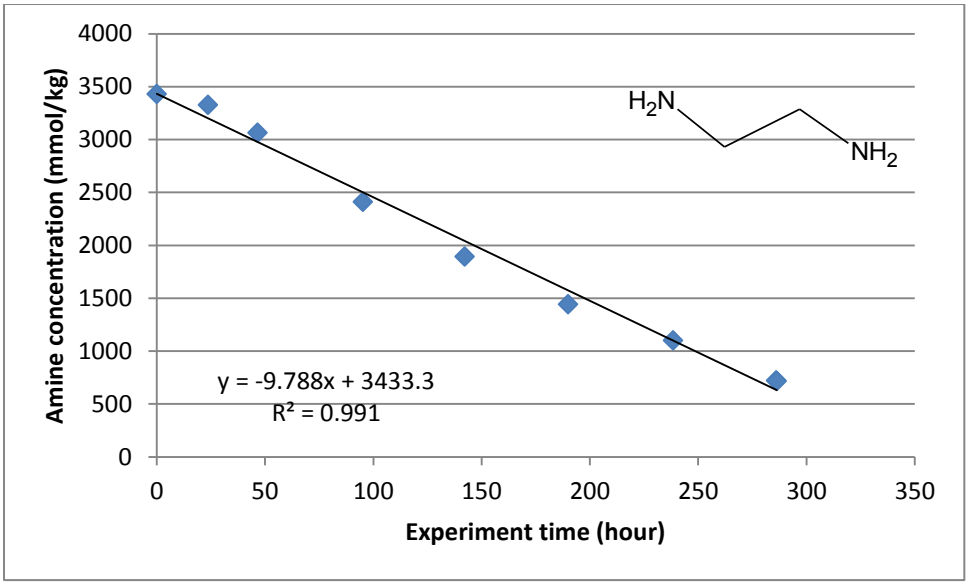

Figure 4. Oxidation of 5 m EDA. Conditions: 70 ℃, 98 kPa O_2, 2 kPa CO_2, 100 ml/min gas flow, 1400 rpm, 0.4 mM Fe, 0.2 mM Mn, 0.1 mM Ni, 0.05 mM Cr.

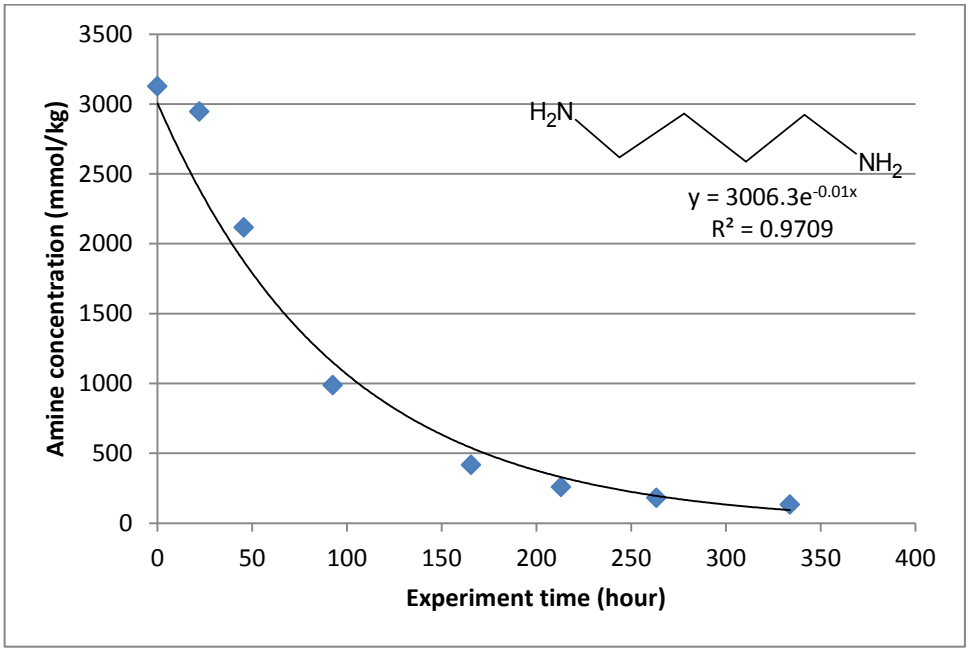

Figure 5. Oxidation of 5 m putrescine. Conditions: 70 ℃, 98 kPa O_2, 2 kPa CO_2, 100 ml/min gas flow, 1400 rpm , 0.4 mM Fe, 0.2 mM Mn, 0.1 mM Ni, 0.05 mM Cr.

Based on the degradation rates of EDA and putrescine, EDA degradation is likely mass transfer controlled or catalytically controlled while putrescine degradation is likely kinetically controlled. Putrescine degradation seems to approach an equilibrium once 90% of the original solvent degraded after approximately 220 hours. These results disagree with Voice in that putrescine is resistant to oxidation, but agree with his observation that EDA is susceptible to oxidation. Voice observed that iron suppressed EDA oxidation, which produced volatile products.

Figure 6 shows the degradation of putrescine. Putrescine seems to undergo a short induction stage where degradation is very slow at first but then rapidly accelerates. Degradation of putrescine is kinetically controlled and follows first order kinetics with rate constant k = 0.01/hr. About 96% of the initial amount of amine was lost to degradation.

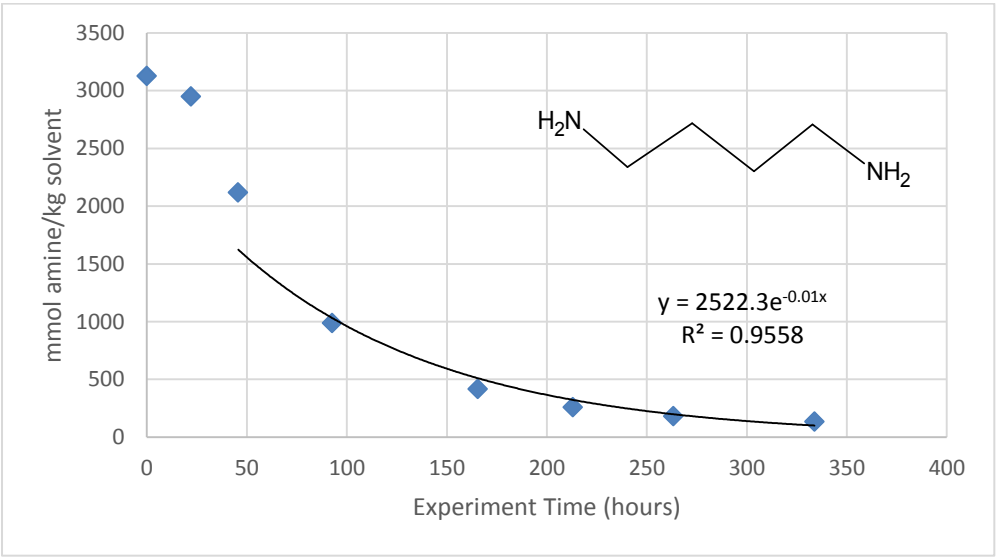

Figure 6. Oxidation of 5 m putrescine. 70 ℃, 98 kPa O_2, 2 kPa CO_2, 100 ml/min gas flow, 1400 rpm.

Anion chromatography data of heat stable salt products formed from putrescine oxidation are shown in Figure 7. The ratio of formate heat stable salts to oxalate heat stable salts is about 3:1.

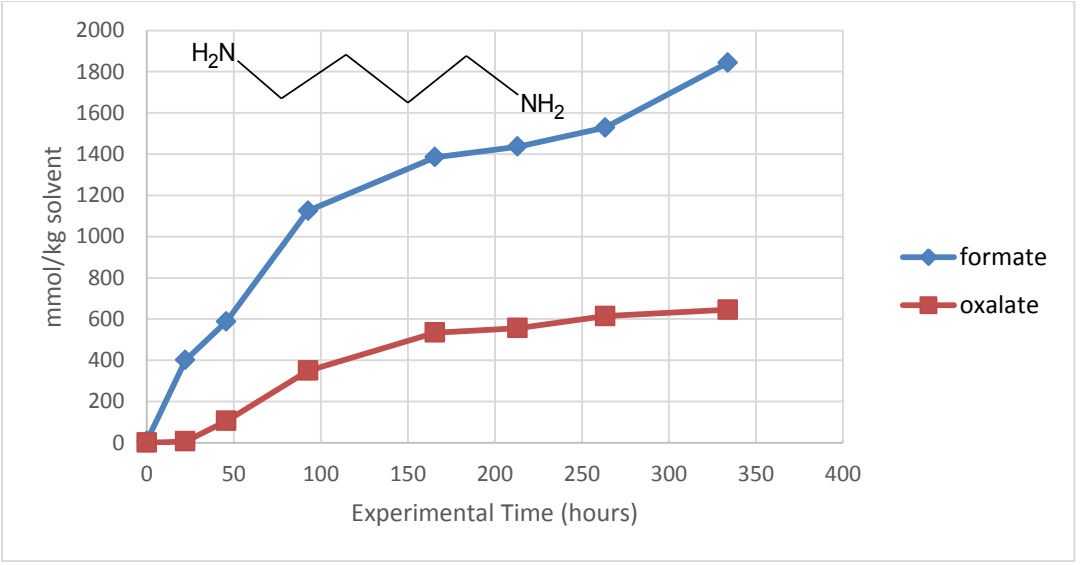

Figure 7. Total formate and total oxalate in oxidation of 5 m putrescine. 70 ℃, 98 kPa O_2, 2 kPa CO_2, 100 ml/min gas flow, 1400 rpm.

Figure 8 shows the degradation of HMDA. An induction period similar to that in putrescine is observed, so only the last four data points were used to calculate the rate of degradation. HMDA shows degradation that is kinetically controlled following first order reaction kinetics with rate constant k = 0.01/hr. About 80% of the initial amount of amine was lost to degradation.

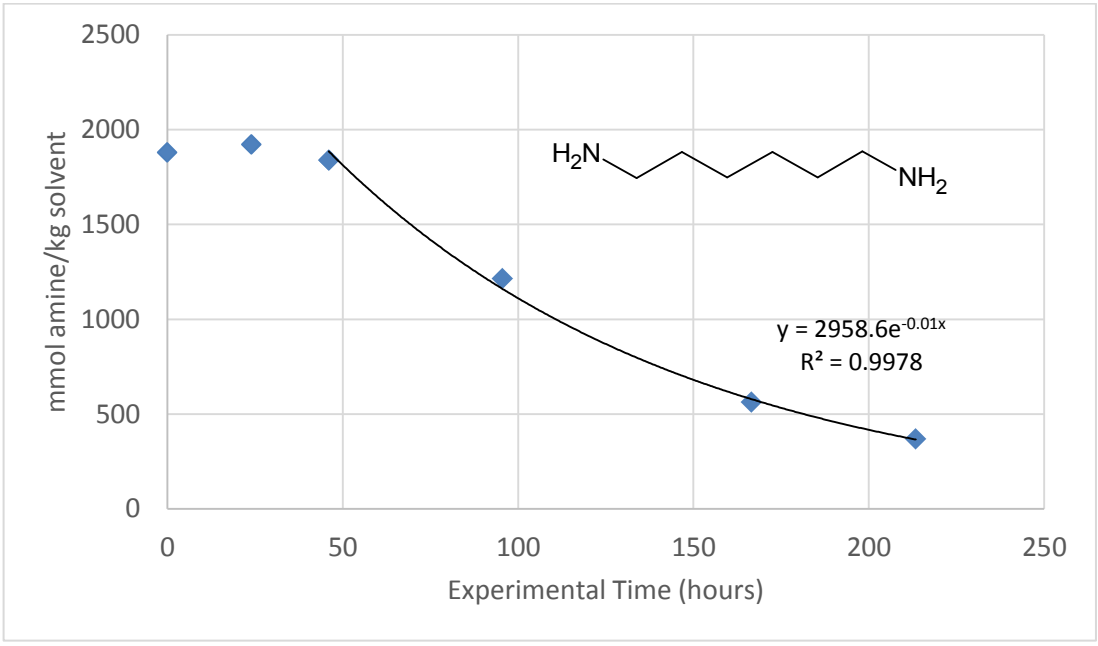

Figure 8. Oxidation of HMDA. 70℃, 98 kPa O_2, 2 kPa CO_2, 100 ml/min gas flow, 1400 rpm.

Figure 9 shows the heat stable salts produced from oxidation of HMDA. Formate forms at a slightly greater rate than oxalate, and the amount of heat stable salts formed is much less than from putrescine. The general trend for heat stable salt formation agrees with the rate of amine loss in Figure 7.

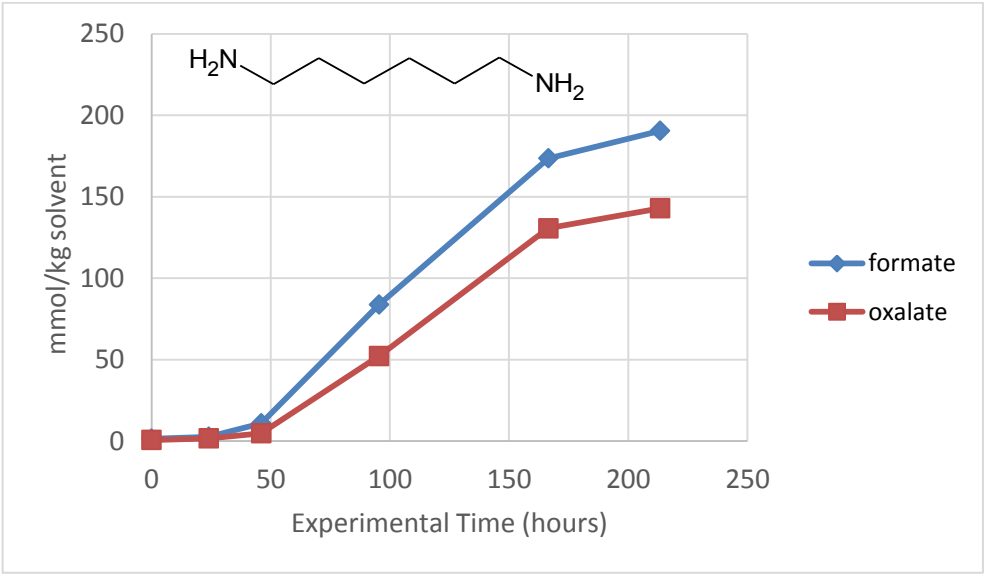

Figure 9. Total formate and total oxalate of HMDA. 70 ℃, 98 kPa O_2, 2 kPa CO_2, 100 ml/min gas flow, 1400 rpm.

Figure 10 shows the degradation of Jeffamine EDR-104®. There is no observable induction stage for this amine, but the degradation is still kinetically controlled following first order reaction kinetics with rate constant k = 0.023/hr. The rate constant is much higher than that of the other amines tested. About 90% of the initial amount of amine was lost to degradation.

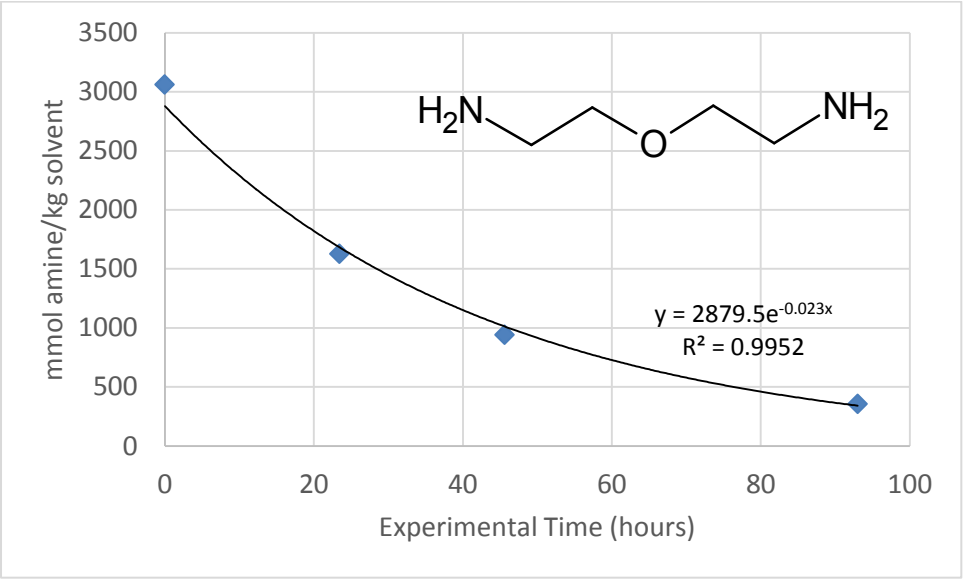

Figure 10. Oxidation of Jeffamine EDR-104®. 70 ℃, 98 kPa O_2, 2 kPa CO_2, 100 ml/min gas flow, 1400 rpm.

Figure 11 shows the formate from oxidation of Jeffamine EDR-104®. Oxalate was detected but could not be quantified.

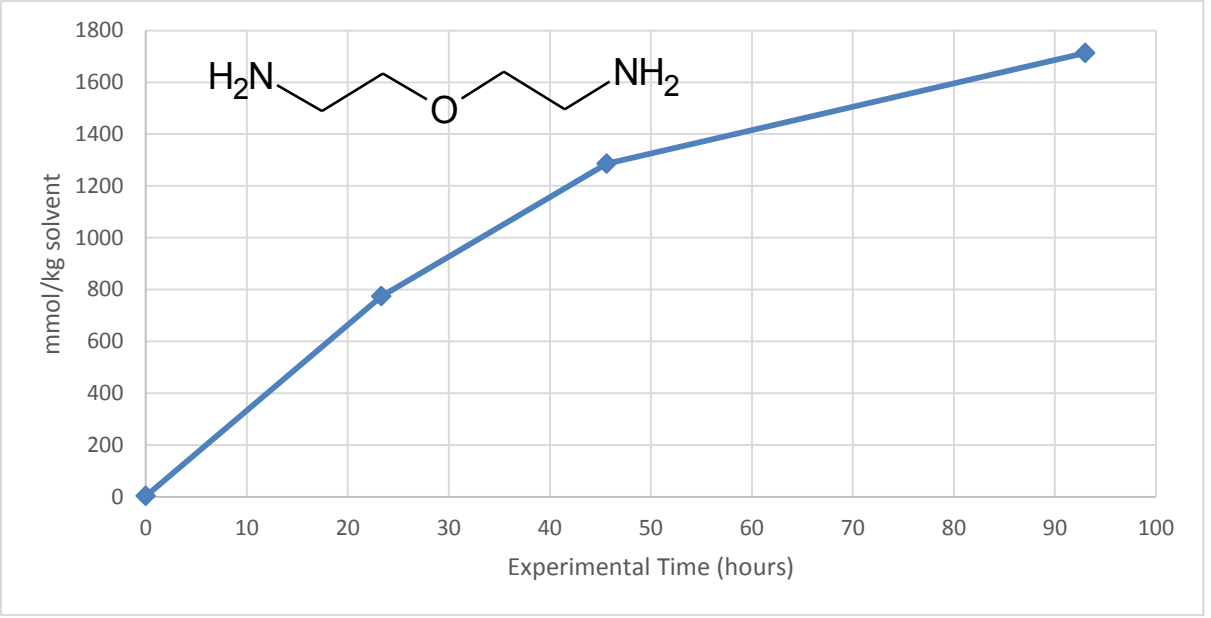

Figure 11. Total formate of Jeffamine EDR-104®. Conditions: 70 ℃, 98 kPa O_2, 2 kPa CO_2, 100 ml/min gas flow, 1400 rpm.

Figures 12 shows the degradation of DGA®. There is no observable induction stage for this amine, but the degradation is still kinetically controlled following first order reaction kinetics with rate constant k = 0.008/hr. About 80% of the initial amount of amine was lost to degradation.

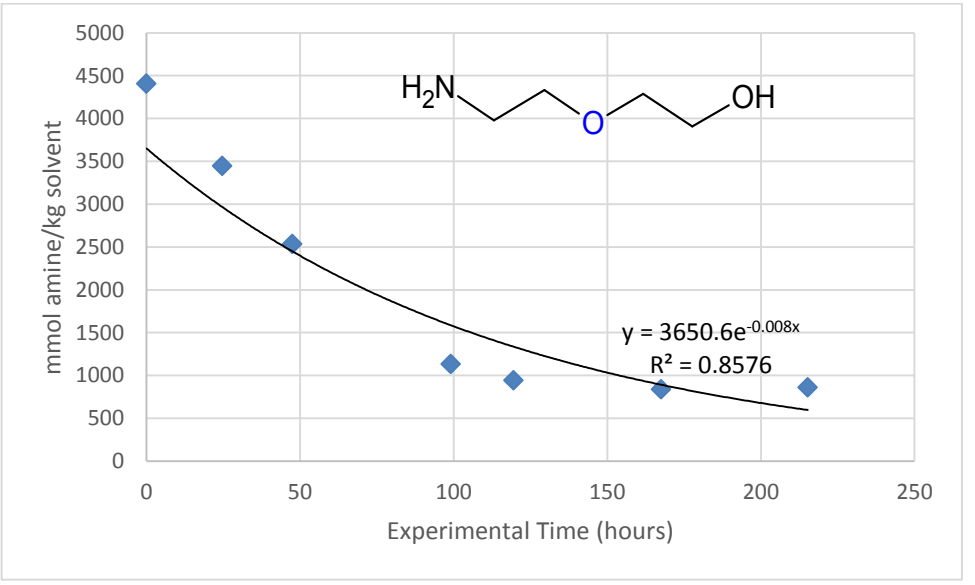

Figure 12. Oxidation of DGA®. Conditions: 70 ℃, 98 kPa O_2, 2 kPa CO_2, 100 ml/min gas flow, 1400 rpm.

Figure 13 shows the degradation of MPA. This amine showed negligible degradation with a 10% amine loss over 260 hours.

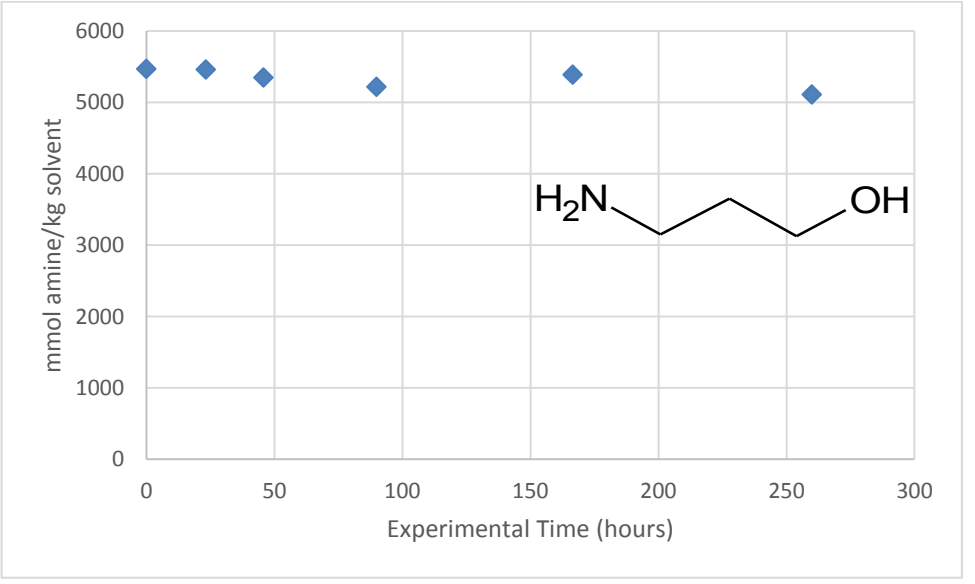

Figure 13. Oxidation of MPA. Conditions: 70 ℃, 98 kPa O_2, 2 kPa CO_2, 100 ml/min gas flow, 1400 rpm.

The amines that showed significant degradation all have even numbers of carbon atoms in their chains. MPA and PDA both contain three carbons in their alkyl chain and both showed negligible degradation. Catalysts form a homogenous solution with the amine samples that degraded significantly, but settled out of solution in the case of MPA and PDA. Data from thermal degradation of PDA showed that PDA and its thermal degradation products are not corrosive, further suggesting that metals likely did not catalyze oxidative degradation due to their insolubility in MPA and PDA [5]. An induction stage was observed in many amines that showed significant degradation. The

initial degradation products may have dissolved the added metals, which subsequently catalyzed degradation and caused rapid amine loss.

4. Conclusions

The table below summarizes experimental observations. A detailed list summarizing degradation behavior of the amines tested follows.

Table 3. Degradation behavior of amines at 70 ℃, 98 kPa O_2, 2 kPa CO_2 , 1400 rpm, 0.4 mM Fe, 0.2 mM Mn, 0.1 mM Ni, and 0.05 mM Cr

Amine Name	Abbreviation	Structure	Rate	Reaction order	Control Mechanism
Ethylenediamine	EDA		k=9.8 mmol/kg*hr	Zeroth order	Mass Transfer Controlled, could be strongly catalyzed
1,3-diaminopropane	PDA		No significant degradation, metal insolubility observed		
1,4-diaminobutane	Putrescine		k=0.01/hr	First order	Kinetically/Catalytically Controlled
Hexamethylenediamine	HMDA	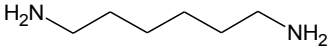	k=0.01/hr	First order	Kinetically/Catalytically Controlled
Propanolamine	MPA	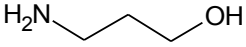	No significant degradation, metal insolubility observed		
Diglycolamine®	DGA®	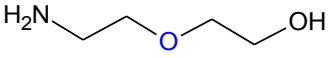	k=0.008/hr	First order	Kinetically/Catalytically Controlled
Bisaminoethyl ether	Jeffamine EDR-104®	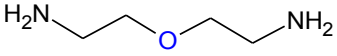	k=0.023/hr	First order	Kinetically/Catalytically Controlled

All of these conclusions were developed at at 70 ℃, 98 kPa O_2, 2 kPa CO_2 with 0.4 mM Fe, 0.2 mM Mn, 0.1 mM Ni, and 0.05 mM Cr.

1. PDA does not show appreciable oxidation with or without antifoam. This shows that foaming is not the reason for PDA resistance to oxidative degradation and experimental observations suggest that metal insolubility may be the cause.
2. EDA oxidizes at 9.8 mmol/kg*h. EDA degradation follows 0th order kinetics and is either mass transfer controlled or strongly catalyzed by the presence of metals.
3. MPA does not show appreciable oxidation. Experimental observations suggest that metal insolubility may cause MPA to be resistant to oxidative degradation.

4. Putrescine oxidizes at 0.01/hr. Putrescine degradation follows first order kinetics and is strongly catalyzed by the presence of metals. Degradation of putrescine produces formate and oxalate at a concentration ratio of approximately 3:1.
5. HMDA oxidizes at 0.01/hr. HMDA degradation follows first order kinetics and appears to be kinetically controlled. Degradation produces about the same amount of formate and oxalate.
6. Bisaminoethyl ether (Jeffamine EDR-104®) oxidizes at 0.023/ r. Its degradation follows first order kinetics and appears to be kinetically controlled.
7. DGA® oxidizes at 0.008/hr. DGA® degradation follows first order kinetics and appears to be kinetically controlled.
8. Amines with three carbons separating the two amino groups (PDA) or the amino group from the hydroxyl group (MPA) seem to be less susceptible to oxidation compared to amines with an even number of carbons separating the amino group from the neighboring functional group.

Acknowledgements

This work was supported by Texas Carbon Management Program.

The authors declare the following competing financial interest(s): One author of this publication consults for Southern Company and for Neumann Systems Group on the development of amine scrubbing technology. The terms of this arrangement have been reviewed and approved by the University of Texas at Austin in accordance with its policy on objectivity in research. The authors have financial interests in intellectual property owned by the University of Texas that includes ideas reported in this paper.

References

[1] Voice AK. Amine Oxidation in Carbon Dioxide Capture by Aqueous Scrubbing. The University of Texas at Austin Ph.D. Dissertation. 2013.

[2] Goff GS. Oxidative Degradation of Aqueous Monoethanolamine in CO_2 Capture Processes: Iron and Copper Catalysis, Inhibition, and O_2 Mass Transfer. The University of Texas at Austin. Ph.D. Dissertation. 2005.

[3] Zhou S, Chen X, Nguyen T, Voice AK, Rochelle GT. Aqueous Ethylenediamine for CO2 Capture. ChemSusChem. Special Issue: Carbon Capture and Sequestration. 2012.

[4] Sexton AJ. Amine Oxidation in CO_2 Capture Pr°Cesses. The University of Texas at Austin. Ph.D. Dissertation. 2008.

[5] Rochelle GT et al. CO_2 Capture by Aqueous Absorption, Fourth Quarterly Progress Report 2013. Texas Carbon Management Program. The University of Texas at Austin. 2014.

[6] Rochelle GT et al. CO_2 Capture by Aqueous Absorption, Second Quarterly Progress Report 2014. Texas Carbon Management Program. The University of Texas at Austin. 2014.

Available online at www.sciencedirect.com

ScienceDirect

Energy Procedia 00 (2013) 000–000

Energy Procedia

www.elsevier.com/locate/procedia

GHGT-12

Thermal Degradation of PZ-Activated Tertiary and Hindered Amines

Omkar Namjoshi[a], Daniel Hatchell[a], Gary Rochelle[a]*

[a]*McKetta Department of Chemical Engineering, The University of Texas at Austin, 200 E Dean Keeton St Stop C0400, Austin, Texas, 78712 USA*

Abstract

The thermal degradation of PZ-activated tertiary amine and PZ-activated hindered amine solvents is presented. Assuming a loss of 2% amine/week, PZ-activated tertiary morpholine solvents were found to be the most stable and are capable of being regenerated at 150 °C or greater. PZ-activated tertiary aliphatic amine solvents without methyl groups can be regenerated between 130 and 140 °C, and PZ-activated tertiary aliphatic amine solvents with at least one methyl group can be regenerated below 130 °C. PZ-activated 2-(tert-butylamino)ethanol and 2-amino-2-methyl-1-propanol were the most stable hindered amines tested and can be regenerated at 140 °C.

Selection and peer-review under responsibility of GHGT.

Keywords: Thermal Degradation; Post-Combustion CO_2 Capture; Pre-Combustion CO_2 Capture; Amines; Tertiary Amines; Hindered Amines;

1. Introduction

Thermal degradation is considered to be a significant contributor to solvent loss in post-combustion capture applications and in pre-combustion applications. In this review, recent results that focus on thermal degradation of PZ-activated tertiary amines and PZ-activated hindered amines are presented.

Piperazine is known to be non-volatile, is oxidatively and thermally stable, and possesses good CO_2 cyclic capacity and absorption rate when used as a CO_2 capture solvent at concentrations varying from 30 wt % PZ to 40

* Corresponding author. Tel.: +1-512-471-7230; Fax: +1-512-471-7060
E-mail address: gtr@che.utexas.edu

Selection and peer-review under responsibility of GHGT.

wt % PZ in water. However, it has a limited solid solubility window, which limits its operational lean loading and can cause plant downtime if the solvent precipitates.

Tertiary amine solvents promoted with PZ have CO_2 capacity and absorption rate that is comparable to concentrated PZ and can avoid the solid solubility limitations of the concentrated PZ. Solvents comprising methyldiethanolamine (MDEA), a tertiary amine, and PZ have been used successfully in high pressure gas treating applications. In coal-derived flue-gas CO_2 capture applications, 7 m MDEA/2 m PZ and 5 m MDEA/5 m PZ have lower regeneration energy requirements than 8 m PZ and comparable CO_2 absorption rates to 8 m PZ. The 5 m MDEA/5 m PZ solvent also has a 10% greater CO_2 cyclic capacity than 8 m PZ [1,2].

PZ-activated hindered amine solvents also have comparable CO_2 absorption rates and capacities to 8 m PZ. A solvent comprising 4 m 2-amino-2-methyl-1-propanol (AMP)/2 m PZ has a similar CO_2 absorption rate and capacity to 8 m PZ [2], and a solvent comprising 3.5 m 2-Amino-2-(hydroxymethyl)-1,3-propanediol (Tris)/3.5 m PZ has a similar CO_2 absorption rate and greater CO_2 capacity than 8 m PZ [3].

PZ/MDEA and PZ/AMP are not as thermally stable as PZ, with maximum stripper temperatures between 120 and 130 °C for PZ/MDEA and between 130 and 140 °C for PZ/AMP. The lower stripper temperatures prevent the solvent from being regenerated at higher temperature and pressure, increasing the cost and energy requirement for CO_2 compression. The low regeneration temperature can also potentially lead to increased nitrosamine concentrations in the circulating solvent [4].

The tertiary amines and hindered amines tested, along with their concentration ranges, are presented in Tables 1 and 2.

Table 1: List of Tertiary Amines Tested

Tertiary Amine Name Abbreviation	Structure	Tertiary Amine Name Abbreviation	Structure
Methyldiethanolamine MDEA	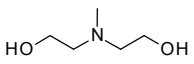	Diethylaminoethanol DEAE	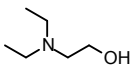
Dimethylaminoethanol DMAE	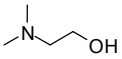	Ethyldiethanolamine EDEA	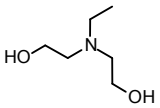
Dimethylaminoisopropanol DMAIP	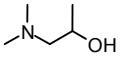		
Dimethylaminopropanol DMAP	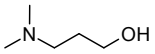	Triethanolamine TEA	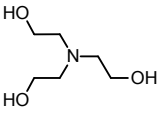
Dimethylaminobutanol DMAB	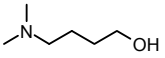		
Dimethylaminoethoxyethanol DMAEE	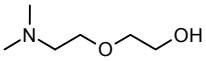	Triisopropanolamine TIPA	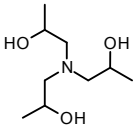
Hydroxyethylmorpholine HEM	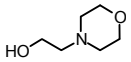		
Hydroxyisopropylmorpholine HIPM	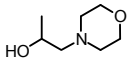	n-Butyldiethanolamine nBuDEA	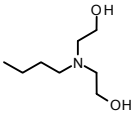
Hydroxypropylmorpholine HPM	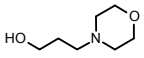		
		tert-Butyldiethanolamine tBuDEA	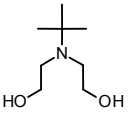

2. Experimental Methods and Modeling

2.1. Solution Preparation

Solvents were prepared gravimetrically. CO_2 was sparged into the solvent using a gas-washing bottle and was measured gravimetrically.

Table 2: List of Hindered Amines Tested

Hindered Amine Name Abbreviation	Structure	Hindered Amine Name Abbreviation	Structure
2-Amino-2-Methyl-1-Propanol AMP	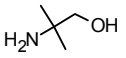	2-Piperidinemethanol PM	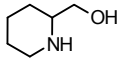
2-Amino-2-Methyl-1,3-Propanediol AMPD	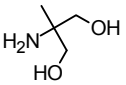	2-Piperidineethanol PE	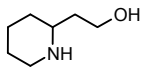
Tris(hydroxymethyl)aminomethane Tris	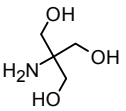	2-(tert-butyl)aminoethanol TBAE	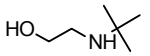

2.2. Thermal Degradation Apparatuses

Solvents were loaded in sealed Swagelok® cylinders with an internal diameter of 0.95 cm and a capacity of 4.5 ml. 4.0 ml of the solvent was loaded into each cylinder, and the cylinders were sealed, weighed, and placed inside convection ovens operating at a set temperature. Cylinders were removed periodically, weighed, and placed inside a chemical refrigerator for storage. Cylinders that lost more than 5% of their mass were discarded and their contents were not analyzed.

2.3. Analytical Techniques – Cation Chromatography

Suppressed cation chromatography was used to determine the concentration of parent amines as well as byproducts in degraded samples. Samples were diluted to roughly 50 ppmw total amine in 18.2 µmho deionized water. A Dionex ICS-2100 chromatograph with a Dionex AS autosampler and a CSRS-300 suppressor was used. 25 µl of the diluted sample was injected into the unit. The mobile phase consisted of a gradient of methylsulfonic acid from 5.5 mM to 38.5 mM in 18.2 µmho deionized water. The separation was carried out using a Dionex CG17 4x50 mm guard column and a Dionex CS17 4x250 mm analytical column with an eluent flow of 0.5 ml/min and a suppressor current of 50 mA.

2.4. Modeling Techniques

Pseudo first-order kinetic models, shown in Equation 1, with respect to parent amine concentration were used to model amine degradation. The activation energy of thermal degradation was calculated using the Arrhenius equation, shown in Equation 2. The pseudo first-order kinetic models predict degradation well for a variety of PZ/tertiary amine solvents and PZ/hindered amine solvents, shown in Figures 1 and 2.

$$\frac{dC_A}{dt} = k * C_A \tag{1}$$

$$k = A * \exp\left(\frac{-E_A}{R*T}\right) \quad (2)$$

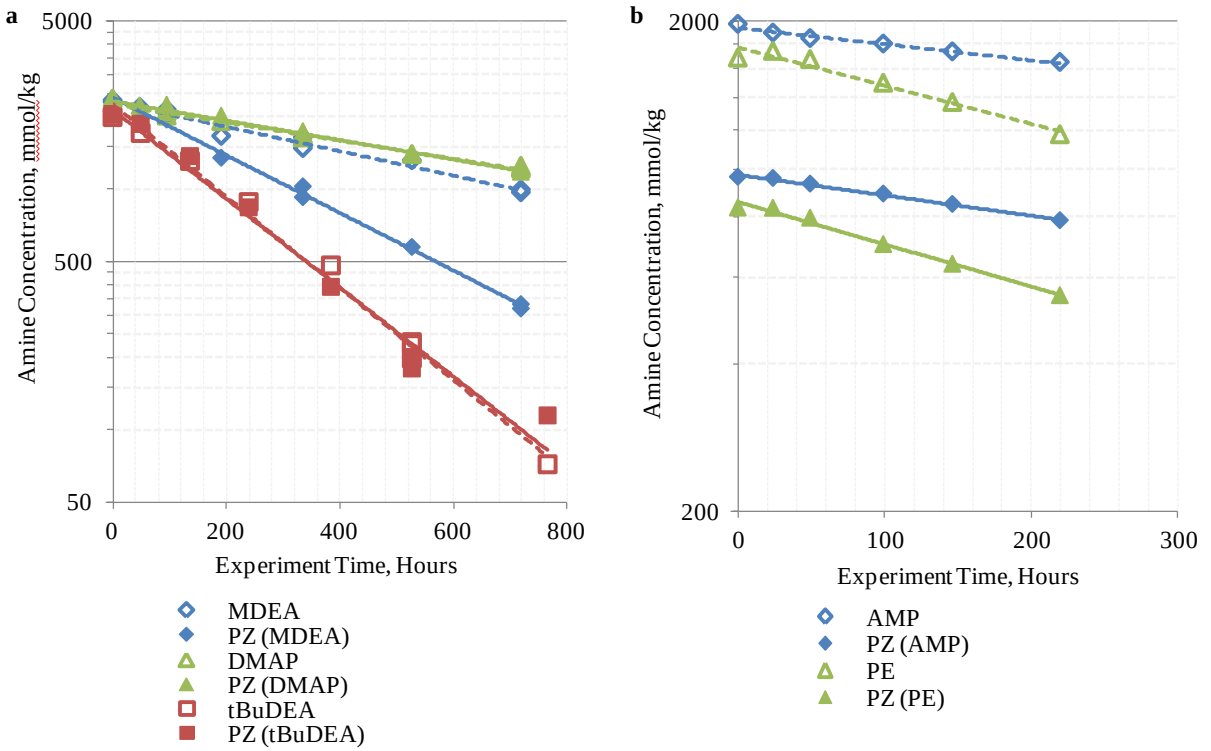

Figure 1: (a) Degradation of 5 m PZ/5 m tertiary amine at 150 °C initially at 0.225 mol CO_2/mol alkalinity and (b) degradation of 1.33 m PZ/2.67 m hindered amine initially at 0.22 mol CO_2/mol alkalinity, showing reasonable agreement with first-order rate models

3. Results

3.1. Degradation of PZ-Activated Tertiary Amines

The degradation of PZ-activated tertiary amines is believed to be initiated via two pathways. In one scheme, shown in Figure 2a, PZ attacks the alpha carbon of the methyl group of protonated MDEA, forming 1-methylpiperazine and diethanolamine. This pathway is believed to occur at moderate CO_2 loading and is reversible [5]. In the other scheme, shown in Figure 2b, PZ attacks the carbon alpha to a hydroxyl group, irreversibly condensing water and creating a polyamine. This occurs at zero loading or in conditions in which the majority of the solvent is protonated and has been observed to occur in DEA-activated MDEA solvents [6].

The byproducts can lead to loss of the activator. The secondary amine byproduct, if capable of forming an oxazolidinone, will react rapidly with the activator via the carbamate polymerization pathway. This can take place between DEA and PZ if CO_2 is present in solution, as shown in Figure 3.

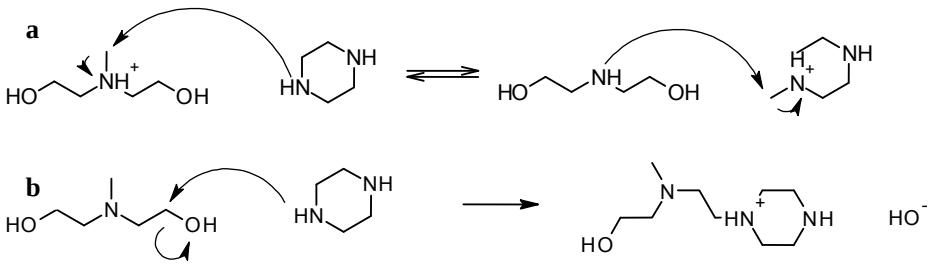

Figure 2: (a) Attack of protonated MDEA by PZ to form diethanolamine and 1-methylpiperazine and (b) attack of the carbon alpha to a hydroxyl group on MDEA by PZ to form a triamine and hydroxide.

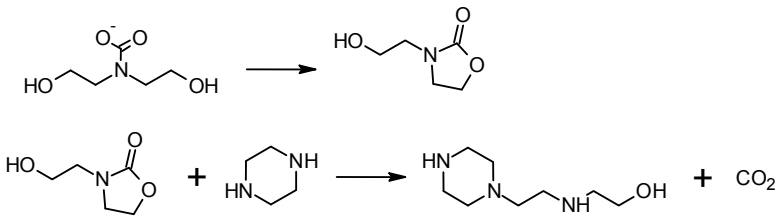

Figure 3: Carbamate polymerization degradation pathway between diethanolamine and PZ

PZ readily attacks methyl substituent groups on the tertiary amine; bulkier substituent groups, such as ethyl or hydroxyethyl groups, are attacked at a lower rate and have higher activation energies of thermal degradation. PZ will rapidly react with intermediate byproducts capable of forming oxazolidinones and thus will have a higher degradation rate than the tertiary amine for solvents whose intermediate degradation products include oxazolidinone-forming amines. Table 3 summarizes the degradation rates of a variety of PZ-activated tertiary amine solvents [7].

Table 3: Degradation rates and activation energies of 5 m tertiary amine (TA)/5 m PZ solvents at an initial loading of 0.225 mol CO_2/mol alkalinity and 150 °C

Tertiary Amine	k_1, TA 10^{-9} sec^{-1}	k_1, PZ 10^{-9} sec^{-1}	E_A, TA/PZ kJ/mol	Tertiary Amine	k_1, TA 10^{-9} sec^{-1}	k_1, PZ 10^{-9} sec^{-1}	E_A, TA/PZ kJ/mol
MDEA	325±35.7	766±40.9	140/139	EDEA	199±12.4	333±21.4	--
DMAE	417±24.3	617±20.4	134/126	DEAE	168±11.7	257±5.14	175/168
DMAIP	202±12.4	278±10.7	--	nBuDEA	177±21.2	291±26.1	--
DMAP	240±20.0	258±23.4	126/131	tBuDEA	1220±95.1	1180±165	--
DMAB	1780±208	1150±164	--	TEA	161±27.2	277±26.3	169/190
DMAEE	339±40.2	302±41.3	--	TIPA	58.3±7.36	129±15.2	--
				HEM	10.7±6.0	17.2±6.9	--
				HIPM	11.0±18.2	14.4±3.8	--
				HPM	5.4±6.0	10.2±4.0	--

3.2. Degradation of PZ-Activated Hindered Amines

The degradation of PZ-activated hindered amines is believed to be initiated via the carbamate polymerization mechanism for the hindered amines that are capable of forming oxazolidinones. This is shown in Figure 4. AMP oxazolidinone as well as the product corresponding to the reaction between PZ/AMP, were identified using direct-injection MS as the main degradation product [8].

All of the hindered amines in this study have structures (two to three carbons between the hydroxyl and amine function) that would lead to oxazolidinone formation. Otherwise, degradation initiated by PZ attack on either the carbon alpha to the hydroxyl or protonated amino functions on the hindered amine would likely dominate. Table 4 summarizes the degradation rates for a variety of PZ-activated hindered amines.

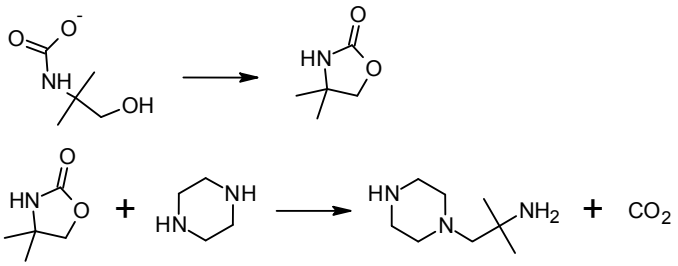

Figure 4: Formation of oxazolidinone from AMP carbamate and subsequent reaction between PZ and oxazolidinone to form a triamine.

Table 4: Degradation rates and activation energies of 2.67 m hindered amine (HA)/1.33 m PZ solvents at an initial loading of 0.223 mol CO_2/mol alkalinity and 165 °C

Hindered Amine	k_1, HA 10^{-9} sec^{-1}	k_1, PZ 10^{-9} sec^{-1}	E_A, HA/PZ kJ/mol	Tertiary Amine	k_1, HA 10^{-9} sec^{-1}	k_1, PZ 10^{-9} sec^{-1}	E_A, HA/PZ kJ/mol
AMP	212±16.7	267±11.4	127/129	2-PM	6907±1228	7764±3632	107/105
AMPD	480±52.4	125±21.1	104/147	2-PE	501±50.3	554±30.5	110/112
TRIS	376±71.6	600±27.4	100/116	TBAE	76.4±7.9	140±7.6	103/125

AMP and TBAE are the most stable hindered amines tested. 2-PM is significantly less stable than 2-PE because it forms a 5-membered oxazolidinone versus a 6-membered oxazolidinone. The rate of PZ degradation in activated TRIS is greater than AMPD or AMP. TRIS has three hydroxyethyl groups, compared to two and one for AMPD and AMP, respectively. The triamine product between TRIS oxazolidinone as well as AMPD oxazolidinone with PZ can also form oxazolidinones, which can lead to additional PZ loss. The rate of hindered amine degradation is greater in AMPD than in TRIS or AMP, but the PZ degradation is the lowest and has the highest activation energy in AMPD/PZ. It is possible that the AMPD oxazolidinone is stable and does not readily react with PZ.

3.3. Maximum Stripping Temperature (T_{MAX})

The maximum stripping temperature (T_{MAX}) of a solvent is defined as the stripper temperature that leads to thermal degradation losses of about 2%/week and is a useful method to rank the relative stability of amines as functions of their initial degradation rates [9]. For MEA, Davis determined that the maximum stripper temperature was 122 °C [10]; gas treating plants and CO_2 capture pilot units using the MEA solvent typically run the stripper between 115 and 120 °C [7,9].

To estimate the T_{MAX}, a first-order degradation rate constant is calculated with respect to total amine concentration at 150 °C for the PZ-activated tertiary amines and at 135 °C for the PZ-activated hindered amines and is shown in Equation 3.

$$\frac{dC}{dt} = k * C_{\sum \text{ParentAmines}} \tag{3}$$

Activation energies are calculated if rate constants calculated using Equation 3 are available at different temperatures. Otherwise, activation energies are estimated based on data available for amines whose structures and degradation mechanisms are similar to the amine of interest and whose activation energy is known [9]. For

example, the activation energy of PZ/TIPA is expected to be similar to PZ/TEA, and the activation energy of the PZ/tertiary morpholine solvents is expected to be similar to concentrated PZ. These data are summarized in Table 4 [7].

PZ-activated aliphatic tertiary amines with at least one methyl group, such as PZ/MDEA and PZ/DMAE, degrade at the greatest rate and have T_{MAX} values between 120 and 130 °C. PZ-activated aliphatic tertiary amines with no ethyl groups, such as PZ/TEA and PZ/DEAE, degrade more slowly than PZ-activated tertiary amines with at least one methyl group and have T_{MAX} values between 130 and 140 °C. PZ-activated tertiary morpholine solvents are the most stable promoted tertiary amine solvent tested with T_{MAX} values above 150 °C. PZ-activated TBAE and AMP are the most stable hindered amine solvents, with stability decreasing as hydroxyethyl substituent groups are added to the hindered amine.

Table 4: T_{MAX} for a variety of PZ/tertiary amine solvents and PZ/hindered amine solvents

Amine System	E_A kJ/mol	MST °C	Amine System	E_A kJ/mol	MST °C
5 m PZ/5 m HPM	180	161	1.33 m PZ/2.67 m TRIS	110	128
5 m PZ/5 m HIPM	180	157	1.33 m PZ/2.67 m 2-PE	110	127
5 m PZ/5 m HEM	180	156	5 m PZ/5 m DMAIP	130	127
1.33 m PZ/2.67 m TBAE	110	147	5 m PZ/5 m DMAP	130	127
5 m PZ/5 m TIPA	190	141	5 m PZ/5 m DMAEE	130	124
1.33 m PZ/2.67 m AMP	130	141	5 m PZ/5 m MDEA	140	122
5 m PZ/5 m TEA	190	135	5 m PZ/5 m DMAE	130	120
5 m PZ/5 m DEAE	170	133	5 m PZ/5 m tBuDEA	130	111
5 m PZ/5 m nBuDEA	170	133	5 m PZ/5 m DMAB	130	107
5 m PZ/5 m EDEA	170	132	1.33 m PZ/2.67 m 2-PM	110	97
1.33 m PZ/2.67 m AMPD	110	131			

4. Conclusions

1. PZ-activated tertiary amines with at least one methyl group, such as PZ/MDEA and PZ/DMAE, degrade at the greatest rate. They typically have activation energies of thermal degradation between 120 and 140 kJ/mol and maximum stability temperatures between 120 and 130 °C.

2. PZ-activated tertiary amines with no ethyl groups, such as PZ/TEA and PZ/DEAE, degrade more slowly than PZ-activated tertiary amines with at least one methyl group. They typically have activation energies of thermal degradation between 160 and 190 kJ/mol and maximum stripper temperatures between 130 and 140 °C.

3. PZ-activated tertiary morpholine solvents are the most stable promoted tertiary amine solvent tested with maximum stripper temperatures above 150 °C.

4. Intermediate degradation products formed from the initial reaction between PZ and the tertiary amine can form oxazolidinones. These compounds can rapidly react with PZ, doubling its degradation rate relative to the tertiary amine.

5. PZ-activated TBAE and AMP are the most stable hindered amine solvents. Stability decreases as hydroxyethyl substituent groups are added to the hindered amine.

Acknowledgements

The authors acknowledge the financial support of the Texas Carbon Management Program.

The authors declare the following competing financial interest(s): One author of this publication consults for Southern Company and for Neumann Systems Group on the development of amine scrubbing technology. The terms of this arrangement have been reviewed and approved by the University of Texas at Austin in accordance with its policy on objectivity in research. The authors have financial interests in intellectual property owned by the University of Texas that includes ideas reported in this paper.

References

[1] Frailie, PT. Modeling Energy Performance of Aqueous MDEA/PZ for CO_2 Capture. Presented at the 6th Trondheim CCS Conference, Trondheim, Norway, 16 June 2011

[2] Li L, Li H, Namjoshi O, Du Y, Rochelle GT. Absorption rates and CO_2 solubility in new piperazine blends. Energy Proc. 2013; 37:370-385

[3] Li L. Solvent Selection for CO_2 Capture-Absorption rates & Capacity. Presented at UTCCS-2, Austin, Texas, USA, 28 January 2014

[4] Fine NA, Nielsen PT, Rochelle GT. Decomposition of Nitrosamines in CO_2 Capture by Aqueous Piperazine or Monoethanolamine. Environ. Sci. Techol. 2014; 48: 5996-6002

[5] Closmann FB. Oxidation and thermal degradation of methyldiethanolamine/piperazine in CO_2 capture. PhD Dissertation, The University of Texas at Austin, Austin, Texas, USA 2011.

[6] Dawodu OF, Meisen A. Degradation of alkanolamine blends by carbon dioxide. Can. J. Chem. Eng. 1996; 74:960-6

[7] Namjoshi O, Rochelle GT. Thermal Degradation of PZ-promoted Tertiary Amine Blends for CO_2 Capture: Comparison of Structure Effects and Process Conditions on Degradation Rate. In preparation

[8] Li H, Voice AK, Personal Communication, May 2014

[9] Freeman SA, Rochelle GT. Thermal Degradation of Aqueous Piperazine for CO_2 Capture. 1.Effect of Process Conditions and Comparison of Thermal Stability of CO_2 Capture Amines. Ind. Eng. Chem. Res. 2012; 51:7719-7725

[10] Davis JD. Thermal Degradation of Aqueous Amines Used for Carbon Dioxide Capture. Dissertation, The University of Texas at Austin, Austin, Texas, USA 2009

Available online at www.sciencedirect.com

ScienceDirect

Energy Procedia 00 (2013) 000–000

Energy Procedia

www.elsevier.com/locate/procedia

GHGT-12

Cyclic oxidation of piperazine in bench and pilot scale CO_2 capture processes

Paul T. Nielsen[a], Alex K. Voice[a], Gary T. Rochelle[a,*]

[a] *McKetta Department of Chemical Engineering, The University of Texas at Austin, Austin, TX 78712, USA.*

Abstract

Concentrated 8 m piperazine was oxidized in the HTOR bench-scale cyclic oxidation apparatus using air and in a campaign conducted at the Tarong pilot plant using a slipstream of post-combustion coal flue gas. The HTOR apparatus closely resembles a real CO_2 capture plant with solvent cycled between low and high temperatures. The profile of oxidation products produced in the HTOR and at Tarong was similar, with formate the most significant liquid-phase product. Ammonia emissions accounted for 50% of the alkalinity oxidized. The oxidation rate observed at Tarong increased by a factor of 3 when the stripper operating temperature was raised 30 °C. The oxidation rate of piperazine at 150 °C was 80% less than monoethanolamine at 120 °C, and was reduced a further 60% by the addition of Inhibitor 8. Oxidation is not limited by the reaction of dissolved oxygen and is enhanced in the stripper and reboiler sump by cyclic oxygen and electron carriers such as organic peroxides and dissolved metal ions.

Keywords: amine oxidation; CO_2 capture; pilot plant; piperazine; cycling system

1. Introduction

The susceptibility of monoethanolamine (MEA), piperazine (PZ), and other amines to oxidation has been studied in batch and semi-batch systems since the 1950s [1]. Amine oxidation rate is a function of CO_2 loading, amine and oxygen concentration, temperature, solvent residence time in the absorber and stripper, and the presence of dissolved metal ions from corrosion [2]. MEA has been the most widely studied baseline solvent due to its low cost and industrial use in acid gas scrubbing. Concentrated aqueous PZ has recently been proposed as an alternative solvent

* Corresponding author. Tel.: +1-512-471-7230; fax: +1-512-471-7060.
E-mail address: grt@che.utexas.edu

due to its increased thermal stability and CO_2 capacity and absorption rate [3]. PZ has also been shown to be resistant to oxidation at absorber conditions [2].

Amine oxidation typically produces volatile ammonia, which will then be emitted in the flue gas leaving the absorber, and heat-stable salts including formate, acetate, and oxalate, which will accumulate in the solvent over time, increasing viscosity and corrosivity [2]. Additional water wash or acid wash treatment and solvent reclaiming may be required to limit the emission of degradation products.

Previous oxidation experiments have typically simulated absorber conditions, where flue gas containing excess oxygen continuously contacts the amine at low temperatures (40 to 70 °C). However, more recent work has shown that amine oxidation is significantly enhanced when the solvent is continuously cycled between absorber and stripper temperatures (100 to 150 °C) [2, 4]. This is most likely caused by the reaction of oxygen carriers (dissolved oxygen, peroxides, nitrite, and dissolved metal ions) with the amine in the cross-exchanger, stripper, and reboiler.

The most accurate picture of amine oxidation can only be made from pilot plant campaigns that mirror the conditions expected in a full-scale capture facility. Previous pilot plant campaigns using MEA [5] and PZ [6] solvents have shown that oxidation will be the dominant cause of amine loss and thermal degradation will be minimal.

Nomenclature

1-MPZ	N-methyl-piperazine
2-PZOH	2-Piperazinol
AEP	N-aminoethyl-piperazine
Cr^{3+}	Chromium ion
CSIRO	Commonwealth Scientific and Industrial Research Organization
DNPH	2,4-Dintro-phenyl-hydrazine
EDA	Ethylenediamine
Fe^{2+}	Ferrous iron ion
FTIR	Fourier Transform Infrared Spectroscopy
HGF	High Gas Flow Oxidation Reactor
HPLC	High performance liquid chromatography
HTOR	High Temperature Oxidation Reactor
Inh	Inhibitor
L/G	ratio of liquid solvent to flue gas flow rate (kg/kg)
MEA	Monoethanolamine
M	Molarity (moles of species per L solution)
m	Molality (moles of species per kg solvent)
mol/kg	moles of species per kg solution
MT	metric ton
NO_x	nitrous oxides
ppm_v	parts per million (molar/volumetric)
PZ	Piperazine
SO_x	sulphur oxides
T.	Total heat-stable salt (summation of free salt and amide)
TR	Thermal Reactor

2. Experimental Methods

In this work, MEA and PZ were oxidized in the High Temperature Oxidative Reactor (HTOR). This apparatus combines low temperature oxidation in the presence of excess oxygen with high temperature oxidation at stripper temperatures. A time series of solvent samples was also collected from a recent campaign using 8 m PZ conducted at the Tarong CO_2 capture pilot plant.

2.1. High Temperature Oxidation Reactor (HTOR) cyclic oxidation apparatus

The HTOR apparatus was constructed to allow the cycling of solvent between a low-temperature atmospheric oxidation reactor and a high-temperature high-pressure thermal reactor. Saturated air mixed with 0.5–2% CO_2 is sparged at 7.5 L/min into a high gas flow (HGF) glass reactor containing 350 mL of amine. The HGF is jacketed by an oil bath at 40 to 55 °C. The solvent is continuously drawn off from the reactor at 0.2 L/min with a peristaltic pump to a bubble-removal vessel before being pumped to the thermal reactor (TR). The TR operates at up to 160 °C and 17.2 bar. A stainless steel plate-and-frame cross-exchanger is used to transfer heat from the solvent leaving the TR to the solvent entering the reactor. The TR is also a stainless steel plate-and-frame exchanger submerged in an oil bath. A trim cooler (a ¼" tube submerged in a temperature-controlled water bath) is used to reduce the solvent temperature before it is returned to the HGF reactor. The total inventory of solvent in the apparatus is 1.6 L. A hot-gas Fourier transform infrared (FTIR) continuously quantifies ammonia leaving with the gas. Liquid samples are taken periodically for analysis of amine loss and degradation product accumulation. A PFD of the HTOR is shown in Figure 1. Additional specifications for the apparatus can be found in the Alex Voice's Ph. D. dissertation [3].

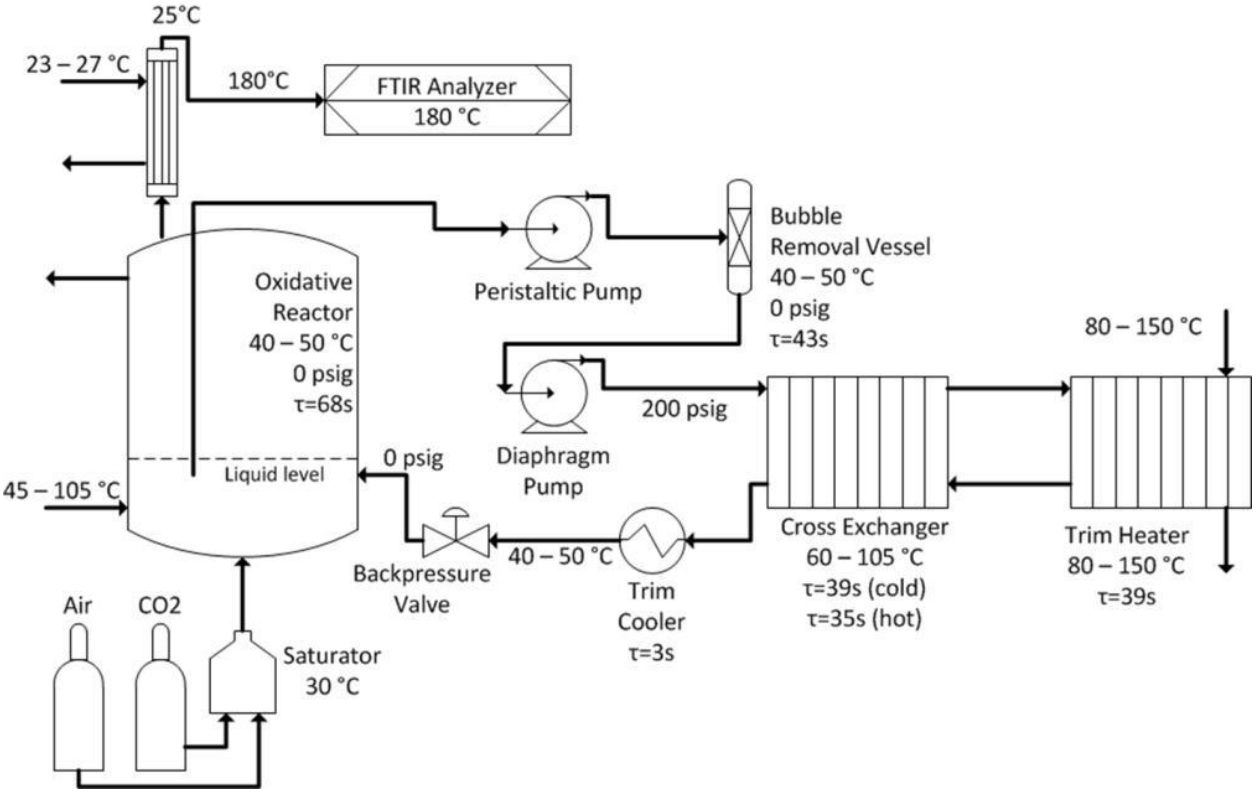

Fig. 1. Process flow diagram of the HTOR apparatus [2]

2.2. Tarong CO_2 Capture Pilot Plant PZ Campaign

The Tarong CO_2 capture pilot plant was constructed and operated by the Commonwealth Scientific and Industrial Research Organization (CSIRO) at the coal-fired Tarong Power Station in Nanango, Queensland, Australia. The pilot plant has been described in detail previously [7]. The plant has the capacity to treat a 0.1 MW_e slip stream of flue gas with 75% to 90% removal of CO_2. 600 kg/hr of flue gas entered the absorber with a typical composition of 11.7 vol % CO_2 and 6.7 vol % O_2 and contacted with 20 L/min of solvent. A caustic wash scrubber before the absorber reduced SO_2 entering with the flue gas to below 1 ppm_v.

CSIRO conducted a campaign at Tarong using 8 m (40 wt %) PZ in 2012 and 2013. After approximately 900 hours of parametric testing to evaluate the energy requirements of the solvent [8] two long-duration tests were conducted, maintaining constant operating conditions. The stripper was operated at 125 °C for 6 weeks before being raised to 155 °C for an additional 6 weeks using the same solvent inventory. Solvent and gas flow rates, rich and lean CO_2 loading, and liquid holdups were kept constant between the two tests. Liquid samples were collected periodically.

2.3. Analytical Methods

Analytical methods used to quantify amine loss and contaminant accumulation are summarized in Table 1.

Table 1. Analytical methods used to quantify amine oxidation.

Method	Analytes	Reference
Sulfuric acid titration	Total alkalinity	[11]
Cation Chromatography	Amines	[3]
Anion Chromatography	Heat-stable salts	[3]
HPLC with UV detection	2-PZOH	[9]
Inductively Coupled Plasma Optical Emission Spectroscopy	Dissolved metal ions	[3]
Fourier-Transform Infrared Spectroscopy	Ammonia	[10]

"Total" heat-stable salts were quantified by treatment of the sample with an equal volume of 5 N NaOH and waiting 24 to 48 hours before analysis by anion chromatography [3].

2-piperazinol (2-PZOH) was quantified by treatment of solvent samples with 2,4-dinitrophenolhydrazine (DNPH) to produce compounds that can be detected via UV absorption on reverse-phase HPLC [9].

3. Results

3.1. PZ Oxidation in the HTOR apparatus

8 m PZ was oxidized in the HTOR with cycling up to 150 °C (Figure 3). The solvent had been slightly degraded in the HTOR during a previous experiment before the start of the 2-week test. Formate was the most significant oxidation product accumulated in the liquid phase, increasing by 45 mmol/kg. 2-piperazinol (2-PZOH) and ethylenediamine (EDA) were also observed in significant molar concentrations, but decreased in concentration over the course of the experiment, indicating that they are unstable intermediary oxidation products. N-(methyl)-piperazine (1-MPZ), acetate, and oxalate were observed to accumulate in lesser molar concentrations than formate. The most significant thermal degradation product was N-(aminoethyl)-piperazine (AEP). AEP accumulated at a much lower rate and concentration than the oxidation products, indicating that thermal degradation was not a significant source of amine loss during the test. Metal ions including iron and chromium accumulated in micromolar concentrations due to corrosion of the stainless steel thermal reactor and cross-exchanger.

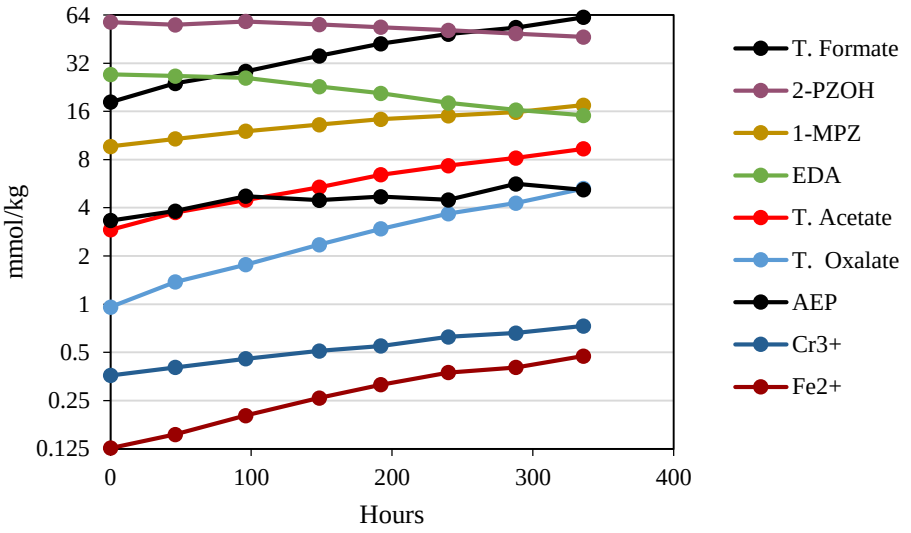

Fig. 2. Accumulation of degradation products in 8 m PZ oxidized in the HTOR. Products ranked by molar concentration in final sample. 40–55 °C 350 mL HGF reactor sparged with 7.5 L/min air + 0.5–2 vol% CO_2, 0.2 L/min cycling to 150 °C, 1.6 L total inventory.

A similar test was done in the HTOR using a solvent of 8 m PZ with the addition of 100 mM Inhibitor 8 (Inh 8) (Figure 4). Inh 8 is proposed to inhibit oxidation via a free-radical scavenger method similar to Inhibitor A, a previously-tested inhibitor [10]. For both solvents, the molar rate of ammonia generation measured by FTIR was nearly identical to the molar rate of PZ loss as measured by cation chromatography. As PZ has 2 equivalents of nitrogen per mole, ammonia accounts for 50% of the total alkalinity oxidized. Inh 8 reduced PZ loss, ammonia generation, and formate accumulation by 55 to 65%. Ferrous iron accumulation was also reduced 60%. However, chromium ion accumulation remained constant. Inh 8 may be reducing the solubility of ferrous iron in solution without affecting the overall corrosion rate.

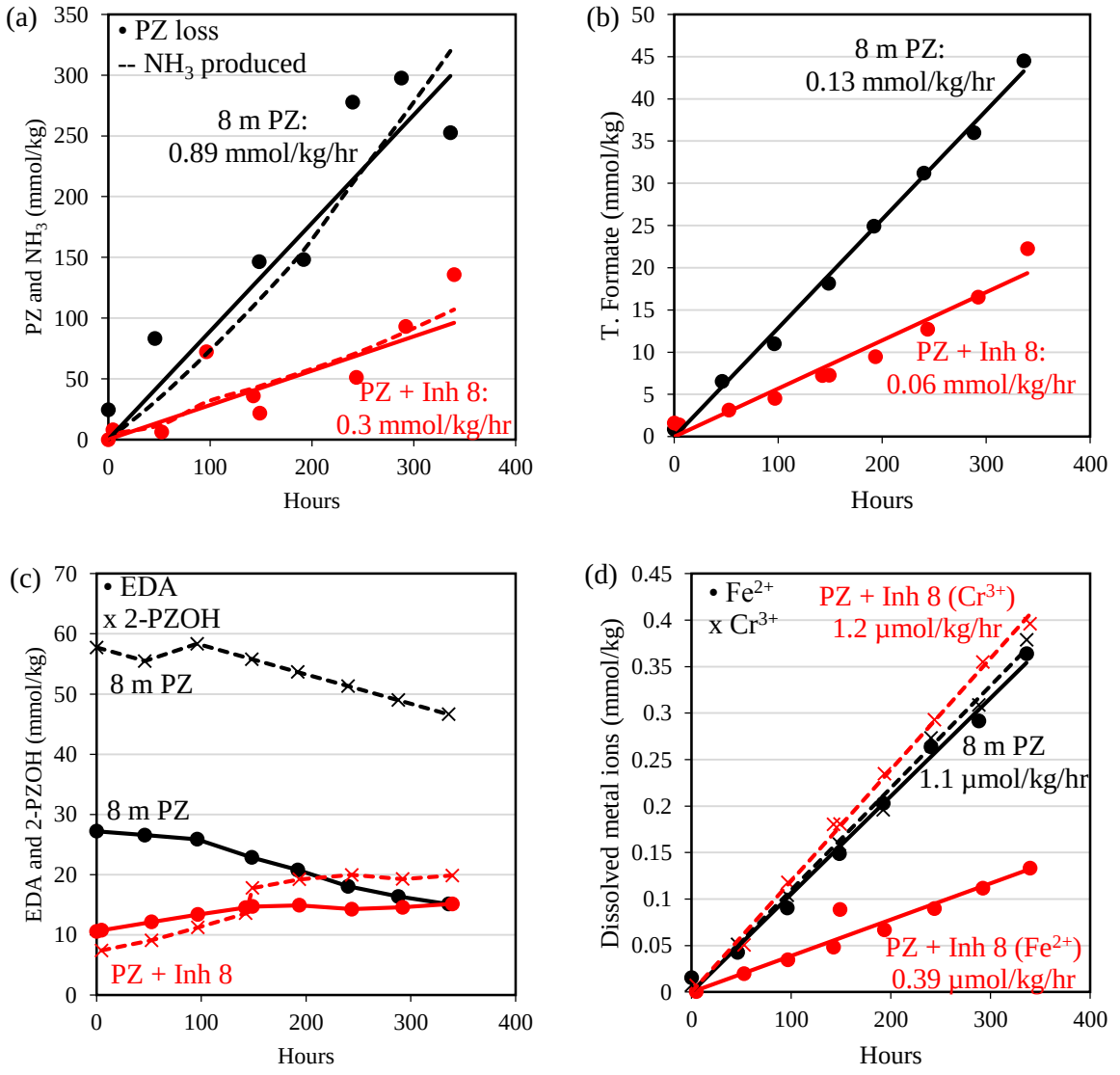

Fig. 3. Oxidation of 8 m PZ and 8 m PZ + 100 mM Inh 8 in HTOR. (a) PZ loss (•, solid line) and ammonia rate (dotted line); (b) formate accumulated; (c) EDA (•, solid line) and 2-PZOH (x, dotted line) accumulation; (d) Fe^{2+} (•, solid line) and Cr^{3+} (x, dotted line) accumulation. Black: 8 m PZ; red: 8 m PZ + 100 mM Inh 8. 40–55 °C 350 mL HGF reactor sparged with 7.5 L/min air + 0.5–2 vol% CO_2, 0.2 L/min cycling to 150 °C, 1.6 L total inventory.

Table 2 summarizes the rates of amine loss, ammonia generation, total formate accumulation, and metal ion accumulation in the 8 m PZ HTOR tests compared to an earlier experiment in the HTOR using 7 m MEA at 120 °C [2]. The oxidation rate of 8 m PZ at 150 °C is 80% less than 7 m MEA at 120 °C even before the addition of Inh 8.

Table 2. Comparison of amine loss, ammonia production, total formate, iron, and chromium ion accumulation rates in the HTOR for 7 m MEA cycled to 120 °C [2], 8 m PZ cycled to 150 °C, and 8 m PZ + 100 mM Inh 8 cycled to 150 °C. 40–55 °C 350 mL HGF reactor sparged with 7.5 L/min air + 0.5–2 vol% CO_2, 0.2 L/min cycling rate, 1.6 L total inventory

Solvent (max T)	Amine loss	Ammonia	T. Formate	Ferrous ions	Chromium ions
	mmol/kg/hr			µmol/kg/hr	

7 m MEA (120 °C) [V]	4.77	3.13	0.32	2.02	0.71
8 m PZ (150 °C)	0.89	0.89	0.13	1.05	1.10
8 m PZ + Inh 8 (150 °C)	0.30	0.31	0.06	0.39	1.20

3.2. Tarong Pilot Plant Long-Duration PZ Campaign

Figure 4 shows the accumulation of contaminants in the PZ solvent during the two long-duration tests. The profile of degradation products is very similar to that observed in the HTOR apparatus, with formate the most significant contaminant on a molar basis. There was also significant accumulation of sulfate and nitrate caused by absorption of SO_x and NO_x from the flue gas. The molar rate of formate accumulation increased by a factor of 3 when the stripper operating temperature was raised from 125 to 155 °C.

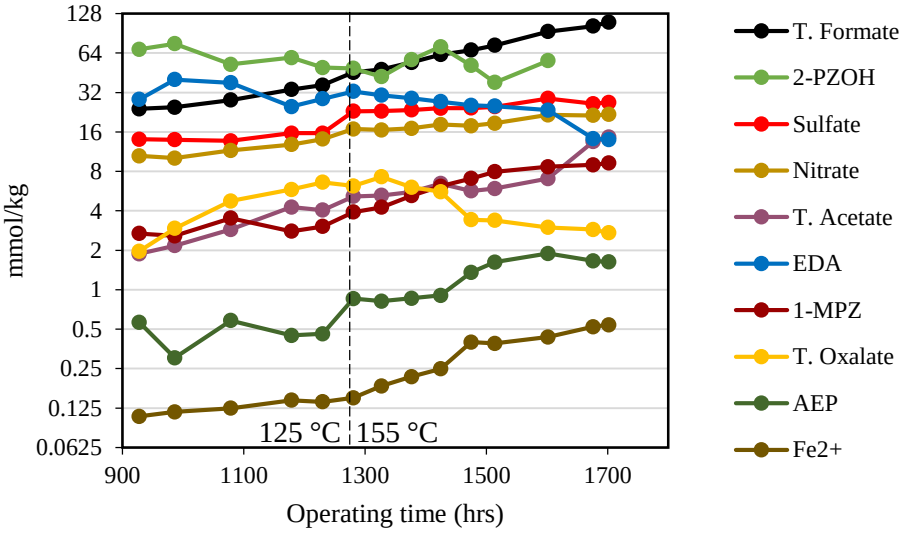

Fig. 4. Contaminant accumulation in Tarong pilot plant long-duration 8 m PZ tests at 125 °C and 155 °C. Contaminants ranked by molar concentration in final sample.

Modeling of PZ Loss at Tarong

Using oxidation rate data collected from the HTOR experiments, a spreadsheet model was created to estimate the total solvent loss rate and accumulation rate of contaminants. Oxidation was assumed to be first order in respect to amine concentration in the solvent and oxygen concentration in the flue gas, and was assumed to be dominated by the residence time of the solvent at the maximum operating temperature in the stripper and reboiler sumps. The activation energy of PZ oxidation was previously quantified at 32 kJ/mol in the HTOR [2]. The spreadsheet also incorporated previously-developed models for thermal degradation [3, 11] and nitrosation of PZ to produce nitrosamines [12]. All SO_2 entering the absorber with the flue gas was assumed to be absorbed as sulfate. Volatile amine emissions in the flue gas leaving the absorber were assumed to be controlled to 1 ppm_v by a water wash scrubber. The spreadsheet model could also be used to calculate the required feed rate and estimated solvent loss for a thermal reclaimer to maintain heat-stable salt concentration at a user-specified value.

Using the operating parameters of the Tarong pilot plant, the loss rate of 8 m PZ at a stripper operating temperature of 155 °C was estimated to be 0.65 kg/MT of CO_2 captured, 67% due to oxidation. By comparison, 7 m MEA at the same operating conditions except a 120 °C stripper would have a loss rate of 1.54 kg/MT CO_2. While PZ is typically

more expensive per kg than MEA, previous modeling work has shown significant energy savings when operating 8 m PZ at 150 °C compared to 7 m MEA at 120 °C [13].

Table 3. Model predictions for solvent loss and ammonia generation rates for 8 m PZ at Tarong as a function of metric tons CO_2 captured. Assumes 90% removal of 12 vol % CO_2 from coal flue gas, L/G of 2.2 kg/kg, 32 minutes total holdup with 11 minutes holdup in stripper and reboiler

Cause of solvent loss	Rate	Assumptions
Thermal degradation	0.03 kg PZ/MT CO_2	155 °C regeneration temperature
Oxidation	0.44 kg PZ/MT CO_2	7 vol% O_2 in flue gas
Nitrosation	0.04 kg PZ/MT CO_2	1 ppm_v NO_2 in flue gas
Volatile PZ emissions	0.02 kg PZ/MT CO_2	Controlled to 1 ppm_v by water wash
Additional loss in reclaimer	0.13 kg PZ/MT CO_2	Feed rate to thermal reclaimer set to maintain 1 wt % steady state heat-stable salt concentration; 95% amine recovery
Total solvent loss	0.65 kg PZ/MT CO_2	

Previously, it has been hypothesized that amine oxidation was the result of the reaction of dissolved oxygen with the amine in the hot end of the CO_2-rich side of the cross exchanger and in any piping between the cross-exchanger and the stripper. Upon entering the stripper, it was postulated that any remaining dissolved oxygen would flash off, ceasing oxidation [4]. However, this assumption under-predicts the observed accumulation of formate at Tarong by 60% (Figure 5). Assuming that oxidation continues into the stripper and reboiler sump due to nonvolatile oxygen carriers (organic peroxides, dissolved metal ions, aldehydes, etc.) matches the final observed accumulation of PZ to within 5%.

Sulfate accumulation matched the model assumption to within 5% of the final concentration, assuming 100% absorption of 0.55 ppm_v SO_2. Tarong employed a caustic scrubber to limit SO_2 in the flue gas entering the absorber to below 1 ppm_v.

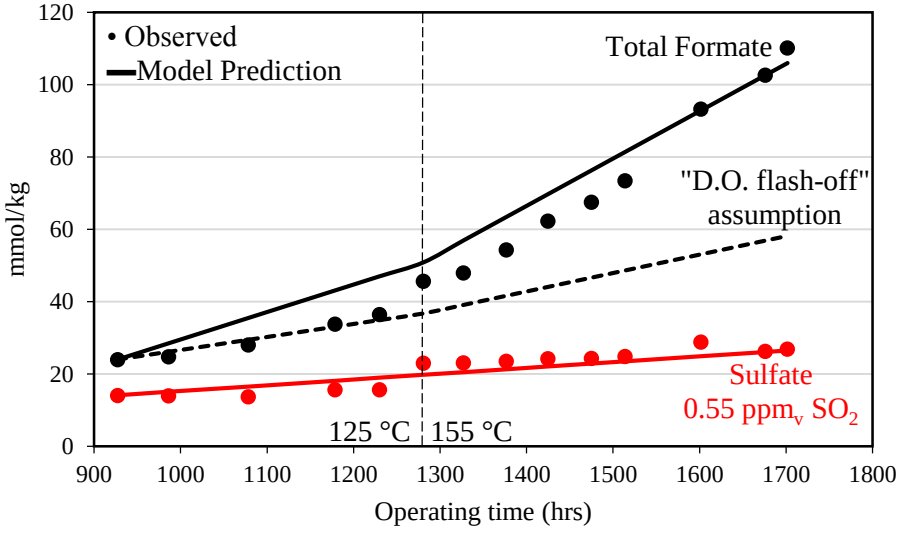

Fig. 5. Observed total formate (black) and sulfate (red) accumulation at Tarong relative to model predictions (lines). Dashed line: predicted formate accumulation assuming oxidation ceases after flash-off of dissolved oxygen upon entering stripper. Solid line: oxidation continues in stripper and reboiler sump.

4. Conclusions

The oxidation rate of 8 m PZ when cycled from 40 to 150 °C in the HTOR apparatus was 80% less than 7 m MEA cycled up to 120 °C. The addition of 100 mM Inh 8 reduced oxidation an additional 60% and also reduced the solubility of ferrous iron ions from stainless steel corrosion. 50% of nitrogen lost due to oxidation was emitted in the gas phase as ammonia. Formate was the most significant stable oxidation product to accumulate in the liquid phase. 2-piperazinol and ethylenediamine were also observed in high concentrations but were not stable.

The accumulation rate of formate in 8 m PZ increased by a factor of 3 when the stripper operating temperature was raised from 125 to 155 °C at the Tarong pilot plant. The accumulation rate could not be explained solely by the reaction of the amine with dissolved oxygen and may be enhanced in the stripper and reboiler sump by nonvolatile oxygen carriers such as organic peroxides and metal ions.

Using first-order approximations, a solvent loss rate of 0.65 kg PZ/MT CO_2 captured was estimated for a capture plant using the same operating parameters as the Tarong campaign.

Acknowledgements

The authors would like to acknowledge support from the Texas Carbon Management Program and the Commonwealth Scientific and Industrial Research Organization (CSIRO). CSIRO wishes to acknowledge financial assistance provided through Australian National Low Emissions Coal Research and Development (ANLEC R&D). ANLEC R&D is supported by Australian Coal Association Low Emissions Technology Limited and the Australian Government through the Clean Energy Initiative.

The authors declare the following competing financial interest(s): One author of this publication consults for Southern Company and for Neumann Systems Group on the development of amine scrubbing technology. The terms of this arrangement have been reviewed and approved by the University of Texas at Austin in accordance with its policy on objectivity in research. The authors have financial interests in intellectual property owned by the University of Texas that includes ideas reported in this paper.

References

[1] Kindrick RC, Atwood K, Arnold MR. *The Relative Resistance to Oxidation of Commercially Available Amines*. Girdler Report No. T2.15-1-30, in "Report: Carbon Dioxide Absorbents", Contract No. NObs-50023, by Girdler Corp., Gas Processes Division, Louisville, KY, for the Navy Department, Bureau of Ships, Washington, DC (Code 649P), 1950a.

[2] Voice AK. *Amine Oxidation in Carbon Dioxide Capture by Aqueous Scrubbing*. The University of Texas at Austin. Ph. D. Dissertation. 2013.

[3] Freeman SA. *Thermal Degradation and Oxidation of Aqueous Piperazine for Carbon Dioxide*. The University of Texas at Austin. Ph.D. Dissertation. 2011.

[4] Closmann FB. *Oxidation and thermal degradation of methyldiethanolamine/piperazine in CO_2 capture.* The University of Texas at Austin. Ph.D. Dissertation. 2011.

[5] da Silva EF, Lepaumier H, Grimstveldt A, Vevelstad SJ, Einbu A, Vernstad K, Svendsen HF, Zahlsen K. Understanding 2-Ethanolamine Degradation in Post-Combustion CO_2 Capture. *Industrial & Engineering Chemistry Research*. 2012;51:13329–13338.

[6] Nielsen PT, Li L, Rochelle GT. Piperazine degradation in pilot plants. *Energy Procedia*. 2013;37:1912–1923.

[7] Cousins A, Cottrell A, Lawson A, Huang S, Feron PHM. Model verification and evaluations of the rich-split process modification at an Australian-based post combustion CO_2 capture pilot plant. *Greenhouse Gases: Science and Technology*. 2012; 2:329–345.

[8] Cousins A, Huang S, Cottrell A, Feron PHM, Chen E, Rochelle GT. Pilot scale parametric evaluation of concentrated piperazine for CO_2 capture at an Australian coal-fired power station. Accepted by *Greenhouse Gases: Science and Technology*. 2014

[9] Fine NA, Nielsen PT, Rochelle GT. Decomposition of secondary nitrosamines in CO_2 capture by aqueous Piperazine or Monoethanolamine. *Environmental Science and Technology*. 2014;48(10):5996–6002.

[10] Goff GS. *Oxidative Degradation of Aqueous Monoethanolamine in CO_2 Capture Processes: Iron and Copper Catalysts, Inhibition, and O_2 Mass Transfer*. The University of Texas at Austin. Ph.D. Dissertation. 2005.

[11] Davis JD. *Thermal Degradation of Aqueous Amines Used for Carbon Dioxide Capture*. The University of Texas at Austin. Ph.D. Dissertation. 2009.

[12] Fine NA, Goldman MJ, Nielsen PT, Rochelle GT. Managing n-nitrosopiperazine and dinitrosopiperazine. *Energy Procedia*. 2013;37:273–284.

[13] Frailie PT. *Modeling of Carbon Dioxide Absorption/Stripping by Aqueous Methyldiethanolamine/Piperazine*. The University of Texas at Austin. Ph.D. Dissertation. 2014.

Available online at www.sciencedirect.com

ScienceDirect

Energy Procedia 00 (2014) 000–000

Energy Procedia

www.elsevier.com/locate/procedia

GHGT-12

Thermodynamic and Kinetic Modeling of Piperazine/2-Methylpiperazine

Brent Sherman[a], Peter T. Frailie[a], Le Li[a], Nina Salta[a], and Gary T Rochelle[a]*

[a]*Department of Chemical Engineering, The University of Texas at Austin, 200 E. Dean Keeton St., C0400, Austin, TX 78712-1589 USA*

Abstract

The equimolal CO_2 solvent, 4 m 2-methylpiperazine (2MPZ)/4 m piperazine (PZ), was modeled in Aspen Plus® using the eNRTL thermodynamic framework. Data were regressed using binary interaction parameters. The sequential regression method was used starting from prior PZ and 2MPZ models. The model correctly predicts the CO_2 equilibrium partial pressure from 40−160 °C. The average differential heat of absorption is close to the expected value of –70 kJ/mol CO_2. Newly reported data show that previous data overpredicted viscosity. Activity-based kinetics were used with pairs of power-law reactions representing the forward and reverse reactions. Fluxes measured in a WWC for lean to rich loading and for 40−100 °C were matched, yielding a SSE of 2.39. The kinetic model used ten different reactions along with the diffusivity of amine-products to capture the rate behavior. This model can be used for techno-economic assessments, pilot plant data reconciliation, and process modeling.

Selection and peer-review under responsibility of GHGT.

Keywords: amine scrubbing; process simulation; eNRTL; carbon capture

1. Introduction

Concentrated piperazine (PZ) has emerged as a solvent of interest due to its multiple advantages over monoethanolamine, such as higher resistance to degradation, higher kinetic rates, and higher capacity. PZ precipitation can be mitigated by blending PZ with another amine. This paper looks at 4 m PZ blended with 4 m 2-methylpiperazine (2MPZ), a moderately hindered secondary amine.

There are no prior open-literature models of 2MPZ/PZ. There are prior models of the subsystems. For 2MPZ there is a thermodynamic and corresponding kinetic model [1,2]. For concentrated PZ, there is an Aspen Plus® model and a proprietary model (Independence) developed by the University of Texas [3].

* Corresponding author. Tel.: +1−512−471−7230; fax: +1−512−471−7060.
E-mail address: gtr@che.utexas.edu

Selection and peer-review under responsibility of GHGT.

Nomenclature

abbreviations

m	molality
eNRTL	electrolyte non-random two-liquid
2MPZ	2-methylpiperazine
PZ	piperazine
MDEA	methyldiethanolamine
MEA	monoethanolamine
WWC	wetted wall column
T	temperature
VLE	vapor-liquid equilibrium

symbols

T_{ref}	reference temperature
$\hat{T}$	$T-T_{ref}$
T	temperature
α	loading, non-randomness parameter
γ	activity coefficient
μ	viscosity
ρ	density
σ^2	standard deviation
G	Gibbs free energy

2. Methods

2.1. Experimental

Amine solutions were prepared gravimetrically and CO_2 was added by bubbling gaseous CO_2 through the solution. The reported composition was measured using total alkalinity for amine concentration and total inorganic carbon for CO_2 concentration. Viscosity data were collected using the same equipment, a Physica MCR 301 cone and plate rheometer. Solution preparation, total alkalinity, TIC, and operating procedure are as described by Freeman [4]. TIC, total alkalinity, and viscosity were performed with triplicates. The standard deviation of the TIC and total alkalinity measurements were less than 2% of the average value while for viscosity the value was up to 14% with a mean of 4%.

2.2. Thermodynamic Modeling

The model is constructed in Aspen Plus® V7.3 using the electrolyte non-random two-liquid (eNRTL) model for the liquid phase, which is a rigorous, activity coefficient model [5,6]. The vapor phase is modeled using Redlich-Kwong. The regressed parameters are the local contribution terms of the excess Gibbs free energy function. This local contribution is partially calculated from Equation 1,

$$G = \exp\left(-\alpha\tau_{i,j}\right) \tag{1}$$

α is the non-randomness parameter, and $\tau_{i,j}$ is the binary interaction parameter defined in Equation 2.

$$\tau_{i,j} = C_{i,j} + \frac{D_{i,j}}{T} + E_{i,j}\left[\frac{\left(T_{ref} - T\right)}{T} + \ln\left(\frac{T}{T_{ref}}\right)\right] \tag{2}$$

$\tau_{i,j}$ ($\tau_{j,i}$) defaults to 10 (−2) for pairs without water, and 8 (−4) for pairs with water. PZ, 2MPZ, and their zwitterions are modeled as Henry's components. The reference state for solutes is asymmetric, infinite dilution, whereas for solvents it is pure, symmetric.

This model draws upon the prior work of Frailie for PZ parameters [3], and Chen for most of the 2MPZ parameters [1]. These models and the 2MPZ/PZ model were developed using sequential regression. First, the pure amine properties were regressed, then the amine and water, followed by the amine, water, and CO_2. This step was done in the two prior models. The current effort started by merging the PZ and 2MPZ submodels. Then, 2MPZ+PZ+H_2O was regressed followed by 2MPZ+PZ+H_2O+CO_2. At each step, the previously regressed parameters are left unchanged.

As the PZ model and the 2MPZ model used different Aspen Plus® property database values for CO_2, merging the two models necessitated choosing which model fit to preserve. The PZ fit was preserved due to higher confidence in its values. In order to resolve this inconsistency, the 2MPZ model would have to be reregressed with the same CO_2 pure component parameters as the PZ model.

Table 1 shows the data available for 2MPZ/PZ thermodynamic regression: density, viscosity[7][7], vapor-liquid equilibrium (VLE), and loaded and unloaded amine volatility. The total number of parameters regressed is twenty-six, of which ten were used for viscosity, eight for density, and eight for VLE. Two additional parameters were adjusted to make the activity coefficient of CO_2 in loaded solution well behaved.

Table 1. Thermodynamic data for the 4 m 2MPZ/4 m PZ system.

Data Type	Number of Points	Points Regressed	Source	Notes
VLE	16	16	[7]	WWC
VLE	11	11	[8]	total pressure
Density	42	42	[4]	
Viscosity	30	0	[7]	
Viscosity	40	40	this work	
Amine volatility	13	0	[9]	
Total	**152**	**109**		

The heat capacity of 2MPZ was assumed to be the same as that of PZ. $\tau_{i,j}$ were regressed using the maximum likelihood method as implemented in the data regression system of Aspen Plus® V7.3.

As no activity coefficient of CO_2 (γ_{CO_2}) data were available for loaded solvent, the trends with loading and temperature were checked for reasonable behavior. The temperature dependent $D_{i,j}$ parameters for ($2MPZH^+$,$PZ(COO^-)_2$), CO_2 and (PZH^+,$2MPZCOO^-$), CO_2 of Equation 2 were adjusted to improve behavior.

The density and viscosity were correlated using least-squares minimization. Density was fit using Equation 3.

$$\rho_{2MPZ+PZ} = x_{H_2O}\rho_{\boldsymbol{H_2O}} + x_{2MPZ}\left(a\hat{T} + b\right) + x_{PZ}\left(c\hat{T} + d\right) + x_{CO_2}\left(e\hat{T} + f\right) + x_{CO_2}\left(x_{2MPZ} + x_{PZ}\right)\left(g\hat{T} + h\right) \quad (3)$$

x_i is the mole fraction, ρ_{H2O} is the density of water, $\hat{T} = T - 313.15$ K, *a*-*h* are adjustable parameters.

The viscosity was fit using Equation 4.

$$\frac{\mu_{2MPZ+PZ}}{\mu_{H2O}} = exp\left\{\begin{matrix}[(ax_{2MPZ} + bx_{PZ} + c)T + dx_{2MPZ} + ex_{PZ} + f] \\ * [(gx_{2MPZ} + hx_{PZ} + iT + j)\alpha + 1] * \frac{x_{2MPZ+PZ}}{T^2}\end{matrix}\right\} \quad (4)$$

Here x_i is mass fraction, μ_{H_2O} is the viscosity of water, α is loading in mol CO_2/mol alk, and *a*-*j* are adjustable parameters. Equations 3 and 4 are referenced to pure water to ensure proper behavior at low amine concentration, such as in the water wash. They both depend on the individual amine concentrations, temperature, and loading. These equations were implemented as Fortran subroutines.

The solvent capacity for coal conditions is calculated using Equation 5, where the rich (α_{rich}) and lean (α_{lean}) loadings are at 5 and 0.5 kPa at 40 °C.

$$\Delta C = \frac{(\alpha_{rich} - \alpha_{lean})(mol\ alk)}{kg\ amine + H_2O} \quad (5)$$

This capacity does not account for viscosity. Considering the effect of viscosity on heat and mass transfer leads to normalizing the capacity as in Equation 6 [10].

$$\Delta C_{\mu} = \frac{\Delta C}{\left({}^{\mu_{\alpha_{mid}}}/_{10\ \mathrm{cP}}\right)^{0.25}} \tag{6}$$

Here α_{mid} is the middle loading between the rich and lean loading at 40 °C.

2.3. Kinetic Modeling

Reaction data collected using a wetted wall column (WWC) were simulated in Aspen Plus® [7]. The WWC interfacial area and gas-side resistance were implemented using custom Fortran subroutines [3]. At each temperature and loading, the WWC is operated to give six fluxes of CO_2: three desorption and three absorption. Only the strongest desorption and absorption fluxes were regressed as these have the least experimental error, being furthest from equilibrium. There were thirty-two points regressed ranging from 40 to 100 °C and at one lean, two middle, and one rich loading.

To account for the highly non-ideal nature of the solvent, the kinetics are modeled with activities as shown in Equation 7.

$$r = k \prod_{i} a_i \tag{7}$$

k is the reaction constant and a_i is the activity of component i. k is computed using Equation 8.

$$k = k_0 \exp\left[\left(\frac{-E_A}{R}\right)\left(\frac{1}{T} - \frac{1}{T_{ref}}\right)\right] \tag{8}$$

Here k_o is the reaction pre-exponential, E_A is the activation energy, R is the universal gas constant, and T_{ref} is set to 40 °C.

The reaction set in Table 2 has two types of reactions: kinetic and equilibrium. Equilibrium reactions are handled by the thermodynamic model calculating the excess Gibbs free energy. Kinetic reactions are a pair of forward and reverse reactions, where each reaction rate is calculated by Equation 7. The reaction pre-exponential and the activation energy in Equation 8 are regressed for the forward reactions, while the reverse rate is backcalculated from the reaction equilibrium constant from the thermodynamic model. This ensures consistency with the thermodynamic model.

Table 2. Reaction set for 2MPZ/PZ.

Type	Stoichiometry	Reaction
kinetic	$PZCOO^- + H_2O + CO_2 \leftrightarrow HPZCOO + HCO_3^-$	1
kinetic	$2MPZCOO^- + H_2O + CO_2 \leftrightarrow H2MPZCOO + HCO_3^-$	2
kinetic	$2\ PZCOO^- + CO_2 \leftrightarrow PZ(COO^-)_2 + HPZCOO$	3
kinetic	$PZCOO^- + 2MPZ + CO_2 \leftrightarrow PZ(COO^-)_2 + 2MPZH^+$	4
kinetic	$PZCOO^- + 2MPZCOO^- + CO_2 \leftrightarrow PZ(COO^-)_2 + H2MPZCOO$	5
kinetic	$PZ + 2MPZ + CO_2 \leftrightarrow PZCOO^- + 2MPZH^+$	6
kinetic	$2\ PZ + CO_2 \leftrightarrow PZH^+ + PZCOO^-$	7
kinetic	$2\ 2MPZ + CO_2 \leftrightarrow 2MPZH^+ + 2MPZCOO^-$	8
kinetic	$2MPZ + PZ + CO_2 \leftrightarrow 2MPZCOO^- + PZH^+$	9
	$2\ 2MPZCOO^- + CO_2 \leftrightarrow 2MPZ(COO^-)_2 + H2MPZCOO$	10
equilibrium	$2MPZCOO^- + 2MPZH^+ \leftrightarrow H2MPZCOO + 2MPZ$	
equilibrium	$2MPZ + HCO_3^- \leftrightarrow 2MPZH^+ + CO_3^{-2}$	
equilibrium	$2MPZ + PZH^+ \leftrightarrow 2MPZH^+ + PZ$	
equilibrium	$PZCOO^- + PZH^+ \leftrightarrow HPZCOO + PZ$	

The reactions that only involved PZ were taken from the prior MDEA/PZ model [3]. Any reaction involving 2MPZ was regressed.

Reaction parameters are regressed alongside the diffusion of amine-products. The prefactor and sensitivity to temperature and viscosity are adjusted as shown in Equation 9.

$$D_{Am-Prod} = D_0 \left(\frac{T}{T_{ref}}\right)^{\alpha} \left(\frac{\mu}{\mu_{ref}}\right)^{\beta} \quad (9)$$

The diffusion of free CO_2 in solvent is shown in Equation 10.

$$D_{CO2-soln} = D_{CO2-water} \left(\frac{\mu_{water}}{\mu_{soln}}\right)^{0.8} \quad (10)$$

$D_{CO2\text{-}water}$ (m^2/s) is the diffusivity of CO_2 in water defined in Equation 11 [11].

$$D_{CO2-water} = 2.35\text{E}-06 * \exp\left(\frac{-2119}{T}\right) \quad (11)$$

These kinetic reactions and diffusivities are calculated throughout the liquid boundary layer. The layer is discretized at thirty-two points.

The experimental loading was adjusted to balance the relative error of the absorption and desorption points. This has the effect of ensuring that at zero driving force, there is zero flux [3]. This adjustment corrects for experimental errors as well any errors in the equilibrium model.

Regression proceeds by changing the reaction pre-exponential, activation energy, and diffusivity of amine-products to match the experimental flux.

3. Results

3.1. Experimental Results

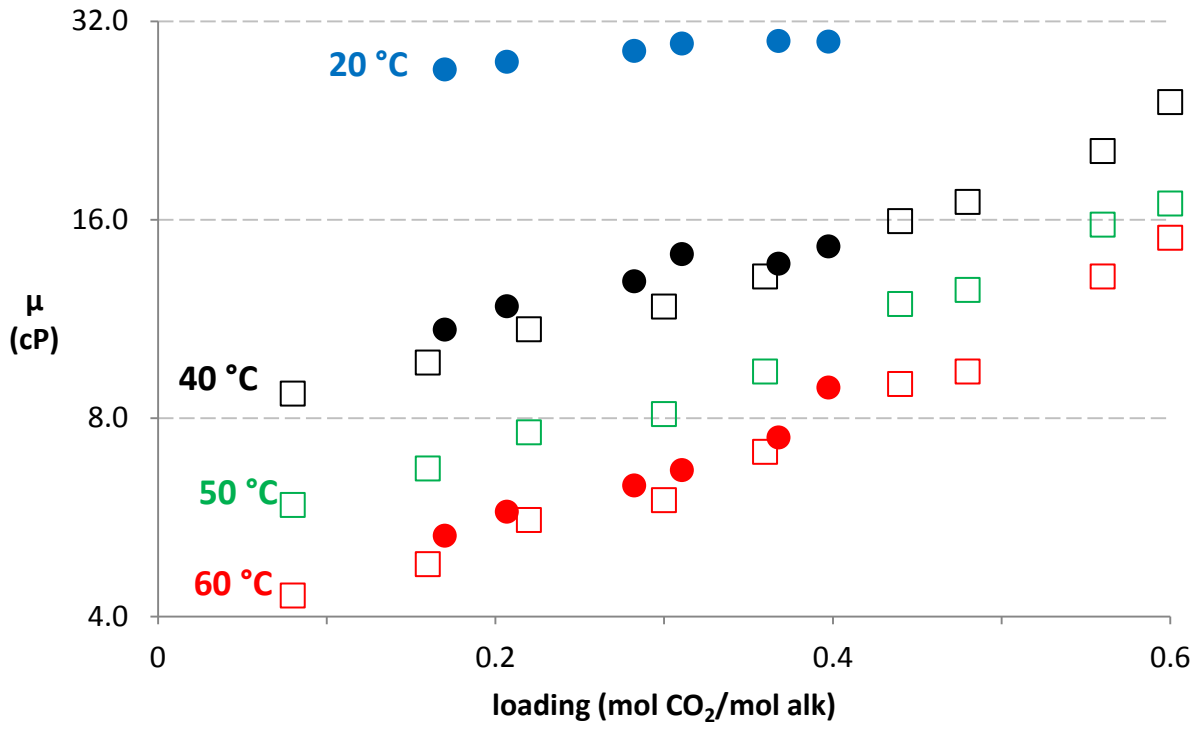

Figure 1. 4 m 2MPZ/4 m PZ viscosity. Data sources: ● this work, □ [7] with loading multiplied by two.

Prior to this work, viscosity was only available for 4 m 2MPZ/4 m PZ [7]. Without varying the ratio of 2MPZ:PZ, the viscosity correlation of Equation 4 cannot account for individual amine effects. For this reason, new data were collected. Figure 1 shows the discrepancy found between the newly collected data and the prior data. The full set of newly collected data is shown in Table 3. It is unclear if the prior data characterized the solution composition using total alkalinity and TIC. Remeasuring 4 m 2MPZ/4 m PZ uncovered a discrepancy that is corrected if the reported loading of Chen is doubled [7].

Table 3. Viscosity data for 2MPZ/PZ.

PZ	2MPZ	Loading	T	μ	PZ	2MPZ	Loading	T	μ
m	m	(mol/mol alk)	C	cP	m	m	(mol/mol alk)	C	cP
4	4	0.170	20	26.99	2	1	0.000	20	3.19
4	4	0.170	40	10.88	2	1	0.000	40	1.54
4	4	0.170	60	5.30	2	1	0.000	60	1.14
4	4	0.207	20	27.74	2	1	0.062	20	3.29
4	4	0.207	40	11.81	2	1	0.062	40	1.71
4	4	0.207	60	5.76	2	1	0.062	60	1.23
4	4	0.282	20	28.80	2	1	0.123	20	3.41
4	4	0.282	40	12.89	2	1	0.123	40	1.49
4	4	0.282	60	6.32	2	1	0.123	60	1.31
4	4	0.311	20	29.55	2	1	0.181	20	3.54
4	4	0.311	40	14.17	2	1	0.181	40	1.70
4	4	0.311	60	6.66	2	1	0.181	60	1.42
4	4	0.368	20	29.83	2	1	0.223	20	3.67
4	4	0.368	40	13.70	2	1	0.223	40	1.77
4	4	0.368	60	7.47	2	1	0.274	20	3.80
4	4	0.397	20	29.75	2	1	0.274	40	2.03
4	4	0.397	40	14.56	2	1	0.325	20	3.97
4	4	0.397	60	8.89	2	1	0.325	40	2.08
					2	1	0.367	20	4.06
					2	1	0.367	40	2.45
					2	1	0.442	20	4.13
					2	1	0.442	40	2.56

3.2. Thermodynamic Modeling

The parameters used to fit VLE are shown in Table 4. All but one has a standard deviation lower than the parameter value. All but the same one parameter are close to the default value of –4. To improve γ_{CO_2}, the two parameters in Table 5 were adjusted.

The viscosity parameters are shown in Table 6. The SSE was 0.78. The density parameters are shown in Table 7. The SEE was 0.001. Using Equations 3 and 4 rather than the native correlations in Aspen Plus® gave a smoother fit with fewer parameters.

An attempt was made to fit the two sets of amine volatility data. They could not be fit along with VLE data, indicating that the data are inconsistent. The volatility data are less reliable, and so the VLE data were trusted.

Table 4. VLE parameters of Equation 2 for 4 m 2MPZ/4 m PZ with their standard deviation.

i	j	$C_{i,j}$	σ^2
($2MPZH^+$, $PZCOO^-$)	H_2O	−3.691	0.157
($2MPZH^+$, $PZ(COO^-)_2$)	H_2O	−5.356	0.523

(PZH^+, 2MPZCOO)	H_2O	−4.095	0.168
($2MPZH^+$, $PZCOO^-$)	H2MPZCOO	−13.262	0.588
($2MPZH^+$, $PZ(COO^-)_2$)	H2MPZCOO	−14.315	0.800
($2MPZH^+$, $PZCOO^-$)	HPZCOO	−0.0536	0.358
(PZH^+, HCO_3^-)	H2MPZCOO	−11.083	1.652
($2MPZH^+$, HCO_3^-)	HPZCOO	−7.060	0.967

Table 5. CO_2 activity coefficient parameters of Equation 2.

i	**j**	$D_{i,j}$ **(K)**
2MPZH+/PZCOO2-	CO_2	-400
PZH+/2MPZCOO-	CO_2	1500

Table 6. Viscosity parameters for Equation 3.

Parameter	**Value**	**Parameter**	**Value**
a	6.43	f	0.08
b	5.43	g	10.01
c	−46.01	h	−29.87
d	−10.10	i	0.01
e	340.20	j	2.72

Table 7. Density parameters for Equation 3.

Parameter	**Value**
a	−2.90
b	1.19E+03
c	−2.90
d	1.19E+03
e	2.06
f	3.29E+03
g	−6.47
h	−7.58E+03

The VLE fit in Figure 2 shows that the two most important temperatures, 40 and 140 ℃, are nicely matched. 40 ℃ is the operating temperature of the absorber, and so matching VLE here ensures proper speciation. The amount of each species present links the thermodynamic model to the kinetic model. 140 ℃ is important to match as it sets the stripper pressure.

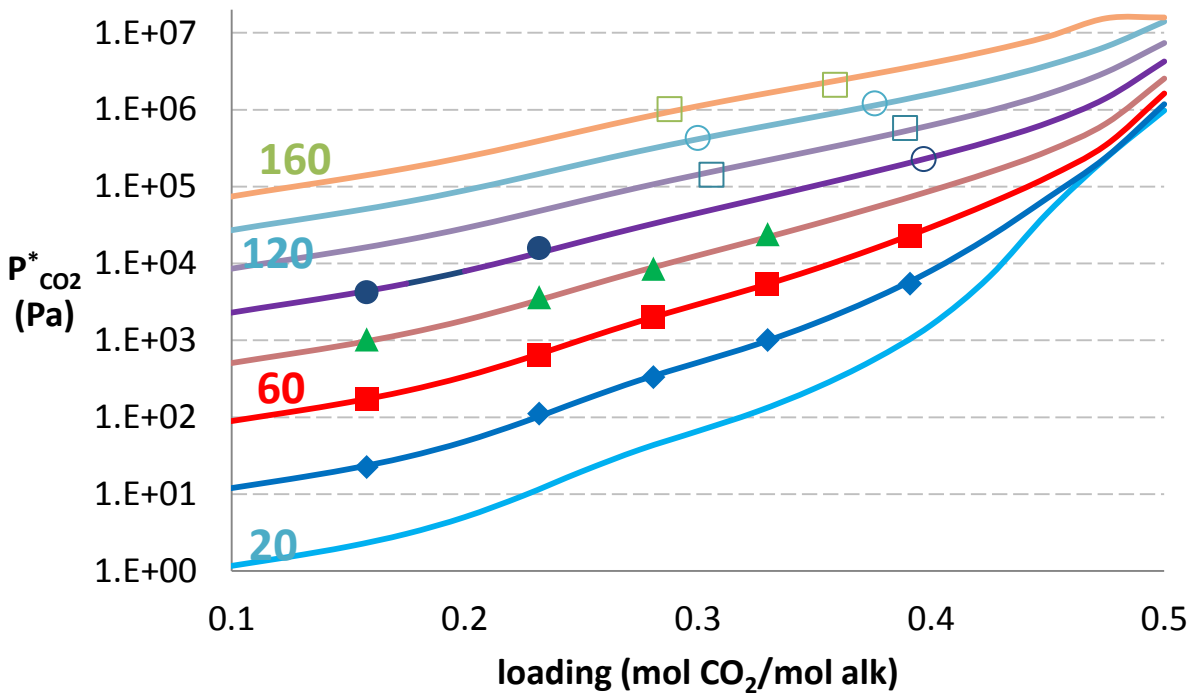

Figure 2. CO_2 solubility of 4 m 2MPZ/4 m PZ. Lines are the model predictions spaced 20 °C apart; filled points WWC data [7]; empty points total pressure [12].

Using the VLE fit along with Equation 5, the capacity is found to be 0.84 mol CO_2/kg amine+H_2O. Normalizing the capacity to viscosity using Equation 6 lowers the value to 0.78 mol CO_2/kg amine+H_2O. This is the same normalized-capacity as 8 m PZ.

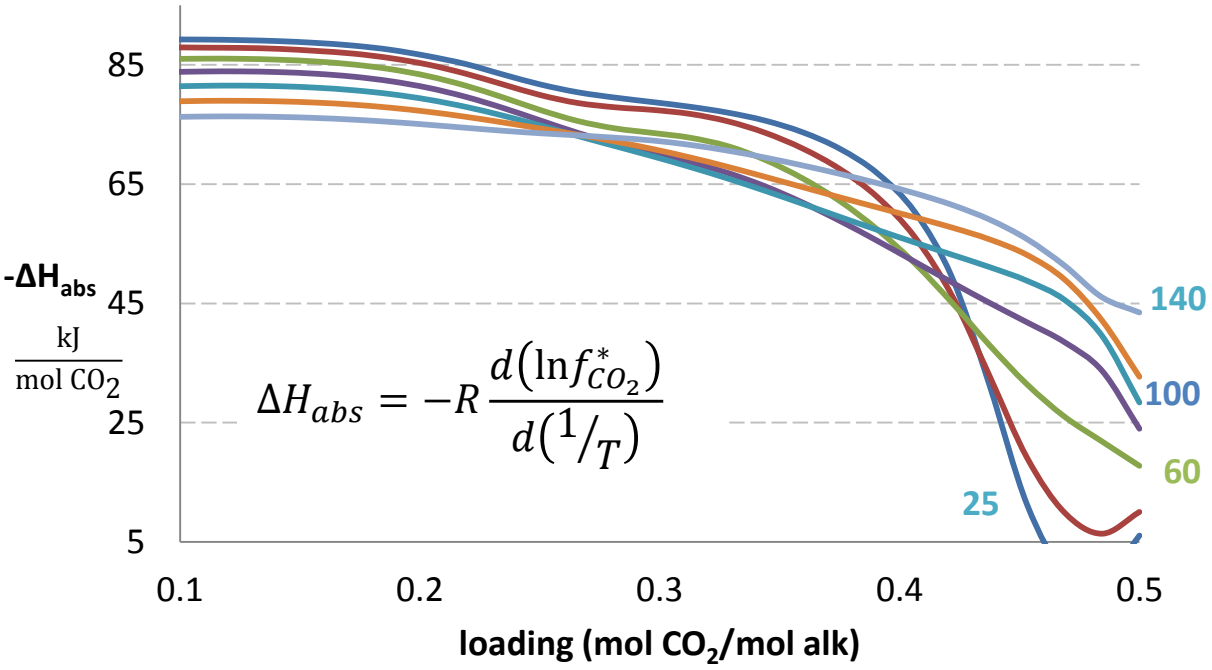

Figure 3. Heat of absorption of 4 m 2MPZ/4 m PZ calculated using the shown equation. Lines are spaced 20 °C apart, except for 25 °C.

The differential heat of absorption as predicted using the thermodynamic relationship shown in Figure 3 is essential to predicting the temperature bulge in the absorber. A precise prediction is needed to determine the amount and location of intercooling. The predicted heat of absorption matches expected magnitude, loading, and temperature trends.

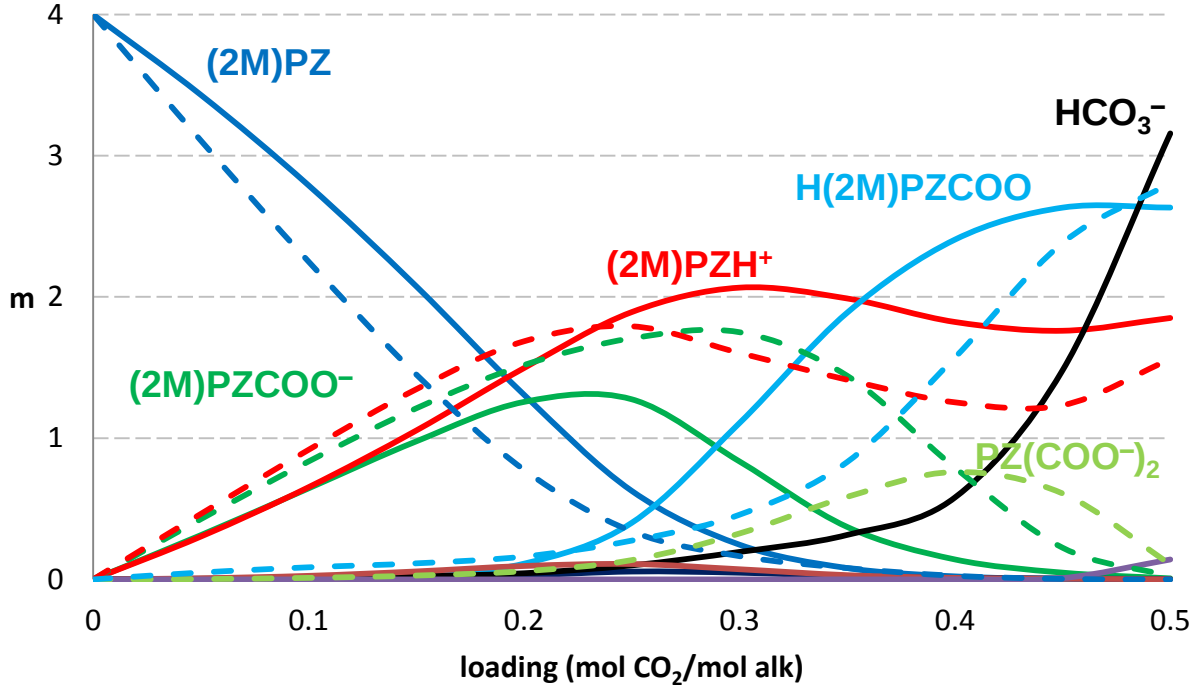

Figure 4. Speciation of 4 m 2MPZ/4 m PZ at 40 °C. Solid lines are 2MPZ species, dashed PZ.

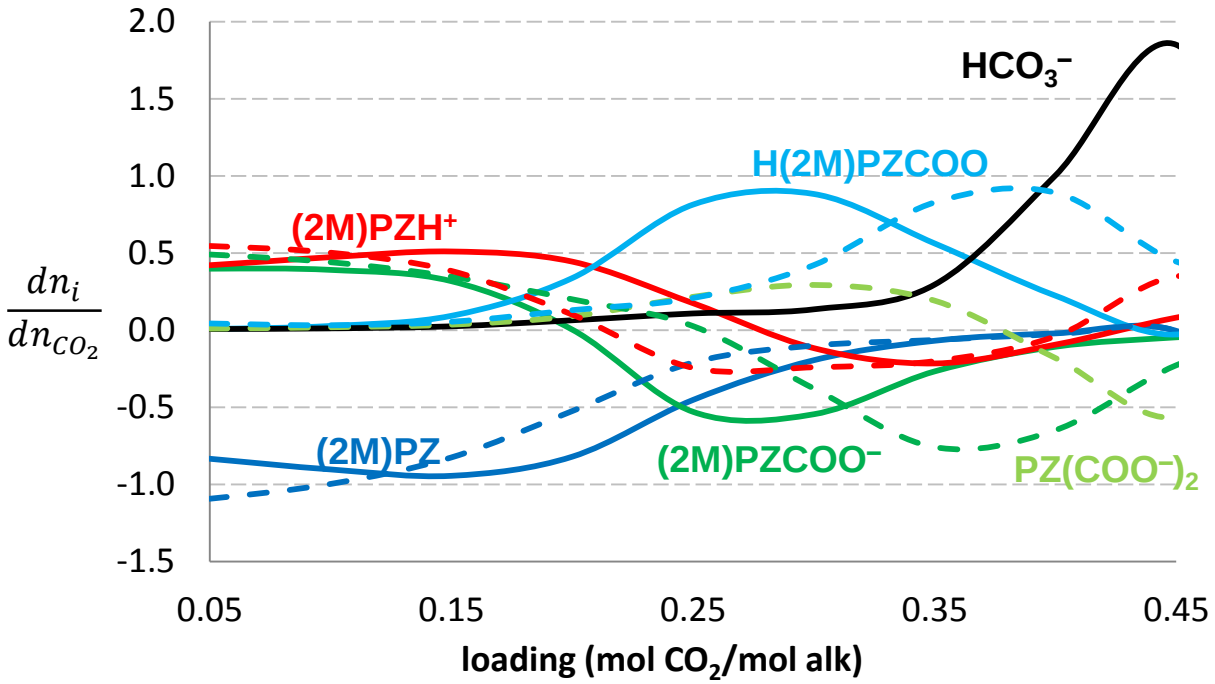

Figure 5. Stoichiometry of 4 m 2MPZ/4 m PZ at 40 °C. Solid lines are 2MPZ species; dashed PZ.

Figure 4 shows that the amount of free PZ decreases faster than 2MPZ, which is attributable to the greater stability of its carbamate and dicarbamate species. For this reason, 2MPZ more often serves as the base rather than forming carbamate. This is why there is more protonated 2MPZ and 2MPZ carbamate.

Another way of interpreting the speciation data is to consider the major reactions at each loading. Figure 5 plots the change in one species relative to the change in CO_2. At a loading of 0.1 mol CO_2/mol alk, the main reactions are PZ+2MPZ +CO_2 → 2MPZCOO$^-$ +PZH^+ and PZ + 2MPZ + CO_2 → $PZCOO^-$ + 2MPZH^+. At a loading of 0.3 mol CO_2/mol alk, the main reaction is 2MPZCOO- + $PZCOO^-$ +CO_2 → H2MPZCOO + $PZ(COO^-)_2$.

3.3. Kinetic Modeling

The reaction parameters are shown in Table 8. They are grouped by the CO_2 product. In changing PZ reactions catalyzed by PZ to PZ reactions catalyzed by 2MPZ, the rates are kept the same as the PZ reaction. This is seen in reactions 3, 5, and 6, 7.

The parameters to represent the diffusion of amine products are shown in Table 9. These parameters are most important at high loading and high temperature. As 4 m 2MPZ/4 m PZ has a high viscosity, the dependence of diffusivities on viscosity is especially important.

Table 8. Reaction parameters for 4 m 2MPZ/4 m PZ for Equation 8.

Stoichiometry	**k_o (kmol/s-m^3)**		**E_A (10^4 J/mol)**	
	fwd	rev	fwd	rev
$PZCOO^- + H_2O + CO_2 \leftrightarrow HPZCOO + HCO_3^-$	2.20E+04	9.74E+01	4.90	7.37
$2MPZCOO^- + H_2O + CO_2 \leftrightarrow H2MPZCOO + HCO_3^-$	2.62E+06	4.28E+05	9.80	17.5
$2\ PZCOO^- + CO_2 \leftrightarrow PZ(COO^-)_2 + HPZCOO$	2.76E+10	2.63E+05	1.42	8.93
$PZCOO^- + 2MPZ + CO_2 \leftrightarrow PZ(COO^-)_2 + 2MPZH^+$	1.00E+10	9.51E+04	6.98	16.6
$PZCOO^- + 2MPZCOO^- + CO_2 \leftrightarrow PZ(COO^-)_2 + H2MPZCOO$	2.76E+12	2.49E+09	1.42	14.1
$PZ + 2MPZ + CO_2 \leftrightarrow PZCOO^- + 2MPZH^+$	2.04E+10	4.27E+04	1.42	8.51
$2\ PZ + CO_2 \leftrightarrow PZH^+ + PZCOO^-$	2.04E+10	6.44E+04	1.42	8.77
$2\ 2MPZ + CO_2 \leftrightarrow 2MPZH^+ + 2MPZCOO^-$	1.45E+10	4.50E+04	1.42	8.93
$2MPZ + PZ + CO_2 \leftrightarrow 2MPZCOO^- + PZH^+$	9.00E+10	1.68E+05	0.4.57	7.95
$2\ 2MPZCOO^- + CO_2 \leftrightarrow 2MPZ(COO^-)_2 + H2MPZCOO$	2.76E+10	6.67E+08	1.42	12.1

Table 9. Diffusivity parameters for Equation 9.

Parameter	**Value**	**Units**
D_o	4.00E-10	m^2/sec
α	-2.5819	—
β	-1	—
T_{ref}	313.15	—
μ_{ref}	0.0137	—

The kinetic fit is shown in Figure 6 and Figure 7. Figure 6 shows that there is a trend towards higher predictions at higher temperatures. It also reveals that there is a large discrepancy between the absorption and desorption points at the temperature extrema. Figure 7 replots the data against loading showing no bias with increasing loading. However, the fit breaks down at the rich end. The overall sum of errors squared is 2.39.

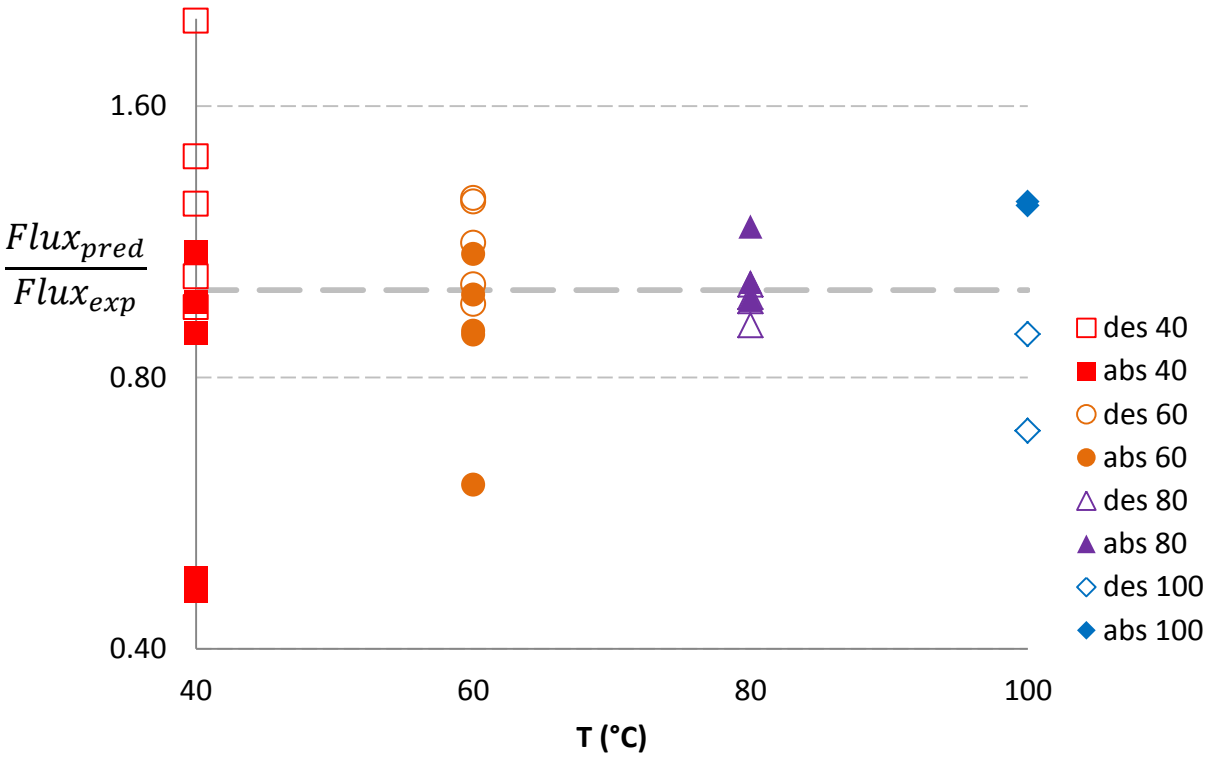

Figure 6. Kinetic predictions ratioed to data [7]. Filled points are absorption; open desorption.

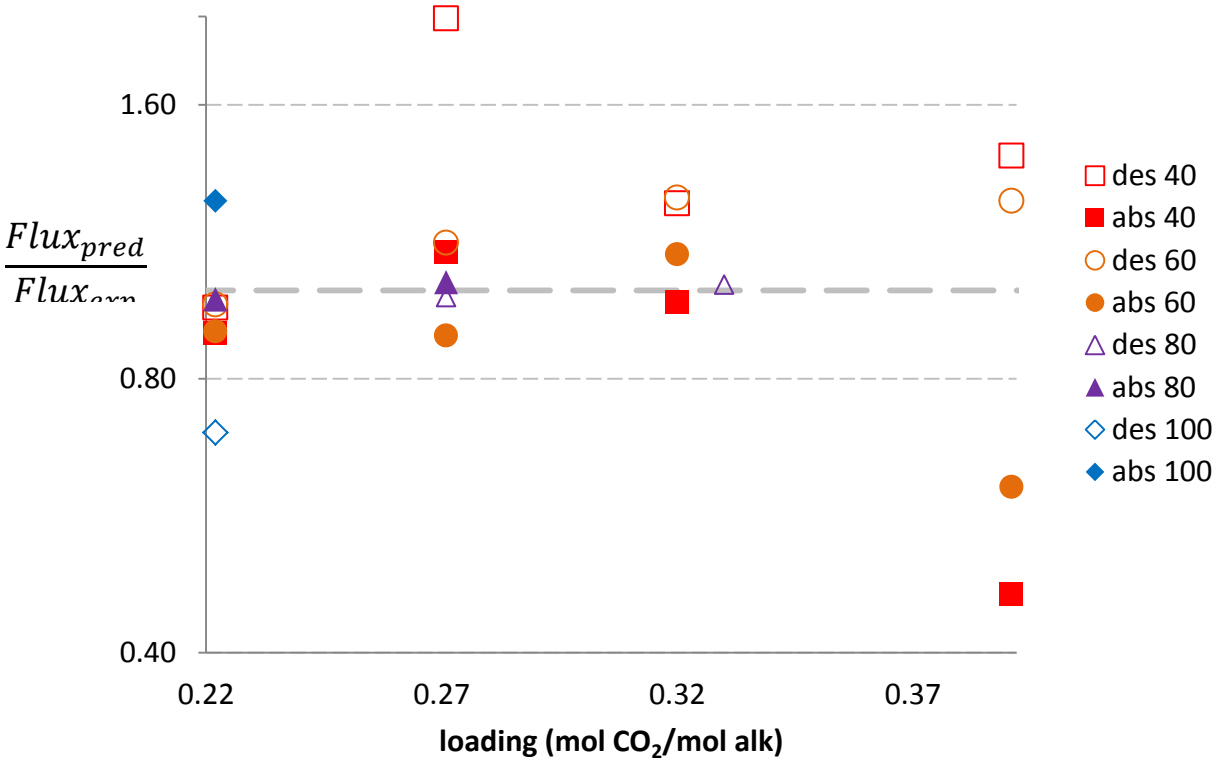

Figure 7. Kinetic predictions ratioed to data [7]. Filled points are absorption; open desorption.

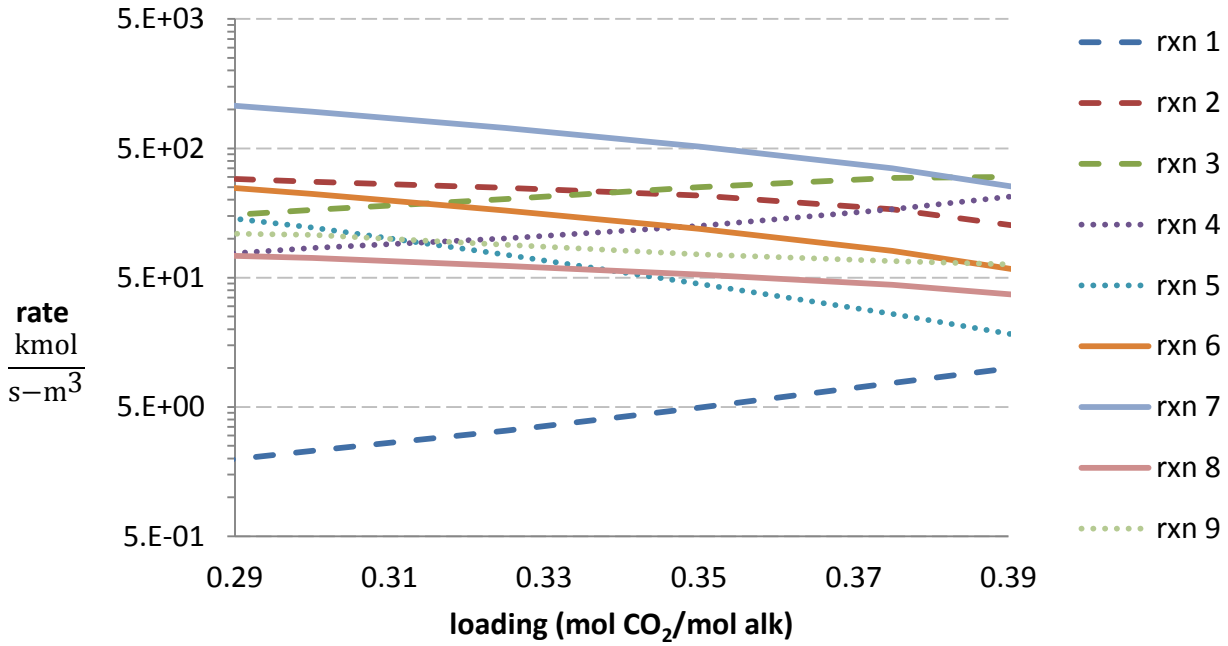

Figure 8. Net rate of kinetic reactions at 40 °C. Numbering corresponds to Table 2.

The individual contributions of each reaction are plotted in Figure 8. Reaction 5, the formation of PZ dicarbamate catalyzed by 2MPZ carbamate, is not plotted as its contribution was negligible. The next slowest reaction is reaction 1, which is the formation of bicarbonate catalyzed by PZ carbamate. The dominant reaction at lean loading is the formation of 2MPZ carbamate catalyzed by PZ (reaction 9). At rich conditions, this is slightly slower than the formation of PZ dicarbamate catalyzed by PZ carbamate (reaction 3).

4. Conclusions

The equimolar 4 m 2MPZ/4 m PZ was modeled in Aspen Plus® using the eNRTL thermodynamic framework. 109 data points for VLE, density, and viscosity were regressed using twenty-six parameters. The resulting thermodynamic model correctly predicts the CO_2 equilibrium partial pressure at absorber and stripper temperatures. The average differential heat of absorption is close to the expected value of –70 kJ/mol CO_2. The predicted speciation and stoichiometry reveal that the 2MPZ carbamate species is less prevalent than the PZ carbamate species, though the 2MPZ zwitterion is more prevalent than its PZ counterpart. The viscosity-normalized capacity is the same as that of 8 m PZ at 0.78 mol CO_2/kg amine+H_2O.

The kinetic model used ten different reactions to capture the rate behavior across the range of lean to rich loadings as well as from 40–100°C. The rate predictions are worst at the temperature extremes as well as at the rich loading. The SSE for the kinetic model was 2.39. The formation of PZ dicarbamate catalyzed by 2MPZ carbamate is negligible. The dominant reaction at lean loading is the formation of 2MPZ carbamate catalazyed by PZ, while at rich conditions the formation of PZ dicarbamate catalyzed by PZ carbamate becomes dominant. Taken as a whole, this thermodynamic and kinetic model can be used for techno-economic assessments, pilot plant data reconciliation, and process modeling.

Acknowledgements

The support of the Department of Energy through the Carbon Capture Simulation Initiative is gratefully acknowledged, as is the support of the Texas Carbon Management Program. Many fruitful discussions were had with Dr. Rochelle and Dr. Frailie. The viscosity data collected by Le Li and Nina Salta were revelatory.

The authors acknowledge the financial support of the Texas Carbon Management Program.

Disclaimer

This presentation was prepared as an account of work sponsored by an agency of the United States Government. Neither the United States Government nor any agency thereof, nor any of their employees, makes any warranty, express or implied, or assumes

any legal liability or responsibility for the accuracy, completeness, or usefulness of any information, apparatus, product, or process disclosed, or represents that its use would not infringe privately owned rights. Reference herein to any specific commercial product, process, or service by trade name, trademark, manufacturer, or otherwise does not necessarily constitute or imply its endorsement, recommendation, or favoring by the United States Government or any agency thereof. The views and opinions of authors expressed herein do not necessarily state or reflect those of the United States Government or any agency thereof.

The authors declare the following competing financial interest(s): One author of this publication consults for Southern Company and for Neumann Systems Group on the development of amine scrubbing technology. The terms of this arrangement have been reviewed and approved by the University of Texas at Austin in accordance with its policy on objectivity in research. The authors have financial interests in intellectual property owned by the University of Texas that includes ideas reported in this paper.

References

[1] Chen X, Rochelle G. Modeling of CO_2 Absorption Kinetics in Aqueous 2-Methylpiperazine. Ind Eng Chem Res 2013;52:4239–48.
[2] Chen X, Rochelle GT. Thermodynamics of CO_2/2-Methylpiperazine/Water. Ind Eng Chem Res 2013;52:4229–38.
[3] Frailie PT. Modeling of Carbon Dioxide Absorption / Stripping by Aqueous Methyldiethanolamine / Piperazine. Ph.D. Dissertation, The University of Texas at Austin, 2014.
[4] Freeman SA. Thermal Degradation and Oxidation of Aqueous Piperazine for Carbon Dioxide Capture. Ph.D. Dissertation, The University of Texas at Austin, 2011.
[5] Chen C-C, Britt HI, Boston JF, Evans LB. Local Composition Model for Excess Gibbs Energy of Electrolyte Systems. AIChE J 1982;28:588–96.
[6] Chen C. A Local Composition Model for the Excess Gibbs Energy of Aqueous Electrolyte Systems 1986;32:444–54.
[7] Chen X. Carbon Dioxide Thermodynamics, Kinetics, and Mass Transfer in Aqueous Piperazine Derivatives and Other Amines. Ph.D. Dissertation, The University of Texas at Austin, 2011.
[8] Xu Q. Thermodynamics of CO_2 Loaded Aqueous Amines. Ph.D. Dissertation, University of Texas at Austin, 2011.
[9] Nguyen T. Amine Volatility in CO_2 Capture. Ph.D. Dissertation, University of Texas at Austin, 2013.
[10] Li L, Li H, Namjoshi O, Du Y, Rochelle GT. Absorption rates and CO_2 solubility in new piperazine blends 2013;00:1–16.
[11] Versteeg GF, Swaaij WPM Van. Solubility and Diffusivity of Acid Gases (CO_2 , N_2O) in Aqueous Alkanolamine Solutions. J Chem Eng Data 1988;33:29–34.

Available online at www.sciencedirect.com

ScienceDirect

Energy Procedia 00 (2013) 000–000

Energy Procedia

www.elsevier.com/locate/procedia

GHGT-12

Effect of liquid viscosity on the liquid phase mass transfer coefficient of packing

Di Song[a,b], A. Frank Seibert[b], Gary T. Rochelle[a,*]

[a]*McKetta Detartment of Chemical Engineering, The University of Texas at Austin, 200 E Dean Keeton St., C0400, Austin, TX 78712-1589, USA*
[b]*Separations Research Program, Pickle Research Center, The University of Texas at Austin, 10100 Burnet Rd., Austin, TX 78758, USA*

Abstract

There are many correlations of liquid phase mass transfer coefficient (k_L) for packings in the literature; most were developed without data that vary liquid viscosity (μ_L) significantly (< 5 cP). In CO_2 capture by amine scrubbing, μ_L, of aqueous amine may be significantly greater than water, which makes it important to know how mass transfer is affected by μ_L. A research plan is proposed to measure the effective mass transfer area (a_e) and k_L in a pilot-scale packed column with μ_L from 1 to 100 cP. Glycerol was chosen as the viscosity enhancer for its complete solubility in water and the Newtonian behavior of its aqueous solution. Models were built to estimate the physical properties (μ_L, ρ, D_{CO2}, H_{CO2}, γ) of CO_2/NaOH/H_2O/glycerol based on literature data. Kinetic data (k_g') for the system were obtained with a wetted wall column (WWC). The kinetic data, k_g', was found to initially increase with glycerol concentration because of the catalytic effect of glycerol, then decrease rapidly because of the increase in μ_L. The overall reaction rate constant (k_{Alk}) was determined from k_g' data, and was found to increase with glycerol concentration until it becomes asymptotic. This model for k_g' will be used for future measurement of a_e and k_L in a pilot-scale column.

Selection and peer-review under responsibility of GHGT.

Keywords: post-combustion CO_2 capture; liquid phase mass transfer coefficient; mass transfer area; packing; liquid viscosity; glycerol

1. Introduction

CO_2 capture and storage (CCS) is an important technology for greenhouse gas control. Post-combustion amine scrubbing is by far the most feasible technique for large scale point source CO_2 capture because of its maturity and

* Corresponding author. Tel.: +1-512-471-7230; fax +1-512-471-7060.
E-mail address: gtr@che.utexas.edu

1876-6102
Selection and peer-review under responsibility of GHGT.

tail-end characteristic. The μ_L of concentrated and CO_2-loaded amine solution can be 10-30 times more viscous than water, which makes it important to know how mass transfer in packed columns is affected by μ_L. Most of the existing k_L (k_La) correlations in the literature examined only water or dilute aqueous solutions with μ_L close to 1 cP. In these correlations, the dependence of k_L on μ_L was indirectly obtained from the dependence on dimensionless numbers such as *Re* and *Sc*. A more reliable prediction can only be made when μ_L is varied directly in a_e and k_L measurements.

Nomenclature

a_e	effective mass transfer area of packing per volume of column, m^2/m^3
a_p	specific (dry) area of packings, m^2/m^3
C	constant in correlation
d	characteristic length, m
D	diffusion coefficient, m^2/s
g	gravitational acceleration, m/s^2
H	Henry's constant, atm L/mol
h	WWC tube length, m
k	reaction rate constant
k_{ALK}	overall reaction rate constant for CO_2/NaOH/H_2O/glycerol, L/mol s
k_g'	liquid phase mass transfer coefficient with chemical reactions expressed in gas unit, mol/m^2 Pa s
k_G	gas phase mass transfer coefficient, mol/m^2 Pa s
k_L	liquid phase mass transfer coefficient, m/s
k_L^0	physical liquid phase mass transfer coefficient, m/s
K	equilibrium constant
K_G	overall mass transfer coefficient expressed in gas unit, mol/m^2 Pa s
L	liquid volumetric flow rate, cm^3/s
N	molar flux, mol/m^2 s
P	pressure, atm or Pa
	wetted perimeter of WWC tube, m
q	pure-component Van der Waals surface area parameter
r	pure-component Van der Waals volume parameter
T	temperature, ℃ or K
u	fluid velocity, m/s
w	weight fraction
x	mole fraction
Z	coordination number in UNIQUAC model

Greek letters

α	dependence of k_L on μ_L
	non-randomness parameter in NRTL model
β	dependence of k_L on D
γ	activity coefficient
	dependence of D on μ_L
δ	liquid film thickness, m
η	parameter in Pigford mass transfer model, defined in Eq. A11
θ	area fraction in UNIQUAC model
Θ	dimensionless concentration change, defined in Eq. A10
μ	viscosity, cP
ρ	density, kg/m^3
σ	surface tension, N/m
τ	exposure time of liquid surface, s
Φ	segment fraction in UNIQUAC model

Dimensionless numbers

Ha	Hatta number, $(k_l D)^{0.5}/k_L^0$
Sc	Schmidt number, $\mu/\rho D$
Sh	Sherwood number, kd/D
Re	Reynolds number, $u\rho d/\mu$

Subscripts

L	liquid phase
G	gas phase
g	glycerol
w	water
Alk	alkalinity

Superscripts

b	bulk solution
i	fluid interface

2. Literature review

2.1. Effect of μ_L on k_L

In packed columns, μ_L affects k_L in two ways: directly through affecting the turbulence in the liquid phase, and indirectly via its influence on the diffusion coefficient, D, of mass transfer species. The total influence of μ_L on k_L is the sum of the two effects.

To illustrate the two effects, assume a k_L (k_La) correlation of the simplified form of Eq. 1, and D is a function of μ_L in the form of Eq. 2. Combining the two equations gives Eq. 3, in which ($\alpha+\beta\gamma$) refers to the total influence of μ_L on k_L, while α and $\beta\gamma$ refer to the direct and indirect effects of viscosity respectively. The value ($\alpha+\beta\gamma$) can be correlated from empirical data with varying μ_L. To obtain separate values of α and $\beta\gamma$, a reliable relationship between D and μ_L is required.

$$k_L(k_La) = C_1\mu^{\alpha}D^{\beta} \tag{1}$$

$$D = C_2\mu^{\gamma} \tag{2}$$

$$k_L(k_La) = C_1C_2^{\beta\gamma}\mu^{\alpha+\beta\gamma} = C_3\mu^{\alpha+\beta\gamma} \tag{3}$$

A comprehensive overview of liquid phase mass transfer properties in packed columns can be found in the literature [1,2]. Au-yeung and Ponter made a detailed review of k_L (k_La) models for packed columns before the 1980s [1]. They pointed out that the lack of data for high viscosity liquids impedes a thorough understanding of k_L. Wang et al. discussed k_L, k_G, and a_e correlations for both random and structured packing in the literature, but they did not focus on the effect of μ_L [2].

2.2. k_L (k_La) correlations for random packing

A number of k_L (k_La) correlations have been developed to predict the mass transfer in columns with random packing. Sherwood and Holloway were the first to systematically measure k_La of several aqueous systems [3].

Van Krevelen and Hoftijzer include the effect of gas-liquid chemical reaction in their k_L correlation for different random packings [4]. Data from a technical plant together with other literature data were used for the correlation. k_L

and a were separated by simply assuming that a_e is equal to a_p. α was found to vary with Ha with an approximate value of -1/3.

Shulman and co-workers, using a 0.25 m diameter (i.d.) column, measured k_G by vaporization of naphthalene packing with known surface area [5,6]. The k_G correlation was used in conjunction with k_Ga data from Fellinger [7] to obtain a_e, which was then used to separate k_L from k_La data from several investigators [3,8-10]. Though α was an unreasonable positive value (0.05) for this correlation, their attempt to separate k_L and k_G from a_e by experimentally measuring a_e is an important contribution to the understanding of mass transfer in packed columns.

Knoedler and Bonilla measured k_La through vacuum desorption of oxygen from water with triangular packing in a 0.15 m diameter (i.d.) column [11]. The direct dependence of k_La on μ_L was found to be 0.52. The unrealistic positive value of α proves the unreliability of the model, which incorporates no variance in μ_L.

Davidson were the first to propose a theoretical k_La model for random packing with the assumption of laminar flow and complete liquid mixing [12]. The packing surface was assumed to consist of a number of inclined surfaces with random angles and length. The model was later adopted and modified by several authors [13-15]. The power, α, was determined to be -1/6.

After comparing k_La data from multiple sources [3,16-18], Norman concluded that the influence of types of random packing on k_La is remarkably small and a universal k_La correlation can be used for random packing [19].

Norman and Sammak measured k_L by absorption of sulphur dioxide into water and carbon dioxide into different aqueous and organic solutions [20,21]. They were the first to vary μ_L over a relatively large range (0.4-20 cP). k_L and a were separated by a preliminary experiment observing the wetted percentage of packing surface as a function of liquid flow rate. Though the packing they examined (vertical disc packing) is not commonly used, their endeavor to examine the specific influence of μ_L on k_L was a step forward.

Onda et al. developed widely-accepted models of a_e and k_L of random packing by correlating extensive literature data and their own experimental data for gas absorption into water and organic solutions [22-25]. The liquid viscosity was not significantly varied in any of the data sources.

Mohunta and Laddha measured k_L with a few experimental runs performed with increased μ_L by adding glycerol to water [26]. Data with increased μ_L fitted well with the bulk of the literature data. While this was the first reported attempt to vary μ_L using aqueous glycerol, the range of μ_L was still small (0.73-1.48 cP).

Cornell and co-workers developed a k_La correlation based on some reported data [27,28]. The databank size was limited and an empirical packing-specific factor was introduced for data fitting. Bolles and Fair modified the model by significantly expanding the databank with a larger range of column size, operating conditions, and packing types [29]. However, the range of μ_L was still limited (0.09-1.5 cP).

Mangers and Ponter were the first to systematically investigate the effect of μ_L on k_La [30]. By the addition of glycerol, the μ_L range (0.9-26 cP) was significantly larger than previous investigators. They found a sharp transition point in the relation between k_La and L/μ_L. The transition was believed to result from whether the packing surface was fully wetted. k_La correlations at both sides of the transition point were provided. The values of α were different before and after the transition point, but both were close to -0.6. Ponter and Au-yeung modified the model by introducing a mixing factor with more empirical data [14].

Linek et al. measured k_La of random packings by desorption of oxygen from water into pure nitrogen [31]. Effective mass transfer area was determined by absorption of carbon dioxide into sodium hydroxide solutions. The overall mass transfer coefficient for this system with fast chemical reaction was known in a theoretical form [32], and was confirmed by experiments with the same system at packing surface with known interfacial area. This approach to measure a_e with a fast reaction system with known mass transfer rates sheds light upon future study of mass transfer in pilot-scale experiments to separate a_e from empirical data of k_La and k_Ga. The k_L data showed good agreement with the correlation of Onda et al. [25].

Echarte et al. examined the desorption of carbon dioxide from water and aqueous glycerol solutions for k_L in a 0.4-m I.D. column [15]. The effective mass transfer area, a_e, were obtained in the same column by water cooling. The use of a_e data obtained from water for k_L of the much more viscous system of water/glycerol is based on the assumption that a_e is not a function of μ_L, which might not be correct. Compared to the experiment of Mangers and Ponter, the μ_L range (0.9-6.1 cP) is smaller but the column size is larger. The correlation is a modification of the theoretical model of Davidson.

Delaloye et al. studied the effect of μ_L on k_La of random packings by stripping oxygen from aqueous solutions of different viscosity enhancers including sodium alginate, glycerol, and polyethylene glycol (PEG) [33]. The μ_L range of was 0.8-9.6 cP. The authors pointed out that, despite the large number of k_L correlations in the literature, few of them gave reliable prediction for α. This was illustrated by the fact that even correlations which agreed for water-like viscosities diverged by an order of magnitude for μ_L of only 10 cP. For sodium alginate and glycerol, α was found to be -0.52, which was in good agreement with the result of Echarte et al. For PEG, α was found to be -0.26. The authors attributed the discrepancy to the inaccuracy of diffusion coefficient, D, model for PEG and the fact actual physical properties of PEG sample might be different from those indicated by the manufacturer.

Billet and Schultes [34,35] developed a semi-theoretical k_L correlation based on penetration theory [36]. The model was correlated by examining an extensive data set involving different packings and systems. However, the range of μ_L was small (0.3-1.66 cP), and the correlation requires knowledge of a packing-specific shape constant, which is not readily available for all packings. The model was updated by further enlarging the data base [37]. The model may provide good prediction for mass transfer properties if shape constants of packing are known and when μ_L is close to water, but its reliability for viscous liquids is doubtful.

Maćkowiak also developed a semi-theoretical k_L model based on penetration theory [38]. Liquid was assumed to flow down along the packing surface in the form of thin rivulets, but change to droplets between individual packing elements. Both rivulets and droplets were believed to provide a_e. Multiple reported data which covered a variety of random packings were used for the correlation. However, the data used only include water-like liquids, and a packing-specific parameter is needed for the correlation.

2.3. k_L (k_La) correlations for structured packing

Since the 1960s structured packing has been applied in industrial distillation and absorption columns [39]. The majority of these studies focused on distillation (e.g., [40-44]), where mass transfer resistance is often thought to be controlled by the vapor phase which makes deducing k_L unreliable.

Bravo et al. were the first investigators to systematically examine mass transfer for structured packings [45]. The model for k_L was derived theoretically based on penetration theory. No parameter for k_L was correlated by empirical data. Though the calculated HETP showed good agreement with extensive literature data from distillation, its use is not recommended for prediction of k_L or α. This model was modified [40,41,46] to include effects of characteristic packing dimension, effective fluid velocity, and contact time. However the correlation of k_L remained in the same form.

The k_L correlation of Billet and Scheltes [34,35,37] for structured packing is the same as with random packing.

Weiland and co-workers measured a_e and k_La by absorption of carbon dioxide into solutions of sodium hydroxide and sodium carbonate/bicarbonate [47]. Though different parameters were assigned to different packings in the correlations, the correlations were the first to be obtained by a system controlled by liquid phase mass transfer resistance. The power, α, was found to be a positive value around 0.5, which is likely a result from the limited range of μ_L.

Hanley et al. developed a theoretical k_L model from an analogy to electrical percolation on a conductor/insulator lattice [48]. In the model, k_L was independent of μ_L.

The k_La correlation of Brunazzi and Paglianti obtained from an aqueous system was verified by data obtained from absorption of chlorinated compounds into solvent with elevated μ_L (mixture of polyethylene glycol dimethylethers with μ_L of 4 cP and 7.7 cP) [49,50]. a_e was measured in a previous study by absorption of 1,1,1-trichloroethane into the same liquid in the same column [51]. Similar to Weiland et al., this correlation also contains packing-specific parameters and gives a positive value of α (0.7) for Mellapak 250Y. This might be caused by the assumption that packing height affects k_L, which is more likely to be the result of liquid maldistribution.

Maćkowiak measured k_L of an aqueous system [52]. The experimental data, together with literature data were used for correlating the model. An assumption was made that a_e is equal to a_p. α was found to be -0.93, which is unreliable because μ_L was not varied.

Murrieta et al. developed a k_L model derived from penetration theory [53]. A packing-specific correction factor was introduced to fit the empirical data. The effective mass transfer area, a_e, was estimated by a previous model [41]. It should be noted that the column diameter is the similar to that to be used in the current study.

Valenz et al. measured k_La of an aqueous system with a_e obtained from absorption of carbon dioxide into sodium hydroxide solution [54]. Strikingly large differences were found between k_La and a_e measured in the work and those predicted by three well-established correlations for structured packings [37,40,55]. No property other than superficial liquid velocity was correlated for the model.

Hanley and Chen [56,57] developed a model for k_L by correlating a large set of literature data for distillation and absorption/desorption systems. Dependence on physical properties was regressed by dimensional analysis and by the least square rule. Data for various packing families were individually analyzed. A universal value of α (-0.67) was found for all packing families examined. The correlation is more of an overall mathematical summary of previously reported data from various sources than an empirical inspection.

2.4. Limitations of existing k_L (k_La) models in the prediction of α

Despite the large number of k_L (k_La) models in literature, few of them provide reliable prediction on how μ_L will affect k_L because of two major problems:

- The total effect of μ_L ($\alpha+\beta\gamma$) was not correlated from actual variance of μ_L in the experiment;
- The direct (α) and indirect ($\beta\gamma$) part of the effects of μ_L were not correctly separated.

To illustrate the first problem, assume k_L correlation takes the form of Eq. 4, which is equivalent to Eq. 5 when dimensionless groups are expanded. In Eq. 5, the total influence of μ_L on k_L is (b-a), which is determined by exponents on *Re* (a), and *Sc* (b). Typically a is correlated by varying the liquid flowrate, and b is directly assigned the value of 0.5 in order to satisfy the 0.5 dependence on D_L dictated by penetration theory [36]. As a result, the μ_L term only appears in Eq. 4 as a part of dimensionless groups without being empirically varied. The α obtained this way is obviously not reliable.

$$Sh = Sh_0 \left(\frac{Re}{Re_0}\right)^a \left(\frac{Sc}{Sc_0}\right)^b \tag{4}$$

$$k_L = k_L^0 \left(\frac{d}{d_0}\right)^{a-1} \left(\frac{\rho}{\rho_0}\right)^{a-b} \left(\frac{u}{u_0}\right)^a \left(\frac{D}{D_0}\right)^{1-b} \left(\frac{\mu}{\mu_0}\right)^{b-a} \tag{5}$$

The second problem arises from the assigned 0.5 dependence on D_L. 26 of the 29 authors assume that β is equal to 0.5 (see Appendix A.1). Since inaccuracy of β will lead to inaccuracy of α, a reliable value for β is of critical importance. Though the 0.5 dependence has been partly confirmed by Vivian and King via desorption of different gases from water in a packed column [58], the conclusion might not necessarily hold for non-aqueous systems or a system with an even larger change in D_L due to a large change in μ_L. Therefore, instead of direct assignment, the reliable approach to obtain β is to determine D_L empirically or to resort to literature that examined D_L for the specific system used in the k_L experiment.

Fig. 1 summarizes the predicted value of α in the k_L (k_La) correlations mentioned earlier. The drastic disagreement on α (-1.03 to +0.7) implies the unreliability of the existing models. For the few correlations in which μ_L was varied over a relatively large range (solid points in Fig. 1), either the column size is too small to avoid the wall effect/entrance effect and to be representative of an industrial scale situation, or only random packings were investigated. Therefore, a systematic investigation of the effect of μ_L on k_L in columns with random and structured packings is necessary.

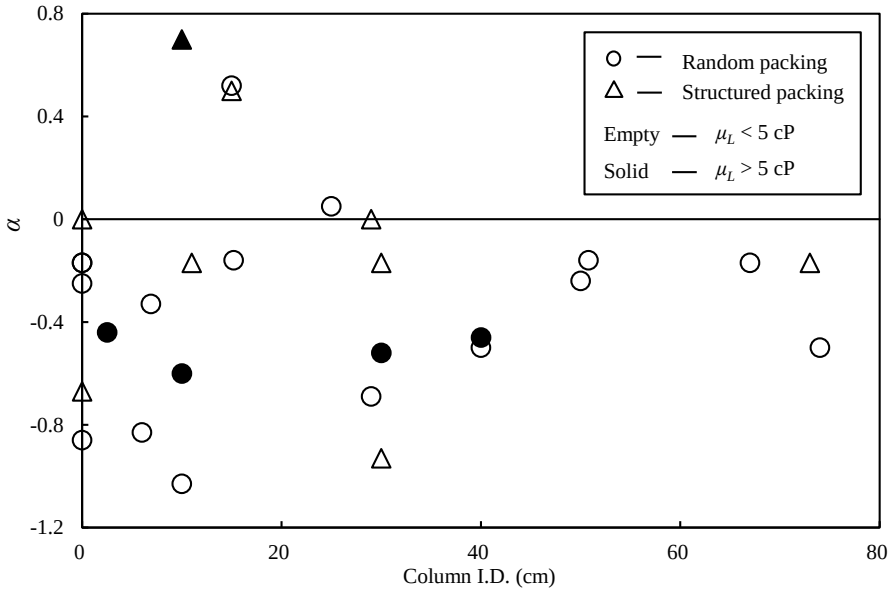

Fig. 1. Prediction of α for k_L (k_La) correlations in literature (for detailed information see Appendix A.1)

3. Experimental details & data analysis

3.1. Overall research plan

A research plan (Table 1) was proposed to systematically investigate the influence of μ_L on k_L in columns with several random and structured packings. The proposed range of μ_L is 1-100 cP. Glycerol was chosen as the liquid viscosity enhancer for its ease of dissolution and complete solubility in water. Aqueous glycerol is Newtonian [59], which guarantees that the μ_L measured by the viscometer is identical with the actual μ_L of the liquid film on the packing surface, and that the fluid exhibits the same μ_L in the WWC and pilot column experiments regardless of the shear rate.

Table 1. Project plan

Stage	1	2	3
Target data	k_g'	a_e	k_L
System	CO_2 + (NaOH/water/glycerol)	CO_2 + (NaOH/water/glycerol)	Toluene + (water/glycerol)
Equipment	WWC	Pilot column (0.46 m I.D.)	Pilot column (0.46 m I.D.)
Packing	N/A	Various random and structured packings	
Approx. range of μ_L	0.9-60 cP	0.9-100 cP	0.9-100 cP
wt% of glycerol	0-89	0-90	0-90

3.2. Experimental equipment, methods, and materials

The WWC was used to measure the k_g' of CO_2/NaOH/H_2O/glycerol. The bench-scale gas-liquid contactor has a known interfacial area, based on which k_g' can be obtained from flux and concentration data by countercurrent gas-liquid contact. The details of the apparatus have been reported by Cullinane [60], Tsai [61], and Chen [62]. The packed column to be used for future measurement of a_e and k_L has been described by Tsai et al. [61,63].

The inorganic carbon (CO_3^{2-} or its equivalent) was measured by total inorganic carbon analysis (TIC) to account for bulk depletion of alkalinity. pH and concentration of total alkalinity were measured by acid titration with a Titrando series titrator (Metrohm, Riverview, FL, USA). A Physica MCR 300 cone and plate viscometer (Anton Paar GmbH, Graz, Austria) was used for liquid viscosity measurement. A Mettler Toledo DE40 densitometer (Mettler-Toledo, Inc., Columbus, OH) was used for density measurement of liquid samples. Details about this equipment and related experimental methods can be found in Rochelle et al. [64].

Distilled and deionized (DDI) water, 1N sodium hydroxide solution (Fisher), 1N sodium carbonate solution (Fisher), and glycerol (Fisher, 0.995-0.998 purity) were used in solution preparation.

3.3. Data analysis

k_g' was obtained from the slope of the flux-driving force plot forced through zero [61]. The empirical k_g', together with other calculated/measured properties (H_{CO2}, D_{CO2}, alkalinity concentration), were used to determine the overall reaction rate constant (k_{Alk}) from Eq. 6 [61]. After the correlation of k_{Alk} has been developed, Eq. 6 will be used to calculate a_e from $k_g'a$ data obtained from pilot column.

$$k_g' = \frac{\sqrt{k_{Alk}[Alk]D_{CO_2,L}}}{H_{CO_2}} \tag{6}$$

Models were built to estimate the physical properties (μ_L, ρ, D_{CO2}, H_{CO2}, γ) of CO_2/NaOH/H_2O/glycerol based on literature data. The correlations used for μ_L and ρ were described by Cheng for H_2O/glycerol [65]. The effect of sodium hydroxide (nominally 0.1 N) and dissolved carbon dioxide on μ_L and ρ was small, which was confirmed by comparing measured and calculated values. Parameters of NRTL and UNIQUAC activity coefficient models (Table 2) for H_2O/glycerol were correlated based on literature data [66]. Predicted values of γ are shown in Fig. 2. It was assumed that sodium hydroxide and dissolved carbon dioxide had insignificant influence on γ. Several sources [67-72] reported that H_{CO2} for CO_2/NaOH/H_2O/glycerol was correlated by Eq. 7 & 8. Parameters in Eq. 7 are summarized in Table 3. The effect of sodium hydroxide and dissolved carbon dioxide on H_{CO2} was neglected because the influence of ions is less than 5% for the worst case scenario using methods of Pohorecki and Moniuk [73]. Predicted and literature values of H_{CO2} are shown in Fig. 3. Correlation of mutual diffusion coefficient of H_2O/glycerol $D_{g\text{-}w}$ is shown in Eq. 9. Calculated and literature data [74-80] are shown in Fig. 4(a). Correlation of diffusion coefficient of CO_2 in H_2O/glycerol $D_{CO2,g\text{-}w}$ is shown in Eq. 10. Calculated and literature data [81-87] are shown in Fig. 4(b).

$$\log\frac{H_{CO_2,g-w}}{H_{CO_2,w}} = (Aw_g + B\ln(w_g+1) + Cln^2(w_g+1)) \times \left(\frac{D}{T(°C)} + E + FT(°C) + G\ln T(°C)\right) \tag{7}$$

$$\log H_{CO_2,w} = -7.8857\times10^{-5}T(K)^2 + 5.9044\times10^{-2}T(K) - 9.1229 \tag{8}$$

$$D_{g-w} = 0.3403T(°C)^{0.3134}\mu^{-0.5557} \tag{9}$$

$$D_{CO_2,g-w} = 0.3169T(°C)^{0.5206}\mu^{-0.7407} \tag{10}$$

Sterilization experiments were performed to check if bacteria growth is a problem in glycerol-rich solutions [88]. It was found that the use of biocide is unnecessary. To check if the mass transfer resistance is still dominated by the liquid phase for toluene/H_2O/glycerol, $\gamma_{Toluene}$ was calculated by correlation of Carrillo-Nava et al. [89] and was found to remain high enough (> 100) at the proposed range of glycerol concentration.

Table 2. NRTL and UNIQUAC parameters for water/glycerol (see Appendix A.2 for details)

Model	A_{12}	A_{21}	B_{12}	B_{21}	α_{12}	Z	σ^2	AAD
NRTL	0.0933	-0.8763	752.1	-193.3	0.4757	-	0.00103	2.93%
UNIQUAC	-0.0101	1.9212	537.9	-284.4	-	10	0.7181	1.39%

Table 3. Parameters in Eq. 7

Parameter	A	B	C	D	E	F	G
Value	3.28	-3.43	-2.26	14.6	-7.09	-0.00416	1.51

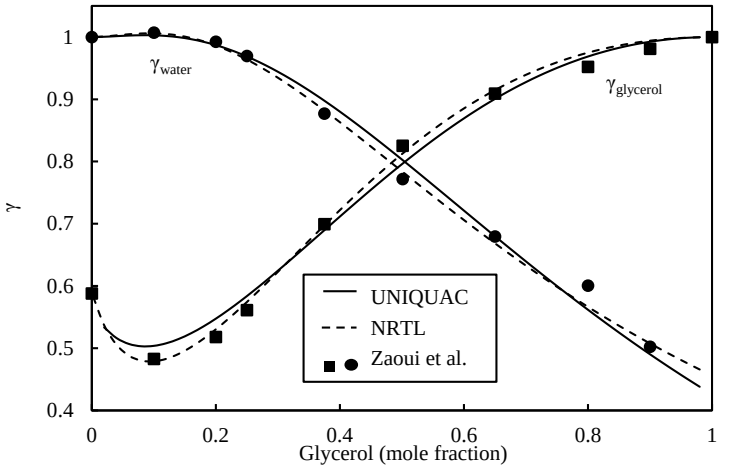

Fig. 2. Activity coefficients of H_2O/glycerol at 20 ℃

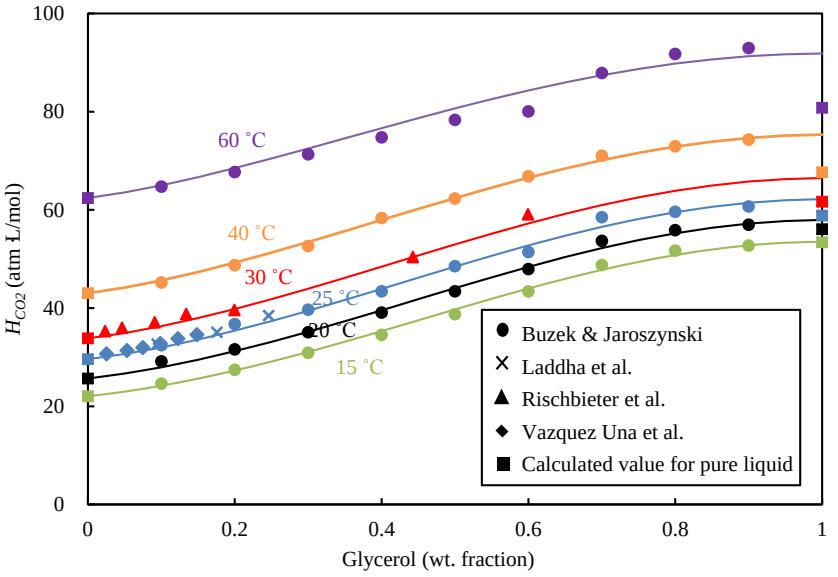

Fig. 3. H_{CO2} of CO_2/NaOH/H_2O/glycerol

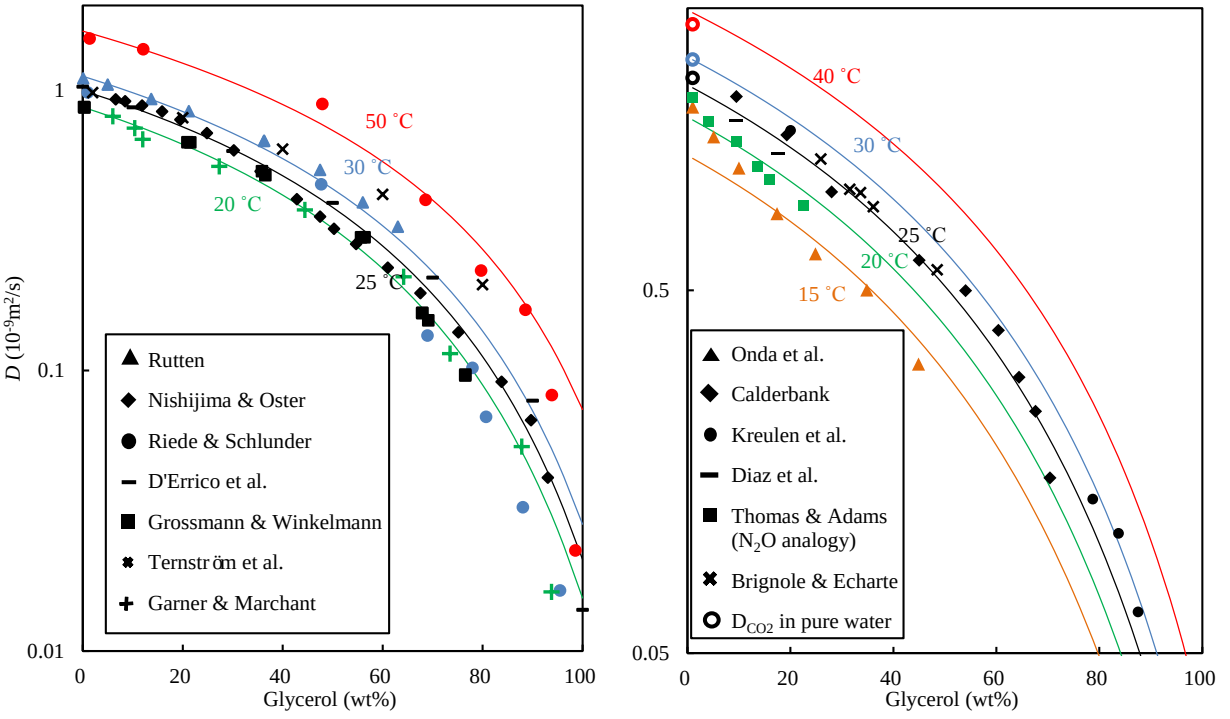

Fig. 4. (a) Mutual diffusion coefficient of H_2O/glycerol; (b) Diffusion coefficient of CO_2 in H_2O/glycerol

4. Results & Discussion

4.1. k_g' & reaction kinetics

The k_g' of the CO_2/NaOH/H_2O/glycerol system obtained from the WWC experiments is shown in Fig. 5. As expected, the k_g' increases with increasing temperature. When glycerol concentration increases, k_g' initially increases and then decreases rapidly.

Several equilibria and reactions are proposed to represent the system:

$$Glycerol + OH^- \overset{K}{\leftrightarrow} Glycerol^- + H_2O \quad \text{(R1)}$$

$$CO_2 + 2OH^- \xrightarrow{k_{OH^-}} CO_3^{2-} + H_2O \quad \text{(R2)}$$

$$CO_2 + 2Glycerol^- + H_2O \xrightarrow{k_{Glycerol^-}} CO_3^{2-} + 2Glycerol \quad \text{(R3)}$$

The overall reaction rate results from the combined effects of R2 and R3, and can be expressed as Eq. 11 & 12. The trend of k_g' as a function of glycerol concentration could be explained by the assumption that $k_{Glycerol^-}$ is larger than k_{OH^-}. When the glycerol concentration is low (< 10 wt %), the increase in μ_L and H_{CO2} is small, so the overall effect of glycerol leads to a higher k_g' because of the catalytic effect of glycerol. When glycerol concentration is further increased, the increase in μ_L, subsequent decrease in D_{CO2}, and increase in H_{CO2} starts to impede the mass transfer and decrease k_g'.

$$k_{Alk} = k_{OH^-}\left(\frac{[OH^-]}{[Alk]}\right) + k_{Glycerol^-}\left(\frac{[Glycerol^-]}{[Alk]}\right) \quad (11)$$

$$[Alk] = [OH^-] + [Glycerol^-] \quad (12)$$

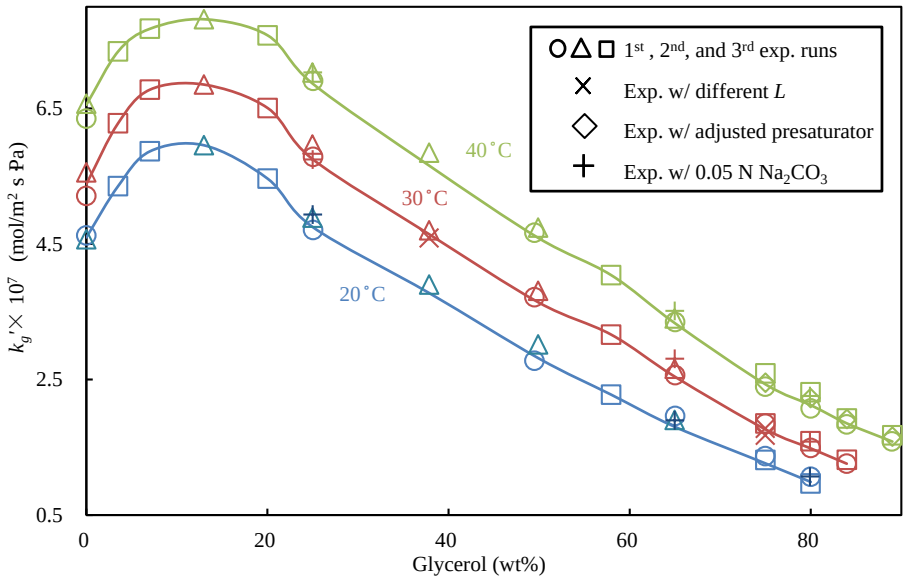

Fig. 5. k_g' of CO_2/NaOH/H_2O/glycerol from WWC experiments, nominally 0.1 M NaOH

Three parallel WWC experiments were performed for reproducibility. Experiments with different liquid flow rates were performed to confirm that k_g' is not a function of L. Experiments with different presaturator temperature (i.e., different partial pressure of water of inlet gas) were performed to investigate the effect of water mass transfer on k_g'. Experiments with 0.05 N sodium carbonate were performed to check the effect of ionic strength and carbon dioxide loading on k_g'. None of these factors was found to be significant.

The k_{Alk} determined from k_g' is shown in Fig. 6. Despite the discrepancy between different experiments, k_{Alk} increases with temperature and glycerol concentration, and finally becomes asymptotic. The trend in Fig. 6 proves the previous assumption that $k_{Glycerol-}$ is larger than k_{OH-}.

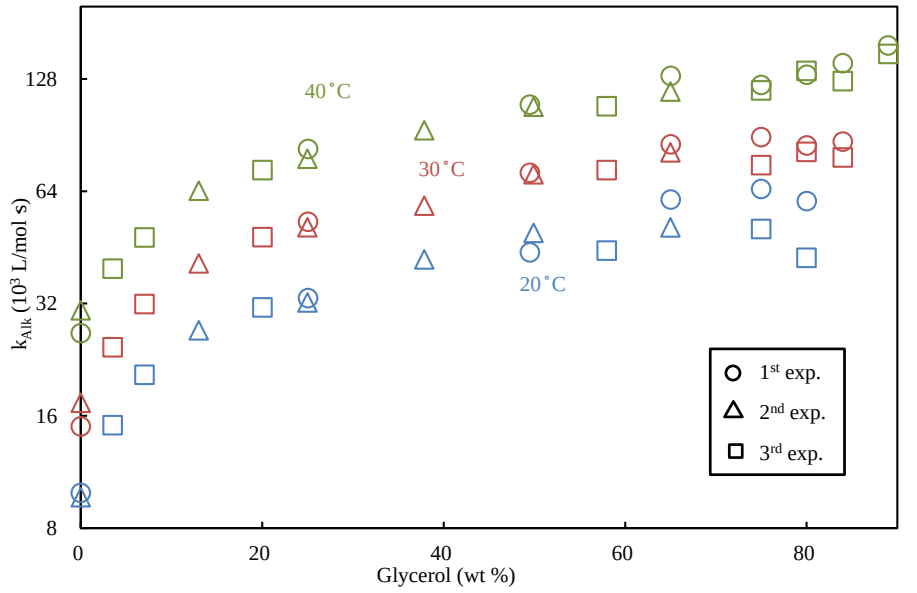

Fig. 6. Back-calculated k_{Alk} based on k_g' of CO_2/NaOH/H_2O/glycerol, nominally 0.1 M NaOH

4.2. Change in μ_L & alkalinity depletion

The μ_L of the WWC samples are shown in Fig. 7. The change of μ_L before and after the experiments is insignificant, and both are close to calculated values. This guarantees that there is no change of μ_L for bulk solution due to mass transfer of water.

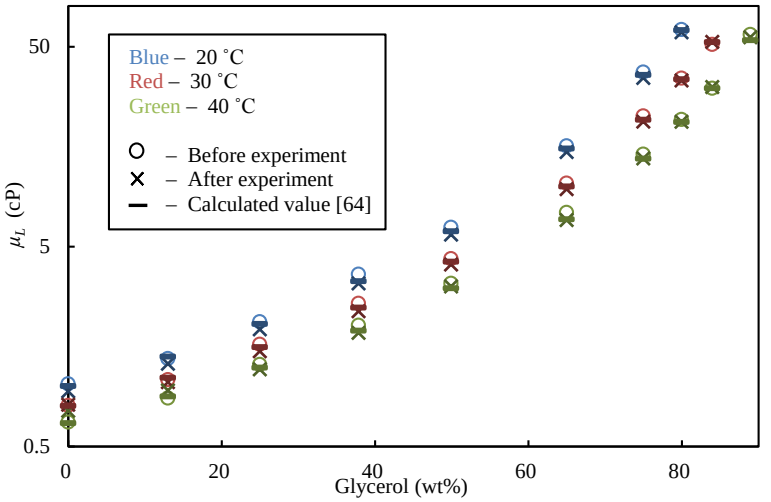

Fig. 7. Change of μ_L before and after WWC experiments

Bulk depletion of alkalinity is about 10% for the worst case scenario, which is acceptable considering the square root dependence of k_g' on alkalinity concentration.

Surface depletion of alkalinity was calculated for each WWC experiment. The pseudo-first-order assumption central to this work is only valid when there is no appreciable depletion of alkalinity at the liquid surface. Flux of alkalinity can be calculated by Eq. 13 through reaction stoichiometry. The interface concentration of alkalinity can be calculated by Eq. 14 with k_L^0 estimated by theory from Pigford [90,91] (see Appendix A.3). The worst case scenario calculated at the highest partial pressure of CO_2 shows an average ratio of surface depletion of 7.6%.

$$N_{Alkalinity} = 2N_{CO_2} \tag{13}$$

$$N_{Alkalinity} = k_L^0\,([Alk]^b - [Alk]^i) \tag{14}$$

5. Conclusions

Prediction of α of existing k_L (k_La) correlations of packing is scattered (-1.03 to +0.7) and unreliable. Models have been built to estimate the physical properties (μ_L, ρ, D_{CO2}, H_{CO2}, γ) of CO_2/NaOH/H_2O/glycerol based on literature data. The k_g' of the system were measured by WWC experiments with μ_L range 0.9-60 cP. The k_g' was found to initially increase about 25% when glycerol increases to 10 wt % because of the catalytic effect of glycerol, and then decreases about 75% when glycerol increases to 89 wt % because of the impeding effect of elevated μ_L on mass transfer. k_{Alk} was estimatedfrom k_g', and was found to increase with glycerol concentration until it becomes asymptotic to a value about five times greater. After k_{Alk} is correlated as a function of K_W, $K_{glycerol}$, k_{OH^-}, and $k_{glycerol^-}$, this model for k_g' will be used for future measurement of effective mass transfer area (a_e) and liquid phase mass transfer coefficient (k_L) using a 42.8 cm diameter (i.d.) packed column.

Acknowledgements

The authors acknowledge the support of Texas Carbon Management Program and Process Science and Technology Center of the University of Texas at Austin.

The authors declare the following competing financial interest(s): One author of this publication consults for Southern Company and for Neumann Systems Group on the development of amine scrubbing technology. The terms of this arrangement have been reviewed and approved by the University of Texas at Austin in accordance with its policy on objectivity in research. The authors have financial interests in intellectual property owned by the University of Texas that includes ideas reported in this paper.

Appendix A. Detailed information for figures, tables, and equations

A.1. Detailed information for Fig. 1

Year	Author	k_L or k_La	α	β	I.D. (cm)	Packing	$\Delta\mu_L > 5$ cP?	system
1940	Sherwood & Holloway	k_La	-0.16	0.5	50.8	random	No	$CO_2/O_2/H_2 + H_2O$ + Air
1942	Molstad et al.	k_La	-0.24	0.5	50	random	No	$O_2 + H_2O$ + Air
1947	Van Krevelen and Hoftijzer	k_L	-0.33	0.67	6.9	random	No	$CO_2 + H_2O$ + Air; O_2 + susp. Purssian white + Air; CO_2 + carbonate soln.; CO_2 + NaOH soln.
1947	Deed et al.	k_La	-0.16	0.5	15.2	random	No	$CO_2/O_2 + H_2O$ + Air
1954	Knoedler and Bonilla	k_La	0.52	0.47	15	random	No	$O_2 + H_2O$ + Air
1955	Shulman et al.	k_L	0.05	0.5	25	random	No	$CO_2/O_2/H_2 + H_2O$ + Air
1959	Davidson et al.	k_La	-0.17	0.5	N/A	random	N/A	N/A
1960	Cornell et al.	k_La	-0.50	0.5	5-76	random	No	$CO_2/O_2/H_2 + H_2O$ + Air
1961	Norman	k_La	-0.25	0.5	0	random	No	$CO_2/O_2/H_2 + H_2O$ + Air
1963	Norman & Sammak	k_L	-0.44	0.5	2.5	random	Yes	$SO_2 + H_2O$; CO_2 + aqueous/organic solutions
1968	Onda et al.	k_L	-0.83	0.5	6	random	No	$CO_2/H_2 + H_2O$; $CO_2/O_2/H_2$ + H_2O + Air
1969	Mohunta & Laddha	k_L	-1.03	0.5	10	random	No	CO_2 + (H_2O+glcerol) + Air
1974	Bridgwater & Scott	k_La	-0.17	0.5	N/A	random	N/A	N/A
1980	Mangers & Ponter	k_La	-0.60	0.5	10	random	Yes	$CO_2 + H_2O$ + glycerol
1982	Bolles & Fair	k_La	-0.50	0.5	25-122	random	No	Multiple

Year	Author	k_L or k_La	α	β	I.D. (cm)	Packing	$\Delta\mu_L$ > 5 cP?	system
1982	Ponter & Au-yeung	k_La	-0.86	0.5	0	random	No	-
1984	Linek et al.	k_La	-0.69	0.5	29	random	No	O_2+H_2O+N_2
1984	Echarte et al.	k_L	-0.46	0.5	40	random	Yes	CO_2 + (H_2O+glycerol) + Air
1991	Delaloye et al.	k_La	-0.52	0.5	30	random	Yes	O_2 + (H_2O+sodium alginate/glycerol/polyethylene glycol) + Air
1999	Billet & Schultes	k_L	-0.17	0.5	6-140	random & structured	No	Multiple
2011	Maćkowiak	k_L	-0.17	0.5	15-120	random	No	CO_2 + H_2O + Air
1985	Bravo et al.	k_L	-0.17	0.5	7-15	random & structured	No	Multiple distillation systems
1993	Weiland et al.	k_L	0.50	0.5	15	structured	No	CO_2 + NaOH/(Na_2CO_3+$NaHCO_3$) solution + Air
1994	Hanley et al.	k_L	0.00	0.5	N/A	random & structured	N/A	N/A
1997	Brunazzi and Paglianti	k_L	0.70	~0.2	10	structured	Yes	CO_2 + H_2O + Air; chlorinated compounds + mixture of polyethylene glycol dimethylethers
1999	Maćkowiak	k_L	-0.93	0.5	30	structured	No	CO_2 + H_2O + Air
2004	Murrieta et al.	k_L	-0.17	0.5	30	structured	No	CO_2 + H_2O + Air
2011	Valenz et al.	k_La	N/A	N/A	29	structured	No	O_2 + H_2O + Air
2012	Hanley & Chen	k_L	-0.67	0.67	0	random & structured	No	Multiple

A.2. Detailed information for Table 2

The models of NRTL and UNIQUAC for binary systems are described by Eq. A1-A4 and Eq. A5-A9, respectively.

$$\ln \gamma_i = x_j^2 \left[\tau_{ji} \left(\frac{G_{ji}}{x_i + x_j G_{ji}} \right)^2 + \frac{\tau_{ij} G_{ij}}{\left(x_j + x_i G_{ij} \right)^2} \right] \tag{A1}$$

$$\ln G_{ij} = -\alpha_{ij} \tau_{ij} \tag{A2}$$

$$\alpha_{ij} = \alpha_{ji} \tag{A3}$$

$$\tau_{ij} = A_{ij} + \frac{B_{ij}}{T} \tag{A4}$$

$$\ln \gamma_i = \ln \frac{\Phi_i}{x_i} + \left(\frac{Z}{2} \right) q_i \ln \frac{\theta_i}{\Phi_i} + \Phi_j \left(l_i - \frac{r_i}{r_j} l_j \right) - q_i \ln\left(\theta_i + \theta_j \tau_{ji} \right) + \theta_j q_i \left(\frac{\tau_{ji}}{\theta_i + \theta_j \tau_{ji}} - \frac{\tau_{ij}}{\theta_j + \theta_i \tau_{ij}} \right) \tag{A5}$$

$$\Phi_i = \frac{r_i x_i}{r_i x_i + r_j x_j} \tag{A6}$$

$$\theta_i = \frac{q_i x_i}{q_i x_i + q_j x_j} \tag{A7}$$

$$\ln \tau_{ij} = A_{ij} + \frac{B_{ij}}{T} \tag{A8}$$

$$l_i = \left(\frac{Z}{2} \right) (r_i - q_i) - (r_i - 1) \tag{A9}$$

Van der Waals parameters were obtained from Aspen Plus®: $q_1 = 1.4$, $q_2 = 3.06$, $r_1 = 0.92$, $r_2 = 3.385$.

Subscript 1 = water; 2 = glycerol.

$\sigma^2 = \sum \frac{\left(\gamma_{calc} - \gamma_{expt} \right)^2}{(\text{no.of data points} - \text{no.of parameters})}$.

$AAD = (100\%/(\text{no. of data points})) \sum \left(\left| \gamma_{calc} - \gamma_{expt} \right| / \gamma_{expt} \right)$.

A.3. Detailed information for Eq. 13 (k_L^0 calculation)

The physical mass transfer coefficient in the liquid phase was calculated by the following equations.

$$\begin{cases} \Theta = 0.7857\exp(-5.121\eta) + 0.1001\exp(-39.21\eta) \\ \qquad +0.036\exp(-105.6\eta) + 0.0181\exp(-204.7\eta), \ \text{for } \eta > 0.01 \\ \Theta = 1 - 3\sqrt{\frac{\eta}{\pi}} \qquad\qquad \text{for } \eta < 0.01 \end{cases} \tag{A10}$$

$$\eta = \frac{D_{Alk} \tau}{\delta^2} \tag{A11}$$

$$\tau = \frac{h}{u_{surf}} \tag{A12}$$

$$\delta = \sqrt[3]{\frac{3 \mu_L Q_L}{\rho_L g P}} \tag{A13}$$

$$u_{surf} = \frac{\rho_L g \delta^2}{2\mu_L} \tag{A14}$$

$$k_L^0 = \left(\frac{Q_L}{a}\right)(1 - \Theta) \tag{A15}$$

Since D_{OH^-} is larger than $D_{glycerol^-}$, and $D_{glycerol^-}$ is approximately equal to $D_{glycerol}$, the mutual diffusion coefficient of H_2O/glycerol (Eq. 9) was used for the k_L^0 calculation.

References

[1] Au-yeung PH, Ponter AB. Estimation of liquid film mass transfer coefficients for randomly packed absorption columns. Can J Chem Eng 1983;61(4):481–93.
[2] Wang GQ, Yuan XG, Yu KT. Review of Mass-Transfer Correlations for Packed Columns. Ind Eng Chem Res 2005;44(23):8715–29.
[3] Sherwood TK, Holloway FAL. Performance of packed towers - Liquid film data for several packings. Trans Am Inst Chem Eng 1940;36(1-2):various pages.
[4] Van Krevelen DW, Hoftijzer PJ. Gas absorption. I. Liquid-film resistance to gas absorption in scrubbers. Recueil des Travaux Chimiques des Pays-Bas et de la Belgique 1947;66(1):49–66.
[5] Shulman HL, DeGouff JJ, Jr. Mass-transfer coefficients and interfacial areas for 1-inch Raschig rings. Ind Eng Chem 1952;44:1915-22.
[6] Shulman HL, Ullrich CF, Proulx AZ, Zimmerman JO. Performance of packed columns. II. Wetted and effective-interfacial areas, gas - and liquid-phase mass transfer rates. AIChE J 1955;1(2):253–8.
[7] Fellinger LL. Absorption of ammonia by water and acids in various standard packigns. 0142216 Dissertation. Ann Arbor: Massachusetts Institute of Technology; 1941.
[8] Vivian JE, Whitney RP. Absorption of chlorine in water. Chem Eng Prog 1947;43(No. 12, Trans. Am. Inst. Chem. Engrs.):691-702.
[9] Whitney RP, Vivian JE. Absorption of sulfur dioxide in water. Chem Eng Prog 1949;45:323-37.
[10] Deed DW, Schutz PW, Drew TB. Comparison of rectification and desorption in packed columns. Ind Eng Chem 1947;39:766-74.
[11] Knoedler EL, Bonilla CF. Vacuum degasification in a packed column. Deoxygenation of water in Stedman packing Chem Eng Prog 1954;50(1):125–33.
[12] Davidson JF. The hold-up and liquid film coefficient of packed towers Part 2: statistical models of the random packing. Trans Inst Chem Eng 1959;37(1):131–6.
[13] Bridgwater J, Scott AM. Statistical models of packing. Application to gas absorption and solids mixing. Trans Inst Chem Eng 1974;52(4):317–24.
[14] Ponter AB, Au-Yeung PH. Estimation of liquid film mass transfer coefficients in columns packed randomly with partially wetted rings. Can J Chem Eng 1982;60(1):94–9.
[15] Echarte R, Campana H, Brignole EA. Effective area and liquid film mass transfer coefficient in packed columns. Ind Eng Chem Process Des Dev 1984;23(2):349–54.
[16] Molstad MC, Abbey RG, Thompson AR, McKinney JF. Performance of drip-point grid tower packings. II. Liquid-film mass transfer data. Trans Am Inst Chem Eng 1942;38(1):410–34.
[17] Koch JHA, Stutzman LF, Blum HA, Hutchings LE. Gas absorption. Chem Eng Prog 1949;45(11):677-82.
[18] Rixon FF. The absorption of carbon dioxide in and desorption from water using packed towers. Trans Inst Chem Engrs 1948;26:119-29, discussion, 29-30.
[19] Norman WS. Absorption, distillation and cooling towers. 1 ed. New York: John Wiley & Sons; 1961.
[20] Norman WS, Sammak FYY. Gas absorption in a packed column Part 1: the effect of liquid viscosity on the mass transfer coefficient. Trans Inst Chem Eng 1963;41(3):109–16.
[21] Norman WS, Sammak FYY. Gas absorption in a packed column part 2: the effect of mixing between packing elements on the liquid film mass transfer coefficient. Trans Inst Chem Eng 1963;41(4):117–9.
[22] Onda K, Sada E, Murase Y. Liquid-side mass transfer coefficients in packed towers. AIChE J 1959;5(1):235–9.
[23] Onda K, Sada E, Takeuchi H. Gas absorption with chemical reaction in packed columns. J Chem Eng Jpn 1968;1(1):62–6.
[24] Onda K, Takeuchi H. Effect of packing materials on the wetted surface area. Kagaku Kogaku 1967;31(2):126-34.
[25] Onda K, Takeuchi H, Okumoto Y. Mass transfer coefficients between gas and liquid phases in packed columns. J Chem Eng Jpn 1968;1(1):56–62.
[26] Mohunta DM, Vaidyanathan AS, Laddha GS. Prediction of liquid-phase mass transfer coefficients in columns packed with Raschig rings Indian Chem Eng 1969;11(3):73–9.
[27] Cornell ID, Knapp WG, Fair JR. Mass-transfer efficiency. Packed columns. Chem Eng Prog 1960;56(No. 7):68-74.
[28] Cornell D, Knapp WG, Close HJ, Fair JR. Mass-transfer efficiency-packed columns. II. Chem Eng Prog 1960;56(No. 8):48-53.
[29] Bolles WL, Fair JR. Improved mass-transfer model enhances packed-column design. Chem Eng (NY) 1982;89(14):109–16.
[30] Mangers RJ, Ponter AB. Effect of Viscosity on Liquid Film Resistance to Mass Transfer in a packed column. Ind Eng Chem Process Des Dev 1980;19(4):530–7.

[31] Linek V, Petricek P, Benes P, Braun R. Effective interfacial area and liquid side mass transfer coefficients in absorption columns packed with hydrophilized and untreated plastic packings Chem Eng Res Des 1984;62(1):13–21.
[32] Sharma MM, Danckwerts PV. Chemical methods of measuring interfacial area and mass transfer coefficients in two-fluid systems. Br Chem Eng 1970;15(4):206–12.
[33] Delaloye MM, Stockar Uv, Lu X-p. The influence of viscosity on the liquid phase mass transfer resistance in packed columns. Chem Eng J (Lausanne) 1991;47(1):51–61.
[34] Billet R, Schultes M. Advantage in correlating packed column performance. Inst Chem Eng Symp Ser 1992;128(Distillation and Absorption '92, Vol. 2):B129-B36.
[35] Billet R, Schultes M. Predicting mass transfer in packed columns. Chem Eng Technol 1993;16(1):1–9.
[36] Higbie R. The rate of absorption of a pure gas into a still liquid during short periods of exposure. Trans Am Inst Chem Eng 1935;31:365-89.
[37] Billet R, Schultes M. Prediction of mass transfer columns with dumped and arranged packings - updated summary of the calculation method of Billet and Schultes. Chem Eng Res Des 1999;77(6):498–504.
[38] Maćkowiak J. Model for the prediction of liquid phase mass transfer of random packed columns for gas–liquid systems. Chem Eng Res Des 2011;89(8):1308-20.
[39] Spiegel L, Meier W. Distillation columns with structured packings in the next decade. Chem Eng Res Des 2003;81(A1):39-47.
[40] Rocha JA, Bravo JL, Fair JR. Distillation Columns Containing Structured Packings: A Comprehensive Model for Their Performance. 2. Mass-Transfer Model. Ind Eng Chem Res 1996;35(5):1660–7.
[41] Bravo JL, Rocha JA, Fair JR. A comprehensive model for the performance of columns containing structured packings. Inst Chem Eng Symp Ser 1992;128(Distillation and Absorption '92, Vol. 1):A489-A507.
[42] Olujic Z. Development of a complete simulation model for predicting the hydraulic and separation performance of distillation columns equipped with structured packings. Chem Biochem Eng Q 1997;11(1):31-46.
[43] Del Carlo L, Olujić Ž, Paglianti A. Comprehensive Mass Transfer Model for Distillation Columns Equipped with Structured Packings. Ind Eng Chem Res 2006;45(23):7967–76.
[44] Schpigel L, Meier W. Performance characteristics of various types of Mellapack packings (productivity, pressure differential, and deficiency). Chem Pet Eng 1994;30(3-4):118–25.
[45] Bravo LJ, Rocha JA, Fair JR. Mass transfer in gauze packings. Hydrocarb Process 1985;64(1):91–5.
[46] Rocha JA, Bravo JL, Fair JR. Distillation columns containing structured packings: a comprehensive model for their performance. 1. Hydraulic models. Ind Eng Chem Res 1993;32(4):641–51.
[47] Weiland RH, Ahlgren KR, Evans M. Mass-transfer characteristics of some structured packings. Ind Eng Chem Res 1993;32(7):1411–8.
[48] Hanley B, Dunbobbin B, Bennett D. A Unified Model for Countercurrent Vapor/Liquid Packed Columns. 2. Equations for the Mass-Transfer Coefficients, Mass-Transfer Area, the HETP, and the Dynamic Liquid Holdup. Ind Eng Chem Res 1994;33(5):1222-30.
[49] Brunazzi E, Paglianti A. Liquid-film mass-transfer coefficient in a column equipped with structured packings. Ind Eng Chem Res 1997;36(9):3792–9.
[50] Brunazzi E, Nardini G, Paglianti A. An improved correlation for estimating liquid phase mass transfer coefficient in absorption columns equipped with structured packings. Inst Chem Eng Symp Ser 1997;142(Distillation and Absorption '97, Vol. 1):477-82.
[51] Brunazzi E, Nardini G, Paglianti A, Petarca L. Interfacial area of Mellapak packing: absorption of 1,1,1-trichloroethane by Genosorb 300. Chem Eng Technol 1995;18(4):248–55.
[52] Mackowiak J. Studies on gas- and liquid-side mass transfer in columns with structured packings. Chem-Ing-Tech 1999;71(1/2):100-4.
[53] Murrieta CR, Seibert AF, Fair JR, Rocha JA. Liquid-side mass-transfer resistance of structured packings. Ind Eng Chem Res 2004;43(22):7113–20.
[54] Valenz L, Rejl FJ, Sima J, Linek V. Absorption Mass-Transfer Characteristics of Mellapak Packings Series. Ind Eng Chem Res 2011;50(21):12134–42.
[55] Olujic Z, Kamerbeek AB, de Graauw J. A corrugation geometry based model for efficiency of structured distillation packing. Chem Eng Process 1999;38(4-6):683-95.
[56] Hanley B, Chen C-C. New mass-transfer correlations for packed towers. AIChE J 2012;58(1):132–52.
[57] Hanley B, Chen C-C. Corrections to "New mass transfer correlations for packed towers". AIChE J 2012;58(7):2290–3.
[58] Vivian JE, King CJ. The mechanism of liquid-phase resistance to gas absorption in a packed column. AIChE J 1964;10(2):221-7.
[59] Dontula P, Macosko CW, Scriven LE. Does the Viscosity of Glycerin Fall at High Shear Rates? Ind Eng Chem Res 1999;38(4):1729-35.
[60] Cullinane JT. Thermodynamics and Kinetics of Aqueous Piperazine with Potassium Carbonate for Carbon Dioxide Absorption. Ph.D. Dissertation. USA: The University of Texas at Austin; 2005.
[61] Tsai RE. Mass Transfer Area of Structured Packing. Ph.D. Dissertation. USA: The University of Texas at Austin; 2010.
[62] Chen X. Carbon Dioxide Thermodynamics, Kinetics, and Mass Transfer in Aqueous Piperazine Derivatives and Other Amines. Ph.D. Dissertation. USA: The University of Texas at Austin; 2011.
[63] Tsai RE, Schultheiss P, Kettner A, Lewis JC, Seibert AF, Eldridge RB, Rochelle GT. Influence of surface tension on effective packing area. Ind Eng Chem Res 2008;47(4):1253–60.
[64] Rochelle GT, Du Y, Fine N, Frailie P, Fulk S, Li L, Lin Y-J, Namjoshi O, Nielsen P, Sachde D, Sherman B, Song D, Walters M, Wang C. "CO_2 Capture by Aqueous Absorption, First Quarterly Progress Report 2014." Texas Carbon Management Program. The University of Texas at Austin. 2014.
[65] Cheng N-S. Formula for the Viscosity of a Glycerol−Water Mixture. Ind Eng Chem Res 2008;47(9):3285–8.
[66] Zaoui-Djelloul-Daouadji M, Negadi A, Mokbel I, Negadi L. (Vapor-liquid) equilibria and excess Gibbs free energy functions of (ethanol+glycerol), or (water+glycerol) binary mixtures at several temperatures. J Chem Thermodyn 2014;69(0):165–71.

[67] Buzek J, Jaroszynski M. Determination of Henry's constant for the ternary system: carbon dioxide-glycerol-water. Inzynieria Chemiczna 1973;3(3):449–60.
[68] Laddha SS, Diaz JM, Danckwerts PV. The nitrous oxide analogy: the solubilities of carbon dioxide and nitrous oxide in aqueous solutions of organic compounds. Chem Eng Sci 1981;36(1):228–9.
[69] Rischbieter E, Schumpe A, Wunder V. Gas Solubilities in Aqueous Solutions of Organic Substances. J Chem Eng Data 1996;41(4):809–12.
[70] Vazquez Una G, Chenlo Romero F, Pereira Goncalves G, Peaguda Lorenzo J. Solubility of CO_2 in Aqueous solutions of Saccharose, Glucose, Fructose, and Glycerin. J Chem Eng Data 1994;39(4):639–42.
[71] Ostonen A, Sapei E, Uusi-Kyyny P, Klemelä A, Alopaeus V. Measurements and modeling of CO_2 solubility in 1,8-diazabicyclo-[5.4.0]-undec-7-ene—Glycerol solutions. Fluid Phase Equilib 2014;374(0):25–36.
[72] Barrett PVL. Gas Absorption on a Sieve Plate. Ph.D. Dissertation: University of Cambridge; 1966.
[73] Pohorecki R, Moniuk W. Kinetics of reaction between carbon dioxide and hydroxyl ions in aqueous electrolyte solutions. Chem Eng Sci 1988;43(7):1677–84.
[74] D'Errico G, Ortona O, Capuano F, Vitagliano V. Diffusion Coefficients for the Binary System Glycerol + Water at 25 °C. A Velocity Correlation Study. J Chem Eng Data 2004;49(6):1665–70.
[75] Garner FH, Marchant PJM. Diffusivities of associated compounds in water. Trans Inst Chem Eng 1961;39(1):397–408.
[76] Grossmann T, Winkelmann J. Ternary Diffusion Coefficients of Glycerol + Acetone + Water by Taylor Dispersion Measurements at 298.15 K. J Chem Eng Data 2005;50(4):1396–403.
[77] Nishijima Y, Oster G. Diffusion in Glycerol-Water Mixture. Bull Chem Soc Jpn 1960;33(12):1649–51.
[78] Riede T, Schlunder EU. Diffusivities of the ternary liquid mixture 2-propanol-water-glycerol and three-component mass transfer in liquids. Chem Eng Sci 1991;46(2):609–17.
[79] Rutten PWM. Diffusion in liquids. C298751 Dissertation. Ann Arbor: Technische Universiteit Delft (The Netherlands); 1992.
[80] Ternström G, Sjöstrand A, Aly G, Jernqvist Å. Mutual Diffusion Coefficients of Water + Ethylene Glycol and Water + Glycerol Mixtures. J Chem Eng Data 1996;41(4):876–9.
[81] Brignole EA, Echarte R. Mass transfer in laminar liquid jets. Measurement of diffusion coefficients. Chem Eng Sci 1981;36(4):695–703.
[82] Calderbank PH. Physical rate processes in industrial fermentation -- 2. Mass transfer coefficients in gas-liquid contacting with and without mechanical agitation. Trans Inst Chem Eng 1959;37(3):173–85.
[83] Diaz JM, Vega A, Coca J. Diffusivities of carbon dioxide and nitrous oxide in aqueous alcohol solutions. J Chem Eng Data 1988;33(1):10–2.
[84] Kreulen H. Microporous hollow fibre membrane modules as gas-liquid contactors. Part 1. Physical mass transfer processes. J Membr Sci 1993;78(3):197–216.
[85] Kreulen H, Smolders CA, Versteeg GF, van Swaaij WPM. Microporous hollow fibre membrane modules as gas-liquid contactors Part 2. Mass transfer with chemical reaction. J Membr Sci 1993;78(3):217–38.
[86] Onda K, Okamoto T, Yamaji Y. Measurement of the diffusivities of CO_2 in liquids by liquid jets. Chem Eng (NY) 1960;24(12):918–25.
[87] Thomas WJ, Adams MJ. Measurement of the diffusion coefficients of carbon dioxide and nitrous oxide in water and aqueous solutions of glycerol. Trans Faraday Soc 1965;61(0):668–73.
[88] Rochelle GT, Du Y, Fine N, Frailie P, Fulk S, Li L, Lin Y-J, Namjoshi O, Nielsen P, Sachde D, Sherman B, Song D, Walters M, Wang C. "CO_2 Capture by Aqueous Absorption, Second Quarterly Progress Report 2014." Texas Carbon Management Program. The University of Texas at Austin. 2014.
[89] Carrillo-Nava E, Dohnal V, Costas M. Infinite dilution activity coefficients for toluene in aqueous solutions of the protein stabilizers glycerol, ethylene glycol, glucose, sucrose and trehalose. J Chem Thermodyn 2002;34(4):443–56.
[90] Pigford RL. Counter-diffusion in a wetted wall column. Ph.D. Dissertation. USA: The University of Illinois at Urbana Champaign; 1942.
[91] Bird RB, Stewart WE, Lightfoot EN. Transport Phenomena. ed. New York: John Wiley & Sons; 2002.

Available online at www.sciencedirect.com

ScienceDirect

Energy Procedia 00 (2013) 000–000

Energy Procedia

www.elsevier.com/locate/procedia

GHGT-12

Dynamic Modeling, Validation, and Time Scale Decomposition of an Advanced Post-Combustion Amine Scrubbing Process

Matthew S. Walters[a], Thomas F. Edgar,[a,b], Gary T. Rochelle[a]*

[a]*McKetta Department of Chemical Engineering, The University of Texas at Austin, 200 E Dean Keaton St. Stop C0400, Austin 78712-1589, USA*
[b]*Energy Institute, The University of Texas at Austin, 2304 Whitis Ave. Stop C2400, Austin 78712-1718, USA*

Abstract

Post-combustion amine scrubbing is a highly integrated process that uses extensive material and energy recycling to reduce costs and increase efficiency. As a result, the process variables exhibit a fast time scale at the unit level associated with the large recycle flows and a slow time scale at the plant level associated with the small feed and product flows. A reduced order model was developed for the system, and the material balances were demonstrated to be in nonstandard singularly perturbed form. Only the stripper vapor mole fractions evolve exclusively on the slow time scale in this model form; all other model states have both slow and fast components. By applying a variable transformation, the model is arranged into standard singularly perturbed form. The slow states in this form are the overall process material hold-ups as well as the stripper vapor mole fractions. An effective control strategy for the process should control the CO_2 removal rate and overall system inventory on the slow time scale using the small stripper overhead flowrate and a cascaded level setpoint controller, respectively. We show that attempting to control CO_2 removal rate with the large solvent recycle rate will likely lead to an ill-conditioned controller.

Selection and peer-review under responsibility of GHGT.

Keywords: Singular Perturbation; Reduced Order Modeling; Time Scale Multiplicity

1. Introduction

The general trend in the chemical industry is the development of increasingly integrated process designs that use extensive material and energy recycling as well as minimize the overall chemical inventory. With large capital and operating costs, post-combustion amine scrubbing adheres to this trend. After the amine solvent has absorbed CO_2

* Corresponding author. Tel.: +1-512-471-7230; fax: +1-512-471-7060.
E-mail address: gtr@che.utexas.edu

1876-6102
Selection and peer-review under responsibility of GHGT.

from the flue gas, it is regenerated at high temperature and completely recycled back to the absorber. Most of the sensible heat from the thermal swing process is recovered either through direct contact packing or a cross heat exchanger. Designing an effective plantwide control strategy of processes with recycle streams is often complicated and is much less studied than systems without recycle [1]. An early solution in the process industry to reduce disturbance propagation in recycle systems was to install large surge tanks between interacting process units [2]. Large surge tanks are unlikely to be acceptable in amine scrubbing because of the added capital cost, along with oxidation, solid solubility, and safety issues associated with large amine hold-ups. Therefore, any storage tank in the plant will not be able to effectively dampen disturbances that propagate through the recycle streams.

In order to develop a plantwide control strategy for recycle systems with minimal inventory, the multiple time scale behavior that emerges as a result of material and energy recycling must be taken into consideration. There are two distinct time scales that exist in the amine scrubbing process dynamics: a fast time scale at the unit level associated with the large recycle flows and a slow time scale at the process level associated with the small feed and product flows. The time scales of the process variable will be identified using singular perturbation theory. Standard singularly perturbed model form is shown in Equations 1–2, where $\boldsymbol{\zeta}$ represents the slow variables, $\boldsymbol{\eta}$ the fast variables, and ε is some small parameter. Arranging the model of the amine scrubbing system in this form allows for the systematic identification of slow and fast variables. In the limit where $\varepsilon \rightarrow 0$, the left hand side of Equation 2 becomes zero and the fast variables are approximately at steady state [3].

$$\dot{\boldsymbol{\zeta}} = f(\boldsymbol{\zeta}, \boldsymbol{\eta}) \tag{1}$$

$$\varepsilon\dot{\boldsymbol{\eta}} = g(\boldsymbol{\zeta}, \boldsymbol{\eta}) \tag{2}$$

The objective of this work is to develop a reduced order model (ROM) with adjustable parameters that adequately represents the physical behavior of the true plant. The ROM is used for process simulation and time scale analysis. The ultimate goal of the ROM is its implementation in a model-based controller, which will be considered in future work.

Nomenclature

a	Wetted area [m^2/m^3]
C	Molar concentration [mol/m^3]
Cp	Specific heat capacity [kJ/mol·K]
D	Diameter [m]
d	Disturbance [-]
F	Molar flowrate [mol/s]
$\widehat{H}$	Specific enthalpy [kJ/mol]
h	Liquid hold-up in packing [m^3/m^3]
K	Overall mass transfer coefficient [$mol/Pa{\cdot}m^2{\cdot}s$]
K^p	Proportional gain constant [varies]
L	Length [m]
l	Level [m]
M	Molar amount [mol]
N	Transfer rate [amount/s]
Ns	Total number of column stages [-]
P	Pressure [Pa]
P^*	Equilibrium pressure of the liquid [Pa]
p_{CC}	Chilton-Colburn parameter [$kJ/m^3{\cdot}K$]
Q_s	Steam heat duty [kW]
R	Gas constant [$m^3{\cdot}Pa/mol{\cdot}K$]
Rc	Recycle number [-]
T	Temperature [K]

UA	Overall heat transfer coefficient [kW/K]
u	Normalized manipulated input [-]
vf	Vapor fraction [mol/mol]
$\boldsymbol{x}$	State vector [varies]
x	Liquid apparent mole fraction [mol/mol]
y	Vapor mole fraction [mol/mol]
Greek	
ΔH	Specific heat of phase change [kJ/mol]
ε	Small perturbation parameter [-]
$\boldsymbol{\zeta}$	Vector of slow variables [varies]
$\boldsymbol{\eta}$	Vector of fast variables [varies]
ω	$\mathcal{O}(1)$ quantity [-]
Subscripts	
i	Component (CO_2, H_2O, PZ, N_2, or O_2)
k	Column stage number
H	Enthalpy
sp	Setpoint
Superscripts	
L	Liquid phase
s	Steady state
V	Vapor phase

2. Reduced Order Model Development and Validation

The model developed in this work is for the advanced amine scrubbing process using 8 molal (m) aqueous piperazine (PZ) described in Fig. 1 [4]. The ROM is nonlinear and based on first principles. Simplifications (discussed in the following paragraphs) have been made to the full first principles model, which results in a ROM that is appropriate for time scale analysis and use in a model-based controller. The ROM differential equations are given in Appendix A.

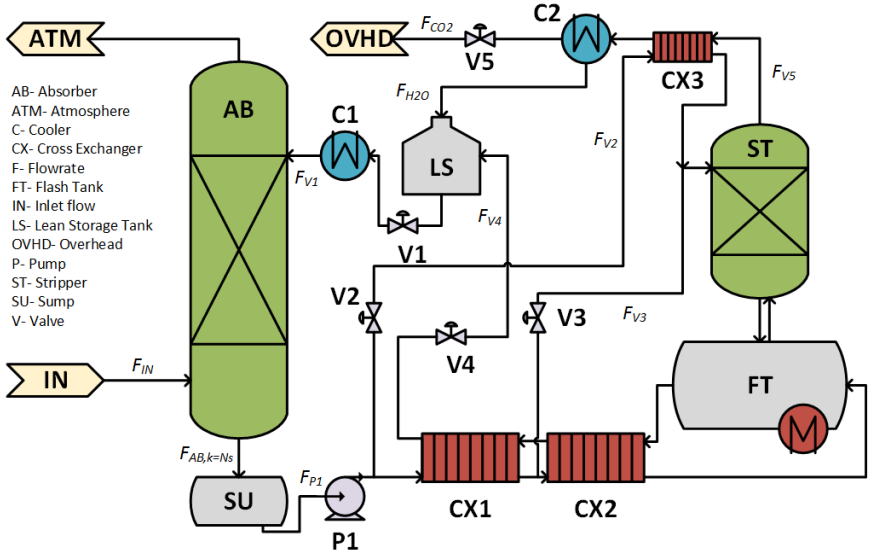

Fig. 1. Process flow diagram with advanced flash stripper configuration [4].

The absorber (AB) and stripper (ST), which contain structured packing, are modeled using constant rate-based mass and energy transfer coefficients that are multiplied by a driving force between the bulk liquid and bulk vapor (Equations 3–4).

$$N_i = K_i a \left(\frac{\pi D^2 L}{4}\right)(P_i - P_i^*),\ i = CO_2, H_2O \tag{3}$$

$$N_H = p_{CC}(K_{H2O}a)\left(\frac{\pi D^2 L}{4}\right)(RT^V)(T^V - T^L) \tag{4}$$

In the AB, the CO_2 mass transfer coefficient implicitly accounts for the rate enhancement due to chemical reaction. Equation 3 shows that bulk convection between the liquid and vapor is ignored. While ignoring bulk convection is a good assumption in the AB since the gas is mostly inert, it may cause deviation from the true

Table 1. ROM inputs, disturbances, and parameters.

Inputs and Disturbances	Thermo and Transport Parameters	Physical Parameters
$F_{V1}^L = 139{,}900\ mol/s$	$Cp^L = 0.11\ kJ/mol \cdot K$	$C^L = 35{,}700\ mol/m^3$
$F_{V2}^L = 0.15 \cdot F_{V1}^L$	$Cp^V = 0.03\ kJ/mol \cdot K$	$C_{AB}^V = 38\ mol/m^3$
$F_{V3}^L = 0.20 \cdot F_{V1}^L$	$\Delta H_{CO2} = 70\ kJ/mol$	$C_{ST}^V = 350\ mol/m^3$
$F_5^V = 2{,}920\ mol/s$	$\Delta H_{H2O} = 40\ kJ/mol$	$D_{AB} = 18\ m$
$Q_s = 385000\ kW$	$K_{AB,CO2}a = 4.83\ X\ 10^{-4}\ mol/Pa \cdot m^3 \cdot s$	$D_{SU} = 18\ m$
$F_{IN} = 18850\ mol/s$	$K_{AB,H2O}a = 1.16\ X\ 10^{-2}\ mol/Pa \cdot m^3 \cdot s$	$D_{FT} = 10.6\ m$
$T_{IN}^V = 313.15\ K$	$K_{ST,CO2}a = 9.66\ X\ 10^{-4}\ mol/Pa \cdot m^3 \cdot s$	$D_{ST} = 3\ m$
$y_{CO2,IN} = 0.147$	$K_{ST,H2O}a = 1.16\ X\ 10^{-2}\ mol/Pa \cdot m^3 \cdot s$	$D_{LS} = 10\ m$
$y_{N2,IN} = 0.752$	$p_{AB,CC} = 0.236\ kJ/m^3 \cdot K$	$h_{AB} = 0.05\ m^3/m^3$
$y_{O2,IN} = 0.027$	$p_{ST,CC} = 0.236\ kJ/m^3 \cdot K$	$h_{ST} = 0.05\ m^3/m^3$
$y_{H2O,IN} = 0.074$	$UA_{CX1} = 600{,}000\ kW/K$	$L_{AB} = 4.72\ m$
$l_{SU,sp}^L = 3\ m$	$UA_{CX2} = 300{,}000\ kW/K$	$L_{ST} = 2\ m$
$l_{FT,sp}^L = 3\ m$	$UA_{CX3} = 4{,}500\ kW/K$	$Ns_{AB} = 10$
		$Ns_{ST} = 4$
		$P_{AB} = 1\ bar$

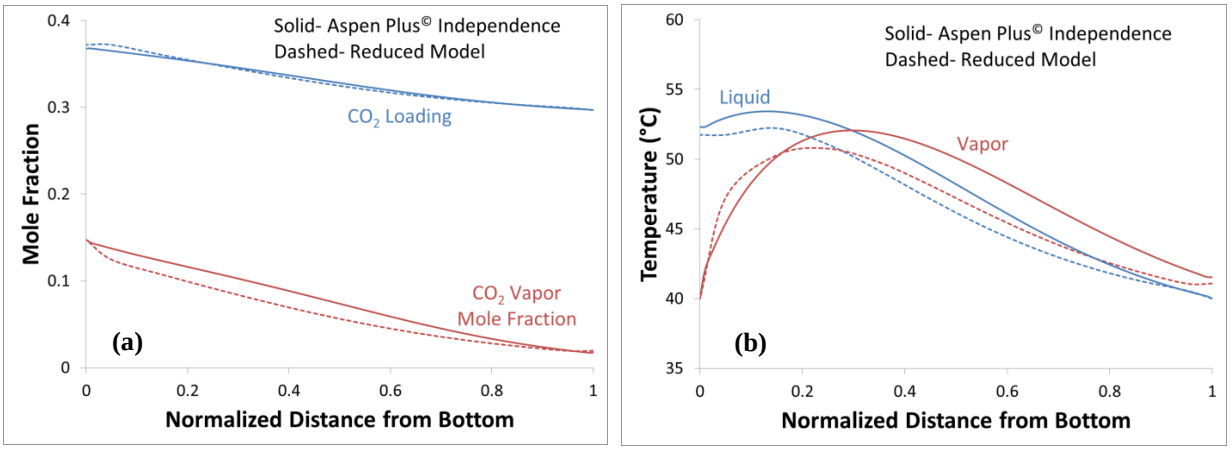

Fig. 2. Comparison of absorber (a) mole fraction and (b) temperature profiles for rigorous Aspen Plus® model [6] and ROM.

behavior of the plant in the ST. The heat transfer coefficient in Equation 4 is proportional to the H_2O mass transfer coefficient through the Chilton-Colburn analogy. The AB and ST packing are coarsely discretized into well-mixed segments for material and energy balances, which greatly reduces the number of model states compared to a finely discretized plug-flow regime. Liquid and vapor molar hold-ups at each segment are assumed to be constant, eliminating the total material balance in the columns.

Tanks, including the absorber sump (SU), flash tank (FT), and lean storage tank (LS) are treated as well-mixed equilibrium stages within the system. They each have material and energy balances on only the liquid hold-up. The main cross exchangers (CX1 and CX2) are assumed to exchange only sensible heat. This is likely a bad assumption for CX2 since flashing is known to occur in the rich solvent on the cold side of the exchanger. The ST and bypass exchanger (CX3) allow energy to be recovered from water vaporized in the FT by heating the bypass streams. It is assumed that heat is applied directly to the FT using steam from the power plant; the steam provides some sensible heat ($\Delta T \sim 5$ °C) and most of the latent heat requirement of the process. The trim cooler (C1) and overhead condenser (C2) are treated as perfect heat exchangers: the lean solvent fed to the absorber is always at 40 °C and all of the water vapor is condensed out of the overhead gas.

Everywhere in the system, PZ is assumed to be nonvolatile and N_2 and O_2 are treated as insoluble components. Thermophysical parameters such as molar density, heat capacity, and heat of absorption are assumed to be constant. Enthalpy and vapor-liquid equilibrium are calculated using the procedure described in Walters et al. [5]. Table 1 summarizes the parameters used in the ROM. The transfer coefficients in the AB are determined by minimizing the square error of the CO_2 mole fraction and temperature profiles between the ROM and a rigorous Aspen Plus® model [6] under the same conditions using 50 stages. In a true plant, uncertain parameters such as these could be found through a system identification. The AB column profiles of the Aspen Plus® and ROM are compared in Fig. 2. The ROM achieves an 86% CO_2 removal rate, while the Aspen Plus® model is designed for 90%. The largest absolute error in the temperature profile is 2.9 °C.

3. Time Scale Analysis

3.1. Material Recycle Number

A time scale analysis was performed on the ROM of the amine process based on the work of Baldea and Daoutidis [7]. Only the material balances have been considered here; energy recycle will be addressed in future work. Fig. 3 shows a rate-based AB where CO_2 is transferring into the solvent from the flue gas at all k segments. The recycle flowrate, F_{V1}, is much greater than the amount of CO_2 fluxing into the system. Furthermore, the flowrate of CO_2 in the lean solvent entering the AB is higher than the flowrate of CO_2 in the flue gas. A material recycle number, Rc, is defined in Equation 5 as the ratio of the large recycle flowrate to the small feed flowrate.

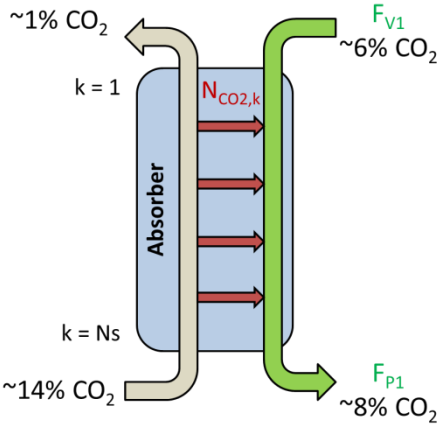

Fig. 3. CO_2 transfers from the flue gas to the liquid at each k segment of the column, but this flow is relatively small compared to the total liquid flow into the column.

$$Rc = \frac{1}{\varepsilon} = \frac{{F_{V1}}^s}{{N_{CO2,k=Ns}}^s} \tag{5}$$

The CO_2 flux is generally expected to be greatest at the bottom of the column, so the flux at the bottom segment is selected for the recycle number definition. An important implication of this selection is that the transfer rates at other segments of the column are of the same order of magnitude or less. The recycle number is substituted into the ROM described in Appendix A. For convenience, other dimensionless quantities have been defined in Table 2.

Table 2. Scaled quantities substituted into ROM.

Manipulated Inputs	Other Parameters
$u_1 = \frac{F_{V1}^L}{{F_{V1}^L}^s}$	$\omega_2 = \frac{{F_{V2}^L}^s}{{F_{V1}^L}^s}$
$u_2 = \frac{F_{V2}^L}{{F_{V2}^L}^s}$	$\omega_3 = \frac{{F_{V3}^L}^s}{{F_{V1}^L}^s}$
$u_3 = \frac{F_{V3}^L}{{F_{V3}^L}^s}$	$\omega_4 = \frac{{F_{V4}^L}^s}{{F_{V1}^L}^s}$
$u_4 = \frac{F_{V4}^L}{{F_{V4}^L}^s}$	$\omega_{AB,CO2,k} = \frac{{N_{AB,CO2,k}}^s}{{N_{AB,CO2,k=Ns}}^s}$
$u_5 = \frac{F_5^V}{{F_5^V}^s}$	$d_{AB,i,k} = \frac{N_{AB,i,k}}{{N_{AB,i,k}}^s}$
$u_p = \frac{F_{P1}^L}{{F_{P1}^L}^s}$	

3.2. Nonstandard Singularly Perturbed Model

After making the substitutions from Section 3.1, the model takes the form of Equation 6:

$$\dot{\boldsymbol{x}} = \boldsymbol{f}(\boldsymbol{x}) + \boldsymbol{G}_{sm}(\boldsymbol{x})\boldsymbol{u}_{sm} + \frac{1}{\varepsilon}\boldsymbol{G}_{lg}(\boldsymbol{x})\boldsymbol{u}_{lg} \tag{6}$$

where $\boldsymbol{x} \in \mathbb{R}^n$ is the state vector, $\boldsymbol{u}_{sm} \in \mathbb{R}^{m_{sm}}$ are the small inlet or outlet flows, $\boldsymbol{u}_{lg} \in \mathbb{R}^{m_{lg}}$ are the large internal flows, $\boldsymbol{f} \in \mathbb{R}^n$ is a vector of small flows which are a functions of the states, and $\boldsymbol{G}_{sm}$ and $\boldsymbol{G}_{lg}$ are matrices of appropriate dimensions. Equation 6 is referred to as nonstandard singularly perturbed form. Unlike the standard form given in Equations 1–2, the variables are not explicitly separated into slow and fast time scales in the nonstandard form. Equation 7–20 show the amine scrubbing ROM from Appendix A (excluding the energy balances and AB vapor material balances) in the form of Equation 6.

$$\dot{x}_{AB,CO2,k} = \frac{1}{M_{AB}^L}\Big[{N_{AB,CO2,k=Ns}}^s d_{AB,CO2,k}\omega_{AB,CO2,k} + x_{AB,CO2,k-1}\textstyle\sum_{k=1}^{k-1} N_{AB,k} - x_{AB,CO2,k}\sum_{k=1}^{k} N_{AB,k} + \frac{1}{\varepsilon}u_1 {N_{AB,CO2,k=Ns}}^s\left(x_{AB,CO2,k-1} - x_{AB,CO2,k}\right)\Big] \tag{7}$$

$$\dot{x}_{AB,PZ,k} = \frac{1}{M_{AB}^L}\Big[x_{AB,PZ,k-1}\textstyle\sum_{k=1}^{k-1} N_{AB,k} - x_{AB,PZ,k}\sum_{k=1}^{k} N_{AB,k} + \frac{1}{\varepsilon}u_1 {N_{AB,CO2,k=Ns}}^s\left(x_{AB,PZ,k-1} - x_{AB,PZ,k}\right)\Big] \tag{8}$$

$$\dot{x}_{ST,CO2,k} = \frac{1}{M_{ST}^L}\Big[N_{ST,CO2,k} + x_{ST,CO2,k-1}\textstyle\sum_{k=1}^{k-1} N_{ST,k} - x_{ST,CO2,k}\sum_{k=1}^{k} N_{ST,k} + \frac{1}{\varepsilon}{N_{AB,CO2,k=1}}^s\left(x_{ST,CO2,k-1} - x_{ST,CO2,k}\right)(u_2\omega_2 + u_3\omega_3)\Big] \tag{9}$$

$$\dot{x}_{ST,PZ,k} = \frac{1}{M_{ST}^{L}}\left[x_{ST,PZ,k-1}\sum_{k=1}^{k-1}N_{ST,k} - x_{ST,PZ,k}\sum_{k=1}^{k}N_{ST,k} + \frac{1}{\varepsilon}N_{AB,CO2,k=1}{}^{s}\left(x_{ST,PZ,k-1} - x_{ST,PZ,k}\right)\left(u_2\omega_2 + u_3\omega_3\right)\right] \quad (10)$$

$$\dot{y}_{ST,CO2,k} = \frac{1}{M_{ST,k}^{V}}\left[\left(y_{ST,CO2,k+1} - y_{ST,CO2,k}\right)\left(u_5 F_{V5}^{V\ s} + \sum_{k=1}^{k-1}N_{ST,k}\right) + y_{ST,CO2,k+1}N_{ST,k} - N_{ST,CO2,k}\right] \quad (11)$$

$$\dot{l}_{SU}^{L} = \frac{4}{\pi {D_{SU}}^2 C^L}\left[\sum_{k=1}^{N_s}N_{AB,k} + \frac{1}{\varepsilon}N_{AB,CO2,k=Ns}{}^{s}\left(u_1 - \omega_p u_P\right)\right] \quad (12)$$

$$\dot{x}_{SU,CO2} = \frac{4}{\pi {D_{SU}}^2 C^L l_{SU}^{L}}\left[\sum_{k=1}^{N_s}N_{AB,k}\left(x_{AB,CO2,k=N_s} - x_{SU,CO2}\right) + \frac{1}{\varepsilon}N_{AB,CO2,k=Ns}{}^{s}u_1\left(x_{AB,CO2,k=N_s} - x_{SU,CO2}\right)\right] \quad (13)$$

$$\dot{x}_{SU,PZ} = \frac{4}{\pi {D_{SU}}^2 C^L l_{SU}^{L}}\left[\sum_{k=1}^{N_s}N_{AB,k}\left(x_{AB,PZ,k=N_s} - x_{SU,PZ}\right) + \frac{1}{\varepsilon}N_{AB,CO2,k=Ns}{}^{s}u_1\left(x_{AB,PZ,k=N_s} - x_{SU,PZ}\right)\right] \quad (14)$$

$$\dot{l}_{FT}^{L} = \frac{4}{\pi {D_{FT}}^2 C^L}\left[-u_5 F_{V5}^{V\ s} + \frac{1}{\varepsilon}N_{AB,CO2,k=1}{}^{s}\left(\omega_p u_p - \omega_4 u_4\right)\right] \quad (15)$$

$$\dot{x}_{FT,CO2} = \frac{4}{\pi {D_{FT}}^2 C^L l_{FT}^{L}}\left[\left(x_{ST,CO2,k=Ns} - y_{FT,CO2}\right)\sum_{k=1}^{N_s}N_{ST,k} + \left(x_{FT,CO2} - y_{FT,CO2}\right)u_5 F_{V5}^{V\ s} + \frac{1}{\varepsilon}N_{AB,CO2,k=1}{}^{s}\left(\left(x_{SU,CO2} - x_{FT,CO2}\right)u_p\omega_p + \left(x_{ST,CO2,k=Ns} - x_{SU,CO2}\right)\left(u_2\omega_2 + u_3\omega_3\right)\right)\right] \quad (16)$$

$$\dot{x}_{FT,PZ} = \frac{4}{\pi {D_{FT}}^2 C^L l_{FT}^{L}}\left[x_{ST,PZ,k=Ns}\sum_{k=1}^{N_s}N_{ST,k} + x_{FT,PZ}u_5 F_{V5}^{V\ s} + \frac{1}{\varepsilon}N_{AB,CO2,k=1}{}^{s}\left(\left(x_{SU,PZ} - x_{FT,PZ}\right)u_p\omega_p + \left(x_{ST,PZ,k=Ns} - x_{SU,PZ}\right)\left(u_2\omega_2 + u_3\omega_3\right)\right)\right] \quad (17)$$

$$\dot{l}_{LS}^{L} = \frac{4}{\pi {D_{LS}}^2 C^L}\left[F_{H2O}^{L} + \frac{1}{\varepsilon}N_{AB,CO2,k=1}{}^{s}\left(\omega_4 u_4 - u_1\right)\right] \quad (18)$$

$$\dot{x}_{LS,CO2} = \frac{4}{\pi {D_{LS}}^2 C^L l_{LS}^{L}}\left[-x_{LS,CO2}F_{H2O}^{L} + \frac{1}{\varepsilon}N_{AB,CO2,k=1}{}^{s}\omega_4 u_4\left(x_{FT,CO2} - x_{LS,CO2}\right)\right] \quad (19)$$

$$\dot{x}_{LS,PZ} = \frac{4}{\pi {D_{LS}}^2 C^L l_{LS}^{L}}\left[-x_{LS,PZ}F_{H2O}^{L} + \frac{1}{\varepsilon}N_{AB,CO2,k=1}{}^{s}\omega_4 u_4\left(x_{FT,PZ} - x_{LS,PZ}\right)\right] \quad (20)$$

In the context of Equation 6, $\boldsymbol{u}_{sm} = u_5$ and $\boldsymbol{u}_{lg} = \begin{bmatrix}u_1 & u_2 & u_3 & u_4 & u_p\end{bmatrix}^T$. The only states that are exclusively slow ($\boldsymbol{G}_{lg} = \boldsymbol{0}$) are the ST vapor mole fractions in Equation 11. All other state variables have both slow and fast components. Fig. 3 demonstrates the pseudo-open loop response of the process to a 10% step reduction in flue gas rate after one hour of steady state operation. The total material balances (Equations 12, 15, and 18) render the system open loop unstable, so perfect level control is assumed in the SU, FT, and LS during the simulation. It is also assumed that the water makeup rate is perfectly controlled so the LS concentration is always 8 m PZ. The AB liquid mole fractions (Fig. 3a) have an initial fast response at the unit level as the amount of CO_2 entering the system is decreased. The fast response is followed by a slow transient period as the system approaches a new steady state. The ST vapor mole fractions (Fig. 3b) are only affected by the small outlet flowrate and therefore only demonstrate a slow response to the step change.

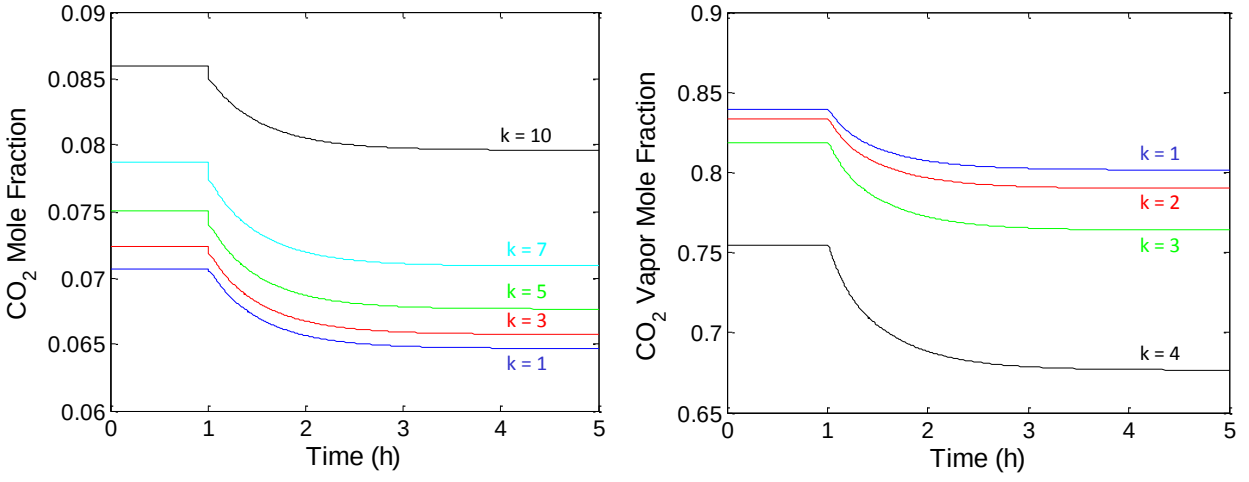

(a) (b)

Fig. 3. Pseudo-open loop response to a 10% decrease in flue gas flow after one hour for (a) the AB liquid mole fractions and (b) the ST vapor mole fractions at segment k of the column.

3.3. Standard Singularly Perturbed Model

In model-based control of a process with time scale multiplicity, the process model needs to be explicitly separated into fast and slow variables [8]. The SU, FT, and LS unit inventories must be stabilized based on the fast time scale, so it is assumed that there is a linear state feedback controller for the tank levels that manipulates the tank effluent flow. Since the energy balance has not yet been taken into consideration, it is also assumed that there is a state feedback law for the exiting cross exchange temperatures ($T_{CX1,h}$ and $T_{CX3,h}$) that manipulates the bypass flowrates. The feedback control laws are given in Equations 21–25, which show that the large flowrates are now a function of the states.

$$u_1 = 1 - K_1^p\left(l_{LS} - l_{LS,sp}\right) \tag{21}$$

$$u_2 = 1 - K_2^p\left(T_{CX3,h}^L - T_{CX3,h,sp}^L\right) \tag{22}$$

$$u_3 = 1 - K_3^p\left(T_{CX3,h}^L - T_{CX3,h,sp}^L\right) \tag{23}$$

$$u_4 = 1 - K_4^p\left(l_{FT} - l_{FT,sp}\right) \tag{24}$$

$$u_p = 1 - K_p^p\left(l_{SU} - l_{SU,sp}\right) \tag{25}$$

It is assumed that the matrix $\boldsymbol{G}_{lg}(\boldsymbol{x})$ can be decomposed according to Equations 26:

$$\boldsymbol{G}_{lg}(\boldsymbol{x}) = \boldsymbol{B}(\boldsymbol{x})\widetilde{\boldsymbol{G}}_{lg}(\boldsymbol{x}) \tag{26}$$

where $\boldsymbol{B} \in \mathbb{R}^{n\times(n-3-Ns_{ST})}$ is a full column rank matrix and $\widetilde{\boldsymbol{G}}_{lg} \in \mathbb{R}^{(n-3-Ns_{ST})\times m_{lg}}$ is a matrix with linearly independent rows [9]. The variable transformation **T(x)** in Equation 27 is applied to explicitly separate the ROM into slow and fast states:

$$\begin{bmatrix}\boldsymbol{\zeta}\\ \boldsymbol{\eta}\end{bmatrix} = \boldsymbol{T}(\boldsymbol{x}) = \begin{bmatrix} M_{total} \\ M_{total,CO2} \\ M_{total,PZ} \\ y_{ST,CO2,k=1} \\ \vdots \\ y_{ST,CO2,k} \\ \vdots \\ y_{ST,CO2,k=Ns} \\ \widetilde{\boldsymbol{G}}_{lg}(\boldsymbol{x})\boldsymbol{u}_{lg}(\boldsymbol{x}) \end{bmatrix} \tag{27}$$

where $\boldsymbol{\zeta} \in \mathbb{R}^{3+Ns_{ST}}$ are the slow states, $\boldsymbol{\eta} \in \mathbb{R}^{n-3-Ns_{ST}}$ are the fast states, and the subscript total denotes the total system molar hold-up. This transformation allows the ROM to be arranged in the form of Equations 1–2, and shows that the total molar hold-ups also evolve on the slow time scale in addition to the stripper vapor mole fractions. Fig. 4 demonstrates the step response of the total system CO_2 hold-up has only a slow component. The steady state liquid residence times in the AB, SU, FT, ST, and LS are 0.3, 3.2, 1.1, 0.02, and 0.9 minutes, respectively, while Fig. 4 shows that the time constant of total CO_2 inventory is ~32 minutes. The total plant inventory time constant is an order of magnitude higher than the individual unit operation residence times because of the material recycle occurring in the process.

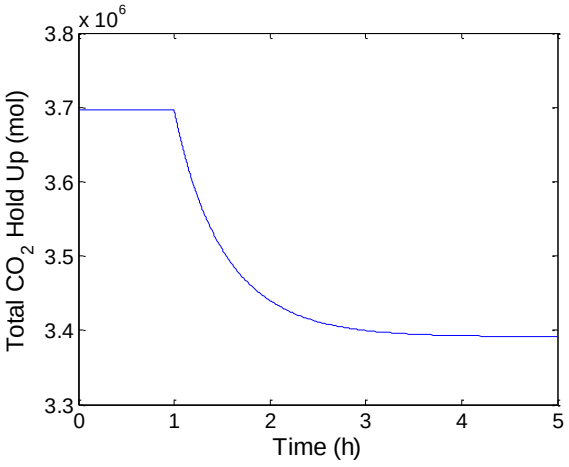

Fig. 4. Pseudo-open loop response to a 10% decrease in flue gas flow after one hour for the total CO_2 inventory.

4. Proposed Control Structure

The overall control objective of the amine scrubbing process is to maintain a desired CO_2 removal rate while minimizing energy use. Additionally, the total material holdup must be stabilized. Based on the singularly perturbed model form, both of these control objectives are related to the slow time scale. In the previous section, state feedback control laws were proposed for the large internal solvent flows in order to stabilize the system on the fast time scale. The only remaining manipulated variable for the slow time scale objectives is the stripper overhead flowrate (F_{V5}^{V}). F_{V5}^{V} is closely tied to the flowrate of CO_2 out of the process, so it should be used to control the removal rate. Since there are no more remaining manipulated variables, the total inventory setpoint can be manipulated by changing the level setpoint on the LS. This structure cascades the fast time scale level control objective with the slow time scale total inventory objective.

Previous work has proposed controlling the removal rate with the large internal recycle flow [10]. However, this strategy will likely lead to an ill-conditioned controller based on the time scale analysis since the slow time scale has not been addressed. Oscillations in stripper pressure were observed by Ziaii when the removal rate was controlled

using the solvent flowrate [11]. The control structure proposed in this work is summarized in Table 3. A state space realization of the slow time scale for use in a model-based controller can be achieved by taking the limit $\varepsilon \rightarrow 0$ (corresponding to infinite recycle) in Equations 1–2. This control structure will be evaluated in future work.

Table 2. Scaled quantities substituted into ROM

Time Scale	Output Variable	Input Variable	Proposed Controller
Fast	Sump Level	Sump Effluent Flowrate (F_{P1})	Proportional
	Flash Tank Level	Recycle Flowrate (F_{V4})	Proportional
	Lean Storage Tank Level	Solvent Flowrate (F_{V1})	Proportional
Slow	Total Material Hold-up	Lean Storage Tank Level Setpoint ($l_{LS,sp}$)	Cascaded, Model-Based
	CO_2 Removal Rate	Stripper Overhead Flowrate (F_{V5})	Model-Based

5. Conclusions

Two time scales exist in the amine scrubbing process dynamics as a result of material recycling. The ROM developed for the time scale analysis and model-based control was compared to a rigorous Aspen Plus® Rate-Sep model. The temperature profile of the ROM is within 2.9 °C of Aspen Plus® model and CO_2 removal rate is within 4%. The time scale decomposition shows that the stripper vapor mole fractions and total system inventories evolve on the slow time scale only. Therefore the CO_2 removal rate and total material hold-up should be controlled using the small stripper overhead flow and fast time scale setpoints. Controlling CO_2 removal with the large solvent recycle flowrate will likely lead to oscillations in process variables.

Acknowledgments

The authors acknowledge the financial support of the Texas Carbon Management Program.

The authors declare the following competing financial interest(s): One author of this publication consults for Southern Company and for Neumann Systems Group on the development of amine scrubbing technology. The terms of this arrangement have been reviewed and approved by the University of Texas at Austin in accordance with its policy on objectivity in research. The authors have financial interests in intellectual property owned by the University of Texas that includes ideas reported in this paper.

Appendix A. Reduced Order Model Material and Energy Balances

The liquid side balances for the absorber are given in Equations 28–29, with the boundary conditions at k = 0 of $F^L_{AB,k=0} = F^L_{V1}$, $x_{AB,i,k=0} = x_{LS,i}$, and $\widehat{H}^L_{AB,k=0} = \widehat{H}^L_{LS}$. The vapor side balances are shown in Equations 30–31, with the boundary conditions at k = Ns + 1 of $F^V_{AB,k=Ns+1} = F^V_{IN}$, $y_{AB,i,k=Ns+1} = y_{IN,i}$, and $\widehat{H}^V_{AB,k=Ns+1} = \widehat{H}^V_{IN}$.

$$\dot{M}^L_{AB,i,k} = x_{AB,i,k-1}F^L_{AB,k-1} - x_{AB,i,k}F^L_{AB,k} + N_{AB,i,k},\ i = CO_2, PZ \tag{28}$$

$$\dot{T}^L_{AB,k} = \frac{1}{Cp^L M^L_{AB,k}}\left[\widehat{H}^L_{AB,k-1}F^L_{AB,k-1} - \widehat{H}^L_{AB,k}F^L_{AB,k} + N_{AB,H,k}\right] + \frac{1}{Cp^L}\left[(\Delta H_{CO2} - \Delta H_{H2O})\dot{x}_{AB,CO2,k} - \Delta H_{H2O}\dot{x}_{AB,PZ,k}\right] \tag{29}$$

$$\dot{M}^V_{AB,i,k} = y_{AB,i,k+1}F^V_{AB,k+1} - y_{AB,i,k}F^V_{AB,k} - N_{AB,CO2,k},\ i = CO_2, N_2, O_2 \tag{30}$$

$$\dot{T}^V_{AB,k} = \frac{1}{Cp^V M^V_{AB,k}}\left[\widehat{H}^V_{AB,k+1}F^V_{AB,k+1} - \widehat{H}^V_{AB,k}F^V_{AB,k} - N_{AB,H,k}\right] \quad (31)$$

The liquid side balances for the stripper are given in Equations 32–33, with the boundary conditions at k = 0 of $F^L_{ST,k=0} = F^L_{V2} + F^L_{V3}$, $x_{ST,i,k=0} = x_{SU,i}$, and $\widehat{H}^L_{AB,k=0} = (\widehat{H}^L_{CX3,c}F^L_{V2} + \widehat{H}^L_{CX1,c}F^L_{V3})/(F^L_{V2} + F^L_{V3})$. The vapor side balances are shown in Equations 34–35, with the boundary conditions at k = 0 of $F^V_{AB,k=0} = F^V_{V5}$ and at k = Ns + 1 of $y_{ST,i,k=Ns+1} = y_{FT,i}$ and $\widehat{H}^V_{ST,k=Ns+1} = \widehat{H}^V_{FT}$.

$$\dot{M}^L_{ST,i,k} = x_{ST,i,k-1}F^L_{ST,k-1} - x_{ST,i,k}F^L_{ST,k} + N_{ST,i,k},\ i = CO_2, PZ \quad (32)$$

$$\dot{H}^L_{ST,k} = \widehat{H}^L_{ST,k-1}F^L_{ST,k-1} - \widehat{H}^L_{ST,k}F^L_{ST,k} + N_{ST,H,k} \quad (33)$$

$$\dot{M}^V_{ST,CO2,k} = y_{ST,CO2,k+1}F^V_{ST,k+1} - y_{ST,CO2,k}F^V_{ST,k} - N_{ST,CO2,k} \quad (34)$$

$$\dot{H}^V_{ST,k} = \widehat{H}^V_{ST,k+1}F^V_{ST,k+1} - \widehat{H}^V_{ST,k}F^V_{ST,k} - N_{ST,H,k} \quad (35)$$

The material and energy balances for the sump, flash tank, and lean storage tank are all treated as well mixed liquid stages in Equations 36–44.

$$\dot{M}^L_{SU} = F^L_{AB,k=N_s} - F^L_{P1} \quad (36)$$

$$\dot{M}^L_{SU,i} = x_{AB,i,k=N_s}F^L_{AB,k=N_s} - x_{SU,i}F^L_{P1},\ i = CO_2, PZ \quad (37)$$

$$\dot{T}^L_{SU} = \frac{1}{Cp^L M^L_{SU}}\left[\widehat{H}^L_{AB,k=N_s}F^L_{AB,k=N_s} - \widehat{H}^L_{SU}F^L_{P1}\right] + \frac{1}{Cp^L}\left[(\Delta H_{CO2} - \Delta H_{H2O})\dot{x}_{SU,CO2} - \Delta H_{H2O}\dot{x}_{SU,PZ}\right] \quad (38)$$

$$\dot{M}^L_{FT} = F^L_{P1} - F^L_{V4} - F^V_{V5} \quad (39)$$

$$\dot{M}^L_{FT,i} = x_{SU,i}(F^L_{P1} - F^L_{V2} - F^L_{V3}) + x_{ST,i,k=Ns}F^L_{ST,k=Ns} - x_{FT,i}F^L_{V4} - y_{FT,i}\left(F^V_{ST,k=Ns} + N_{ST,k=N_s}\right),\ i = CO_2, PZ \quad (40)$$

$$\dot{T}^L_{FT} = \frac{1}{Cp^L M^L_{FT}}\left[\widehat{H}^L_{CX2,c}(F^L_{P1} - F^L_{V2} - F^L_{V3}) + \widehat{H}^L_{ST,k=Ns}F^L_{ST,k=Ns} - \widehat{H}^L_{FT}F^L_{V4} - \widehat{H}^V_{FT}\left(F^V_{ST,k=Ns} + N_{ST,k=N_s}\right) + Q_s\right] + \frac{1}{Cp^L}\left[(\Delta H_{CO2} - \Delta H_{H2O})\dot{x}_{FT,CO2} - \Delta H_{H2O}\dot{x}_{FT,PZ}\right] \quad (41)$$

$$\dot{M}^L_{LS} = F^L_{V4} + F^L_{H2O} - F^L_{V1} \quad (42)$$

$$\dot{M}^L_{LS,i} = x_{FT,i}F^L_{V4} - x_{LS,i}F^L_{V1},\ i = CO_2, PZ \quad (43)$$

$$\dot{T}^L_{LS} = \frac{1}{Cp^L M^L_{LS}}\left[\widehat{H}^L_{FT}F^L_{V4} + \widehat{H}^L_{H2O}F^L_{H2O} - \widehat{H}^L_{LS}F^L_{V1}\right] + \frac{1}{Cp^L}\left[(\Delta H_{CO2} - \Delta H_{H2O})\dot{x}_{LS,CO2} - \Delta H_{H2O}\dot{x}_{LS,PZ}\right] \quad (44)$$

The energy balance for the cross heat exchangers is given in Equations 45–50, where the energy flux, N_H, is calculated by multiplying the overall heat transfer coefficient by a log mean driving force.

$$\dot{T}^L_{CX1,c} = \frac{1}{Cp^L M^L_{CX1,c}}\left[\left(T^L_{SU} - T^L_{CX1,c}\right)(F^L_{P1} - F^L_{V2}) + N_{CX1,H}\right] + \frac{1}{Cp^L}\left[(\Delta H_{CO2} - \Delta H_{H2O})\dot{x}_{SU,CO2} - \Delta H_{H2O}\dot{x}_{SU,PZ}\right] \quad (45)$$

$$\dot{T}^L_{CX1,h} = \frac{1}{Cp^L M^L_{CX1,h}}\left[\left(T^L_{CX2,h} - T^L_{CX1,h}\right)F^L_{V4} - N_{CX1,H}\right] + \frac{1}{Cp^L}\left[(\Delta H_{CO2} - \Delta H_{H2O})\dot{x}_{FT,CO2} - \Delta H_{H2O}\dot{x}_{FT,PZ}\right] \quad (46)$$

$$\dot{T}^L_{CX2,c} = \frac{1}{Cp^L M^L_{CX2,c}}\left[\left(T^L_{CX1,c} - T^L_{CX2,c}\right)\left(F^L_{P1} - F^L_{V2} - F^L_{V3}\right) + N_{CX2,H}\right] + \frac{1}{Cp^L}\left[\left(\Delta H_{CO2} - \Delta H_{H2O}\right)\dot{x}_{SU,CO2} - \Delta H_{H2O}\dot{x}_{SU,PZ}\right] \quad (47)$$

$$\dot{T}^L_{CX2,h} = \frac{1}{Cp^L M^L_{CX2,h}}\left[\left(T^L_{FT} - T^L_{CX2,h}\right)F^L_{V4} - N_{CX2,H}\right] + \frac{1}{Cp^L}\left[\left(\Delta H_{CO2} - \Delta H_{H2O}\right)\dot{x}_{FT,CO2} - \Delta H_{H2O}\dot{x}_{FT,PZ}\right] \quad (48)$$

$$\dot{T}^L_{CX3,c} = \frac{1}{Cp^L M^L_{CX3,c}}\left[\left(T^L_{SU} - T^L_{CX3,c}\right)F^L_{V2} + N_{CX3,H}\right] + \frac{1}{Cp^L}\left[\left(\Delta H_{CO2} - \Delta H_{H2O}\right)\dot{x}_{SU,CO2} - \Delta H_{H2O}\dot{x}_{SU,PZ}\right] \quad (49)$$

$$\dot{T}^L_{CX3,h} = \frac{1}{Cp^L M^L_{CX3,h}}\left[\widehat{H}^V_{ST,k=1}F^V_{V5} - \widehat{H}^L_{CX3,h}(1 - vf_{CO2})F^T_{V5} - \widehat{H}^V_{CX3,h}vf_{CO2}F^T_{V5} - N_{CX3,H}\right] \quad (50)$$

References

[1] Luyben WL. Dynamics and Control of Recycle Systems. 1. Simple Open-Loop and Closed-Loop Systems. Ind Eng Chem Res 1993;32:466-75.

[2] Seborg DE, Edgar TF, Mellichamp DA, Doyle FJ. Process Dynamics and Control, 3rd Ed. Hoboken, NJ: John Wiley & Sons; 2011.

[3] Kokotović P, Khalil HK, O'Rielly J. Singular Perturbation Methods in Control: Analysis and Design. London: Academic Press; 1986.

[4] Lin Y-J, Madan T, Rochelle GT. Regeneration with Rich Bypass of Aqueous Piperazine and Monoethanolamine for CO_2 Capture. Ind Eng Chem Res 2014;53:4067-74.

[5] Walters MS, Dunia RH, Edgar TF, Rochelle GT. Two-Stage Flash for CO_2 Regeneration: Dynamic Modeling and Pilot Plant Validation. Energy Procedia 2013;37:2133-44.

[6] Frailie PT. Modeling of Carbon Dioxide Absorption/Stripping by Aqueous Methyldiethanolamine/Piperazine. The University of Texas at Austin. Ph.D. Dissertation. 2014.

[7] Baldea M, Daoutidis P. Dynamics and Nonlinear Control of Integrated Process Systems. New York: Cambridge University Press; 2012.

[8] Chen X, Heidarinejad M, Liu J, Christofides PD. Composite Fast-Slow MPC Design for Nonlinear Singularly Perturbed Systems. AIChE J 2012;58:1802-11.

[9] Baldea M, Daoutidis P. A General Analysis and Control Framework for Process Systems with Inventory Recycling. Int J Robust Nonlin 2013;In Press.

[10] Panahi M, Karimi M, Skogestad S, Hillestad M, Svendsen HF. Self-Optimizing and Control Structure Design for a CO_2 Capturing Plant. 2nd Ann Gas Proc Symp, Qatar. 2010.

[11] Ziaii, SF. Dynamic Modeling, Optimization, and Control of Monoethanolamine Scrubbing for CO_2 Capture. The University of Texas at Austin. Ph.D. Dissertation. 2012.

Available online at www.sciencedirect.com

ScienceDirect

Energy Procedia 00 (2013) 000–000

Energy Procedia

www.elsevier.com/locate/procedia

GHGT-12

Packing characterization for post combustion CO_2 capture: mass transfer model development

Chao Wang[a,b], Micah Perry[b], Frank Seibert[b], Gary Rochelle[a,*]

[a] *Texas Carbon Management Program, McKetta Department of Chemical Engineering, The University of Texas at Austin, 200 E. Dean Keeton St., C0400, Austin, TX 78712-1589*

[b] *Separations Research Program, Pickle Research Campus, The University of Texas at Austin, 10100 Burnet Road, Austin, TX 78758*

Abstract

Three mass transfer properties: the effective area (a_e), liquid film and gas film mass transfer coefficients (k_L and k_G) are measured consistently for eleven packings with different surface area and corrugation angle. The effective area and liquid film mass transfer coefficient increases with liquid velocity while gas film mass transfer coefficient increases with gas velocity. The fractional effective area decreases with surface area and barely changes with corrugation angle. k_L and k_G increase as surface area increases or corrugation angle decreases. A new concept-mixing point density is proposed to represent the packing geometry influence on k_L and k_G. Correlations for a_e, k_L, and k_G are developed including effects of gas and liquid rates and packing geometry.

Selection and peer-review under responsibility of GHGT.

Keywords: CO_2 capture, structured packing, effective area, mass transfer coefficient, mass transfer model.

1. Main text

Nomenclature

A	column cross section area, m^2
a_e	effective mass transfer area, m^2/m^3
a_P	packing physical area, m^2/m^3
C	experimental constant used in effective area correlation

Selection and peer-review under responsibility of GHGT.

HTU	height of transfer unit, m
K_{OG}	overall mass transfer coefficient, m/s
k_G	gas film mass transfer coefficient, m/s
k_L	liquid film mass transfer coefficient, m/s
M	mixing point density, pts/m^3
NTU	number of transfer units
Q	volumetric flow rate, m^3/s
u_G	gas superficial velocity, m/s
u_L	liquid superficial velocity, m/s
σ	surface tension, N/m
θ	packing corrugation angle, deg

1.1. Introduction

Among the major systems for CO_2 capture, post-combustion capture with amines is the most mature and readily employable technology. Packing is widely used in post-combustion CO_2 capture because of its low pressure drop, good mass transfer efficiency, and ease of installation. In the CO_2 capture process, absorber and stripper performance are highly dependent on the effective mass transfer area of the packing (a_e). The stripper performance depends on the liquid film mass transfer coefficient (k_L), while gas cooler and water wash performance depend on the gas film mass transfer coefficient (k_G).

A number of mass transfer models for packing are described in the literature.[1,2,3] In these models, the combination of mass transfer coefficient and area (Ka) was measured. However, a common defect in the previous models is that either a theoretical assumption of area or proposed K models from other work were used to separate K and a. In other words, none of the mass transfer values (k_G, k_L, a_e) were independently validated. In distillation systems, most cases only required the combination (Ka) values, where these models were acceptable, but the design and optimization of the amine scrubbing CO_2 capture system requires validated separate values for k_G, k_L, and a_e.

This research is focused on the consistent measurement and mechanistic model development of a_e, k_G, k_L for packing. The specific objective is to explore effects of operating conditions and packing geometry on mass transfer properties. Finally, mechanistic mass transfer models are developed.

2. Experimental

2.1. Apparatus

All experiments were conducted in a pilot-scale PVC column with an inner diameter of 0.428 m (16.8 in) and a total height of 7.62 m (25 ft) located in the Separation Research Program in the University of Texas at Austin (UT SRP). The same column has been used by previous researchers to measure a_e.[4,5] A DeltaV® control system provided by Emerson was utilized to operate the system and collect data. The experiment setup is shown in Figure 1.

A packed bed of 3.3 m (10 ft) was used to measure the pressure drop, liquid hold-up, and effective area. A packed bed of 1.83 m (6 ft) was used for the k_L measurement to avoid the peak tailing in GC analysis of outlet toluene. The packed bed height was further shortened to approximately 0.51 m (20 in) for the k_G measurement to obtain a reliable outlet SO_2 concentration.

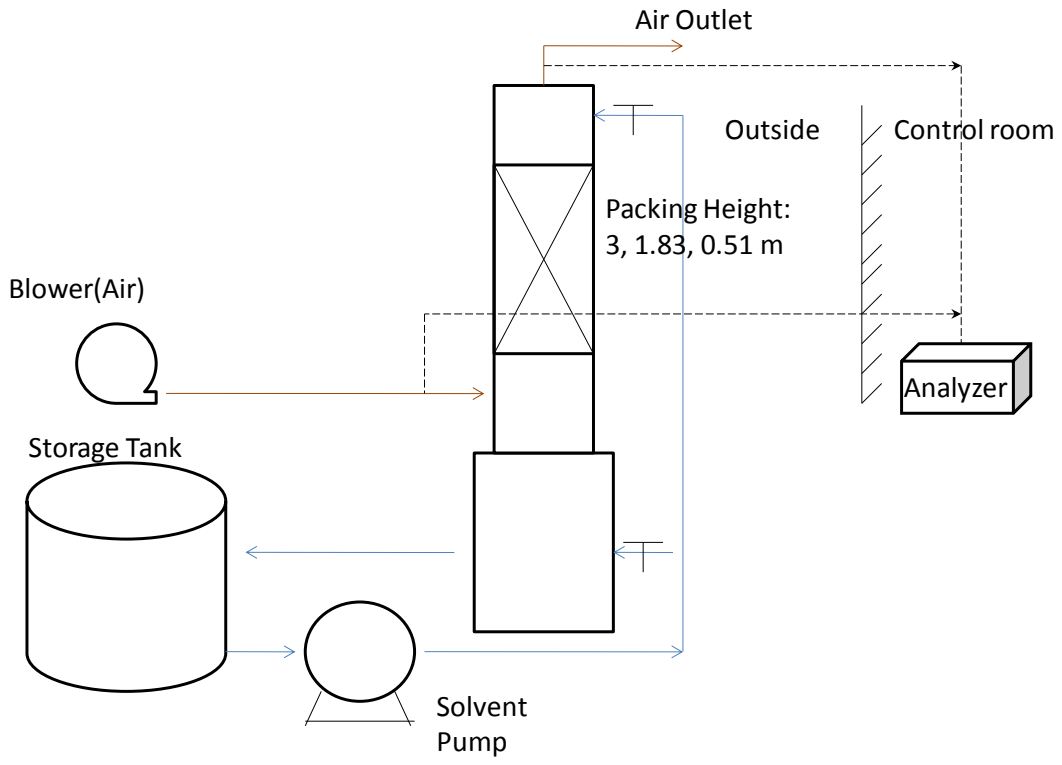

Fig. 1. Flow Process Diagram for the Packed Column

2.2. Experimental methods

The effective mass transfer area (a_e) was measured by the absorption of atmospheric CO_2 with 0.1 gmol/L NaOH solution. This method was first proposed by Danckwerts.[6] The reaction between CO_2 and NaOH is a pseudo first-order reaction, and the CO_2 flux is controlled by CO_2 diffusion and reaction in the liquid boundary layer. The liquid film mass transfer coefficient with chemical reactions can be calculated by Equation 1The effective area and mass transfer coefficient can be separated, and the area calculated by Equation (2).

$$k_g^{'} = \frac{\sqrt{k_{OH^-}[OH^-]D_{CO2,L}}}{H_{CO2}} \tag{1}$$

$$a_e = \frac{u_G \ln(\frac{y_{CO_2in}}{y_{CO_2out}})}{ZK_G RT} \approx \frac{u_G \ln(\frac{y_{CO_2in}}{y_{CO_2out}})}{Zk_G^{'} RT} \tag{2}$$

Where:
k_{OH^-} is the second-order reaction constant, $m^3/(kmol*s)$;
$[OH^-]$ is the concentration of free hydroxyl ion in the liquid phase, gmol/L;
$D_{CO2,L}$ is the diffusivity of CO_2 in the liquid phase, m^2/s;
H_{CO2} is the Henry's constant of CO_2, m^3*bar/kmol;
y_{CO2in} and y_{CO2out} are the concentration of CO_2 in the gas phase at inlet and outlet, ppmv;
Z is the packed bed height, m.

Physical absorption or desorption of low solubility gas with water has been used by others [7, 8] to measure k_L. In this work, the liquid film mass transfer coefficient (k_L) was measured by stripping toluene from water into air. This is a liquid phase controlled system because of its very high Henry's constant. The overall mass transfer can be assumed to be equal to the liquid phase mass transfer coefficient. Once the inlet and outlet toluene concentration in water have been measured, the following equation can be used to calculate k_La:

$$k_L a = \frac{u_L}{Z} \ln(c_{LA1} / c_{LA2}) \tag{3}$$

Where:

u_L is the liquid superficial velocity, m/s;

c_{LA1}/c_{LA2} are the inlet and outlet toluene concentrations in water, ppm.

k_L can then be determined directly from the measured k_La and the measured effective area (a_e) under the same liquid and gas rates:

$$k_L = \frac{k_L a}{a_e} \tag{4}$$

Absorption of reactive gas with aqueous sodium hydroxide has been used by previous researchersto measure k_G [9, 10]. In this study, the gas film mass transfer coefficient was measured by absorption of SO_2 mixed with air with 0.1 gmol/L NaOH. The reaction between SO_2 and NaOH is an instantaneous reaction making the liquid phase mass transfer resistance negligible. Thus, the overall mass transfer coefficient (K_{OG}) can be assumed to be equivalent to the gas film mass transfer coefficient (k_G). The gas film mass transfer coefficient can be calculated by:

$$k_G = \frac{u_G \ln(\frac{y_{SO2in}}{y_{SO2out}})}{ZRTa_e} \tag{5}$$

Where:

u_G is the gas superficial velocity, m/s;

y_{SO2in}/y_{SO2out} are the inlet and outlet SO_2 concentrations, ppmv;

a_e is the effective mass transfer area, m^2/m^3.

Because of the high efficiency of SO_2 removal with NaOH, the packed height was reduced from 10 feet to 30–40 inches to obtain a reliable and measurable outlet SO_2 concentration. In this case, the mass transfer from the top section above the packing and the bottom section below the packing became comparable with the mass transfer from the packing section. In the k_G measurement, the mass transfer from these two ends (NTU_{end}) was measured and deducted from the overall mass transfer (NTU_{total}).

2.3. Packing list and operating conditions

Eleven structured packings with different surface area (a_P) and corrugation angle (θ) were measured to explore how packing geometry influences the mass transfer properties. The packing information is listed in Table 1. Seven liquid flow rates (L) and five gas velocities (u_G) were measured to explore the impact of operating conditions on mass transfer performance. The operating conditions are listed in Table 2. The gas and liquid mass transfer coefficients (k_G and k_L) were separated from the Ka value with the measured effective area (a_e) at the same operating condition. The physical properties are listed in Table 3.

Table 1. Packing information

Packing	125Y	2X	200X	250Y	250Y	250X	350Y	350Z	350Y	350X	500Y
Type	Mellapak	Mellapak	Raschig Hybrid	Raschig, Hybrid	Mellapak	Mellapak	GT-Pak	GT-Pak	A	B	GT-Pak
Area, m^2/m^3	125	205	200	250	250	250	350	350	350	350	500
Corrugation angle	45	60	60	45	45	60	45	70	45	60	45
Channel base B, m	0.0635	0.0302	0.0318	0.0318	0.0302	0.0254	0.0167	0.0175	0.0254	0.0175	0.0143
Crimp height h, m	0.0254	0.0143	0.0048	0.0048	0.0111	0.0111	0.0075	0.0079	0.008	0.009	0.00635
Mixing point density M, pts/m^3	58583	266509	721574	1249766	593478	483197	2863768	902394	1171656	1256854	4628764

Table 2. Operating conditions

	Liquid load (L), m^3/m^2*h							Gas velocity (u_G), m/s				
	6.1	12.2	24.4	36.7	48.9	61	73.3	0.6	1	1.5	2	2.3
a_e	✓	✓	✓	✓	✓	✓	✓	✓	✓	✓	✓	✓
k_G	✓			✓	✓			✓	✓	✓	✓	✓
k_L	✓	✓	✓	✓	✓	✓	✓	✓	✓	✓		

Table 3. Average physical properties at 298K

	Liquid density, ρ_L	Gas density, ρ_G	Liquid diffusivity, D_L	Gas diffusivity, D_G	Liquid viscosity, μ_L	Gas viscosity, μ_G	Surface tension, σ_L
Units	kg/m^3	kg/m^3	m^2/s	m^2/s	kg/(m*s)	kg/(m*s)	N/m
Values	998	1.204	8.6E-10	1.31E-5	1.002E-3	1.98E-5	0.072

3. Results and discussion

3.1. Effective area

To explore the influence of surface area, the fractional effective area of four structured packings with the same corrugation angle (45 degrees) and surface area ranging from 125 to 500 m^2/m^3 is compared in Figure 2. The gas velocity is 0.99 m/s (300 ACFM) for all packings. Every packing shows an increase in effective area with

increasing liquid load. At the same liquid load, the fractional effective area decreases with surface area. Rivulets, ripples, and droplets, those mass-transfer-enhancing film instabilities according to Henriques[11] form easily between the sheets in coarser packing with high void fraction. End effects and wall effects could also have a greater impact on coarser packing. Finer packing such as 350Y and 500Y could be more subject to maldistribution and insufficient wetting, causing a lower fractional effective area.

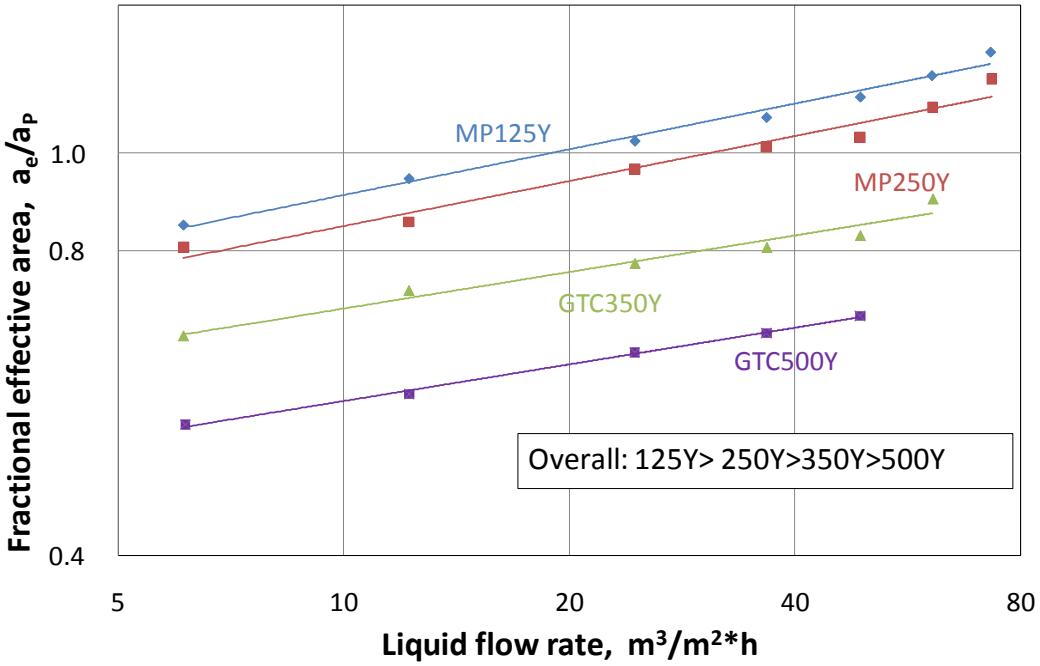

Figure 2. Fractional effective area as a function of specific dry area.

The effective area of MP250Y and 250X is compared in Figure 3 to show the effect of corrugation angle. MP250X has equivalent surface area and geometric structure except for a higher corrugation angle (60 degrees), compared with MP250Y (45 degrees). The measured effective area of MP250Y is only 6% higher than MP250X within the range of the experimental error. A comparison of GT-PAK™ 350Y and 350Z also shows that the corrugation angle has an insignificant effect on the effective area. 350Y has a 45-degree corrugation angle while 350Z has a 70-degree angle. The difference in effective area between these two packings is 7%, which is within the 10% experimental error.

The effective area should be determined by the wettability of the packing surface, which is influenced by: (1) the surface tension, which determines the contact angle of liquid and packing surface; and (2) the liquid phase velocity, which determines the liquid flow pattern. Other factors such as gas velocity, liquid viscosity, and packing corrugation angle do not have a significant impact on effective area.

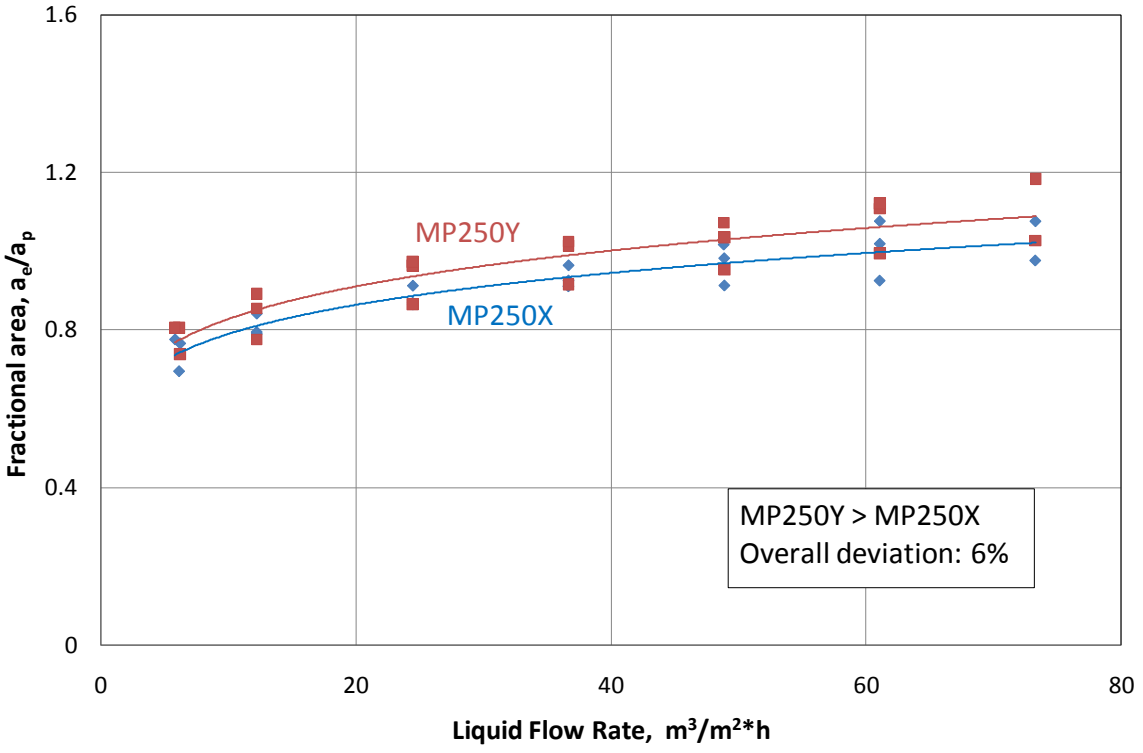

Fig. 3. Fractional effective area comparison between MP250Y and MP250X

3.2. Liquid and gas film mass transfer coefficient (k_L and k_G)

Figures 4 and 5 compare liquid film and gas film mass transfer coefficients for packings with different surface area. For all packings, k_L increases with liquid velocity. At the same gas and liquid flow rate, k_L increases as surface area increases. On average, the k_L of 500Y is 33% higher than 350Y, and the k_L of 350Y is 21% higher than 250Y. These differences are significantly more than the 10% experimental noise. A similar conclusion is reached when gas film mass transfer coefficient of packings with different surface areas is compared (Figure 5). At the same gas and liquid flow rate, the k_G of 500Y is 23% higher than 350Y, and the k_G of 350Y is 22% higher than 250Y. The difference between 250Y and 125Y is negligible (only 3%) since there could be extra bubbles or ripples creating mass transfer in coarse packing like 125Y.

The liquid film and gas film mass transfer coefficients for packings with different corrugation angles are compared in Figure 6 and Figure 7. At the same liquid and gas flow rate, both k_L and k_G increase as the corrugation angle decreases from 70 to 45 degrees (350Z to 350Y). The mass transfer coefficient difference between these two packings is between 25% and 35%.

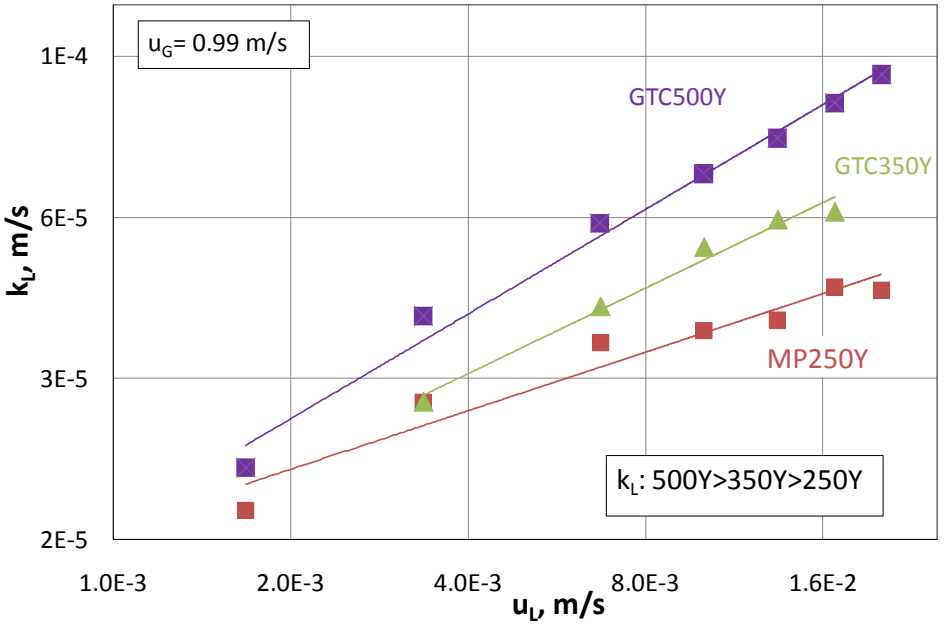

Fig 4. k_L comparison of 250Y, 350Y, and 500Y

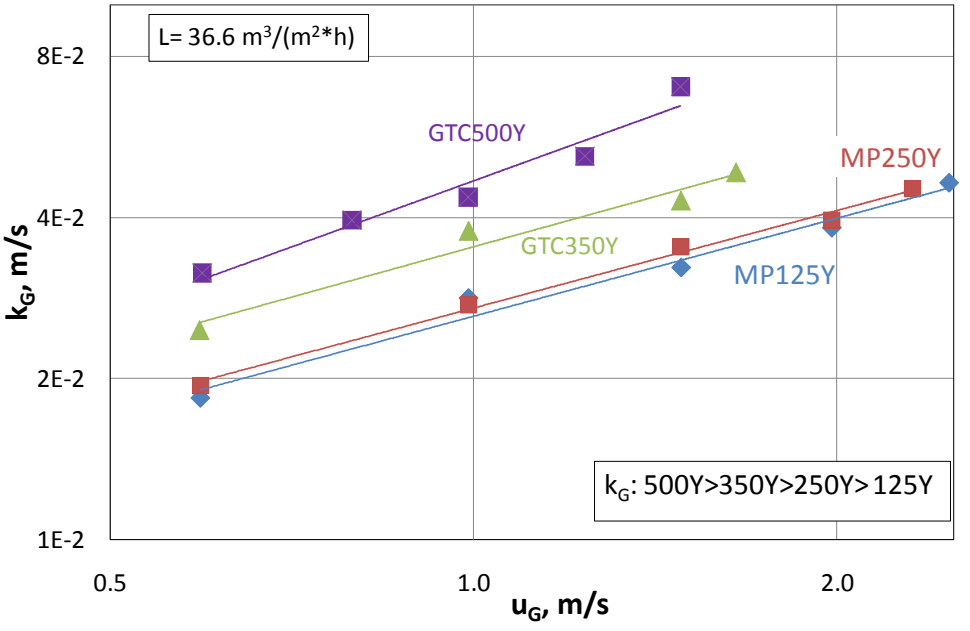

Fig 5. k_G comparison of 125Y, 250Y, 350Y, and 500Y

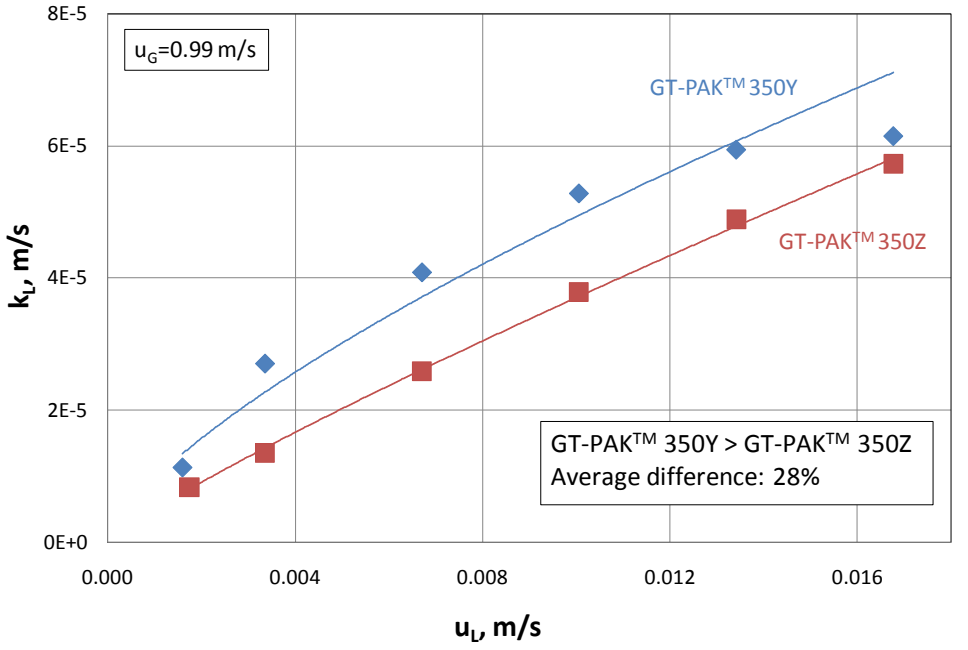

Fig 6. k_L comparison of GT-PAK™ 350Y and 350Z

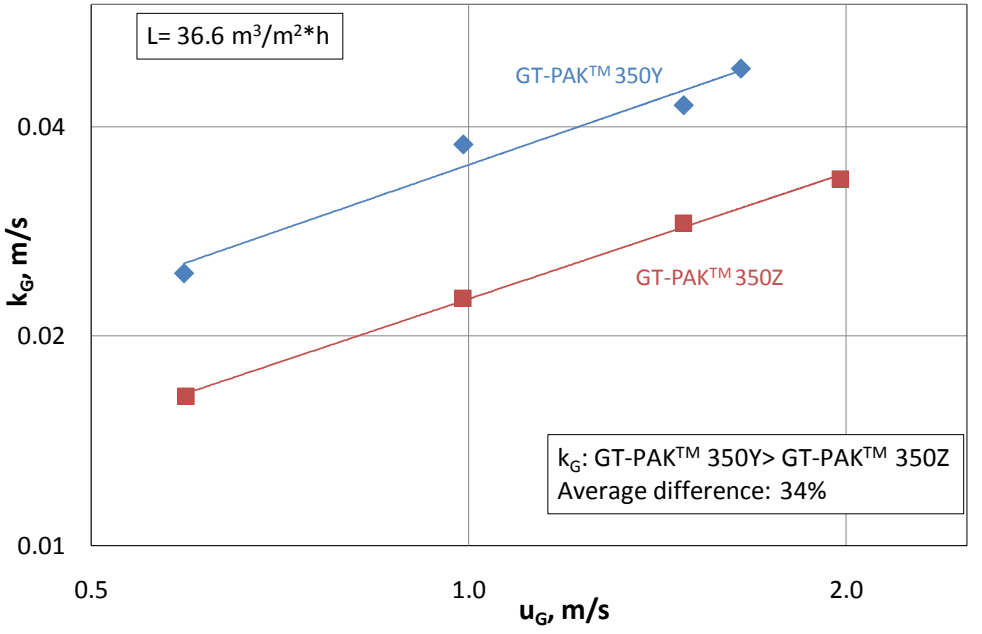

Fig 7. k_G comparison of GT-PAK™ 350Y and 350Z

In general, both k_L and k_G increase with packing surface area (a_p) and decrease with packing corrugation angle (θ). Structured packing geometries are studied to understand this phenomenon.

3.3. Mixing point density

Figure 8 shows the flow mechanism in the corrugated metal sheets that compose structured packing. Liquid flow inside the packing can be seen flowing along these corrugated sheets. At the joint points of metal sheets (marked by circles in Figure 8), flows mix with each other, change directions, and create turbulence. Thus, these mixing points are believed to be the key points for mass transfer in structured packing. In packing with a lower corrugation angle or larger surface area, there will be more mixing points, which means liquid and gas flows mix with each other more often, change direction more frequently, and create more turbulence. Both k_L and k_G increase as corrugation angle decreases or surface area increases.

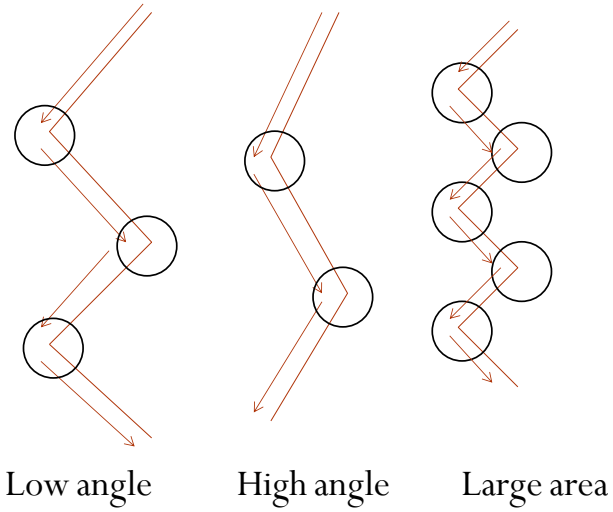

Fig 8. Liquid flow along corrugated metal sheets

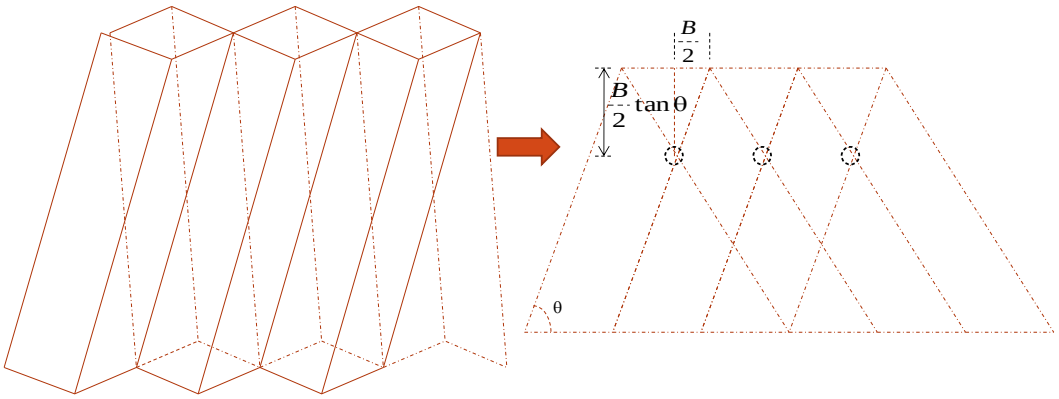

Fig 9. Lateral view of a structured packing with a corrugation angle (θ)

The number of mixing points vary with the packing geometry. Figure 9 shows the lateral view of a structured packing with a corrugation angle θ. From the lateral view, the corrugated metal sheets can be seen as a series of

parallel lines with a tilt angle to the horizontal line. In the structured packing, each corrugated metal sheet contacts the one next to it. In the lateral view, this is expressed by the parallel lines crossing with another set of parallel lines in a different direction. The crossed corrugated metal sheets form hundreds of square pyramids, which are the triangles in the lateral view. The mixing points are the vertices of the triangles, which are marked in black circles in the lateral view.

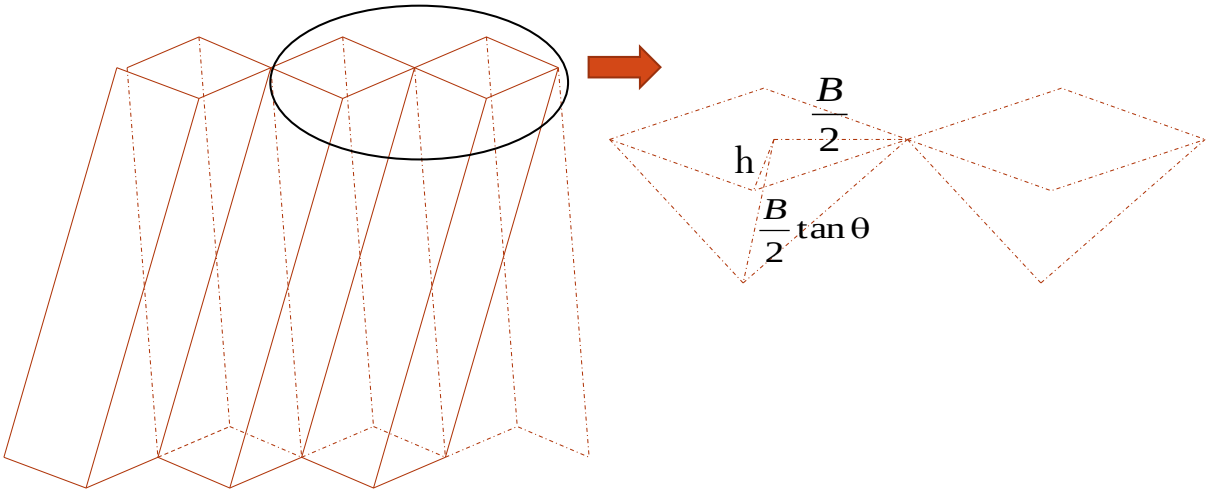

Fig 10. Top view of a structured packing with a corrugation angle (θ)

The square pyramids formed by the crossed metal sheets can be better seen from the top view of the packing (Figure 10). The height of the square pyramid is B/2*tanθ, the bottom area of the pyramid is B*h. Both B and h are structured packing geometric characteristics. B is the channel base length (m) while h is the crimp height length (m).

The volume of the square pyramid is (BhB*tanθ)/6. Thus, the number of square pyramids per m^3 volume is 6/(BhB*tanθ). Each pyramid has five mixing points; however, each pyramid also shares mixing points with four adjacent pyramids, making the number of mixing points per pyramid 5/5. The number of mixing point per m^3 (mixing point density M) can be calculated by Equation 6.

$$M = \frac{6}{BhB\tan\theta} \tag{6}$$

Where:
B is the channel base, m;
h is the crimp height, m;
θ is the corrugation angle, deg.

4. Model development

The effective area model in this study is based on the model by Tsai[12]. The updated model uses liquid superficial velocity per total area (u_L/a_P) as the liquid flow rate per perimeter term (Q/L_P), and changes the experimental coefficient from 1.34 to 1.42, which provides a better fit for our larger data base. The effective area model is:

$$\frac{a_e}{a_P} = 1.42[(\frac{\rho_L}{\sigma})g^{1/3}(\frac{u_L}{a_P})^{4/3}]^{0.116} \tag{6}$$

Figure 11 shows the comparison of experimental data and the effective area model. It includes the data for all packings measured in this work. The effective area model fits most of the experimental data well except for GT-PAK™ 500Y. Some of the packing surface area cannot be wetted efficiently for high surface area packings, causing the measured fractional area for GT-PAK™ 500Y to be lower than expected. The average deviation between the model and experimental results is 10%.

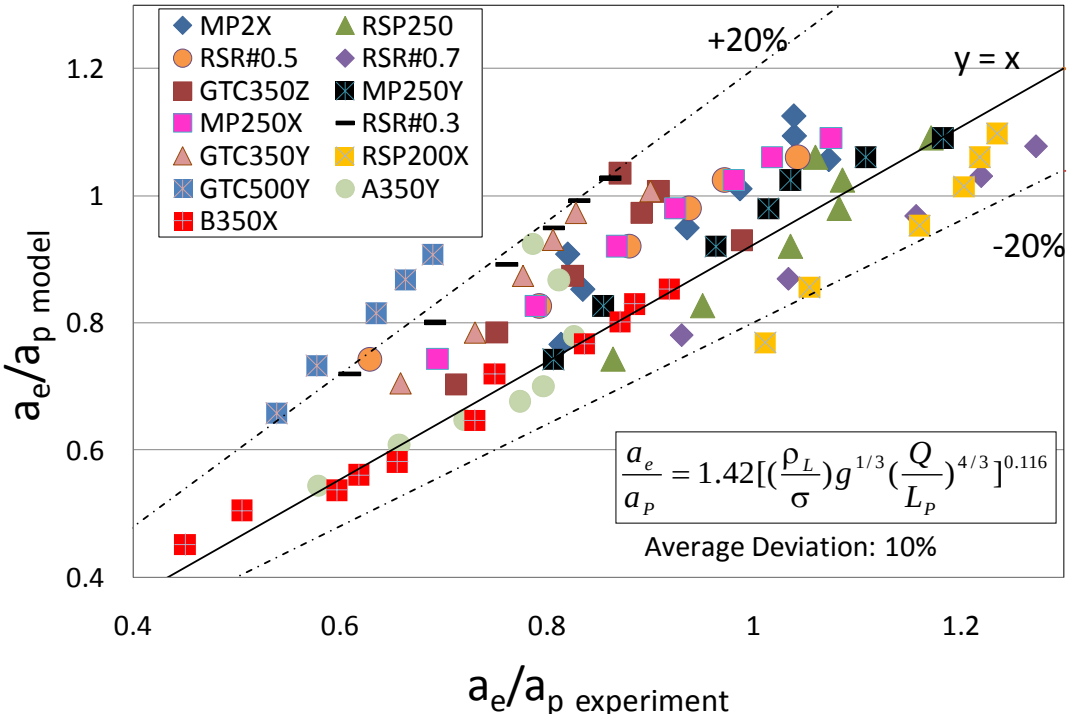

Fig 11. Comparison of experimental data a nd the effective area model

The gas and liquid film mass transfer coefficients (k_G and k_L) are a function ofthe gas and liquid superficial velocity (u_G, u_L), the packing surface area (a_p), and the mixing point density (M). M is the number of mixing points per m^3, which represents the effect of the corrugation angle and packing size. M is given by by Equation 6. The mass transfer coefficients models are given by Equation 7 and 8.

$$k_L = 3.08E-3 * u_L^{0.72} M^{0.42} a_P^{-1.15} \quad (7)$$

$$k_G = 1.08E-2 * u_G^{0.55} M^{0.22} a_P^{-0.36} \quad (8)$$

The comparison of experimental data and values predicted by the k_L and k_G models is shown in Figures 12 and 13. The deviation between k_L, experiment and k_L, model is 22% while the deviation between k_G, experiment and k_G, model is 13%. The standard errors of each parameter in the k_L and k_G models are listed in Table 4 and Table 5. The p-value for each term tests the null hypothesis that the coefficient is equal to zero (no effect). A predictor that has a low p-value (<0.05) is likely to be a meaningful addition to the model because changes in the predictor's value are related to changes in the response variable. Conversely, a larger (insignificant) p-value suggests that changes in the predictor are not associated with changes in the response. P-values are all less than 0.05 except the p-value for a_P in the k_G model, indicating that more work is still needed to find out the dependence of gas film mass transfer coefficient (k_G) on packing surface area (a_P).

Previous k_G models (Rocha[2], Hanley and Chen[15]) are compared with data in this work (Figure 13). Both of them are developed based on data measured in distillation systems. Rocha's model under-predicts k_G value by 32%, and Hanley's model under-predicts k_G by 69%.

Table 4. k_L correlation standard error

	Average Power	Standard error	P-Value
u_L	0.72	0.045	2.59E-23
M	0.42	0.086	6.93E-6
a_P	-1.15	0.252	2.47E-5

Table 5. k_G correlation standard error

	Average Power	Standard error	P-Value
u_G	0.55	0.055	3.09E-13
M	0.22	0.056	1.05E-3
a_P	-0.36	0.179	0.0308

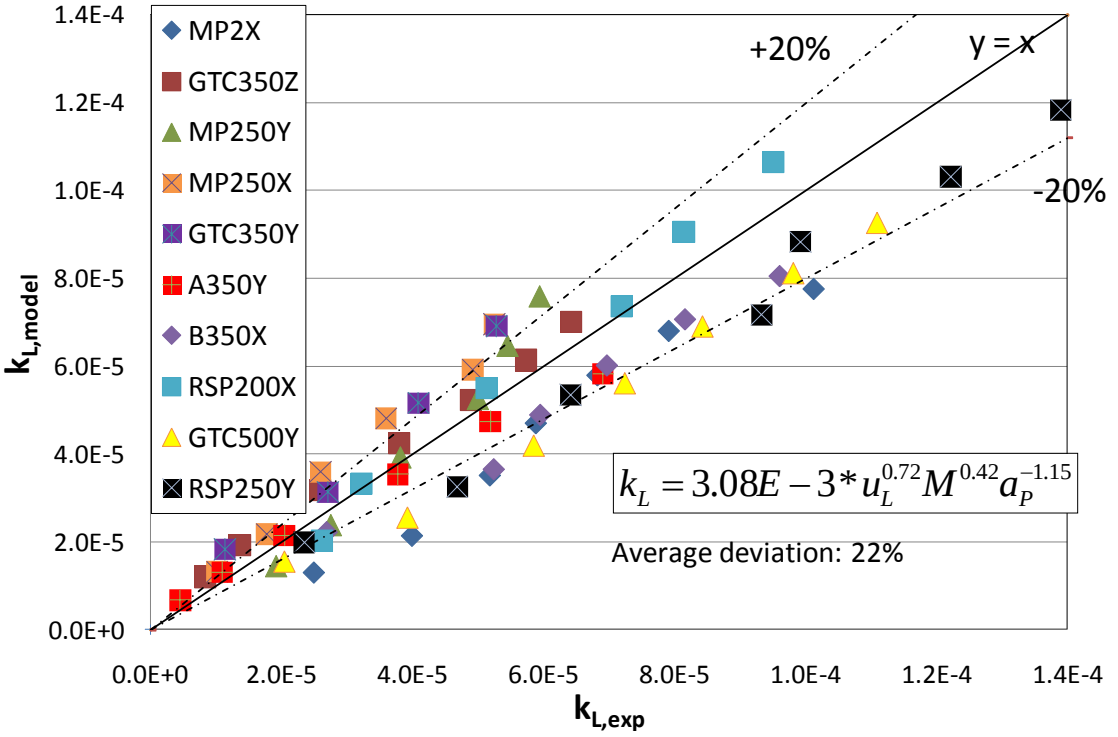

Fig 12. Liquid film mass transfer coefficient model

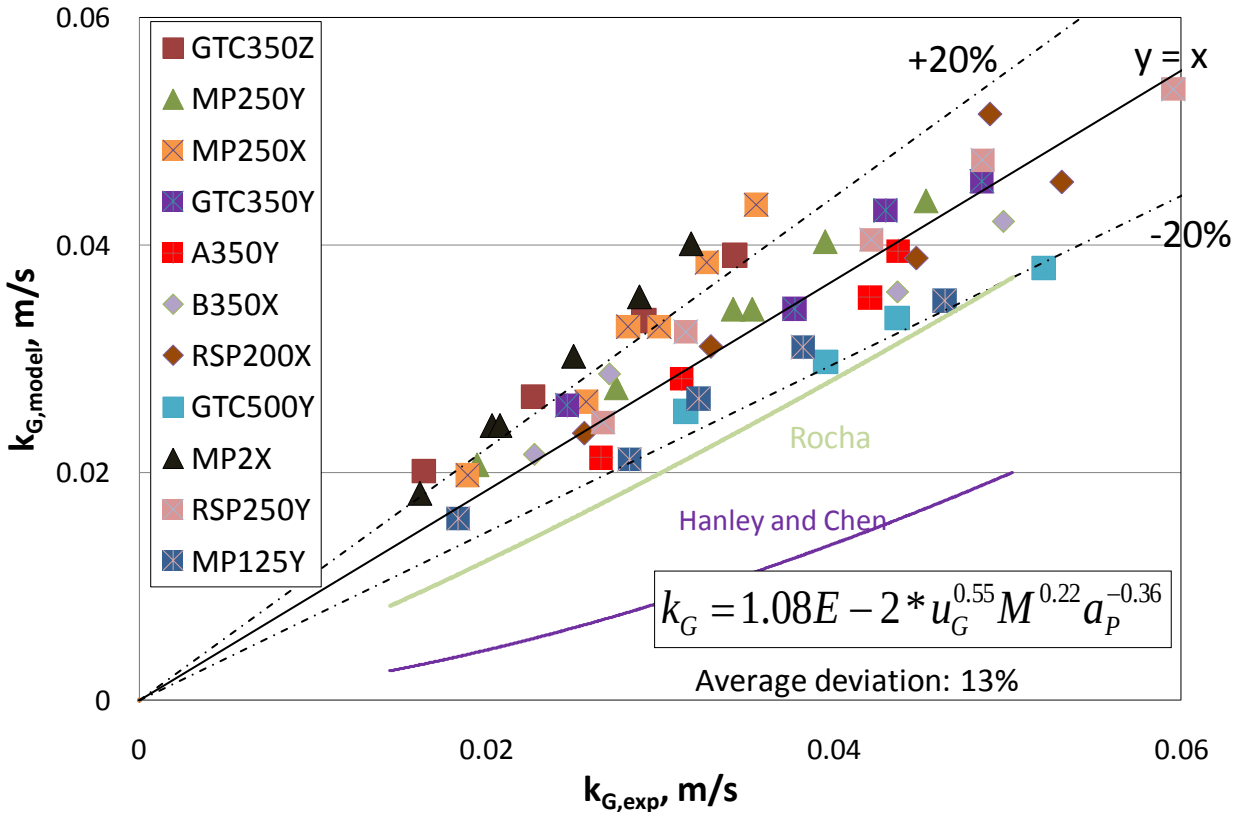

Fig 13. Gas film mass transfer coefficient model

5. Data comparison with previous work

The mass transfer data (a_e, k_L, and k_G) measured in this work is compared with previous work in this section. Figure 14 compares the effective area measured in this work for data from Tsai[12] Linek[13]. The system used is CO_2/air-NaOH for all three researchers. The differences between data in this work and data by previous researchers are 2-3%, showing good agreement.

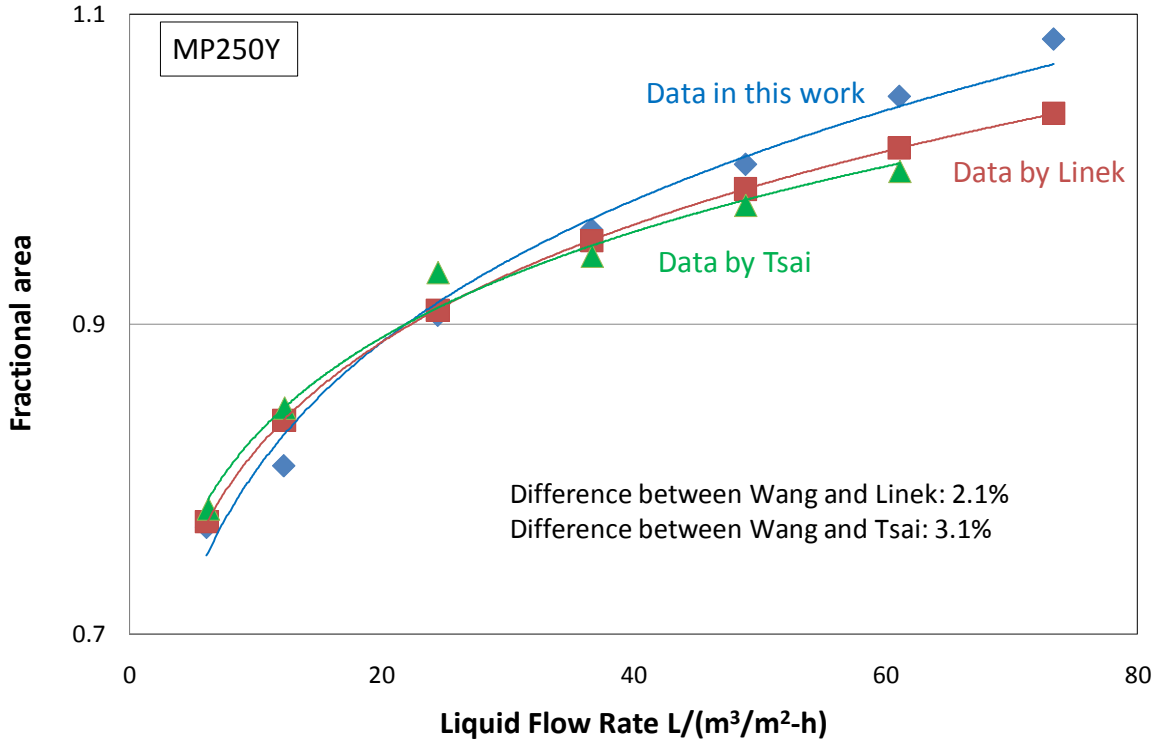

Fig 14. Effective area comparison between data in this work and data by previous researchers

Figure 15 compares the k_La predicted by the model in this work to models by previous researchers for MP250Y. The models by Laso and Linek are semi-empirical based on measured data. The system was O_2 desorption from water by air (Laso[14]), or by N_2 (Linek[13]). The packed height was 0.42 m (Laso) and 0.84 m (Linek) compared to 1.83 m in this work. Because of the diffusivity differences between different systems, the k_La measured in O_2-water system is converted to toluene-water system by Equation 9 (assume k_La changes with u_L to the 0.5 power).

$$\frac{(k_La)_{tol}}{(k_La)_{O_2}} = \left(\frac{D_{tol,L}}{D_{O2,L}}\right)^{0.5} = 0.661 \quad (9)$$

Where:

$D_{tol,L}$ = 8.6E-10 m^2/s;

$D_{O2,L}$ = 1.97E-9 m^2/s

k_La measured by Laso is 54% higher than k_La measured in this work, and k_La measured by Linek is 31% higher than k_La measured in this work. Since the packed heights in Laso's work and Linek's work were shorter than the packed height used in this work, end effect could play a more significant role in their results, making the k_La value higher than expected. Another reason could be the dependence of k_L on u_L, which is still quite uncertain. According to previous researchers, the dependence is believed to be in the range of 0.5-1.[15, 16] If higher value of dependence is used, the corrected k_La value from Laso and Linek would be lower, making it closer to k_La value in this work.

Two previous mass transfer models developed from data in distillation systems (Hanley and Chen[17], Rocha[2]) were also compared with the data in this work. Because of the systematic differences, it is suggested to use k_La value, which is the combination of k_L model and area model from the same author. The k_La value predicted by Hanley and Chen is 29% lower than k_La predicted in this work, while k_La value predicted by Rocha is 38% lower.

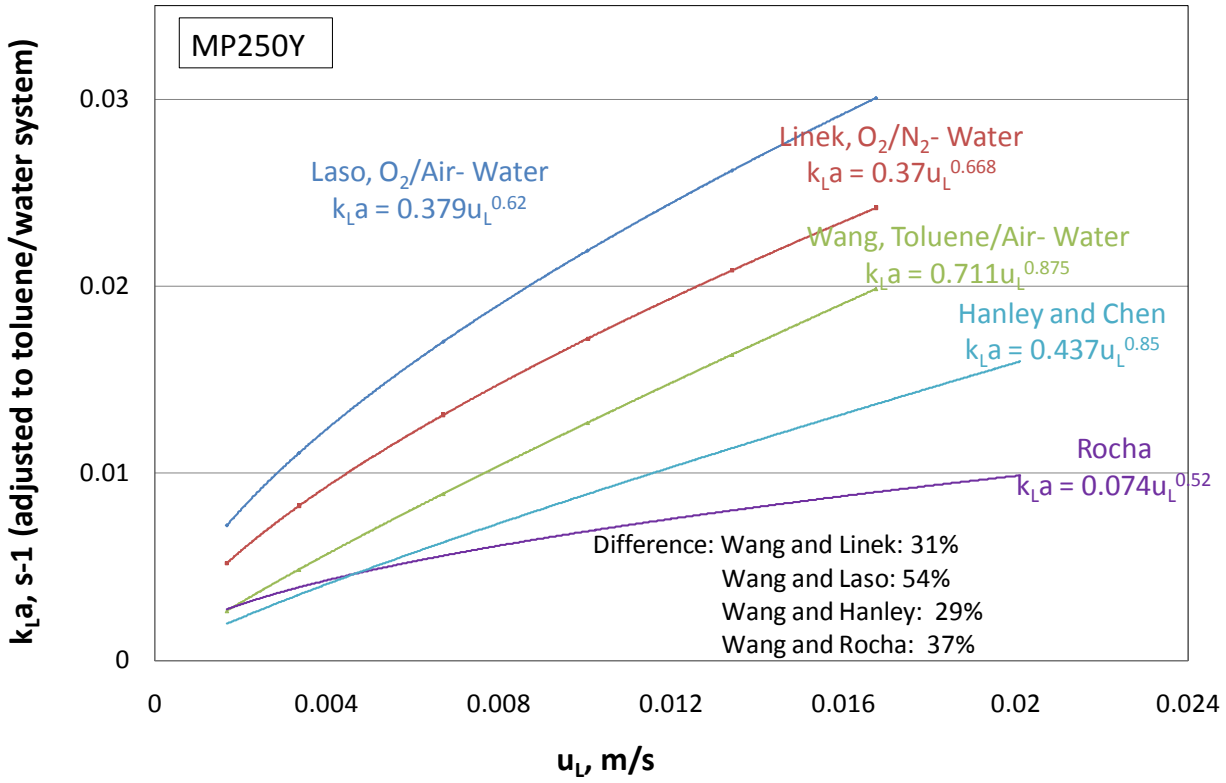

Fig 15. k_La comparison between data in this work and data by previous researchers

6. Conclusions

In this work, the effective mass transfer area (a_e), liquid film mass transfer coefficient (k_L), and gas film mass transfer coefficient (k_G) were measured consistently in a pilot-scale packed column. Eleven structured packings with varying surface area (a_P) and corrugation angle (θ) were tested to explore the influence of packing geometry on mass transfer performance. For each packing, seven different liquid velocities (u_L) and five different gas velocities (u_G) were tested to explore the influence of operating condition on mass transfer performance. The effective area (a_e) and liquid film mass transfer coefficient (k_L) increases with liquid velocity (u_L) and barely changes with gas velocity (u_G); gas film mass transfer coefficient (k_G) increases with gas velocity and barely changes with liquid velocity (u_L).

The fractional effective area (a_e/a_P) decreases with surface area (a_P) since coarse packing gets good wetting and additional mass transfer area from mass-transfer-enhancing film instabilities at the same liquid flow rate. The effective area barely changes when the corrugation angle increases from 45 degrees to 70 degrees. The liquid film and gas film mass transfer coefficients increase as packing surface area (a_P) increases or packing corrugation angle (θ) decreases. Packing geometry was studied and a new concept-mixing point density (M) proposed to explain this phenomenon. Mixing point density represents the packing geometry influence and can be quantified.

Mass transfer models are developed in this work. The effective area model is based work by Tsai, slightly changing the experimental constant and exponent. The mass transfer coefficients models are developed based on three factors influencing mass transfer: the liquid/gas superficial velocity ($u_{L/G}$), the packing size (a_P), and the mixing points density (M). The mass transfer models are:

$$\frac{a_e}{a_P} = 1.42[(\frac{\rho_L}{\sigma})g^{1/3}(\frac{u_L}{a_P})^{4/3}]^{0.116}$$

$$k_L = 3.08E-3 * u_L^{0.72} M^{0.42} a_P^{-1.15}$$
$$k_G = 1.08E-2 * u_G^{0.55} M^{0.22} a_P^{-0.36}$$

Appendix A. Calculation of HTU_G and HTU_L using models developed in this work

An example of calculation for the gas phase and liquid phase Individual Height of Transfer Unit (HTU_G and HTU_L) is shown in this section. Mellapak 250Y is chosen in this example calculation. The base case operating conditions are listed in Table 6. The gas flow rate (G) is 8.5 m^3/min or 300 ACFM in English units, and the liquid flow rate (L) is 36.7 $m^3/(m^2*h)$ or 15 gpm/ft^2 in English units. The superficial gas and liquid velocities can be calculated.

$$u_L = \frac{36.7m^3}{m^2 * 3600s} = 0.0102\ m/s \tag{10}$$

$$u_G = \frac{8.5m^3}{0.144m^2 * 60s} = 0.98\ m/s \tag{11}$$

Table 6. Operating conditions in HTUG and HTUL calculation

Parameters	Liquid flow rate, L	Gas flow rate, G	Cross-section area, A	Superficial liquid velocity, u_L	Superficial gas velocity, u_G	Packed height, Z
Units	$m^3/(m^2*h)$	m^3/min	m^2	m/s	m/s	m
Values	36.7	8.5	0.144	0.0102	0.98	3.048

The effective area (a_e), liquid film mass transfer coefficient (k_L), and gas film mass transfer coefficient (k_G) can be calculated using the mass transfer models developed in this work.

$$a_e = a_P * 1.42[(\frac{\rho_L}{\sigma}) g^{1/3} (\frac{u_L}{a_P})^{4/3}]^{0.116}$$
$$= 250m^2/m^3 * 1.42[(\frac{998kg/m^3}{0.072N/m} * 9.8m/s^2 * (\frac{0.0102m/s}{250m^2/m^3})^{4/3}]^{0.116} = 245\ m^2/m^3$$
$$k_L = 3.08E-3 * u_L^{0.72} M^{0.42} a_P^{-1.15}$$
$$= 3.08E-3 * (0.0102m/s)^{0.72} * (593478\,pts/m^3)^{0.42} * (250m^2/m^3)^{-1.15} = 5.27E-5\ m/s$$

$$k_G = 1.08E-2 * u_G^{0.55} M^{0.22} a_P^{-0.36}$$
$$= 1.08E-2 * (0.98m/s)^{0.55} * (593478\,pts/m^3)^{0.22} (250m^2/m^3)^{-0.36} = 2.73E-2\ m/s$$

Then the HTU_L and HTU_G can be calculated.

$$HTU_L = \frac{u_L}{k_L a_e} = \frac{0.0102 m/s}{5.27E-5 m/s * 245 m^2/m^3} = 0.79\ m$$

$$HTU_G = \frac{u_G}{k_G a_e} = \frac{0.98 m/s}{2.73E-2 m/s * 245 m^2/m^3} = 0.15\ m$$

The measured HTU_L is 1.07 m and measured HTU_G is 0.14 m for MP250Y at the corresponding operating conditions, showing that the mass transfer models developed in this work have good prediction.

References

[1] Billet R, Schultes M. Predicting mass transfer in packed column. *Chem. Eng. Technol.* 1996;16: 1-9

[2] Rocha JA, Bravo JL, Fair JR. Distillation Columns Containing Structured Packings: A Comprehensive Model for Their Performance. 2. Mass-Transfer Models. *Ind. Eng. Chem. Res.* 1996; 35:1660

[3] Brunazzi E, Paglianti A. Liquid-Film Mass-Transfer Coefficient in a Column Equipped with Structured Packings. *Ind. Eng. Chem. Res.* 1997; 36: 3792-3799

[4] Wilson I. Gas-Liquid Contact Area of Random and Structured Packing.. The University of Texas at Austin. M.S. Thesis. 2004

[5] Tsai RE, Schultheiss P, Kettner A, Lewis JC, Seibert AF, Eldridge RB, Rochelle GT. Influence of surface tension on effective packing area. *Ind. Eng. Chem. Res.* 2008; 47: 1253-1260

[6] Danckwerts PV, Sharma MM. Absorption of carbon dioxide into solutions of alkalis and amines. *Chem Engr.* 1966; 202: 244-280

[7] Onda K, Sada E. Liquid-side mass transfer coefficient packed towers. *AIChE Journal.* 1959;5:235-239

[8] Linek V, Petericek P. Effective interfacial area and liquid side mass transfer coefficients in aborption columns packed with hydrophilised and untreated plastic packings. *Chem Eng Res Des.* 1984;62:13-21

[9] Mehta VD, Sharma MM. Effect of diffusivity on gas-side mass transfer coefficient. *Chemical Engineering Science.* 1966;21: 361-365

[10] Yaici W, Laurent A. Determination of gas-side mass transfer coefficients in trickle-bed reactors in the presence of an aqueous or an organic liquid phase. *International Chemical Engineering.* 1988;28(2):299-305

[11] Henriques de Brito, von Stockar U, Bangerter, AM, Bomio P. Effective Mass-Transfer Area in a Pilot Plant Column Equipped with Structured Packings and with Ceramic Rings. *Ind. Eng. Chem. Res.* 1994;33(3):647-656

[12] Tsai R. Mass Transfer Area of Structured Packing. The University of Texas at Austin. Ph.D Dissertation. 2010

[13] Valenz L, Rejl FJ, Sima J, Linek V. Absorption Mass-Transfer Characteristics of Mellapak Packings Series. *Ind. Eng. Chem. Res.* 2011; 50: 12134-12142

[14] Laos M, Henriques de Brito M, Bomio P, von Stockar U. Liquid-side mass transfer characteristics of a structured packing. *The Chemical Engineering Journal.* 1995; 58: 251-258

[15] Hanley B, Dunbobbin B, Bennett D. A unified model for countercurrent vapour/liquid packed columns. 2. Equations for the mass-transfer coefficients, mass-transfer area, the HETP, and the dynamic liquid holdup. *Ind. Eng. Chem. Res.* 1994; 33: 1222

[16] Brunazzi E, Paglianti A. Liquid-film mass-transfer coefficient in a column equipped with structured packings. *Ind. Eng. Chem. Res.* 1997; 36: 3792

[17] Hanley B, Chen CC. New Mass-Transfer Correlations for Packed Towers. *AIChE Journal.* 2012; 58: 132-152

Available online at www.sciencedirect.com

ScienceDirect

Energy Procedia 00 (2013) 000–000

Energy Procedia

www.elsevier.com/locate/procedia

GHGT-12

Absorber Performance with High CO_2

Yue Zhang[a], Gary T. Rochelle[a]

[a]*The University of Texas at Austin, Department of Chemical Engineering, 200 E Dean Keeton St. Stop C0400, Austin, TX 78712-1589 USA*

Abstract

Previous studies of CO_2 absorption mainly focused on coal-fired flue gas with 12% CO_2. However, in a hybrid process combining amine scrubbing with membrane technology, the CO_2 concentration in the flue gas may be enriched to 20%. This work simulates absorber performance at 12 to 20% CO_2 with the Independence model for piperazine (PZ) in Aspen Plus®. 5 molal (m) PZ was chosen as the solvent with a solvent rate of 1.1*L_{min}. To estimate the absorber performance in this range, a factorial design has been used to define the model inputs. Both in-and-out intercooling and pump-around intercooling have been simulated for the absorber. The model calculates the solvent rate, packing height, rich loading, and optimized position of intercooling for each case. Empirical correlations for rich loading and a semi-empirical correlation for normalized packing have been derived. When estimating real absorber performance, K_G equals $k_g^{'}$ measured in wetted wall column times a correction factor φ. For 99% removal, φ varies from 1.6 to 2.6. For 60% removal, φ varies from 0.6 to 0.8.

Selection and peer-review under responsibility of GHGT.

Keywords: absorber; piperazine; factorial design; mass transfer coefficient; correction factor; normalized packing

1. Introduction

Membrane Technology and Research, Inc., has proposed a hybrid system combining amine scrubbing with membrane technology to reduce energy cost [1]. Previous studies of CO_2 absorption mainly focused on coal-fired flue gas with 12% CO_2. However, in the hybrid process, the CO_2 concentration in the flue gas may be enriched to 20%.

Selection and peer-review under responsibility of GHGT.

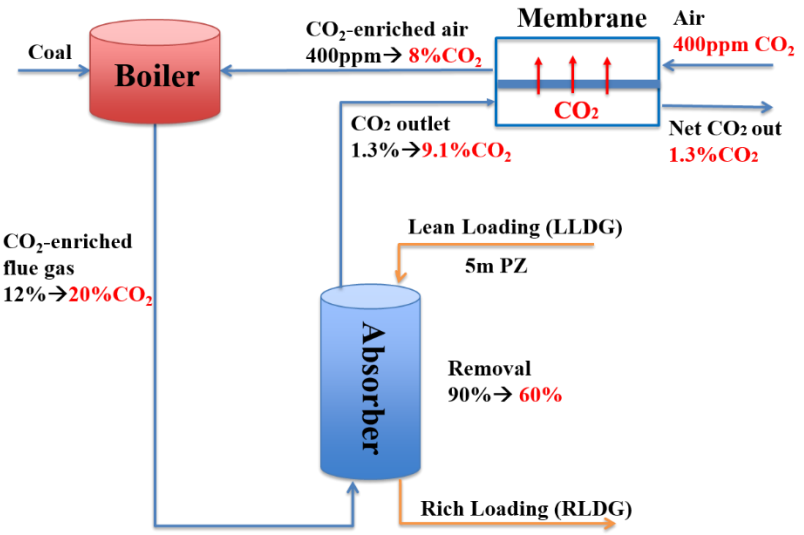

Fig. 1. Hybrid-series system combining amine scrubbing with membrane technology

In the hybrid-series arrangement (Figure 1) [1] the outlet CO_2 can be increased to 9.1% and removal can be reduced to 60%, which will result in smaller absorber packing height. With a larger driving force at the top and bottom of the absorber, higher lean loading can be used to minimize energy use.

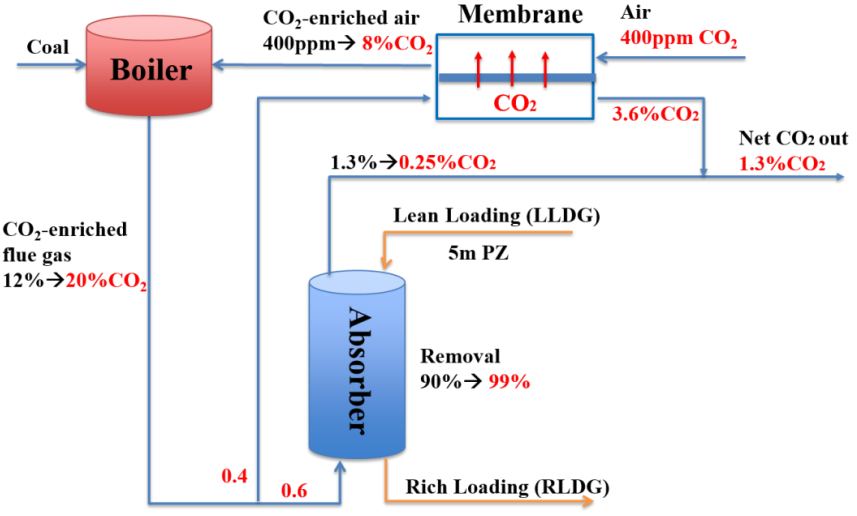

Fig. 2. Hybrid-parallel system combining amine scrubbing with membrane technology

In hybrid-parallel arrangement (Figure 2), removal can be increased to 99%. Both the absorber and the membrane will deal with less CO_2, which will result in smaller diameter and smaller membrane area. This work simulates absorber performance at 12 to 20% CO_2 and 60 to 99% removal with the Independence model [2] for 5 m PZ in Aspen Plus®.

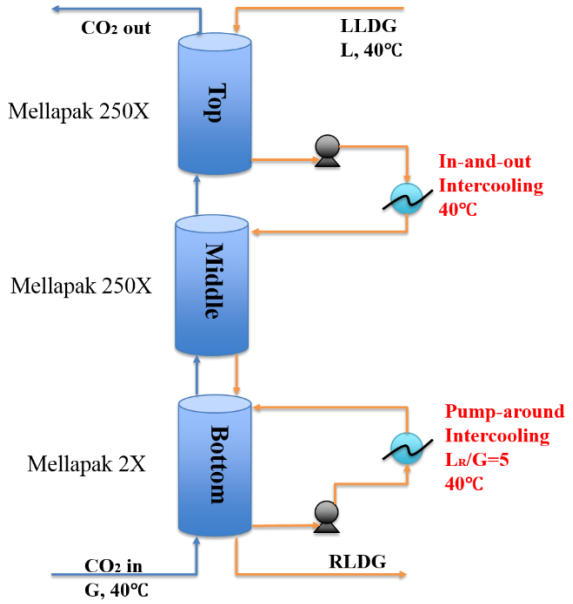

Fig. 3. Two types of intercooling

To improve the mass transfer rate, both in-and-out intercooling and pump-around intercooling have been simulated for the absorber [3] (Figure 3). In order to calculate the optimized position of intercooling, the absorber is considered in parts: top, middle, and bottom. In-and-out intercooling draws and returns the solvent to the first stage of the middle part. Pump-around intercooling draws the solvent out from the last stage of the bottom part, and sends it back to the first stage of the bottom part after cooling. Each case has been simulated to find the best position for intercooling

2. Safety

In order to improve the mass transfer rate, both in-and-out intercooling and pump-around intercooling have been added to the absorber. However, this can result in gasket failure of the plate intercooling heat exchanger. Gasket failure will result in solvent splash and personnel exposure to amine. To avoid exposure, the plate heat exchanger should be put on ground level.

If the heat exchanger is installed above ground level, solvent will splash over people when gasket fails. A splash protector should be added around the heat exchanger, and a spill containment system should be implemented to collect solvent.

3. Absorber Performance with In-and-out and Pump-around Intercooling

In order to predict the absorber performance using data calculated by Aspen Plus®, a factorial design was used to define the model inputs (Table 1). There are three degrees of freedom: CO_2 into the absorber, absorber CO_2 removal (f), and lean loading (LLDG). The factorial design includes 18 cases: three different CO_2 concentrations (coal-fired flue gas with 12% CO_2, and the hybrid process with 15% and 20% CO_2), three different removals (60%, 90%, and 99%), as well as two different lean loadings (over-stripping and normal lean loading was defined by the ratio of the partial pressure of CO_2 in the lean solvent and the partial pressure of CO_2 coming out of the absorber). With the results from the factorial design, correlations between these factors have been developed to predict the rich loading and packing area from the CO_2 concentration, CO_2 removal, and LLDG. The top and middle sections of the absorber use Mellapak 250X. The bottom section uses Mellapak 2X. 5 m PZ was chosen as the solvent with a solvent rate of $1.1*L_{min}$. Both in-and-out intercooling and pump-around intercooling have been simulated for the absorber. The solvent rate is $1.1*L_{min}$. The pump-around intercooling solvent recycle rate L/G is 5 mol/mol. The model calculates the solvent rate, packing areas, rich loading, and optimized position of intercooling for each case (Table 1).

Table 1. Model Inputs and Calculated Absorber Packing Distribution

Case	CO_2 (%)	f (%)	$P^*_{CO_2}/P_{CO_2,out}$	LLDG (mol CO_2/mol alk)	RLDG (mol CO_2/mol alk)	L/G (mol/mol)	Total Area (1000*m^2)	Area Fraction Top	Mid	Bot	NP (sec*m^2 /mol)
1	12	60	0.037	0.265	0.397	3.3	301	0.4	0.2	0.4	222
2	12	60	0.370	0.36	0.405	9.7	737	0.5	0.2	0.3	543
3	12	90	0.037	0.192	0.390	3.3	382	0.3	0.3	0.4	188
4	12	90	0.370	0.307	0.398	7.2	656	0.5	0.2	0.3	323
5	12	99	0.037	0.061	0.379	2.3	393	0.4	0.3	0.3	176
6	12	99	0.370	0.192	0.382	3.8	514	0.4	0.2	0.4	230
7	15	60	0.037	0.275	0.401	4.3	316	0.4	0.2	0.4	186
8	15	60	0.370	0.368	0.410	13.0	825	0.5	0.2	0.3	486
9	15	90	0.037	0.206	0.392	4.4	367	0.4	0.3	0.4	144
10	15	90	0.370	0.318	0.404	9.5	689	0.5	0.2	0.3	271
11	15	99	0.037	0.071	0.382	2.9	403	0.4	0.3	0.3	144
12	15	99	0.370	0.208	0.386	5.0	484	0.5	0.2	0.3	173
13	20	60	0.037	0.290	0.406	6.2	342	0.4	0.2	0.4	151
14	20	60	0.370	0.378	0.416	19.0	996	0.5	0.2	0.3	440
15	20	90	0.037	0.226	0.397	6.4	370	0.4	0.2	0.4	109
16	20	90	0.370	0.332	0.411	13.8	828	0.6	0.2	0.3	244
17	20	99	0.037	0.088	0.386	4.0	389	0.4	0.3	0.4	104
18	20	99	0.370	0.227	0.397	7.1	520	0.6	0.1	0.3	139

Normalized packing (NP) can reflect the absorber efficiency.

$$NP = \frac{\text{Total surface area}}{\text{Total Gas flow rate} * CO_2 \text{ Conc} * \text{Removal}} \quad (1)$$

In Case 1,

$$NP = \frac{301 * 1000\ \text{m}^2}{18.8\ \text{kmol/sec} * 0.12 * 0.99} = 222\ \text{sec} * \text{m}^2/\text{mol}.$$

A lower value for NP indicates better absorber performance, because the absorber needs less packing to capture the same amount of CO_2. The NP is also the reciprocal of the average CO_2 flux. Cases with low lean loading and high removal have lower normalized packing, which indicates better absorber performance. When using intercooling, the rich loading increases as expected with the inlet CO_2, but it does not vary significantly, which indicates that the solvent practically reaches equilibrium with the CO_2 at the bottom of the absorber.

4. Rich loading empirical correlation

In order to derive the RLDG empirical correlation, further experiments were performed at different lean loadings (Table 2).

Table 2: Data for RLDG Empirical Correlation

Cases	CO_2	ln(CO_2)	f	ln(f)	LLDG (mol CO_2/mol alk)	ln(LLDG)	RLDG (mol CO_2/mol alk)
1	0.12	-2.12	0.6	-0.51	0.265	-1.33	0.397
2	0.12	-2.12	0.6	-0.51	0.36	-1.02	0.405
3	0.12	-2.12	0.9	-0.11	0.192	-1.65	0.39
3-1	0.12	-2.12	0.9	-0.11	0.231	-1.47	0.388

4	0.12	-2.12	0.9	-0.11	0.307	-1.18	0.398
4-1	0.12	-2.12	0.9	-0.11	0.327	-1.12	0.401
4-2	0.12	-2.12	0.9	-0.11	0.336	-1.09	0.402
5	0.12	-2.12	0.99	-0.01	0.061	-2.80	0.379
6	0.12	-2.12	0.99	-0.01	0.192	-1.65	0.382
7	0.15	-1.90	0.6	-0.51	0.275	-1.29	0.401
8	0.15	-1.90	0.6	-0.51	0.368	-1.00	0.41
9	0.15	-1.90	0.9	-0.11	0.206	-1.58	0.392
10	0.15	-1.90	0.9	-0.11	0.318	-1.15	0.404
11	0.15	-1.90	0.99	-0.01	0.071	-2.65	0.382
12	0.15	-1.90	0.99	-0.01	0.208	-1.57	0.386
13	0.2	-1.61	0.6	-0.51	0.29	-1.24	0.406
14	0.2	-1.61	0.6	-0.51	0.378	-0.97	0.416
15	0.2	-1.61	0.9	-0.11	0.226	-1.49	0.397
15-1	0.2	-1.61	0.9	-0.11	0.261	-1.34	0.402
16	0.2	-1.61	0.9	-0.11	0.332	-1.10	0.411
16-1	0.2	-1.61	0.9	-0.11	0.35	-1.05	0.413
16-2	0.2	-1.61	0.9	-0.11	0.358	-1.03	0.414
17	0.2	-1.61	0.99	-0.01	0.088	-2.43	0.386
18	0.2	-1.61	0.99	-0.01	0.227	-1.48	0.397
19	0.2	-1.61	0.95	-0.05	0.303	-1.19	0.408

There are three degrees of freedom: inlet CO_2 (CO_2), removal (f), and LLDG. The original terms (CO_2, 1-f, and LLDG) and logarithm terms (ln(CO_2), ln(1-f), and ln(LLDG)) were chosen as variables for regression (Table 2). After the statistical significance test, the empirical correlation of rich loading is:

$$\mathrm{RLDG} = 0.374 + 0.001 * \ln(1 - \mathrm{f}) + 0.018 * \ln(CO_2) + 0.160 * \mathrm{LLDG} - 0.014 * \ln(\mathrm{LLDG})$$

R^2=0.984 (2)

For all removals, the RLDG calculated by Aspen Plus® and RLDG predicted by correlation are plotted against LLDG at 12%, 15%, and 20% inlet CO_2 concentration (Figure 4).

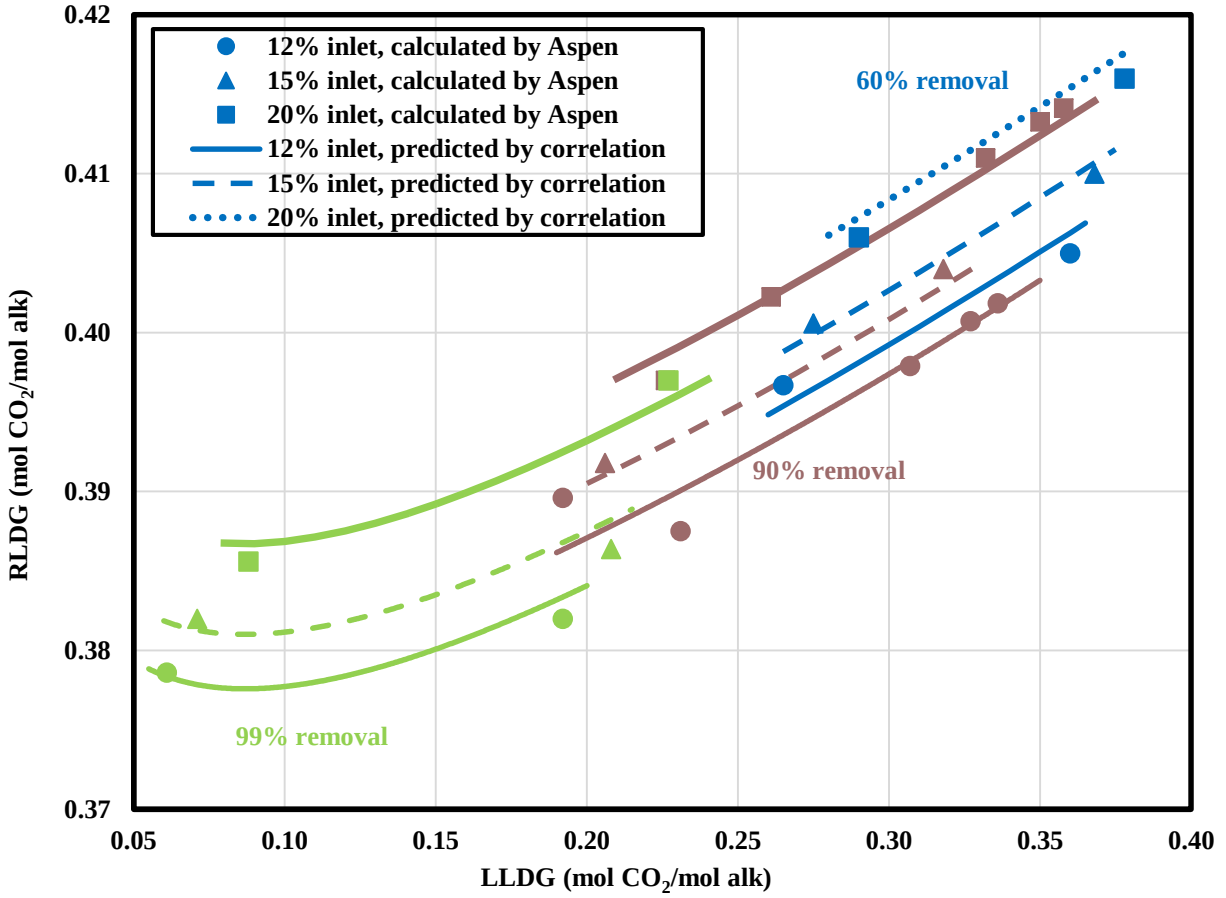

Figure 4: RLDG calculated by Aspen Plus®

Figure 4 shows that the RLDG predicted by the correlation is close to the RLDG calculated by Aspen Plus® from 0.05 to 0.4 LLDG. It also shows that rich loading behaves linearly in the high lean loading range and increases with lean loading. Rich loading lies between 0.37 and 0.42, suggesting that solvent practically reaches equilibrium with the inlet CO_2.

5. Normalized packing semi-empirical correlation

In the absorber, if we assume plug flow for the gas, the average CO_2 flux ($\overline{N_{CO_2}}$) is related to the overall mass transfer coefficient related to gas phase driving force (K_G) and the log mean CO_2 partial pressure driving force ($\overline{\Delta P_{CO_2}}$).

$$\overline{N_{CO_2}} = \frac{G*(y_{in}-y_{out})}{A} = K_G * \overline{\Delta P_{CO_2}} \quad (3)$$

As discussed above, the NP is the reciprocal of $\overline{N_{CO_2}}$, which can be written as Equation 4.

$$K_G = \frac{1}{NP*\overline{\Delta P_{CO_2}}} \quad (4)$$

K_G is related to the liquid-film mass transfer coefficient k_g' and gas phase mass transfer coefficient k_g in this series resistance relationship:

$$\frac{1}{K_G} = \frac{1}{k_g} + \frac{1}{k_g'} \quad (5)$$

k_g' has been measured in a wetted wall column and K_G can reflect the real absorber performance. However, when estimating absorber performance, k_g' is usually substituted for K_G for convenience [4]. Of course this substitution is

not accurate. The dimensionless group $\frac{K_G}{k'_g}$ can be defined as a correction factor φ, which can show how K_G varies with k'_g. If both sides of Equation 4 are divided by k'_g, and then the dimensionless group $\varphi$is on the left side, as is shown in Equation 6.

$$\varphi = \frac{K_G}{k'_g} = \frac{1}{NP * k'_g * \overline{\Delta P_{CO_2}}} \tag{6}$$

To predict NP, the dimensionless group φ was chosen as the term to be regressed. Comparison between φ predicted by correlation and φ calculated by Aspen Plus® shows how well the data is correlated. Equation 6 was used to calculate φ for each case. Since $k'_g * \overline{\Delta P_{CO_2}}$ will change along the column, $k'_g * \overline{\Delta P_{CO_2}}$ requires a good approximation. Equation 7 provides an approximation of $k'_g * \overline{\Delta P_{CO_2}}$, using the log mean average of $k'_g * \Delta P_{CO_2}$ at both lean and rich end to calculate φ.

$$k'_g * \overline{\Delta P_{CO_2}} \approx \overline{k'_g * \Delta P_{CO_2}}_{rich,lean} = \frac{k'_{g,rich} * \left(P_{CO_2,in} - P^*_{CO_2,rich}\right) - k'_{g,lean} * \left(P_{CO_2,out} - P^*_{CO_2,lean}\right)}{\ln \frac{k'_{g,rich} * \left(P_{CO_2,in} - P^*_{CO_2,rich}\right)}{k'_{g,lean} * \left(P_{CO_2,out} - P^*_{CO_2,lean}\right)}} \tag{7}$$

In Equation 7, $P^*_{CO_2}$ and k'_g at the both lean and rich ends are required to calculate φ. $P^*_{CO_2,lean}$ was found from the 5 m PZ VLE curve at 40 °C, while $P^*_{CO_2,rich}$ was predicted from RLDG using Equation 8, which was regressed from the 5 m PZ VLE curve at 40 °C. RLDG was predicted from LLDG, 1-f, and CO_2 inlet concentration using Equation 2.

$$\ln P^*_{CO_2} = 29.29 * (CO_2 \text{ loading})^2 + 7.24 * CO_2 \text{ loading} - 5.56 \qquad R^2 = 0.995 \tag{8}$$

To predict k'_g at the lean and rich ends, CO_2 rate data from Dugas [5] was used for the k'_g correlation (Table 3).

Table 3. CO_2 Rate Data for 5 m PZ Solution at 40 ˚C

CO_2 loading mol CO_2/mol alk	kg' mol/s*Pa*m^2
0.226	4.39E-06
0.299	2.57E-06
0.354	1.69E-06
0.402	7.93E-07

Equation 9 is the k'_g correlation during 0.226 to 0.402 CO_2 loading regressed from the Dugas data. k'_g is a linear function of $\ln(CO_2 \text{ loading})$. Equation 9 was also used to extrapolate k'_g outside this CO_2 loading range.

$$k'_g = -6 \times 10^{-6} \ln(CO_2 \text{ loading}) - 5 \times 10^{-6} \qquad R^2 = 0.998 \tag{9}$$

Table 4. Data for NP semi-empirical Correlation

	$P_{CO_2,in}$ kPa	$P_{CO_2,out}$ kPa	$P^*_{CO_2,lean}$ kPa	$P^*_{CO_2,rich}$ kPa	$k'_{g,lean}$ mol/s*Pa*m^2	$k'_{g,rich}$ mol/s*Pa*m^2	$\overline{k'_g * \Delta P_{CO_2}}$ mol/s*m^2	NP sec*m^2/mol	φ
1	12.2	5.2	0.2	6.8	3.0E-06	5.5E-07	7.4E-03	222	0.61
2	12.2	5.2	1.9	8.8	1.1E-06	4.2E-07	2.4E-03	543	0.76
3	12.2	1.4	0.0	5.5	4.9E-06	6.6E-07	5.3E-03	188	1.00
3-1	12.2	1.4	0.1	5.2	3.8E-06	6.9E-07	4.8E-03	189	1.10
4	12.2	1.4	0.5	7.1	2.1E-06	5.3E-07	2.2E-03	323	1.39
4-1	12.2	1.4	0.8	7.7	1.7E-06	4.9E-07	1.5E-03	425	1.58
4-2	12.2	1.4	1.0	8.0	1.5E-06	4.7E-07	1.1E-03	505	1.76
5	12.2	0.1	0.0	4.0	1.2E-05	8.3E-07	3.6E-03	176	1.60
6	12.2	0.1	0.1	4.4	4.9E-06	7.7E-07	2.1E-03	230	2.06

7	15.2	6.7	0.2	7.7	2.7E-06	4.9E-07	8.9E-03	186	0.60
8	15.2	6.7	2.4	10.2	1.0E-06	3.5E-07	2.8E-03	486	0.74
9	15.2	1.8	0.1	5.9	4.5E-06	6.2E-07	6.7E-03	144	1.04
10	15.2	1.8	0.6	8.5	1.9E-06	4.4E-07	2.5E-03	271	1.48
11	15.2	0.2	0.0	4.4	1.1E-05	7.7E-07	4.3E-03	144	1.60
12	15.2	0.2	0.1	5.0	4.4E-06	7.1E-07	2.5E-03	173	2.30
13	20.3	9.2	0.3	9.0	2.4E-06	4.1E-07	1.1E-02	151	0.60
14	20.3	9.2	3.4	12.4	8.4E-07	2.6E-07	3.3E-03	440	0.69
15	20.3	2.5	0.1	6.9	3.9E-06	5.4E-07	8.3E-03	109	1.11
15-1	20.3	2.5	0.2	8.1	3.1E-06	4.6E-07	6.3E-03	133	1.19
16	20.3	2.5	0.9	10.6	1.6E-06	3.3E-07	2.9E-03	244	1.42
16-1	20.3	2.5	1.4	11.4	1.3E-06	3.0E-07	1.9E-03	322	1.61
16-2	20.3	2.5	1.8	11.7	1.2E-06	2.9E-07	1.5E-03	383	1.78
17	20.3	0.3	0.0	4.9	9.6E-06	7.2E-07	5.6E-03	104	1.71
18	20.3	0.3	0.1	6.9	3.9E-06	5.4E-07	2.7E-03	139	2.65
19	20.3	1.3	0.5	9.6	2.2E-06	3.8E-07	2.7E-03	197	1.86

Table 4 shows the data used for NP semi-empirical correlation. The regressed dimensionless group φ is related to three degrees of freedom: CO_2, f, and LLDG. The original terms, logarithm terms, and crossing terms were chosen as variables for φ correlation. With φ correlation, NP can be calculated using Equation 6. After the statistical significance test, the semi-empirical correlation is shown as Equation 10.

$$\ln\varphi = \ln\frac{K_G}{k_g'} = -1.21 - 0.29 * \ln(1-f) + 1.3 * LLDG - 0.64 * \ln(1-f) * LLDG \quad R^2 = 0.955 \tag{10}$$

For all inlet CO_2 concentrations, φ calculated by Aspen Plus® and φ predicted by correlation are plotted against LLDG at 60%, 90%, 95%, and 99% CO_2 removal in Figure 5.

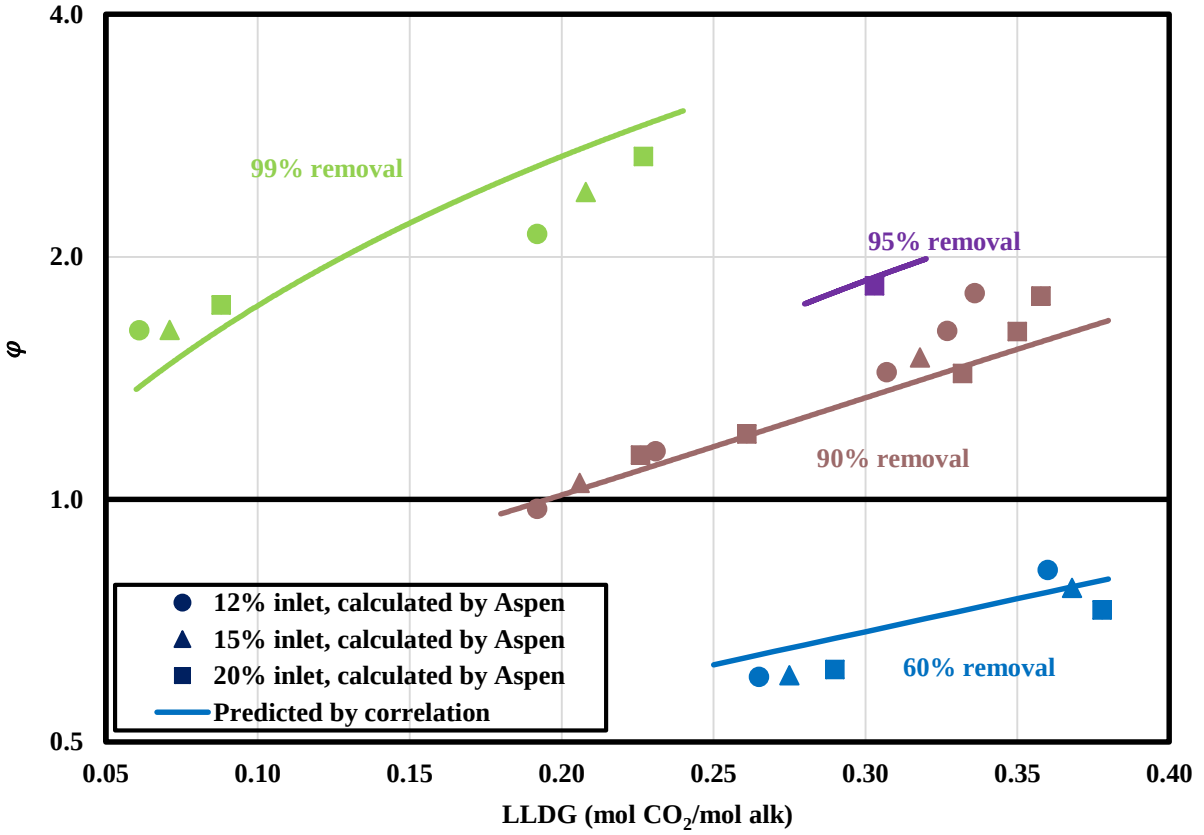

Figure 5: φ calculated by Aspen Plus®

As is shown in Figure 5, the dimensionless group φ varies from 0.5 to 4 and the curve shifts at different CO_2 removal levels. When estimating real absorber performance, simply substituting k'_g measured in the wetted wall column for K_G is not accurate. K_G equals k'_g times a correction factor φ, and the correction factor φ is a function of LLDG and f (Equation 10). For 99% removal, φ varies from 1.6 to 2.6. For 60% removal, φ varies from 0.6 to 0.8.There are two reasons for the deviation between the φ calculated by Aspen Plus® and φ predicted by correlation. The first reason is that the log mean average of $k'_g * \Delta P_{CO_2}$ at both the lean and rich ends is chosen as the $k'_g * \overline{\Delta P_{CO_2}}$ approximation. Since k'_g varies with CO_2 loading, k'_g will change along the column. At high CO_2 removal, the column is closer to the lean end pinch, thus $k'_g * \Delta P_{CO_2}$ at the lean end should be weighted more. At high CO_2 removal, the column is closer to the rich end pinch and $k'_g * \Delta P_{CO_2}$ at the rich end should be weighted more. The second reason is the inaccuracy when using Equation 2 & 8 to predict $P^*_{CO_2}$ and Equation 9 to predict k'_g.

6. Conclusion

1. The absorber performance can be represented by normalized packing (NP): the lower, the better.

$$NP = \frac{\text{Total surface area}}{\text{Total Gas flow rate} * CO_2 \text{ Conc} * \text{Removal}} \quad (1)$$

2. RLDG can be predicted by Equation 2. RLDG increases with lean loading, but does not vary much with removal. RLDG lies between 0.37 and 0.42, suggesting that the solvent practically reaches equilibrium with the inlet CO_2

$$\text{RLDG} = 0.374 + 0.001 * \ln(1 - \text{f}) + 0.018 * \ln(CO_2) + 0.160 * \text{LLDG} - 0.014 * \ln(\text{LLDG}) \quad (2)$$

3. NP can be predicted by Equation 2, 6, 7, 8, 9, &10.

$$\begin{cases} \varphi = \dfrac{1}{NP * k_g^{'} * \overline{\Delta P_{CO_2}}} & (6) \\ k_g^{'} * \overline{\Delta P_{CO_2}} \approx \overline{k_g^{'} * \Delta P_{CO_2}}_{rich,lean} & (7) \\ \ln P_{CO_2}^{*} = 29.29 * (CO_2 \text{ loading})^2 + 7.24 * CO_2 \text{ loading} - 5.56 & (8) \\ k_g^{'} = -6 \times 10^{-6} \ln(CO_2 \text{ loading}) - 5 \times 10^{-6} & (9) \\ \ln \varphi = -1.21 - 0.29 * \ln(1-f) + 1.3 * LLDG - 0.64 * \ln(1-f) * LLDG & (10) \end{cases}$$

4. When estimating real absorber performance, simply substituting k_g' measured in the wetted wall column for K_G is not accurate. K_G equals k_g' times a correction factor φ, and the correction factor φ is a function of LLDG and f (Equation 10). For 99% removal, φ varies from 1.6 to 2.6. For 60% removal, φ varies from 0.6 to 0.8.

Acknowledgements

This material is based on work supported in part by the Department of Energy under Award Number DE-FE0013188. The authors also acknowledge the financial support of the Texas Carbon Management Program.

The authors declare the following competing financial interest(s): One author of this publication consults for Southern Company and for Neumann Systems Group on the development of amine scrubbing technology. The terms of this arrangement have been reviewed and approved by the University of Texas at Austin in accordance with its policy on objectivity in research. The authors have financial interests in intellectual property owned by the University of Texas that includes ideas reported in this paper.

References

[1] Freeman B, Hao P, Baker R, Kniep J, Chen E, Ding J, Zhang Y, Rochelle GT. Hybrid membrane-absorption CO_2 capture process. Presented at GHGT-12, Austin, United States, October 5-9, 2014. *Energy Procedia*, 2014;

[2] Frailie PT. *Modeling of Carbon Dioxide Absorption/Stripping by Aqueous Methyldiethanolamine / Piperazine*. PhD Dissertation, The Univeristy of Texas at Austin: Austin, 2014;

[3] Sachde D, Rochelle GT. Absorber Intercooling Configurations using Aqueous Piperazine for Capture from Sources with 4 to 27% CO_2. Presented at GHGT-12, Austin, United States, October 5-9, 2014. *Energy Procedia*, 2014;

[4] Chen E. *Carbon Dioxide Absorption into Piperazine Promoted Potassium Carbonate using Structured Packing*. PhD Dissertation, The Univeristy of Texas at Austin: Austin, 2007;

[5] Dugas RE. *Carbon Dioxide Absorption , Desorption , and Diffusion in Aqueous Piperazine and Monoethanolamine*. PhD Dissertation, The Univeristy of Texas at Austin: Austin, 2009;

[6] Ding J, Rochelle GT. Optimization of Stripping of Concentrated Piperazine Over a Wide Range of Rich Loading. Presented at GHGT-12, Austin, United States, October 5-9, 2014. *Energy Procedia*, 2014.

Exergy Analysis of the Advanced Flash Stripper Using Aqueous Piperazine for CO_2 Capture

Yu-Jeng Lin[a] and Gary T. Rochelle[a]*

[a]Texas Carbon Management Program, McKetta Department of Chemical Engineering, The University of Texas at Austin, 200 E Dean Keeton St, C0400 Austin, TX 78712-1589, USA

*Corresponding author gtr@che.utexas.edu

Abstract

Amine scrubbing is the most mature CO_2 capture technology for coal-fired power plants. However, the energy consumption for regeneration incurs a 20–25% penalty on electricity output. The objective of this work is to identity and minimize inefficiencies in the capture process. The regeneration process and the compressor train were simulated in Aspen Plus®. The minimum work of the process and the lost work of each unit operation were quantified by exergy balance. The two major sources of lost work for the simple stripper are the lean/rich solvent cross exchanger and the stripper overhead condenser. The advanced flash stripper was proposed to reduce the lost work of the condenser by recovering stripping steam heat from the stripper. The advanced flash stripper reduces the heat duty and total equivalent work by 16% and 11%, respectively, compared to the simple stripper. Lean vapor compression, another regeneration process, reduces heat duty and total equivalent work by 8% and 3%, respectively. With these advanced stripping processes, the major source of lost work is from the cross exchanger, which should be optimized by including both energy and capital cost.

Keywords: amine scrubbing, post-combustion, irreversibility, Aspen Plus®

1. Introduction

The amine scrubbing process is considered the most feasible technology for CO_2 capture from coal-fired flue gas with 12% CO_2.[1,2] A typical amine scrubbing process includes an absorber, a stripper, and a cross exchanger (Figure 1). Desulfurized flue gas is contacted with the aqueous amine in the absorber to remove 90% of the CO_2. The rich solvent carrying the CO_2 from the bottom of the absorber is sent to the stripper and heated for CO_2 regeneration. After condensing the water, the stripped CO_2 is compressed to 150 bar for further storage and sequestration.

For post-combustion CO_2 capture, steam usage for CO_2 regeneration in the stripper and CO_2 compression work are the main contributions to energy use. CO_2 capture will reduce electricity output by 20–25% at a typical coal-fired power plant.[3,4]

Lost work (exergy) analysis can be used to quantify thermodynamic inefficiencies in the process.[5,6] The actual work required can be improved by reducing the lost work. Previous investigators have evaluated minimum work and lost work of the CO_2 capture process.[7–10] The isothermal minimum work at 40 ºC required to get from 12% CO_2 at 1 bar to pure CO_2 at 150 bar is 18.2 kJ/mol CO_2, which includes 7.3 kJ/mol CO_2 separation work (12% CO_2 to pure CO_2 at 1 bar) and 10.9 kJ/mol compression work (pure CO_2 from 1 bar to 150 bar). Geuzebroek et al.[10]

evaluated exergy loss in amine scrubbing with monoethanolamine (MEA) and concluded that the major sources of lost work are the absorber, the stripper overhead condenser, and the flue gas blower.

Previous studies did not evaluate the interactions between solvent selection, operating conditions, and alternative process configurations, which are the most important factors determining the energy performance. Lean vapor compression is a promising stripper configuration[11–13] that has been applied in pilot scale CO_2 capture plants[14,15]. Lin has demonstrated the energy improvement by recovering the stripping steam heat using rich solvent bypasses.[16] Among the proposed configurations with this strategy, the advanced flash stripper (flash stripper with the warm rich bypass and rich exchanger bypass) provides the best energy performance.

The objective of this work is to quantify the minimum work and the lost work of the CO_2 capture process, so the inefficient parts can be identified and improved. 8 molal piperazine (8 m PZ), a publicly characterized, second generation solvent, will be used in this work.[17] Three stripper configurations will be simulated in Aspen Plus® and compared, including a simple stripper, lean vapor compression, and the advanced flash stripper. The most important operating parameter, lean loading, will be varied to show how it affects performance.

2. Simulation methods

2.1 Simulation model

Simulation results were obtained from Aspen Plus® version 7.3 with "Independence", a thermodynamic model created by Frailie to represent 8 m PZ.[18] The Electrolyte Non-Random Two-Liquid (e-NRTL)[19] property method is used to describe the CO_2-amine-H_2O chemistry accounting for the non-ideality in the aqueous electrolyte system. To model the stripper, Aspen Plus® RateSep™ provides a rigorous rate-based model for heat and mass transfer with equilibrium reactions in the boundary layer. The application of the rate-based model to the amine scrubbing process accurately represented pilot plant data.[20]

8 m PZ has been demonstrated as an advanced solvent that has a higher reaction rate and CO_2 capacity,[21] and is more thermally stable than the conventional solvent, MEA. It can be used up to 150 ^{o}C without significant thermal degradation.[22] The thermodynamic model used in this

work was "Independence,"[18] which was rigorously regressed in Aspen Plus® with experimental data including amine volatility, heat capacity, CO_2 solubility, and amine pK_a over a range of amine concentration and CO_2 loading.

2.2 Process specifications

Process specifications used in the simulations are shown in Table 1. This work simulates the whole process shown in Figure 1 except the absorber. Typically, with an intercooled absorber using 8 m PZ over a range of lean loading,[23] the rich solvent is at 46 ºC with 0.40 CO_2 mol CO_2/mol alkalinity. In this work, the temperature and the CO_2 loading of the rich solvent were fixed. The stripper used Mellapak 250X structured packing. The Bravo Correlation was used to calculate the mass transfer coefficient and interfacial area.[24]

Operating the stripper at higher temperature is usually more energy efficient. However, the elevated temperature could result in significant thermal degradation of the amine in the reboiler. A reasonable compromise of 150 ºC for PZ was used.[22] The log mean temperature difference (LMTD) of the rich exchanger that transfers heat from condensing steam to cold rich solvent was specified as 20 K. In the cross exchanger, rich solvent is vaporized after being heated above its bubble point. The LMTD of both rich exchanger and cross exchangers was obtained by integrating the temperature profile instead of relying solely on inlet/outlet temperatures. The LMTD of the cross exchanger was specified as 5 K.

For the advanced flash stripper which has two cross exchangers the average LMTD, $\Delta T_{LM,avg}$ was calculated using Equation 1, which weights the LMTD of each exchanger ($\Delta T_{LM,1}$ and $\Delta T_{LM,2}$) by their exchanger duties (Q_1 and Q_2).

$$\Delta T_{LM,avg} = \frac{Q_1 + Q_2}{\frac{Q_1}{\Delta T_{LM,1}} + \frac{Q_2}{\Delta T_{LM,2}}} \quad (1)$$

2.3 Multi-stage compressor

The multi-stage compressor shown in Figure 2 was simulated in Aspen Plus®. The inlet pressure of the compressor train is determined by the stripper pressure, which is dependent on the lean loading and reboiler temperature. To sequester the CO_2 underground, the final pressure is specified as 150 bar. A supercritical pump is used for the last stage when the density is above

500 kg/m^3.[25] To decrease the pipeline diameter, aftercooling can be applied to increase CO_2 density and reduce volume flow rate.[26] In this work, aftercooling to 30 ºC is employed before the supercritical pump.

The specifications of the multi-stage compressor are shown in Table 2. The Benedict-Webb-Rubin-Starling (BWRS) equation of state was used to represent the gas density. The multi-stage compressor compresses the CO_2 from the stripper pressure to 76 bar that includes 2 bar of net positive suction head (NPSH) for the supercritical pump that pressurizes to 150 bar. The pressure ratio of the compressor was evenly distributed into each stage but does not exceed 2 per stage. The gas is intercooled to 40 ºC between each stage. The compression work with varied inlet pressure is shown in Figure 3, and is compared with the isothermal minimum work of compression at 40 ºC. The compression work requirement was regressed in Equation 2 as a function of inlet pressure from 1 to 20 bar.

$$W_{comp}\left(\frac{kJ}{mol\ CO_2}\right) = -3.48\ln(P_{in}) + 14.85,\ \ 1 < P_{in}(bar) < 20 \qquad (2)$$

2.4 Minimum work and lost work

The minimum work (theoretical work, reversible work) of the whole process can be calculated by the difference of Gibbs free energy between inlet and outlet states.

The lost work (exergy loss, irreversibility, available work) is defined as the maximum useful work that could be obtained during the process if the system were brought into equilibrium with the heat sink. The lost work is due to irreversible operation and the sources could be heat and mass transfer driving forces, mixing, flashing, and mechanical inefficiency. By exergy balance using Equation 3, the lost work of the whole process and for each unit operation can be calculated. The sink temperature, T_o, is set at 313.15 K (40 ºC). T_k (K) is the temperature of the heat source or sink. Q and W are the heat duty and work input/output. The enthalpy, H, and the entropy, S, are obtained from Aspen Plus® simulations. The actual work of the process, W_{act}, will be the minimum work plus the total lost work (Equation 4). The minimum work is the thermodynamic limit, which is determined only by inlet and outlet conditions, but the amount of lost work depends on how the process is operated. The lost work can be reduced by a better process design that makes the operation more reversible, and leads to less actual work required.

$$W_{lost} = \sum \left(1 - \frac{T_o}{T_k}\right) \dot{Q} + \sum \dot{W} + \sum_{in} \left(\dot{H} - T_o \dot{S}\right) - \sum_{out} \left(\dot{H} - T_o \dot{S}\right) \quad (3)$$

$$W_{act} = W_{min} + \sum W_{lost} \quad (4)$$

2.5 Total equivalent work

The total equivalent work is similar to the actual work, W_{act} in Equation 4, which gives the energy requirement, but more usefully represents the electricity penalty caused by the steam extraction from the power plant. Equation 5 shows that total equivalent work consists of pump work, compression work, and heat work, and is normalized by the moles of CO_2 removed.

The equivalent work is determined for reboiler heat duty by multiplying turbine efficiency (η_T) and Carnot cycle efficiency, as shown in Equation 6. In the Carnot efficiency the temperature approach between the reboiler/steam heater and the steam condensing temperature is taken as 5 K, and the heat sink is assumed to be 40 ºC. The effective turbine efficiency, η_T, is set at 90%. The equivalent work uses the same heat-work conversion method as Equation 3, except for the 90% turbine efficiency, which converts the work to electricity.

The pump work includes the head to move the rich solvent from the absorber to the pressure of the stripper with an efficiency of 65%. The compression work was calculated using Equation 2.

$$W_{eq}\left(\frac{kJ}{mol\ CO_2}\right) = W_{Heat} + W_{pump} + W_{comp} \quad (5)$$

$$W_{Heat}\left(\frac{kJ}{mol\ CO_2}\right) = \eta_T \left(\frac{T_{steam} - T_{sink}}{T_{steam}}\right) Q_{reb} \quad (6)$$

3. Stripper configurations

3.1 Simple stripper

The simple stripper is shown in Figure 1. The cold rich solvent is heated by the hot lean solvent in the cross exchanger and then sent to the top of the stripper. The reboiler provides the sensible heat, the heat of CO_2 desorption, and the heat of water vaporization. The hot lean solvent from the reboiler is returned to the absorber after being cooled to 40 ºC by the trim cooler. The hot CO_2 vapor from the top of stripper is cooled to 40 ºC in the overhead condenser with loss of the

latent heat of the excess water vapor.

3.2 Lean vapor compression

Figure 4 shows solvent regeneration including lean vapor compression. The simple stripper is modified by adding a flash tank and a single compressor stage. The hot lean solvent coming from the reboiler is flashed, and produces steam and CO_2 in the flash tank at lower pressure. The flashed vapor is pressurized by the lean vapor compressor, and sent to the bottom of the packing section in the stripper. The additional stripping steam provides a heat source for heating the rich solvent in the stripper with packing. Compared to the simple stripper at the same operating lean loading, the stripper pressure with lean vapor compression is higher, and the rich solvent coming into the top of the stripper is colder. The lean vapor compressor is analogous to the first stage of the multi-stage compressor. The stripper serves as a direct contact cooler that recovers the latent heat of steam.

The temperature of the flashed vapor at the lean vapor compressor inlet is approximately 140 ºC. After compression the hot vapor is over 200 ºC, which might exceed the temperature limit of typical compressor materials. The lean vapor compression work is included in the calculation of the total equivalent work. The pressure ratio of the lean vapor compressor for each lean loading was optimized to minimize the total equivalent work. If a higher pressure ratio is used, less stripping steam heat will be lost in the higher pressure stripper but the lean vapor compression work will increase.

3.3 Advanced flash stripper

Figure 5 shows the advanced flash stripper, which is referred to as the flash stripper with warm rich bypass and rich exchanger bypass in the previous study.[16] In this configuration, warm rich bypass and cold rich bypass are added to recover the stripping steam heat and improve energy performance.

The rich exchanger is used to preheat the cold rich solvent by hot CO_2 vapor coming out of the stripper. A portion of the cold rich solvent obtains latent heat of steam from the stripped vapor. Warm rich bypass is extracted between two cross exchangers and fed to the top of the stripper after mixing with cold rich bypass. The temperature was selected as the bubble point temperature at the stripper operating pressure. In the stripper packing, the gas stream strips CO_2

from the warm rich bypass, and the solvent condenses a portion of stripping steam. The warm rich bypass at the bubble point that avoids flashing provides the highest CO_2 partial pressure of the solvent at given pressure and rich loading. The optimized warm rich bypass rate will maximize the potential benefits of CO_2 mass transfer and heat transfer between solvent and vapor in the stripper. The rest of the rich solvent is heated by a steam heater and fed into the bottom of the stripper. The regeneration temperature of the stream coming from the flash tank was specified as 150 ºC.

The reboiler in a typical stripper is replaced by a steam heater and a flash vessel. Since the convective steam heater has less solvent hold-up and residence time, it will minimize thermal degradation. The cold and warm rich bypasses were optimized to obtain minimum total equivalent work at each lean loading. Higher rich solvent bypass is required at lower lean loading where the heat loss of stripping steam is significant.

4. Results and discussion

4.1 Minimum work and lost work

Figure 6 shows the minimum work and lost work of a simple stripper using 8 m PZ. The boundary conditions of the minimum work are defined in Table 3. The minimum work of separation purifies the inlet 12% CO_2 at 1 bar to pure CO_2 at stripper pressure, which depends on the operating lean loading. The minimum work of compression brings the pure CO_2 from stripper pressure to final pressure at 150 bar. Both these values vary with lean loading since the stripper pressure is not constant. The sum of separation and compression minimum work is 18.2 kJ/mol CO_2, which is independent of lean and rich loading.

The work lost during the process was analyzed. The lost work of regeneration was calculated first and the lost work of the absorber was determined by difference. Because the CO_2 partial pressure decreases with lean loading, a larger driving force of CO_2 partial pressure causes the lost work of the absorber to increase at a lower lean loading. This implies that the work lost from the absorber has to be compensated by the stripper with more work input. For the stripper, the minimum work of regeneration is defined as the minimum work of separation plus the lost work of the absorber (Equation 7), which corresponds to the boundary conditions with inlet rich solvent, outlet lean solvent, and outlet pure CO_2 at stripper pressure. The minimum work of regeneration more equitably represents the efficiency of the stripper configurations than the

minimum work of separation, which includes the lost work of the absorber. At higher lean loading, even though the minimum work of regeneration required is lower, the absorber may need more packing area due to insufficient mass transfer driving force.

$$W_{min,rgn} = W_{min,sep} + W_{lost,abs} \quad (7)$$

Figure 6 also shows the lost work that results from regeneration, compression, and unrecovered solvent pressure with varied lean loading. The lost work of regeneration includes the irreversibility of the cross exchanger, the condenser, the stripper, the trim cooler, and the rich solvent pump.

The lost work of compression is obtained from the difference between the actual work of compression and the isothermal minimum work of compression at 40 ºC shown in Figure 3. The lost work of compression comes from the inefficiency of the compressors and non-isothermal operation. The lost work of unrecovered solvent pressure shows the amount of work that the lean solvent at the stripper pressure can generate if it is brought to 1 bar. Practically, the unrecovered solvent pressure of the lean solvent will be used to overcome the pressure drop through the cross exchangers, the trim cooler, and the static head of the absorber.

The actual work required by the process is the sum of the minimum work values and all of the lost work. The lost work of regeneration accounts for 60–70% of total lost work. It is the major reason that makes the simple stripper inefficient and is possibly improved by alternative stripper configurations.

4.2 Simple stripper

The lost work of regeneration can be distributed into the unit operations. Figure 7 shows this distribution for a simple stripper using 8 m PZ with varied lean loading. For each lean loading, 5 m packing is used in the stripper and 5 K is specified for the cross exchanger LMTD.

The lost work of the reboiler reflects the heat duty requirement and the temperature approach between the solvent and the heating steam. The temperature of the heating steam is 155 ºC, 5 K higher than the reboiler temperature. The lost work of the trim cooler and the pump increases when the lean loading increases due to decreasing solvent capacity (increasing solvent rate) and increasing stripper pressure.

The cross exchanger and the overhead condenser account for over 70% of the lost work of regeneration. When the CO_2 is stripped out, a large amount of water vapor leaves the stripper and is removed in the overhead condenser. The lost work of the condenser is mainly caused by the loss of latent heat of the stripping steam. From the Gibbs-Helmholtz equation of CO_2 desorption reaction (Equation 8), either increasing the regeneration temperature or using solvents that have higher heat of absorption (ΔH_{des}) will increase the partial pressure of CO_2 (P_{CO_2}), providing better selectivity of CO_2 over the stripping steam. However, elevated regeneration temperature will cause more solvent degradation and a higher pressure heating steam requirement. Externally, the stripping steam generated can be recovered by the advanced flash stripper.

$$\frac{d\left(lnP_{CO_2}\right)}{dT} = \frac{\Delta H_{des}}{RT^2} \tag{8}$$

The heat transferred between the cold rich and the hot lean solvent in the cross exchanger is 2 to 5 times the reboiler duty input to the system. Therefore, even when a tight LMTD of 5 K is used, the lost work of the cross exchanger is still significant. It is sensitive to the lean loading mainly because of the change in solvent capacity. The circulating solvent flow rate at 0.34 lean loading is twice that at 0.28 lean loading, which almost doubles the lost work of the cross exchanger.

4.3 Lean vapor compression

There are two reasons that lean vapor compression works better than the simple stripper. First, additional stripping steam is produced in the flash tank by releasing the solvent pressure, providing the opportunity for the rich solvent to obtain that extra heat in the stripper. However, the stripping steam has to be pressurized before the heat is recovered, which requires additional compression work. Second, similar to multi-pressure and double matrix configurations,[27–29] the stripper is operated at higher pressure, which inherently reduces the stripping steam.

Figure 8 shows the lost work of regeneration with lean vapor compression. Even though the stripper is operated at higher pressure than the simple stripper at the same lean loading, the lost work of the condenser is only reduced by 1/3. Compared to the simple stripper, a portion of the lost work is shifted from the reboiler to the stripper since the rich solvent is also heated by the

superheated stripping steam coming into the bottom of the stripper. The lean vapor compressor and the flash tank also incur inefficiencies and lost work.

5.4 Advanced flash stripper

The advanced flash stripper reduces the stripping steam externally by using cold rich and warm bypasses. Figure 9 shows the lost work of the advanced flash stripper using 8 m PZ. For each lean loading, the cold and warm bypasses were optimized to minimize the total equivalent work.

The lost work of the condenser is almost eliminated. The water vapor content from the rich exchanger is only 5 mol %. Similar to lean vapor compression, the lost work of the stripper is more significant at lower lean loading because more warm rich solvent is bypassed and heated by the stripping steam in the stripper. Figure 10 compares the lost work of the condenser and stripper, which indicates how efficiently the stripping steam is recovered. The advanced flash stripper saves 3–5 kJ/mol CO_2 lost work of the condenser and stripper compared to the simple stripper.

Figure 11 compares the heat duty of the three stripper configurations with varied packing height from 2–10 m. The advanced flash stripper is most improved by adding packing. Compared to the simple stripper, lean vapor compression reduces the heat duty by 8.4% and the advanced flash stripper reduces it by 16.1% at optimum lean loading. Even though an additional heat source is provided in the lean vapor compression, the total stripping steam cannot be fully recovered.

Figure 12 compares the total equivalent work, which includes the compression work, pump work, heat duty work, and the lean vapor compression work. The advanced flash stripper reduces the total equivalent work by 11.2% at optimum lean loading while the lean vapor compression reduces it by only 3.4%. The additional compression work required to pressurize the stripping steam makes lean vapor compression less attractive.

4.5 Second law efficiency of regeneration

The second law efficiency can be used to quantify and differentiate between alternative process designs. The second law efficiency, η_{2nd}, is defined as the ratio of minimum work to actual work input. If the process is totally reversible, there will be no lost work, implying the second law

efficiency is 100%. Higher efficiency indicates less lost work so less actual work is required. The efficiency also quantifies the opportunity for improving the process.

As shown in Equation 9, the second law efficiency of regeneration, $\eta_{2nd,rgn}$, is defined as the ratio of the minimum work of regeneration to the actual work of regeneration. The efficiency of compression can be calculated in the same approach, which is around 73% throughout the operating range of lean loading.

$$\eta_{2nd,rgn} = \frac{W_{min,rgn}}{W_{act,rgn}} \tag{9}$$

Figure 13 shows the comparison of the second law efficiency of regeneration. The efficiency of the simple stripper is 50–60% and the advanced flash stripper is 50–75% in the range of operating lean loading.

For the simple stripper, the low efficiency at high lean loading is mainly due to the dominating lost work of the cross exchanger. At lower lean loading where the lost work of the condenser dominates, the efficiency is relatively flat because the minimum work also increases. The advanced flash stripper is nearly stripping steam free, so the efficiency is only driven by the lost work of the cross exchanger for the entire lean loading range. The advanced flash stripper improves the most at lower lean loading where the stripping steam is significant. The advanced flash stripper at 0.20 lean loading provides the highest efficiency, 74% in this operating lean loading range. The rest of the inefficiency comes from the lost work of the cross exchanger, the steam heater, and the rich exchanger.

4.6 Lost work of the cross exchanger

The cross exchanger is the major source of lost work left in the advanced flash stripper. The lost work of the cross exchanger decreases with increasing solvent capacity. The solvent capacity is dependent on solvent properties and can be increased by operating at lower lean loading. Another way to reduce the lost work of the cross exchanger is to use a small temperature approach. Figure 14 shows the sensitivity analysis of the LMTD of the cross exchanger. The total equivalent work increases 10–20% when the LMTD increases from 5 K to 10 K. This implies that the LMTD of the cross exchanger has a significant impact on the energy

performance. The capital cost of the cross exchanger is one of the cost centers of the process,[18] and is 20–30% of the total capital cost of the CO_2 capture process. Reducing the lost work of the cross exchanger by a tight temperature approach is not straightforward. The tradeoffs between energy consumption and capital cost must be considered.

5. Conclusions

The minimum work and lost work of the CO_2 capture process using 8 m PZ were quantified. The minimum work, including separation and compression from 12% CO_2 to pure CO_2 at 150 bar, is 18.2 kJ/mol. The total lost work of the simple stripper is 15–19 kJ/mol and the regeneration accounts for 60–70% of this. The two major sources of lost work are the cross exchanger and the stripper overhead condenser. The advanced flash stripper can effectively eliminate the lost work of the condenser by recovering the stripping steam heat using cold and warm rich bypasses. The advanced stripper reduces the total equivalent work by 11.2% while the lean vapor compression reduces it by 3.4% compared to the simple stripper.

The second law efficiency of regeneration can be used to differentiate the performance of stripper configurations and indicate how much room is left for energy reduction. At low lean loading, the advanced flash stripper has second law efficiency of regeneration above 70%. At higher lean loading, where the lost work of the cross exchanger is significant due to the reduced solvent capacity, the efficiency of regeneration is only around 50%. The advanced flash stripper provides the most improvement over the simple stripper at low lean loading where a large amount of stripping steam is produced. Since the capital cost of the cross exchanger is one of the cost centers, the capital-energy tradeoffs must be considered in any attempt to reduce the lost work of the cross exchanger.

6. Acknowledgements

The authors gratefully acknowledge financial support from the Texas Carbon Management Program in the preparation of this work.

One author of this publication consults for Southern Company and for Neumann Systems Group on the development of amine scrubbing technology. The terms of this arrangement have been reviewed and approved by the University of Texas at Austin in accordance with its policy on

objectivity in research. The authors have financial interests in intellectual property owned by the University of Texas that includes ideas reported in this paper.

References

(1) Rochelle, G. T. Amine Scrubbing for CO_2 Capture. *Science* **2009**, *325*, 1652–1654.

(2) IEA. *Technology Roadmap- Carbon Capture and Storage*; France, 2013.

(3) Romeo, L. M.; Espatolero, S.; Bolea, I. Designing a Supercritical Steam Cycle to Integrate the Energy Requirements of CO_2 Amine Scrubbing. *Int J Greenh Gas Cont* **2008**, *2*, 563–570.

(4) Aroonwilas, A.; Veawab, A. Integration of CO_2 Capture Unit Using Single- and Blended-Amines into Supercritical Coal-Fired Power Plants: Implications for Emission and Energy Management. *Int J Greenh Gas Cont* **2007**, *1*, 143–150.

(5) Sama, D. The Use of the Second Law of Thermodynamics in Process Design. *J Energy Resour Technol* **1995**, *117*, 179–185.

(6) Leites, I..; Sama, D.; Lior, N. The Theory and Practice of Energy Saving in the Chemical Industry: Some Methods for Reducing Thermodynamic Irreversibility in Chemical Technology Processes. *Energy* **2004**, *29*, 301–304.

(7) Amrollahi, Z.; Ertesvåg, I. S.; Bolland, O. Thermodynamic Analysis on Post-Combustion CO_2 Capture of Natural-Gas-Fired Power Plant. *Int J Greenh Gas Cont* **2011**, *5*, 422–426.

(8) McGlashan, N. R.; Marquis, A. J. Availability Analysis of Post-Combustion Carbon Capture Systems: Minimum Work Input. *Proc Inst Mech Eng Part C J Mech Eng Sci* **2007**, *221*, 1057–1065.

(9) Rochedo, P. R. R.; Szklo, A. Designing Learning Curves for Carbon Capture Based on Chemical Absorption according to the Minimum Work of Separation. *Appl Energy* **2013**, *108*, 383–391.

(10) Geuzebroek, F. H.; Schneiders, L. H. J. M.; Kraaijveld, G. J. C.; Feron, P. H. M. Exergy Analysis of Alkanolamine-Based CO_2 Removal Unit with AspenPlus. *Energy* **2004**, *29*, 1241–1248.

(11) Sanchez Fernandez, E.; Bergsma, E. J.; de Miguel Mercader, F.; Goetheer, E. L. V.; Vlugt, T. J. H. Optimisation of Lean Vapour Compression (LVC) as an Option for Post-Combustion CO_2 Capture: Net Present Value Maximisation. *Int J Greenh Gas Cont* **2012**, *11*, S114–S121.

(12) Benson, H.; Mccrea, D. Removal of Acid Gases from Hot Gas Mixtures. EP0004043 A1, 1979.

(13) Cousins, A.; Wardhaugh, L. T.; Feron, P. H. M. Preliminary Analysis of Process Flow Sheet Modifications for Energy Efficient CO_2 Capture from Flue Gases Using Chemical Absorption. *Chem Eng Res Des* **2011**, *89*, 1237–1251.

(14) Thimsen, D.; Maxson, A.; Smith, V.; Cents, T.; Falk-Pedersen, O.; Gorset, O.; Hamborg, E. Results from MEA Testing at the CO_2 Technology Centre Mongstad . Part I : Post-Combustion CO2 Capture Testing Methodology. Presented at *GHGT-12*. Austin, TX, USA, October 5–9, 2014.

(15) Singh, A.; Stéphenne, K. Shell Cansolv CO_2 Capture Technology : Achievement from First Commercial Plant. Presented at *GHGT-12*. Austin, TX, USA, October 5–9, 2014.

(16) Lin, Y.-J.; Madan, T.; Rochelle, G. T. Regeneration with Rich Bypass of Aqueous Piperazine and Monoethanolamine for CO_2 Capture. *Ind Eng Chem Res* **2014**, *53*, 4067-4074.

(17) Rochelle, G. T.; Chen, E.; Freeman, S. A.; Van Wagener, D. H.; Xu, Q.; Voice, A. K. Aqueous Piperazine as the New Standard for CO_2 Capture Technology. *Chem Eng J* **2011**, *171*, 725–733.

(18) Frailie, P. T. Modeling of Carbon Dioxide Absorption/Stripping by Aqueous Methyldiethanolamine/Piperazine. Ph.D. Dissertation, The University of Texas at Austin, 2014.

(19) Chen, C.-C.; Song, Y. Generalized Electrolyte-NRTL Model for Mixed-Solvent Electrolyte Systems. *AIChE J* **2004**, *50*, 1928–1941.

(20) Zhang, Y.; Chen, H.; Chen, C. Rate-Based Process Modeling Study of CO_2 Capture with Aqueous Monoethanolamine Solution. *Ind Eng Chem Res* **2009**, *48*, 9233–9246.

(21) Dugas, R. E. Carbon Dioxide Absorption, Desorption, and Diffusion in Aqueous Piperazine and Monoethanolamine. Ph.D. Dissertation, The University of Texas at Austin, 2009.

(22) Freeman, S. A. Thermal Degradation and Oxidation of Aqueous Piperazine for Carbon Dioxide Capture. Ph.D. Dissertation, The University of Texas at Austin, 2011.

(23) Plaza, J. M. Modeling of Carbon Dioxide Absorption Using Aqueous Monoethanolamine, Piperazine and Promoted Potassium Carbonate. Ph.D. Dissertation, The University of Texas at Austin, 2011.

(24) Bravo, J. L.; Rocha, J. A.; Fair, J. R. Mass Transfer in Gauze Packings. *Hydrocarb Process* **1985**, *64*, 91–95.

(25) Bergamini, L.; Vescovo, C.; Milone, F. Centrifugal Pumps for CO_2 Applications. In *Proceedings of the Twenty-Seventh International Pump User Symposium*; 2011; pp. 45–49.

(26) Moore, J.; Nored, M. Novel Concepts for the Compression of Large Volumes of Carbon Dioxide. In *Proceedings of ASME Turbo Expo: Power for Land, Sea and Air*; 2008.

(27) Oyenekan, B. A.; Rochelle, G. T. Alternative Stripper Configurations for CO_2 Capture by Aqueous Amines. *AIChE J* **2007**, *53*, 3144–3154.

(28) Jassim, M.; Rochelle, G. T. Innovative Absorber/stripper Configurations for CO_2 Capture by Aqueous Monoethanolamine. *Ind Eng Chem Res* **2006**, *45*, 2465–2472.

(29) Van Wagener, D. H.; Rochelle, G. T. Stripper Configurations for CO_2 Capture by Aqueous Monoethanolamine. *Chem Eng Res Des* **2011**, *89*, 1639–1646.

Tables/Figures

Table 1: Process simulation specifications.

Solvent	8 m PZ
Process modeling tool	Aspen Plus® v7.3
Thermodynamic model	Independence
Packing	Mellapak 250X
Reboiler T (ºC)	150
Steam T (ºC)	155
Rich loading (mol CO_2/mol alkalinity)	0.40
Rich solvent T (ºC)	46
Cross exchanger LMTD (K)	5
Rich exchanger LMTD (K)	20

Table 2. Multi-stage compressor specifications

Process modeling tool	Aspen Plus® v7.3
Thermodynamic model	BWRS
Maximum pressure ratio/stage	2
Compressor polytropic efficiency (%)	86
Intercooling temperature (ºC)	40
Aftercooling temperature (ºC)	30
Supercritical pump efficiency (%)	65
Multi-stage compressor outlet P (bar)	76
Final target P (bar)	150

Table 3. Specifications of minimum work calculations

Minimum work	Inlet	Outlet
Separation ($W_{min,sep}$)	12% CO_2 (40 ºC, 1 bar)	Pure CO_2 (40 ºC, stripper P)
Compression ($W_{min,comp}$)	Pure CO_2 (40 ºC, stripper P)	Pure CO_2 (40 ºC, 150 bar)
Regeneration ($W_{min,rgn}$)	Rich solvent (46 ºC, 1 bar, 0.40 Ldg)	Lean solvent (40 ºC, 1 bar, varied Ldg) Pure CO_2 (40 ºC, 150 bar)

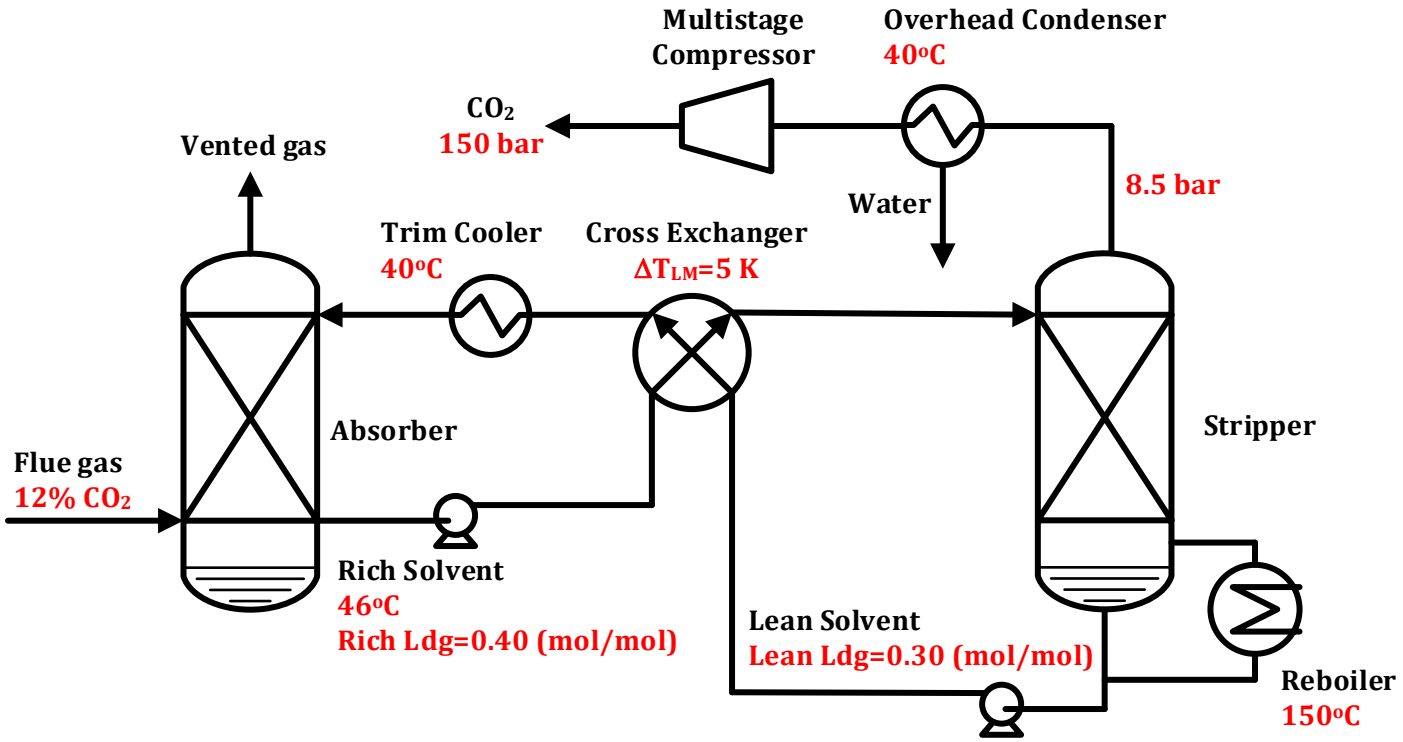

Figure 1: Amine scrubbing process with simple stripper

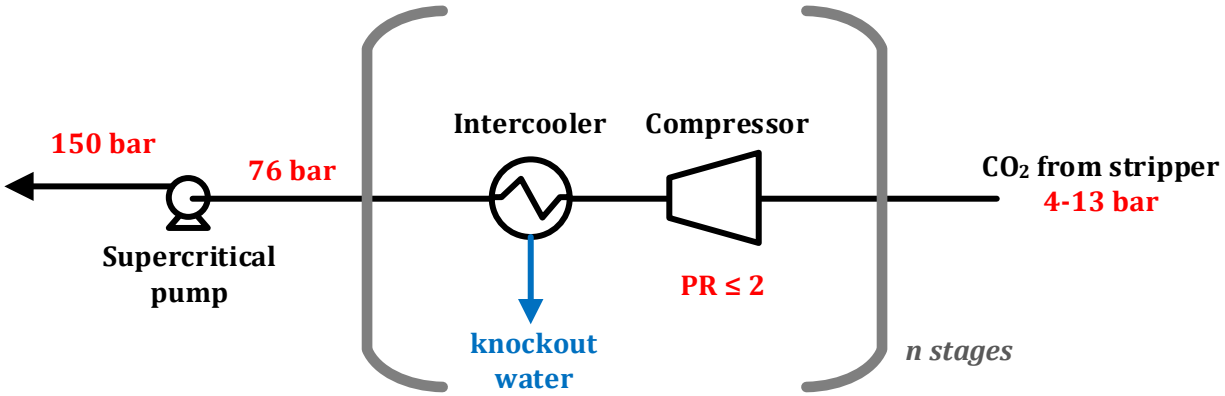

Figure 2: Multi-stage compressor

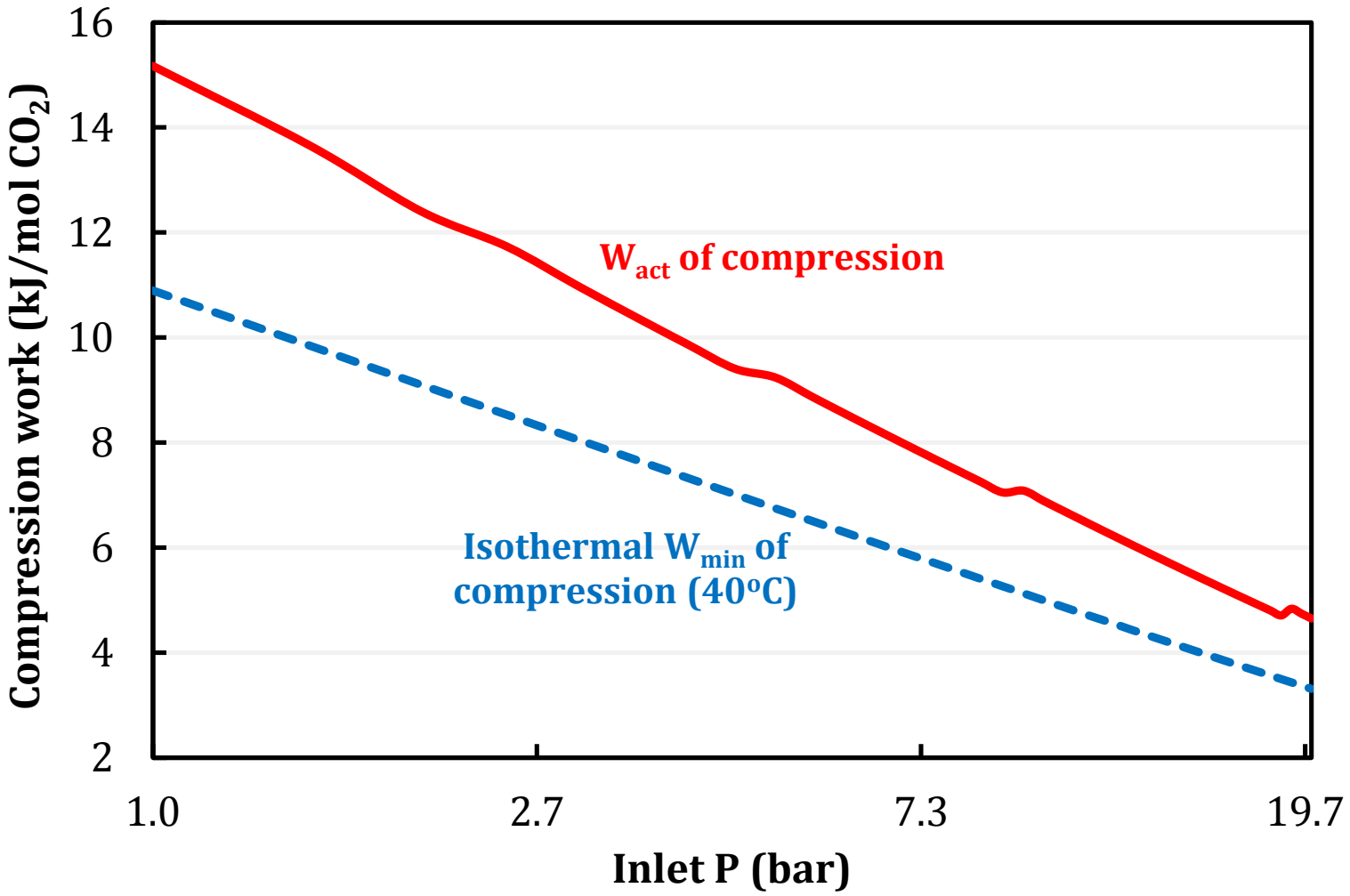

Figure 3: Actual and minimum work for pure CO_2 compression with varied inlet pressure: final pressure 150 bar.

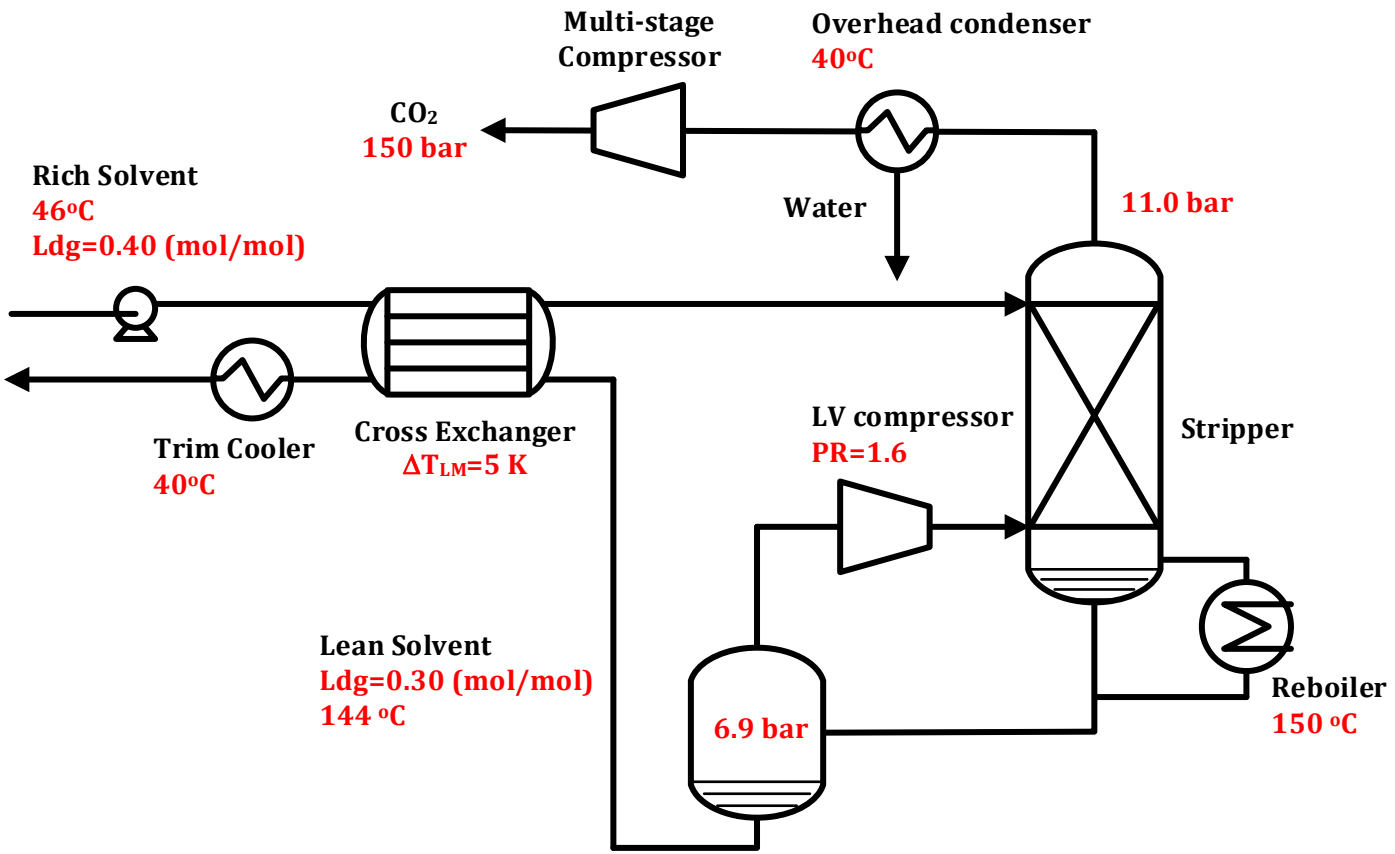

Figure 4: Lean vapor compression

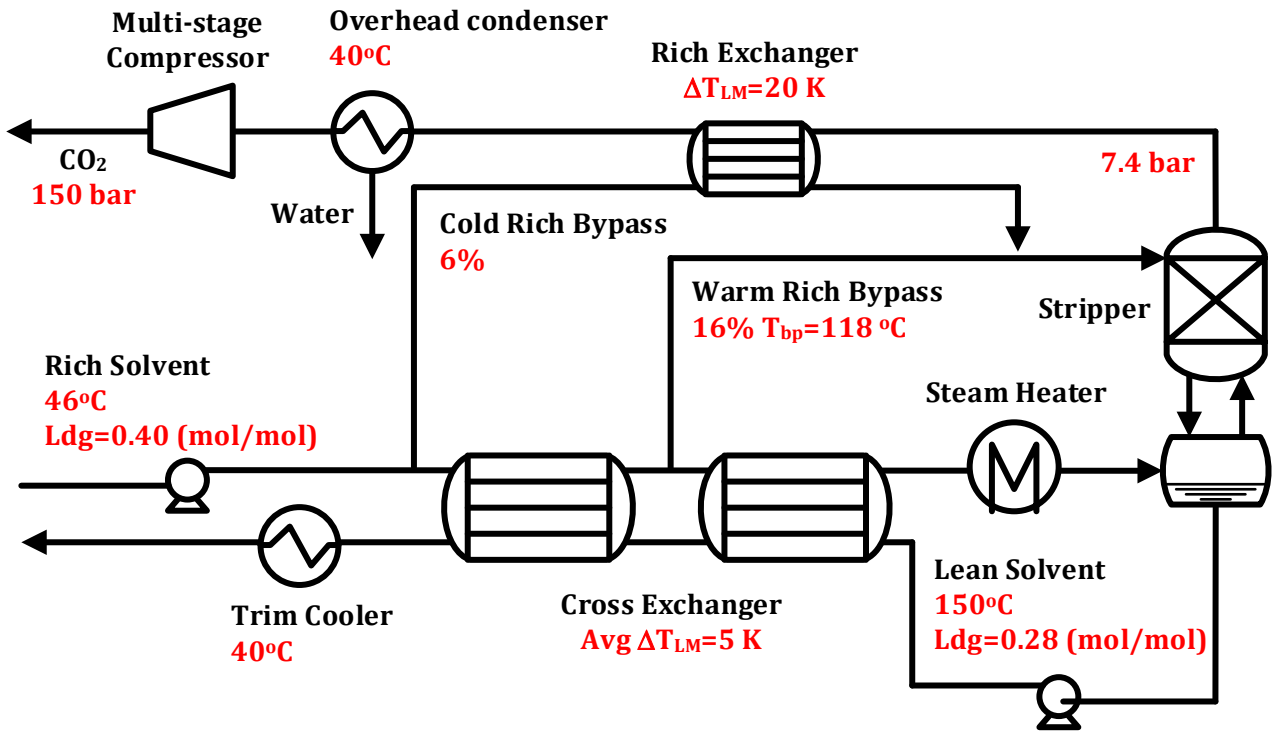

Figure 5: Advanced flash stripper

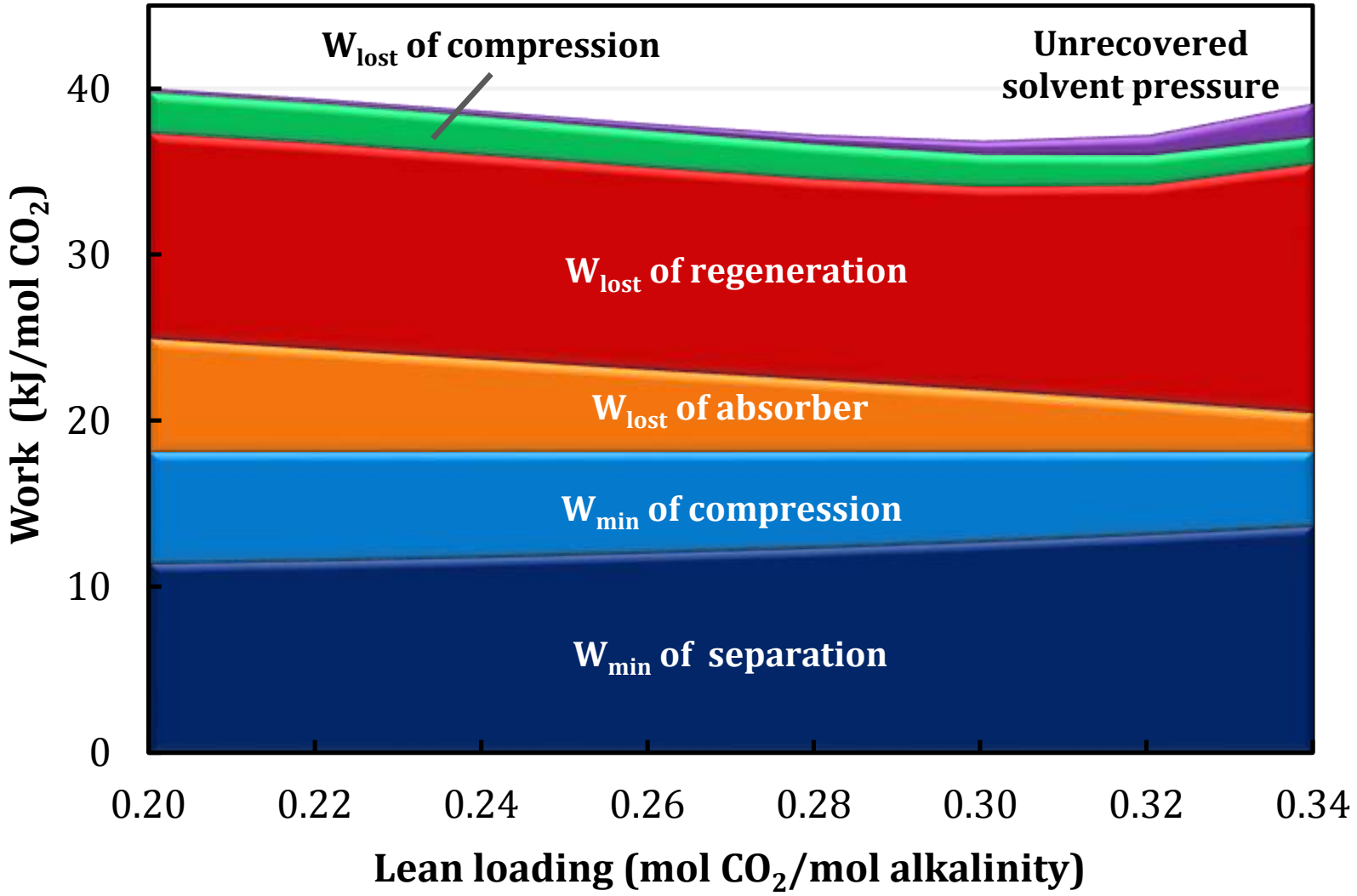

Figure 6: Minimum work and lost work of simple stripper using 8 m PZ; 5 m stripper packing; 5 K cross exchanger ΔT_{LM}; 150 °C reboiler T.

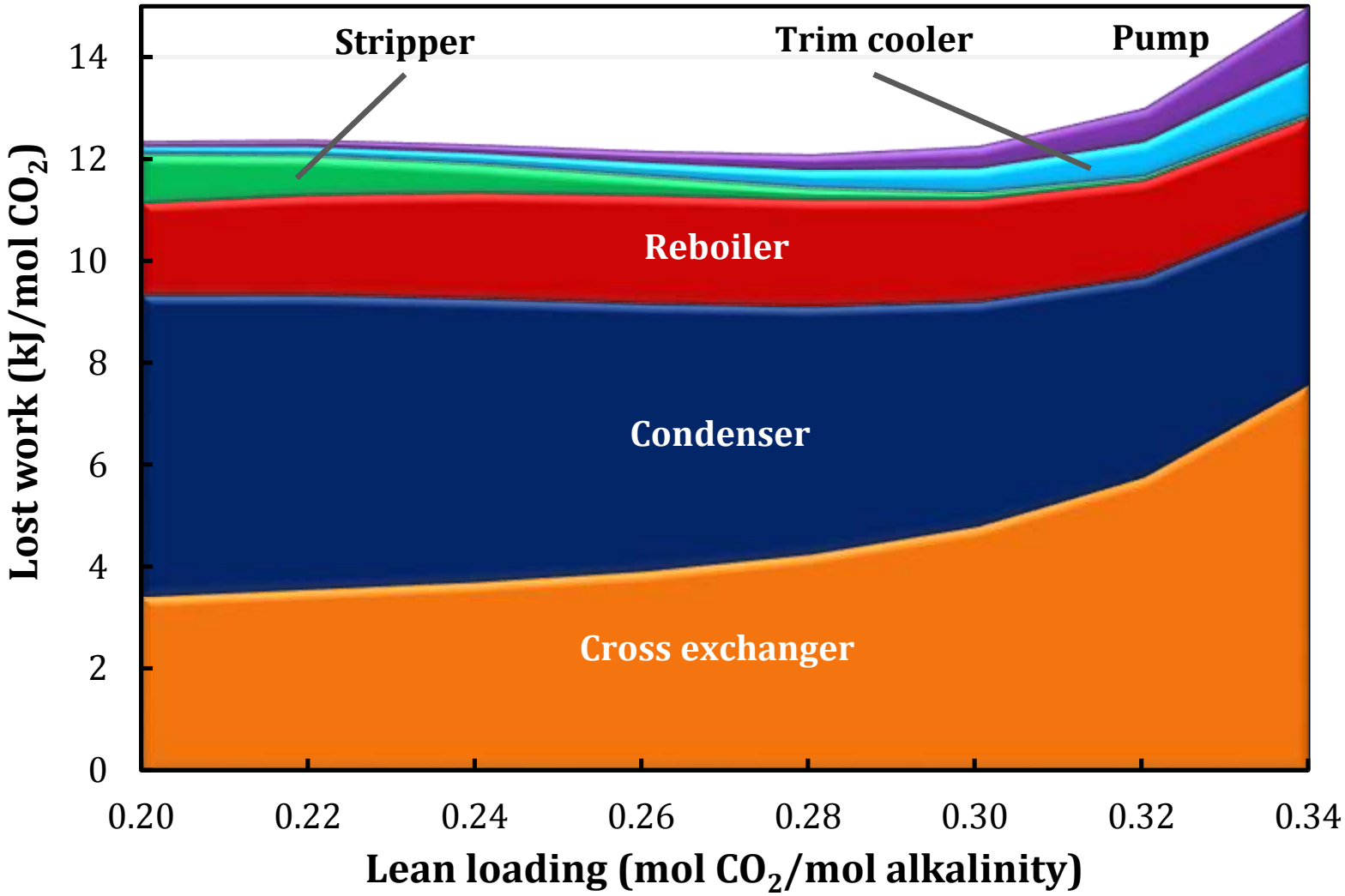

Figure 7: Lost work of regeneration of simple stripper using 8 m PZ; 5 m stripper packing; 5 K cross exchanger ΔT_{LM}; 150 °C reboiler T.

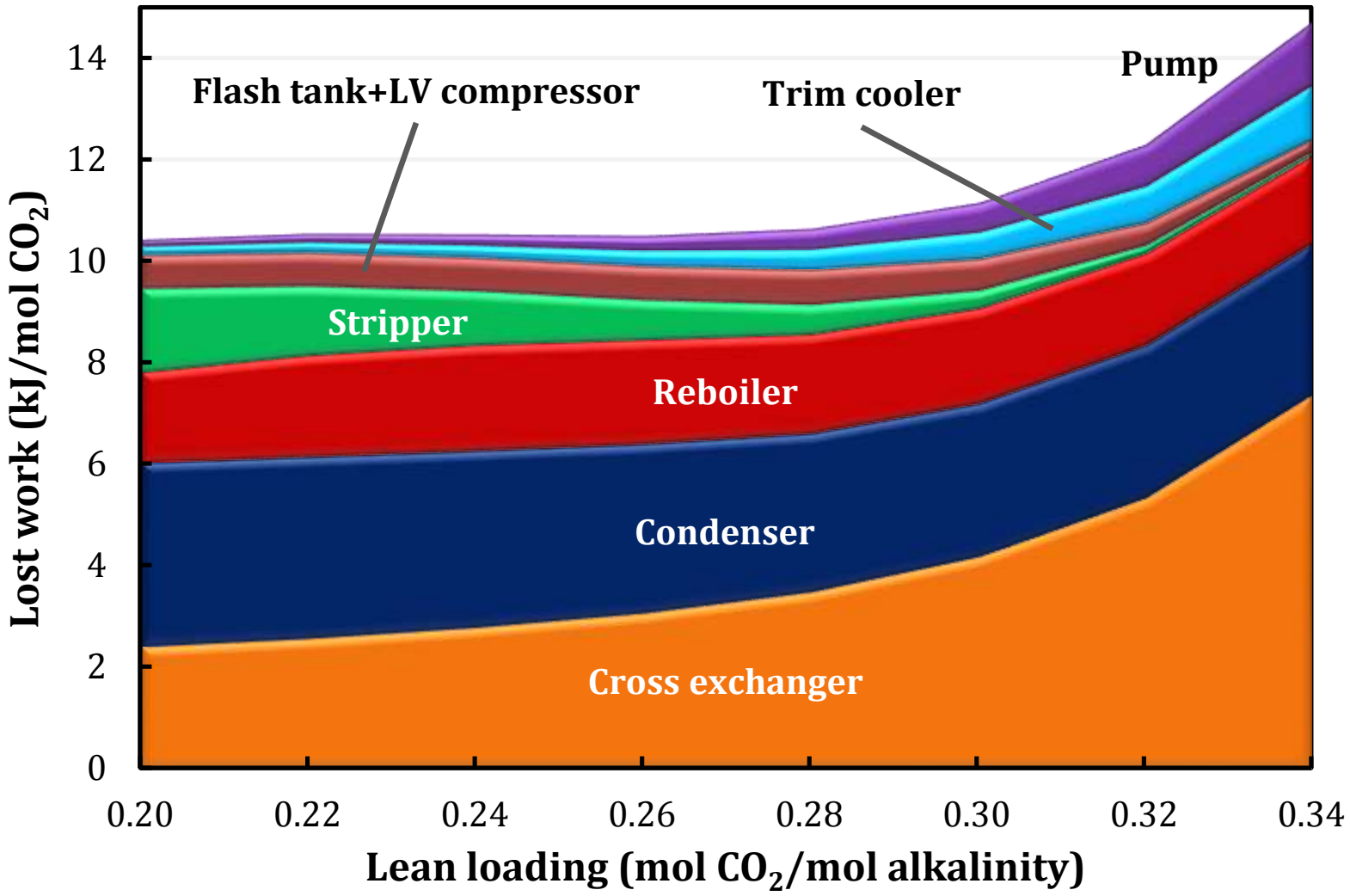

Figure 8: Lost work of regeneration of lean vapor compression using 8 m PZ; 5 m stripper packing; 5 K cross exchanger ΔT_{LM}; 150 °C reboiler T.

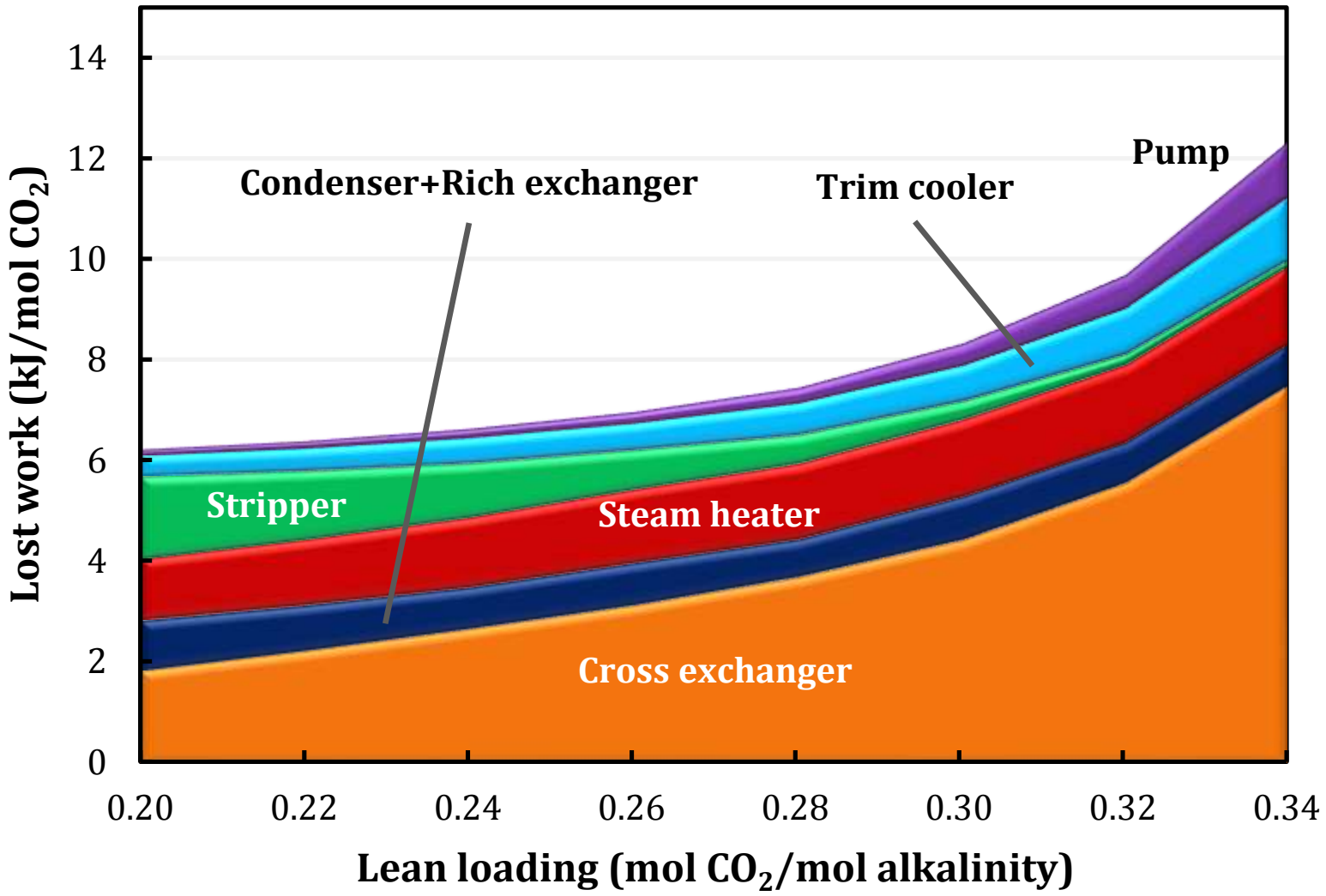

Figure 9: Lost work of regeneration of advanced flash stripper using 8 m PZ; 5 m stripper packing; 5 K cross exchanger ΔT_{LM}; 150 °C regeneration T.

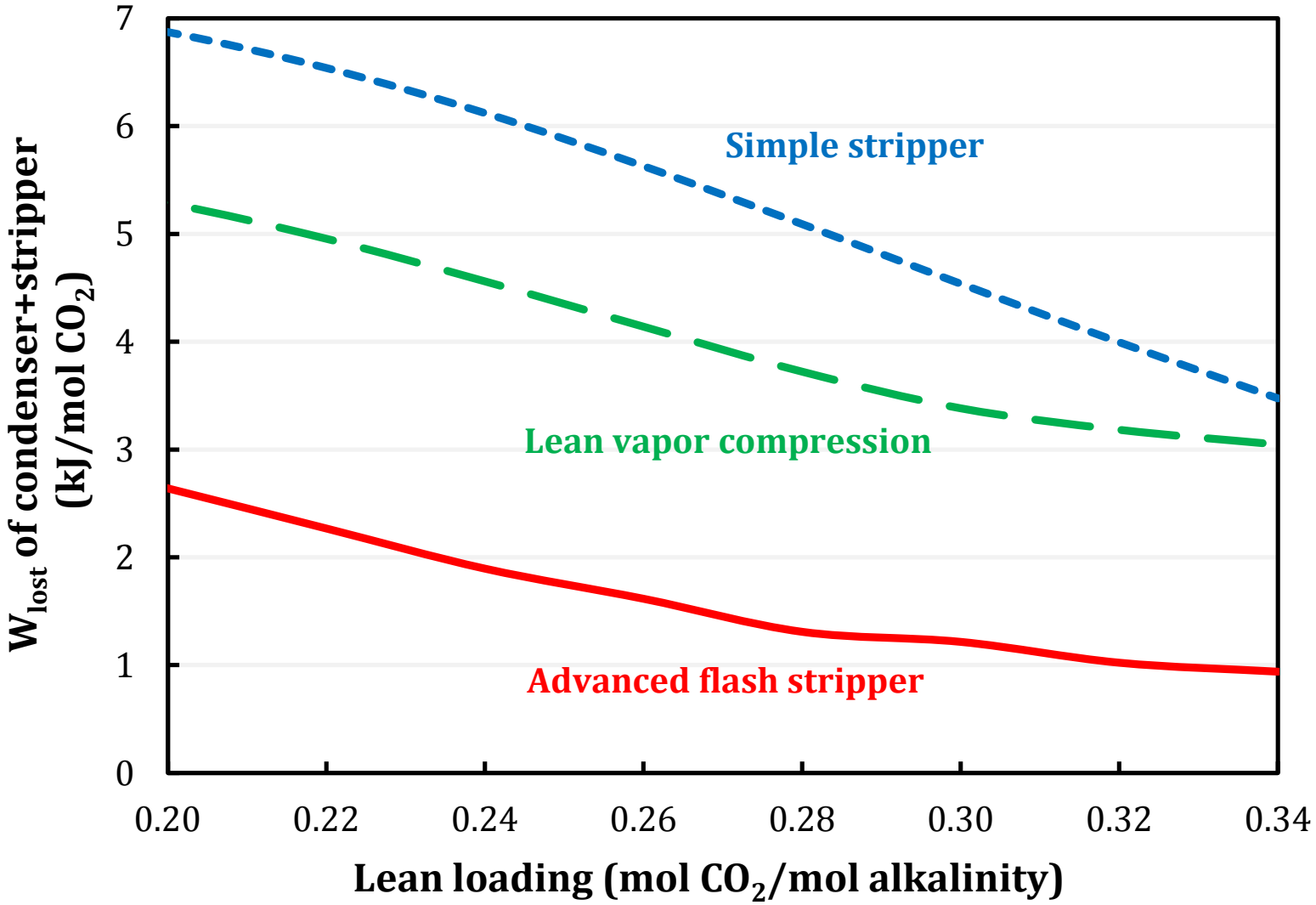

Figure 10: Comparison of lost work of condenser and stripper; 5 m stripper packing; 5 K cross exchanger ΔT_{LM}; 150 ºC regeneration T.

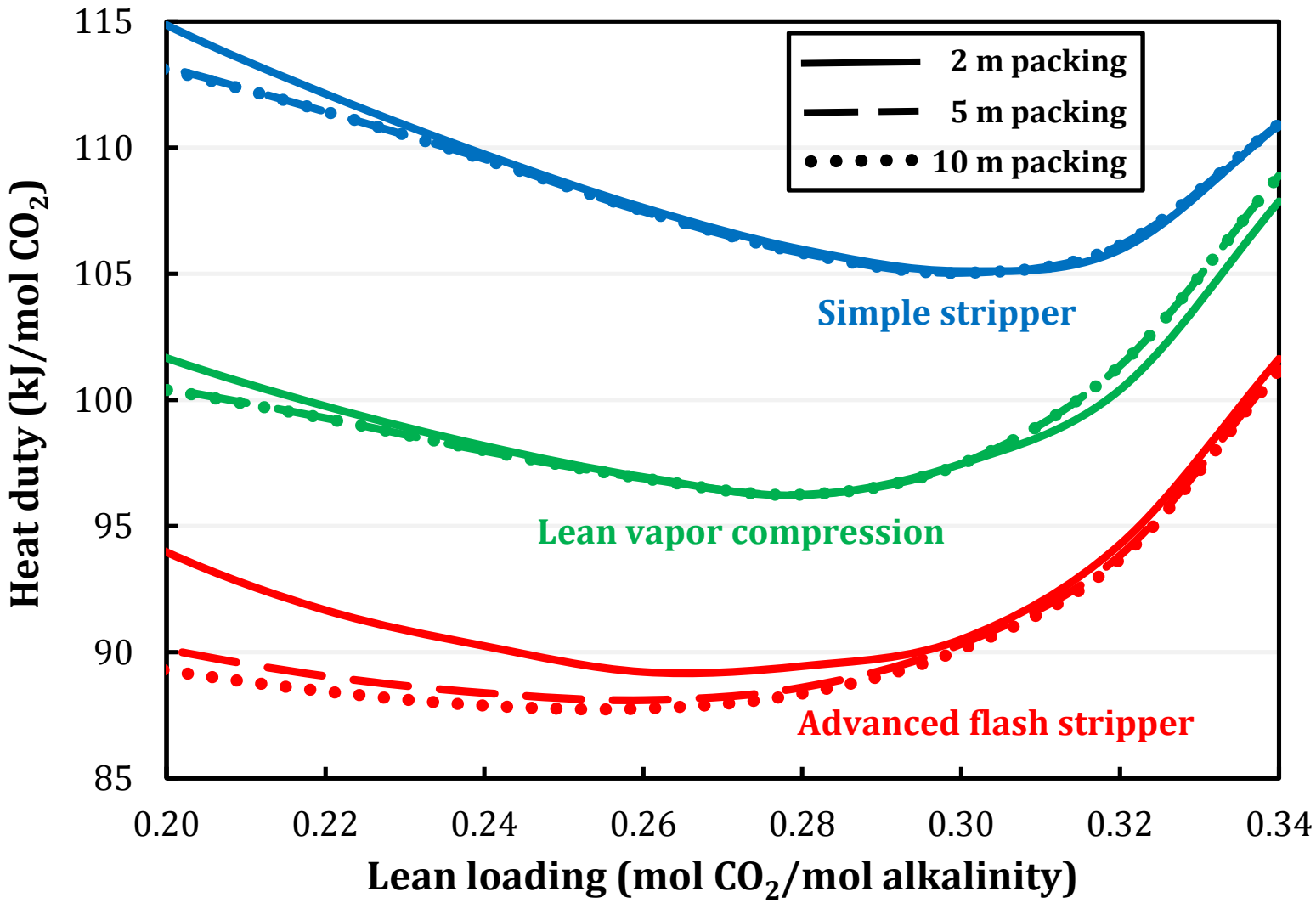

Figure 11: Comparison of heat duty of reboiler/steam heater with varied stripper packing height; 5 K cross exchanger ΔT_{LM}; 150 ºC regeneration T.

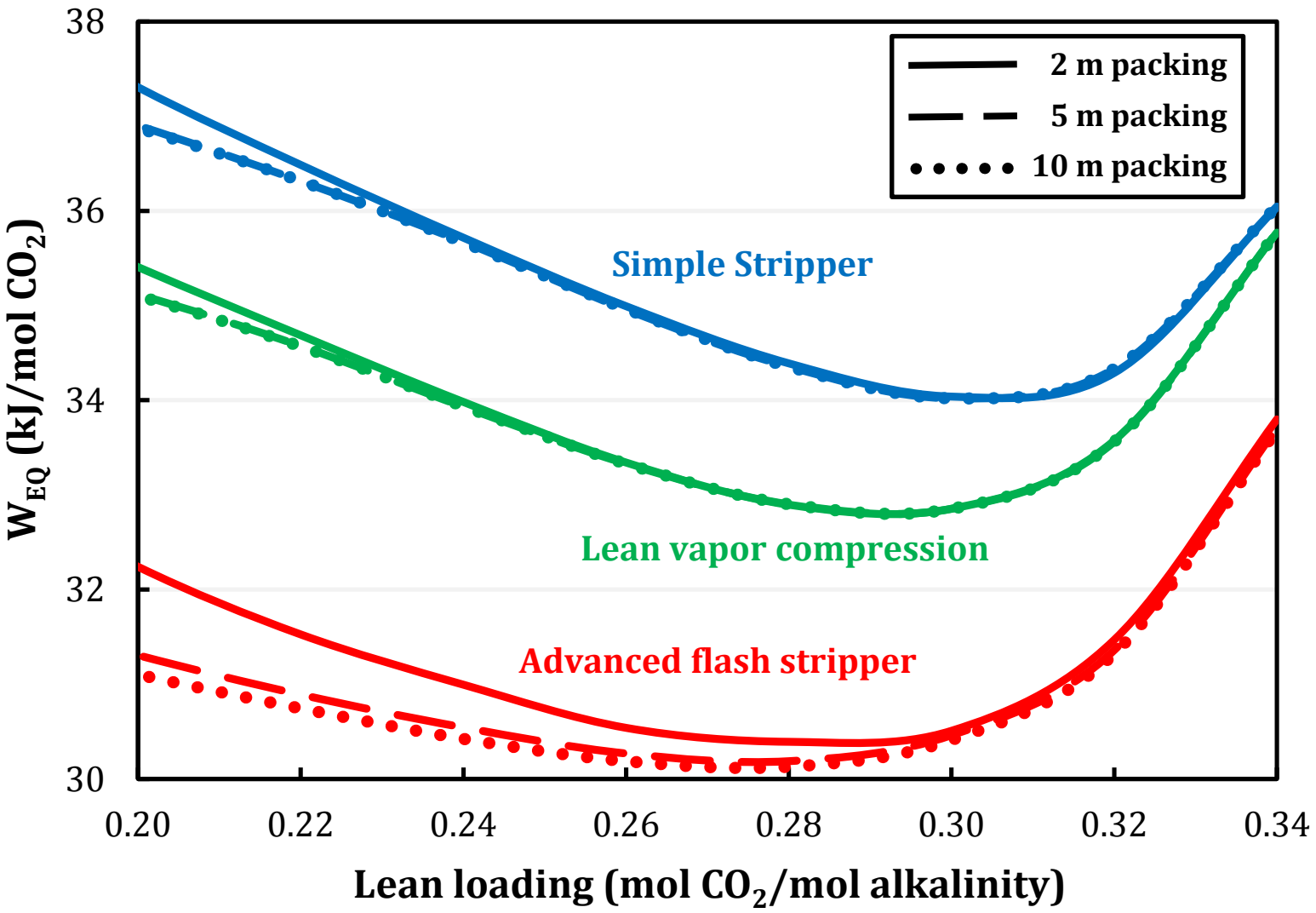

Figure 12: Comparison of total equivalent work with varied stripper packing height; 5 K cross exchanger ΔT_{LM}; 150 °C regeneration T.

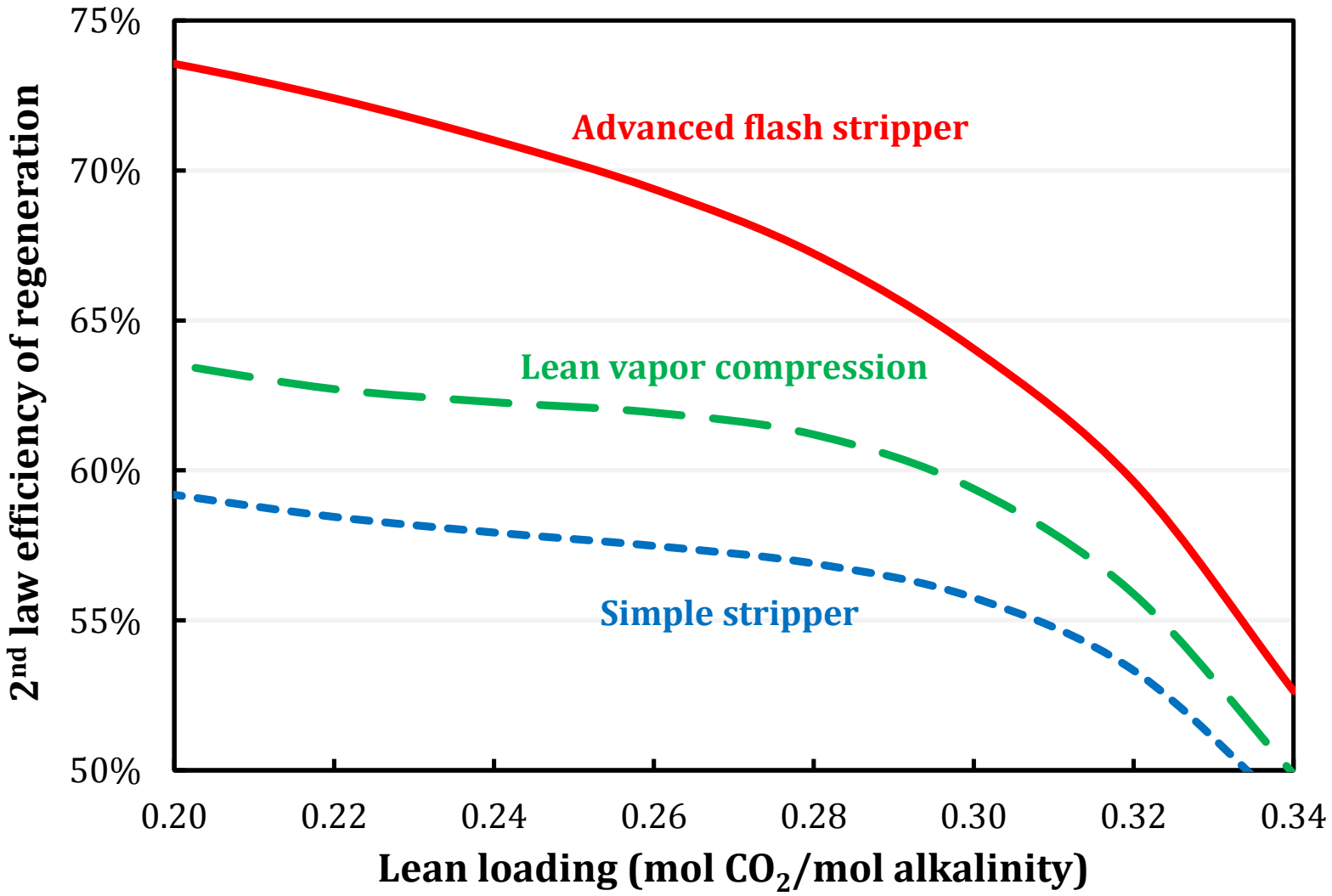

Figure 13: Comparison of second law efficiency of regeneration; 5 m stripper packing; 5 K cross exchanger ΔT_{LM}; 150 ºC regeneration T.

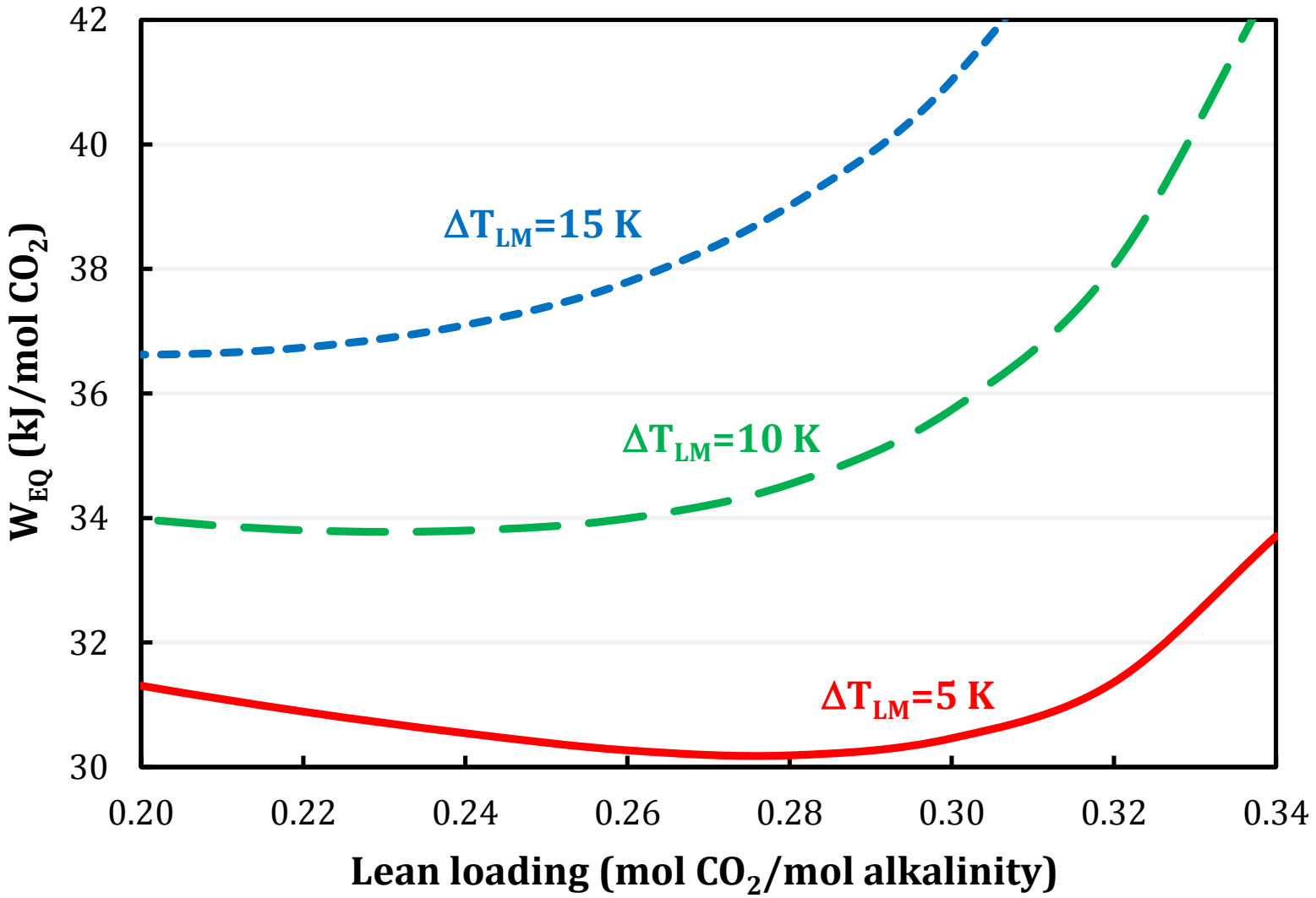

Figure 14: Total equivalent work of the advanced flash stripper with varied cross exchanger ΔT_{LM}; 5 m stripper packing; 150 ºC regeneration T.